

# Polymer Colloids

## Formation, Characterization and Applications

## Soft Matter Series

### *Series editors:*

Hans-Jürgen Butt, *Max Planck Institute for Polymer Research, Germany*

Ian W. Hamley, *University of Reading, UK*

Howard A. Stone, *Princeton University, USA*

Karen J. Edler, *University of Bath, UK*

Amy Shen, *Okinawa Institute of Science and Technology Graduate University, Japan*

### *Titles in this series:*

- 1: Functional Molecular Gels
- 2: Hydrogels in Cell-based Therapies
- 3: Particle-stabilized Emulsions and Colloids: Formation and Applications
- 4: Fluid–Structure Interactions in Low-Reynolds-Number Flows
- 5: Non-wettable Surfaces: Theory, Preparation and Applications
- 6: Wormlike Micelles: Advances in Systems, Characterisation and Applications
- 7: Electrospinning: From Basic Research to Commercialization
- 8: Polymer-modified Liquid Crystals
- 9: Polymer Colloids: Formation, Characterization and Applications

### *How to obtain future titles on publication:*

A standing order plan is available for this series. A standing order will bring delivery of each new volume immediately on publication.

### *For further information please contact:*

Book Sales Department, Royal Society of Chemistry, Thomas Graham House, Science Park, Milton Road, Cambridge, CB4 0WF, UK

Telephone: +44 (0)1223 420066, Fax: +44 (0)1223 420247

Email: [booksales@rsc.org](mailto:booksales@rsc.org)

Visit our website at [www.rsc.org/books](http://www.rsc.org/books)

# *Polymer Colloids*

## *Formation, Characterization and Applications*

Edited by

**Rodney D. Priestley**

*Princeton University, USA*

*Email: rpriestl@princeton.edu*

and

**Robert K. Prud'homme**

*Princeton University, USA*

*Email: prudhomm@princeton.edu*



## Soft Matter Series No. 9

Print ISBN: 978-1-78801-417-5  
PDF ISBN: 978-1-78801-647-6  
EPUB ISBN: 978-1-83916-121-6  
Print ISSN: 2048-7681  
Electronic ISSN: 2048-769X

A catalogue record for this book is available from the British Library

© The Royal Society of Chemistry 2020

*All rights reserved*

*Apart from fair dealing for the purposes of research for non-commercial purposes or for private study, criticism or review, as permitted under the Copyright, Designs and Patents Act 1988 and the Copyright and Related Rights Regulations 2003, this publication may not be reproduced, stored or transmitted, in any form or by any means, without the prior permission in writing of The Royal Society of Chemistry or the copyright owner, or in the case of reproduction in accordance with the terms of licences issued by the Copyright Licensing Agency in the UK, or in accordance with the terms of the licences issued by the appropriate Reproduction Rights Organization outside the UK. Enquiries concerning reproduction outside the terms stated here should be sent to The Royal Society of Chemistry at the address printed on this page.*

*Whilst this material has been produced with all due care, The Royal Society of Chemistry cannot be held responsible or liable for its accuracy and completeness, nor for any consequences arising from any errors or the use of the information contained in this publication. The publication of advertisements does not constitute any endorsement by The Royal Society of Chemistry or Authors of any products advertised. The views and opinions advanced by contributors do not necessarily reflect those of The Royal Society of Chemistry which shall not be liable for any resulting loss or damage arising as a result of reliance upon this material.*

The Royal Society of Chemistry is a charity, registered in England and Wales, Number 207890, and a company incorporated in England by Royal Charter (Registered No. RC000524), registered office: Burlington House, Piccadilly, London W1J 0BA, UK, Telephone: +44 (0) 20 7437 8656.

For further information see our web site at [www.rsc.org](http://www.rsc.org)

Printed in the United Kingdom by CPI Group (UK) Ltd, Croydon, CR0 4YY, UK

# Preface

The formation, characterization, and application of polymer colloids, a subject that has been extensively investigated, remains a topic of great scientific and technological importance, rich in unexplored and far from understood phenomena and observations. Polymer colloids represent a class of soft matter that has enabled mature technologies including latexes for paints and coatings, personal and home care formulations, cosmetics, food additives, and reinforcing additives in composite materials. While these fields continue to advance, emerging technologies such as targeted-controlled drug delivery, medical imaging, enhanced oil recovery, and photonics are rapidly developing. Continued advancement of the field of polymer colloids will require: (i) new synthetic and physical-based approaches to generating colloids with internal and external structure, encapsulation of hydrophobic and hydrophilic cargo, hybrid and multi-functional properties, and autonomous and triggered activity, (ii) the development of tools for physical and chemical characterization, and (iii) theory and simulations to enable detailed molecular-scale understanding that will provide new insights and accelerate the finding of new structures *via* machine-learning. Indeed, the field remains filled with the potential for new advances in the formation, characterization and application of polymer colloids.

This book was, in part, motivated by a short course organized by the editors at the 2017 American Physical Society Annual Meeting as part of the Division of Polymer Physics programming, aimed at providing an overview of recent advances in the formation, characterization and application of polymer colloids. The book is meant to both provide an update on mature topics and introduce new ones for the seasoned soft matter scientist. Part I of the book focuses on recent advances in polymer colloid formation including Dow Chemical's Bluewave Technology and Flash NanoPrecipitation.

Part II highlights recent advances in colloid characterization including simulations, microscopy, and physical property measurements. Finally, Part III addresses recent advances in the application of polymer colloids, including Pickering emulsions, medical applications, and personal care. It is our desire that this book, as part of the Soft Matter Series, will serve as a reference to both the novice and expert in polymer colloid science, and help inspire new fundamental insights and disruptive technologies.

Finally, we'd like to offer our sincere gratitude to our colleagues who have contributed their expertise to this book, and for their commitment to the creation and dissemination of new knowledge in the field of polymer colloid science. We'd also like to acknowledge the staff of the Royal Society of Chemistry for their support of the book. RDP gratefully acknowledges the support of a Leverhulme Trust Visiting Professor Fellowship that allowed him to visit Imperial College, London and co-develop this book.

Rodney D. Priestley  
Robert K. Prud'homme

To Nathaniel and Nolan

In memory of Mr Kofi Aidoo

# Contents

## Section I: Emerging Methods in Polymer Colloid Formation

<b>Chapter 1 Development, Characterization, and Application of Novel High Temperature Thermoplastic and Thermosetting Dispersions</b>	<b>3</b>
<i>D. L. Malotky, D. L. Dermody, D. Schmidt, T. J. Young and M. Kalinowski</i>	
1.1 Introduction	3
1.2 Droplet Breakup Theory	6
1.2.1 Classical Droplet Breakup Theory	6
1.2.2 Concentrated Emulsion Systems	7
1.2.3 Beyond Steady State – Transient Breakup	8
1.2.4 Surfactant Effects on Rheology and Droplet Breakup	9
1.2.5 Confined Boundaries and Wall Effects	10
1.2.6 Surfactant Optimization	10
1.2.7 Surfactant Selection for Emulsification in Water at Elevated Temperature	11
1.2.8 Conclusions	13
1.3 Applications	13
1.3.1 Considerations for Design of Aqueous Polyolefin Dispersions and their Applications	15
1.3.2 Hybrid Particles for Optical Hiding	18
1.3.3 Polyolefin Dispersions as Adhesion Promoters for Plastic Substrates	20

1.3.4 Dispersion Enabled Heat Activated Pressure Sensitive Adhesive	23
1.4 Conclusions	25
Acknowledgements	25
References	25
<b>Chapter 2 Synthesis of Core–Shell Polymer-based Colloids</b>	<b>30</b>
<i>Mengchen Wu and Rui Liu</i>	
2.1 Introduction	30
2.2 Grafting Approach	32
2.2.1 “Grafting To”	32
2.2.2 “Grafting From”	34
2.3 Polymer Deposition	41
2.3.1 Resin or Polydopamine Coating	41
2.3.2 Biopolymer Coating	43
2.3.3 Layer-by-layer Deposition	45
2.4 Self-assembly	47
2.4.1 Co-precipitation	47
2.4.2 Flash NanoPrecipitation (FNP)	50
2.4.3 Microfluidics	51
2.5 Electro-spraying/Jetting	53
2.5.1 Electro-spraying	53
2.5.2 Electro-jetting	53
2.6 Conclusion	54
Acknowledgements	55
References	55
<b>Chapter 3 Flash Nano-precipitation and -complexation to Produce Polymer Colloids</b>	<b>61</b>
<i>Victoria E. Lee, Douglas M. Scott, Robert K. Prud'homme and Rodney D. Priestley</i>	
3.1 Introduction	61
3.2 The Flash NanoPrecipitation Process	62
3.2.1 Polymer Collapse, Nucleation, and Aggregation	62
3.2.2 Solvent and Polymer Choice	66
3.2.3 Mechanism of Stabilization	67
3.2.4 Equipment	69
3.3 Homopolymer Colloids	70
3.3.1 Concentration Effects	70
3.3.2 Mixing Time Effects	71

*Contents*

xi

3.4	Colloids from Homopolymer Blends	72
3.4.1	Janus Particles	75
3.4.2	Patchy Particles	75
3.4.3	Core–Shell Particles	78
3.5	Hybrid Polymer–Inorganic Colloids	79
3.6	Block Copolymer Microphase Separation in Colloids	81
3.6.1	Molecular Weight Effect	81
3.6.2	Blends of Block Copolymers and Homopolymers	82
3.7	Polyelectrolyte Complexation	85
3.7.1	Mechanism of Polyelectrolyte Complexation	85
3.7.2	Effect of Mixing Timescales on PEC Formation	86
3.7.3	Flash NanoComplexation (FNC)	88
3.7.4	Encapsulation <i>via</i> FNC	89
3.8	Summary	91
	References	91

**Chapter 4 Design and Fabrication of Polymer Microparticles and Capsules Using Microfluidics**

100

*William N. Sharratt and João T. Cabral*

4.1	Introduction	100
4.2	Single- and Multi-phase Microfluidics and Devices	102
4.3	Chemical Approaches to Particle Solidification	104
4.3.1	Polymerisation of Monomer-containing Droplets	104
4.3.2	Flow Lithography in Single- (and Multi-)phase Flows	109
4.3.3	Covalent Crosslinking of Polymer-containing Droplets	114
4.3.4	Ionic Crosslinking of (Bio)polymer-containing Droplets	117
4.3.5	Interfacial Complexation for Capsule Formation	119
4.4	Physical Approaches to Particle Solidification	122
4.4.1	Particle Assembly at Interfaces	122
4.4.2	Block Co-polymer Self-assembly in Double Emulsions	128
4.4.3	Solvent Extraction of Polymer-containing Droplets	131
4.5	Summary and Outlook	138
4.5.1	Particle Formation Strategies	139

4.5.2 Scalability	139
4.5.3 Full Process Integration, Feedback and Learning	140
References	140
<b>Chapter 5 Recent Advances in Colloidal Polyelectrolyte Brushes</b>	<b>148</b>
<i>Qingsong Yang, Xiaofeng Niu, Zhinan Fu, Li Li and Xuhong Guo</i>	
5.1 Introduction	148
5.2 Generation of Metallic Nanoparticles in SPBs	151
5.2.1 Synthesis of Monometallic Nanoparticles	153
5.2.2 Synthesis of Bimetallic Nanoparticles	154
5.2.3 Catalytic Performance	155
5.2.4 Preparation of Metallic Compound Nanoparticles	156
5.3 Preparation of Organic-Inorganic Hybrid Nanoparticles Tempered by SPBs	161
5.4 Controlled Protein Immobilization in SPBs	164
5.4.1 Interactions Between Protein and SPB	164
5.4.2 Characterization Methods for Protein Immobilization on SPBs	168
5.4.3 Effect of SPB Structure on Protein Immobilization in SPBs	173
5.4.4 Effect of pH and Ionic Strength on Protein Immobilization in SPBs	175
5.5 Conclusion and Perspective	179
References	183

## Section II: Recent Advances in Colloid Characterization

<b>Chapter 6 The Advanced Microscopy of Colloids</b>	<b>193</b>
<i>Daniel G. Gregory and Nan Yao</i>	
6.1 Introduction	193
6.2 A Brief History of Microscopy	194
6.3 Narrowing our Focus – The Specimen: Colloids	196
6.4 Polymer Colloids	197
6.5 Natural Opals and Colloidal Silica	198
6.5.1 Colloidal Crystals	199
6.5.2 Characterization of Colloids	200
6.6 Basics of Microscopy	202
6.6.1 Microscope Probes	202

*Contents*

xiii

6.6.2	The Wave-like Nature of Light, Electrons, and Electromagnetic Radiation	203
6.6.3	Lens Basics	205
6.6.4	Aberrations	206
6.6.5	Apertures	208
6.6.6	Magnification	209
6.6.7	Resolution	209
6.6.8	Diffraction Limit of Resolution	210
6.6.9	Resolution Criteria	211
6.6.10	Inspiration for the Electron, Ion, and X-ray Microscope	212
6.7	The “Spectrum” of Microscopes	213
6.8	Optical Microscopes	213
6.8.1	The Visible Light Microscope	213
6.8.2	The Fluorescence Microscope	215
6.8.3	The Confocal Microscope	216
6.9	The X-ray and Atomic Force Microscopes	217
6.9.1	The X-ray Microscope	217
6.9.2	The Atomic Force Microscope (AFM)	218
6.10	Electron Microscopes	220
6.10.1	Electron Microscopy Background	220
6.10.2	The Scanning Electron Microscope (SEM)	223
6.10.3	The Transmission Electron Microscope (TEM)	224
6.10.4	Scanning Transmission Electron Microscopy (STEM)	226
6.10.5	The Ion Microscope	226
6.10.6	The Focused Ion Beam System	227
6.10.7	The Helium Ion Microscope	229
6.11	Instrument Selection for Colloid Analysis	230
6.12	The Microscopy of Colloids – A Summary	232
	References	233
<b>Chapter 7</b>	<b>Simulations in Polymer Colloid Formation</b>	<b>240</b>
	<i>Arash Nikoubashman</i>	
7.1	Introduction	240
7.2	Particle-based Modeling	241
7.2.1	General Considerations	241
7.2.2	Model Details	246
7.3	Kinetic Monte Carlo Simulations	252
	Acknowledgements	259
	References	259

<b>Chapter 8 Glass Transition and Crystallization in Colloidal Polymer Nanoparticles</b>	<b>263</b>
<i>Daniele Cangialosi and Aurora Nogales</i>	
8.1 Introduction	263
8.2 Glassy Dynamics in Colloidal Polymer Nanoparticles	264
8.2.1 The Glass Transition	265
8.2.2 Glass Transition in Geometrical Confinement	267
8.2.3 Specific Features of the Glass Transition in Colloidal Polymer Nanoparticles	268
8.2.4 Specific Features of Physical Aging in Colloidal Polymer Nanoparticles	271
8.2.5 Connection with Molecular Mobility	272
8.3 Semicrystalline Colloidal Particles	274
8.3.1 Methods for Generation of Nanoparticles from Preformed Semicrystalline Polymers	276
8.3.2 Chain Conformation by Confinement of Polymers in Nanoparticles	278
8.3.3 Modification of Crystallization in Polymer Nanoparticles	279
8.3.4 Polymer Nanocrystals from Crystallizable Nanoparticles	281
8.4 Conclusions	281
Acknowledgements	282
References	283
<b>Chapter 9 Transport of Polymer Colloids in Porous Media</b>	<b>289</b>
<i>Navid Bizmark, Joanna Schneider, Emily de Jong and Sujit S. Datta</i>	
9.1 Introduction	289
9.2 Mathematical Modeling	291
9.2.1 Macro-scale Modelling: 1D Continuum Advection-dispersion Equation (ADE)	291
9.2.2 Pore-scale Events: Filtration Theory	292
9.2.3 The Lattice-Boltzmann Method (LBM) and Pore Network Modeling (PNM)	295
9.3 Experiments on Colloidal Particle Transport in Porous Media	296
9.3.1 Macro-scale Studies	296
9.3.2 Indirect Pore-scale Assessments	299

*Contents*

xv

9.3.3 Direct Pore-scale Assessments	303
9.4 Conclusions and Outlook	310
References	312
<b>Section III: Advanced Applications of Polymer Colloids</b>	
<b>Chapter 10 Pickering Emulsions Stabilized by Polymer Colloids</b>	<b>325</b>
<i>Yang Lan, Yankai Jia and Daeyeon Lee</i>	
10.1 Introduction	325
10.1.1 Emulsions	325
10.1.2 Pickering Emulsions	326
10.2 Pickering Emulsions Stabilized by Anisotropic Homogeneous Particles	328
10.3 Janus-particle Stabilized Pickering Emulsions	331
10.3.1 Janus Particles at Liquid–Liquid Interfaces	332
10.3.2 Thermodynamically Stable Pickering Emulsions Stabilized by Janus Particles	334
10.3.3 Janus Balance	335
10.3.4 Stimuli-responsive Pickering Emulsion Stabilized by Janus Particles	335
10.4 Microgel-stabilized Pickering Emulsions	335
10.4.1 Microgels	335
10.4.2 Stimuli-responsive Pickering Emulsions Stabilized by Microgels	337
10.4.3 Microgels at Liquid–Liquid Interfaces	338
10.4.4 High Internal Phase Emulsions Stabilized by Microgels	339
10.5 Pickering Emulsions Stabilized by Polymer-grafted Particles	340
10.6 Biopolymer Colloid-stabilized Pickering Emulsions	342
10.6.1 Cellulose Nanocrystal-stabilized Pickering Emulsions	342
10.6.2 Protein-stabilized Pickering Emulsions	343
10.6.3 Fat Crystal-stabilized Pickering Emulsions	343
10.7 Conclusions and Outlook	344
References	345
<b>Chapter 11 Latexes for Advanced Coatings</b>	<b>349</b>
<i>J. Klier, S. Trevenen and P. J. Beltramo</i>	
11.1 Evolution of Latexes for Advanced Coatings	349
11.1.1 Background	349

11.1.2	Architectural Coatings	350
11.1.3	Industrial Coatings	351
11.1.4	New Technological Applications of Anisotropic Latexes	352
11.2	Experimental	353
11.2.1	Film Formation	353
11.2.2	Sample Preparation	353
11.3	Results and Discussion	354
11.4	Conclusion	355
	References	357
<b>Chapter 12</b>	<b>Polymer Colloids Enable Medical Applications</b>	<b>358</b>
	<i>Christina Tang, Shani Levit, Michael Zeevi, Chris Vasey and Catherine Fromen</i>	
12.1	Introduction	358
12.2	Material Selection	360
12.2.1	Natural Polymers	361
12.2.2	Synthetic Polymers	362
12.3	Responsive Nanoparticle Platforms	365
12.3.1	pH Responsive	365
12.3.2	Temperature Responsive	366
12.3.3	Chemoresponsive Polymer Systems	367
12.4	Processing Methods	367
12.4.1	Bottom-up Methods	367
12.4.2	Top-down Methods	371
12.5	Effect of Physiochemical Properties	375
12.5.1	Size	375
12.5.2	Shape	376
12.5.3	Mechanical Properties	377
12.5.4	Surface Chemistry	377
12.6	Emerging Applications	381
12.6.1	Multifunctional Particles	381
12.6.2	Encapsulation of Biologics	381
12.6.3	Alternative Routes of Administration	382
12.6.4	Immune Engineering	383
12.7	Clinical Translation	385
12.8	Outlook	386
	Acknowledgements	386
	References	387

<i>Contents</i>	xvii
<b>Chapter 13 Polymer Colloids for Cosmetics and Personal Care</b>	<b>399</b>
<i>Liangchen Xu, Yao Zhou and Samiul Amin</i>	
13.1 Introduction	399
13.2 Key Polymer Colloid Properties	400
13.2.1 Particle Size, Particle Size Distribution	400
13.2.2 Film Formation	401
13.2.3 Adhesion	402
13.2.4 Waterproofing	402
13.2.5 Chemistry Modification	402
13.2.6 Lubrication and Tribology	403
13.3 Applications of Polymer Colloids	404
13.3.1 Facial Makeup	404
13.3.2 Sunscreen	405
13.3.3 Mascara	405
13.3.4 Nail Polish	406
13.3.5 Lipstick, Liquid Lipstick	407
13.3.6 Shampoo and Conditioner	407
13.4 Novel Polymer Particles	408
13.4.1 Janus Particle	408
13.4.2 Amphiphilic Particles	409
13.4.3 Sustainable Particles	409
13.4.4 Smart Particles – Stimuli-responsive Polymers	409
13.5 Environmental and Safety Concerns of Polymer Colloids	410
13.5.1 Health and Safety	410
13.5.2 Environmental Safety	412
13.6 Conclusion	413
References	414
<b>Subject Index</b>	<b>418</b>



## **Section I: Emerging Methods in Polymer Colloid Formation**



## CHAPTER 1

# *Development, Characterization, and Application of Novel High Temperature Thermoplastic and Thermosetting Dispersions*

D. L. MALOTKY, D. L. DERMODY,\* D. SCHMIDT,  
T. J. YOUNG AND M. KALINOWSKI

Dow Chemical Company, Michigan, USA

\*Email: DLDermody@dow.com

## 1.1 Introduction

Dow's HIPE (High Internal Phase Emulsion) process, also known as BLUEWAVE™ technology, has been practiced at Dow for over 20 years. It is a process and formulation approach for creating aqueous emulsions or dispersions of polymers, which cannot otherwise be made *via* polymerization of monomers in aqueous systems (*i.e.* by emulsion or suspension polymerization). Examples of such polymers include polyurethanes, epoxies, polyolefins, silicones, polyesters, and alkyds. Advantages of this process include:

- Controlled internal phase concentration (very dilute to >95% internal phase)
- Controlled particle or droplet size (200 nm–50 µm, although 500 nm–5 µm is most typical)

- Minimal surfactant requirements (typically 2–6% based on internal phase)
- Ability to process high viscosity materials (>100 000 cP)
- Solvent free

Compared to emulsion polymerization, BLUEWAVE™ technology generally requires slightly higher surfactant amounts and generates slightly larger particle size because it is a direct emulsification technique, as opposed to a polymer synthesis technique. The use of appropriate process equipment and surface active ingredients also allows for the creation of emulsions of polymer melts at temperatures above the boiling point of water. For example, an emulsion of high density polyethylene (HDPE, melting temperature = 135 °C) in water can be generated at a process temperature of 150 °C and then cooled down to room temperature to give a stable HDPE in water dispersion.

Once the polymer is present in the form of a water-borne dispersion, it can be processed using standard emulsion application tools, such as printing or coating processes, dipping, spraying, and froth foaming. This provides a very different set of physical properties, such as the high crystallinity and melting temperature of a polyolefin, with the application convenience of an emulsion polymer. Compared with an extruder applied coating of the same polymer chemistry, water-borne submicron particles allow for significant down gauging of coating thickness.

There are a number of commercial products made with BLUEWAVE™ technology, including:

- CANVERA™ polyolefin dispersions for metal beverage packaging
- ECOSMOOTH™ polyolefin dispersions for skin and hair care
- HYPOD™ polyolefin dispersions for paper coating
- ProSperse™ epoxy dispersions
- ACCENT™ polyolefin co-polymer dispersions for oil and gas

Small particle size emulsions can be generated by a range of mechanical equipment or non-mechanical processes. Examples of mechanical emulsification techniques include rotor-stator mixing systems,<sup>1,2</sup> ultrasound,<sup>3</sup> high pressure impingement systems,<sup>4–6</sup> and membrane emulsification.<sup>7,8</sup> The non-mechanical processes for emulsion formation include phase inversion,<sup>9</sup> either by composition or temperature, as well as precipitation and solvent exchange.<sup>10</sup> However, the ability of these standard processes to create very small (sub-micron) particle dispersed systems of very high viscosity materials, such as polyolefin elastomers, is limited. BLUEWAVE™ technology combines mechanical (process) and non-mechanical (formulation) approaches to generate challenging dispersions.

A general schematic of the continuous process used in BLUEWAVE™ technology is shown in Figure 1.1. The particular equipment that is used for the primary mixer and dilution mixer unit operations depends upon the material properties of the polymer being fed into the process. For example,

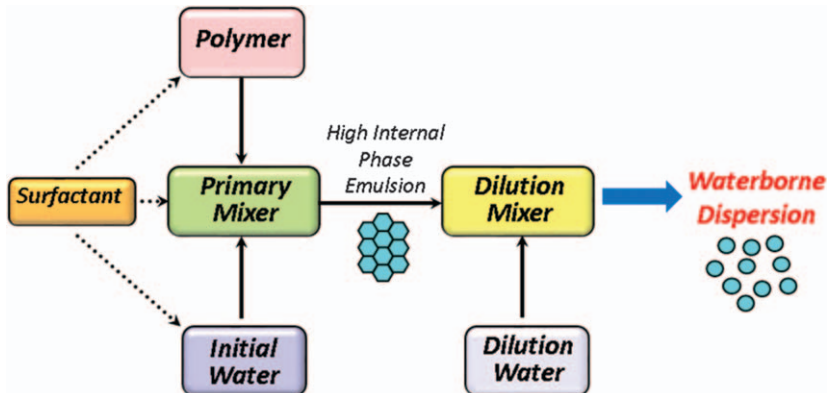


**Figure 1.1** General schematic for BLUEWAVE<sup>TM</sup> technology process.

a thermoplastic polyolefin may have both mixing operations performed in series in a single twin screw extruder. For an amorphous polymer feed, such as an alkyd or high molecular weight polydimethylsiloxane, it may be more effective to use separate rotor stator mixers as the primary and secondary mixers.

In the BLUEWAVE<sup>TM</sup> technology, a polymer melt phase, a surfactant, and a small amount of initial water are combined in a primary mixing device at a temperature above the glass transition temperature ( $T_g$ ) and melting temperature ( $T_m$ ) of the polymer to create a polymer melt in water High Internal Phase Emulsion (HIPE). The HIPE can be thought of as a liquid/liquid foam, and is, by definition, an emulsion where the internal phase is greater than 74.5% of the total volume, which is the limit for close packed mono-dispersed spheres. Figure 1.2 shows a scanning electron micrograph of a polyolefin high internal phase ratio emulsion that has been allowed to cool below the polymer  $T_m$  without dilution. The polyhedral nature of the solid internal phase particles, as well as their high volume fraction, is clear.

With the BLUEWAVE<sup>TM</sup> technology, the particle size of the internal phase droplet is set with the creation of this HIPE, which is then combined with additional dilution water to yield the final dispersion product at the desired internal phase volume concentration. For some applications, such as cosmetic emollient concentrates,<sup>11</sup> the final product may itself be a HIPE, as it is desirable that it contains as little water as possible. In other applications where a low viscosity dispersion is desired for spray coating, the final solids level may be in the range of 50% by volume. Internal phase polymers that solidify above room temperature must be diluted down below ~60% by volume before the polymers cool and solidify to avoid mechanical interlocking of the HIPE, which makes further dilution of the dispersion impossible.

The rest of this chapter is separated into two sections. In Section 1.2, we will discuss the advantages, in the context of droplet breakup theory, of passing through this HIPE phase to produce small, mono-disperse emulsion

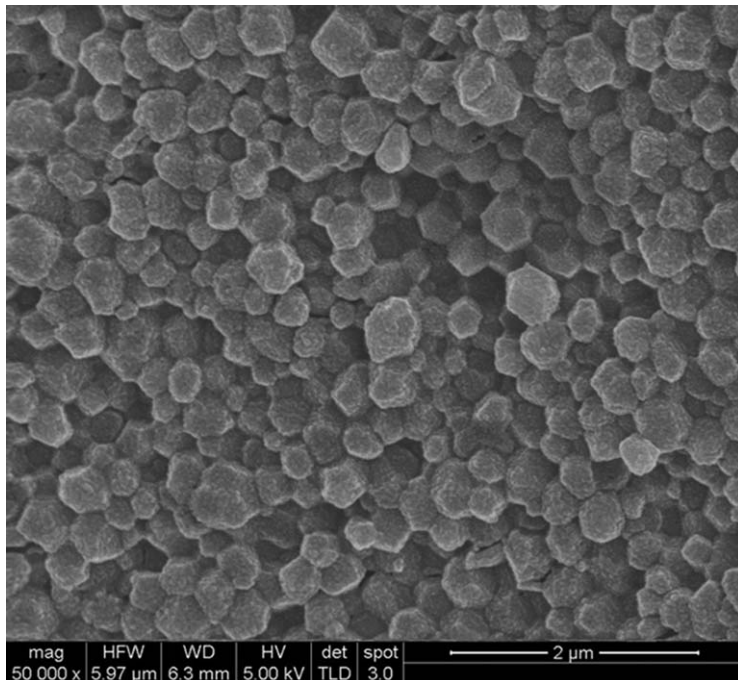


Figure 1.2 SEM of cooled polyolefin co-polymer in water HIPE.

particles. The mechanism of droplet breakup in the concentrated (concentrated internal phase) system differs from the droplet breakup in the conventional (dilute internal phase) system. These differences result in the production of the small, monodisperse droplets generated by our process. We will also discuss the complications of finding a stabilizing agent that is effective at helping to form this polymer melt/water interface at high temperatures. In Section 1.3, we will discuss the applications that are enabled by the BLUEWAVE™ technology.

## 1.2 Droplet Breakup Theory

In the following sections we will discuss classical droplet breakup theory, and how it has been extended to more concentrated systems in order to gain insight into the mechanisms that allow for the formation of small, mono-disperse particles with our BLUEWAVE™ mechanical dispersion process technology.

### 1.2.1 Classical Droplet Breakup Theory

The particle or droplet size of an aqueous emulsion depends upon how the internal oil phase breaks up during mixing. Promoting drop deformation and breakup is the shear stress,  $\tau$ , caused by the flow field within the mixer,

which is generally defined as  $\tau = \eta_c \dot{\gamma}$  where  $\eta_c$  is the continuous phase viscosity and  $\dot{\gamma}$  is the shear rate. Counteracting that force is the interfacial stress  $\sigma/R$ , where  $\sigma$  is the oil–water interfacial tension and  $R$  is the drop radius. The ratio of these values is the dimensionless capillary number  $Ca$ :

$$Ca = \frac{\tau}{\sigma/R} = \frac{\eta_c \dot{\gamma} R}{\sigma} \quad (1.1)$$

Taylor<sup>12</sup> was the first to provide a theoretical analysis of droplet deformation and breakup. Within the constraints of his system (simple steady-state shear flow, no droplet–droplet interactions, small drop deformation, and zero inertial effects), Taylor showed that the drop behavior depends on only the capillary number and the viscosity ratio,  $\lambda$ , defined as follows, where  $\eta_i$  is the internal phase viscosity:

$$\lambda = \frac{\eta_i}{\eta_c} \quad (1.2)$$

For a given flow field and viscosity ratio, there exists a critical capillary number,  $Ca_{\text{crit}}$ , above which a drop of radius  $R$  is unstable and breaks up into smaller drops. The maximum droplet radius,  $R_{\text{max}}$ , which can exist at a given critical capillary number is expressed in eqn (1.3). Drops with a radius below  $R_{\text{max}}$  are stable; drops with a radius above  $R_{\text{max}}$  will break up into smaller drops.

$$R_{\text{max}} = \frac{\sigma}{\eta_c \dot{\gamma}} Ca_{\text{crit}} \quad (1.3)$$

Numerous theoretical and experimental studies on droplet breakup have been reviewed by Rallison,<sup>13</sup> Bentley and Leal,<sup>14</sup> Stone,<sup>15</sup> Leng and Calabrese,<sup>2</sup> Cristini and Renardy,<sup>16</sup> and others. One of the most widely cited works is the extensive experimental study conducted by Grace.<sup>17</sup> Grace determined the critical capillary numbers,  $Ca_{\text{crit}}$ , below which a drop in dilute conditions would remain stable and not break for both simple shear and elongational flows under steady-state conditions. His work showed that for steady-state conditions, the smallest droplet size is always attainable at a viscosity ratio of 1 and that above a viscosity ratio of about 4, droplet breakup in simple shear is impossible.

### 1.2.2 Concentrated Emulsion Systems

In BLUEWAVE™ technology, small droplet sizes are achievable across a very broad viscosity ratio range. There are several reasons why this technology is effective even when the viscosity ratio is far from unity. One is that a HIPE, because of the close-packed nature of the droplets, is more effective at transferring shear energy to the small droplet than would be the case for a single droplet in a dilute system. The use of a HIPE to control particle size

in a batch process has been known for some time.<sup>18</sup> Aronson<sup>19</sup> created emulsions of controlled droplet size by preparing surfactant solutions of 20–60 wt% and then slowly adding oil while mixing to create a concentrate. He showed an inverse relationship between the viscosity of the surfactant solution and the particle size of the droplets and proposed that instead of the true continuous viscosity, an effective continuous viscosity should be used that takes into effect the increased viscosity due to the surfactant and the packing of the system. By using the effective continuous phase viscosity, he argued that his system had a droplet breakup similar to that observed by Taylor.

Jansen, Agterof, and Mellema<sup>20</sup> also showed that in concentrated systems under steady-state simple shear flow, the experimental Grace curve will shift downward and to the right. They looked at emulsion concentrations from about 0% up to 70% oil phase. At 70% oil, the critical capillary number was reduced by a factor of about 10 and the optimum viscosity ratio increased by close to two orders of magnitude. The authors found that if they replaced the continuous phase viscosity in  $Ca_{crit}$  and  $\lambda$  with the emulsion viscosity at the critical shear rate (a necessary correction since the emulsion is shear thinning), the data fell very close to that reported by Grace. Finally, Tcholakova *et al.* experimentally demonstrated that by increasing the drop volume fraction up to HIPE concentrations ( $\Phi > 75\%$ ) they could dramatically improve the efficiency of emulsification for viscous oils in turbulent flow. They were then able to describe the behavior of the concentrated emulsions using a simple scaling expression.<sup>21</sup>

### 1.2.3 Beyond Steady State – Transient Breakup

Another reason for the insensitivity to the viscosity ratio is the nature of the shear stress experienced by the droplet. Up to this point, only steady-state shearing conditions or systems with changes in shear rate so small that they can be considered steady state have been reviewed. Under real mixing conditions, shear rates will be far from equilibrium. Torza, Cox and Mason<sup>22</sup> observed that the rate of increasing shear rate ( $d\dot{\gamma}/dt$ ) influences both when and how the droplet will burst. In particular, they observed that large and viscous drops were more easily pulled into liquid threads than smaller, inviscid drops. This is explained by a relaxation time in which large, viscous drops readjust their shapes very slowly so that high rates of increasing shear stretch the drops directly into threads which have no time to relax but break up into many drops *via* Rayleigh instabilities. This capillary breakup mode is quite different from the splitting of a drop into two daughter droplets (binary breakup) which is characteristic of most of the steady-state work. A schematic comparing the mechanisms for breakup of different size drops is shown in Figure 1.3.

Elemans, Bos, Janssen, and Meijer<sup>23</sup> observed that under transient simple shear flow conditions where a shear stress is suddenly applied such that the  $Ca \gg Ca_{crit}$ , a Newtonian droplet within another Newtonian fluid will extend

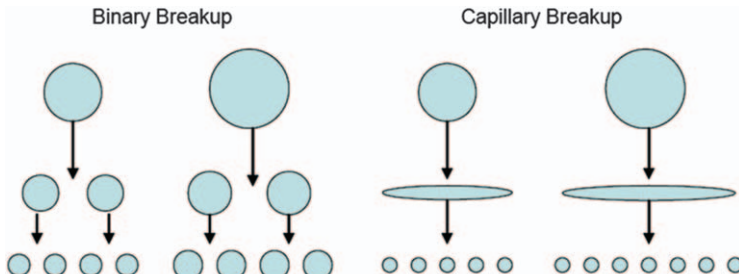


**Figure 1.3** Binary vs. capillary breakup.

into a thread. After a certain time, the thread will exhibit sinusoidal distortions and break up into several droplets. Also, Janssen and Meijer<sup>24,25</sup> examined the transient breakup mechanisms for Newtonian fluids in both simple shear and elongational flow. The extending thread formed under flow undergoes capillary instabilities at the interface. In quiescent conditions, one wavelength will dominate at the thread diameter and lead to breakup. With an extending thread, the dominant wavelength is continuously changing as the thread thins and thus the breakup of the thread is delayed compared to the fixed width thread. Eventually, the amplitude of a wavelength will exceed the diameter of the continuously decreasing thread and breakup will occur. The droplets formed will be independent of the original droplet radius. The conclusion of their work is that the optimum viscosity ratio for transient breakup is much larger than unity. This is partly because capillary disturbances develop more slowly on a highly viscous thread and thus it has more time to thin before breakup.

Janssen and Meijer's theoretical and experimental work was only carried out with Newtonian fluids. The presence of a viscoelastic continuous phase may help further improve the droplet breakup. Zhao and Goveas<sup>26</sup> experimentally observed that a viscoelastic continuous phase greatly narrowed the distribution of thread widths at breakup, as well as the resulting droplet size distribution compared to a Newtonian continuous phase.

Similar to Aronson, Mason and Bibette<sup>27,28</sup> also created stable, monodispersed emulsions by shearing a pre-emulsion within a mixing apparatus containing a well-defined, narrow shear gap and by creating viscoelasticity within the emulsion either through increasing the emulsion volume fraction to create a HIPE or varying the surfactant concentration to create a viscoelastic continuous phase. A similar thread breakup mechanism has been proposed to explain their work<sup>29</sup> and their observations further suggest that partial elasticity in the emulsion is necessary to achieve the monodispersity.<sup>30</sup>

#### 1.2.4 Surfactant Effects on Rheology and Droplet Breakup

The surfactant added to reduce the interfacial tension and stabilize the final emulsion against agglomeration will also affect the interfacial rheology.

It has been recognized as early as Rumscheidt and Mason<sup>31</sup> that droplet breakup changed when emulsifiers were present, most likely because of the formation of viscoelastic interfaces. Flumerfelt<sup>32,33</sup> modeled droplet deformation in steady-state simple shear and elongational flows that accounted for interfacial properties such as surface shear viscosity and surface dilatational viscosity. When interfacial properties are significant, they can dominate over the viscosity ratio. Davies and co-workers<sup>34</sup> compared emulsion drop size to rates of turbulent energy dissipation for a series of high shear emulsifiers and noted the critical role of the non-continuous phase viscosity in final droplet size as well as the role in adsorbed surfactant in droplet breakup. The influence of surfactant on interfacial rheology may also amplify the transient breakup effects discussed above by increasing the effective continuous viscosity and dampening out the disturbance formed at the interface, allowing the thread to extend and thin even more before breakup. The viscoelastic nature of the interfacial film may also help to narrow the size distribution similar to that observed for viscoelastic fluids by Zhao and Goveas. Mabille and co-workers,<sup>30</sup> in extending the work of Mason and Bibette, argue that the elasticity of the emulsion is absolutely necessary to get a monodisperse emulsion and that this elasticity can be controlled either by controlling the rheology of the continuous phase using surfactant and polymers or by concentrating the emulsion into the HIPE regime.

### 1.2.5 Confined Boundaries and Wall Effects

A final factor that can affect drop breakup is the nature of the boundaries within the shear field. Migler and co-workers<sup>35–37</sup> have shown that drops in confined shear flow will form strings or threads more readily than in the bulk. In tight gaps, the walls will act to stabilize the formation of the threads and prevent them from rupturing during flow. The threads will remain stable until they thin down to a point where they no longer experience the stabilizing effect of the walls, at which point they break up into droplets by Rayleigh instabilities. Thus, smaller drops can be generated within small gaps as long as the drop size is not significantly smaller than half of the gap width. More recently, Squires and co-workers<sup>38</sup> characterized droplet breakup of closely spaced fluid threads using a microfluidic multi-inlet co-flow system. Their experiments indicated that the Rayleigh–Plateau instability of adjacent, closely spaced threads (HIPE-like conditions) were collective and the cooperative breakup led to reduced polydispersity in the emulsion.

### 1.2.6 Surfactant Optimization

A simple way of expressing the effects of different variables on the droplet size is shown in eqn (1.4), where the droplet radius ( $R$ ) is directly proportional to the oil–water interfacial tension ( $\sigma$ ), inversely proportional to

the shear rate ( $\dot{\gamma}$ ), and a function of the viscosity ratio, temperature ( $T$ ) and time ( $t$ ).

$$R \propto \frac{\sigma}{\dot{\gamma}} * f\left(\frac{\eta_i}{\eta_c}\right) * f(T, t) \quad (1.4)$$

It is quickly apparent that reducing interfacial tension is an easy way to reduce droplet size with the same energy input. The interfacial tension is dependent not only on the identity and concentration of the surfactant, but on the concentration of all of the phases: surfactant, oil, and water. In a batch process, the local concentrations of the phases will vary widely as the surfactant, water, and oil are mixed together. In BLUEWAVE™ technology, the ratio of oil phase, water phase, and surfactant can be precisely controlled at the point where they first meet and mix together, allowing for precise optimization of the interfacial tension for the creation of emulsion droplets of controlled size. By concentrating the surfactant in the water phase, the effects of dynamic interfacial tension, or the increase of the interfacial tension due to the time required for surfactant to diffuse to the newly created interface, can also be reduced. Of course, the viscosity of the continuous phase can also be influenced by the presence of the surfactant, especially in the concentrated (low amount of dispersed phase) system, where a HIPE is formed.

### 1.2.7 Surfactant Selection for Emulsification in Water at Elevated Temperature

A unique obstacle with many polymer systems is that they require high temperatures, typically over 100 °C, in order to flow. Besides the complications of maintaining pressure in the equipment above the boiling point of water, there is the additional problem of finding a surfactant that will be effective above 100 °C. The use of a surfactant is required because even at higher temperatures, the interfacial tension of a typical polymer in water system without surfactant will still be too high for good emulsification. For example, the interfacial tension of a styrene-isoprene (SI) oligomer (a free flowing room temperature liquid) with water in the absence of surfactant is shown in Figure 1.4. These measurements are made with a high temperature pendant drop tensiometer (Tracker, from IT Concept-Teclis), similar to the work done by Chaverot and co-workers.<sup>39</sup>

Also, most surfactants lose their effectiveness at high temperatures. For example, non-ionic surfactants become less soluble at high temperatures and become ineffective above their cloud point, at which point the solubility drops enough that the surfactant precipitates into separate phase.<sup>40</sup> Anionic surfactants also change in both solubility and effectiveness at elevated temperatures, sometimes in counterintuitive fashion. As temperature increases, the hydrophobicity of the surfactant hydrocarbon tail can decrease rendering the molecule more hydrophilic, and therefore less interfacially

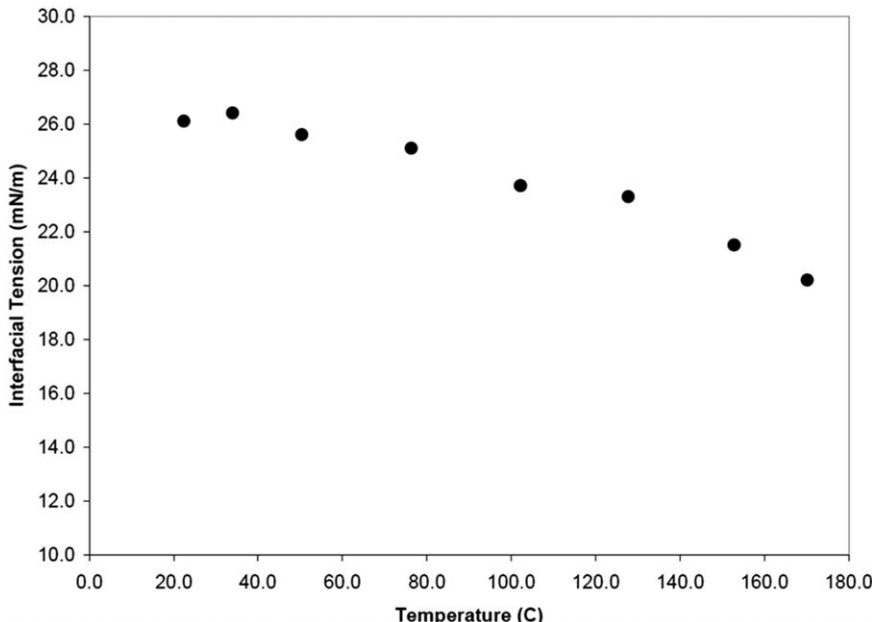


**Figure 1.4** Interfacial tension of styrene-isoprene (SI) oligomer in water measured with Tracker pendent drop tensiometer.

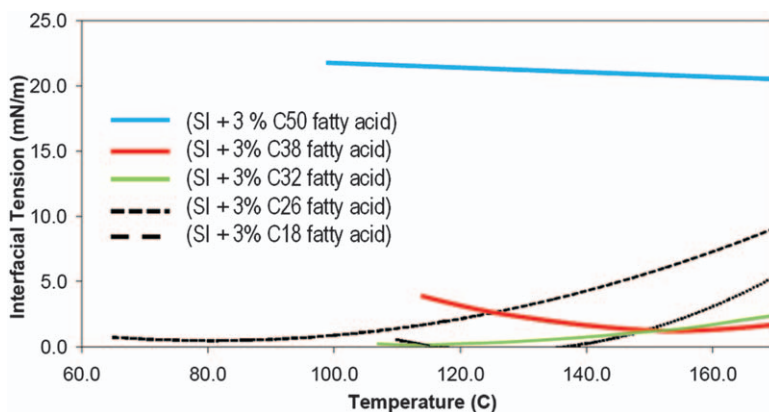


**Figure 1.5** Interfacial tension of styrene-isoprene oligomer (SI) in water with KOH neutralized fatty acids measured with Tracker pendent drop tensiometer.

active and less effective at reducing interfacial tension. The anionic surfactant head group will also increase in solubility with higher temperature, further reducing the interfacial activity of shorter hydrocarbon chain surfactants.

Figure 1.5 shows the interfacial tension of the same styrene-isoprene (SI) oligomer as in Figure 1.4 with water in the presence of a series of carboxylic

acid potassium soaps, as a function of carbon chain length. As temperature increases, the size of the surfactant hydrocarbon tail required for a minimum interfacial tension also increases. The much higher molecular weight C50 fatty acid has a much lower interfacial activity at these temperatures.

By measuring interfacial tension of materials at elevated temperatures, we have identified materials that are not particularly interfacially active, or water soluble, at room temperature, but are effective surfactants at elevated temperature. Use of these materials by themselves can cause issues in room temperature storage stability, since they lose their interfacial activity as the dispersions cool. This is usually remedied by blending them with surfactants that are more effective at room temperature.

Some conventional ionic and non-ionic surfactants are effective at elevated temperatures. For example, some EO-PO type surfactants have cloud points over 100 °C, as do some alkyl polyglucosides where the -OH functionality loses its hydrophilic nature slowly with increasing temperature because of strong hydrogen bonding interactions.<sup>41</sup>

### 1.2.8 Conclusions

In conclusion, the BLUEWAVE™ dispersion technology can be used to produce sub-micron sized, low polydispersity dispersions for many challenging high viscosity resin systems. We do this by taking advantage of high concentration emulsion conditions to better enable more efficient mechanical mixing of the oil and water phases as well as to promote a thread breakup mechanism within our dispersion devices. Through careful selection of surfactants we are able to maintain low interfacial tension during particle formation and stabilize the resultant dispersion formulations to ensure good shelf stability.

Classical droplet breakup theory can provide many useful insights into high concentration emulsification approaches such as the BLUEWAVE™ mechanical dispersion process. However, a rigorous description is more challenging because of the difficulty in directly characterizing interfacial tension and internal and external phase rheology under normal BLUEWAVE™ technology process conditions, which can be significantly above the boiling point of water. In addition, selecting the most effective high temperature interfacial stabilizer for a particular resin can be challenging for similar reasons. Continued research in the area of high temperature emulsification as well as the development of new *in-situ* characterization methods would greatly assist the improvement of fundamental understanding of these interesting and useful colloidal systems.

## 1.3 Applications

As mentioned previously, a wide range of polymer types can be converted into a water-borne form factor through the BLUEWAVE™ mechanical dispersion technology. This includes materials such as high molecular weight

and/or high viscosity polyurethanes, epoxies, polyolefins, silicones, polyesters, and alkyds, which cannot be synthesized by emulsion polymerization. Once these chemistries are incorporated into a water-borne dispersion, they can be processed using the standard emulsion polymer application tools such as rotogravure coating, dipping, spray application, and even frothed foam. This range of chemistries and application techniques allows for a wide variety of uses including coatings on substrates such as metal, paper, or plastic, as well as additives for oil and gas applications, or use as personal care ingredients in products such as skin creams or lotions, shampoos, and body wash.

Other form factors for the polymer chemistries can be generated with water-borne dispersions as the starting point. With proper additives, many of the higher  $T_g/T_m$  materials such as polyolefins and polyesters can be spray dried into a powder, such as that shown in Figure 1.6. This powder may or may not be water re-dispersible, depending upon the application. For example, a spray dried polyolefin elastomer powder could be used in rotomolding applications, where it would have benefits in both cost to manufacture and flowability, compared to a powder of the same elastomer generated by cryo-grinding.<sup>42</sup> Powder coating with these dispersion based powders is also possible, as well as the generation of interesting combinations of chemistries not possible with traditional techniques.<sup>43</sup>

An aqueous dispersion can also be used in place of a viscous polymer melt/resin in the creation of a composite part.<sup>44</sup> Typically, a viscous resin is forced into a dense fiber weave under pressure and it is challenging to fully coat all the fiber with the resin. When the resin phase is emulsified into an aqueous dispersion the viscosity of the resin is effectively decoupled from the viscosity of the material being infused into the fiber. This allows the fiber to be completely wetted without the use of high pressure infusion techniques and can result in the creation of composite parts with the same strength as the conventionally manufactured piece utilizing less resin, reducing both weight and cost.

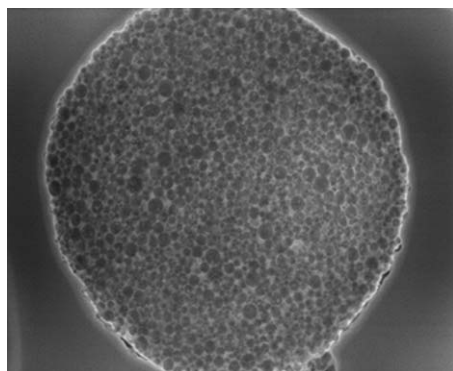


**Figure 1.6** Micrograph of a 50 micron diameter composite particle generated by spray drying of polyolefin dispersion.

### 1.3.1 Considerations for Design of Aqueous Polyolefin Dispersions and their Applications

In the next sections, we will discuss additional application areas for some specific polyolefin dispersions in more detail. However, first we will describe why polyolefins are a particularly useful polymer type to use from a water-borne form factor. There are a wide range of polyolefin chemistries available, with widely differing physical properties such as flexibility and melting temperature. In general, as the amount of crystallinity in a polyolefin increases, both its melting temperature and its modulus increase, but it becomes more brittle. For example in Figure 1.7 the low crystallinity elastomer would have a low melting temperature (perhaps 65 °C) and be very flexible. However, it would be a poor barrier to the diffusion of water or grease because of its low level of crystallinity. The highly crystalline HDPE would provide good barrier properties, but would require a high melting temperature to generate a cohesive film ( $T > 135$  °C), and would be inflexible and more prone to cracking upon large deformations.

In all cases, a temperature above the melting temperature of the polyolefin base resin is required to generate a coalesced film from the dispersion particles. This is in contrast to materials such as the emulsion polymers used for architectural paints, which are amorphous and have a  $T_g$  below room temperature, and are therefore able to coalesce into cohesive films without additional heat. Because of this required “cure temperature” for the polyolefin dispersions to form a continuous film, they are best suited for factory applied or OEM (original equipment manufacturer) applications, as opposed to “field applied” applications; however, the polyolefin dispersions can be used as additives in another film forming polymer.

After it is generated with the BLUEWAVE™ technology, the polyolefin dispersion has the general morphology of a core of non-functional “base resin,” such as the highly crystalline HDPE discussed above, and a shell of the dispersant, which is used to lower the interfacial tension during the manufacturing process and provide colloidal stability at room temperature, as seen in Figure 1.8.

Figure 1.9 shows the formation of a coalesced film from a collection of polyolefin dispersion particles. As the temperature increases, the

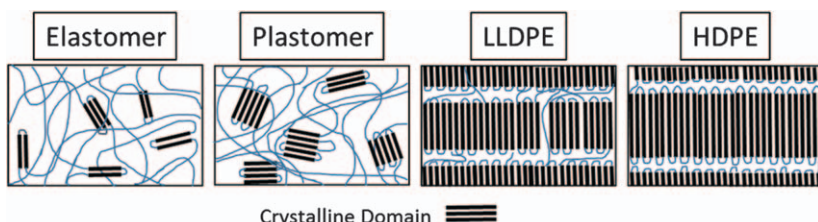


**Figure 1.7** Illustration of polyolefin morphology as a function of crystallinity. LLDPE is linear low density polyethylene, HDPE is high density polyethylene.

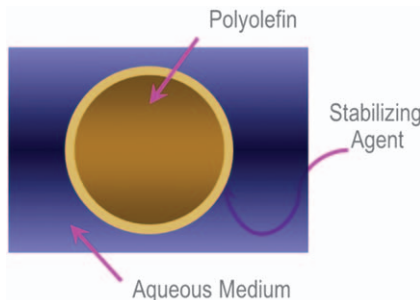


**Figure 1.8** Illustration of aqueous polyolefin dispersion particle generated by BLUEWAVE™ technology.

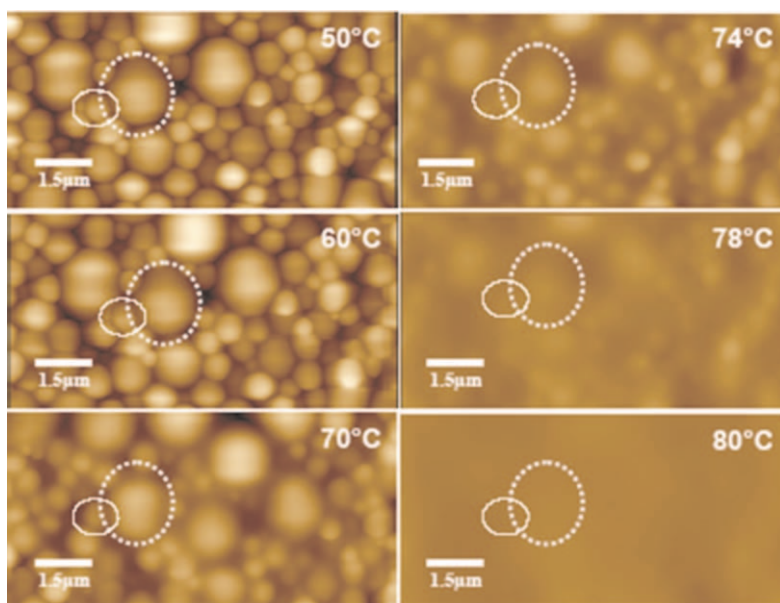


**Figure 1.9** Coalesced coating formation from a polyolefin dispersion with applied temperature.

morphology of the film changes from being a collection of individual particles continuous in the stabilizing agent (upper left), to become a phase inverted film continuous in the base resin. At this point, the individual particles are no longer observed in the coating morphology (lower right).

When developing a dispersion for a specific application, we need to select the components of the dispersion to take into account both the needs of the BLUEWAVE™ process technology, as well as the performance requirements of the application. For example, in a paper coating application, it may be important to have a low cure temperature to allow for fast coating line speeds, and a high barrier may not be as important, as the coated article is

intended only for a single, short term use (e.g. paper beverage cup). For a metal coating application, it will likely be more important to have the barrier from the higher crystallinity polyolefin, even if it requires a higher curing temperature.

A dispersion for metal coating may also require some functional olefin to help with the adhesion of the coating to the metal substrate. Fortunately, in many cases this functional olefin can double as the dispersant for the BLUEWAVE™ technology. This dispersant may not be melt miscible with the base resin in certain cases, such as a functional polyethylene dispersant and a polypropylene base resin. The representative coating morphologies that result from “compatible” and “incompatible” base resin and stabilizing agent are shown in Figure 1.10.

These large domains of stabilizing agent in the coating can act as defects for coating failure and are undesirable. Even in the system with the “compatible” stabilizing agent, the coating morphology may not be entirely single phase, as can be seen in the cross sectional micrograph of the “compatible” system shown in Figure 1.11. The stabilizing agent is visible as very small domains scattered throughout the coating thickness.

In addition to control of coating morphology through the use of specific base resin and stabilizing agent combinations, it can also be controlled through the blends of different dispersions. This concept is well known in the emulsion polymer field,<sup>45</sup> but we propose that the BLUEWAVE™

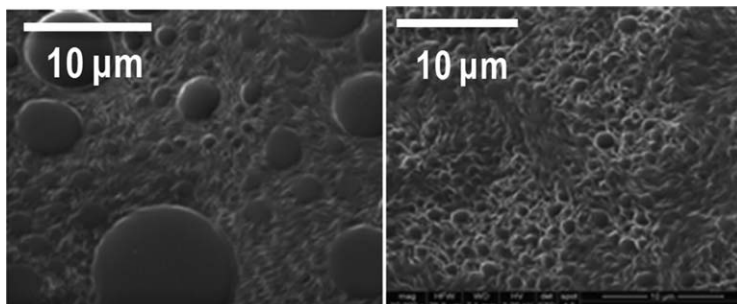


**Figure 1.10** Surface microscopy of a coating generated with a stabilizing agent that is “incompatible” (left) with the base resin, compared to a coating generated with a stabilizing agent that is “compatible” (right) with the base resin.

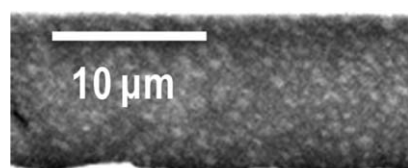


**Figure 1.11** Cross section microscopy of compatible base resin and stabilizing agent system from Figure 1.10 (right).

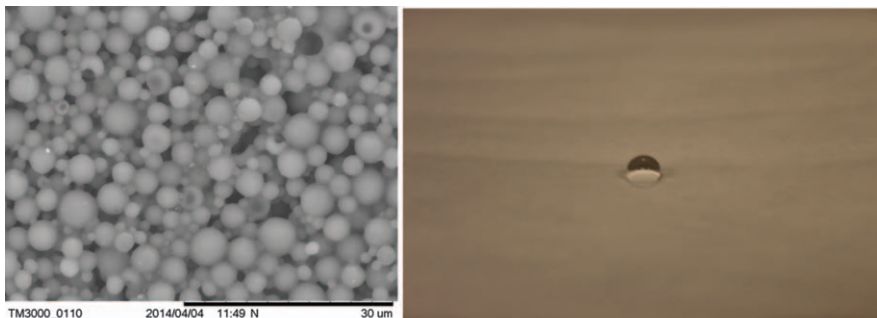


**Figure 1.12** Surface micrograph (left) of porous, hydrophobic polyolefin coating from a bi-modal blend, and a macroscopic image of a water droplet on the same coating (right).

technology provides an advantageous way of creating specifically designed dispersions of other types of polymers for the design of exotic coating morphologies. For example, a water vapor permeable hydrophobic coating can be generated from a bi-modal aqueous polyolefin dispersion.<sup>46</sup>

A population of large particle size, high melting point ( $T_{mH}$ ) particles of a hydrophobic polymer, such as HDPE, is combined with a population of small particle size, lower melting point ( $T_{mL}$ ) polymer particles in an appropriate ratio to create a coating that is porous, but mechanically robust, when cured at a temperature  $T_{mL} < T < T_{mH}$ . Appropriate selection of composition, formulation, and cure conditions result in a coating that assembles into a water vapor permeable morphology, but is resistant to liquid water (contact angle  $\sim 130^\circ$ ). Key to achieving this useful combination of properties is both the very hydrophobic nature of the large particle population and its presence above the critical pigment volume concentration, such that the cured coating is porous with a rough surface. However, a sufficient population of lower melting point binder particles is still required to provide mechanical integrity. A surface micrograph of such a coating is shown in Figure 1.12, as well as the image of a water droplet beading up with a high contact angle on the same coating.

### 1.3.2 Hybrid Particles for Optical Hiding

In addition to the morphology of a stabilizing agent shell around a base resin core, shown in Figure 1.8, it is easy to imagine other possible particle morphologies<sup>47</sup> that could be prepared by the BLUEWAVE™ mechanical dispersion process technology. Illustrations of some possible morphologies are shown in Figure 1.13, with the morphology of Figure 1.8 represented by the upper left drawing. The illustrations of the lower middle and lower left of Figure 1.13 show a more substantial shell than that from the stabilizing agent alone. This type of shell may be generated by interfacial polymerization, for example.<sup>48</sup> This type of morphology would have the benefits of

the controlled particle size distribution generated by the BLUEWAVE™ technology, combined with the protective barrier of an interfacially polymerized shell, perhaps for the encapsulation of actives in a cosmetic application.

In the two middle illustrations of Figure 1.13, the added element of an individual inorganic particle, on the order of size of the dispersion particle itself, is included within the dispersion particle. A micrograph of a polyester + TiO<sub>2</sub> dispersion system, with the upper middle morphology of Figure 1.13, is shown in Figure 1.14. Because of the small volume % loading of the TiO<sub>2</sub> in this particular example, not every dispersion particle contains a TiO<sub>2</sub> particle.

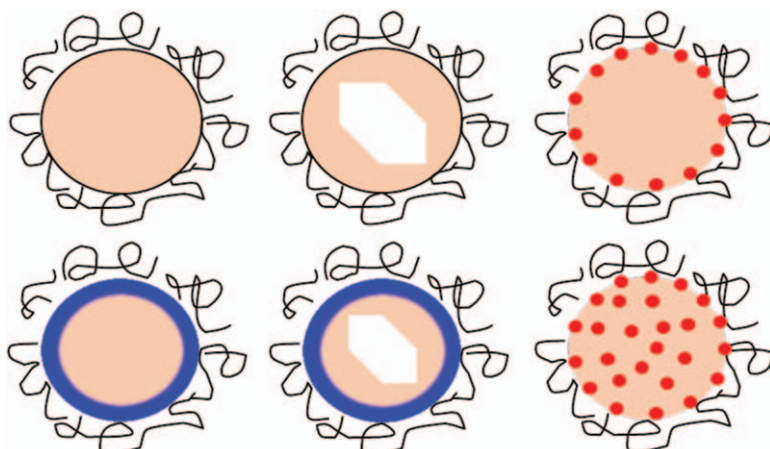


**Figure 1.13** Illustrations of possible dispersion particle morphologies. White hexagons and red circles represent inorganic materials, blue and pink represent different polymer compositions, and black is dispersant.

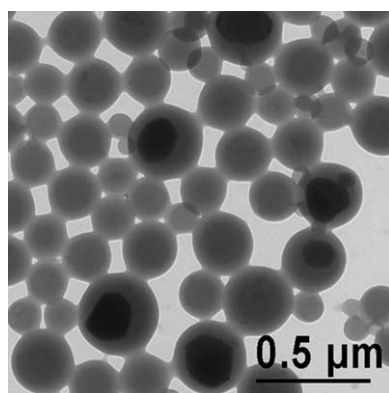


**Figure 1.14** TiO<sub>2</sub> pigment encapsulated in polyester dispersion particles.

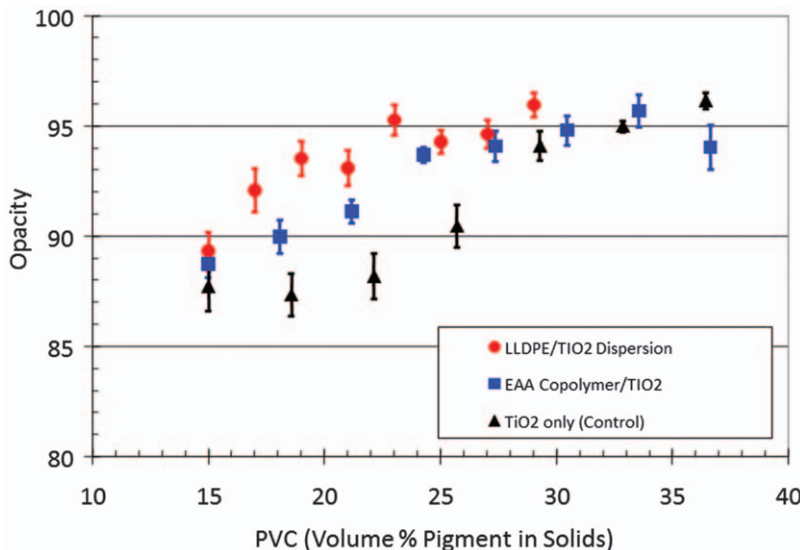


**Figure 1.15** Coating opacity, as a function of pigment volume concentration, for different pigment preparations.

This “encapsulated pigment” morphology is particularly useful in enhancing the efficiency of a pigment in an optical hiding application.<sup>49</sup> Figure 1.15 shows opacity data for three different architectural paint formulations, where a TiO<sub>2</sub> pigment is added alone (control), added with an ethylene acrylic (EAA) co-polymer to help act as a pigment dispersant, or added encapsulated in a linear low density polyethylene (LLDPE) dispersion. As the pigment goes from unmodified, to well dispersed by the EAA, to fully encapsulated in the LLDPE, the pigment efficiency (opacity at a given volume % loading) increases until it hits a limiting value of ~95%. The pigment volume % at this limiting value is lowest for the fully encapsulated pigment, at ~23 vol%, compared to ~27 vol% for the EAA dispersed pigment, and ~32 vol% for the TiO<sub>2</sub> control.

The advantage of the encapsulated pigment comes from keeping each individual pigment particle separate, and therefore able to scatter at the maximum efficiency. The more efficient hiding of the encapsulated pigment greatly reduces the total amount of pigment required in the formulation to reach the desired level of opacity. There may also be the advantage of another refractive index mismatch between the LLDPE encapsulating polymer and the coating matrix.

### 1.3.3 Polyolefin Dispersions as Adhesion Promoters for Plastic Substrates

Polyolefins have excellent mechanical properties, recyclability, and chemical resistance<sup>50,51</sup> at a reasonable cost. However, because of their low surface

energy and lack of polar functional groups, polyolefins have poor adhesion to paints requiring modification of both the substrate and paint for practical use in applications where paintability is required. Various technologies have been developed to improve the paintability of polyolefins. These include bulk modification by blending with polar polymers or additives like polyurethane,<sup>52,53</sup> surface pretreatment such as flame, corona, or plasma treatments,<sup>54,55</sup> and application of primers such as solvent-borne or aqueous-based chlorinated polymers as adhesion promoters.<sup>56,57</sup> However, there is still a need for better performing, more environmentally friendly solutions such as a chlorine-free and solvent-free aqueous adhesion promoter system.

In a recent study by Wan and co-workers,<sup>58</sup> the BLUEWAVE™ mechanical dispersion technology was used to produce water-borne dispersions of functional polyolefins. These materials were proposed as an adhesion promoter to improve the paintability of treated thermal plastic olefins (TPO). The functional polyolefins contain a polar functional group that increases the surface energy relative to that of the TPO substrate, which allows for good adhesion with a conventional polyurethane or acrylic top coat.

Three different polyolefin dispersions were evaluated as adhesion promoters: a dispersion of an unfunctional polyolefin base resin (control), a dispersion of an -OH functional polyolefin base resin, and a blend of the -OH functional dispersion with a dispersion of a maleic anhydride (MAH) functional polyolefin base resin. These dispersions were all low viscosity (<500 cP), and high solids (44%–52%), similar to a conventional water-borne latex. They were coated onto a TPO substrate with a Meyer rod to form a 20 µm wet film thickness and dried at 90 °C for 15 minutes. The primed substrates were then coated with 50 µm wet film thickness layer of either a water-borne acrylic topcoat, or a solvent-borne polyurethane topcoat (PU) and dried at 60 °C for 15 minutes.

Crosshatch adhesion was used to evaluate the adhesion strength of primer + topcoat system to the TPO substrate. In the crosshatch adhesion test, a crosshatch scribe is used to make parallel linear cuts through the coating. A similar set of linear cuts is then made perpendicular to the original cuts in order to obtain a checker board pattern. Adhesive tape (3M #810) is then applied to the scribed surface and rubbed down with fingers in order to apply adequate pressure to ensure good contact between the tape and coating. The loose end of the tape is then pulled smoothly at an angle of 135° to remove the tape from the surface. After the tape is removed, the coating is visually evaluated for adhesion and ASTM D3359 is followed to rank the adhesion strength. The adhesion is ranked from 0B to 5B with 0B being the worst (>65% squares fail) and 5B being the best (0% squares fail). Representative photographs of a “0B” and a “5B” crosshatch adhesion rank are shown in Figure 1.16.

Table 1.1 summarizes the crosshatch adhesion ranking of three primers with polyurethane (PU) and acrylate top coating on the thermoplastic

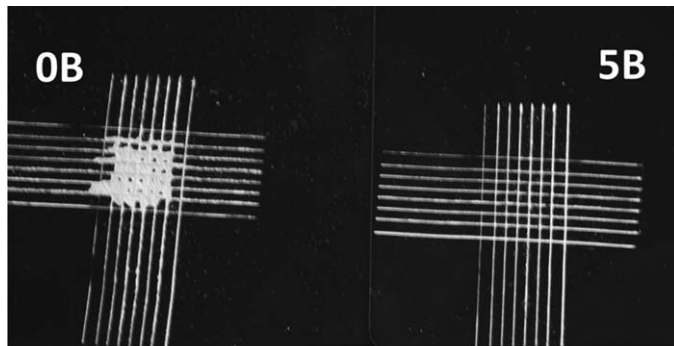


**Figure 1.16** Representative photographs of typical crosshatch adhesion ranks.

**Table 1.1** TPO crosshatch adhesion for polyolefin dispersion primers with top coats.<sup>a</sup>

Primer dispersion	PU top coating	Acrylic top coating
Control polyolefin (unfunctional)	0B	0B
-OH functional polyolefin	5B	4B
Blend of MAH functional and -OH functional polyolefin dispersions	5B	5B

<sup>a</sup>Adhesion rating: 0B – No adhesion; 5B – Excellent adhesion.

polyolefin substrate (TPO). The unmodified polyolefin dispersion primer has poor adhesion for both PU and acrylate topcoats, with crosshatch adhesion ranking of 0B, where the majority of the squares would peel off with the ASTM tape, as illustrated in Figure 1.16 (left image). The MAH-g-polyolefin and OH-g-polyolefin blend dispersion has excellent crosshatch adhesion to both PU and acrylate topcoats, with crosshatch adhesion ranking of 5B, where none of the scribed squares peeled off, as illustrated in Figure 1.16 (right image). Maleic anhydride modified polyolefin dispersion has excellent adhesion to the PU topcoat (5B), and slightly inferior adhesion (4B) to the acrylic topcoat.

Both PU and acrylic topcoats are more polar than unmodified polyolefin, and therefore do not adhere well to the unfunctional polyolefin primer layer or to the unprimed TPO substrate (data not shown), and easily delaminate in the crosshatch adhesion test. Maleic anhydride or hydroxyl functionalized polyolefins increase the polarity, and thus, the surface energy, of the primed surface. These functional groups can also provide some chemical bonding, polar–polar surface interaction, or hydrogen bonding of primed surfaces with PU or acrylic topcoats. Therefore, the overall adhesion performance is greatly improved, and there is little, to no, adhesive failure in the top coated systems with these primers.

### 1.3.4 Dispersion Enabled Heat Activated Pressure Sensitive Adhesive

Pressure sensitive labels represent a large and growing market segment within the packaging industry.<sup>59</sup> A typical pressure sensitive label consists of a facestock (either paper or plastic), a pressure sensitive adhesive (PSA), and a siliconized release liner, which serves the purpose of protecting the label during manufacture and storage, and which must be disposed of at the time of application. The siliconized release liner is not currently recyclable and represents a large amount of waste. Labels which do not require a release liner, or “linerless” labels, are gaining popularity in order to reduce waste and overall cost (Figure 1.17). The most widely adopted solution for linerless labels is to top-coat the label surface with a silicone release coating. This eliminates the liner stock, but not the cost associated with the silicone itself. The top coating approach also does nothing to address the problems associated with the adverse impact on the appearance of the label or difficulty printing, which a topcoated silicone release layer creates. An alternative approach is to use an activatable adhesive, which can be transformed from hard to tacky with heat, UV, or some other activation method.

There are several potential approaches to a heat-activated adhesive, such as the encapsulation of the adhesive,<sup>60,61</sup> or blending a dispersed polymer with a solid plasticizer (a dispersed tackifier is also commonly included in the formulations), which then combine upon heating. The requirement of heterogeneity on the micro scale precludes solvent-borne or hot melt polymers from being used in this application. Therefore, a water-borne adhesive must be used in order to prevent premature mixing of the polymer and the plasticizer.

The water-borne formulation has the advantage of being highly tunable with a variety of additives such as rheology modifiers, wetting agents, and other surfactants. It can be applied by a broad range of coating methods such as curtain, gravure, reverse gravure, and pattern coating techniques that are not accessible with hot melt polymers, which must be coated by extrusion methods.

The materials used as tackifiers and plasticizers in the deconstructed water-borne pressure sensitive adhesive (PSA) are low molecular weight, low melting temperature molecules that can be dispersed by conventional phase

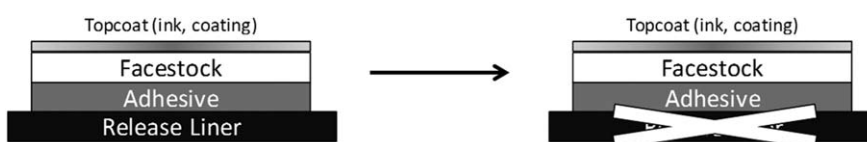


**Figure 1.17** Structure of a typical pressure sensitive label construction (left) and a linerless label with a heat-activated adhesive (right).

inversion or direct emulsification<sup>17</sup> processes. The polymers typically used in this water-borne approach are those readily available in a water-borne form factor such as acrylics, styrene-acrylics, polyurethanes, and natural rubber derivatives.<sup>62–64</sup> It would be advantageous to be able to use styrene-isoprene-styrene (SIS) type block co-polymers in these deconstructed pressure sensitive adhesive formulations, but it is not possible to synthesize this type of polymer *via* emulsion polymerization. However, through the use of BLUE-WAVE™ mechanical dispersion technology, it is possible to generate SIS dispersions to combine with water-borne tackifier, and plasticizer to form the novel pressure sensitive adhesive.<sup>65</sup> Alternative methods to generate SIS dispersions including grinding<sup>66</sup> and using solvent to aid the dispersion process, are not desirable from a process economics standpoint because of the elastomeric nature of the polymer, and the need to remove the solvent from the dispersion before use, respectively.

Neat SIS polymers are of such high modulus that they have very low room temperature tack. There are many tackifiers for SIS that have glass transitions above room temperature, are available as dispersions, and also have limited tack at room temperature. At higher temperatures, above the  $T_g$  of the tackifier, a precipitous drop in modulus is measured as the phases mix and the adhesive activates. The wide range of tackifier molecular weight, glass transition temperature, and hydrophobicity that are readily available offer many additional formulating options. These changes can markedly affect rheology, tackifier partitioning, and can be used to engineer the performance targets for a given adhesive application. The plasticizer for the SIS-based PSA is selected based on its compatibility with the styrene domains.

Scanning electron microscopy (SEM) was used to visually observe the morphological changes within the SIS-based PSA coating during the heat activation step. A formulation containing SIS (tri-block co-polymers with 16% polymerized styrene units and 56% diblock) dispersion, benzyl-2-naphthyl ether plasticizer dispersion, and Snowtack 100G rosin ester tackifier dispersion is shown in the SEM image of Figure 1.18, both before and after activation at 110 °C. In the image of the unactivated adhesive film (Figure 1.18, left), the large benzyl-2-naphthyl ether crystals are dominant at the surface. After heat activation at 110 °C (Figure 1.18, right), the film is much more uniform.

Pressure sensitive adhesives (PSAs), suitable for use in label applications without a silicone-coated release liner (so-called “linerless” labels), were developed utilizing heat-activated aqueous adhesive formulations comprised of dispersed styrenic block copolymers (SIS), dispersed plasticizers, and dispersed tackifiers. A water-borne system of an SIS polymer with 19% di-block dispersed with a long-chain primary carboxylic acid combined with a sucrose benzoate plasticizer resulted in the best combination of high peel and low blocking in the end-use application. Peel forces upwards of 10 N/in were obtained for the heat-activated adhesive, indicating their applicability for many label applications.

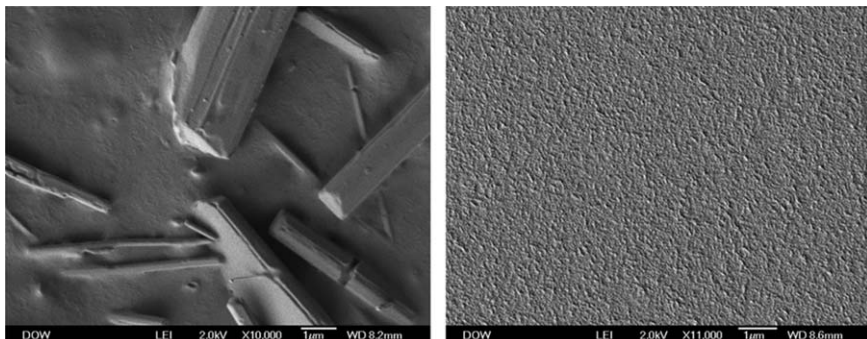


**Figure 1.18** SEM Images of PSA containing SIS (triblock copolymers with 16% polymerized styrene units and 56% diblock) dispersion, benzyl-2-naphthyl ether plasticizer dispersion, and Snowtack 100G rosin ester tackifier dispersion both before (left) and after (right) heat activation.

## 1.4 Conclusions

The previous sections have provided an introduction to the types of particles that can be generated and applications that can be addressed by thermoplastic polyolefin dispersions generated by the BLUEWAVE™ mechanical dispersion technology. We have also pointed out the limitations of these systems, such as the requirement of heat above the polymer  $T_g/T_m$  to coalesce the particles to form a defect-free film for protective coating applications. The application sections are not intended to be exhaustive, but to provide examples of the types of problems that can be addressed with BLUEWAVE™ mechanical dispersion technology. Some important application areas, such as polyurethane dispersions, and reactive systems such as dispersion enabled thermosetting composites,<sup>44</sup> are not discussed here because of their complexity.

## Acknowledgements

The authors would like to gratefully acknowledge the assistance and technical insights of Rick Lundgard, Manesh Sekharan, Jodi Mecca, Grace Wan, Bobby Moglia, Jinghang Wu, Mike Hus, Grace Wan, Ralph Even, Dan Himmelberger, Ray Drumright, and Jay Romick in the writing of this chapter.

## References

1. V. A. Atiemo-Obeng and R. V. Calabrese, Rotor-Stator Mixing Devices, in *Handbook of Industrial Mixing: Science and Practice*, ed. E. L. Paul, V. A. Atiemo-Obeng and S. M. Kresta, John Wiley & Sons, 2004, pp. 479–505.

2. D. E. Leng and R. V. Calabrese, Immiscible Liquid-Liquid Systems, in *Handbook of Industrial Mixing: Science and Practice*, ed. E. L. Paul, V. A. Atiemo-Obeng and S. M. Kresta, John Wiley & Sons, Hoboken, 2004, pp. 639–753.
3. M. J. W. Povey, Ultrasound particle sizing: A review, *Particuology*, 2013, **11**(2), 135–147.
4. E. Dumay, *et al.*, Technological aspects and potential applications of (ultra) high-pressure homogenisation, *Trends Food Sci. Technol.*, 2013, **31**(1), 13–26.
5. B. Freudig, S. Tesch and H. Schubert, Production of Emulsions in High-Pressure homogenizers – Part II: Influence of Cavitation on Droplet Breakup, *Eng. Life Sci.*, 2003, **3**(6), 266–270.
6. M. Stang, H. Schuchmann and H. Schubert, Emulsification in High-Pressure Homogenizers, *Eng. Life Sci.*, 2001, **1**(4), 151–157.
7. S. M. Joscelyne and G. Trägårdh, Membrane emulsification – a literature review, *J. Membr. Sci.*, 2000, **169**(1), 107–117.
8. E. Piacentini, E. Drioli and L. Giorno, Membrane emulsification technology: Twenty-five years of inventions and research through patent survey, *J. Membr. Sci.*, 2014, **468**, 410–422.
9. A. Perazzo, V. Preziosi and S. Guido, Phase inversion emulsification: Current understanding and applications, *Adv. Colloid Interface Sci.*, 2015, **222**, 581–599.
10. H. Schubert and R. Engel, Product and Formulation Engineering of Emulsions, *Chem. Eng. Res. Des.*, 2004, **82**(9), 1137–1143.
11. J. E. Pate, *et al.*, Process for Preparing a Cosmetic Formulation, *U. S. Pat.*, US 6783766, Aug. 31, 2004.
12. G. I. Taylor, The formation of emulsions in definable fields of flow, *Proc. R. Soc. London, Ser. A*, 1934, **146**, 501–523.
13. J. M. Rallison, The deformation of small viscous drops and bubbles in shear flows, *Annu. Rev. Fluid Mech.*, 1984, **16**, 45–66.
14. H. A. Stone, B. J. Bentley and L. G. Leal, An experimental study of transient effects in the breakup of viscous drops, *J. Fluid Mech.*, 1986, **173**, 131.
15. H. A. Stone, Dynamics of drop deformation and breakup in viscous fluids, *Annu. Rev. Fluid Mech.*, 1994, **26**, 65–102.
16. V. Cristini and Y. Renardy, Scalings for Droplet Sizes in Shear-Driven Breakup: Non-Microfluidic Ways to Monodisperse Emulsions, *FDMP*, 2006, **1**(1), 101–117.
17. H. P. Grace, Dispersion phenomena in high viscosity immiscible fluid systems and application of static mixers as dispersion devices in such systems, *Chem. Eng. Commun.*, 1982, **14**, 225–277.
18. T. J. Lin, *et al.*, Low-energy emulsification. II: Evaluation of emulsion quality, *J. Soc. Cosmetic Chem.*, 1978, **29**(12), 745–756.
19. M. P. Aronson, The Role of Free Surfactant in Destabilizing Oil-in-Water Emulsions, *Langmuir*, 1989, **5**, 494–501.
20. K. M. B. Jansen, W. G. M. Agterof and J. Mellema, Droplet breakup in concentrated emulsions, *J. Rheol.*, 2001, **45**(1), 227–236.

21. S. Tcholakova, *et al.*, Efficient emulsification of viscous oils at high drop volume fraction, *Langmuir*, 2011, **27**(24), 14783–14796.
22. S. Torza, R. G. Cox and S. G. Mason, Particle Motions in Sheared Suspensions XXVII. Transient and Steady Deformation and Burst of Liquid Drops, *J. Colloid Interface Sci.*, 1972, **38**(2), 395–411.
23. P. H. M. Elemans, *et al.*, Transient Phenomena in Dispersive Mixing, *Chem. Engng. Sci.*, 1993, **48**(2), 267–276.
24. J. M. H. Janssen and H. E. H. Meijer, Droplet breakup mechanisms: Stepwise equilibrium versus transient dispersion, *J. Rheol.*, 1993, **37**(4), 597–608.
25. H. E. H. Meijer and J. M. H. Janssen, Mixing of Immiscible Liquids, in *Mixing and Compounding of Polymers*, ed. I. Manas-Zloczower and Z. Tadmor, Hanser, New York, 1994.
26. X. Zhao and J. L. Goveas, Size Selection in Viscoelastic Emulsions under Shear, *Langmuir*, 2001, **17**, 3788–3791.
27. T. G. Mason and J. Bibette, Emulsification in Viscoelastic Media, *Phys. Rev. Lett.*, 1996, **77**(16), 3481–3484.
28. T. G. Mason and J. Bibette, Shear Rupturing of Droplets in Complex Fluids, *Langmuir*, 1997, **13**, 4600–4613.
29. C. Mabille, *et al.*, Monodisperse fragmentation in emulsions: Mechanisms and kinetics, *Europhys. Lett.*, 2003, **61**(5), 708–714.
30. C. Mabille, *et al.*, Rheological and Shearing Conditions for the Preparation of Monodisperse Emulsions, *Langmuir*, 2000, **16**, 422–429.
31. F. D. Rumscheidt and S. G. Mason, Particle Motions in Sheared Suspensions XII. Deformation and Burst of Fluid Drops in Shear and Hyperbolic Flow, *J. Colloid Interface Sci.*, 1961, **16**, 238–261.
32. R. W. Flumerfelt, Effects of Dynamic Interfacial Properties on Drop Deformation and Orientation in Shear and Extensional Flow Fields, *J. Colloid Interface Sci.*, 1980, **76**(2), 330–349.
33. W. J. Phillips, R. W. Graves and R. W. Flumerfelt, Experimental Studies of Drop Dynamics in Shear Fields: Role of Dynamic Interfacial Effects, *J. Colloid Interface Sci.*, 1980, **76**(2), 350–370.
34. J. T. Davies, Drop sizes of emulsions related to turbulent energy dissipation rates, *Chem. Eng. Sci.*, 1985, **40**(5), 839–842.
35. K. B. Migler, String Formation in Sheared Polymer Blends: Coalescence, Breakup, and Finite Size Effects, *Phys. Rev. Lett.*, 2001, **86**(6), 1023–1026.
36. J. A. Pathak, *et al.*, Layered Droplet Microstructures in Sheared Emulsions: Finite-Size Effects, *J. Colloid Interface Sci.*, 2002, **255**, 391–402.
37. J. A. Pathak and K. B. Migler, Droplet-String Deformation and Stability during Microconfined Shear Flow, *Langmuir*, 2003, **19**, 8667–8674.
38. V. Mansard, *et al.*, Collective Rayleigh-Plateau Instability: A Mimic of Droplet Breakup in High Internal Phase Emulsion, *Langmuir*, 2016, **32**(11), 2549–2555.
39. P. Chaverot, *et al.*, Interfacial Tension of Bitumen – Water Interfaces. Part 1: Influence of Endogenous Surfactants at Acidic pH, *Energy Fuels*, 2008, **22**(2), 790–798.

40. M. J. Rosen, *Surfactants and Interfacial Phenomena*, 2nd edn, John Wiley & Sons, New York, 1989, p. 219.
41. D. Balzer, Cloud point phenomena in the phase behavior of alkyl polyglucosides in water, *Langmuir*, 1993, **9**(12), 3375–3384.
42. P. H. Walia, H. Liang, M. Jones, D. Malotky and M. Sekharan, Spray dried polyolefin elastomer powder for rotational molding processes, *Eur. Pat.*, EP 3277764 A1, Feb. 7, 2018.
43. J. Romick, D. Malotky, R. Lundgard and L. Chen, Powder Coatings, *Eur. Pat.*, EP 3155052 A2, April 19, 2017.
44. M. Sekharan, M. Hus, D. Bank, D. Dermody, D. Malotky, P. Cate, S. Burr and T. Young, Premolding article from thermoset and thermoplastic polymer dispersions, *U. S. Pat.*, US 9303131 B2, April 5, 2016.
45. S. Eckersley and B. Helmer, Mechanistic considerations of particle size effects of film properties of hard/soft latex blends, *J. Coat. Technol.*, 1997, **69**(864).
46. J. Romick, D. Malotky and M. Crimmins, Polyolefin dispersion compositions for making high vapor transport hydrophobic coatings, *U. S. Pat.*, US 9701824 B2, July 11, 2017.
47. J. Vyroykka, D. Malotky and R. Wevers, Coating composition, a process of producing a coating composition, a coated article, and a method of forming such articles, *U. S. Pat.*, US 9221940 B2, Dec. 29, 2015.
48. D. Schmidt and D. Malotky, Process for encapsulating a hydrophobic active, *U. S. Pat.*, US 20140271751 A1, Sept. 18, 2014.
49. R. Lundgard and J. Mecca, Coating composition, a process of producing a coating composition, a coated article, and a method of making such articles, *U. S. Pat.*, US 8829083 B2, Sept. 9, 2014.
50. D. J. Burnett, F. Thielmann and R. A. Ryntz, Correlating thermodynamic and mechanical adhesion phenomena for thermoplastic polyolefins, *J. Coat. Technol. Res.*, 2007, **4**(2), 211–215.
51. K. Deng, *et al.*, Influence of position and composition on adhesion to injection-molded TPO plaques as model automotive parts, *Polymer*, 2009, **50**(21), 5084–5093.
52. K. Deng, *et al.*, Characterizing interfacial structure of TPO/CPO/TPO adhesive joints by PFM–AFM and SEM, *Polymer*, 2009, **50**(14), 3225–3233.
53. J. Song, *et al.*, Polyethylene/polyurethane blends for improved paint adhesion, *Prog. Org. Coat.*, 2011, **72**(3), 492–497.
54. C. Chan, T. Ko and H. Hiraoka, Polymer surface modification by plasmas and photons, *Surf. Sci. Reports*, 1996, **24**, 1–54.
55. E. M. Liston, L. Martinu and M. R. Wertheimer, Plasma surface modification of polymers for improved adhesion: a critical review, *J. Adhes. Sci. Technol.*, 1993, **7**(10), 1091–1127.
56. E. Tomasetti, *et al.*, Diffusion of adhesion promoter (CPO) into polypropylene/ethylene-propylene (PP/EP) copolymer blends: mechanism, *J. Adhes. Sci. Technol.*, 2001, **15**(13), 1589–1600.
57. Z. Yin, *et al.*, Adhesion of CPO onto high modulus TPO: Lap-shear tests in conjunction with microscopy studies of the fracture surface structure, *Polymer*, 2005, **46**(25), 11610–11623.

58. G. Wan, D. Malotky, K. Anderson, S. Anderson, K. Lutz, M. Read and C. Li Pi Shan, Development of Novel Functional Polyolefin Primers/ Adhesives, in *2015 Adhesion Society Meeting*, Savannah, GA, 2015.
59. A. A. W. Associates, *Global Pressure-Sensitive Label Market Study*, 2017.
60. J. Empereur, M. N. Belgacem and D. Chaussy, Silicone Liner-Free Pressure-Sensitive Adhesive Labels, *Macromol. Mater. Eng.*, 2008, **293**(3), 167–172.
61. T. Schwantes, In situ microencapsulated adhesive, US 6592990 B2, July 15, 2003.
62. T. Shin, Water soluble heat sensitive self adhesive composition and heat sensitive self adhesive sheet, *Jp. Pat.*, JP 2001303019 A, Oct. 31, 2001.
63. I. Akira, Production of thermo-adhesive label, *Jp. Pat.*, JP 2001064603 A, March 13, 2001.
64. M. Seiji, Thermoplastic resin composition, heat sensitive adhesive sheet and method for producing heat-sensitive adhesive sheet, *Jp. Pat.*, JP 2001098162 A, April 10, 2001.
65. M. Einstla, W. Griffith, D. Himmelberger, S. Zolynski, S. Zhang, T. Powell and D. Malotky, Heat Activated pressure sensitive adhesives for linerless labels, *J. Appl. Polym. Sci.*, 2019, **136**(6), 47048.
66. J. Bassam and E. Daniels, Efficient proces for making tackifiers and adhesives, *U. S. Pat.*, US 7410110 B2, Aug. 12, 2008.

## CHAPTER 2

# *Synthesis of Core–Shell Polymer-based Colloids*

MENGCHEN WU AND RUI LIU\*

Key Laboratory of Advanced Civil Engineering Materials of Ministry of Education, School of Materials Science and Engineering, Tongji University, Shanghai 201804, China

\*Email: ruiliu@tongji.edu.cn

## 2.1 Introduction

Nanoparticles (NPs) have become an important topic in colloid and materials science with diverse applications in energy, the environment and bioengineering.<sup>1–5</sup> A particle with spatially core–shell architecture on a nanoscopic length scale is an engrossing subject by virtue of the fascinating improved physical/chemical properties over its single-component counterpart.<sup>6–9</sup> Huge interest has been elicited in the usage of core–shell NPs in drug delivery,<sup>10</sup> catalysis,<sup>11</sup> sensors,<sup>12</sup> etc. Being partitioned in space, the core and the shell can perform independent or complementary functions. The two divisions are both interfaced and molecularly permeable to build molecular interactions between them, i.e., one side is able to affect the other.<sup>13,14</sup> For example, a hydrophilic shell not only provides different surface functional groups, but also protects the core from environmental corrosion. The core, on the other hand, can endow appropriate mechanical functionality (e.g., hard or soft) or particular properties (e.g., physical or biological), making the whole NPs effective in practical applications.

With regard to the core–shell type, the core generally features a single sphere (Figure 2.1A) or an aggregation of several small spheres (Figure 2.1B)

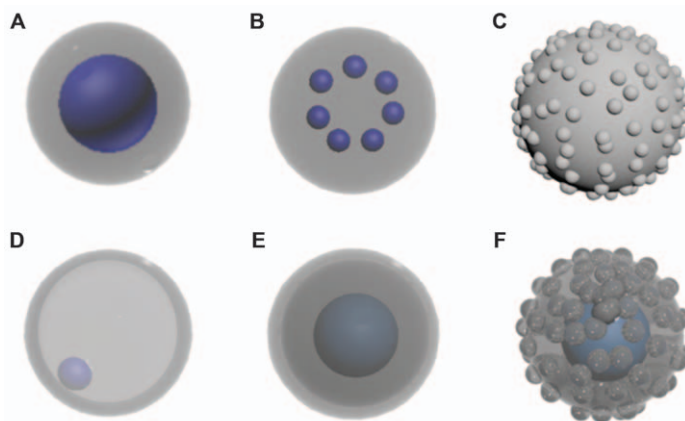


**Figure 2.1** Schematic representation of different types of core–shell particles.

within a continuous layer.<sup>15</sup> An outer layer of minor spheres attached to the core is also accepted as a core–shell structure (Figure 2.1C).<sup>16</sup> Derivative structures include rattle-like or yolk–shell NPs, where a core is encapsulated in a hollow shell (Figure 2.1D), and NPs with complex multiple continuous or scattering shells (Figure 2.1E and F).<sup>17</sup> Alternatively, depending on the compositions of the core and the shell, they can be categorized into four classes: inorganic/inorganic,<sup>18</sup> inorganic/organic,<sup>19</sup> organic/inorganic<sup>20</sup> and organic/organic.<sup>21</sup> Publications that deal with the fabrication of particles consisting of inorganic materials can be found elsewhere.<sup>22–25</sup> Here, we will focus on the polymer related morphology.

Synthetic protocols that enable the feasible production of core–shell NPs with controlled size, shape and composition, have a profound interdisciplinary effect on scientific research. Moving forward, an understanding of how to carefully select methods to harness the specific strengths of different technologies has the potential to be transformative. Understanding of the process by which polymer-based core–shell structures with an array of features are formed is becoming clearer. Contemporary methodologies involve a wide range of available techniques, which can be generally categorized into four types: (i) grafting approaches, (ii) polymer deposition, (iii) self-assembly and (iv) electro-spinning or electro-jetting.<sup>26–30</sup> The first three methods are conducted in solution, which utilizes the mutual relationship between pristine core and shell resources or unique properties inherent in polymer self-assembly. The last method relies on particular extrinsic forces.

It is the intention in this chapter to review the current state of knowledge about the preparation of polymer-based core–shell particles. At the same time, it will provide researchers with relevant information about their choice of targeted applications. We will look at both theoretical and experimental insights to identify modern techniques used in this paradigm and finally discuss future prospects.

## 2.2 Grafting Approach

Grafting is a conventional method involving either a two-step or a multiple-step process, which begins with an initial modification of the pre-synthesized cores and then their use as seeds in a subsequent polymerization.<sup>31,32</sup> The key point that governs the manufacture of core–shell particles is the efficiency of the initiation from the achieved core and the uniform formation of the desired shell. An attractive feature is the independence of the steps, which allows the particle size to be chosen ranging from a few nanometers to micrometers.

### 2.2.1 “Grafting To”

In the “grafting to” approach, the polymer chain grows primarily in the polymerization media rather than directly from the core surface. The fundamental idea is to solidly incorporate an orthogonal functional group onto the core surface which will serve as a link to couple the pre-synthesized polymer. A typical example is grafting polyethylene glycol (PEG) onto polystyrene (PS) cores. PEG molecules with different end-functionalized groups and molecular weights suit various synthetic routes to form PEG shells. As shown in Figure 2.2a, PS@PEG core–shell NPs can be prepared through: (i) a diisocyanate-coupling agent linking the hydroxyl-functionalized PEG chain to amine-functionalized PS NPs,<sup>33</sup> (ii) a carbodiimide-coupling reaction occurring between amine-functionalized PEG chains and carboxyl-functionalized PS NPs<sup>34</sup> and (iii) a Decker–Forster reaction between PEG-bearing Schiff base end groups and chloromethylated PS NPs.<sup>35</sup> Similarly, bromo-functionalized cores could also serve as desirable handles with grafting efficiency. For example, Liu and co-workers successfully anchored poly(4-vinyl pyridine) (PVP) on mesoporous silica by simply grafting PVP with a bromo-functionalized silica surface through quaternized pyridine groups, yielding polymer-mesoporous silica core–shell hybrid materials as responsive drug carriers.<sup>36</sup>

Much current investigation is focusing on the control of chain-end functionality and the efficiency of click chemistry between the shell and the core. Until now, copper-catalyzed azide/alkyne (CuAAC) is the most frequently used “click” reaction, consisting of copper-catalyzed Huisgen 1,3-dipolar cycloaddition of azides and terminal alkynes.<sup>37</sup> Other available catalysts include  $\text{Ni}^{2+}$ ,  $\text{Pd}^{2+}$ ,  $\text{Pt}^{2+}$  and  $\text{Au}^+$ .<sup>38,39</sup> Breed *et al.* used an alkyne-azide click reaction to graft PEG molecules to the surface of PS particles (Figure 2.2b).<sup>40</sup> Initially polymerized PS particles were reacted with sodium azide ( $\text{NaN}_3$ ) through nucleophilic substitution of the halide group to prepare azide-functionalized nanoparticles, followed by a CuAAC reaction. It is this functional group that provides an adequate quantity to produce the requisite density of sites and serves as a link to the PEG segment. The reaction may also be extended to other exotic polymer beads, such as different functionalized latexes or poly(methyl methacrylate).<sup>41</sup>

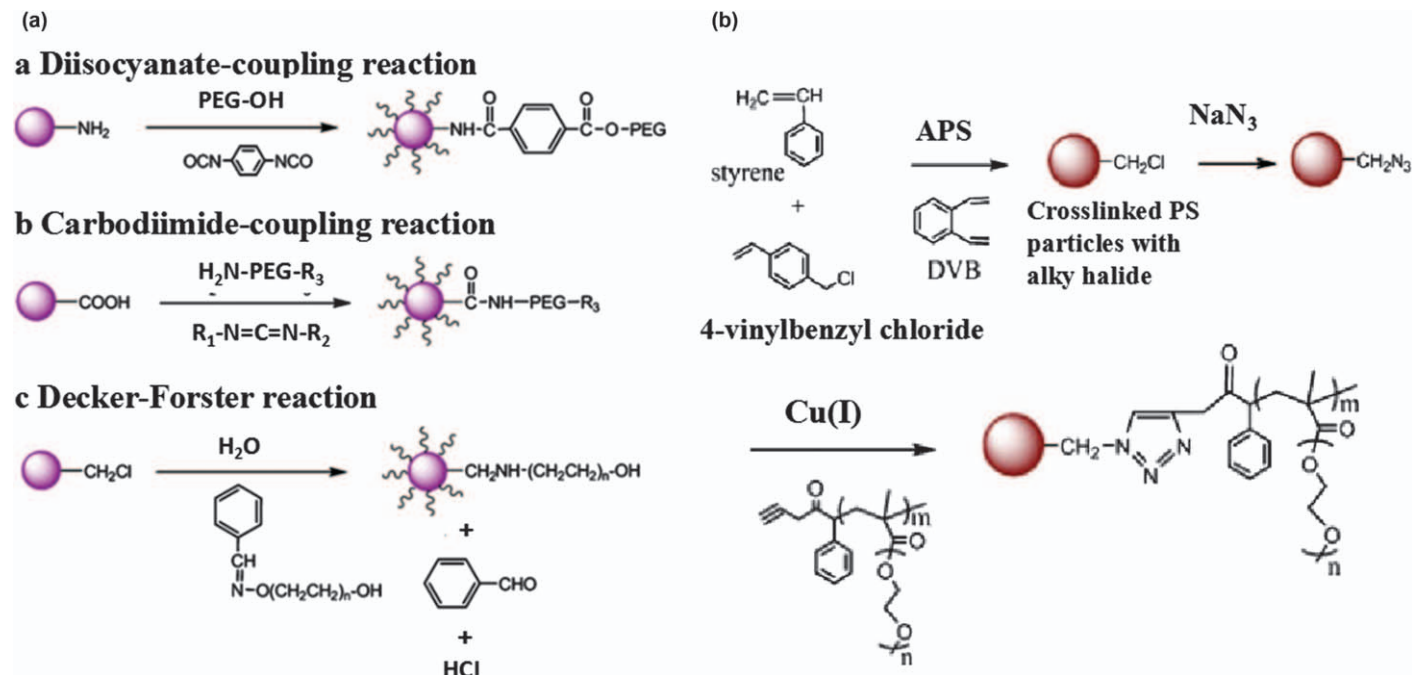


**Figure 2.2** (a) Varied “grafting to” approaches for the formation of a PEG shell. Adapted from ref. 26 with permission from Springer Nature, Copyright 2010. (b) The preparation of PS@PEG core–shell particle *via* “grafting-to” click reaction. Reproduced from ref. 40 with permission from American Chemical Society, Copyright 2009.

Dual click reactions from a surface with dual clickable functionalities have greatly facilitated the synthesis of hybrid macromolecular structures. Kang *et al.*, used a primitive silica@poly(methacrylic acid-*co*-propargyl methacrylate-*co*-divinylbenzene) ( $\text{SiO}_2@\text{P}(\text{MAA-}co\text{-PMA-}co\text{-DVB})$ ) core–shell hybrid nanosphere as a structured template, where alkyne–azide and thiol–ene surface click reactions were given in sequence to obtain hybrid core–shell nanospheres (Figure 2.3).<sup>42</sup> A dense silica core was encapsulated by a rough polymer shell by a prior distillation–precipitation polymerization. Subsequent alkyne–azide and thiol–ene click reactions of PS and PEG in the “grafting to” process consequently increased the average diameter. Similarly, quantum dots,<sup>43,44</sup> or Au NPs,<sup>45</sup> have also been grafted with various polymers through the “grafting to” approach. However, it should be noted that an obstacle to achieving a high grafting density is the steric hindrance of reactive surface sites occupied by the prior grafted polymers. Hence, the thickness of the shell layer is usually limited to below 100 nm.

## 2.2.2 “Grafting From”

In the “grafting from” approach, the polymer chains grow from initiators attached to the surface prior to polymerization. Alternatively, an initial preparation of seed cores with reactive functional groups or initiators incorporated onto them, followed by the consecutive attachment and growth of monomer molecules can be used. The method is also known as surface-initiated polymerization (SIP).<sup>46,47</sup> In this realm, atom transfer radical polymerization (ATRP), nitroxide mediated polymerization (NMP) and reversible addition fragmentation transfer polymerization (RAFT) are extensively described SIP techniques, where the polymer chain growth can be well controlled.

### 2.2.2.1 ATRP

The ATRP reaction happens in a multi-component system, consisting of an initiator, a metal halide complexed with ligand(s) and a monomer.<sup>48</sup> The initiator, in most cases, should have a structure homologous to the corresponding polymer end group. Control over the reaction is dependent on all the parameters used in the polymerization (*e.g.*, the nature of the catalyst complex and solvent). Thus far, the copper-based ATRP system has been adapted for controlled/living polymerization and shell formation from a series of monomers (*e.g.*, styrene, acrylate, methacrylate, acrylonitrile).<sup>49</sup> Patten *et al.* prepared  $\text{SiO}_2@\text{PS}$  core–shell NPs by ATRP; spherical silica particles tethered with a surface ATRP initiator (2-(4-chloromethylphenyl)ethyl)-dimethylethoxylsilane (CDES)) were used as macro-initiators for ATRP of styrene with  $\text{CuCl}/4,4'\text{-di-(5-nonyl)-2,2'-bipyridyl}$  ( $\text{CuCl}/2\text{dNbipy}$ ) as the catalysis system.<sup>50</sup>

As well as the addition of an ATRP initiator onto the core, the residual surface groups from the core can also be used as initiation sites for

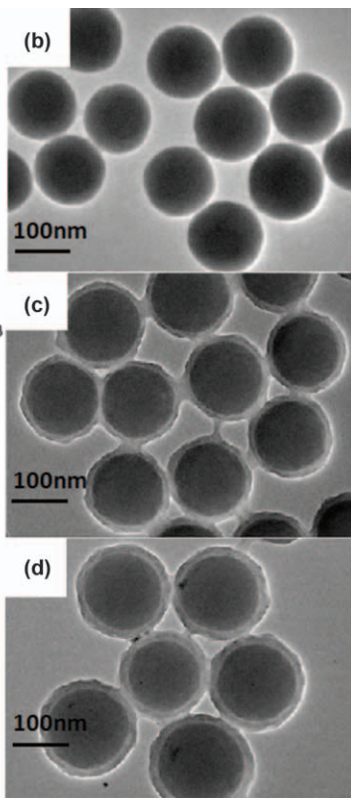
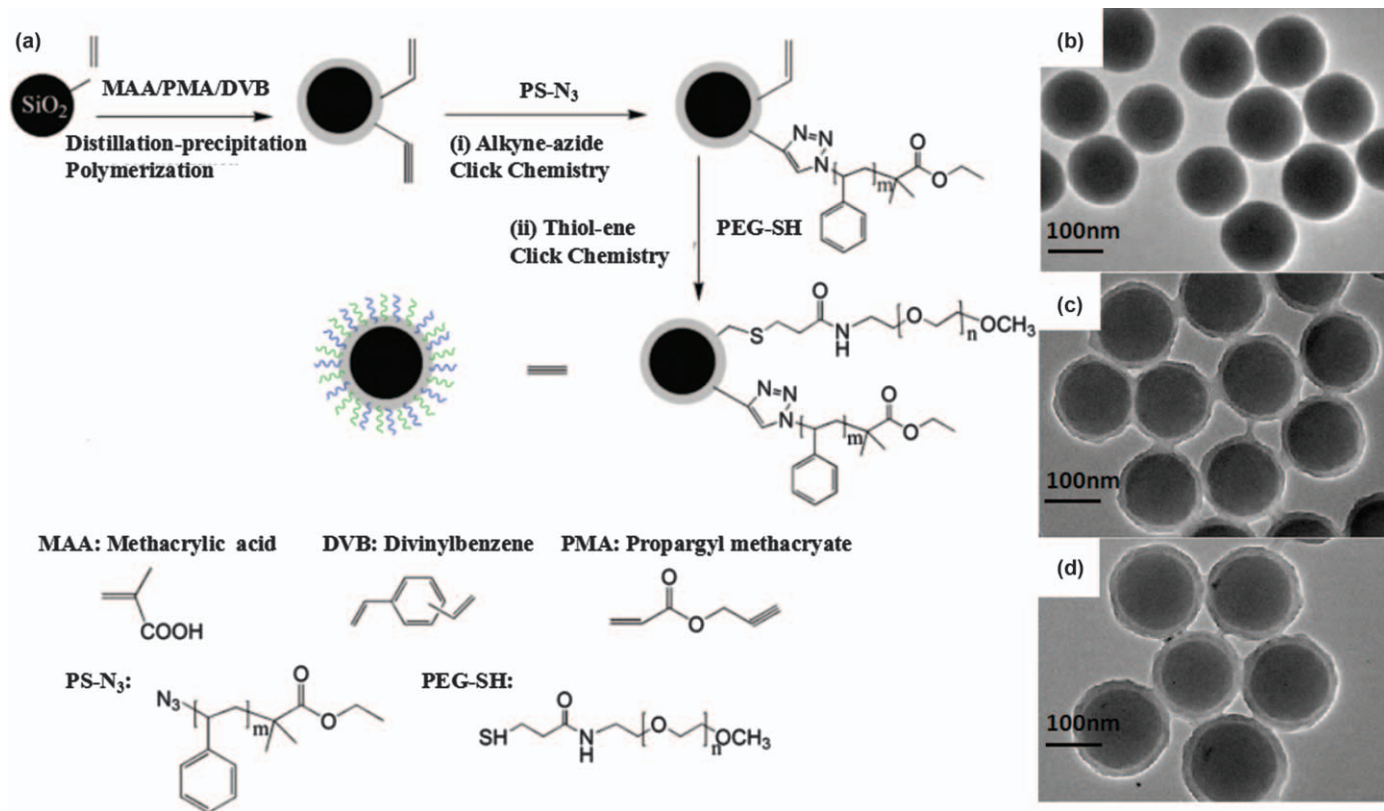


**Figure 2.3** (a) Illustration of the synthesis of silica@co-polymer core–shell hybrid nanosphere surface *via* the alkyne–azide and thiol–ene dual click reactions. TEM micrographs of (b)  $\text{SiO}_2$  NPs, (c)  $\text{SiO}_2@P(\text{MAA}-\text{co}-\text{PMA}-\text{co}-\text{DVB})$  NPs and (d)  $\text{SiO}_2@P(\text{MAA}-\text{co}-\text{PMA}-\text{co}-\text{DVB})$ -click-PS/PEG nanospheres.

Reproduced from ref. 42 with permission from American Chemical Society, Copyright 2010.

subsequent ATRP. For instance, Stöver *et al.* reported grafting an outer PS layer from poly(divinylbenzene) (PDVB80) microspheres using ATRP.<sup>51</sup> As illustrated in Figure 2.4a, PDVB80 microspheres were prepared by precipitation polymerization of DVB80 using AIBN as the initiator, which consequently left residual vinyl groups outside the core. Then ATRP of styrene was started from these initiator sites using a CuBr/2bipy catalyst system. TEM images showed that PS was uniformly grafted from the particle surfaces with increased particle size.

### 2.2.2.2 NMP

NMP is based on coupling an active chain-end radical with a nitroxide leaving group. There are two different systems applicable to this polymerization. One is bimolecular, in which a conventional free radical initiator is grafted onto the surface of particles and then nitroxides are introduced. The other is unimolecular, where alkoxyamine is directly grafted onto the surface of the particle. For either alternative, surface-initiated NMP requires the presence of a sacrificial initiator to achieve good control of the polymerization.<sup>47</sup> Bérangère and co-workers have grafted PS chains onto the surface of silica NPs through NMP and obtained silica-PS core–shell particles *via* further mini-emulsion polymerization through two steps. *N*-tert-butyl-1-diethylphosphono-2,2-dimethylpropyl nitroxide (DEPN) was used as an alkoxyamine initiator to develop a terminal functional group *in situ*, which then grafted onto the silica surface. The resultant functional groups were employed to initiate the growth of PS chains. The as-prepared PS-grafted Stöber silica could be successfully redispersed into styrene by mini-emulsification, giving rise to the formation of silica-PS core–shell particles. One advantage of this route was that it was possible to control inter-particle distance, and the spatial distribution of the core within the polymer shell.<sup>52</sup>

Developments in the elaboration of new materials have enabled this technique to fabricate core–shell structures comprising a wide range of organic polymers tethered onto special surfaces. Hawker *et al.* have reported the synthesis of a series of well-defined, three-dimensional nanostructures *via* NMP.<sup>53</sup> As described in Figure 2.4b, the structure features a PEG outer shell, a hydrophilic DOTA (1,4,7,10-tetraazacyclododecane-1,4,7,10-tetraacetic acid) inner shell and a central hydrophobic core. In the experiment, PEG was coupled to a chloro-functional NMP initiator to obtain macro-initiators. By starting with well-defined linear diblock co-polymers, the thickness of each layer, overall size/molecular weight and the number of internal reactive functional groups could be tuned accurately, all of which led to final products with varied outer- and inner-shell thicknesses. It is important to note that, due to the use of the DOTA metal chelator in this system, all synthetic methodology was designed to be metal-free to avoid trace contamination.

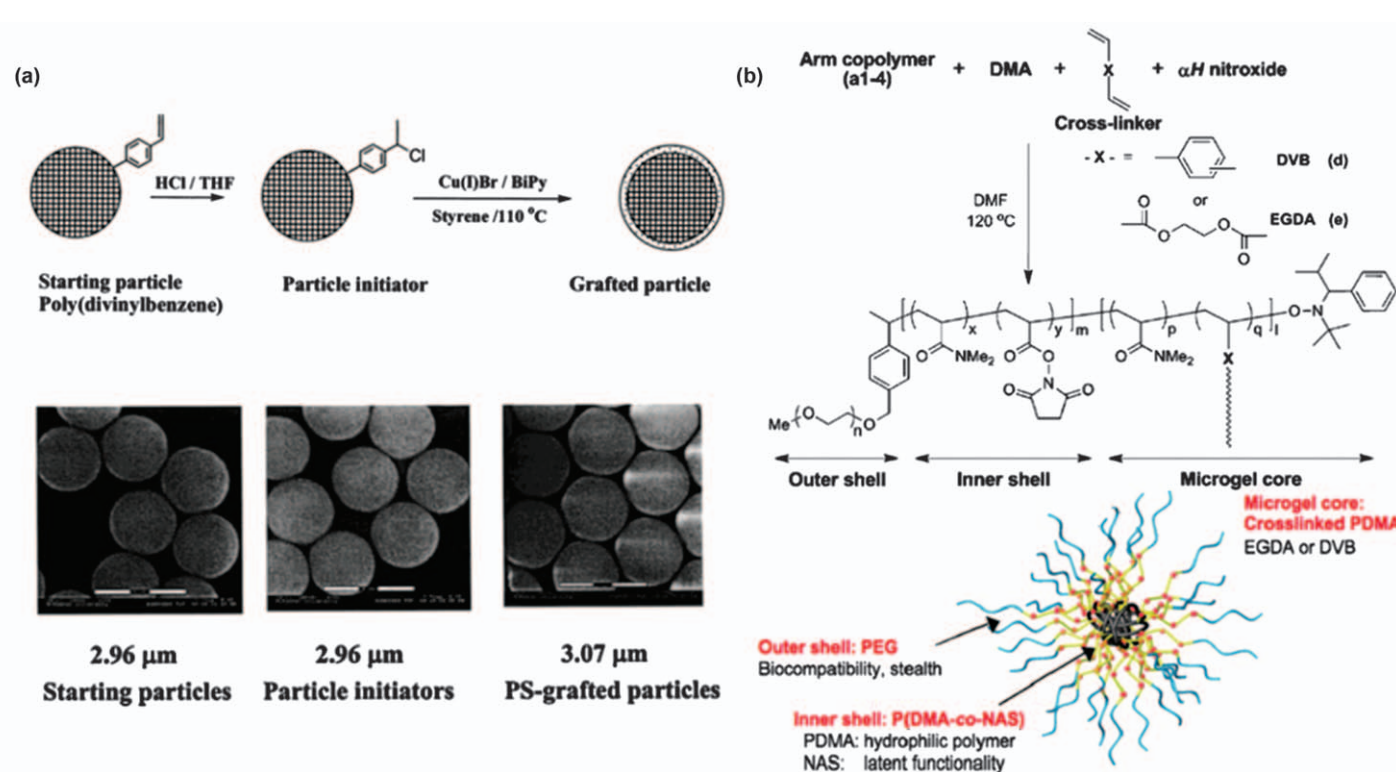


**Figure 2.4** (a) ATRP from initiated PDVB-80 to obtain a PS outer layer and the corresponding SEM images of starting particles, particle initiators and polystyrene-grafted particles. Reproduced from ref. 51 with permission from American Chemical Society, Copyright © 2002. (b) NMP synthetic process and structure model. Adapted from ref. 53 with permission from American Chemical Society, Copyright 2008.

### 2.2.2.3 RAFT

RAFT polymerization involves a series of reversible addition-fragmentation steps based on the transfer of a moiety, *e.g.*, dithioester, between active and dormant species. Either conventional free radical initiators (usually an azo-initiator such as AIBN, 2,2-dimethoxy-2-phenylactopheneone (DMPA)), or RAFT agents can be grafted onto the surface of particles to conduct surface-initiated polymerization. Huang *et al.* reported the grafting of PS from the surface of BaTiO<sub>3</sub> by an *in situ* RAFT polymerization to obtain core–shell structured BaTiO<sub>3</sub>/PS nanocomposites (Figure 2.5a).<sup>54</sup> BaTiO<sub>3</sub> NPs were treated with H<sub>2</sub>O<sub>2</sub> to provide an amount of -OH groups. Then a certain amount of free RAFT agent activated *N*-hydroxysuccinimide-*S*-1-ethyl-*S'*-( $\alpha,\alpha'$ -dimethyl- $\alpha''$ -acetic acid) trithiocarbonate (NHS-EDMAT) and styrene was added to the system to control the polymerization. TEM images in Figure 2.5b and c suggested that a higher monomer concentration contributed to a thicker shell. To conclude, not only was the additional functionality successfully conferred to the spheres by grafting from the surface of the cores, but also the size could be tailored by changing the feed ratio.

RAFT works with a range of conventional radical polymerization monomers and can be carried out in various experimental conditions, such as in bulk, solution or emulsion. As an enticing approach to functionalization of a solid, conceptually, the nature of the polymer shell allows for a great versatility. Feng and co-workers grafted poly(*N*-acryloxsuccinimide) (PNAS) onto mesoporous silica (MS) through RAFT to achieve intelligent polymer coated nanocomposites (PNAS-MS).<sup>55</sup> MCM-41-type mesoporous silica particles were used as nanocontainers for the attachment of chain transfer agent to the pore outlets. RAFT polymerization occurred when AIBN was introduced into the system. In Figure 2.5e and f, a uniform, thick polymer coating shell can be observed around the silica particle after grafting, which would work as an on-off switch in response to redox signals. In view of the omission of a metal catalyst in RAFT polymerization and the versatility of monomers, it provides a promising synthesis, especially for biosensors and *in vivo* site-specific drug delivery.

### 2.2.2.4 Other Polymerization Techniques

Ionic, metal-catalyzed and UV- or photo-induced polymerizations are other types of surface-initiated polymerization in the manner of core–shell construction. Ballauff *et al.* prepared well-defined poly(*N*-isopropylacrylamide) (PS-PNIPA) core–shell particles using photoemulsion polymerization (Figure 2.6a).<sup>56</sup> The PS cores were covered by a thin layer of the photo initiator 2-[*p*-(2-hydroxy-2-methylpropiophenone)]-ethylene glycol methacrylate (HMEM). Shining light onto a suspension of these particles could thereby generate radicals on the surface for further photo-emulsion polymerization of cross-linked *N*-isopropyl-acrylamide (NIPA) chains. TEM images of PS@PNIPA in Figure 2.6b show that a homogeneous and regular PNIPA shell was affixed on the spherical PS core as well as the desired monodispersity.

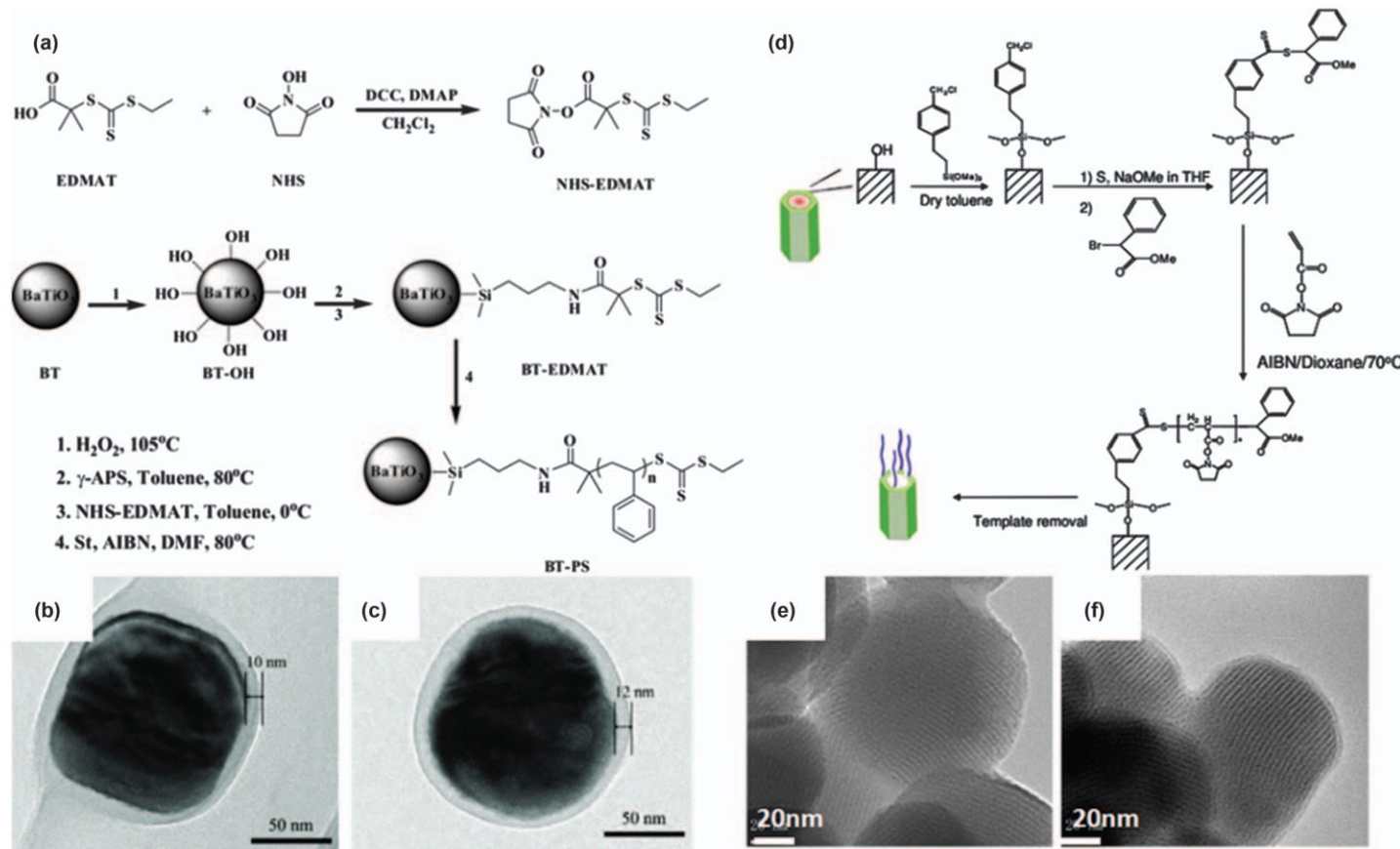


**Figure 2.5** (a) Illustration of the synthesis of activated RAFT agent NHS-EDMA and preparation of core–shell nanocomposites *via* RAFT. (b, c) TEM images of core–shell structure with monomer increased. Reproduced from ref. 54 with permission from John Wiley and Sons, Copyright © 2012 WILEY-VCH Verlag GmbH & Co. KGaA, Weinheim. (d) The synthesis of PNAS-MS. (e, f) TEM images of MCM-41 and PNAS-MS core–shell nanoparticles. Reproduced from ref. 55 with permission from American Chemical Society, Copyright 2008.

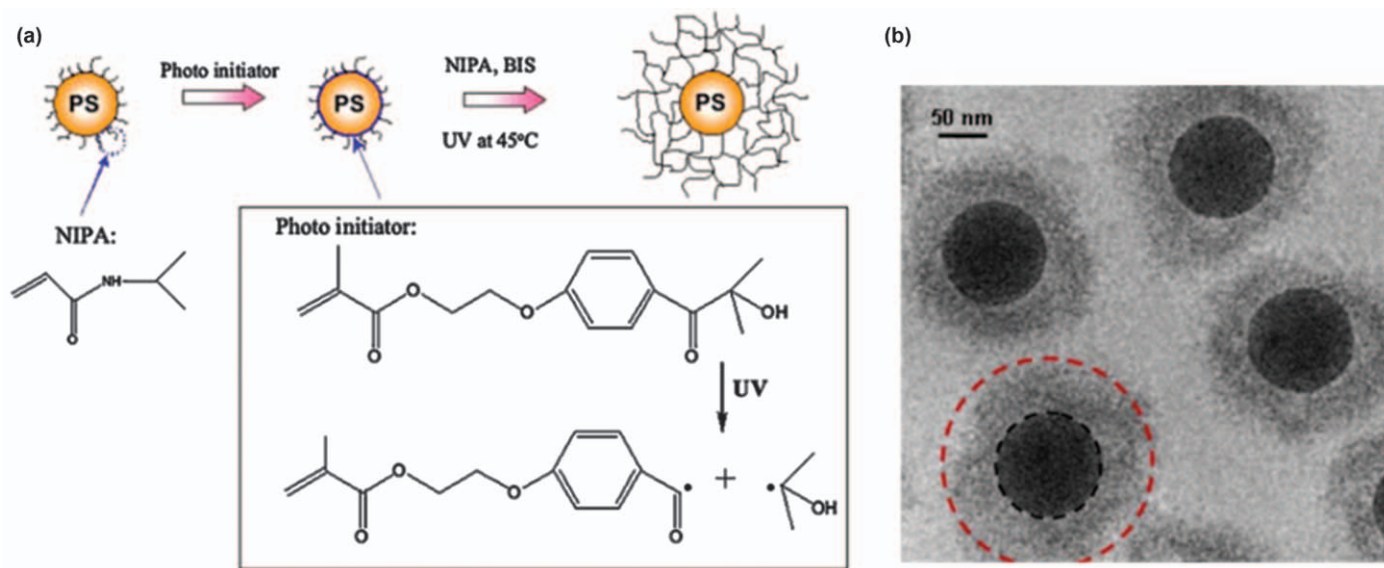


**Figure 2.6** (a) Schematic representation of the preparation of PS@PNIPA core-shell particles by photo-emulsion polymerization and (b) TEM images of PS@PNIPA core-shell particles.

Reproduced with permission from ref. 56 with permission from John Wiley and Sons, Copyright © 2006 WILEY-VCH Verlag GmbH & Co. KGaA, Weinheim.

## 2.3 Polymer Deposition

A coating can be constructed and deposited atop a substrate of almost any composition or topology lying on complementary affinities from polymer molecules. The fabrication methods rely on different mechanisms to form coatings on substrates, including *in situ* formation of resin or polydopamine coating, covalent linkages and supramolecular assemblies of bio-polymer coatings, and electrostatic interactions between layered materials.

### 2.3.1 Resin or Polydopamine Coating

Stöber method is a classical synthetic approach of a silica sphere and coating, in which the hydrolysis and condensation of silica precursors such as tetraethylorthosilicate (TEOS) occur in a solvent of alcohol, water and ammonia at room temperature.<sup>57–60</sup> Resorcinol-formaldehyde (RF) or phenol-formaldehyde (PF) resin nanospheres have been synthesized by a protocol analogous to the silicate sol-gel process. Interest has been generated by the excellent properties of the extension of the Stöber coating in the fabrication of core resin/polymer shell nanostructures with a smooth surface and a controllable shell thickness. For example, Yu and co-workers reported a facile one-pot route for the large-scale synthesis of mono-core and multi-core/shell silver-PF nanospheres with controlled particle size.<sup>61</sup> A mono-core/shell structure was prepared as a result of the parallel reduction of silver NPs by formaldehyde (HCHO) and *in situ* polymerization of phenol and HCHO around silver NPs. The size of core–shell spheres is related to phenol-to-hexamethylenetetramine (HMT) molar ratio. In addition, multi-core/shell spheres were produced from high starting concentrations of AgNO<sub>3</sub>.

Fuertes and co-workers developed a one-step synthesis of highly monodisperse silica enveloped within RF polymer (SiO<sub>2</sub>@RF) under Stöber conditions<sup>62</sup> (Figure 2.7a), which amplified the formation mechanism. NH<sub>4</sub><sup>+</sup> ions aggressively covered the negatively charged Stöber silica spheres, while, OH<sup>-</sup> ions catalyzed the slower reaction between resorcinol and formaldehyde to form hydroxymethyl-substituted species, which diffused onto the NH<sup>4+</sup> modified silica particles through electrostatic interaction. These species condensed within the nanospace of the silica particles to create RF polymeric layers (Figure 2.7b). Furthermore, internal cavities could be generated within the RF shell by dissolving the silica core of the SiO<sub>2</sub>@RF sphere (Figure 2.7c). The one-step fabrication of core–shell nanospheres and related capsules immediately foreshadowed the possibility of simplifying the multiple coating process. For example, Priestley and co-workers reported an Ag, AgBr-silica-RF core–shell–shell (CSS) structure based on the simultaneous reduction of AgNO<sub>3</sub> and the polymerization of silica and RF from a one-step process.<sup>63</sup> Simply feeding AgNO<sub>3</sub>, TEOS, resorcinol and formaldehyde into hexadecyl trimethyl ammonium bromide (CTAB) in an alcohol and aqueous ammonia mixture constructed a CSS architecture (Figure 2.7d). The CSS

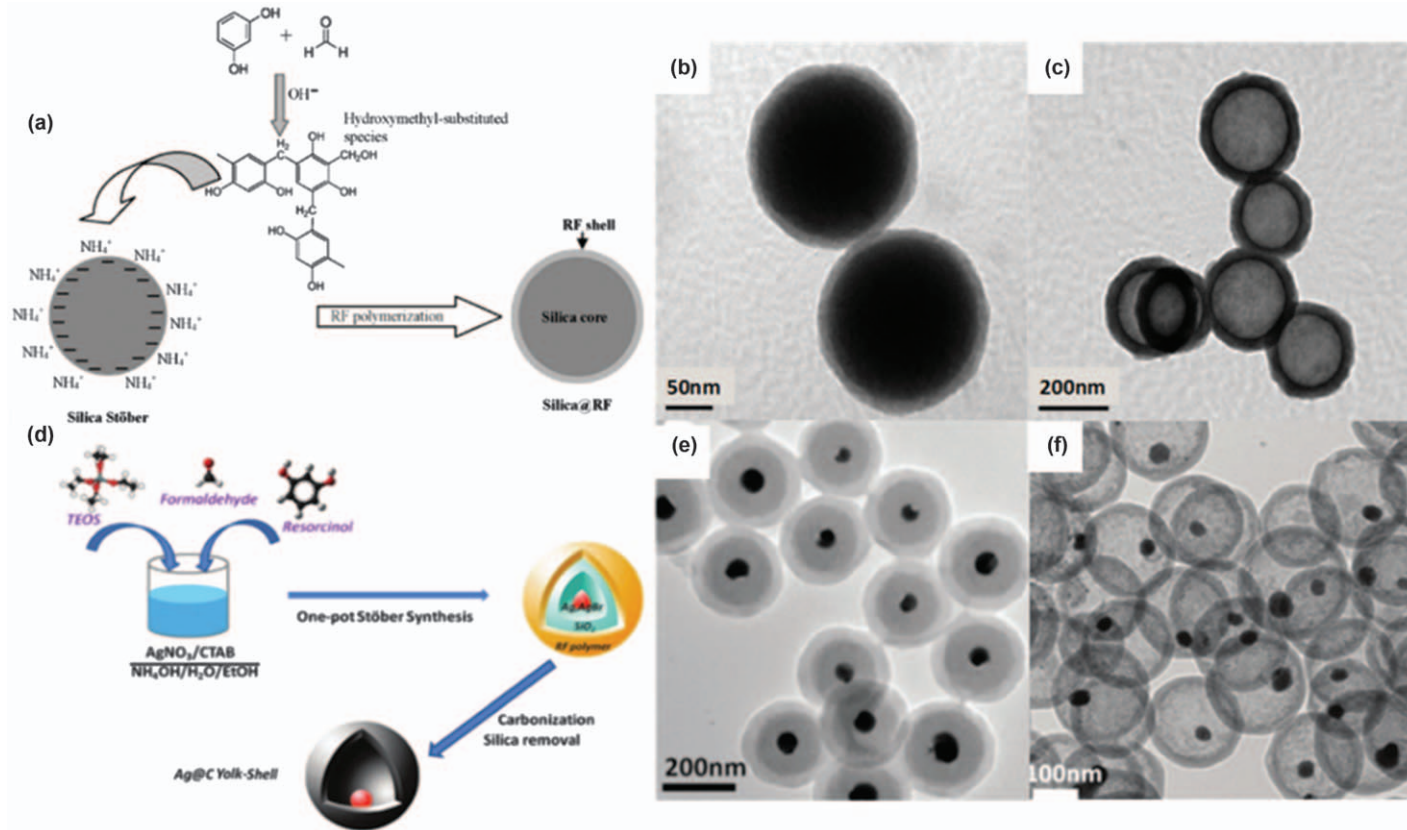


**Figure 2.7** (a) Synthesis scheme for the formation of silica@RF spheres. TEM images of (b) SiO<sub>2</sub>@RF core-shell particles and (c) RF hollow capsules. Reproduced from ref. 62 with permission from the Royal Society of Chemistry. (d) One-pot Stöber Synthesis of Ag, AgBr-SiO<sub>2</sub>-RF core-shell-shell and Ag@C yolk shell nanoparticle. TEM images of (e) Ag, AgBr-SiO<sub>2</sub>-RF and (f) Ag@C yolk shell nanoparticles after carbonization and etching silica, respectively. Reproduced from ref. 63 with permission from the Royal Society of Chemistry.

structure of these particles is obvious from the TEM image in Figure 2.7e. In addition, Ag@carbon yolk–shell spheres can be easily derived through carbonization of the composite and etching silica, which is vital for extended applications in catalysis (Figure 2.7f).

Polydopamine (PDA) is another type of surface engineered coating to obtain core–shell topology, which is exclusively carried out in aqueous solution. Inspired by the adhesive proteins in mussels, Messersmith *et al.* proposed an adherent PDA coating approach, where dopamine (DA) containing both catechol and amine functional groups self-polymerizes at weakly alkaline pH values. The thickness of the PDA layer could be simply controlled by varying the dopamine concentration or reaction time.<sup>64</sup> This approach has been demonstrated as a straightforward functionalizable platform for immobilization atop a series of materials, including nanocarbon, metal particles and cells.<sup>65–67</sup> Priestley *et al.* prepared Fe<sub>3</sub>O<sub>4</sub>@PDA core–shell nanoparticles through the classical PDA coating method. They further exploited the fascinating properties of Fe<sub>3</sub>O<sub>4</sub>@PDA as a metal catalyst support, carbon adsorbent and drug carrier (Figure 2.8a–b).<sup>68</sup> Deng *et al.* developed a simple technique for the preparation of nanoscale PDA-encapsulated porous sulfur (S@PDA) core–shell nanospheres as cathodes for lithium–sulfur batteries (Figure 2.8c).<sup>69</sup> Monodispersed porous sulfur spheres were prepared through the reaction of sodium thiosulfate (Na<sub>2</sub>S<sub>2</sub>O<sub>3</sub>) with hydrochloride acid (HCl) in the presence of polyvinylpyrrolidone (PVP). The PDA-coated sulfur nanocomposites could then be obtained through *in situ* self-polymerization of PDA in aqueous solution (pH = 8.2) for 1 h. From the TEM image in Figure 2.8d the PDA shell was measured to be ~20 nm thick and the sulfur core was about 500 nm in diameter.

### 2.3.2 Biopolymer Coating

A number of interesting physicochemical phenomena can be observed in the range of ubiquitous natural entities, such as proteins, bacteria and polysaccharides, which show that these biopolymers are also capable of capturing target molecules effectively in proximity to the surface through a multiplex bonding mechanism.

Phase-transitioned lysozyme (PTL) coating makes use of superfast amyloid-like lysozyme assembly on a range of particle surfaces, from which a robust and biocompatible nanoscale film can be obtained. This method is widely applicable to various materials because of its general and multiplex surface binding affinity to virtually arbitrary material surfaces.<sup>70</sup> Yang and co-workers reported that the  $\alpha$ -helix of native lysozyme could assemble into a  $\beta$ -sheet structure to form amyloid-like assembled oligomers in a lysozyme buffer solution. These assembled oligomers would preferentially aggregate at the air/water interface to form a PTL-nanofilm. When macroscopic substrates were directly immersed and incubated in the PTL solution, PTL-nanofilms could be attached atop the substrates. The PTL coating is colorless and stable over a wide pH window ranging from 1 to 12. With this

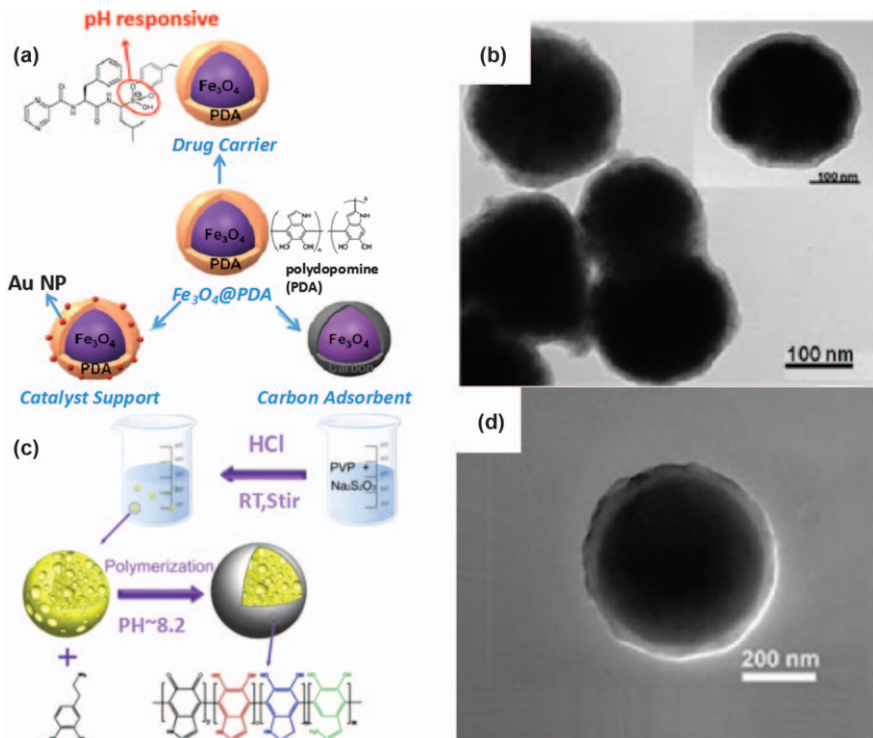


**Figure 2.8** (a)  $\text{Fe}_3\text{O}_4@PDA$  as a versatile NP platform and (b) TEM image of  $\text{Fe}_3\text{O}_4@PDA$  core–shell nanoparticles. Adapted from ref. 68 with permission from American Chemical Society, Copyright 2013. (c) Synthesis of S@PDA composites and (d) TEM image of S@PDA. Adapted from ref. 69 with permission from Elsevier, Copyright 2015.

strategy, the same group recently reported a PTL-shell coating on micro/nanoparticles (*e.g.*, PS,  $\text{SiO}_2$ , and metal particles) and extended this technique to prepare Janus particles and hollow capsules (Figure 2.9a).<sup>71</sup> Since the PTL nanofilm inherently includes a series of functional groups (*e.g.*  $-\text{NH}_2$ ,  $-\text{COOH}$ ,  $-\text{OH}$ ,  $-\text{SH}$ ,  $-(\text{CH})_n-\text{CH}_3$ , and aromatic rings), it can afford further modification. For instance, a continuous layer of Ag or Cu was successfully deposited on the surface of PS particles with PTL as the adhesion promotion layer between them, giving rise to Ag-coated PS particles. From this point, the PTL coating is important in offering a new generation of bio-inspired adhesives that harness the ability to couple the centre core strongly with the outer features.

A biopolymer shell can also be constructed by electrostatic interactions between oppositely charged molecules. The formation of an electrostatic complex is usually a reversible process and is influenced by variables such as pH and ionic strength. Chitosan is polycationic due to the presence of amino groups, which has been previously used to establish a secondary layer around negative charged particles, such as emulsion droplets and

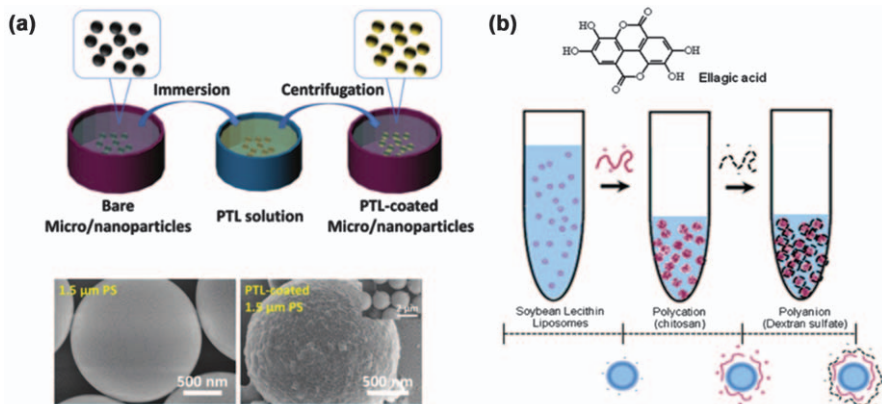


**Figure 2.9** (a) Schematic illustration of the PTL coating process on particles, SEM images of PS micro/nanoparticles before (left) and after (right) coating with the PTL film. Reproduced from ref. 71 with permission from John Wiley and Sons, © 2018 WILEY-VCH Verlag GmbH & Co. KGaA, Weinheim. (b) Chemical structure of ellagic acid and the process of preparing multi-layered biopolymer shell. Adapted from ref. 75 with permission from Elsevier, Copyright 2010.

biopolymeric particles.<sup>72</sup> Laye *et al.* mixed cationic chitosan solutions with anionic liposome suspensions produced by homogenizing 1% soy lecithin in acetate buffer to obtain stable dispersions of chitosan-coated food-grade liposomes.<sup>73</sup> Similarly, Santipanichwong *et al.* successfully prepared core-shell biopolymer particles using electrostatic deposition of an anionic polysaccharide (beet pectin) onto cationic heat-denatured protein  $\beta$ -lactoglobulin [ $\beta$ -lg].<sup>74</sup> These biopolymer-coated particles were freed from aggregation when the pH value was in the range 4 to 6 or even in NaCl solution, indicating the possibility of protecting functional food components (*i.e.*, aspeptide, protein or nutraceutical). Likewise, Madrigal-Carballo *et al.* prepared biopolymer-coated liposomes by adding cationic (chitosan) and anionic (dextran sulphate) biopolymers to a suspension of anionic liposomes (soybean lecithin) under carefully controlled solution compositions. Furthermore, ellagic acid was loaded onto the liposome core during the process to evaluate the release capability (Figure 2.9b).<sup>75</sup>

### 2.3.3 Layer-by-layer Deposition

Layer-by-layer (LbL) methodology is a bottom-up strategy for the construction of core–shell structures by building up multi-layered films on various templates. A prominent feature is the electrostatic attraction between oppositely charged surfaces of alternating layers of polyelectrolytes.<sup>76</sup> Components with distinct structures can be intimately and harmoniously combined within LbL assembled nanofilms. Accordingly, LbL has rapidly

emerged as a versatile methodological platform for core–shell products. Caruso and co-workers have reported the deposition of polymer multi-layers atop enzymes with positive charge. Polyelectrolyte layers, such as negatively charged polystyrenesulfonate (PSS) and positively charged poly(allylamine hydrochloride) (PAH), were deposited sequentially through the surface charge reversal that occurred upon adsorption of each layer.<sup>77</sup> As another example, PS particles covered with polyelectrolyte (PE) multi-layer films were prepared through LbL assembly of poly(diallyldimethylammonium chloride) (PDDA) and poly(sodium 4-styrenesulfonate) (PSS) in NaCl aqueous solution.<sup>78</sup> TEM images directly showed discernible changes between the uncoated and coated PE shell on PS particles (Figure 2.10a). Similarly, negatively charged polyacrylic acid (PAA) combined with the positively charged PAH also gave core–shell formation *via* this route.<sup>76</sup>

Apart from the frequently used electrostatic interactions, other molecular interactions have also been developed to construct core–shell architectures using the LbL assembly technique. For example, Huang *et al.* reported a core–corona structure with a raspberry-like polymer composite using a hydrogen interaction mechanism.<sup>79</sup> Small poly(ethylene glycol dimethacrylate-*co*-acrylic acid) (poly(EGDMA-*co*-AA)) microspheres effectively self-assembled on poly(ethylene glycol dimethacrylate-*co*-4-vinylpyridine) (poly(EGDMA-*co*-VPy)) surfaces through an affinity complex between the carboxylic acid and pyridine groups. Caruso's group reported a versatile and robust coating method using one-step assembly of coordination complexes on various substrates (Figure 2.10b). The natural polyphenol tannic acid (TA) and Fe(<sup>III</sup>) were chosen as the organic ligand and the inorganic cross-linker to make TA-Fe coordination layers.<sup>80</sup>

Host–guest interaction is another force that can be chosen to fabricate LbL multi-layer assemblies.<sup>81</sup> Ma and co-workers reported the engineering of

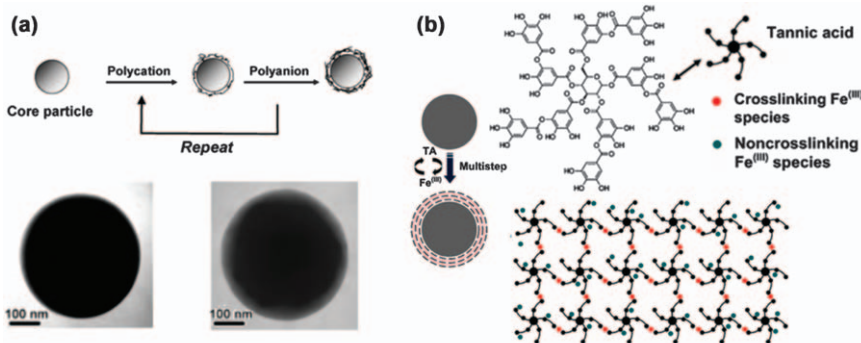


**Figure 2.10** (a) Multi-layer film formation on a PS core achieved by LbL and TEM images of the uncoated and coated particles. Adapted from ref. 78 with permission from American Chemical Society, Copyright 2004. (b) Illustration showing the coordination interaction modes of TA and Fe(<sup>III</sup>) for LbL coatings. Reproduced ref. 80, <https://doi.org/10.1021/cm403903m>, with permission from American Chemical Society, Copyright 2014.

core–shell nanospheres by interaction between a host macromolecule and a guest substance.<sup>82</sup>  $\beta$ -cyclodextrin ( $\beta$ -CD) with a hydrophilic block was selected as the host unit for a link with another hydrophilic segment, such as a diblock hydrophilic co-polymer, polyethylene glycol-*b*-polycyclodextrin (PEG-*b*-PCD) or hydrophobic small molecules. Based on the different solubilization effects of various cyclodextrins ( $\alpha$ ,  $\beta$  or  $\gamma$ ) in a broad range of hydrophobic compounds, these could be developed into novel types of universal nanocarriers. But it should be emphasized that host–guest interactions demand explicit recognition provided by selective interactions between the host cavities and corresponding guest molecules.<sup>83</sup>

## 2.4 Self-assembly

A feature of amphiphilic block co-polymers is the simplicity with which they can form ordered nanoscale structures under special circumstances. Self-assembly is the preferred method for providing access to core–shell morphology through purely physical forces (noncovalent forces). The advantage of omitting washing steps or reducing synthetic steps has created huge interest.

### 2.4.1 Co-precipitation

A selective solvent will preferentially dissolve one part of the molecule (comprising both hydrophobic and hydrophilic parts) over another. As a result, the hydrophobic segment is shielded from the solvent in the core of the structure whereas the hydrophilic part primarily dissolves in the solvent. Co-precipitation involving the spontaneous self-assembly of inorganic NPs and amphiphilic block co-polymers in a selective solvent is a method for locking the preformed inorganic NPs into polymer micelles to form core–shell colloids. Taton *et al.* synthesized  $\gamma\text{-Fe}_2\text{O}_3$ @polymer core–shell nanostructures from the co-assembly of magnetic particles and PS<sub>250</sub>-*b*-PAA<sub>13</sub> co-polymer (Figure 2.11a).<sup>84</sup> The block co-polymer and oleic acid-stabilized  $\gamma\text{-Fe}_2\text{O}_3$  were dissolved in the corresponding good solvents *N,N*-dimethylformamide (DMF) and tetrahydrofuran (THF). The anti-solvent water (H<sub>2</sub>O) was then added gradually into the mixture to desolvate both the particles and the hydrophobic polymer block simultaneously. It was observed that the hydrophobic PS block from PS<sub>250</sub>-*b*-PAA<sub>13</sub> enveloped the hydrophobic NPs through hydrophobic–hydrophobic interactions. In addition, the average number of encapsulated particles per micelle could be controlled by varying the starting concentrations of NPs and block co-polymer. Au NPs, single-walled carbon nanotubes and other inorganic materials have been functionalized using a similar approach.<sup>85</sup> Subtly tuning interactions between the inorganic NPs and corona blocks, such as the composition of the block co-polymers, the functional ligands on the inorganic NPs or the environmental conditions, may remodel self-assembled structures. For example, Park and co-workers have studied the influence of

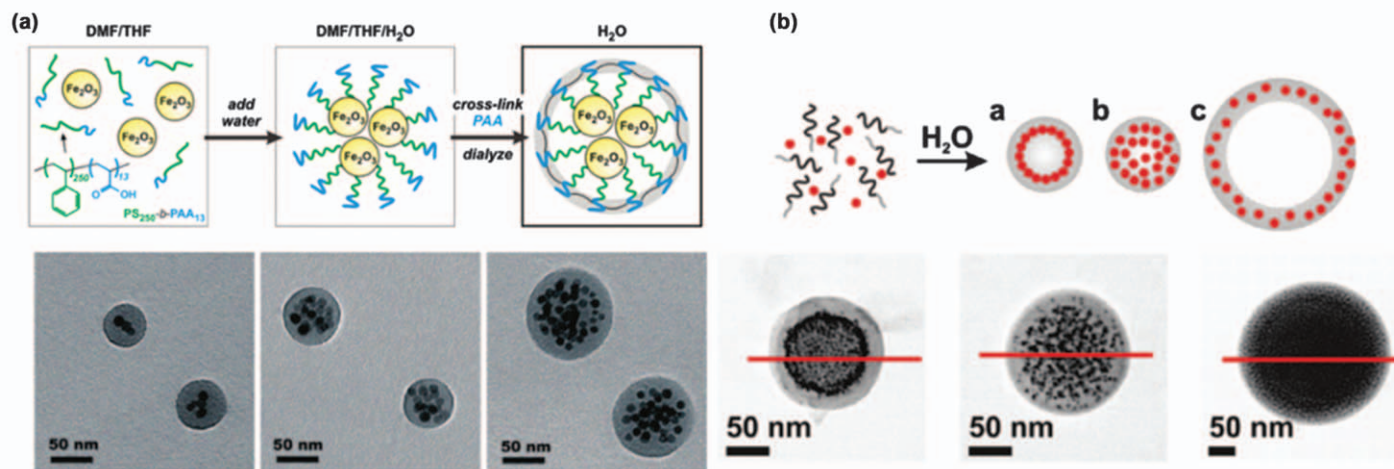


**Figure 2.11** (a) Schematic illustration and TEM of co-precipitation of PS-*b*-PAA and Fe<sub>2</sub>O<sub>3</sub> NPs. Adapted from ref. 84 with permission from American Chemical Society, Copyright 2005. (b) Self-assemble of nanoparticles and block co-polymers for three different morphologies, as well as the corresponding TEM images. Adapted from ref. 86 with permission from American Chemical Society, Copyright 2011.

solvent/polymer combinations on the final structures.<sup>86</sup> Figure 2.11b depicts three different morphologies of nanoparticle-polymer assemblies: (i) polymersomes with NPs packed in the wall (magneto-polymersomes), (ii) core-shell assemblies with NPs radially arranged at the interface between the polymer core and the shell (magneto-core/shell) and (iii) polymer micelles with NPs homogeneously incorporated (magneto-micelles). It was revealed that the overall morphology and the NP arrangement in the polymer matrix could be precisely tuned by parameters, such as the relative volume ratio between the hydrophobic block and the hydrophilic blocks of the amphiphilic block co-polymer, solvent and the intimate NP-polymer interaction.

Apart from the aforementioned solvent exchange process, solvent evaporation is another co-precipitation process for the generation of self-assembled core–shell structures. Due to the physical generality of the formation mechanism, this evaporation method opened up a wide variety of polymers, particularly block polymers, for constructing complex structures (*i.e.*, one-dimensionally stacked lamellar, Janus and core–shell structures). For example, Yabu and co-workers prepared fine-sized PS NPs by means of evaporating the volatile THF from a PS solution containing both a poor (water) and a good solvent (THF).<sup>87</sup> The same group used amphiphilic block co-polymer stabilized Au micelles as templates to prepare Au NPs/polymer composite particles. In relation to the solvent evaporation process, the solution of polymer (*e.g.*, polyisobutylene (PIB), PS or polymethylmethacrylate (PMMA)) was mixed with block co-polymer-stabilized Au NPs in THF. The different hydrophobicity of these homopolymers led to three different self-assembled structures, including: (i) a core–shell particle with Au NPs in the shell (Figure 2.12a), (ii) a Janus structure with Au NPs located only in one domain (Figure 2.12b) and (iii) a core–shell structure with Au NPs congregating in the core (Figure 2.12c).<sup>88</sup> Light-absorbing dyes, paramagnetic particles and other functional materials were introduced into similar polymer composite particles.<sup>89</sup>

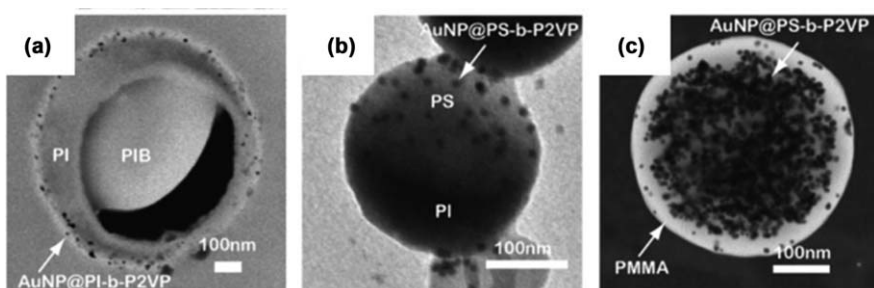


**Figure 2.12** TEM images of Au/polymer composite NPs produced by evaporating THF from different mixed solutions.

Adapted from ref. 88 with permission from John Wiley and Sons, Copyright © 2010 WILEY-VCH Verlag GmbH & Co. KGaA, Weinheim.

## 2.4.2 Flash NanoPrecipitation (FNP)

FNP is a rapid self-assembly technique using a small chamber, such as a multi-inlet vortex (MIV) or confined impinging jets (CIJ) mixer to create NPs of uniform size ranging from 30 to 800 nm.<sup>90</sup> In general, two high velocity linear jets of fluid, *i.e.*, one containing the block co-polymer solution and the other containing a non-solvent for the polymer, will be expelled manually from two different syringes into a chosen reservoir. Depending on the rapid super saturation after mixing, the polymer swiftly assembles and precipitates into NPs. Note that the process has facile-operation, high reproducibility and low energy consumption. The particle size can be precisely controlled *via* changing the polymer and/or the electrolyte concentration.<sup>91</sup> In particular, the technique successfully tackled the possibility of engulfing active components within polymers that have distinctive solubility properties. Prud'homme *et al.* reported the co-encapsulation of hydrophobic organic actives ( $\beta$ -carotene) and inorganic Au NPs into poly(ethylene glycol)-block-poly( $\epsilon$ -caprolactone) (PEG-*b*-PCL) using FNP in a four-stream vortex mixer.<sup>92</sup> In Figure 2.13a, hydrophobic Au NPs in conjunction with  $\beta$ -carotene and PEG-*b*-PCL were dissolved in THF. A custom-designed MIV mixer

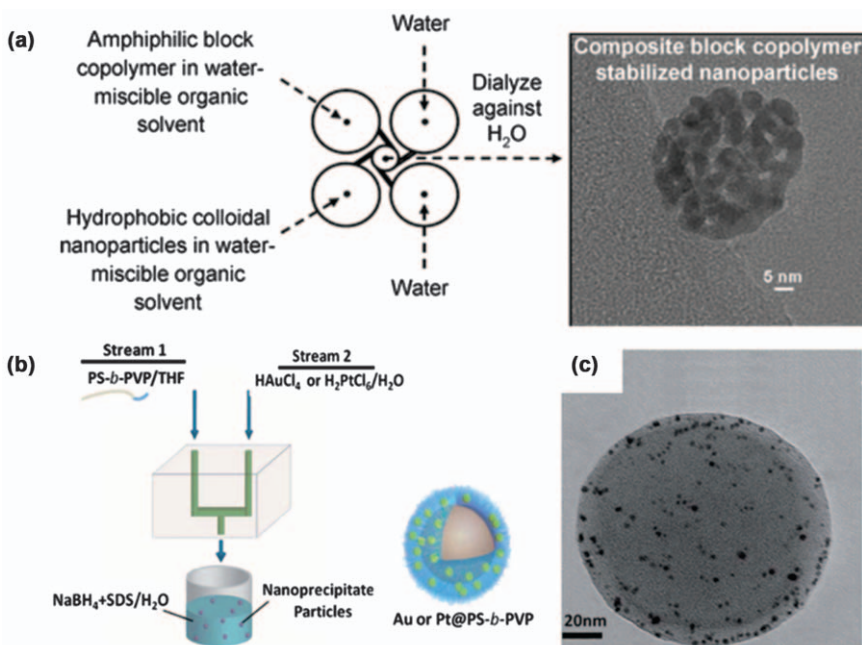


**Figure 2.13** (a) Preparation of multi-component core–shell nanoparticles *via* FNP in a MIV and corresponding TEM image. Adapted from ref. 92 with permission from American Chemical Society, Copyright 2008. (b) Schematic process of FNP to produce metal@PS-*b*-PVP. (c) TEM image of Au@PS-*b*-PVP. Adapted from ref. 95 with permission from the Royal Society of Chemistry.

afforded the mixture with an anti-solvent of H<sub>2</sub>O and precipitation of all hydrophobic components, including Au NPs, β-carotene and the hydrophobic block of PEG-*b*-PCL. Sterically, β-carotene was encapsulated, in conjunction with Au NPs, within the cores of PEG-*b*-PCL shells. Likewise, magnetic and quantum dot, photo-sensitizer and organic dye NPs have also been encapsulated into co-polymers by FNP.<sup>93,94</sup>

On the other hand, an outer layer of inorganic NPs attached to polymer NPs can be obtained through FNP. Priestley *et al.* prepared Au NPs decorated polymer core–shell particles with tunable overall particle size and metal nanoparticle arrangement.<sup>95</sup> As schematically showed in Figure 2.13b, a syringe containing polystyrene-*b*-poly(4-vinylpyridine) (PS-*b*-PVP) dissolved in THF was placed at the inlet of stream 1, and a syringe containing HAuCl<sub>4</sub> in H<sub>2</sub>O was placed at the inlet of stream 2. These two streams were merged into a mixing stream and then diluted into a water medium containing NaBH<sub>4</sub> and sodium dodecyl sulfate (SDS). The AuCl<sub>4</sub><sup>−</sup> ions converted into Au seeds due to the reducing capability of NaBH<sub>4</sub> and grew within the PVP layer to form stable Au@PS-*b*-PVP composites NPs (Figure 2.13c). Likewise, Liu and co-workers successfully prepared other metal (*e.g.*, Ag, Pt) NPs loaded atop co-polymer NPs through the same methodology.<sup>96,97</sup>

#### 2.4.3 Microfluidics

Microfluidics concerns small (from 10<sup>−18</sup> to 10<sup>−9</sup> liter) volumes of fluids, whose appendix channels have dimensions from tens to hundreds of micrometers. Self-assembly is preceded by a mixing step that rapidly distributes the reactant molecules within a microreactor. It ordinarily requires the generation of single- or multi-phase emulsions, *e.g.*, W/O/W (water/oil/water), O/O/W and O/W/O emulsions. Subsequent solidification or gelling of these droplets yields core–shell particles, which are carried toward the outlet of the reactor.<sup>98–101</sup> Michael *et al.* fabricated monodisperse poly(lactic-co-glycolic acid) (PLGA)-alginate core–shell microspheres by using a capillary microfluidic device. A schematic diagram is illustrated in Figure 2.14a: fluids of three phases were guided into the microfluidic device to generate PLGA-alginate double emulsion droplets,<sup>102</sup> specifically, a PLGA solution in dichloromethane (DCM) containing rifampicin, a polyvinyl alcohol (PVA) solution containing alginate and toluene containing span 80. They were used as the inner oil phase, middle aqueous phase and outer oil phase, respectively. After mixing, the double emulsion droplets were collected in a beaker containing calcium chloride solution to cross-link the alginate shell layer.

Alternatively, the self-assembly of core–shell structures can be triggered in a reactor by radiation/high temperature, or by the diffusion of reactants to the locus of targeted cores. Fleischmann *et al.* fabricated a core–shell elastomer containing liquid crystalline elastomer (LCE) shells filled with a liquid core in a designed microfluidic set-up (Figure 2.14b).<sup>103</sup> The microfluidic device comprised a triple-channel: a concentric cylindrical glass

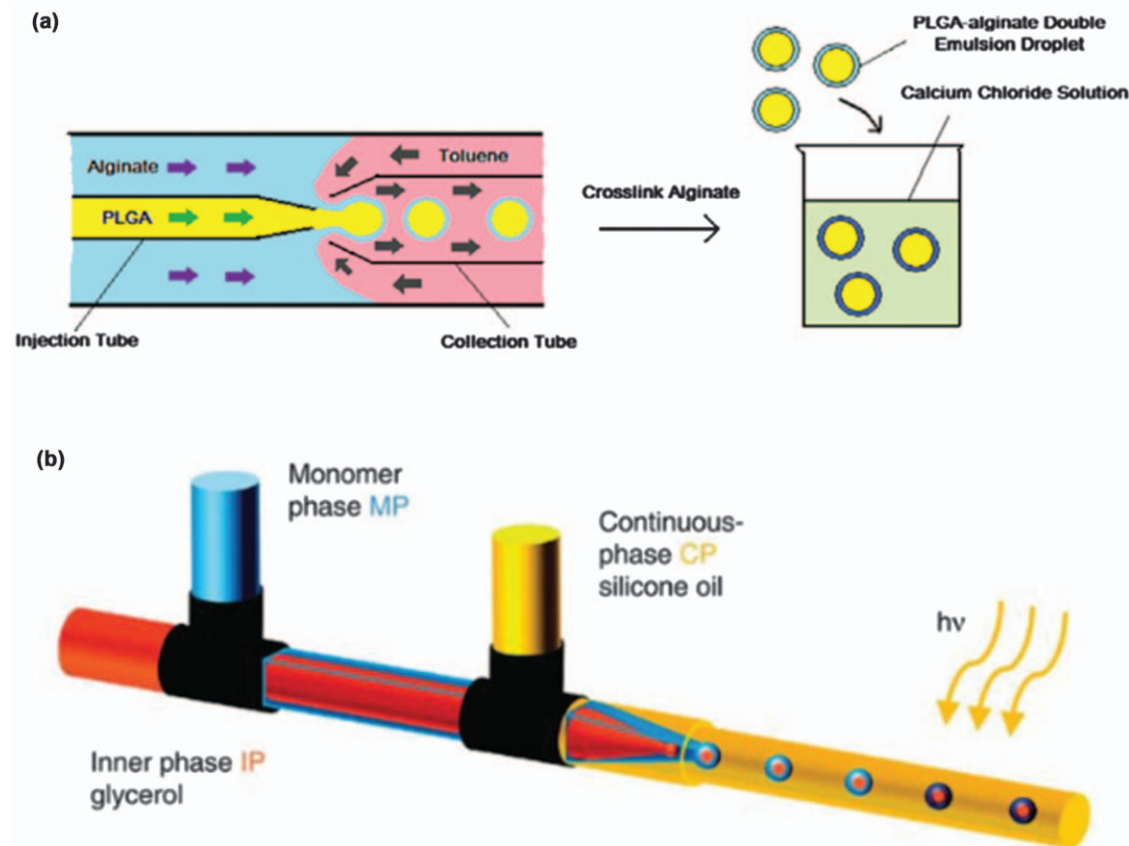


**Figure 2.14** (a) Fabrication process of PLGA-alginate core-shell microspheres. Adapted from ref. 102 with permission from Elsevier, Copyright 2013. (b) Preparation of core-shell elastomers through microfluidics in a designed reactor. Reproduced from ref. 103 with permission from Springer Nature, Copyright 2012.

micropipette containing the LC monomer (blue), a tapered square glass capillary containing glycerol (red) and an outer cylindrical glass micropipette containing silicone oil (yellow). The low viscosity of the monomer in its high-temperature isotropic phase made it easily continuous in a microfluidic device for the formation of the core–shell particles. Glycerol droplets encapsulated by a monomer shell were then placed into silicone oil. This co-flow microfluidic geometry allowed good control of the preparation of core–shell particles, and avoided coalescence of the particles until they were photo-polymerized downstream.

## 2.5 Electro-spraying/Jetting

### 2.5.1 Electro-spraying

The electro-spraying process involves an external electrical field of high voltage and a coaxial set-up. During electrospraying, micro/nano-sized solids directly reach the receptor, accompanied by the quick solvent evaporation of the charged droplets and the entrapment of targeted materials (such as drugs and cells). One outstanding feature is the ability to tune the size and morphology of the generated droplets by optimizing the overall physical/chemical properties of the precursor solution and processing parameters (e.g., flow rate, external voltage). Wu and co-workers prepared core–shell structured polymeric particles with protein as the core and an amphiphilic biodegradable polymer as the shell.<sup>104</sup> Figure 2.15a described the single-step electrospraying process. PCL-PPE-EA [poly(e-caprolactone)-polyamino-ethyl ethylene phosphate] was used as the amphiphilic polymer. Aqueous protein was dispersed drop by drop into a dichloromethane (DCM) solution containing PCL-PPE-EA co-polymer to produce a water-in-oil (W/O) emulsion, which was then electrosprayed and delivered onto a collector. The electro-sprayed PCL-PPE-EA polymeric core–shell spherical particles had rather smooth surfaces and uniform size distribution. Additionally, this process hints at an innovative way of constructing core–shell polymeric particles, which enables hydrophilic and hydrophobic parts to be ideally randomly distributed.<sup>105–107</sup>

### 2.5.2 Electro-jetting

Electro-jetting is a cost effective and versatile technique to optimize core–shell particles on an industrial scale. As an electro-hydrodynamic process, it is governed by the interactions between the electrostatic repulsion induced by an applied electric field and the polymer concentration to guarantee a liquid droplet.<sup>108,109</sup> Daniel and co-workers reported a type of alginate-based hydrogel microcapsule with core–shell structures using a two-fluid co-axial electro-jetting system.<sup>110</sup> As shown in Figure 2.15b, the shell fluid consisted of a cell-free alginate solution while the core fluid contained the cell aggregates or therapeutic cells. Under an electrostatic force, microdroplets

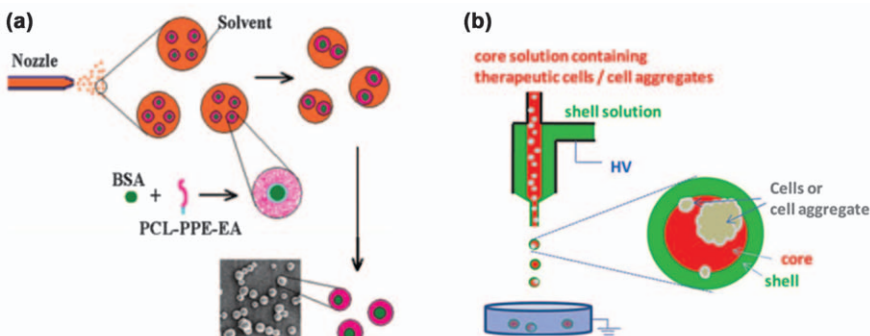


**Figure 2.15** (a) Schematic representation of the formation of core–shell structured particles through electro-spraying an emulsion solution. Adapted from ref. 104 with permission from John Wiley and Sons, Copyright © 2013 WILEY-VCH Verlag GmbH & Co. KGaA, Weinheim. (b) Schematic depictions of two-fluid co-axial electro-jetting for core–shell capsules and cell encapsulation. Reproduced from ref. 110 with permission from the Royal Society of Chemistry.

with core–shell structures were formed and dropped into the gelling bath. The composition and thickness of both the core and the shell were adjustable by the material selection and their respective flow rates. Analogous to electro-jetting, coaxial electro-spinning is another electro-hydrodynamic method for manufacturing core–shell materials, especially preferred in one-dimensionally arranged nanofibers.<sup>111</sup>

## 2.6 Conclusion

In this review we have discussed different synthetic routes that are capable of creating an explicit polymer-based core–shell morphology with sizes ranging from a few nanometers to micrometers. The strategies included: (i) the attachment of particular polymer chains onto the surface of functionalized cores (“grafting to”) and the surface-initiated polymerization of monomer from reactive seeded cores (“grafting from”); (ii) direct deposition or LbL coating; (iii) self-assembly approaches and (iv) electro-spraying/jetting. By using the different synthesis methods, functional NPs or polymers can be located in a particular configurable structure, which in turn changes or adjusts the properties of the whole materials.

Whilst assorted approaches to fabricating core–shell structures have been outlined, there are nevertheless crucial concerns to be taken into account. It is advisable for the research community to rationally evaluate the advantages and disadvantages of various methods with a view to improving its future burgeoning developments. Note that most current grafting methodologies often require stringent experimental conditions. Ideally avoiding organic solutions, metal catalysts or tedious purification processes is a great benefit for environmental concerns. At this point, ionic

liquid, an environmentally friendly, nontoxic and nonaqueous solvent is of technological interest.<sup>112–115</sup>

The development of new coating layer has become of great importance with the emergence of promising versatile materials. Among them, diverse coordination polymers appear to be broadly compatible and suggest several potentially fruitful avenues for constructing complex polymer networks as thin films or coatings on particle surfaces.<sup>116–118</sup> Regarding self-assembly, it is challenging to find a feasible, commercially viable way to produce various functional core-shell polymer NPs. The continuous self-assembly process seems to have a major advantage in industrial scale production.<sup>119,120</sup> For example, using continuous flow in the current FNP geometry would enable production of 3.5 kg day<sup>-1</sup> of NPs and scale-up is possible from laboratory apparatus to industrial continuous production at 1400 kg day<sup>-1</sup>.<sup>91</sup>

The engrossing core-shell types of polymer have the advantage of unlimited applicability in versatile areas, such as biomedicine, imaging and chemical sensing, and catalytic applications. Meanwhile, more chemical or physical transformation mechanisms are emerging that will expand the scope of innovative preparation. From these perspectives, stimulating challenges for the creation of core-shell polymer-based NPs with different compositions as well as properties in practical utilization still await us, while huge efforts are being elicited for versatile approaches with the hope of promoting commercial merit and industrial scalability.

## Acknowledgements

We would like to acknowledge the National Natural Science Foundation of China (Grant No. 21774095).

## References

1. G. M. Odegard, T. C. Clancy and T. S. Gates, *Polymer*, 2005, **46**, 553.
2. D. Qian, W. K. Liu and R. S. Ruoff, *Compos. Sci. Technol.*, 2003, **63**, 1561.
3. A. Bajaj, O. R. Miranda, I. B. Kim, R. L. Phillips, D. J. Jerry, U. H. F. Bunz and V. M. Rotello, *PNAS*, 2009, **106**, 10912.
4. H. Zhang, J. Han and B. Yang, *Adv. Funct. Mater.*, 2010, **20**, 1533.
5. J. S. Smith, D. Bedrov and G. D. Smith, *Compos. Sci. Technol.*, 2003, **63**, 1599.
6. P. K. Sudeep and T. Emrick, *Polym. Rev.*, 2007, **47**, 155.
7. A. K. Khan, B. C. Ray and S. K. Dolui, *Prog. Org. Coat.*, 2008, **62**, 65.
8. R. H. Ottewill, A. B. Schofield, J. A. Waters and N. S. J. Williams, *Colloid Polym. Sci.*, 1997, **275**, 274.
9. C. D. Jones and L. A. Lyon, *Macromolecules*, 2000, **33**, 8301.
10. B. Mandal, H. Bhattacharjee, N. Mittal, H. Sah, P. Balabathula, L. A. Thoma and G. C. Wood, *Nanomed. Nanotechnol.*, 2013, **9**, 474.
11. Y. Lu, Y. Mei, M. Drechsler and M. Ballauff, *Angew. Chem. Int. Ed. Engl.*, 2006, **45**, 813.

12. L. He, Y. Liu, J. Liu, Y. Xiong, J. Zheng, Y. Liu and Z. Tang, *Angew. Chem., Int. Ed.*, 2013, **52**, 3741.
13. X. Sun and Y. Li, *Angew. Chem. Int. Ed. Engl.*, 2004, **116**, 607.
14. F. Zhang, R. C. Che, X. M. Li, C. Yao, J. P. Yang, D. K. Shen, P. Hu, W. Li and D. Y. Zhao, *Nano Lett.*, 2012, **12**, 2852.
15. X.-l. Zhang, H.-y. Niu, W.-h. Li, Y.-l. Shi and Y.-q. Cai, *Chem. Commun.*, 2011, **47**, 4454.
16. H. H. Park, K. Woo and J. P. Ahn, *Sci. Rep.*, 2013, **3**, 1497.
17. X. Lai, J. Li, B. A. Korgel, Z. Dong, Z. Li, F. Su, J. Du and D. Wang, *Angew. Chem., Int. Ed.*, 2011, **50**, 2738.
18. T. Li, J. Moon, A. A. Morrone, J. J. Mecholsky, D. R. Talham and J. H. Adair, *Langmuir*, 1999, **15**, 4328.
19. S. Balakrishnan, M. J. Bonder and G. C. Hadjipanayis, *J. Magn. Magn. Mater.*, 2009, **321**, 117.
20. R. A. Caruso, A. Susha and F. Caruso, *Chem. Mater.*, 2001, **13**, 400.
21. S. Shi, Y. Yu, T. Wang, Q.-M. Wang, C. Wang and S.-I. Kuroda, *Chin. J. Polym. Sci.*, 2014, **32**, 524.
22. Z. Xiong, L. Zhang and X. S. Zhao, *Chem. – Eur. J.*, 2014, **20**, 14715.
23. J. Chen, R. Zhang, L. Han, B. Tu and D. Zhao, *Nano Res.*, 2013, **6**, 871.
24. J. Du, J. Qi, D. Wang and Z. Tang, *Energy Environ. Sci.*, 2012, **5**, 6914.
25. J.-M. Yan, X.-B. Zhang, T. Akita, M. Haruta and Q. Xu, *J. Am. Chem. Soc.*, 2010, **132**, 5326.
26. K. M. Ho, W. Y. Li, C. H. Wong and P. Li, *Colloid Polym. Sci.*, 2010, **288**, 1503.
27. H. N. Yow and A. F. Routh, *Soft Matter*, 2006, **2**, 940.
28. R. Ghosh Chaudhuri and S. Paria, *Chem. Rev.*, 2011, **112**, 2373.
29. O. J. Cayre, N. Chagneux and S. Biggs, *Soft Matter*, 2011, **7**, 2211.
30. Y. Wang, X. W. Teng, J. S. Wang and H. Yang, *Nano Lett.*, 2003, **3**, 789.
31. H. Chen, J. Gao, M. Ruan, J. Shi and D. Yan, *Microporous Mesoporous Mater.*, 2004, **76**, 209.
32. K. Zhang, H. T. Chen, X. Chen, Z. M. Chen, Z. C. Cui and B. Yang, *Macromol. Mater. Eng.*, 2003, **288**, 380.
33. K. N. Jayachandran and P. R. Chatterji, *J. Macromol. Sci., A*, 1998, **35**, 1971.
34. F. Meng, G. H. Engbers and J. Feijen, *J. Biomed. Mater. Res., Part A*, 2004, **70**, 49.
35. Y. B. Wang, Q. G. Du and J. L. Huang, *Macromol. Rapid Commun.*, 1998, **19**, 247.
36. R. Liu, P. Liao, J. Liu and P. Feng, *Langmuir*, 2011, **27**, 3095.
37. J.-F. Lutz, *Angew. Chem., Int. Ed.*, 2007, **46**, 1018.
38. C. Chowdhury, S. B. Mandal and B. Achari, *Tetrahedron Lett.*, 2005, **46**, 8531.
39. P. L. Golas, N. V. Tsarevsky, B. S. Sumerlin and K. Matyjaszewski, *Macromolecules*, 2006, **39**, 6451.
40. A. S. Goldmann, A. Walther, L. Nebhani, R. Joso and D. Ernst, *Macromolecules*, 2009, **42**, 3707.

41. D. R. Breed, R. Thibault, F. Xie, Q. Wang, C. J. Hawker and D. J. Pine, *Langmuir*, 2009, **25**, 4370.
42. G. L. Li, D. Wan, K. G. Neoh and E. T. Kang, *Macromolecules*, 2010, **43**, 10275.
43. J. Xu, J. Wang, M. Mitchell, P. Mukherjeeet, M. Jeffries-EL and Z. Q. Lin, *J. Am. Chem. Soc.*, 2007, **129**, 12828.
44. J. Ye, Y. Hou, G. Z. Zhangand and C. Wu, *Langmuir*, 2008, **24**, 2727.
45. M. Q. Zhu, L. Q. Wang, G. J. Exarhosand and A. D. Q. Li, *J. Am. Chem. Soc.*, 2004, **126**, 2656.
46. A. Olivier, F. Meyer, J.-M. Raquez, P. Damman and P. Dubois, *Prog. Polym. Sci.*, 2012, **37**, 157.
47. S. Edmondson, V. L. Osborne and W. T. Huck, *Chem. Soc. Rev.*, 2004, **33**, 14.
48. K. Matyjaszewski, *Macromolecules*, 2012, **45**, 4015.
49. T. Pintauer and K. Matyjaszewski, *Chem. Soc. Rev.*, 2008, **37**, 1087.
50. T. Von Werne and T. E. Patten, *J. Am. Chem. Soc.*, 1999, **121**, 7409.
51. G. D. Zheng and H. D. H. Stover, *Macromolecules*, 2002, **35**, 6828.
52. B. Bailly, A. C. Donnenwirth, C. Bartholom, C. Bartholome and E. Beyou, *J. Nanomater*, 2006, **2006**, 10.
53. K.-i. Fukukawa, R. Rossin, A. Hagooly, E. D. Pressly, J. N. Hunt, B. W. Messmore, K. L. Wooley, M. J. Welch and C. J. Hawker, *Biomacromolecules*, 2008, **9**, 1329.
54. K. Yang, X. Y. Huang, L. Y. Xie and P. K. Jiang, *Macromol. Rapid. Commun.*, 2012, **33**, 1922.
55. R. Liu, X. Zhao, T. Wu and P. Y. Feng, *J. Am. Chem. Soc.*, 2008, **130**, 14418.
56. Y. Lu, A. Wittemann, M. Ballauff and M. Drechsler, *Macromol. Rapid Commun.*, 2006, **27**, 1137.
57. J. Chen, R. Zhang, L. Han, B. Tu and D. Zhao, *Nano Res.*, 2013, **6**, 871.
58. R.-P. Ye, L. Lin, J.-X. Yang, M.-L. Sun, F. Li, B. Li and Y.-G. Yao, *J. Catal.*, 2017, **350**, 122.
59. J. Liu, S. Z. Qiao, H. Liu, J. Chen, A. Orpe, D. Zhao and G. Q. Lu, *Angew. Chem. Int. Ed.*, 2011, **50**, 5947.
60. Q. Yao, Z.-H. Lu, Z. Zhang, X. Chen and Y. Lan, *Sci. Rep.*, 2014, **4**, 7597.
61. S.-R. Guo, J.-Y. Gong, P. Jiang, M. Wu, Y. Lu and S.-H. Yu, *Adv. Funct. Mater.*, 2008, **18**, 872.
62. A. B. Fuertes, P. Valle-Vigón and M. Sevilla, *Chem. Commun.*, 2012, **48**, 6124.
63. R. Liu, Y. W. Yeh, V. H. Tam, F. Qu, N. Yao and R. D. Priestley, *Chem. Commun.*, 2014, **50**, 9056.
64. H. Lee, S. M. Dellatore, W. M. Miller and P. B. Messersmith, *Science*, 2007, **318**, 426.
65. Y. Tian, Y. Cao, Y. Wang, W. Yang and J. Feng, *Adv. Mater.*, 2013, **25**, 2980.
66. W. Wei, H. Liang, K. Parvez, X. Zhuang, X. Feng and K. Müllen, *Angew. Chem., Int. Ed.*, 2014, **53**, 1570.

67. Z. Xia, Z. Lin, Y. Xiao, L. Wang, J. Zheng, H. Yang and G. Chen, *Biosens. Bioelectron.*, 2013, **47**, 120.
68. R. Liu, Y. Guo, G. Odusote, F. Qu and R. D. Priestley, *ACS Appl. Mater. Interfaces*, 2013, **5**, 9167.
69. Y. Deng, H. Xu, Z. Bai, B. Huang, J. Su and G. Chen, *J. Power Sources*, 2015, **300**, 386.
70. D. Wang, Y. Ha, J. Gu, Q. Li, L. Zhang and P. Yang, *Adv. Mater.*, 2016, **28**, 7414.
71. R. R. Liu, J. Zhao, Q. Han, X. Hu, D. Wang, X. Zhang and P. Yang, *Adv. Mater.*, 2018, **30**, 1802851.
72. M. Thibault, M. Astolfi, N. Tran-Khanh, M. Lavertu, V. Darras, A. Merzouki and M. D. Buschmann, *Biomaterials*, 2011, **32**, 4639.
73. C. Laye, D. J. McClements and J. Weiss, *J. Food Sci.*, 2008, **73**, N7.
74. R. Santipanichwong, M. Suphantharika, J. Weiss and D. J. McClements, *J. Food Sci.*, 2008, **73**, N23.
75. S. Madrigal-Carballo, S. Lim, G. Rodriguez, A. O. Vila, C. G. Krueger, S. Gunasekaran and J. D. Reed, *J. Funct. Foods*, 2010, **2**, 99.
76. F. X. Xiao, M. Pagliaro, Y. J. Xu and B. Liu, *Chem. Soc. Rev.*, 2016, **45**, 3088.
77. F. Caruso, D. Trau, H. Mohwald and R. Renneberg, *Langmuir*, 2000, **16**, 1485.
78. K. Katagiri and F. Caruso, *Macromolecules*, 2004, **37**, 9947.
79. G. Li, X. Yang, F. Bai and W. Huang, *J. Colloid Interface Sci.*, 2006, **297**, 705.
80. M. A. Rahim, H. Ejima, K. L. Cho, K. Kempe, M. Müllner, J. P. Best and F. Caruso, *Chem. Mater.*, 2014, **26**, 1645.
81. B. Andrade, Z. Song, J. Li, S. C. Zimmerman, J. Cheng, J. S. Moore, K. Harris and J. S. Katz, *ACS Appl. Mater. Interfaces*, 2015, **7**, 6359.
82. J. Zhang and P. X. Ma, *Angew. Chem.*, 2009, **121**, 982.
83. J. X. Zhang, H. L. Sun and P. X. Ma, *ACS Nano*, 2010, **4**, 1049–1059.
84. B. S. Kim, J. M. Qiu, J. P. Wang and T. A. Taton, *Nano Lett.*, 2005, **5**, 1987.
85. Y. Kang and T. A. Taton, *Angew. Chem., Int. Ed.*, 2005, **44**, 409.
86. R. J. Hickey, A. S. Haynes, J. M. Kikkawa and S. J. Park, *J. Am. Chem. Soc.*, 2011, **133**, 1517.
87. H. Yabu, T. Higuchi, K. Ijiro and M. Shimomura, *Chaos*, 2005, **15**, 047505.
88. H. Yabu, K. Koike, K. Motoyoshi, T. Higuchi and M. Shimomura, *Macromol. Rapid Commun.*, 2010, **31**, 1267.
89. Y. Chen, J. Cho, A. Young and T. A. Taton, *Langmuir*, 2007, **23**, 7491.
90. B. K. Johnson and R. K. Prud'homme, *AIChE J.*, 2003, **49**, 2264.
91. C. Zhang, V. J. Pansare, R. K. Prud'homme and R. D. Priestley, *Soft Matter*, 2012, **8**, 86.
92. M. E. Gindy, A. Z. Panagiotopoulos and R. K. Prud'homme, *Langmuir*, 2008, **24**, 83.

93. H. D. Lu, T. L. Lim, S. Javitt, A. Heinmillerand and R. K. Prud'homme, *ACS Comb. Sci.*, 2017, **19**, 397.
94. J. N. Shan, S. J. Budijono, G. H. Hu, N. Yao, Y. B. Kang, Y. G. Ju and R. K. Prud'homme, *Adv. Funct. Mater.*, 2011, **21**, 2488.
95. R. Liu, C. Sosa, Y.-W. Yeh, F. Qu, N. Yao, R. K. Prud'homme and R. D. Priestley, *J. Mater. Chem. A*, 2014, **2**, 17286.
96. Y. Z. He, B. J. Wang, X. X. Hu, L. Sun, R. Liu and R. D. Priestley, *Colloid Polym. Sci.*, 2017, **295**, 521.
97. M. M. Liu, J. Zhao, R. D. Priestley, W. Teng and R. Liu, *Colloids. Surf., A*, 2018, **552**, 118.
98. A. Abou-Hassan, O. Sandre and V. Cabuil, *Angew. Chem., Int. Ed.*, 2010, **49**, 6268.
99. S. Marre and K. F. Jensen, *Chem. Soc. Rev.*, 2010, **39**, 1183.
100. W. Wang, M. J. Zhang and L. Y. Chu, *Acc. Chem. Res.*, 2014, **47**, 373.
101. W. Wang, M. J. Zhang and L. Y. Chu, *Curr. Opin. Pharmacol.*, 2014, **18**, 35.
102. J. Wu, T. Kong, K. W. K. Yeung, H. C. Shum, K. M. C. Cheung, L. Wang and M. K. T. To, *Acta Biomater.*, 2013, **9**, 7410.
103. E.-K. Fleischmann, H.-L. Liang, N. Kapernaum, F. Giesselmann, J. Lagerwall and R. Zentel, *Nat. Commun.*, 2012, **3**, 1178.
104. Y. Wu, I. C. Liao, S. J. Kennedy, J. Du, J. Wang, K. W. Leong and R. L. Clark, *Chem. Commun.*, 2010, **46**, 4743.
105. L. Cao, J. Luo, K. H. Tu, L. Q. Wang and H. L. Jiang, *Colloid Surf., B*, 2014, **115**, 212.
106. S. T. Zhao, P. Agarwal, W. Rao, H. S. Huang, R. L. Zhang, Z. G. Liu, J. H. Yu, N. Weisleder, W. J. Zhang and X. M. He, *Integr. Biol.*, 2014, **6**, 874–884.
107. Y. Mao, C. J. Li, P. Ge, F. J. Wang and L. Wang, *Molecular and Cellular Biomechanics*, 2018, vol. 15, p. 143.
108. Y. Chen, Z. L. Yue, S. E. Moulton, P. Hayes and G. G. Wallace, *J. Mater. Chem. B*, 2015, **3**, 7255.
109. L. F. Yu, C. Ni, S. M. Grist and K. C. Cheung, *Biomed. Microdevices*, 2015, **17**, 33.
110. M. Ma, A. Chiu, G. Sahay, J. C. Doloff, N. Dholakia, R. Thakrar, J. Cohen, A. Vegas, D. Chen, K. M. Bratlie, T. Dang, R. L. York, J. Hollister-Lock, G. C. Weir and D. G. Anderson, *Adv. Healthcare Mater.*, 2013, **2**, 667.
111. A. L. Yarin, *Polym. Adv. Technol.*, 2011, **22**, 310.
112. J. Wang, C. Q. Yuan, Y. C. Han, Y. L. Wang, X. M. Liu, S. J. Zhang and X. H. Yan, *Small*, 2017, **13**, 1702175.
113. F. L. Zhou, L. M. Azofra, M. Ali, M. Kar, A. N. Simonov, C. McDonnell-Worth, C. H. Sun, X. Y. Zhang and D. R. MacFarlane, *Energy Environ. Sci.*, 2017, **10**, 2516–2520.
114. M. A. Gebbie, A. M. Smith, H. A. Dobbs, A. A. Lee, G. G. Warr, X. Banquy, M. Valtiner, M. W. Rutland, J. N. Israelachvili, S. Perkin and R. Atkin, *Chem. Commun.*, 2017, **53**, 1214–1224.

115. A. Strate, T. Niemann, D. Michalik and R. Ludwig, *Angew. Chem., Int. Ed.*, 2017, **56**, 496.
116. K. Liang, J. J. Richardson, C. J. Doonan, X. Mulet, Y. Ju, J. Cui, F. Caruso and P. Falcaro, *Angew. Chem., Int. Ed.*, 2017, **56**, 8510.
117. K. Liang, R. Ricco, C. M. Doherty, M. J. Styles, S. Bell, N. Kirby, S. Mudie, D. Haylock, A. J. Hill, C. J. Doonan and P. Falcaro, *Nat. Commun.*, 2015, **6**, 7240.
118. R. Ameloot, L. Stappers, J. Fransaer, L. Alaerts, B. F. Sels and D. De Vos, *Chem. Mater.*, 2009, **21**, 2580.
119. D. F. Liu, H. B. Zhang, S. Cito, J. Fan, J. Salonen, T. M. Sikanen and D. A. Weitz, *Nano Lett.*, 2017, **17**, 606.
120. W. S. Saada and R. K. Prud'homme, *Nano Today*, 2016, **11**, 212.

## CHAPTER 3

# *Flash Nano-precipitation and -complexation to Produce Polymer Colloids*

VICTORIA E. LEE,<sup>a</sup> DOUGLAS M. SCOTT,<sup>a</sup>  
ROBERT K. PRUD'HOMME<sup>a</sup> AND RODNEY D. PRIESTLEY<sup>\*a,b</sup>

<sup>a</sup> Department of Chemical and Biological Engineering, Princeton University, Princeton, NJ 08540, USA; <sup>b</sup> Princeton Institute for the Science and Technology of Materials, Princeton University, Princeton, NJ 08540, USA

\*Email: rpriestl@princeton.edu

### 3.1 Introduction

Polymeric nanoparticles and colloids have generated a great deal of interest for their realized and potential applications in a variety of fields.<sup>1,2</sup> Polymer colloids can be used to deliver therapeutics or imaging aids to specific targets in the body<sup>3–6</sup> or to probe biological responses to foreign objects.<sup>7</sup> Those which respond to chemical or physical stimuli can assemble to create nanocircuits or electronic displays,<sup>8,9</sup> and their propulsion behavior can give insights into the microrheology of their environment.<sup>10,11</sup> In other systems, immiscible mixtures can be compatibilized upon the introduction of polymer colloids which act as interfacial property modifiers.<sup>12,13</sup> Many of these applications require polymer colloids with anisotropic surface chemistries, complex internal morphologies, or specific surface charges. In order to be utilized in industrial applications, these colloids must be produced at large scale using an economical process.

Motivated by this array of applications, significant effort has been made in the last few decades to develop processes to produce such complex polymer colloids. Current techniques such as emulsion polymerization and microfluidic approaches can be used to reliably generate kilograms of material per day but can be limited in the range of sizes and complexity of the colloid morphologies that can be produced. Other processes such as masking or solvent exchange can generate more complex morphologies, but this is often at the expense of yield, requiring multiple time-consuming or chemistry-specific steps. Flash NanoPrecipitation (FNP) and Flash NanoComplexation (FNC) have recently emerged as promising platforms to generate complex polymer colloids on industrial scales with a high degree of flexibility. Operated in a continuous manner at room temperature, FNP is a solvent-exchange process based on the precipitation, nucleation, and agglomeration of polymer chains upon exposure to a poor solvent to produce monodisperse polymer colloids. Phase separation between different polymers and electrostatic interactions between components can be exploited to create internally-structured and hybrid polymer-inorganic colloids with simple changes to the process. Using the same equipment, FNC relies on the electrostatic complexation of oppositely-charged polymers upon mixing to form polymer colloids, instead of the precipitation and aggregation behavior of polymer chains.

In this chapter, we will introduce the fundamental concepts behind the FNP and FNC processes as well as discuss practical considerations for their use. We will also review examples of polymer colloids generated by these processes, highlighting the variety of polymer colloid morphologies which can be produced from these economical and scalable processes and their utility in a variety of applications.

## 3.2 The Flash NanoPrecipitation Process

Flash NanoPrecipitation has been used to prepare polymer colloids of a wide range of sizes, compositions, and morphologies. It is particularly attractive as a processing platform as it can be scaled up from the lab bench to industrial production while product attributes can be controlled by making simple adjustments to a set of process parameters.<sup>14–16</sup> In the following sections, we review the dynamics of polymer chain collapse and particle stabilization as well as the equipment and material properties to consider when performing FNP.

### 3.2.1 Polymer Collapse, Nucleation, and Aggregation

The formation of colloids *via* FNP is enabled by the collapse, nucleation, and aggregation of individual polymer chains upon a change in solvent quality. When the polymer feed stream and the anti-solvent stream are rapidly mixed, the polymer is suddenly placed under high supersaturation conditions, thereby inducing chain collapse into globules which each act as a nucleation point. In traditional crystallization theory, fluctuations in the

concentration of molecular species result in the formation of nuclei. In such systems, the nucleation rate,  $J$ , is defined in eqn (3.1):

$$J = A \exp\left(\frac{-\Delta G_{\text{cr}}}{kT}\right) \quad (3.1)$$

where  $A$  is a constant,  $k$  is Boltzmann's constant,  $T$  is the absolute temperature, and  $\Delta G_{\text{cr}}$  is the critical free energy for nucleation, comprising the energy required to form an interface and the free energy of the bulk phase.<sup>17</sup> This critical free energy can be defined in terms of the supersaturation, surface tension, and solute properties to result in eqn (3.2):

$$J = A \exp\left(\frac{-16\pi\gamma^3\nu^2}{3k^3T^3(\ln(S))^2}\right) \quad (3.2)$$

in which  $\gamma$  is the surface tension,  $\nu$  is the molar volume, and  $S$  is the supersaturation ratio of the solute. From eqn (3.2), it can be seen that the nucleation rate increases as the solution supersaturation increases.<sup>18</sup> The formation of nuclei results in a drop in the solute concentration and a halt to the formation of new nuclei. The individual polymer globules then diffuse and aggregate until stabilization occurs. Low levels of supersaturation or inhomogeneous mixing result in the formation of polydisperse particles as uniform nucleation may not occur. Fast mixing, on the order of a few milliseconds, is therefore essential to create high supersaturation and uniform nucleation conditions which produce monodisperse polymer colloids.<sup>19</sup> These short mixing times are a critical feature of the FNP process, and millisecond mixing times have been confirmed using known reaction kinetics as benchmarks (see Characteristic Times of the FNP Process for more detail).<sup>20</sup>

Each of the nuclei that forms upon mixing is composed of a single collapsed polymer chain. The Flory theory can be used to relate the radius of gyration,  $R_g$ , of this collapsed polymer chain to its degree of polymerization,  $N$ , in different solvent conditions.<sup>21,22</sup> Before mixing, when polymer chains are dissolved in a good solvent at dilute concentrations, the interactions between the polymer and the solvent are thermodynamically favorable. This results in an extended and swollen chain conformation, such as that shown in Figure 3.1a, in which  $R_g$  is proportional to  $N$  according to eqn (3.3):

$$R_g \sim N^{0.588} \quad (3.3)$$

In a poor solvent, however, the interactions between the polymer chain and the solvent are less favorable and the polymer collapses in on itself to form a globule, such as that in Figure 3.1b, with a new relation between  $R_g$  and  $N$  according to eqn (3.4):

$$R_g \sim N^{1/3} \quad (3.4)$$

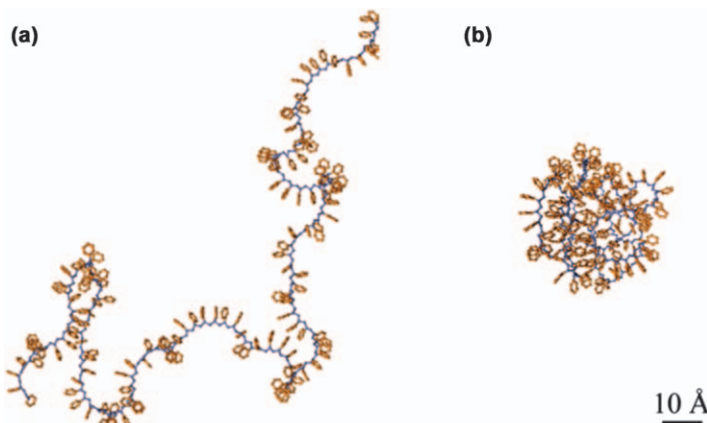


**Figure 3.1** Polystyrene chain conformation in good solvent conditions (a) and poor solvent conditions (b).

Adapted from ref. 22 with permission from American Chemical Society, Copyright 2018.

It will be shown in Section 3.3.1 that for rapid mixing conditions, the size of homopolymer colloids formed *via* FNP scales with polymer concentration according to a power law with an exponent of approximately 0.30. This indicates that the number of polymer chains in each colloid is proportional to the polymer concentration in the mixture and that the process is growth-controlled under these conditions rather than nucleation-controlled.

In some cases, an amphiphilic block copolymer is used to form a protective shell, or corona, around the colloid core. This is advantageous for certain applications, for instance in medical applications where a corona of polyethylene glycol (PEG) can lengthen circulation in the bloodstream and prevent protein adsorption.<sup>23–25</sup> The amphiphilic block copolymers are incorporated in the feed stream with the other polymeric components and experience the same change in solvent quality upon rapid mixing with the anti-solvent stream, leading to the collapse of one block of the copolymer. From here, the adsorption of the partially-collapsed block copolymers atop the collapsed polymer globule nuclei follows adsorption kinetics with two stages.<sup>26,27</sup> The first fast stage involves diffusion of the block copolymer to the nucleus surface and continues until an overlapping brush layer forms on the surface of the particles. This first stage is followed by a second, slower stage in which further adsorption of block copolymers is limited by the ability of the block copolymers to penetrate the adsorbed overlapping brush layer. The brush density can be controlled by tuning the percent of core material in the system and varies between two regimes. In the mushroom regime, block copolymer chains act as if they were free chains in solution at the particle surface. In the more dense brush regime, the block copolymer chains are more crowded at equilibrium and are stretched to create a thicker layer at the interface.<sup>28,29</sup> With or without amphiphilic block copolymers, the

aggregation of the collapsed polymer chains continues as they diffuse through the solvent until stabilization conditions are met. The mechanism of stabilization has been found to depend on the polymers and solvent system used, and the various forces at work will be discussed in Section 3.2.3.

## Characteristic Times of the FNP Process

The rapid mixing time,  $\tau_{\text{mix}}$ , and the particle formation time,  $\tau_{\text{flash}}$ , are important parameters of the FNP process (Figure 3.2).<sup>32</sup> When multiple components are incorporated in the process,  $\tau_{\text{flash}}$  can be broken down into the times for each of the components to nucleate and grow. For example, when a core material is being encapsulated and stabilized by an amphiphile,  $\tau_{\text{flash}}$  consists of the time for nucleation and growth of the core material,  $\tau_{\text{ng}}$ , and the aggregation time of the amphiphilic stabilizer,  $\tau_{\text{agg}}$ . When these two timescales are matched by tuning the properties of the amphiphilic block copolymer, the block copolymer can adsorb on the surface of the growing core material.<sup>28</sup> Similarly, if two hydrophobic polymers with similar dynamics are incorporated in the feed stream, they can interact to form internally-structured colloids.<sup>30,31</sup>

One key to creating monodisperse polymer colloids using the FNP process is to achieve uniform and homogeneous nucleation, in which the effect of the mixing time is minimized. This is the case when mixing is rapid and  $\tau_{\text{mix}}$  is smaller than  $\tau_{\text{flash}}$ . The Damköhler number,  $Da$ , is the ratio of these two values ( $\tau_{\text{mix}}/\tau_{\text{flash}}$ ), so this condition is met when  $Da < 1$ .

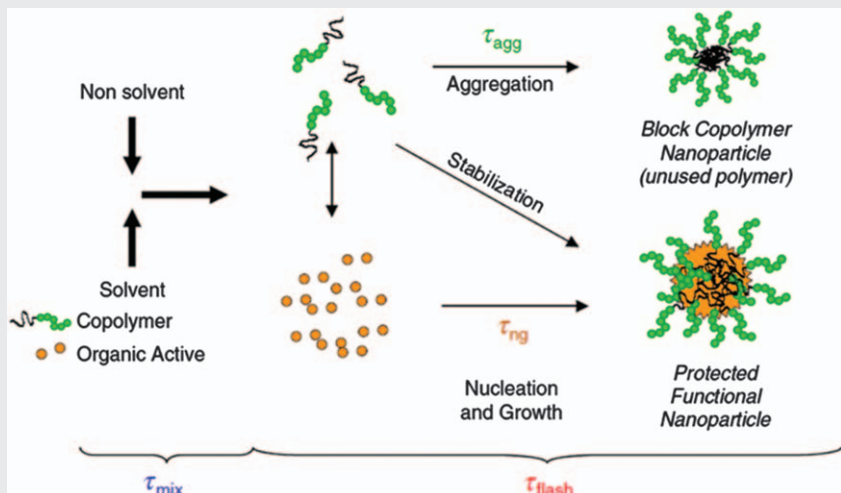


**Figure 3.2** Characteristic timescales involved in the formation of stabilized nanoparticles *via* FNP.

Reproduced from ref. 32 with permission from CSIRO Publishing.

This results in a ‘homogeneous’ starting condition which removes the effect of mixing time on the final particle properties. When  $Da > 1$  and mixing is slow, the particle formation is transport-controlled, and the particle size is a function of mixing speed. When  $Da = 1$  and the values of  $\tau_{mix}$  and  $\tau_{flash}$  are equal, the particle size ceases to be a function of the mixing rate.

To better understand the process and develop scaling laws for FNP, it was necessary to determine these characteristic times for different injection rates and mixer geometries. A set of competitive chemical reactions with known reaction rates was therefore used as a “chemical ruler” to determine the value of  $\tau_{mix}$ .<sup>20</sup> These reactions took place while the particles were in the process of forming, where the amount of one of the products could be measured. Because the initial concentrations and reaction rates were known for the reactions, the value of  $\tau_{mix}$  could then be calculated from the measured concentration of the reaction’s product. Further, the value of  $\tau_{agg}$  for a variety of amphiphilic block copolymer stabilizers was determined once  $\tau_{mix}$  was known for a specific geometry and injection rate. With only an amphiphilic block copolymer in the FNP feed stream,  $\tau_{flash}$  was equal to  $\tau_{agg}$  for that specific block copolymer and therefore,  $Da = \tau_{mix}/\tau_{agg}$ . As described, colloid formation transitions from being transport-controlled when  $Da > 1$  to being independent of mixing time when  $Da < 1$ . The value of  $\tau_{agg}$  could therefore be determined by identifying the mixing time where particle size became homogeneous as a function of mixing rates, the point when  $Da = 1$ .<sup>32</sup>

### 3.2.2 Solvent and Polymer Choice

Based on the mechanism of polymer collapse and aggregation, there are certain constraints on the solvents and polymers used in the FNP system to create monodisperse, stable polymer colloids. The first is that the solvent in the feed stream and the solvent in the anti-solvent stream must be a good and poor solvent for the chosen polymers, respectively. FNP is a solvent exchange process, and the formation of uniform polymer colloids relies on the quick transition from complete dissolution of the polymer in the feed stream to high supersaturation conditions where polymer chains collapse to form globules. The complete dissolution of the polymer in the feed stream allows for uniform formation of globule nuclei which then aggregate to form larger colloids.

The second constraint is that the two solvents must be miscible. This allows for uniform and rapid solvent exchange upon mixing of the two solvents and for the immediate collapse of the polymers, which are super-saturated in the new solvent conditions. Table 3.1 includes a list of example polymers, solvents, and anti-solvents that have been used to form colloids via the FNP process. The most common combination is a solution of a hydrophobic polymer in THF flashed against water as the anti-solvent.

**Table 3.1** Examples of polymers, solvents, and anti-solvents that have been used in FNP.

Polymer	Good Solvent	Anti-solvent	References
Polystyrene (PS)	THF	Water	33
Polyisoprene (PI)	Acetone		30
Polybutadiene (PB)			34
Polylactic acid (PLA)			35
Polycaprolactone (PCL)			36
Poly(lactic-co-glycolic acid) (PLGA)			
Poly(butyl acrylate)- <i>b</i> -Poly(acrylic acid)	DMSO Methanol	Water Chloroform Acetone	37 38
Poly(ethylene glycol)- <i>b</i> -dimyristoyl lipid (PEG- <i>b</i> -DMG)	Ethanol	Water	39 40

When forming more complex polymer colloid morphologies such as Janus or core-shell particles which include the use of more than one polymer, the interactions between different polymers and between any additives and the polymers will affect the final colloid morphology. The molecular weights of the polymers, charge of polymer functional groups, and surface charge of additives will significantly change the morphology of the products. These effects will be discussed in later sections. Block copolymers with different properties have been tested for their ability to stabilize particles against coalescence, suggesting that the amorphous content and glass transition temperature ( $T_g$ ) of the polymer affect the stability of the formed nanoparticles.<sup>36</sup> In addition, nanoparticles which will be used in drug delivery or personal care applications may also necessitate the use of biocompatible or biodegradable polymers. These properties must be considered when preparing polymer colloids *via* FNP for various applications.

### 3.2.3 Mechanism of Stabilization

The formation of monodisperse, stable aggregates of collapsed polymer chains is made possible due to the presence of stabilizing forces during FNP processing. These forces can arise from electrostatic repulsion between colloids or from steric stabilization of polymer brushes on the surface of the colloids. Electrostatic stabilizing forces between colloids are often described in terms of the  $\zeta$ -potential, or the electric potential at the slipping plane of the colloid, and absolute  $\zeta$ -potential values above 30 mV are generally deemed sufficient to stabilize colloids.<sup>41</sup> In the case where hydrophobic polymers such as polystyrene (PS) or polyisoprene (PI) are incorporated in the feed stream, the resulting polymer colloids exhibit a significant negative  $\zeta$ -potential between  $-30.0$  and  $-40.0$  mV, shown in Figure 3.3, despite the lack of charged groups in the polymer itself. The origin of this negative charge has generated debate for decades.<sup>42-44</sup> Microbubbles in water have

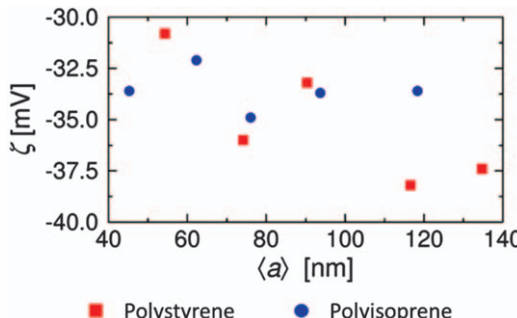


**Figure 3.3**  $\zeta$ -potential of PS and PI particles prepared *via* FNP, and  $\langle a \rangle$  is radius of the colloid.

Reproduced from ref. 33 with permission from American Chemical Society, Copyright 2016.

been experimentally observed to exhibit significant negative surface charges, and oil droplets in oil/water emulsions have had similar charges which stabilize them against coalescence for months either in the presence of non-ionic surfactants or in the absence of surfactants altogether.<sup>45–49</sup> The surface charges on these air and oil droplets, indicated by the measurement of  $\zeta$ -potentials, are negative at high pH and become less negative as pH decreases until finally becoming positive at pH  $\sim$ 2–4, suggesting that it may be the preferential adsorption of hydroxyl ions at the interface which generates this negative charge.<sup>42,50,51</sup> This mechanism is further supported by observations that the pH of an oil/water emulsion decreases linearly with an increase in surface area and more NaOH is required to maintain a constant pH.<sup>52</sup> However, competing theories propose that the negative charge at water/hydrophobic interfaces is due to the adsorption of bicarbonate anions rather than hydroxyl ions or carboxyl impurities in the oil containing system.<sup>53</sup>

Other theoretical simulations and spectroscopic measurements have suggested that hydronium cations are more strongly attracted to water/vapor interfaces than hydroxyl anions, in contrast with the experimentally-observed negative charge on air bubbles and oil droplets.<sup>43,54,55</sup> Alternatively, molecular dynamics (MD) simulations have proposed that water molecules can collectively organize at an interface, producing a charge transfer effect that would result in a negative  $\zeta$ -potential, though the magnitude of that  $\zeta$ -potential does not match experimental results.<sup>56</sup> While the magnitude of the negative  $\zeta$ -potential for plain PS or PI particles more closely matches that of air bubbles and oil droplets, suggesting that the preferential adsorption of hydroxyl ions results in the stabilization of homopolymer colloids prepared *via* FNP, the mechanism behind this stabilization clearly remains a topic of debate.

Many polymer colloids formed *via* FNP are sterically stabilized with amphiphilic block copolymers. As described in Section 3.2.1, the hydrophilic block of the amphiphilic block copolymers can adopt different conformations on the surface of the polymer colloids depending on the polymer

surface density (*i.e.* chains per nm<sup>2</sup>). In the brush regime, colloids with solvophilic coronas are sterically stabilized by that polymer brush on the colloid surface. This brush resists chain interpenetration when two colloids approach one another, creating a repulsive force between colloids.

### 3.2.4 Equipment

In practice, there are two main mixing designs used to perform FNP: the confined impingement jets (CIJ) mixer and the multi-inlet vortex mixer (MIVM). The designs of these two setups are illustrated in Figure 3.4. Irrespective of geometry, the colloid formation mechanism is common to both. However, as noted below, the MIVM can provide some additional capabilities. A video tutorial of the operation of the CIJ and MIVM mixers has been presented by Markwalter *et al.*<sup>57</sup>

The CIJ mixer has two inlet streams, one for the polymer feed solution, and another for the anti-solvent. The two streams must have equal momentum when they are injected to ensure rapid and complete mixing of the two solvents.<sup>56</sup> The two inlet streams can be attached to pumps to use the CIJ mixer in a continuous manner. Alternatively, small volumes of colloidal suspensions can be prepared manually to conserve material, which is advantageous for small-scale research projects.<sup>58</sup> One syringe can be loaded with the polymer solution to be used as the feed stream and another loaded with the anti-solvent, and these syringes can be depressed manually. After mixing of the two feed streams, the effluent is deposited in an anti-solvent reservoir to provide an additional quenching step. Additional components can be incorporated in the anti-solvent reservoir, giving the FNP process more flexibility.

For certain applications, it is advantageous to have more than two inlet streams or to have different flow rates for different components. The four-stream MIVM can accommodate both options.<sup>59</sup> Rather than

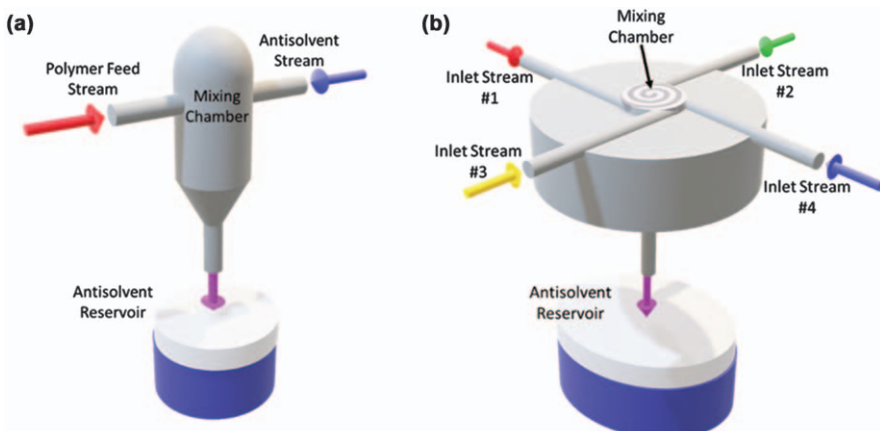


**Figure 3.4** Schematic illustrations of the (a) CIJ mixer configuration and (b) MIVM configuration for FNP.

impinging directly into one another as the streams do in the CIJ mixer, in the MIVM, they inject tangentially into the mixing chamber allowing for imbalances in stream momentum. MIVM setups can range in size. The original design used syringe pumps to control the feed rates of each stream. The process of priming the pumps and reaching steady state can result in waste that may be unacceptable if the materials being used are limited in quantity or expensive. To prevent this waste, a scaled-down version of the MIVM system, termed the micro-MIVM, has been designed where syringes are used for the feed streams, as they can be for the CIJ mixer.<sup>60</sup>

### 3.3 Homopolymer Colloids

In its most basic configuration, FNP can be used to produce homogeneous polymer colloids with uniform surface composition by incorporating a single homopolymer in the feed stream. These homopolymer colloids remain suspended and stable due to the net negative surface charge as described in Section 3.2.3. Even with this setup, a range of particle sizes can be achieved by tuning various process parameters such as polymer feed concentration and mixing time. These effects will be discussed in the following section.

#### 3.3.1 Concentration Effects

Homogeneous colloids of various hydrophobic polymers such as PS and PI have been generated *via* FNP and range from 50 to 500 nm in diameter. With the same simple setup in a CIJ or MIVM configuration, the particle size can be tuned by controlling the concentration of polymer in the feed stream.

As the concentration of polymer in the system increases, more collision events occur between collapsed globules before stabilization is achieved, and each colloid is composed of more polymer chains. The radius of the final colloids,  $a$ , showed a dependence on polymer concentration,  $\Phi$ , that could be fit to a power law relation to give  $a \sim \Phi^{1/3}$ , as shown for both PS and PI colloids in Figure 3.5.<sup>33</sup> Simulations of the FNP process have confirmed this scaling law and also revealed that while polymer chains near the core of the colloid assume a melt conformation, those at the surface are more collapsed due to their proximity to the poor solvent environment.<sup>33</sup> This scaling relation also applies for colloids prepared from block copolymers of these two hydrophobic polymers.<sup>61</sup>

The collapse and aggregation of individual polymer chains is essential to the formation of monodisperse polymer colloids *via* FNP. Above the overlap concentration, however, polymer chains become entangled and can form networks that lead to large aggregates rather than monodisperse colloids.<sup>62</sup> Therefore, there is an upper limit on polymer concentration in the FNP process at that polymer's overlap concentration, and the higher the polymer molecular weight used, the lower that limit is.<sup>63,64</sup>

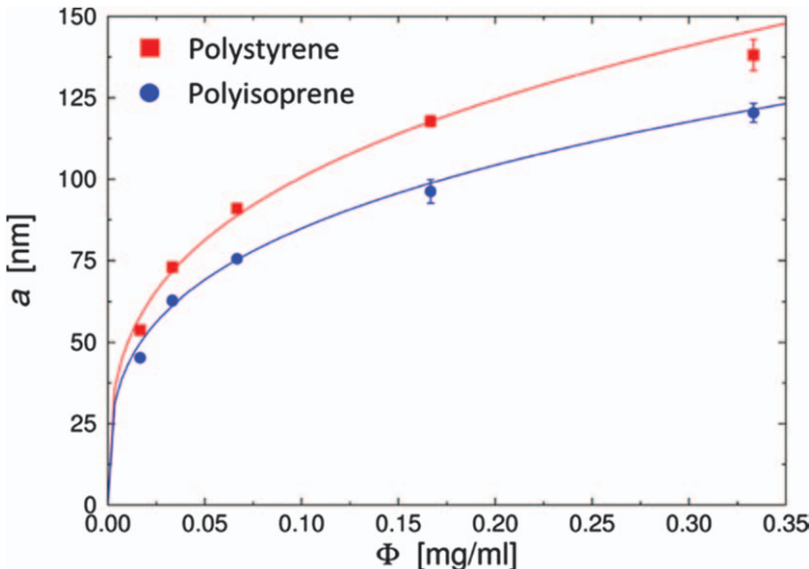


**Figure 3.5** Effect of polymer concentration on colloid radius.

Adapted from ref. 33 with permission from American Chemical Society,  
Copyright 2016.

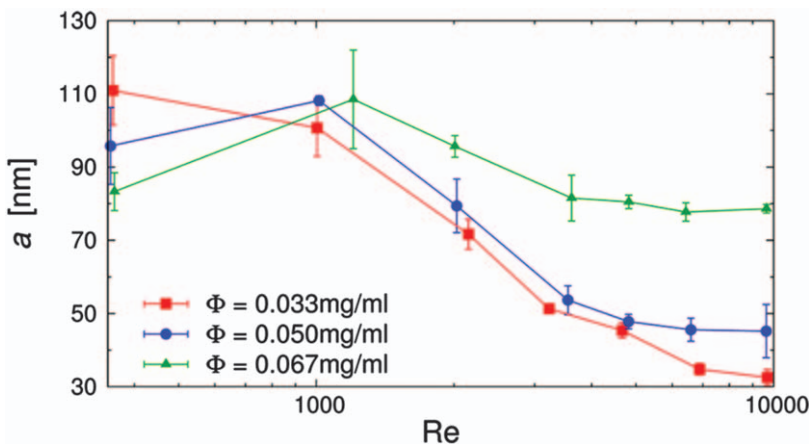


**Figure 3.6** Effect of inlet stream flow rate during FNP on colloid radius.

Reproduced from ref. 33 with permission from American Chemical Society, Copyright 2016.

### 3.3.2 Mixing Time Effects

Colloid size can also be controlled by varying the mixing rate of the good and poor solvents in FNP, which is controlled by varying the flow rate of the inlet streams. As shown in Figure 3.6, as the mixing time decreases,

corresponding to an increase in the Reynolds number,  $Re$ , colloid diameter decreases until, at sufficiently high  $Re$ , colloid diameter remains roughly constant. This is due to changes in the nucleation rate as a function of supersaturation, described in Section 3.2.1. As discussed with respect to eqn (3.2), the nucleation rate increases as the supersaturation ratio increases. Under slower mixing conditions, the polymer is exposed to lower supersaturation conditions with fewer nuclei, and the colloid growth proceeds by a nucleation and growth mechanism where growth proceeds as polymer is depleted from the solution. The smaller number of nuclei therefore results in the formation of larger colloids. As  $Re$  increases and the mixing time is reduced, the solvent quality changes more rapidly, creating higher initial levels of supersaturation, and therefore, more collapsed polymer chains, which act as nuclei. Formation of the colloids then proceeds according to a nucleation-aggregation model, resulting in colloids with smaller diameters as faster mixing times are achieved.

The effect of mixing time on homopolymer colloid formation can also be thought of in terms of the  $Da$ . As described in Section 3.2.1,  $Da = \tau_{\text{mix}}/\tau_{\text{flash}}$ . It was shown in such systems that when  $\tau_{\text{mix}}$  is large and mixing is slow ( $Da > 1$ ), particle size is a function of mixing speed. However, a minimum size plateau is reached when  $Da < 1$ .<sup>32</sup> The data in Figure 3.6 are generated without the presence of a stabilizing block copolymer; therefore stabilization is due to electrostatic surface charging, as described in Figure 3.3. At low  $Re$ , the larger particle sizes reflect the heterogeneity in supersaturation and nucleation under poor mixing conditions. The smaller sizes and plateau in size, at high  $Re$ , reflects assembly under diffusion limited aggregation (DLA), where the solvent exchange has happened more rapidly than the DLA assembly time.<sup>28</sup> Under these conditions, nanoparticle size follows  $a \sim \Phi^{1/3}$ .

### 3.4 Colloids from Homopolymer Blends

The polymer colloids discussed up to this point have been prepared from solutions of a single homopolymer and have, therefore, had homogenous surface compositions. However, more complex colloid morphologies can be generated *via* FNP by exploiting the propensity of sufficiently dissimilar polymers to phase separate. By incorporating blends of homopolymers in the feed stream, FNP can be used to produce Janus, core–shell, and patchy spherical particles as well as non-spherical colloids.

To form internally-structured polymer colloids, the component homopolymers must experience a driving force to phase separate. This driving force arises from the difference in interaction energies between mixture components and is captured by the Flory interaction parameter,  $\chi$ . Using expressions for the free energy of mixing for a polymer blend, binodal and spinodal curves can be determined which delineate between regions of

stability in terms of  $\chi$ . The critical interaction parameter,  $\chi_c$ , is the minimum or maximum of the spinodal curve, or the value of  $\chi$  which separates a single-phase system from a two-phase system, and is given by the expression in eqn (3.5):

$$\chi_c = \frac{1}{2} \left( \frac{1}{\sqrt{N_A}} + \frac{1}{\sqrt{N_B}} \right)^2 \quad (3.5)$$

in which  $N_A$  and  $N_B$  are the degrees of polymerization of the component polymers. Longer polymer chains thus have lower critical interaction parameters and are more likely to phase separate while shorter polymer chains are more likely to be miscible.

An empirical relationship has been developed to capture the temperature dependence of the Flory interaction parameter and is indicated by eqn (3.6):

$$\chi(T) \cong A + \frac{B}{T} \quad (3.6)$$

In this expression,  $A$  denotes the entropic contribution, and  $\frac{B}{T}$  indicates the enthalpic contribution to the interaction parameter. Values of  $A$  and  $B$  have been determined for many polymer blends and can be used to determine the value of  $\chi$  for the system of choice.<sup>65</sup> In order to produce phase-separated colloids *via* FNP, the interaction parameter must be greater than the critical value ( $\chi > \chi_c$ ), indicating that there are sufficient repulsive forces between the polymers to induce phase separation.

Once a homopolymer blend is determined to phase separate, the morphology of the final colloid is then dependent on the surface tensions of the two polymers with one another and of each with the surrounding solvent environment. Examining a drop of water in contact with a polymer solid phase as in Figure 3.7, the contact between the solid and liquid at equilibrium can be described by the Young eqn (3.7):

$$\cos \theta = \frac{\gamma_{SA} - \gamma_{SL}}{\gamma_{LA}} \quad (3.7)$$

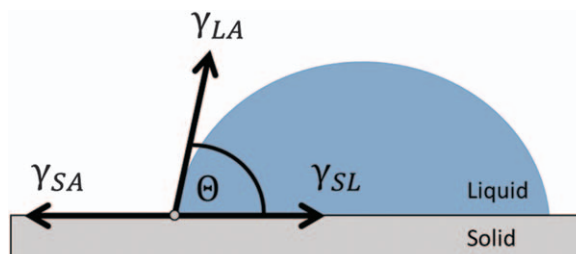


**Figure 3.7** Surface tension components involved in the formation of a liquid droplet on a solid substrate.

in which  $\theta$  is the contact angle, and  $\gamma_{SA}$ ,  $\gamma_{SL}$ , and  $\gamma_{LA}$  are the interfacial tensions between the solid and air, the solid and liquid, and the liquid and air phases, respectively.<sup>66</sup> The values of  $\theta$  and  $\gamma_{LA}$  can be easily measured experimentally while  $\gamma_{SA}$  and  $\gamma_{SL}$  are more difficult to obtain.

The coalescence of immiscible liquid drops has been studied extensively and can be used to explain the equilibrium morphologies of polymer colloids as well.<sup>67–71</sup> For two immiscible liquid droplets in a third liquid medium, a critical parameter is the spreading coefficient,  $S$ , defined in eqn (3.8):

$$S_i = \gamma_{jk} - (\gamma_{ij} + \gamma_{ik}) \quad (3.8)$$

where  $\gamma$  is the interfacial tension between the different liquids. When the three spreading coefficients are calculated, the results fall under one of three situations, as illustrated in Figure 3.8. In the first case, shown in Figure 3.8a, when the spreading coefficient of one liquid and the surrounding medium are negative and that of the other liquid is positive, complete engulfing occurs. This creates a core–shell droplet in which one liquid covers the entire surface of the other. In the case where all three spreading coefficients are negative, as in Figure 3.8b, partial engulfing is observed, and a Janus morphology emerges. Finally, when the spreading coefficients of both liquids are negative and that of the surrounding medium is positive, a non-engulfing morphology is observed in which the two liquids form separate droplets, as is illustrated in Figure 3.8c. The same phenomenon is seen for a system of two polymers in a liquid medium, as will be discussed.

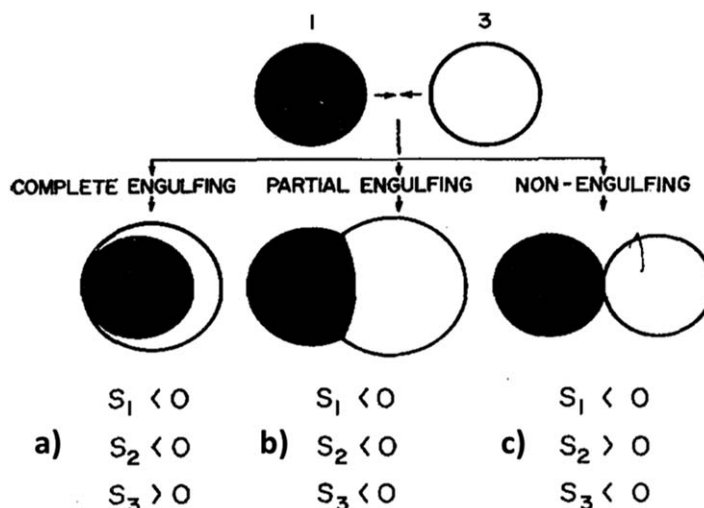


**Figure 3.8** Potential colloid morphologies and the spreading coefficient values which correspond to each.

Reproduced from ref. 67 with permission from Elsevier, Copyright 1970.

Together, the values of the Flory interaction parameter,  $\chi$ , and the spreading coefficients,  $S$ , determine the morphology of colloids prepared *via* FNP with blends of homopolymers in the feed stream. Examples of such morphologies will be discussed in the following sections.

### 3.4.1 Janus Particles

The simplest iteration of a homopolymer blend in FNP is the use of two hydrophobic polymers in the feed stream which have similar collapse times and solvent interactions. We showed in Section 3.3 that homopolymer PS and homopolymer PI particles can be generated *via* FNP and have similar properties with regards to surface charge and colloid diameter. For PS and PI of moderate molecular weights, the Flory interaction parameter is greater than the critical value ( $\chi > \chi_c$ ) at most temperatures, driving the polymers to phase separate. These two hydrophobic polymers also have high and approximately equal interfacial tensions with the solvent mixture employed ( $\gamma_{\text{PS-Water}} \sim \gamma_{\text{PI-Water}}$ ) and the interfacial tension between the two polymers is significantly lower ( $\gamma_{\text{PS-PI}} \ll \gamma_{\text{PS-Water}}$  and  $\gamma_{\text{PI-Water}}$ ). According to eqn (3.8), the spreading coefficients for the three components are as follows:  $S_{\text{PS}} < 0$ ,  $S_{\text{water}} < 0$ , and  $S_{\text{PI}} < 0$ . When equilibrated, therefore, the combination of these properties drives the colloids made from a mixture of PS and PI to adopt a Janus morphology with two distinct surface domains.

With this system, the diameter and the composition of each Janus colloid can be independently controlled. As described in Section 3.3.1 the colloid size can be controlled by the polymer concentration in the system. Simultaneously, the composition of each Janus colloid can be tuned by adjusting the composition of the feed stream. As the ratio of the homopolymers in the feed stream changes, it is directly reflected in the composition of each colloid, as shown in Figure 3.9. Like homopolymer colloids, these Janus colloids are stable without the use of additional stabilizers, but rather by a negative surface charge of approximately  $-33$  mV.

### 3.4.2 Patchy Particles

More complex spatial distribution of heterogeneity on the surface of patchy particles is of interest for the unique self-assembly behavior that the patches can impart to the colloidal systems. These patchy particles can form porous Kagome lattices, photonic crystals, or flexible chains depending on the number of patches and their spatial distribution on the colloid surface.<sup>72–75</sup> Producing these patchy particles with control over the particle size and morphology can be difficult, with several current approaches requiring multiple synthetic steps and post-fabrication sorting to achieve patchy equilibrium structures.<sup>76,77</sup> Kinetic trapping of block copolymer colloids in non-equilibrium morphologies has also been demonstrated with the use of one polymer component which vitrifies at processing temperatures.<sup>78,79</sup>

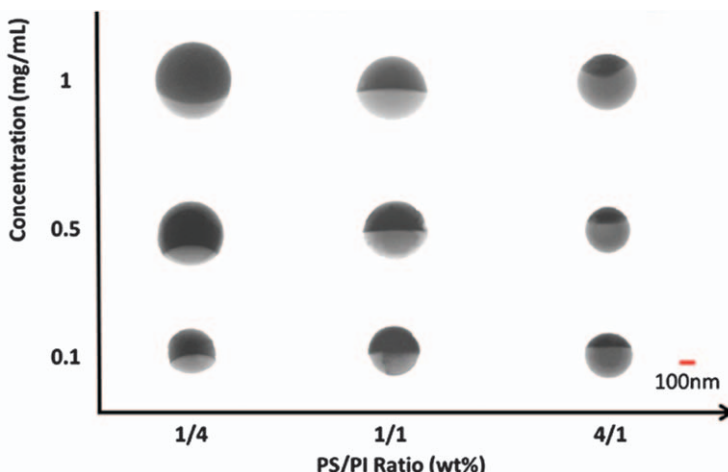


**Figure 3.9** Control over PS/PI Janus colloid size and anisotropy using FNP.  
Reproduced from ref. 30 with permission from American Chemical Society, Copyright 2016.

However, with mixing times on the order of a few milliseconds, FNP can be used to create patchy particles by arresting polymer diffusion before equilibrium morphologies can be achieved.

Patchy particles have been generated *via* FNP with a blend of homopolymers in the feed stream. The patchiness of these colloids can be controlled by tuning the composition of the feed stream, the overall feed concentration, and the glass transition temperature ( $T_g$ ) of the vitrifying polymer.<sup>80</sup> In experiments with PS and PI blends in the feed stream, the PS acts as the vitrifying agent due to its  $T_g$  of approximately 100 °C and therefore, its glassy properties at room temperature. From Figure 3.10 it can be seen that at higher feed concentrations, colloids prepared with an excess of PS formed patchy colloids with surface PI patches while the patchy particles prepared with an excess of PI had PS surface patches. The emergence of these surface patches can be explained by comparing timescales of vitrification with those of homopolymer demixing, and a scaling argument has been developed to delineate the boundary between Janus and patchy colloid formation conditions.<sup>30</sup> The number of patches on the colloid surface can also be controlled by tuning the amount of the vitrifying polymer in the feed stream; as more PS is incorporated, more surface PI patches form.

As these patchy particles are kinetically arrested in non-equilibrium morphologies, the  $T_g$  of the vitrifying agent was shown to be an important parameter in their formation. Colloids prepared from blends of PI and low-molecular weight PS (850 g mol<sup>-1</sup>) adopted Janus morphologies while those prepared with high-molecular weight PS (1 600 000 g mol<sup>-1</sup>) were patchy. The increase in PS molecular weight corresponded to an increase in  $T_g$  and zero shear viscosity which increased polymer viscosity sufficiently to slow

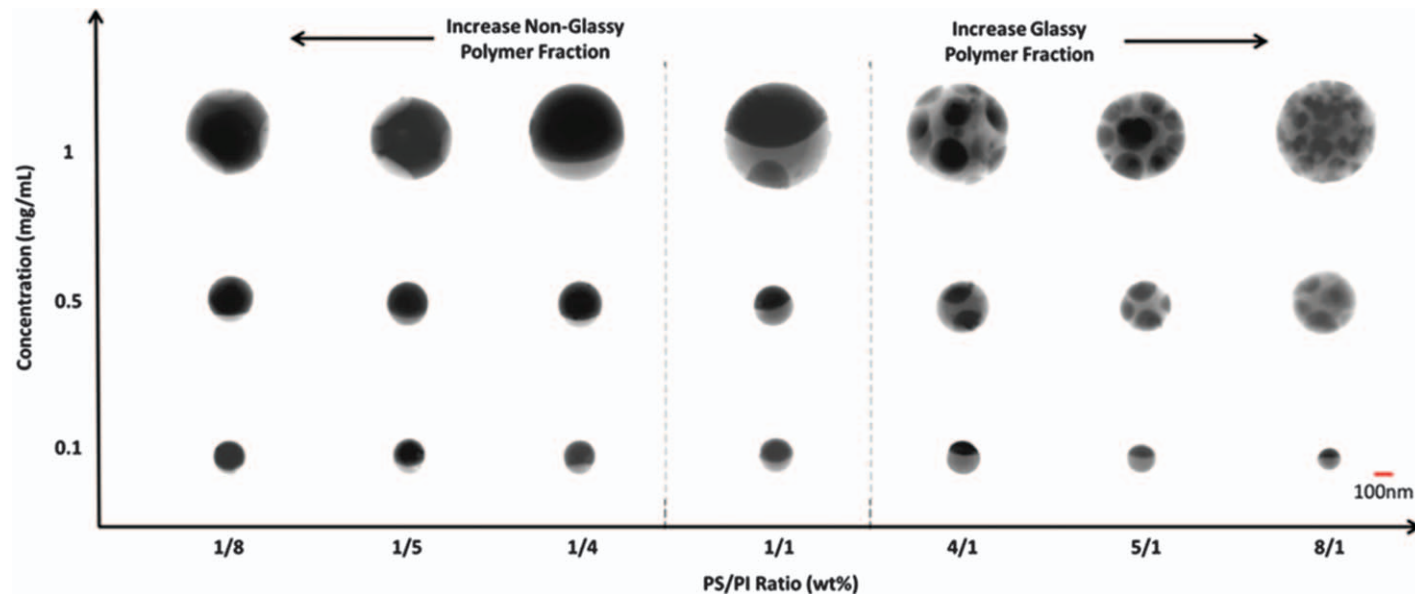


**Figure 3.10** Colloid morphologies for homopolymer blends of PS and PI over a range of feed concentrations and polymer ratios.  
Reproduced from ref. 80 with permission from American Chemical Society, Copyright 2017.

polymer diffusion, and to allow vitrification before complete separation to a Janus state. The ease of independently tuning colloid size and patchiness by adjusting the polymer concentration, ratio, and  $T_g$ , is an attractive feature of the FNP process.

### 3.4.3 Core–Shell Particles

Core–shell particles can be formed when there is a driving force for one of the polymers to preferentially interact with the solvent environment. This can be realized if one of the homopolymers has a higher or lower interfacial tension than the other with the surrounding solvent. Simulations of this scenario show that the polymer with the lower interfacial tension forms a shell that encapsulates the other polymer which has a higher interfacial tension with the solvent environment, illustrated in Figure 3.11.<sup>31</sup> This engulfing morphology should be observed when the spreading coefficient of one polymer and the liquid medium are negative and that of the other polymer is positive, as illustrated in Figure 3.8a.

Experimentally, core–shell particles have been created with a few different combinations of functionalized homopolymers and solvent environments, as shown in Figure 3.12. With a mixture of amine-terminated polystyrene

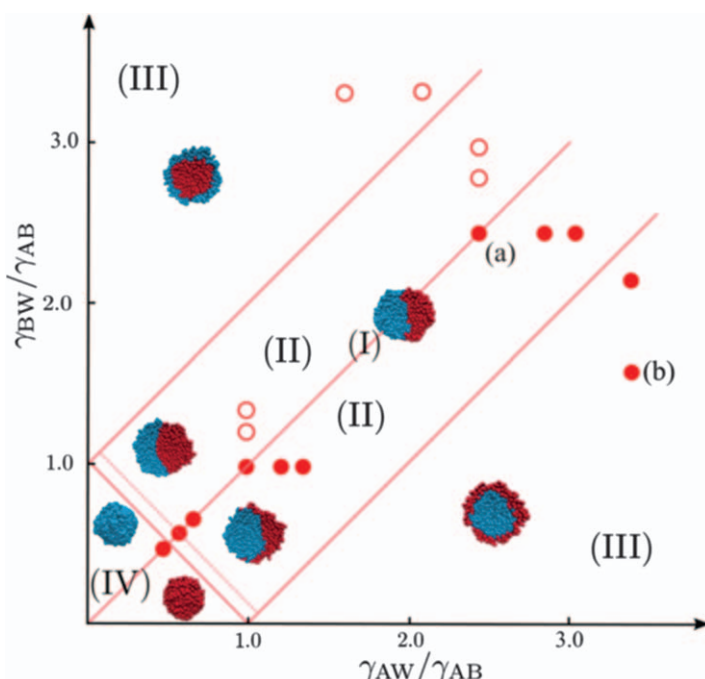


**Figure 3.11** Phase diagram of potential morphologies created from blends of homopolymers via FNP.

Reproduced from ref. 31 American Chemical Society, Copyright 2017.

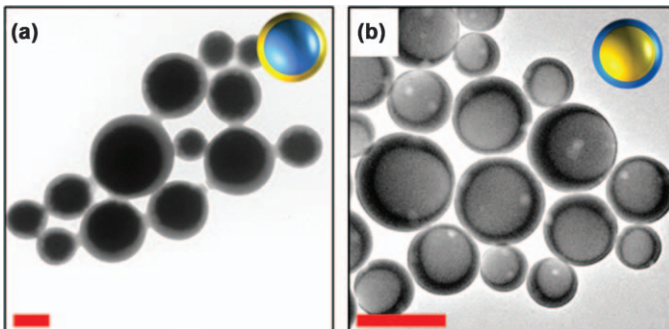


**Figure 3.12** Core–shell polymer colloids prepared from blends of (a) PS–NH<sub>2</sub> and PI or (b) PS and PB-COOH *via* FNP. Scale bars are 200 nm.  
Adapted from ref. 34 with permission from American Chemical Society, Copyright 2017.

(PS–NH<sub>2</sub>) and PI in the feed stream and a mixture of THF and water as the final solvent environment, a core–shell polymer colloid with a PI core and PS–NH<sub>2</sub> shell is formed.<sup>34</sup> Alternatively, colloids prepared from PS and carboxy-terminated polybutadiene (PB-COOH) in the feed stream have been shown to form core–shell particles in an aqueous environment. These preliminary examples demonstrate the potential to form core–shell colloids *via* FNP with a variety of polymers and solvent conditions.

### 3.5 Hybrid Polymer–Inorganic Colloids

An additional level of functionality can be imparted to these colloids by incorporating inorganic nanoparticles. These hybrid colloids can be used to enhance Raman spectroscopy signals, to enhance the selectivity of catalysts in biphasic reactions, and as self-propelled nanomotors.<sup>81–84</sup> For these applications, the ability to control the placement of the inorganic nanoparticles is essential, and this can be accomplished using FNP.

We previously described how Janus particles can be formed using a blend of PS and PI homopolymers. When citrate-stabilized gold nanoparticles (Au NPs) are incorporated in the anti-solvent stream, the resulting colloids retain their Janus morphology, and the Au NPs align at the PS/PI/water contact line, as shown in Figure 3.13a.<sup>34</sup> Nanoparticles have been known to adsorb at liquid–liquid interfaces, and in mixtures with phase-separating diblock copolymers, the nanoparticles assembled at the interfaces between the microdomains.<sup>85–87</sup> The hydrophilic surface of the citrate-stabilized Au NPs similarly leads them to localize to the contact line between the two hydrophobic polymer domains and the aqueous solvent environment to minimize the interfacial energy between the polymers. The ability to generate this complex structure with a one-step process is unique.

The Au NPs align at the contact line between two polymers if the NP surface is neutral with respect to both polymers, as is the case with the

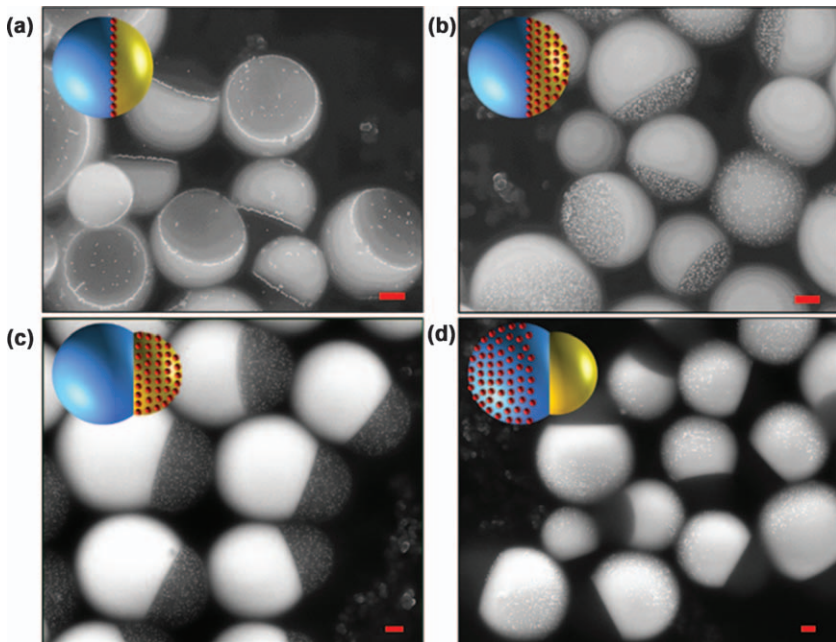


**Figure 3.13** Incorporation of Au NPs on different domains of polymer Janus colloids. (a) Au NPs align at the interface between PS and PI domains, (b) Au NPs are incorporated throughout one domain of PS-NH<sub>2</sub>/PI colloids, non-spherical or dumbbell Janus colloids can be prepared by introducing surfactants in the FNP process with Au NPs on the (c) PS-NH<sub>2</sub> domain of PS-NH<sub>2</sub>/PI colloids or the (d) PI domain of PS/PI colloids. Scale bars are 200 nm.

Adapted from ref. 34 with permission from American Chemical Society, Copyright 2017.

homopolymers PS and PI. Alternatively, colloids can be designed with favorable interactions between the polymers and the nanoparticles. When a mixture of PS-NH<sub>2</sub> and PI is used in the feed stream and the citrate-stabilized Au NPs are incorporated in the anti-solvent stream, the resulting colloids exhibit a Janus structure caused by the phase separation of the two polymers, as shown in Figure 3.13b. The Au NPs in this case are distributed throughout the PS-NH<sub>2</sub> domain due to electrostatic interactions between the positively-charged amine groups on the PS-NH<sub>2</sub> and the negatively-charged citrate groups on the Au NPs at neutral pH. This control of nanoparticle location can enable their use in biphasic catalysis and allow for further functionalization with thiol-Au chemistries.

The placement of the inorganic nanoparticles can further be adjusted using surfactants. As described in Section 3.4, equilibrium colloid morphology is dictated by the interactions between individual polymers and between polymers and the solvent media. Surfactants can alter the overall colloid shape by changing the interfacial tensions between the hydrophobic

polymers and the aqueous environment. The incorporation of a non-ionic surfactant, such as Tween 80, in the anti-solvent stream or the anti-solvent reservoir along with PI and either PS or PS-NH<sub>2</sub> in the feed stream results in the formation of non-spherical dumbbell Janus colloids.<sup>34</sup> This effect is maintained upon addition of Au NPs, whereas the surfactant does not appear to interfere with the electrostatic interactions between PS-NH<sub>2</sub> amine groups and citrate groups on the Au NPs. This combination results in dumbbell Janus particles with Au NPs incorporated in the PS-NH<sub>2</sub> domain, as shown in Figure 3.13c. Alternatively, if the homopolymer mixture is of PS and PI, the dumbbell Janus shape is maintained, but the Au NPs are dispersed in the PI domain, as shown in Figure 3.13d. With FNP, hybrid polymer-inorganic colloids can be prepared with precise control over the placement of inorganic nanoparticles.

### 3.6 Block Copolymer Microphase Separation in Colloids

The same principles that govern the phase separation of homopolymers apply to the microphase separation of block copolymers. While the blends of two homopolymers completely phase separate into distinct domains within the colloid, the covalent bond between chemically distinct blocks of the diblock copolymers limit the phase separation to smaller scales, which can lead to the creation of more complex colloid morphologies, discussed below.

#### 3.6.1 Molecular Weight Effect

Symmetric poly(styrene-*b*-isoprene) (PS-*b*-PI) diblock copolymers microphase separate and form a lamellar morphology in thin films and bulk systems at certain values of the Flory-Huggins interaction parameter,  $\chi$ , and sufficiently high molecular weights or degrees of polymerization,  $N$ .<sup>88</sup> When the same diblock copolymer is incorporated in the FNP feed stream, the resulting spherical colloids exhibit a concentric lamellar morphology, as shown in Figure 3.14a.<sup>61</sup> The lamellar period within each colloid, indicated by the arrows in Figure 3.14a, matches small-angle X-ray scattering (SAXS) measurements of the unprocessed block copolymer powder as well as the lamellar spacing in the bulk. While increasing the concentration of block copolymer in the feed stream results in an increase in colloid diameter, as it does for homopolymer particles, the lamellar period is maintained across all colloid diameters. Molecular dynamics (MD) simulations performed on a similar block copolymer system qualitatively agree and are illustrated below the experimental results in Figure 3.14a.

A transition in morphology occurs when the molecular weight of the PS-*b*-PI diblock copolymer in the feed stream is increased. With this higher molecular weight diblock copolymer, a lamellar structure is still observed,

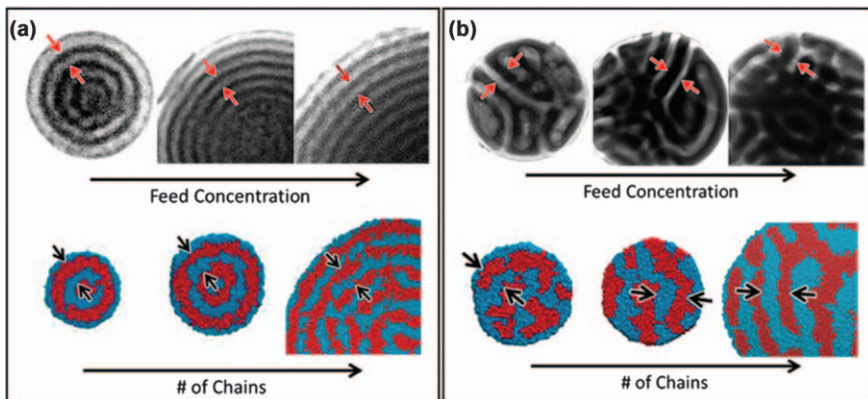


**Figure 3.14** Concentric lamellar colloid formation with the use of PS-*b*-PI block copolymers in FNP.

Adapted from ref. 61 with permission from American Chemical Society, Copyright 2018.

and the lamellar period is larger than for the lower molecular weight block copolymer, again matching SAXS measurements of unprocessed powder. However, defects in the phase-separated layers are observed which introduce disorder in the lamellar morphology, shown in Figure 3.14b. This change in morphology is also observed in MD simulations. The higher molecular weight diblock copolymer chains diffuse sufficiently slowly in the colloids formed *via* FNP for the defects in the lamellae not to be eliminated, resulting in the disordered lamellar colloids.

### 3.6.2 Blends of Block Copolymers and Homopolymers

We have previously discussed the colloids formed when blends of two homopolymers are incorporated in the feed stream of the FNP system in Section 3.4. The use of blends of diblock copolymers and homopolymers in FNP can further increase the complexity of colloid morphology by combining the dual effects of the phase separation of the two polymers and the microphase separation of the diblock copolymer.

The concentric lamellar morphology described in Section 3.6.1 is observed when a low-molecular weight PS-*b*-PI diblock copolymer is mixed with a low-molecular weight PS homopolymer in the feed stream at low homopolymer contents. The addition of more and more homopolymer results in swelling of the lamellae as the PS homopolymer is incorporated into the PS domain of the microphase separated diblock copolymer. At sufficiently high homopolymer content, the lamellar structure becomes disordered and is then replaced by an internal micellar morphology, as shown in Figure 3.15. This transition has been observed in bulk and is attributed to the free energy penalty of disturbing the copolymer chains due to homopolymer swelling.<sup>89,90</sup>

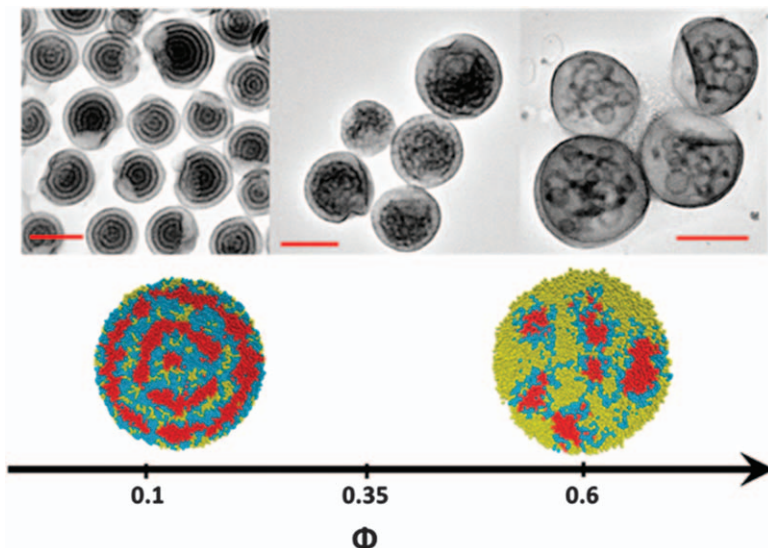


**Figure 3.15** Evolution of concentric lamellar colloids to micellar colloids observed experimentally and in simulations with the inclusion of more homopolymer PS with PS-*b*-PI block copolymers. Simulations show that the homopolymer PS swells the PS domain of the phase-separated block copolymer lamellae. Scale bars are 200 nm.

Adapted from ref. 61 with permission from American Chemical Society, Copyright 2018.

Increasing the molecular weight of the PS homopolymer creates two-phase lamellar morphologies with a homopolymer-rich domain and a block copolymer-rich domain, as illustrated in Figure 3.16. This results in lamellar Janus morphologies at homopolymer volume fractions,  $\Phi$ , up to 0.5 and overall polymer concentrations at or below  $0.5 \text{ mg mL}^{-1}$  in the feed stream. However, increasing feed concentration and homopolymer content yields lamellar patchy particles. The kinetic trapping effect of the higher molecular weight homopolymer PS begins to come into play, as described in Section 3.4.2 for homopolymer blends. In these hierarchically structured colloids, the patches are composed of microphase-separated diblock copolymer.

Upon an increase in molecular weight of the PS-*b*-PI diblock copolymer, the micellar morphology forms for all blend compositions. In these colloids, micelles of block copolymer are embedded in a continuous phase of homopolymer PS, shown in Figure 3.17. As  $\Phi$  increases and more homopolymer of any molecular weight is incorporated in the feed stream, the overall particle size remains constant, but the internal micelles become more dispersed within the homopolymer PS matrix.

Microphase separation of block copolymers has been extensively studied in thin film and bulk systems, while less is understood about the effects of confinement on microphase separation within the volume of a colloid.

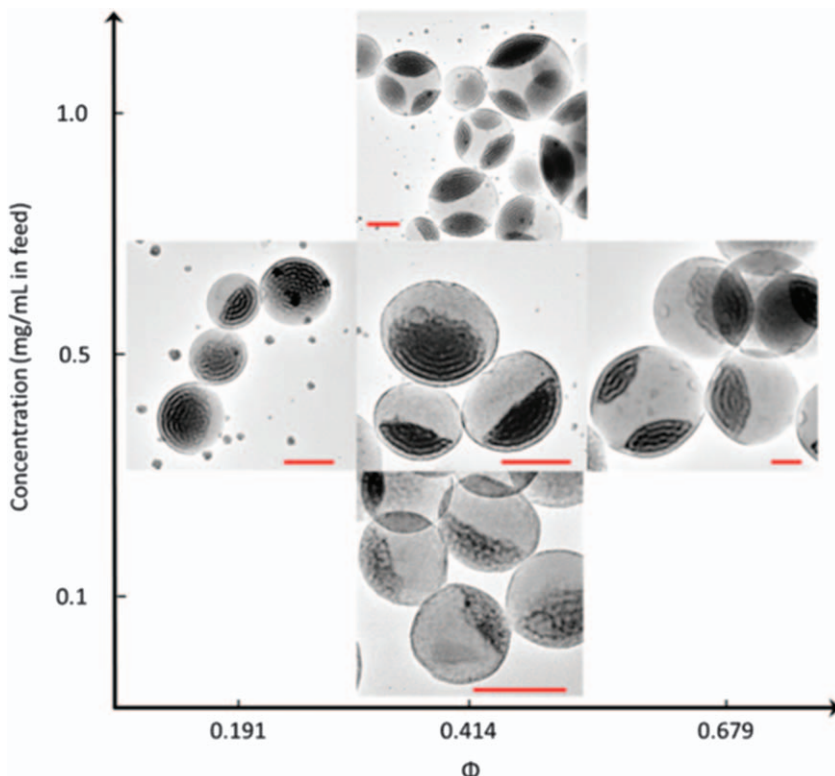


**Figure 3.16** Hierarchical colloid morphologies with blends of PS-*b*-PI block copolymers and homopolymer PS. Scale bars are 200 nm.  
Adapted from ref. 61 with permission from American Chemical Society, Copyright 2018.

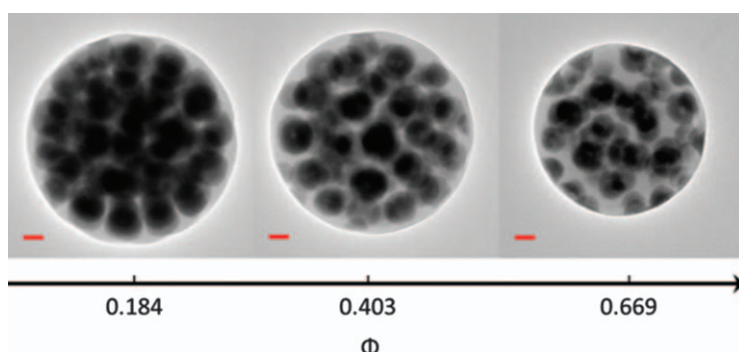


**Figure 3.17** Micellar colloid morphologies formed by blends of homopolymer PS and PS-*b*-PI block copolymers. Scale bars are 200 nm.  
Adapted from ref. 61 with permission from American Chemical Society, Copyright 2018.

Through these early studies involving a set of diblock copolymer systems, FNP has been demonstrated as a feasible means to produce a range of colloid morphologies, some of which have not been observed previously. However, a large design space remains to be explored in the use of diblock copolymers of different compositions as well as triblock copolymers.

### 3.7 Polyelectrolyte Complexation

Polyelectrolytes (PEs) are polymers with a high-volume percent of ionizable monomers that may carry either positive, negative, or zwitterionic charges. Common ionic groups present in PEs include conjugate acids or bases, both originating from weak and strong bases or acids *via* proton exchange, salt forms of permanent ionic groups (*e.g.*, salts of quaternary amines), and reactive groups (*e.g.*, acid anhydrides). While PEs are generally soluble in aqueous conditions, their utility has been derived from the process of complexation. Manipulation of process parameters relevant to this process has been employed to control both the formation kinetics and the final morphologies of complexes for use in applications including structured colloids<sup>91–95</sup> and encapsulation.<sup>96–99</sup>

#### 3.7.1 Mechanism of Polyelectrolyte Complexation

Upon mixing solutions of two oppositely charged PEs with low to moderate ionic strengths, the PE chains will spontaneously associate and form complexes. This is understood through the changes in enthalpy and entropy during complexation: (1) solubilized PEs are surrounded by electrostatic double layers consisting of concentrated counter-ions; (2) two oppositely charged PEs interact and associate *via* electrostatic interactions, thereby reducing configurational entropy of both chains while their respective double layers are disrupted and counter-ions are released into the less concentrated solution phase, resulting in a significant net increase in the entropy of the overall solution; (3) complexation continues until sterically hindered *via* mismatch in constituent chain charge densities and lengths; (4) complexation yields stable, soluble polyelectrolyte complexes (PECs) or macroscopic coacervates.<sup>100,101</sup>

Factors affecting the result of PE complexation include the concentration, charge density, charge group spacing, molecular weight, and  $pK_a$  of respective PEs as well as the concentration and valency of simple electrolytes in the system. These constitute important process variables such as the ionic strength and the monomer charge ratio of the PE system. In contrast to the complexation process described previously for low/moderate ionic strengths, interactions between charged groups on PEs are diminished (“salted out”) at high ionic strengths as the expulsion of counter-ions from a double layer into a concentrated solution phase becomes less entropically favored. Additionally, multivalent ions can act as point crosslinkers between charged

groups on PE chains.<sup>102</sup> With regards to the monomer charge ratio, the relative concentrations of PEs (or charged repeat units) and the degrees of ionization based on respective pKas in relation to solution pH strongly influence the formation, net charge, and stability of complexes.

### 3.7.2 Effect of Mixing Timescales on PEC Formation

Traditionally, PECs are fabricated *via* polyelectrolyte titration in which a solution of a constituent PE is introduced at a specified rate to a complementary PE solution with simple stirring. The initial constituent PE solutions are chosen to give a final mixture with a target PEC concentration and charge ratio. While the characteristics of generated PECs have been studied with respect to PE chain architecture, charge ratio, and ionic strength of the final mixture, an important feature of PE titration is the time of addition during which the charge ratio and concentration of constituent PEs is transient. To this end, Dragan *et al.* systematically studied the impact of the titrant addition rate (TAR) on final PEC formation.<sup>103,104</sup>

When titrating poly(sodium 2-acryloamido-2-methylpropanesulfonate) (NaPAMPS), a polyanion, into a polycation solution of poly(diallyl dimethylammonium chloride) (PDADMAC) or 5 mol% branched poly(*N,N*-dimethyl-2-hydroxypropleneammonium chloride), the authors detected the formation of small PEC nanoparticles ( $R_h = 50\text{--}75\text{ nm}$ ) for cationic non-stoichiometric charge ratios which exhibited little dependence on TAR. At the stoichiometric charge ratio, or isoelectric point, of each PE pair, average PEC particle size and mixture turbidity sharply increased, accompanied by a reduction in polydispersity. Interestingly, this transition in particle size was found to vary inversely with TAR, with the smallest PECs being generated at the highest TAR (Figure 3.18a). As charge ratio was further varied into the regime of excess polyanions, PEC size was found to remain constant. However, higher TAR also reduced the relative increases in polydispersity with greater charge ratio asymmetry (polyanion excess). As a result, the dip in polydispersity observed at the stoichiometric charge ratio was maintained at more asymmetric charge ratios. TAR was also modulated during titration, revealing size dependence only on the TAR specified as the PEC mixture passed through the isoelectric point. From these observations, the authors posited the following mechanism: neutral PECs formed at the isoelectric point can aggregate and coalesce without the electrostatic stabilization afforded by excess charge. At slow TAR, the introduction and therefore migration of excess polyanions to the surfaces of these coalescing neutral PECs is slower in comparison to the timescale of PEC aggregation. Conversely, higher TARs flood the PE quicker with excess polyanion and the two competing timescales become more commensurate, stabilizing neutral PECs quicker and resulting in smaller final particles (Figure 3.18b).

Given the importance of the TAR and the associated timescales of stabilization when preparing PECs *via* titration, the use of micro-mixing

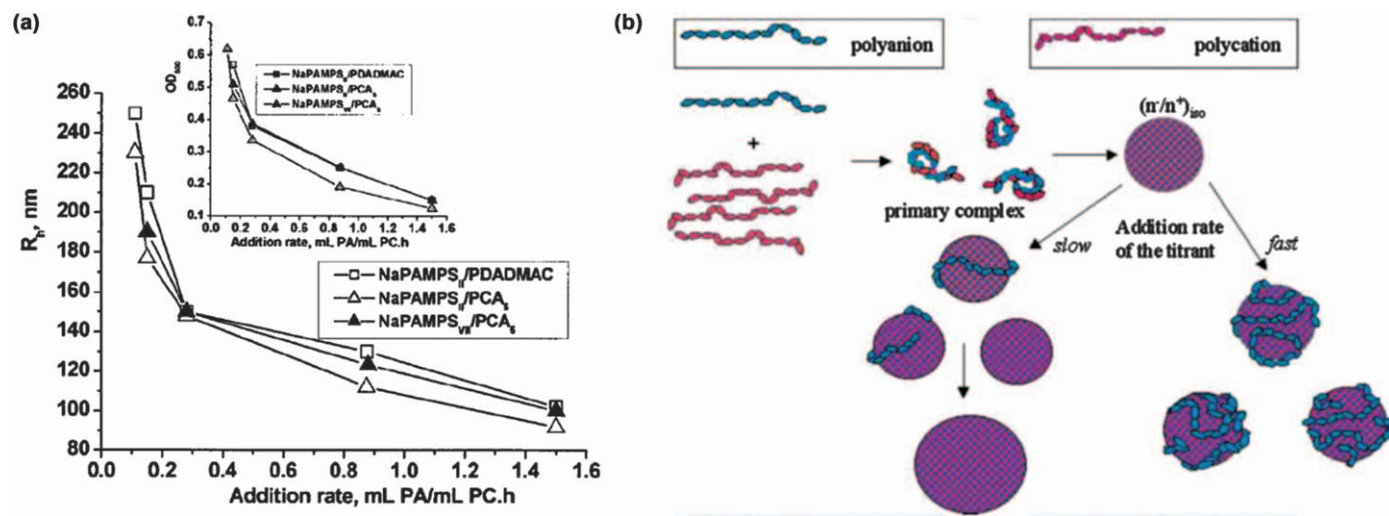


**Figure 3.18** (a) PC size ( $R_h$ ) and turbidity ( $OD_{500}$ ) vs. TAR for various PE pairs. (b) Proposed mechanism of PEC formation and stabilization for slow and fast TARs.

Reproduced from ref. 103 with permission from John Wiley and Sons, Copyright © 2004 Wiley Periodicals, Inc.

technologies such as CIJ and MIVM mixing with shorter mixing timescales could impact PEC formation and open new pathways for continuous, high-throughput PEC fabrication for a variety of applications.

### 3.7.3 Flash NanoComplexation (FNC)

The benefit and influence of process parameters intrinsic to CIJ mixing such as  $\tau_{\text{mix}}$  as well as characteristics of the constituent PEs were explored by Ankerfors *et al.*<sup>105</sup> to develop the process later coined by Santos *et al.*<sup>106</sup> as Flash NanoComplexation (FNC). Experimentally, aqueous solutions of poly(allylamine hydrochloride) (PAH) and poly(acrylic acid) (PAA) were impinged inside a CIJ mixer and the resultant PECs were characterized by dynamic light scattering (DLS). By systematically varying PE molecular weight, charge ratio, concentration, and flow velocity, particle size trends were elucidated. Specifically, higher molecular weights, concentrations, and charge ratios closer to the isoelectric point yielded larger particles. When increasing  $\tau_{\text{mix}}$ , little increase in size was observed except for short times ( $\tau_{\text{mix}} < 20$  ms) in which particles composed of higher molecular weight PAA were larger in size as  $\tau_{\text{mix}}$  was reduced (Figure 3.19a). This observation was posited to stem from a resistance to flow by longer chains leading to branching between pre-complexes and subsequent aggregation. The invariance of particles size to  $\tau_{\text{mix}}$  was investigated by measuring the diffusion of PEs *via* DLS. An estimate for the timescale of diffusion and association was found to be 0.21 ms, shorter than the shortest  $\tau_{\text{mix}}$  attained *via* CIJ mixers (~2 ms) and thus strongly decoupled to the mixing time (*i.e.*  $Da \gg 1$ ). Yet, when compared to titration of PE mixtures, CIJ mixing consistently produced smaller particle sizes (Figure 3.19b), highlighting the potential benefit of the technique.

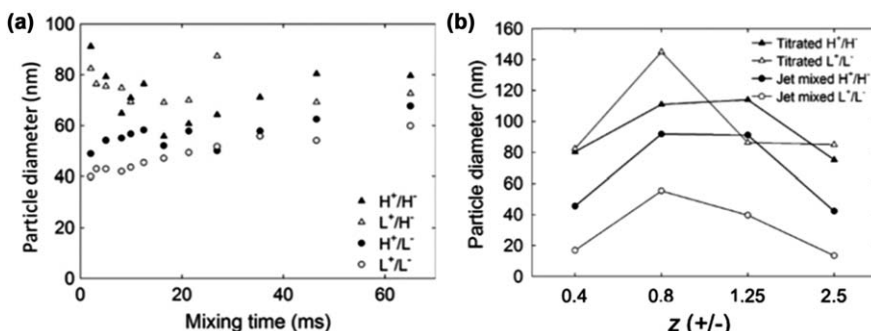


**Figure 3.19** (a) Particle diameters generated from CIJ mixing at various stream flow rates and corresponding mixing times. (b) Comparison between titration and CIJ methods for PEC fabrication. Notation: “H” = high molecular weight (15k PAH/5k PAA); “L” = lower molecular weight (70k PAH/240k PAA); “+” = PAH; “−” = PAA.  
Adapted from ref. 105 with permission from Elsevier, Copyright 2010.

### 3.7.4 Encapsulation *via* FNC

Polyelectrolyte complexation has been employed to encapsulate a wide range of substances. For encapsulation of higher molecular weight ingredients, Black *et al.* utilized poly(lysine) to form pre-complexes with bovine serum albumin (BSA) proteins which were subsequently complexed with poly(glutamic acid) to form microscale coacervates exhibiting pH dependent release characteristics.<sup>107</sup> Conversely, PEC formation has also been used for small molecule encapsulation. Zhu *et al.* studied the size stability of precipitated β-carotene NPs alone and in the presence of poly(ethylene imine) and chitosan (CS), identifying a reduction in particle growth. The authors suggested that the increase in stability arose from both steric and electrostatic interactions, serving as an alternative to standard diblock copolymer stabilization layers.<sup>96</sup> Alternatively, instead of using pre-formed PE chains to create complexes, Zhang *et al.* ion paired 2-acylamide-2-methylpropanesulfonic acid (AMPS) with ammonium groups on CS followed by polymerization to form CS-PAMPS complexes encapsulating doxorubicin.<sup>108</sup>

The use of FNC for encapsulation and delivery of active ingredients has been demonstrated in investigations conducted by collaborations between Mao, Leong, and Chen *et al.*<sup>106,109–111</sup> Santos *et al.* studied CIJ mixing of aqueous solutions of linear polyethyleneimine (*l*PEI) and plasmid DNA to reproducibly produce complex nanoparticles for transfection.<sup>106</sup> Similar to the aforementioned results,<sup>105</sup> as stream flow rate was increased, complex size was reduced for intermediate flow rates with a slight increase at the highest flow rate of 50 mL min<sup>-1</sup>. Adjusting the pH of the *l*PEI stream to modulate its protonation, and therefore the charge ratio of complexation, resulted in a transition from spherical to rod-like particles. This was attributed to lessening charge associations between *l*PEI and DNA plasmids which prevented complexes from being tightly bound, resulting in less spherical particles. Similarly, as the overall PE concentrations were increased, rod-like particles were generated. This outcome suggested a transition from the  $Da < 1$  to  $Da > 1$  regime in which an increasingly higher number of PE associations can occur during  $\tau_{mix}$  leading to a higher coordination number per PE chain and less efficient packing associated with rod-like particles. *In vitro* and *in vivo* transfection efficiency studies of the *l*-PEI/DNA complexes generated from bulk mixing and FNC showed insignificant differences, validating FNC as a suitable continuous process alternative.

Further studies have demonstrated the efficacy of FNC for encapsulation. He *et al.* utilized the ionic gelation of chitosan with tripolyphosphate in a MIVM geometry to encapsulate insulin for intended oral delivery applications.<sup>109</sup> FNC generated the smallest, most monodisperse particles when compared to injection, drop-wise addition, or bulk mixing methods. Furthermore, release of insulin into pH 7.4 buffer solution showed greater linearity with time compared to PECs fabricated *via* drop-wise addition. The encapsulation efficiency of insulin correlated with the pH of the final

mixture with the highest value, 90%, achieved at the highest tested pH of 6.5. This was attributed to a shift in the isoelectric point of the insulin due to self-association and charge masking from fast mixing. Similarly, Tian *et al.* explored FNC to produce PECs with insulin for penetration of mucus and intestinal epithelium barriers in the GI tract which limit oral delivery formulations.<sup>110</sup> Using a two-step process, modified chitosan was mixed with insulin in a MIVM, and then next mixed against hyaluronic acid (HA) with and without thiol functionalization (Figure 3.20). The first stage was optimized to generate PECs 75 nm in diameter with an encapsulation efficiency of 91% and mass loading of 64.5%. The second stage coated HA onto these PECs, increasing their size to 101 nm and inverting their surface charge in a similar manner to layer-by-layer adsorption of polyelectrolytes. Photo-quenching of HA-coated PECs in mucin demonstrated higher mobility in comparison to the positively charged precursors which interact strongly with the negatively charged mucin matrix and, therefore, are immobilized. Application of PECs to rat jejunum tissue loops showed significantly higher penetration of insulin through the mucin layer as well as into the epithelial cell layer with HA-coated PECs when compared to precursor chitosan PECs. Further improvements in penetration *via* thiol-functionalized HA coatings were also observed, ascribed to the favorable disulfide bonding at the epithelial cell level.

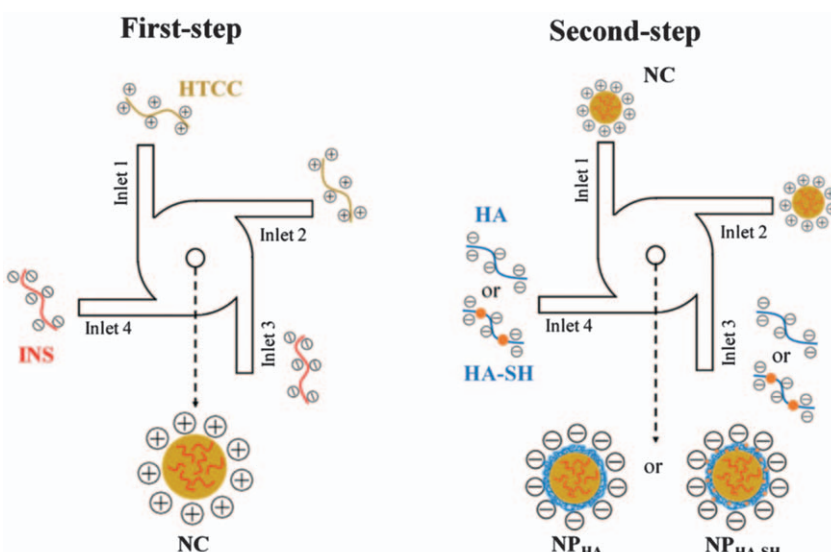


**Figure 3.20** Schematic of step-by-step FNC for encapsulating insulin (INS) with modified chitosan (HTCC) and coating with HA or thiol-functionalized HA (HA-SH).

Reproduced from ref. 110 with permission from John Wiley and Sons, © 2018 WILEY-VCH Verlag GmbH & Co. KGaA, Weinheim.

Also using the MIVM technique, Qiao *et al.* fabricated PECs of chitosan and heparin to coencapsulate the subunit antigen protein VP1 with an adjuvant, TNF or CpG.<sup>111</sup> In comparing the activity of adjuvants encapsulated inside the PECs with VP1 and free in solution with PECs containing VP1, a significant increase in activity was observed for the former case, highlighting the enhancing benefits of FNC encapsulation.

### 3.8 Summary

In this chapter, we have reviewed FNP and FNC as two promising processes with which to prepare polymer colloids. While rapid mixing and subsequent solvent exchange during FNP result in collapse and aggregation of polymer globules to form monodisperse polymer colloids, phase separation between chemically distinct polymers can further result in the formation of colloids with complex internal structures, including those with Janus, core–shell, and hierarchically-structured morphologies. Alternatively, FNC relies on the complexation of two oppositely-charged species upon mixing to create polymer colloids without the need for organic solvents and has been shown to effectively encapsulate a variety of payloads. We have reviewed the various equipment configurations that can be used to perform both FNP and FNC and emphasize that these processes can be run in a continuous manner at room temperature, making them economical options and requiring relatively few alterations to scale up the production of polymer colloids.

## References

1. M. A. C. Stuart, W. T. S. Huck, J. Genzer, M. Müller, C. Ober, M. Stamm, G. B. Sukhorukov, I. Szleifer, V. V. Tsukruk and M. Urban, *et al.*, Emerging Applications of Stimuli-Responsive Polymer Materials, *Nat. Mater.*, 2010, **9**(2), 101–113.
2. E. S. Daniels, E. D. Sudol and M. S. El-Aasser, Overview of Polymer Colloids: Preparation, Characterization, and Applications, in *Polymer Colloids*, 2001, pp 1–12.
3. J. W. Hickey, J. L. Santos, J.-M. Williford and H.-Q. Mao, Control of Polymeric Nanoparticle Size to Improve Therapeutic Delivery Graphical Abstracts HHS Public Access, *J. Controlled Release*, 2015, **219**, 536–547.
4. M. E. Gindy and R. K. Prud'homme, Multifunctional Nanoparticles for Imaging, Delivery and Targeting in Cancer Therapy, *Expert Opin. Drug Delivery*, 2009, **6**(8), 865–878.
5. A. Shahrvan and T. Matsoukas, Encapsulation and Controlled Release from Core–Shell Nanoparticles Fabricated by Plasma Polymerization, *J. Nanopart. Res.*, 2012, **14**(1), 668–678.
6. H. D. Lu, B. K. Wilson, T. L. Lim, A. Heinmiller and R. K. Prud'homme, Real-Time and Multiplexed Photoacoustic Imaging of Internally Normalized Mixed-Targeted Nanoparticles, *ACS Biomater. Sci. Eng.*, 2017, **3**(3), 443–451.

7. S.-H. Hu and X. Gao, Nanocomposites with Spatially Separated Functionalities for Combined Imaging and Magnetolytic Therapy, *J. Am. Chem. Soc.*, 2010, **132**(21), 7234–7237.
8. S. N. Yin, C. F. Wang, Z. Y. Yu, J. Wang, S. S. Liu and S. Chen, Versatile Bifunctional Magnetic-Fluorescent Responsive Janus Supraballs towards the Flexible Bead Display, *Adv. Mater.*, 2011, **23**(26), 2915–2919.
9. S. K. Smoukov, S. Gangwal, M. Marquez and O. D. Velev, Reconfigurable Responsive Structures Assembled from Magnetic Janus Particles, *Soft Matter*, 2009, **5**, 1285–1292.
10. J. Wu and L. L. Dai, Apparent Microrheology of Oil-Water Interfaces by Single-Particle Tracking, *Langmuir*, 2007, **23**(8), 4324–4331.
11. A. I. Campbell and S. J. Ebbens, Gravitaxis in Spherical Janus Swimming Devices, *Langmuir*, 2013, **29**, 14066–14073.
12. A. Walther and A. H. E. Müller, Well-Defined Nanostructured Polymer Blends with Janus Particles, *Interface*, 2009, **2**, 1–2.
13. B. T. T. Pham, C. H. Such and B. S. Hawkett, Synthesis of Polymeric Janus Nanoparticles and Their Application in Surfactant-Free Emulsion Polymerizations, *Polym. Chem.*, 2015, **6**, 426–435.
14. R. J. Demyanovich, Production of Commercial Dyes via Impingement-Sheet Mixing Part I. Testing of a Device Suitable for Industrial Application, *Chem. Eng. Process.*, 1991, **29**, 173–177.
15. M. Midler Jr., E. L. Paul, E. F. Whittington, M. Futran, P. D. Liu, J. Hsu, S.-H. Pan Crystallization Method to Improve Crystal Structure and Size. *U. S. Pat.* 5, 314, 506, 1994.
16. D. L. Marchisio, L. Rivautella and A. A. Barresi, Design and Scale-Up of Chemical Reactors for Nanoparticle Precipitation, *AICHE J.*, 2006, **52**(5), 1877–1887.
17. S. M. D'Addio and R. K. Prud'homme, Controlling Drug Nanoparticle Formation by Rapid Precipitation, *Adv. Drug Delivery Rev.*, 2011, **63**(6), 417–426.
18. W. S. Saad and R. K. Prud'homme, Principles of Nanoparticle Formation by Flash Nanoprecipitation, *Nano Today*, 2016, **11**(2), 212–227.
19. A. J. Mahajan and D. J. Kirwan, Nucleation and Growth Kinetics of Biochemicals Measured at High Supersaturations, *J. Cryst. Growth*, 1994, **144**, 281–290.
20. B. K. Johnson and R. K. Prud'homme, Chemical Processing and Micromixing in Confined Impinging Jets, *AICHE J.*, 2003, **49**(9), 2264–2282.
21. M. Rubinstein and R. H. Colby, Polymer Solutions, in *Polymer Physics*, Oxford University Press, 2003, pp. 171–198.
22. T. I. Morozova and A. Nikoubashman, Coil – Globule Collapse of Polystyrene Chains in Tetrahydrofuran – Water Mixtures, *J. Phys. Chem. B*, 2018, **122**(7), 2130–2137.
23. S. M. Moghimi, A. C. Hunter and J. C. Murray, Long-Circulating and Target-Specific Nanoparticles: Theory to Practice, *Pharmacol. Rev.*, 2001, **53**(2), 283–318.

24. C. Monfardini and F. M. Veronese, Stabilization of Substances in Circulation, *Bioconjugate Chem.*, 1998, **9**(4), 418–450.
25. D. Bazille, C. Prud'homme, M.-T. Bassoulet, M. Marlard, G. Spenlehauer and M. Veillard, Stealth Me. PEG-PLA Nanoparticles Avoid Uptake by the Mononuclear Phagocytes System, *J. Pharm. Sci.*, 1995, **84**(4), 493–498.
26. C. Liguore and L. Leibler, Thermodynamics and Kinetics of Grafting End-Functionalized Polymers to an Interface, *J. Phys.*, 1990, **51**(12), 1313–1328.
27. C. Amiel, M. Sikka, J. W. Schneider, Y.-H. Tsao, M. Tirrell and J. W. Mays, Adsorption of Hydrophilic-Hydrophobic Block Copolymers on Silica from Aqueous Solutions, *Macromolecules*, 1995, **28**(9), 3125–3134.
28. R. F. Pagels, J. Edelstein, C. Tang and R. K. Prud'homme, Controlling and Predicting Nanoparticle Formation by Block Copolymer Directed Rapid Precipitations, *Nano Lett.*, 2018, **18**(2), 1139–1144.
29. S. J. Budijono, B. Russ, W. Saad, D. H. Adamson and R. K. Prud'homme, Block Copolymer Surface Coverage on Nanoparticles, *Colloids Surf., A*, 2010, **360**, 105–110.
30. C. Sosa, R. Liu, C. Tang, F. Qu, S. Niu, M. Z. Bazant, R. K. Prudhomme and R. D. Priestley, Soft Multifaced and Patchy Colloids by Constrained Volume Self-Assembly, *Macromolecules*, 2016, **49**(9), 3580–3585.
31. N. Li, A. Z. Panagiotopoulos and A. Nikoubashman, Structured Nanoparticles from the Self-Assembly of Polymer Blends through Rapid Solvent Exchange, *Langmuir*, 2017, **33**, 6021–6028.
32. B. K. Johnson and R. K. Prud'homme, Flash NanoPrecipitation of Organic Actives and Block Copolymers Using a Confined Impinging Jets Mixer, *Aust. J. Chem.*, 2003, **56**(10), 1021–1024.
33. A. Nikoubashman, V. E. Lee, C. Sosa, R. K. Prud'homme, R. D. Priestley and A. Z. Panagiotopoulos, Directed Assembly of Soft Colloids through Rapid Solvent Exchange, *ACS Nano*, 2016, **10**(1), 1425–1433.
34. V. E. Lee, C. Sosa, R. Liu, R. K. Prud'homme and R. D. Priestley, Scalable Platform for Structured and Hybrid Soft Nanocolloids by Continuous Precipitation in a Confined Environment, *Langmuir*, 2017, **33**(14), 3444–3449.
35. C. Zhang, V. J. Pansare, R. K. Prud'homme and R. D. Priestley, Flash Nanoprecipitation of Polystyrene Nanoparticles, *Soft Matter*, 2012, **8**(1), 86–93.
36. K. M. Pustulka, A. R. Wohl, H. S. Lee, A. R. Michel, J. Han, T. R. Hoye, A. V. McCormick, J. Panyam and C. W. Macosko, Flash Nanoprecipitation: Particle Structure and Stability, *Mol. Pharmacol.*, 2013, **10**(11), 4367–4377.
37. B. K. Johnson and R. K. Prud'homme, Mechanism for Rapid Self-Assembly of Block Copolymer Nanoparticles, *Phys. Rev. Lett.*, 2003, **91**(11), 118302.
38. R. F. Pagels and R. K. Prud'homme, Inverse Flash NanoPrecipitation for Biologics Encapsulation: Nanoparticle Formation and Ionic

- Stabilization in Organic Solvents, in *Control of Amphiphile Self-Assembling at the Molecular Level: Supra-Molecular Assemblies with Tuned Physico-chemical Properties for Delivery Applications*, ed. M. A. Ilies, 2017, vol. 1271, pp. 249–274.
- 39. M. E. Gindy, K. DiFelice, V. Kumar, R. K. Prud'homme, R. Celano, R. M. Haas, J. S. Smith and D. Boardman, Mechanism of Macromolecular Structure Evolution in Self-Assembled Lipid Nanoparticles for SiRNA Delivery, *Langmuir*, 2014, **30**(16), 4613–4622.
  - 40. K. Margulis, S. Magdassi, H. S. Lee and C. W. Macosko, Formation of Curcumin Nanoparticles by Flash Nanoprecipitation from Emulsions, *J. Colloid Interface Sci.*, 2014, **434**, 65–70.
  - 41. R. W. O'Brien, B. R. Midmore, A. Lamb and R. J. Hunter, Electro-acoustic Studies of Moderately Concentrated Colloidal Suspensions, *Faraday Discuss. Chem. Soc.*, 1990, **90**, 301–312.
  - 42. J. K. Beattie, A. M. Djerdjev and G. G. Warr, The Surface of Neat Water Is Basic, *Faraday Discuss.*, 2009, **141**, 31–39.
  - 43. V. Buch, A. Milet, R. Vácha, P. Jungwirth and J. P. Devlin, Water Surface Is Acidic, *Proc. Natl. Acad. Sci. U. S. A.*, 2007, **104**(18), 7342–7347.
  - 44. R. Vacha, V. Buch, A. Milet, J. P. Devlin and P. Jungwirth, Autoionization at the Surface of Neat Water: Is the Top Layer PH Neutral, Basic, or Acidic?, *Phys. Chem. Chem. Phys.*, 2007, **9**(34), 4736–4747.
  - 45. M. Takahashi, Potential of Microbubbles in Aqueous Solutions: Electrical Properties of the Gas-Water Interface, *J. Phys. Chem. B*, 2005, **109**(46), 21858–21864.
  - 46. R.-H. Yoon and J. L. Yordan, Zeta-Potential Measurements on Microbubbles Generated Using Various Surfactants, *J. Colloid Interface Sci.*, 1986, **113**(2), 430–438.
  - 47. S. Usui and H. Sasaki, Zeta Potential Measurements of Bubbles in Aqueous Surfactant Solutions, *J. Colloid Interface Sci.*, 1978, **65**(1), 36–45.
  - 48. J. C. Carruthers, The Electrophoresis of Certain Hydrocarbons and Their Simple Derivatives as a Function of PH, *Trans. Faraday Soc.*, 1938, **34**, 300–307.
  - 49. D. E. Dunstan and D. A. Saville, Electrokinetic Potential of the Alkane/Aqueous Electrolyte Interface, *J. Chem. Soc. Faraday Trans.*, 1993, **89**(3), 527–529.
  - 50. R. Zimmermann, S. Dukhin and C. Werner, Electrokinetic Measurements Reveal Interfacial Charge at Polymer Films Caused by Simple Electrolyte Ions, *J. Phys. Chem. B*, 2001, **105**(36), 8544–8549.
  - 51. K. G. Marinova, R. G. Alargova, N. D. Denkov, O. D. Velev, D. N. Petsev, I. B. Ivanov and R. P. Borwankar, Charging of Oil-Water Interfaces Due to Spontaneous Adsorption of Hydroxyl Ions, *Langmuir*, 1996, **12**(8), 2045–2051.
  - 52. J. K. Beattie and A. M. Djerdjev, The Pristine Oil/Water Interface: Surfactant-Free Hydroxide-Charged Emulsions, *Angew. Chem., Int. Ed.*, 2004, **43**(27), 3568–3571.

53. X. Yan, M. Delgado, J. Aubry, O. Gribelin, A. Stocco, F. Boisson-Da Cruz, J. Bernard and F. Ganachaud, Central Role of Bicarbonate Anions in Charging Water/Hydrophobic Interfaces, *J. Phys. Chem. Lett.*, 2018, **9**(1), 96–103.
54. R. Vacha, S. W. Rick, P. Jungwirth, A. G. F. de Beer, H. B. de Aguiar, J.-S. Samson and S. Roke, The Orientation and Charge of Water at the Hydrophobic Oil Droplet/Water Interface, *J. Am. Chem. Soc.*, 2011, **133**(26), 10204–10210.
55. T. L. Tarbuck, S. T. Ota and G. L. Richmond, Spectroscopic Studies of Solvated Hydrogen and Hydroxide Ions at Aqueous Surfaces, *J. Am. Chem. Soc.*, 2006, **128**(45), 14519–14527.
56. R. Vacha, O. Marsalek, A. P. Willard, D. Jan Bonthuis, R. R. Netz and P. Jungwirth, Charge Transfer between Water Molecules as the Possible Origin of the Observed Charging at the Surface of Pure Water, *J. Phys. Chem. Lett.*, 2012, **3**(1), 107–111.
57. C. E. Markwalter, R. F. Pagels, B. K. Wilson, K. D. Ristrop and R. K. Prud'homme, Flash NanoPrecipitation for the Encapsulation of Hydrophobic and Hydrophilic Compounds in Polymeric Nanoparticles, *J. Visualized Exp.*, 2019, (143), e58757.
58. J. Han, Z. Zhu and H. Qian, *et al.*, A Simple Confined Impingement Jets Mixer for Flash Nanoprecipitation, *J. Pharm. Sci.*, 2012, **101**(10), 4018–4023.
59. Y. Liu, C. Cheng, Y. Liu, R. K. Prud'homme and R. O. Fox, Mixing in a Multi-Inlet Vortex Mixer (MIVM) for Flash Nano-Precipitation, *Chem. Eng. Sci.*, 2008, **63**, 2829–2842.
60. C. E. Markwalter and R. K. Prud'homme, Design of a Small-Scale Multi-Inlet Vortex Mixer for Scalable Nanoparticle Production and Application to the Encapsulation of Biologics by Inverse Flash NanoPrecipitation, *J. Pharm. Sci.*, 2018, **107**(9), 2465–2471.
61. L. S. Grundy, V. E. Lee, N. Li, C. Sosa, W. D. Mulhearn, R. Liu, R. A. Register, A. Nikoubashman, R. K. Prud'Homme and A. Z. Panagiotopoulos, *et al.*, Rapid Production of Internally Structured Colloids by Flash Nanoprecipitation of Block Copolymer Blends, *ACS Nano*, 2018, **12**(5), 4660–4668.
62. Q. Ying and B. Chu, Overlap Concentration of Macromolecules in Solution, *Macromolecules*, 1987, **20**(2), 362–366.
63. W. W. Graessley, Polymer Chain Dimensions and the Dependence of Viscoelastic Properties on Concentration, Molecular Weight and Solvent Power, *Polymer*, 1980, **21**(3), 258–262.
64. M. Rubinstein and R. H. Colby Introduction, in *Polymer Physics*; 2003.
65. H. B. Eitouni and N. P. Balsara, Thermodynamics of Polymer Blends. in *Physical Properties of Polymers Handbook*, ed. J. E. Mark, Springer, 2007, pp. 339–356.
66. E. Bormashenko, Physics of Solid-Liquid Interfaces: From the Young Equation to the Superhydrophobicity (Review Article) The Cassie-Wenzel Transition of Fluids on Nanostructured Substrates: Macroscopic Force

- Balance versus Microscopic Density-Functional Theory, *Low Temp. Phys.*, 2016, **42**, 114704.
- 67. S. Torza and S. G. Mason, Three-Phase Interactions In Shear and Electrical Fields, *J. Colloid Interface Sci.*, 1970, **33**(1), 67–83.
  - 68. S. Torza and S. G. Mason, Coalescence of Two Immiscible Liquid Drops, *Science*, 1969, **163**(3869), 813–814.
  - 69. N. Pannacci, H. Bruus, D. Bartolo, I. Etchart, T. Lockhart, Y. Hennequin, H. Willaime and P. Tabeling, Equilibrium and Nonequilibrium States in Microfluidic Double Emulsions, *Phys. Rev. Lett.*, 2008, **101**(16), 164502.
  - 70. X. Cao, W. Li, T. Ma and H. Dong, One-Step Fabrication of Polymeric Hybrid Particles with Core-Shell, Patchy, Patchy Janus and Janus Architectures via a Microfluidic-Assisted Phase Separation Process, *RSC Adv.*, 2015, **5**, 79969–79975.
  - 71. Y. L. Fan, C. H. Tan, Y. Lui, D. Zudhistira and S. C. J. Loo, Mechanistic Formation of Drug-Encapsulated Janus Particles through Emulsion Solvent Evaporation, *RSC Adv.*, 2018, **8**, 16032–16042.
  - 72. J. Zhang, Z. Sun and B. Yang, Self-Assembly of Photonic Crystals from Polymer Colloids, *Curr. Opin. Colloid Interface Sci.*, 2009, **14**(2), 103–114.
  - 73. Q. Chen, S. C. Bae and S. Granick, Directed Self-Assembly of a Colloidal Kagome Lattice, *Nature*, 2011, **469**, 381–384.
  - 74. Z. Zhang, A. S. Keys, T. Chen and S. C. Glotzer, Self-Assembly of Patchy Particles into Diamond Structures through Molecular Mimicry, *Langmuir*, 2005, **21**(25), 11548–11551.
  - 75. A. H. Gröschel, A. Walther, T. I. Löbling, F. H. Schacher, H. Schmalz and A. H. E. Müller, Guided Hierarchical Co-Assembly of Soft Patchy Nanoparticles, *Nature*, 2013, **503**, 247–251.
  - 76. Y. Wang, Y. Wang, D. R. Breed, V. N. Manoharan, L. Feng, A. D. Hollingsworth, M. Weck and D. J. Pine, Colloids with Valence and Specific Directional Bonding, *Nature*, 2012, **491**, 51–55.
  - 77. D. J. Kraft, W. S. Vlug, C. M. van Kats, A. van Blaaderen, A. Imhof and W. K. Kegel, Self-Assembly of Colloids with Liquid Protrusions, *J. Am. Chem. Soc.*, 2009, **131**, 1182–1186.
  - 78. D. J. Pochan, J. Zhu, K. Zhang, K. L. Wooley and C. Miesch, Multi-compartment and Multigeometry Nanoparticle Assembly, *Soft Matter*, 2011, **7**, 2500–2506.
  - 79. T. Higuchi, K. Motoyoshi, H. Sugimori, H. Jinnai, H. Yabu and M. Shimomura, Phase Transition and Phase Transformation in Block Copolymer Nanoparticles, *Macromol. Rapid Commun.*, 2010, **31**(20), 1773–1778.
  - 80. C. Sosa, V. E. Lee, L. S. Grundy, M. J. Burroughs, R. Liu, R. K. Prud'homme and R. D. Priestley, Combining Precipitation and Vitrification to Control the Number of Surface Patches on Polymer Nanocolloids, *Langmuir*, 2017, **33**, 5835–5842.

81. D. Suzuki and H. Kawaguchi, Janus Particles with a Functional Gold Surface for Control of Surface Plasmon Resonance, *Colloid Polym. Sci.*, 2006, **284**, 1471–1476.
82. A. Kirillova, C. Schliebe, G. Stoychev, A. Jakob, H. Lang and A. Synytska, Hybrid Hairy Janus Particles Decorated with Metallic Nanoparticles for Catalytic Applications, *ACS Appl. Mater. Interfaces*, 2015, **7**, 21218–21225.
83. M. Pera-Titus, L. Leclercq, J.-M. Clacens, F. De Campo and V. Nardello-Rataj, Pickering Interfacial Catalysis for Biphasic Systems: From Emulsion Design to Green Reactions, *Angew. Chem., Int. Ed.*, 2015, **54**(7), 2006–2021.
84. A. M. Pourrahimi and M. Pumera, Multifunctional and Self-Propelled Spherical Janus Nano/Micromotors: Recent Advances, *Nanoscale*, 2018, **10**, 16398–16415.
85. A. Böker, J. He, T. Emrick and T. P. Russell, Self-Assembly of Nanoparticles at Interfaces, *Soft Matter*, 2007, **3**, 1231–1248.
86. B. J. Kim, G. H. Fredrickson, C. J. Hawker and E. J. Kramer, Nanoparticle Surfactants as a Route to Bicontinuous Block Copolymer Morphologies, *Langmuir*, 2007, **23**(14), 7804–7809.
87. Y. Lin, H. Skaff, T. Emrick, A. D. Dinsmore and T. P. Russell, Nanoparticle Assembly and Transport at Liquid-Liquid Interfaces, *Science*, 2003, **299**(5604), 226–229.
88. A. K. Khandpur, S. Ftirster, F. S. Bates, I. W. Hamley, A. J. Ryan, K. Almdal and K. Mortensen, Polyisoprene-Polystyrene Diblock Copolymer Phase Diagram near the Order-Disorder Transition, *Macromolecules*, 1995, **28**(26), 8796–8806.
89. M. W. Matsen, Phase Behavior of Block Copolymer/Homopolymer Blends, *Macromolecules*, 1995, **28**(17), 5765–5773.
90. H. Yabu, S. Sato, T. Higuchi, H. Jinnai and M. Shimomura, Creating Suprapolymer Assemblies: Nanowires, Nanorings, and Nanospheres Prepared from Symmetric Block-Copolymers Confined in Spherical Particles, *J. Mater. Chem.*, 2012, **22**, 7672–7675.
91. I. K. Voets, A. de Keizer and M. A. C. Stuart, Complex Coacervate Core Micelles, *Adv. Colloid Interface Sci.*, 2009, **147–148**, 300–318.
92. I. K. Voets, R. Fokkink, T. Hellweg, S. M. King, P. de Waard, A. de Keizer and M. A. C. Stuart, Spontaneous Symmetry Breaking: Formation of Janus Micelles, *Soft Matter*, 2009, **5**(5), 999–1005.
93. I. K. Voets, F. A. Leermakers, A. de Keizer, M. Charlaganov and M. A. C. Stuart Co-Assembly Towards Janus Micelles, in *Self Organized Nanostructures of Amphiphilic Block Copolymers I*, ed. A. H. E. Müller and O. Borisov, Springer Berlin Heidelberg, Berlin, Heidelberg, 2011, pp 163–185.
94. S. van der Burgh, R. Fokkink, A. de Keizer and M. A. C. Stuart, Complex Coacervation Core Micelles as Anti-Fouling Agents on Silica and Polystyrene Surfaces, *Colloids Surf. A*, 2004, **242**(1–3), 167–174.

95. I. K. Voets, A. de Keizer, M. A. Cohen Stuart, J. Justynska and H. Schlaad, Irreversible Structural Transitions in Mixed Micelles of Oppositely Charged Diblock Copolymers in Aqueous Solution, *Macromolecules*, 2007, **40**(6), 2158–2164.
96. Z. Zhu, K. Margulis-Goshen, S. Magdassi, Y. Talmon and C. W. Macosko, Polyelectrolyte Stabilized Drug Nanoparticles via Flash Nanoprecipitation: A Model Study With  $\beta$ -Carotene, *J. Pharm. Sci.*, 2010, **99**(10), 4295–4306.
97. D. Kulig, A. Zimoch-Korzycka and A. Jarmoluk, Cross-Linked Alginate/Chitosan Polyelectrolytes as Carrier of Active Compound and Beef Color Stabilizer, *Meat Sci.*, 2017, **123**, 219–228.
98. L. George, M. C. Bayya, K. V. Rohan and R. Srivastava, A Therapeutic Polyelectrolyte–Vitamin C Nanoparticulate System in Polyvinyl Alcohol–Alginate Hydrogel: An Approach to Treat Skin and Soft Tissue Infections Caused by *Staphylococcus Aureus*, *Colloids Surf., B*, 2017, **160**, 315–324.
99. G. Sukhorukov, A. Fery and H. Möhwald, Intelligent Micro- and Nanocapsules, *Prog. Polym. Sci.*, 2005, **30**(8), 885–897.
100. J. van der Gucht, E. Spruijt, M. Lemmers and M. A. C. Stuart, Polyelectrolyte Complexes: Bulk Phases and Colloidal Systems, *J. Colloid Interface Sci.*, 2011, **361**(2), 407–422.
101. X. Liu, M. Haddou, I. Grillo, Z. Mana, J.-P. Chapel and C. Schatz, Early Stage Kinetics of Polyelectrolyte Complex Coacervation Monitored Through Stopped-Flow Light Scattering, *Soft Matter*, 2016, **12**(44), 9030–9038.
102. Y. Senuma, C. Lowe, Y. Zweifel, J. G. Hilborn and I. Marison, Alginate Hydrogel Microspheres and Microcapsules Prepared by Spinning Disk Atomization, *Biotechnol. Bioeng.*, 2000, **67**(5), 616–622.
103. E. S. Dragan and S. Schwarz, Polyelectrolyte Complexes. VII. Complex Nanoparticles Based on Poly(Sodium 2-Acrylamido-2-Methylpropane-sulfonate) Tailored by the Titrant Addition Rate, *J. Polym. Sci., Part A: Polym. Chem.*, 2004, **42**(20), 5244–5252.
104. E. S. Dragan, M. Mihai and S. Schwarz, Polyelectrolyte Complex Dispersions with a High Colloidal Stability Controlled by the Polyion Structure and Titrant Addition Rate, *Colloids Surf., A*, 2006, **290**(1), 213–221.
105. C. Ankerfors, S. Ondaral, L. Wågberg and L. Ödberg, Using Jet Mixing to Prepare Polyelectrolyte Complexes: Complex Properties and Their Interaction with Silicon Oxide Surfaces, *J. Colloid Interface Sci.*, 2010, **351**(1), 88–95.
106. J. L. Santos, Y. Ren, J. Vandermark, M. M. Archang, J.-M. Williford, H.-W. Liu, J. Lee, T.-H. Wang and H.-Q. Mao, Continuous Production of Discrete Plasmid DNA-Polycation Nanoparticles Using Flash Nano-complexation, *Small*, 2016, **12**(45), 6214–6222.

107. K. A. Black, D. Priftis, S. L. Perry, J. Yip, W. Y. Byun and M. Tirrell, Protein Encapsulation via Polypeptide Complex Coacervation, *ACS Macro Lett.*, 2014, **3**(10), 1088–1091.
108. L. Zhang, J. Wang, C. Ni, Y. Zhang and G. Shi, Preparation of Poly-electrolyte Complex Nanoparticles of Chitosan and Poly(2-Acrylamido-2-Methylpropanesulfonic Acid) for Doxorubicin Release, *Mater. Sci. Eng., C*, 2016, **58**, 724–729.
109. Z. He, J. L. Santos, H. Tian, H. Huang, Y. Hu, L. Liu, K. W. Leong, Y. Chen and H.-Q. Mao, Scalable Fabrication of Size-Controlled Chitosan Nanoparticles for Oral Delivery of Insulin, *Biomaterials*, 2017, **130**, 28–41.
110. H. Tian, Z. He, C. Sun, C. Yang, P. Zhao, L. Liu, K. W. Leong, H.-Q. Mao, Z. Liu and Y. Chen, Uniform Core–Shell Nanoparticles with Thiolated Hyaluronic Acid Coating to Enhance Oral Delivery of Insulin, *Adv. Healthcare Mater.*, 2018, **7**(17), 1800285.
111. D. Qiao, L. Liu, Y. Chen, C. Xue, Q. Gao, H.-Q. Mao, K. W. Leong and Y. Chen, Potency of a Scalable Nanoparticulate Subunit Vaccine, *Nano Lett.*, 2018, **18**(5), 3007–3016.

## CHAPTER 4

# *Design and Fabrication of Polymer Microparticles and Capsules Using Microfluidics*

WILLIAM N. SHARRATT AND JOÃO T. CABRAL\*

Department of Chemical Engineering, Imperial College London,  
South Kensington, London SW7 2AZ, UK

\*Email: j.cabral@imperial.ac.uk

## 4.1 Introduction

Demand for micron scale polymer particles and capsules has boomed in recent decades, evidenced by the growth in citations of academic papers in the field, alongside consistently over 100 patents granted annually, illustrated in Figure 4.1(a) and (b), respectively. The significant interest stems from the plethora of precise fabrication approaches and growing applications for polymer microparticles and capsules as functional materials.<sup>1–3</sup> Applications include encapsulation of small molecules, colloids and biomolecules and subsequent release following an appropriate stimulus, employed in common laundry and food products, to advanced drug delivery and therapeutic uses.<sup>4–6</sup> For instance, recent developments have demonstrated the encapsulation of fluorescently labelled colloids or quantum dots to impart optical ‘barcodes’ onto particles, paving the way for big data approaches, such as high-throughput multiplexed biomolecular detection.<sup>7,8</sup> Microparticles comprising organic polymers can exploit both their tuneable chemistry and high surface area in catalysis, and chiral and gas separations.<sup>9,10</sup> A number of applications benefit from the ability to form

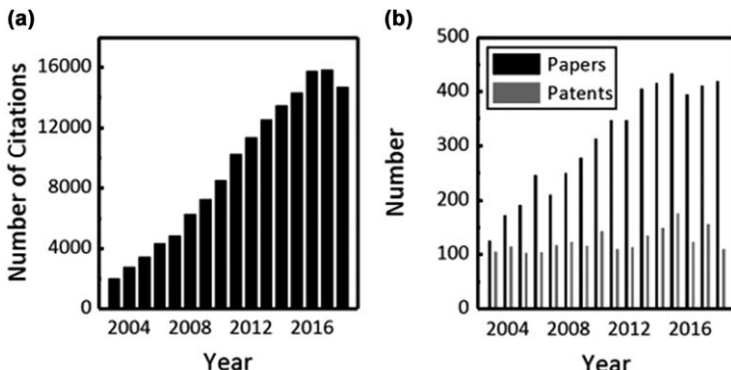


**Figure 4.1** Published literature analysis for: “polymer” and “microcapsule” OR “microparticle” in terms of (a) total number of citations per year and (b) total number of papers and patents published per year (Web of Science, October 2018).

microparticles of non-spherical shapes, and/or patchiness, access a plethora of unique physical,<sup>11–13</sup> optical and sensory properties,<sup>14,15</sup> and enable the predictive self-assembly of such colloidal ‘building blocks’ into highly ordered structures.<sup>16–18</sup>

Since the advent of microfluidics in the late 1990s, accompanied by advances in soft lithography,<sup>19</sup> academic research on polymer microparticles has exploited microdevices and confined flows. Industrial use and commercialisation of products using microfluidics are also becoming more widespread.<sup>20–23</sup> Kumacheva and Garstecki’s 2011 book provides a comprehensive overview of “Microfluidic Reactors for Polymer Particles” (its title), including considerable detail into microfluidic droplet generation.<sup>24</sup> A number of reviews have also focused on droplet microfluidics and emulsification,<sup>1,25–28</sup> as well as microfluidic approaches to particle formation.<sup>3,29–37</sup>

In this chapter, we summarise recent developments in the use of microfluidics for polymer particle and capsule formation, outlining fabrication routes from monomers, polymers and colloids, within single and multi-phase flows. After introducing microdevices and flow operation in Section 4.2, we describe a range of representative chemical (Section 4.3) and physical (Section 4.4) approaches that illustrate the current state of the art in the field. Rather than exhaustively reviewing the literature of the past two decades, we seek to provide an overview of significant approaches, categorised in terms of (4.3.1) Polymerisation of monomer-containing droplets, (4.3.2) Flow lithography in single- (and multi-) phase flows, (4.3.3) Covalent crosslinking of polymer-containing droplets, (4.3.4) Ionic crosslinking of (bio)polymer-containing droplets, (4.3.5) Interfacial complexation for capsule formation, (4.4.1) Particle assembly at interfaces, (4.4.2) Block co-polymer self-assembly in double emulsions and finally (4.4.3) Solvent extraction of polymer-containing droplets. These are depicted in Figure 4.2.

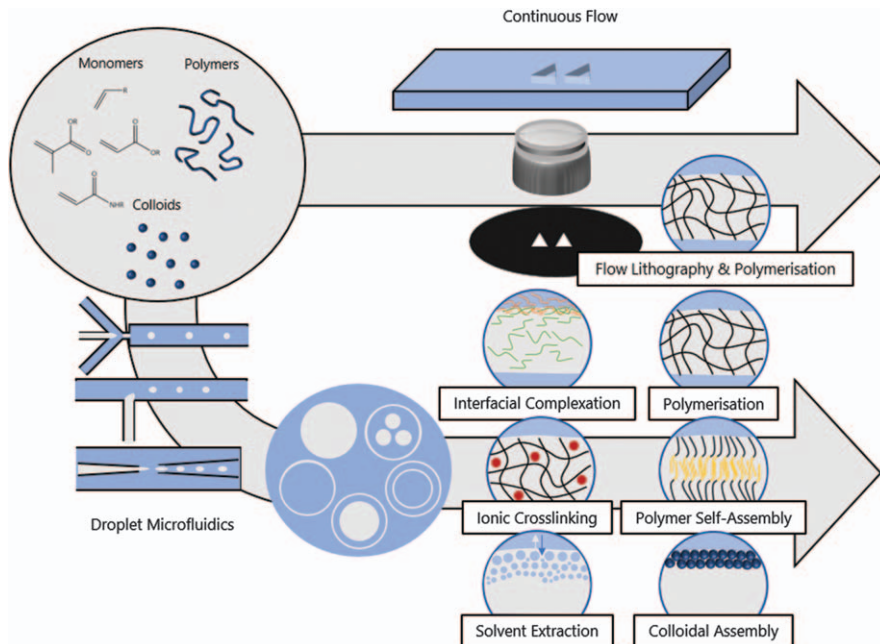


**Figure 4.2** Schematic of microfluidic approaches to microparticle and capsule formation, from monomers, polymers and colloids. Two categories are shown: continuous flow, which comprises flow-lithography and other polymerisation approaches, and droplet templating approaches. The latter exploit droplet microfluidics to generate structured emulsions and a variety of solidification strategies available with ‘soft’ precursor materials.

Evidently, this list is not comprehensive but hopefully provides an inspiring perspective of the capabilities and limitations of microfluidic methods in designing and fabricating a vast array of hierarchical and complex particle motifs.

## 4.2 Single- and Multi-phase Microfluidics and Devices

Microfluidic approaches for polymer particle and capsule generation can employ single-phase as well as multi-phase flows, including co-flowing streams and droplet flows. The precision and control afforded by these methods has been exploited for a range of biological, chemical and physical processes, including fast reaction screening in compartmentalised volumes with control of individual droplet composition and mixing.<sup>38</sup> A significant class of such processes involves the formation of polymeric microparticles and capsules (as well as fibres), benefiting from the uniformity and predictability characteristic of microfluidic systems.

Methods for the controlled generation of structured emulsions are thus central to numerous polymer particle technologies. Whilst droplet generation can be achieved through traditional emulsification methods, microfluidics can precisely harness fluid instabilities, which can be passive or active (*i.e.* in the presence of external fields).<sup>27,39</sup> Typically, the injection of immiscible fluids at a microchannel junction leads to the formation of droplets *via* mechanisms of squeezing (largely dominated by geometry), dripping, jetting, tip-streaming and tip-multi-breaking (governed by the capillary, or Rayleigh–Plateau, instability under confinement). Under prescribed conditions, microdevices enable the high frequency production ( $\sim$ kHz) of monodisperse droplets, with coefficients of variation in size of the order of 1%, and volumes ranging from typically fL to  $\mu$ L (corresponding to diameters of 1–1000  $\mu$ m). Confinement facilitates geometric control over the fluid streams but also allows precise control over the flow fields required to break up such streams into droplets, and suppresses emulsion coalescence and destabilisation mechanisms, such as Ostwald ripening, prior to solidification. Employing multiple junctions and through control of channel geometry, fluid and surface chemistry, and appropriate flow rates, hierarchically structured droplets can be produced, paving the way to ‘designer emulsions’.<sup>1</sup> These can be subsequently converted into particles and capsules, with exceptional precision and reproducibility. Both planar<sup>40</sup> and co-axial<sup>41</sup> devices for multiple emulsion formation have been demonstrated, with not only the emulsion order (double, triple *etc.*) but the number and composition of internal phases varied, as illustrated in Figure 4.3. The majority of droplet generation for microfluidic particle formation occurs with three basic geometries; flow-focussing,<sup>42,43</sup> co-flow (or coaxial flow)<sup>44</sup> and cross-flow.<sup>45,46</sup>

While droplet production can operate at relatively high frequencies (kHz) with a single junction, throughput can be further extended by scaling-out *via* parallelisation or *via* membrane emulsification approaches.<sup>47–49</sup> Microfluidic approaches appear thus suited to high-value, low quantity manufacturing, or approaches requiring complex hierarchical droplets, which are difficult to generate by bulk methods, in addition to mechanistic and kinetic studies into particle and capsule formation (and dissolution).

Microfluidic devices can be fabricated from a range of materials, with glass and poly(dimethyl siloxane) (PDMS) being widely used in droplet microfluidics. PDMS and other polymeric devices are typically favoured for rapid prototyping to optimise microchannel geometries, design and dimensions, and are typically fabricated by soft lithographic and photopolymerisation techniques, as shown in Figure 4.4(a–d) and (e–g), respectively.<sup>19,50,51</sup> Other rapid prototyping techniques, such as laser ablation and micromachining,<sup>52,53</sup> are possible, albeit less widely used.<sup>54</sup> The most common approach for droplet microfluidic device fabrication in glass is shown in Figure 4.4(h–k). It involves the co-axial alignment of a tapered inlet and outlet glass capillary within an outer capillary,<sup>36,55</sup> whose assembly can be challenging. Each microfabrication approach is

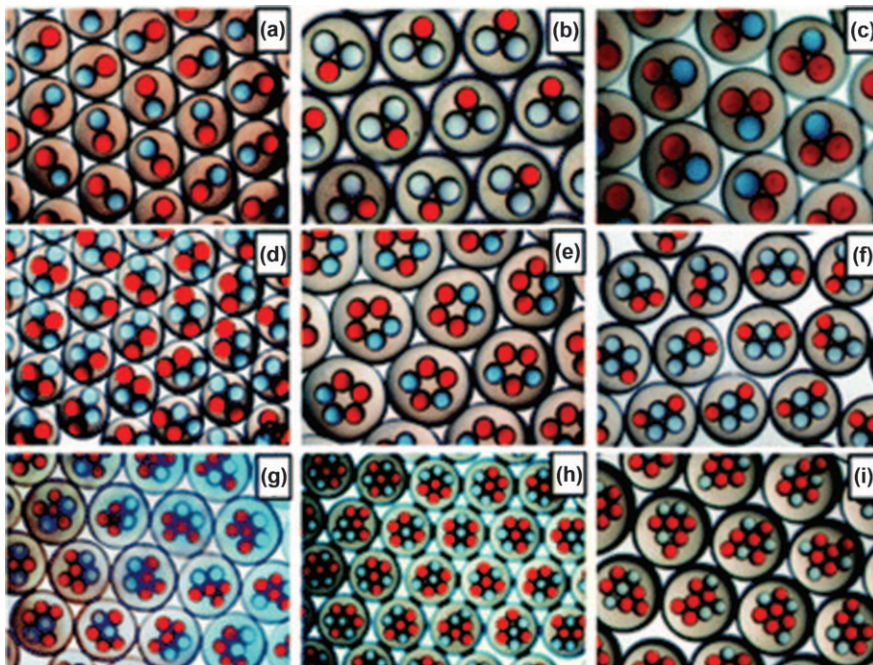


**Figure 4.3** Multiple emulsions generated from a sequential coaxially aligned glass capillary devices with multiple inlets; shown here are double emulsions with prescribed number of inner droplets.

Reproduced from ref. 41 with permission from The Royal Society of Chemistry.

generally best suited to a given flow geometry, or geometries, which must be considered when generating particles in microfluidics.

## 4.3 Chemical Approaches to Particle Solidification

### 4.3.1 Polymerisation of Monomer-containing Droplets

Droplet microfluidics provides compartmentalised reactors capable of undergoing chemical reactions suspended within an immiscible carrier phase that imposes a barrier to reagent diffusion. Microdroplets have therefore been extensively used as polymerisation reactors for the formation of polymeric particles. Reactions which do not require particularly demanding conditions (atmosphere, extreme temperature, specific monomer purity, long reaction times) are naturally suited to microfluidic synthesis.<sup>58</sup> Free-radical polymerisation chemistries are most frequently employed, while polycondensation, an interfacial approach to generating microcapsules,<sup>59,60</sup> is comparatively less used in droplet microfluidics, in part due to the lower flexibility of the chemistries available. Polymerisation within microfluidics can be initiated externally, for instance by heating or exposure to ultra-violet

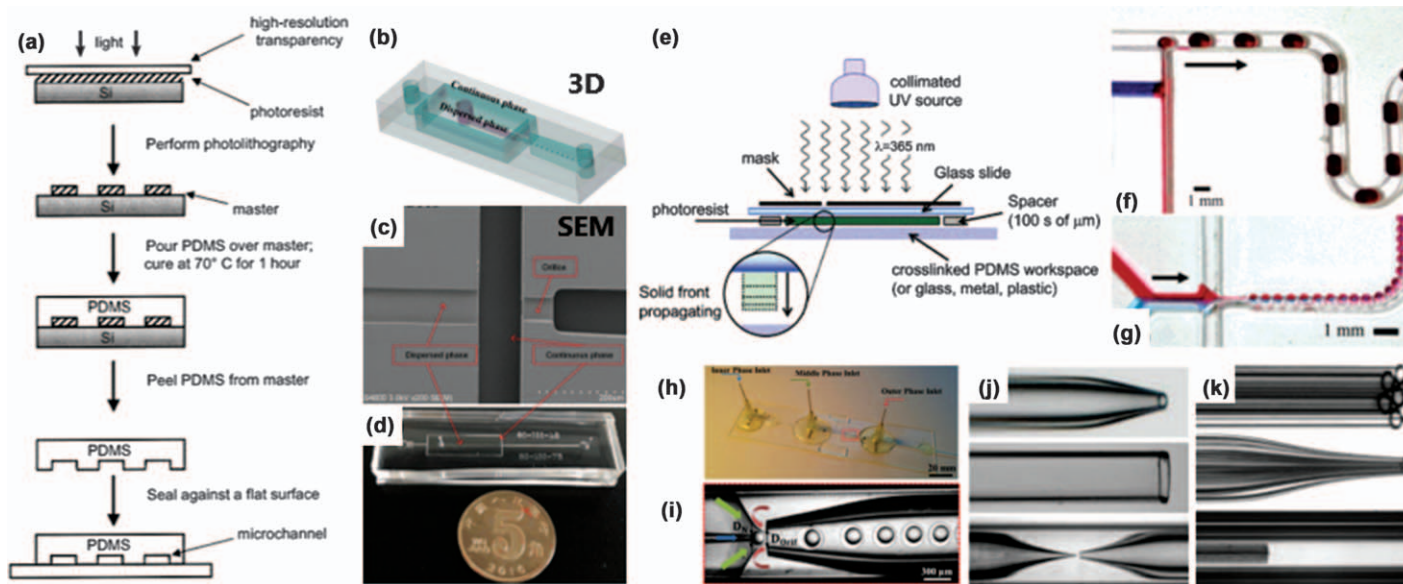


**Figure 4.4** (a) Schematic of PDMS microfluidic device fabrication by a soft lithographic approach.<sup>50</sup> (b) 3D illustration of a microfluidic flow-focussing device. (c) SEM image of a detail of the design in (b). (d) Image of overall device, with a coin shown for scale. (e) Schematic of frontal photopolymerisation (FPP) for rapid prototyping of polymeric microfluidic devices. A 365 nm UV source and photomask are used to pattern an enclosed resist material with the channel design.<sup>51</sup> Height is defined by spacers. (f, g) Example of droplet generation, by cross-flow (f) and flow-focussing (g) geometries, from microfluidic devices fabricated by FPP. (h) Photograph of coaxial capillary microfluidic device used for double emulsion generation. (i) Optical microscopy image of the flow-focussing junction in (h). (j) Optical images of glass capillaries used to fabricate coaxial devices. (k) Examples of multi-inlet capillaries used to precisely generate 'designer emulsions'.

(a) Adapted from ref. 50 with permission from American Chemical Society, Copyright 2002. (b-d) Adapted from ref. 56, <https://doi.org/10.3390/mi9040139>, under the terms of the CC BY 4.0 licence, <https://creativecommons.org/licenses/by/4.0/>. (e) Reproduced from ref. 51 with permission from American Chemical Society, Copyright 2004. (f) and (g) Reprinted with permission from Z. T. Cygan, J. T. Cabral, K. L. Beers and E. J. Amis, Microridic platform for the generation of organic-phase microreactors, *Langmuir*, 2005, **21** (8), 3629–34, Copyright 2005 American Chemical Society. (h) and (i) Reproduced from ref. 57, <https://doi.org/10.1016/j.ces.2015.03.004>, under the terms of the CC BY 4.0 licence, <https://creativecommons.org/licenses/by/4.0/>. (j) and (k) Adapted from ref. 28 with permission from American Chemical Society, Copyright 2017.

(UV) light,<sup>61,62</sup> with high reaction rates and monomer conversions, and can be used within a multitude of precursor template droplet structures. UV irradiation in the presence of a photoinitiator is, so far, the most commonly used approach. However, polymerisation can also be chemically initiated by droplet fusion, rupture of internal droplet compartment,<sup>63</sup> or diffusion across a droplet interface.<sup>25,64</sup> Below, general guidelines for microfluidic droplet polymerisation are discussed and selected applications are illustrated. In these, most monomers contain more than one polymerisable moiety or an additional crosslinking agent is added to yield a polymeric network.

Polymerisation within microfluidics can be initiated *on-chip*, or externally by collecting droplets in a vessel which are subsequently polymerised *ex-situ*.<sup>65</sup> As in traditional polymerisation approaches, the initiator content must be optimised for the target molecular weight of the polymer in the particle (less important for crosslinked networks), reaction rate and to prevent the excessive heating of droplets under exothermic polymerisation conditions. If the initiator is activated by irradiation with light, consideration of the absorption the microfluidic device and photoinitiator, as well as light source emission spectrum is required. Owing to its optical transparency, PDMS is a suitable device material for most applications, as well as glass or quartz. Due to the wetting of channel walls by a thin layer of the carrier fluid and the shrinkage of droplets or plugs upon polymerisation, channel blockages can generally be avoided during solidification. The resulting particle size is thus largely determined by the droplet size (in turn governed by the operation and geometry of the droplet generator) and can be further modulated by microchannel confinement (if one channel dimension is smaller than the droplet radius), flow fields, or active droplet manipulation.

A pioneering demonstration of polymer particle formation, and shape control, combining UV photopolymerisation and droplet microfluidics is illustrated in Figure 4.5(a).<sup>30</sup> Acrylic and vinylic monomer droplets were emulsified with an aqueous surfactant solution in PDMS or poly(urethane) flow-focussing devices, before on-chip UV photopolymerisation downstream. The concept of varying particle morphology by manipulation of channel aspect ratio (height/width) is depicted in Figure 4.5(b-d), and resulting microscopy images of acrylic microparticles, with prescribed spherical, discoidal, rod-like and ellipsoidal morphologies and dimensions, are shown in Figure 4.5(e-h). Additional encapsulants (*e.g.* liquid crystals, quantum dots and porogens) can be added to functionalise the particles. Other functionalised monomers (*e.g.* acrylic acid) can be co-polymerised into particles by this approach and change the particle surface chemistry for application in biological macromolecule isolation, immobilisation and detection.<sup>62</sup>

By incorporation of multiple inlet streams of immiscible monomers into the microfluidic droplet generator, multi-component oil in water (O/W) droplets can also be templated into Janus and patchy particles. The particle

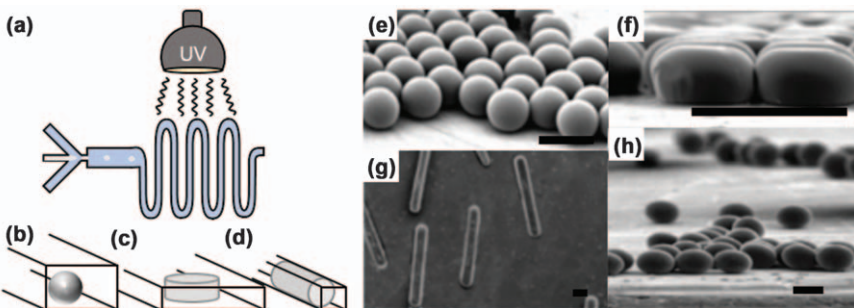


**Figure 4.5** (a) Schematic of the planar PDMS microfluidic flow-focussing device for photocurable monomer droplet formation and *on-chip* UV photopolymerization. (b-d) Schematic depiction of the range of morphologies achievable by manipulation of relative droplet size and channel dimensions. (e-h) Microscopy images of (e) microspheres, (f) disks (g) rods, and (h) ellipsoids.

Adapted from ref. 62 with permission from American Chemical Society, Copyright 2005.

structure can be manipulated through the number of inlet streams of immiscible monomers and their ratio of flow rates, to vary the volume fraction of each stream in the resulting droplet and particle,<sup>66,67</sup> and the spreading parameter, which reflects the balance of interfacial tensions between monomers in the droplet and with the carrier phase.<sup>68</sup> Janus and biphasic particles are generated from combinations of components in the droplet phase with similar interfacial tensions (with respect to the carrier phase). If a non-curable oil (silicone oil), is introduced into the droplet phase, as schematically shown in Figure 4.6(a) and (b),<sup>69</sup> multi-component O/W droplets are readily formed. Upon photopolymerisation and washing of the particles, to remove the silicone oil, a range of hemispherical and biconcave particles can be prepared, shown in Figure 4.6(c-f).<sup>70</sup> Further, core-shell particles can be formed when the interfacial tension between one of the monomers or oils, within the O/W droplet, is lower than the other, leading to a preferential wetting at the O/W interface, before UV photopolymerisation.<sup>68</sup>

Structured, or higher order, emulsion droplets from polymerisable monomers can equally be templated and transformed into polymeric particles. Their shape and morphology is dictated by the multiple emulsion template and appropriate chemistry, or physical phenomena occurring prior to or during polymerisation, *e.g.* phase separation. Figure 4.7 depicts two approaches resulting in the formation of porous polymer particles.<sup>71,72</sup> In the first example, capillary microfluidics was used to generate double emulsions, with a monomer-containing oil phase, and single or multiple encapsulated droplets, as dictated by the relative flow rate of the outer fluid phase. Hierarchically porous particles are formed from photopolymerisation of the middle fluid in a water in oil in water (W/O/W) emulsion, schematically depicted in Figure 4.7(a).<sup>71</sup> Micron sized pores, or voids, are generated from removal of encapsulated aqueous droplets, as shown in the SEM

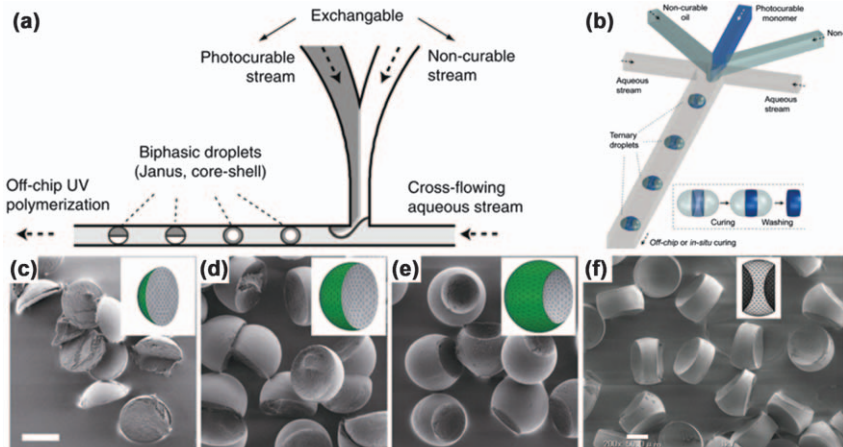


**Figure 4.6** (a) Schematic of the microfluidic cross-flow junction used to generate O/W biphasic droplets and shape-controlled polymeric microparticles through UV photopolymerisation. (b) Schematic representation of ternary O/W droplet formation within a planar microfluidic flow-focussing device. Oil inlet streams comprise one UV curable oil stream (centre) and two non-curable streams. (c–e) SEM images of microparticles, and evolution of morphology, as flow rate ratio of curable and non-curable oil phases are varied from 1 : 4 to 1 : 1 and 4 : 1, yielding two different thicknesses of hemispherical particles and concave dimpled particles, respectively. (f) SEM image of biconcave particle following photopolymerisation with oil droplet ratio of 1 : 1 : 1 prior to washing to remove the non-curable oil phases. (a) and (c–e) Reproduced from ref. 69 with permission from Springer Nature, Copyright 2009. (b) and (f) Reproduced from ref. 70 with permission from John Wiley and Sons, © 2014 Wiley VCH Verlag GmbH & Co. KGaA, Weinheim.

images in Figure 4.7(b) and (e), for single and double droplet cores, respectively. Pores within the shell are induced from the minute partial miscibility of water in the monomer and formation of surfactant stabilised water in oil (W/O) nanodroplets during emulsion formation, as shown in Figure 4.7(c, d) and (f, g). An alternative approach to generating porosity in microparticles involves the addition of an inert amphiphilic molecule (*e.g.* long chain alcohol) into the oil phase of a W/O/W emulsion. Upon photopolymerisation, the alcohol causes phase separation of the growing polymer domains into small spherical aggregates, and the subsequent alcohol removal results in the consolidation of a porous shell, depicted in Figure 4.7(h). The final dry microcapsule structure is shown in Figure 4.7(i) and the structure of the porous shell in (j). Liquid cores could be encapsulated by this approach and applied in, for example, biomolecular sensing.<sup>73</sup> Other polymerisation-induced phase separations have been shown to lead to core–shell particle morphologies, *e.g.* poly(ethylene glycol diacrylate) (PEGDA)-alginate core–shell hydrogel particles, which could be exploited as a drug-delivery vehicle with a sustained release profile.<sup>74</sup>

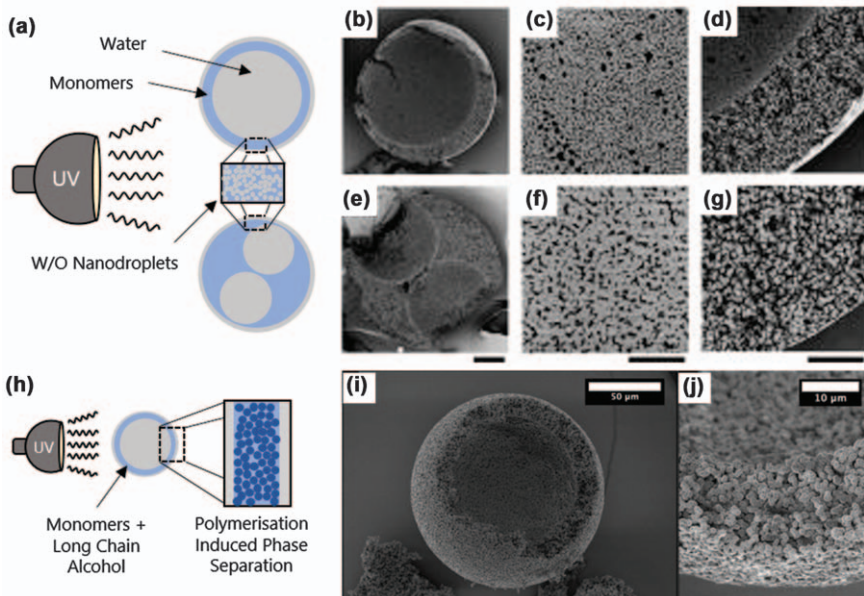
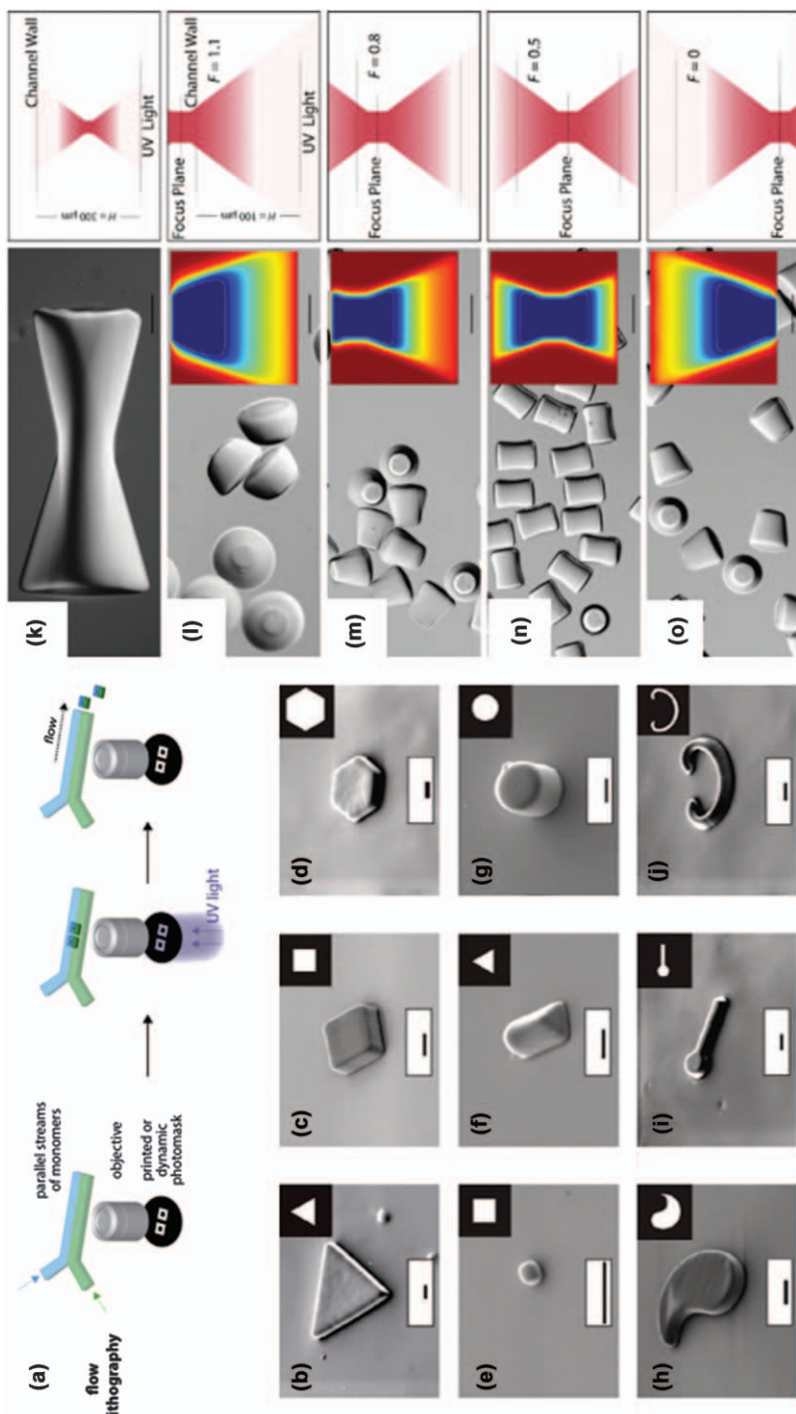


**Figure 4.7** (a) Schematic for UV photopolymerisation of double emulsions, with single and multiple core droplets, generated within a capillary microfluidic device. W/O nanodroplet formation in the middle phase is indicated and arises from the partial miscibility of water in the monomeric oil phase and presence of surfactant. (b–g) SEM images of microparticles formed from photopolymerisation of acrylic co-polymers with micron and nano scale pores. (b–d) Ruptured hierarchical porous poly(MMA-*co*-EGDMA) microparticles with a single micron scale pore. (e–g) Magnetic hierarchical porous poly(MMA-*co*-EGDMAco-GMA) microparticles with two micrometer-sized pores. Scale bars are 50  $\mu\text{m}$  in (b), (e) and 20  $\mu\text{m}$  in (c, d) and (f, g). (h) Schematic of capsule formation by UV photopolymerization of a W/O/W emulsion droplet containing monomers and a long-chain alcohol (30% w/w undecan-1-ol). Polymerisation-induced phase separation results in a porous shell structure. (i) SEM image of a ruptured capsule. (j) SEM image of the shell cross-section, highlighting the porous structure.  
 (a–g) Adapted from ref. 71 with permission from American Chemical Society, Copyright 2015. (h–j) Adapted from ref. 72 with permission from American Chemical Society, Copyright 2017.

### 4.3.2 Flow Lithography in Single- (and Multi-)phase Flows

A range of polymer particles can also be produced by the combination of photopolymerisation and lithographic techniques in single-phase flows, as shown in Figure 4.8(a), without requiring droplet templating. This approach was pioneered by Doyle and co-workers and is referred to as continuous-flow lithography (CFL). The photomask can define arbitrary shapes in the  $x$ – $y$  plane and these 2D patterns are transferred to template polymer particles. Photomasks are generally projected using a microscope objective and a high-intensity, pulsed, UV light source onto a flowing stream of monomer(s) and



photoinitiator within custom-designed PDMS microfluidic devices.<sup>75</sup> Given that a number of photopolymerisation reactions (including acrylates) are inhibited by oxygen, and PDMS exhibits partial permeability to air, light exposure leaves an unpolymerised layer near the channel walls which allows the particles to flow continuously, rather than becoming immobilised at the channel walls. Selected examples of shapes fabricated by this technique are shown in Figure 4.8(b–j). This approach is, however, broadly limited to use of acrylic monomers and formation of dense crosslinked polymer network structures. PDMS also limits reagent compatibility to mostly water-soluble monomers, *e.g.* PEGDA which does not swell and deform the device. The particle size is determined by the height of channel (minus the oxygen inhibition layers on the top and bottom surfaces), photomask feature size and optical resolution (largely defined by the objective). As the optical resolution increases, the depth of field decreases, effectively modulating the distance over which incoming light beam has a fixed diameter. Consequently, the side walls of the particle can also be designed if the depth of field is made smaller than the channel size, thereby resulting in particles with an inhomogeneously polymerised/crosslinked profile. This was exploited in flow-lithography for the generation of 3D particles.<sup>76</sup> Figure 4.8(k–o) shows accessible shapes by variation of the focal plane relative to the channel height, *i.e.* manipulating the depth of field. The resulting particles may thus exhibit non-uniform mechanical responses as well as non-uniform responses to environmental stimuli.

Stopped-flow or pulsed-flow approaches can further increase the spatial resolution of the patterned particles. Typically in CFL, particle shape becomes smeared at high fluid flow rates, which limits either throughput or particle shape definition. To circumvent this, flow can be stopped,

---

**Figure 4.8** (a) Schematic of CFL: photocurable monomers, typically acrylic molecules, are flowed through microchannels. UV light is passed through a photomask and focussed onto the channel with an objective to selectively cure the shape and dimensions defined by the photomask. (b–j) SEM images of PEGDA microparticles formed by CFL and shapes defined by the photomasks shown in the respective insets. Vertical dimensions are defined by the channel height. All scale bars are 10 µm. (k–o) 3D PEGDA microparticles synthesized using a 40× objective (N. A. = 0.6). Optical microscopy images show the shapes resulting from changing the focal plane of UV light within the microchannel relative to the channel height. The height in (k) is 300 µm and 100 µm in (l–o). The relative focal distance value,  $F$ , is 0.5, 1.10, 0.80, 0.50 and 0 in (k–o) respectively. Insets show the simulated oxygen concentration,  $a$ , on surface plots. All scale bars are 50 µm. The right panel shows a schematic diagram of focal plane position relative to the channel height in each case. Insets show the simulated critical monomer conversion contour as the white line, which gives predicted particle shapes in each case.

(a) Reproduced from ref. 83 with permission from Elsevier, Copyright 2015. (b–j) Reproduced from ref. 75 with permission from Springer Nature, Copyright 2006. (k–o) Reproduced from ref. 76 with permission from John Wiley and Sons, © 2013 Wiley VCH Verlag GmbH & Co. KGaA, Weinheim.

monomers polymerised and then flushed out of the microchannels, for instance with compressed air driven flows, which give improved response times. The resulting particles, in the 1–10 µm size range, are thus considerably better resolved by the stop-flow lithography (SFL) approach.<sup>77</sup> Further 3D surface structure can be imparted to particles generated by SFL. By incorporating a PDMS phase mask between the chip and the incoming UV light, generation of a complex interference pattern spatially modulates the light intensity within the masked region to create areas on the surface of the particle which will not crosslink.<sup>78</sup> A combination of SFL, channel topography, and pressure-induced channel deformation can also be used to generate 3D structured particles. In this case, photopolymerisation in CFL is performed with a PDMS microchannel with topographically patterned surfaces, such as pillars (positive relief structures). The resulting particles are held ‘locked’ until sufficient pressure is applied to deform the PDMS and release the particles. As monomer streams can readily flow past the ‘locked’ particle, composite polymer particles with spatially controlled chemical compositions and shapes can be fabricated by an initial ‘locked’ polymerisation followed by replacement of the monomer and a second polymerisation, with a new photomask, to encase the first polymeric precursor.<sup>79</sup>

A non-PDMS based stopped-flow lithography approach has also been developed by Doyle and co-workers to complement their PDMS-based approach.<sup>80</sup> A vertical flow-focussing approach sandwiches a monomer layer between fluid layers, which are inert to UV exposure and a radical trap, in a gas-impermeable microfluidic device, *e.g.* an NOA81 (a thiolene-based resin commercialised by Norland Optical Products) device. Particle heights were then tuned *in situ* by controlling the flow rate of the inert fluid, rather than fixing through the channel height in PDMS devices. The chemical resistance of NOA81 devices facilitates the use of organic solvent and water-insoluble monomers to generate particles with different chemistries, encapsulants (*e.g.* quantum dots, ruthenium dyes) and with well-defined shapes.

Most particle shapes generated by flow-lithographic approaches rely on the projection of 2D patterns, from light focussed through a photomask, with a fixed depth of field and result in shape control in predominately the *x*-*y* plane. Controlling the photopolymerisation in the third dimension (*z* or channel height direction) is thus not trivial. A similar approach to SFL, referred to as optofluidic fabrication, relies on the photopolymerisation of monomer within multi-phase microfluidic flows perturbed by inertial effects, either from curved channel walls or additional structures placed in single channels, such as pillars. Flow then modulates the fluid cross section and defines particle shape in the third dimension to allow fabrication of a plethora of 3D particle shapes. Several examples of particles are shown in Figure 4.9(a) and schematically illustrated in (b), where a photopolymerisable monomer stream is encased within an inert fluid and perturbed by the inertial effects of half pillars adorning the channel walls. Once the fluid cross section has deformed into the desired shape, projection photolithography through a photomask with defined shape is carried

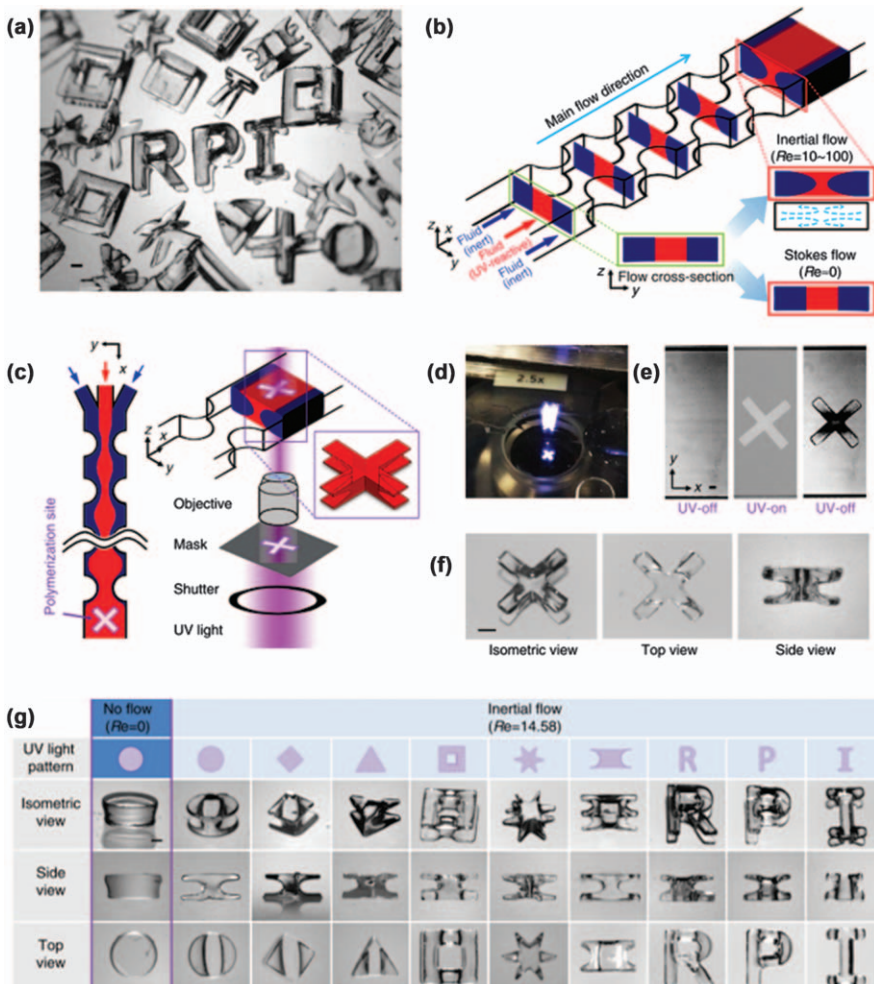


**Figure 4.9** Optofluidic fabrication of 3D microparticles. (a) Examples formed through this approach. (b) Design and operation of inertial flow in a microfluidic device. A jet of photopolymerisable monomer is created with an inert carrier fluid and the flow cross-section is deformed by local vortex formation near the multiple half pillars of the sides of the channels. (c) A schematic of the inertial flow deformation and polymerisation of the deformed monomer stream downstream by flow lithography. Once sufficient deformation is attained, the flow is stopped and the channel illuminated through the photomask with UV light. (d) Image of photomask projection with UV light from a microscope objective onto a microchannel. (e) UV photopolymerisation of a cross shape following pulsing of UV light. (f) Isometric, top and side view of the cross-shaped particle formed. (g) Images of particles formed from different photomasks under identical flow conditions ( $Re = 14.58$ ). Scale bars represent 500  $\mu\text{m}$ . Reproduced from ref. 81, <https://doi.org/10.1038/ncomms7976>, under the terms of the CC BY 4.0 licence, <https://creativecommons.org/licenses/by/4.0/>.

out (c–e). Figure 4.9(f) and (g) shows a subset of shapes patterned under the same flow conditions by this approach. Lateral variation of the pillar position and additional density-driven stratification have further been shown to anisotropically deform the fluid cross section and allow access to a greater range of structured particles.<sup>81,82</sup>

CFL and SFL techniques find a range of encapsulation and delivery applications, which are further extended in flow lithography, particle-based multiplexing, and detection and quantification of biomolecules.<sup>83</sup> For example, acrylate-modified oligonucleotide probes for DNA sequence detection were incorporated into Janus encoded particles by SFL, offering the potential for up to  $2^{20}$  unique particle codes. The biomolecular targets were fluorescently labelled, *e.g.* oligonucleotides with complementary sequences, and therefore allowed detection by fluorescent microscopy within a microfluidic flow-focussing device, which aligned particles before decoding.<sup>84</sup> Multiple analyte detection was also achieved through an SFL approach, detecting attamol quantities of biomolecules without signal amplification. The versatility of this platform not only competes with current commercial screening sensitivity, but at a high throughput, and with a wider array of chemical and fluidic approaches to tune particle morphology and encapsulate a greater range of biomacromolecular analytes.<sup>85,86</sup>

### 4.3.3 Covalent Crosslinking of Polymer-containing Droplets

So far, we have predominantly described particle formation from hydrophobic monomers. However, water-soluble acrylic monomers offer a range of functionalities including thermo-responsive behaviour. Typically, particle formation requires monomer polymerisation and crosslinking or, alternatively, the crosslinking of (pre-formed) polymers in solution, to form hydrogels. Both approaches have been exploited to generate hydrogel microparticles, or ‘microgels’. For example, Kim *et al.* have demonstrated the formation of crosslinked poly(*N*-isopropylacrylamide) (pNIPAm) microgels in a capillary microfluidic device from W/O emulsion droplets.<sup>87</sup> Rapid mixing ( $\simeq 90$  ms) of two aqueous inlets, one containing the radial initiator and the other containing NIPAm monomers, co-monomers and crosslinker, initiates radical polymerisation and crosslinking to form microgel particles. Attractively, spherical particle formation can occur within seconds and consequently no stabiliser is required to prevent coalescence in the outlet stream. Expectedly, particle size is controlled by the droplet size and is a function of the flow rate and size of the capillary orifice. The resulting crosslinked pNIPAm particles can be loaded with a variety of nanoparticle cargoes, which have been shown to not affect the volume phase transition temperature of the thermo-responsive pNIPAm microgel matrix. The temperature-induced swelling and contraction of microgel particles therefore offers a facile release strategy of encapsulated material.

Other morphologies are accessible by polymerising monomers in the presence of crosslinkers. Hollow microgel capsules have been generated

from W/O emulsions by dissolving the initiator in the carrier (outer) phase and relying on diffusion into the monomer and crosslinker-containing droplet to selectively polymerise at the interface.<sup>64</sup> The polymerisation and crosslinking is thus directional and self-limiting, as the radicals generated in the continuous phase by UV photoinitiation cannot diffuse across a sufficiently thick, dense pNIPAm layer. Additionally, Janus ‘snowman’ type morphologies can be designed by combining solvent evaporation from a W/O droplet template, inducing a phase separation and density-driven stratification into an adjoining monomer-rich and monomer-poor droplet, prior to photopolymerisation.<sup>88</sup> Uniquely here, the Janus morphology is obtained with the same chemistry, resulting in particles that exhibit amphiphilic behaviours without any change in chemical functionality.

Polymers with crosslinkable functional groups, or which are readily functionalised *e.g.* polyacrylates or polyacrylamides, are excellent precursors to microgel particles *via* the crosslinking route. For example, pNIPAm, functionalised with photosensitive crosslinking agents, can be dissolved in water and emulsified, through microfluidic flow-focussing, into droplets; upon UV irradiation, the polymers crosslink and form a hydrogel network, yielding a micro-gel particle.<sup>89,90</sup> Fluorescently labelling inlet streams shows that Janus particles and liquid core microgels can be formed through this approach. Alternatively, pre-formed microgels can be injected as the inner phase of a microgel in water in oil droplet, where the middle water phase is a crosslinkable solution of pNIPAm.<sup>90,91</sup> Depending of the chemistry of the microgel particle precursors, the resulting core-shell structures can have multiple thermo-responsive behaviours, from the core and pNIPAm shell, or just the pNIPAm shell alone. Further modifications of microgel structures can be achieved by incorporation of an O/W emulsion into a single aqueous droplet in a capillary microfluidic device.<sup>92</sup> In one example, a solution of pNIPAm and crosslinker was used as the water phase and the inner emulsion oil droplets were over 10 times smaller than the overall droplet. UV crosslinking followed droplet formation and, with removal of the inner oil droplets by washing or temperature cycling and washing, open-celled internal porous structures in the microgel particles could be obtained. No change in the volume phase transition temperature was observed with the change in internal structure of the microgel, although the dynamic response (to temperature cycling) was found to improve due to the porous structure.

Microgel particles can also be crosslinked in microfluidic devices through biocompatible chemistries, which avoid generation of free radicals, such as thiol–ene click chemistry.<sup>93</sup> Hyperbranched poly(glycerols) terminated with thiol groups and PEG-macro crosslinkers can be mixed and broken up into droplets by an oil carrier phase, before coupling agents can crosslink them into a ‘cell-friendly’ microgel. A more recent approach to hydrogel formation involves the phase separation of all-aqueous systems before crosslinking to arrest the structure. Droplet formation from biocompatible dextran and PEG, which can spontaneously form two phases with a low interfacial tension ( $\simeq 0.1 \text{ mN m}^{-1}$ ),<sup>94</sup> generally requires active approaches, which have

been detailed by Sauret and Shum.<sup>95</sup> Droplets can be formed by perturbation of a jet of one aqueous phase in the other, or by using mixtures of the phase separating components as the inner phase of a W/O emulsion. The first approach has been successfully used to generate hydrogel particles from droplets containing methacrylate functionalised dextran, by diffusion of crosslinker from the PEG carrier phase.<sup>96</sup> The second exploits the internal phase separation of PEG monomer-dextran mixtures, followed by cross-linking. Watanabe *et al.* report W/O droplet formation in a capillary microfluidic device followed by internal phase separation of the all-aqueous system, to form water in water in oil (W/W/O) droplets. Subsequently, two end functionalised tetra-PEG macromonomers could then spontaneously cross-couple to form a hydrogel shell, as schematically illustrated in Figure 4.10(a).<sup>97</sup> Much like the biphasic, Janus and core-shell particles described in Figure 4.6, the equilibrium morphology of droplets containing dextran and PEG are determined by the spreading parameter in the three

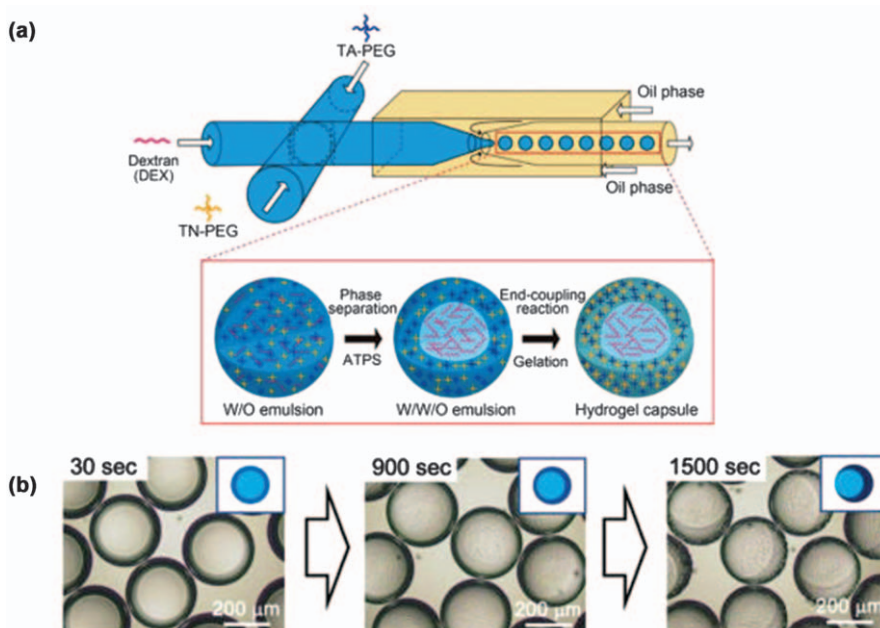


**Figure 4.10** (a) Schematic of the microfluidic formation of dextran-PEG W/O droplets. Following generation, internal phase separation causes formation of a W/W/O core-shell droplet, where an end-coupling reaction can crosslink the two PEG-macromonomers into a hydrogel shell. (b) The kinetics of crosslinking can be slowed by reducing the pH to 4, which allows for a density-difference driven migration of the inner dextran droplet and deviation away from the core-shell structure before the crosslinking arrests the structure. (insets) Schematic of the observed structures.

Adapted from ref. 97 with permission from American Chemical Society, Copyright 2019.

phase system. PEG–oil interfaces have a lower interfacial tension than dextran–oil interfaces and therefore dextran core–PEG shell droplets, and consequently particles, could be expected under neutral pH conditions. However, as depicted by the series of images in Figure 4.10(b), through kinetic control of the crosslinking, the particle morphology can be varied. Here, decreases in pH can be used to slow the kinetics of PEG–macromonomer crosslinking and allow for the inner dextran core to ‘sink’ and result in Janus structures. Subsequent washing can remove the dextran droplet and result in crescent shaped particles. Other morphologies are possible by speeding up the crosslinking process and arresting the particle with multiple cores from the phase separated dextran–PEG mixtures. Alternatively, Ma *et al.* used UV photopolymerisation to solidify internally phase separated dextran–PEGDA droplets into core–shell hydrogel particles.<sup>98</sup> By altering the ratio of dextran to PEGDA in the aqueous phase, the core–shell hydrogels can be transformed into dimpled hydrogels, with a ‘socket’, which are reminiscent of ‘lock and key’ colloids.<sup>99</sup>

#### 4.3.4 Ionic Crosslinking of (Bio)polymer-containing Droplets

Polyelectrolytes, including a number of biopolymers, can undergo ionic crosslinking upon addition of multi-valent ions,<sup>100–103</sup> and a number of microfluidic methods to produce polyelectrolyte particles have been reported.<sup>104–106</sup> Although the approach is applicable to a range of polyelectrolytes,<sup>107,108</sup> sodium alginate has been a ‘workhorse’ for research on ionically crosslinked microparticles. Sodium alginate is a water-soluble linear polysaccharide consisting of linked  $\beta$ -D-mannuronate (M) and  $\alpha$ -L-guluronate (G) monomer units arranged in a non-regular pattern. Diad sequential blocks of GG units create cavities, referred to as an ‘eggbox’, in which carboxylic acid functional groups can strongly complex divalent cations such as calcium.<sup>109</sup> Upon addition of a sufficient concentration of divalent ions to a solution containing alginate, multi-valent ions act as ionic crosslinking point and induces lateral aggregation of chains.<sup>110</sup> When these solutions are contained within micron-size droplets, ionically crosslinked/gel particle formation takes place.

Droplet microfluidic approaches offer greater control over the the ionic crosslinking process and the resulting particle size and shape than bulk approaches, and the formation of gel particles have been demonstrated by several groups. Ionic crosslinking of W/O emulsion droplets can be induced by the incorporation of calcium ions into the water phase. This can be achieved by suspending an ‘inactive’ source of calcium inside the aqueous droplet, such as calcium carbonate, and adding a partially oil-soluble acid into the carrier phase, such as acetic acid.<sup>111</sup> Diffusion of acid into the droplet releases calcium ions and induces ionic crosslinking of the alginate-containing droplet. Alternatively, a simple and widely used technique is to induce passive diffusion of calcium from the oil phase, from a partially oil-soluble calcium salt *e.g.* calcium acetate, across the droplet interface.<sup>111</sup>

Both approaches can be performed *on-chip*, leading to particle morphologies defined by the channel geometry, or externally, by immersion within an ion-containing medium, which will be discussed below. Another route consists in separately generating alginate- and calcium-containing droplets, within microfluidic droplet generators, and combining them downstream in an expansion channel, which slows down the droplet velocities and causes droplets to collide and coalesce.<sup>105</sup> With precise control over droplet size and generation frequency, this technique allows spherical, disk and plug-like particles to be fabricated. During passive diffusion, at stagnation points in the multi-phase flows, crosslinking from free ions to form gel particles can cause clogging of channels. By chelating the active crosslinking ion in the carrier phase, or in an additional aqueous stream, and exchanging with chelated inert divalent ions within an alginate inlet stream, crosslinking can be finely controlled. Divalent ions remain bound, to either a chelating agent or alginate, and therefore no free ions are present to clog the channels. Additionally, with this approach crosslinking occurs within a stable, biologically compatible pH range and therefore can be used for cell encapsulation. Both fibres and droplets are suitable templates to ionically crosslink by this approach. An alternative approach involves the selective coalescence of multiple core W/O/W droplets, containing both a divalent crosslinking ion and alginate separated by a thin oil layer.<sup>112</sup> Once the thin lubricating oil layer separating the inner calcium chloride and alginate droplets is drained, the inner droplets can selectively coalesce, allowing ionic crosslinking and microparticle formation to take place. With this approach, spherical particle morphologies dominate and, whilst asymmetric droplet templates can be generated by varying inner fluid flow rates, asymmetry only affects the crosslinking density and size of the gelled particle.

Considerable research has been devoted to tuning the morphology when particles are ionically crosslinked *ex situ*. Typically, microfluidic approaches are first used to generate W/O emulsion drops before immersion of the outlet stream into a bath containing crosslinking ions, as depicted in Figure 4.11(a). A thin oil layer, containing an oil-soluble salt of the crosslinking agent, is also often added to the bath. Whilst many authors have addressed aspects of this issue,<sup>113–115</sup> Hu *et al.* provide a compelling demonstration of how to control particle morphology by *ex situ* ionic crosslinking.<sup>116</sup> Multiple processing parameters can be used to tune the crosslinked particle morphology, which are shown in the optical microscopy images in Figure 4.11(b–j). The parameters exploited are the outlet tubing height above the bath, viscosity of the bath (through glycerol addition), interfacial tension of the droplet (through surfactant addition) and level of oil added to the surface of the bath, and result in a range of particle morphologies (spherical, hemi-spherical, red-blood cell shaped, tadpole shaped, mushroom shaped). The precise details leading to their formation can be found in the supplementary information of their paper. In general, these morphologies arise from the interplay of forces which deform the droplet (*e.g.* viscous forces) and interfacial tension, which acts to retain

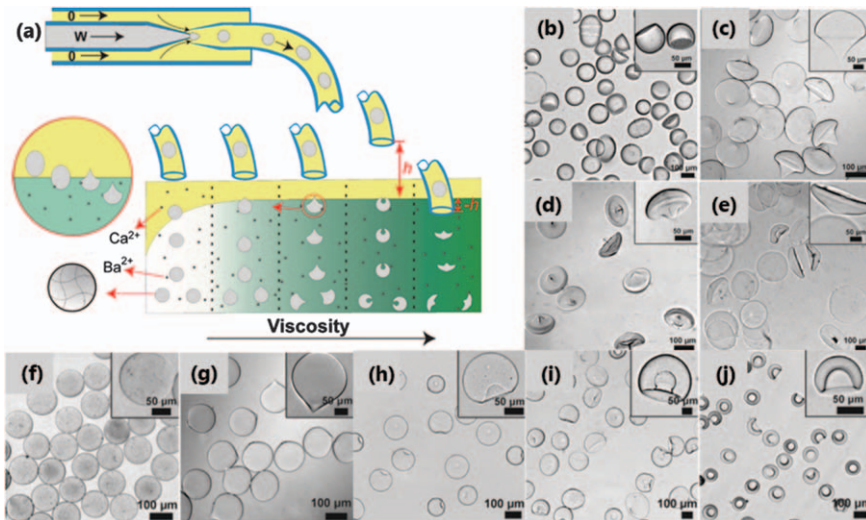


**Figure 4.11** (a) Schematic of the generation of W/O droplets in capillary microfluidics before immersion of the outlet stream into a gelation bath containing a high concentration of divalent ions, typically calcium or barium. Particle morphology can be tuned by variation of the bath salt concentration, viscosity and height of outlet above/or immersed in the bath. (b–j) Show optical microscopy images of sodium alginate particles formed by external gelation with barium acetate.  
Reprinted from Y. Hu, Q. Wang, J. Wang, *et al.*, Biomicrofluidics, **6**, 026502, (2012), with the permission of AIP Publishing.

sphericity, within the timescale of ionic diffusion and crosslinking of the droplet. For example, addition of surfactant to the alginate-containing droplet allows the droplets to deform during crosslinking, leading to dimpled and bowl-shaped particles, as shown in Figure 4.11(h, i).

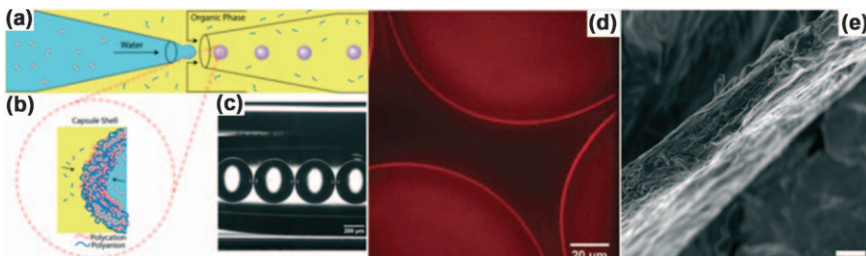
#### 4.3.5 Interfacial Complexation for Capsule Formation

Traditional synthesis of polyelectrolyte microcapsules relies on the assembly of oppositely charged polyelectrolytes on a charged, spherical, colloidal or inorganic template.<sup>117</sup> This requires multiple steps to deposit polyelectrolytes onto the template before its removal. Droplet microfluidic approaches show great promise by avoiding drawbacks of bulk syntheses. The main challenge is to solubilise a polyelectrolyte in an oil/organic liquid so when microfluidic droplets are generated, the polyelectrolyte can diffuse to the W/O or O/W droplet interface and complex with an oppositely charged polyelectrolyte in the aqueous phase. Two approaches have been established to solubilise polyelectrolytes in an organic phase, namely by the use of hydrophobic polymers partially functionalised with charged groups, *e.g.* sulfonated poly(styrene-*b*-ethylene/butylene)-*b*-styrene (*s*-SEBS) or poly(ethyleneimine) (PEI), which have pH-dependent degrees of ionisation;

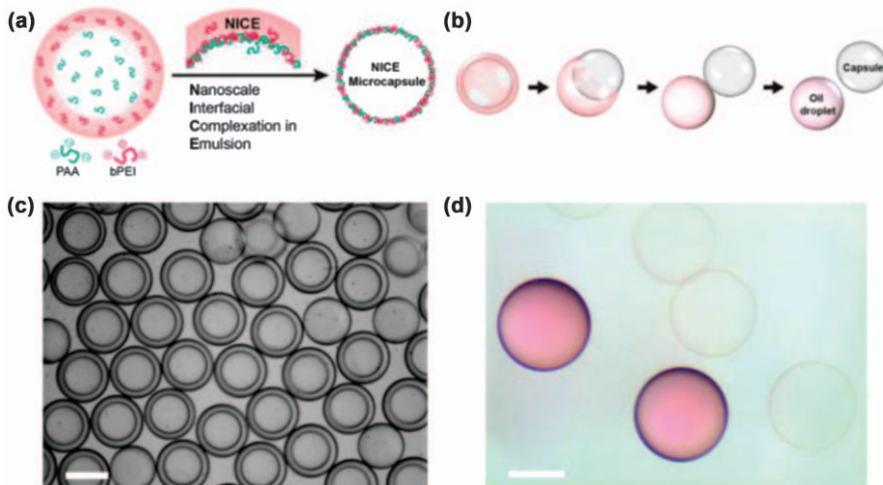
or alternatively by exchange of polyelectrolyte counterions with charged low hydrophobic–hydrophilic balance surfactants to generate oil-soluble ion pairs.

Figure 4.12 shows an example of polyelectrolyte capsule formation at the interface of W/O emulsion droplets.<sup>118</sup> In this example, partially charged polyelectrolyte s-SEBS, dissolved in the oil phase, complexes with a weak, naturally derived, cationic polyelectrolyte chitosan at the W/O droplet interface. Structurally similar microcapsules have also been observed for the interfacial complexation of polyelectrolytes with oppositely charged nanoparticles.<sup>119</sup> Droplet formation and complexation are schematically depicted in Figure 4.12(a) and (b). Microscopy images of the corresponding structures are shown in Figure 4.12(c–e). Stable, spherical, monodisperse capsules ( $\approx 200 \mu\text{m}$ ) are formed within the length of the capillary device in  $<60$  s, comprising a core–shell structure and thin, micron scale shell, as shown in Figure 4.12(d) and (e). As shell thicknesses are significantly larger than molecular dimensions, either the complexation kinetics are slower than the diffusion of polyelectrolytes across the interface or the capsule shell formed does not inhibit diffusion across the interface. The shell thickness is thus independent of both polymer concentration and, for polyelectrolytes above a critical size, molecular weight, as shown by Zhang *et al.* for capsules generated in all-aqueous conditions.<sup>120</sup> However, shell thickness has been found to be sensitive to the presence of salt but not the concentration or type.<sup>118</sup>

Microcapsules have also been fabricated by interfacial complexation of PEI and poly(acrylic acid) (PAA) within a W/O/W double emulsion.<sup>121,122</sup> In this case, the branched PEI was dissolved in a similar mixture of organic



**Figure 4.12** (a) Schematic of W/O emulsion droplet formation within a capillary flow-focussing device and interfacial complexation of oppositely charged polyelectrolytes, dissolved in each phase. (b) Schematic representation of the complexation of chitosan, from the aqueous inner phase, and s-SEBS from the oil phase resulting in formation of a polymeric shell. (c) Optical microscopy image of the stable capsules exiting the capillary device. Scale bar is  $200 \mu\text{m}$ . (d) Confocal microscopy image showing the core–shell structure of the microcapsules. (e) SEM image of the microcapsule shell with  $\sim\mu\text{m}$  thickness.  
Reproduced from ref. 118 with permission from The Royal Society of Chemistry.



**Figure 4.13** (a) Schematic illustration of the formation of polyelectrolyte complex microcapsules from water in oil in water (W/O/W) double emulsions by interfacial complexation. (b) Schematic of the dewetting of the oil middle phase following complexation within the emulsion, leaving a hollow polyelectrolyte microcapsule. (c) Optical microscopy image of W/O/W double emulsions generated through capillary microfluidics. (d) Optical microscopy image of microcapsules completely separated from dyed oil droplets (pink).  
Adapted from ref. 122 with permission from American Chemical Society, Copyright 2016.

solvents used for polymersome generation. Schematically, the complexation, followed by a dewetting transition that separates the oil droplet from the aqueous core capsule, is depicted in Figure 4.13(a) and (b). Optical microscopy images of the W/O/W droplets and capsules, following dewetting, are shown in (c) and (d). The formation of an oleophobic surface, upon complexation of the polyelectrolytes, aids full dewetting of the oil droplet. Acid-base reactivity of the polyelectrolytes, alongside a low pH (<4) of the inner aqueous phase, has been proposed as a driving force for the complexation between the two macromolecules. Evidently, this approach is applicable to a range of poly-electrolyte combinations. The resulting capsules show pronounced swelling with increase in pH and capsule rupture upon increase in ionic strength.

Another approach to solubilising polyelectrolytes in an organic phase of emulsion droplets, and formation of ion pairs, has been demonstrated with W/O/W double emulsions with combinations of polyelectrolyte and oppositely charged surfactant, *e.g.* poly(styrene sulfonate)(PSS)-didodecyldimethylammonium bromide (DDAB).<sup>123</sup> Ion pairs are formed from bulk emulsification of the polyelectrolyte dissolved in water with the surfactant dissolved in oil. The mechanism of microcapsule formation is conceptually the same as for

PEI-PAA microcapsules; complexation of poly(diallyldimethylammonium chloride) (PDADMAC), dissolved in the inner aqueous phase, with PSS solubilised in the organic phase (as a PSS-DDAB ion pair) results in shell formation. In the absence of monovalent salt in the inner phase, microcapsules are unstable. This suggests charge screening facilitates complexation of the two polyelectrolytes. Salt also promotes the dewetting of the oil phase and isolation of the capsules. As before, these capsules show tuneable release behaviour as a function of ionic strength; at low external salt concentrations (60 mM), capsules become permeable and slowly release encapsulated material, whilst at high salt concentrations (2 M), capsules rupture rapidly.

Complexation of dilute aqueous solutions of oppositely charged polyelectrolytes results in the spontaneous phase separation into polyelectrolyte-rich droplets, which rapidly coalesce to form a bulk phase, and a depleted supernatant, *via* a coacervation process. The molecular crowded and charged environment is similar to that of biological cells, and thus provides a desirable encapsulation medium for biomacromolecules, while bulk syntheses cannot prevent coalescence of coacervate microdroplets and macroscopic phase separation. However, droplet microfluidics has been shown to be able to immobilise coacervate droplets within liposomes that can potentially act as artificial cells.<sup>124</sup> Figure 4.14(a) schematically depicts the microfluidic generation of coacervates and encapsulation into liposomes. Oppositely charged polyelectrolytes are mixed and loaded as the inner phase of W/O/W double emulsions in a capillary microfluidic device. The middle oil phase, which contains a lipid, undergoes dewetting and forms a liposome shell. Concurrently, micron size coacervate droplets in the inner aqueous phase fuse and migrate to the centre of the liposome. Optical and confocal microscopy images depicting the dewetting processes, to form a liposome, and coalescence of encapsulated coacervate droplets are shown in Figure 4.14(b) and (c).

Coacervates formed from specific precursors yield cell mimics that facilitate storage and release of high concentrations of specific biomolecules, *e.g.* RNA. Figure 4.14(d) shows a schematic of the thermo-reversible coacervate formation from poly(uridylic acid) (PolyU) and spermine, and within a liposome, to store and release fluorescently labelled DNA. Figure 4.14(e) shows fluorescent images as temperature is cycled below the lower critical solution temperature (LCST) of the coacervate, to release DNA, and then increased above the LCST, to store DNA again. The corresponding fluorescent signal within the liposome and coacervate as a function of time, during the temperature cycle, is shown in Figure 4.14(f).

## 4.4 Physical Approaches to Particle Solidification

### 4.4.1 Particle Assembly at Interfaces

The adsorption of colloids at droplet interfaces, such as in Pickering emulsions,<sup>12</sup> has long been proposed as a route to fabricating a range of

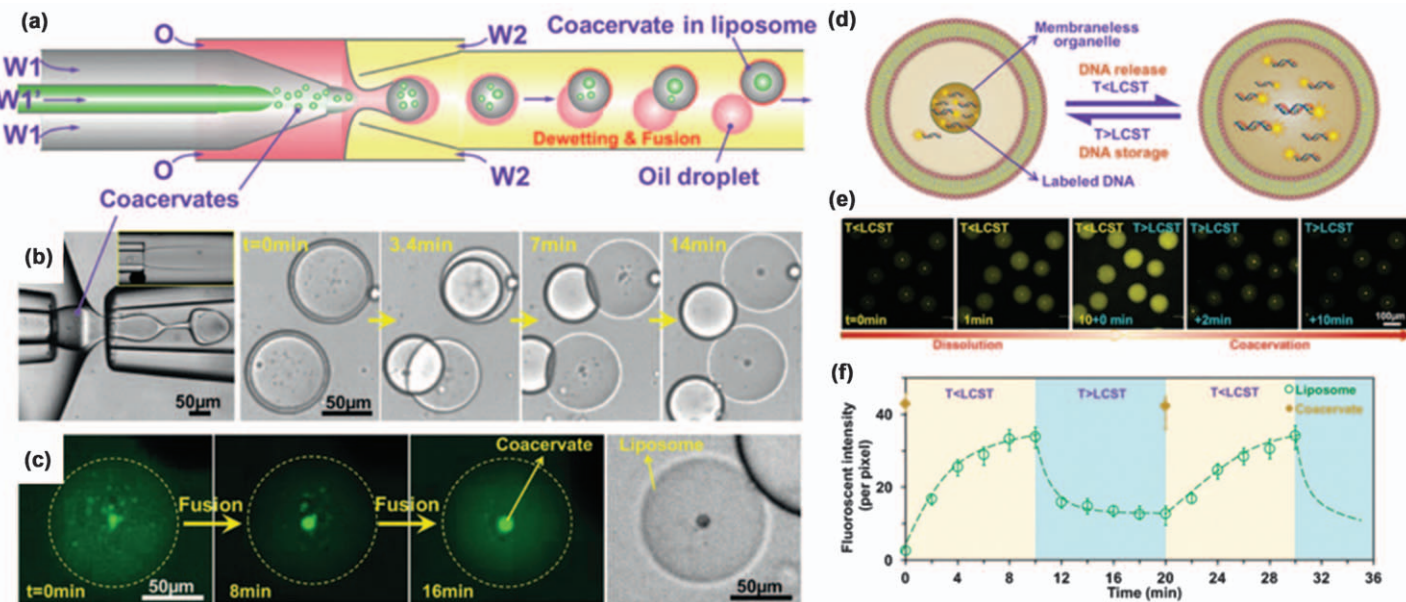


**Figure 4.14** (a) Schematic of encapsulation of coacervate droplets within the inner phase of W/O/W double emulsion droplets with a capillary flow-focussing device. W1 and W1' are poly(lysine) and adenosine triphosphate, which form coacervates in the inner water phase. (b) Optical microscopy images of the W/O/W emulsion formation and subsequent dewetting of the middle oil phase, forming a hollow vesicle with an encapsulated coacervate droplet. (c) Confocal microscopy images of coalescence of coacervate droplets into a larger central droplet. (d) Schematic of encapsulation of DNA in a vesicle, containing a polyuridylic acid (polyU)/spermine coacervate droplet, and the thermal storage and release cycling properties. (e) Fluorescent microscopy images of the thermally triggered storage and release of labelled DNA molecules. (f) Kinetic profile of the fluorescent signal in the vesicle and coacervate droplet during the storage/release cycle.

Reproduced from ref. 124, <https://doi.org/10.1002/anie.201703145>, under the terms of the CC BY 4.0 licence, <https://creativecommons.org/licenses/by/4.0/>.

microstructured particles.<sup>125</sup> In emulsion droplets containing colloidal suspensions, such as poly(styrene) latexes, self-assembly at the liquid–liquid interface can result in the kinetic arrest of highly ordered layers. The resulting assemblies range from densely packed particles<sup>126</sup> to hollow vesicular structures, analogous to liposomes, with mechanically stable shells, or ‘colloidosomes’.<sup>127</sup> These hollow elastic core–shell particles provide encapsulation vehicles with tuneable physical properties; they can be formed at numerous liquid–liquid, solid–liquid and air–liquid interfaces, from a variety of colloidal particles, and combined with film-forming polymers to tune the permeability and release properties.<sup>128</sup>

The simplest approach to generating microparticles from the directed self-assembly of colloids at interfaces is to remove solvent from emulsion droplets, where the dispersed phase comprises a colloidal suspension. Upon sufficient solvent removal, phase inversion occurs and the packed colloids become the majority component in the newly formed particle. This approach has been demonstrated to form densely packed spherical ‘supraparticles’ of poly(styrene) latexes which exhibit photonic properties owing to the highly ordered packing.<sup>126</sup> Much like other solvent extraction processes, control of the resulting particle structure is governed by the rate of solvent removal relative to the diffusion of soft material inside the droplet, defined by the Péclet number (Pe). Rapid solvent removal does not allow time for structurally homogenising processes such as diffusion, coarsening or reorganisation of colloids to occur before the particle forms. If the rate of solvent removal from the colloidal suspension droplets is enhanced, *e.g.* by microwave irradiation, packing of colloids within the ‘supraparticle’ can be tuned,<sup>129</sup> and consequently the characteristic length, the inter-particle spacing, can be tuned to exhibit different photonic properties.<sup>130</sup> The ability to tune to the overall particle morphology has been demonstrated by Velev and co-workers.<sup>127</sup> Whilst particles were not formed *via* a microfluidic approach, and instead droplets were dried whilst floated on a dense fluorinated oil, the overall morphology was shown to be determined by the interplay of droplet radii ( $R$ ), gravity and interfacial tension ( $\gamma$ ). The resulting morphology could be classified by the Bond number  $\left(Bo \sim \frac{\Delta\rho g R^2}{\gamma}\right)$  of the initial droplet template, where  $\Delta\rho$  is the density difference between the droplet and surrounding fluid and  $g$  is acceleration due to gravity. By tuning the initial droplet size (volume  $> 3 \mu\text{L}$ ), and concentration of the colloids inside the droplet ( $< 20\% \text{ v/v}$ ), the droplet templates can be deformed (at corresponding  $Bo > 1$ ) and solidified into disk and ellipsoidal shapes. Further control can be exerted by reduction of the interfacial tension, through surfactant addition, which induces mechanical instabilities in the packed colloidal shells, during drying and volume reduction, to form dimpled and toroidal-shaped particles. Overall, the ability to control the interfacial packing and particle morphology during drying of colloid-containing droplets appears a facile way to generate particles with tuneable optical properties and shape.

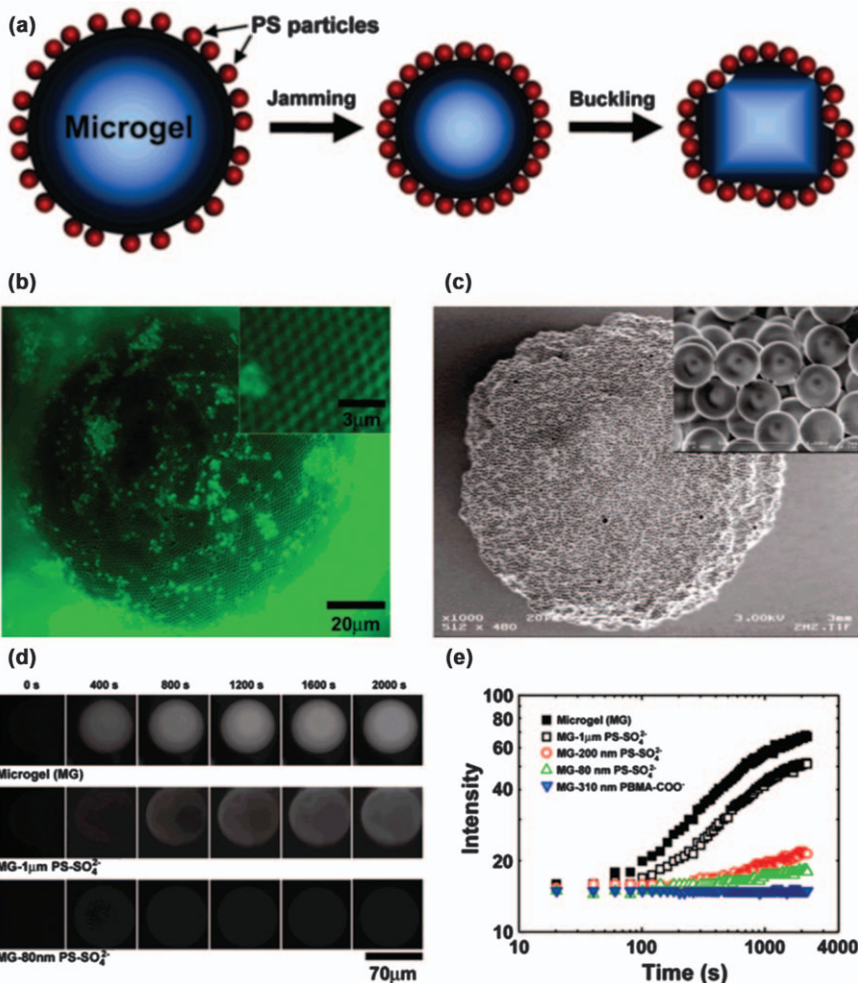


**Figure 4.15** (a): Schematic of surface colloid packing when surface area is reduced for adsorbed poly(styrene) colloids on a microgel core. Surface area reduction is induced by an increase in temperature. (b) Fluorescent microscopy image of jammed 1  $\mu\text{m}$  sulfate functionalised PS colloids on the microgel surface at 50  $^{\circ}\text{C}$ . (c) SEM micrograph of colloidosome surface after drying at 60  $^{\circ}\text{C}$  for 24 h. (inset) Magnified area showing packing of PS colloids. (d) Fluorescent microscopy time-series of the permeation of fluorescein sodium salt solution (0.5  $\mu\text{M}$ ) into microgel-core colloidosomes compared to the native microgel particle. (e) Effect of colloidal particle diameter on the permeation of fluorescein salt into the colloidosome, depicted in a plot of fluorescence intensity *vs* time.

Adapted from ref. 133 with permission from American Chemical Society.

Colloidosomes can be templated from double emulsions in the bulk and with microfluidic approaches. Microfluidic approaches benefit from the reduced processing required to generate double emulsion droplets used for templating. For example, Lee *et al.* demonstrated the formation of silica and silica/poly(lactic acid) (PLA) composite colloidosomes from W/O/W double emulsions.<sup>131</sup> Upon extraction of the oil phase solvent, here toluene or toluene/chloroform mixtures, *in-situ* colloidosome formation occurred by consolidation of the two particle saturated interfaces without need for any additional processing. The resulting colloidosomes show size selective permeability, owing to the interstitial voids between packed colloids. This inherent permeability of the colloidosomes, leading to passive release of encapsulated material, is determined by the void size between particles in the shell and, assuming hexagonal packing, is proportional to the constituent colloid size.<sup>128</sup> Voids can be further reduced in size and number through a variety of approaches, including sintering the shell (near the  $T_g$  for polymer colloids),<sup>128</sup> incorporation of additional polymer<sup>131</sup> or colloids into the shell, and chemical crosslinking.<sup>132</sup> Furthermore, they can exhibit stimuli-responsive behaviour and thus complex function. For example, including a PNIPAm microgel core and adsorbing negatively charged poly(styrene) colloids onto the surface, as shown schematically in Figure 4.15(a), can generate thermo-responsive colloidosomes.<sup>133</sup> Colloid coverage on the microgel was tuned by increasing the temperature, and reducing the volume of the microgel core, until the adsorbed colloids jammed, buckled and formed a porous shell with thickness independent of colloid size, shown in Figure 4.15(b) and (c). The rate of diffusion of small fluorescent molecules into the core is vastly reduced by the presence of the colloid shell, as shown in Figure 4.15(d) and (e). The jamming transition leading to shell formation is expected to be irreversible, and the shell to rupture upon core expansion. Reversible thermo-responsiveness requires the use of soft colloidal particles within the shell, as demonstrated by Weitz and co-workers,<sup>134</sup> who used pNIPAm colloids, adsorbed at the interface of an O/W emulsion droplet, and crosslinked with gluteraldehyde to form a colloidosome. The thermo-responsive colloids comprising the shell can cause a  $\approx 80\%$  volume reduction upon thermal actuation, and offer potential for pulsed or triggered release.

Spatial control of colloids within the shell in colloid–polymer composite capsules, can also be achieved by modifying the surface chemistry (*e.g.* with silanes) of the colloid and tuning the contact angle at the middle/inner (and outer) phase interface.<sup>36</sup> Layered as well as homogeneously distributed shells can be realised by this approach. By fixing the colloid surface chemistry, and encapsulating multiple inner droplets with a capillary microfluidic double emulsion templating approach shown in Figure 4.16(a) and (b), the overall morphology of microcapsule could be controlled.<sup>135</sup> Dispersion of silica colloids within the oil phase of a W/O/W double emulsion, comprising an acrylic monomer and photoinitiator, allows the capsule structure to be arrested in a range of non-spherical morphologies by subsequent photopolymerisation of the acrylic monomer. The internal structures of the

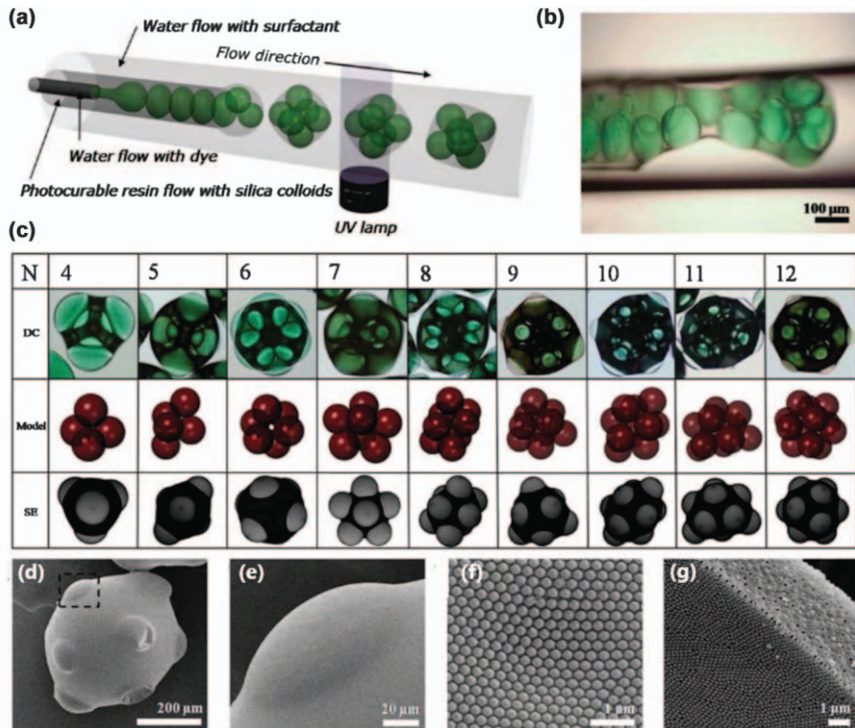


**Figure 4.16** (a) Schematic of W/O/W emulsion formation within a coaxial co-flow capillary microfluidic device. (b) Optical microscopy image of double emulsion formation comprising multiple internal water droplets. (c) Table showing the experimentally measured droplet clusters within double emulsions (first row), model predictions (second row) and Surface Evolver calculations (third row). (d) SEM image of a microcapsule with number of encapsulated droplets ( $N = 10$ ). (e) Magnified area from (d) showing the distortion of the colloidosome shell arising from the presence of internal droplets; (f) and (g) show the hexagonally packed colloids at the outer and inner surfaces of the colloidosomes respectively. Reproduced from ref. 135 with permission from John Wiley and Sons, Copyright © 2011 WILEY-VCH Verlag GmbH & Co. KGaA, Weinheim.

precursor emulsion droplets, encapsulating multiple aqueous droplets, are shown in Figure 4.16(c). Differential contrast microscopy images and model structures, where the inner aqueous cores from microscopy images are taken as spheres and the oil phase ignored, are compared to Surface Evolver calculations, which minimise the interfacial energy of the structure with a fixed contact angle between the aqueous droplets and oil phase. Particles and surface dimples arising from the internal aqueous core droplets are illustrated in Figure 4.16(d) and (e), respectively. Owing to the surface chemistry of the colloids used, the inner and outer surfaces of such particles are arrested with packed colloids within a polymeric matrix, as shown in Figure 4.16(f) and (g).

#### 4.4.2 Block Co-polymer Self-assembly in Double Emulsions

Polymersomes, bilayers of self-assembled block co-polymers (BCPs),<sup>136</sup> yield capsules, with mechanically robust structures superior to lipid vesicles (liposomes) and tuneable physical properties. The overall molecular weight of the BCP determines the membrane thickness, whilst permeability is largely controlled by the glass transition temperature of the hydrophobic block. Self-assembly of polymersomes is induced by changes in solvent quality and therefore they can be templated by double emulsion droplets, where the BCP is typically dissolved in an organic phase comprising a volatile good solvent for both blocks and a non-volatile selective solvent for one of the blocks.

Figure 4.17(a) shows the formation of BCP-containing double emulsions with a capillary microfluidic device.<sup>137</sup> Evaporation of the chloroform induces self-assembly of the PEG-*b*-PLA BCP dissolved in a toluene/chloroform mixture at the water/oil interfaces before a dewetting transition occurs, as shown in Figure 4.17(b). The dewetting transition occurs over a small range of solvent compositions, where adhesion of the BCP-covered interfaces to form a bilayer and a separate oil phase is energetically favoured.<sup>138</sup>

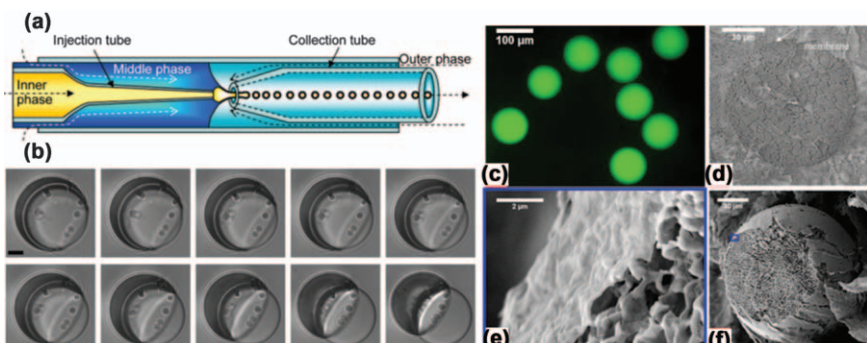


**Figure 4.17** (a) Schematic of coaxial capillary microfluidic device for formation of W/O/W double emulsion droplets. Here the oil phase comprises a PEG-*b*-PLA block co-polymer in a 2:1 v/v toluene/chloroform mixture. (b) Microscopic images of the solvent evaporation induced dewetting transition to generate the polymersome. The organic solution droplet is the darker (left) and the aqueous polymersome the more transparent (right) in each image. Scale bar is 10  $\mu\text{m}$ . (c) Confocal laser scanning microscope image of PEG(5000)-*b*-PLA(5000) polymersomes encapsulating a fluorescent dye in the aqueous core. (d) Cryo-SEM image of a single polymersome. (e) Magnified view of the shell region in (d). (f) SEM image of a freeze-dried PEG(5000)-*b*-PLA(5000) polymersome encapsulating a PEG solution. The internal foam-like morphology is typical of a dried PEG solution, indicating the polymersome shell does not affect the encapsulated core. The shell appears uniformly thin. (a) and (b) Adapted from ref. 137 with permission from American Chemical Society, Copyright 2008. (c-f) Adapted from ref. 138 with permission from American Chemical Society, Copyright 2011.

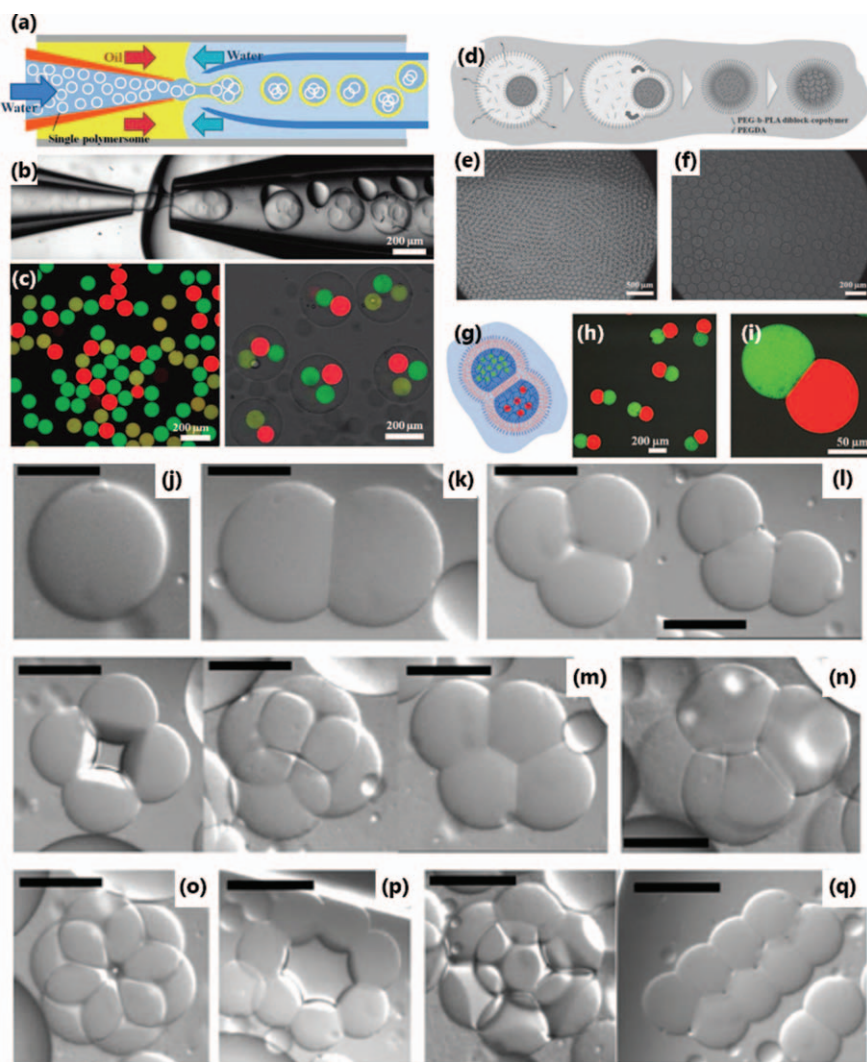
Owing to the comparable magnitude of the surface energy of the co-polymer bilayer and the co-polymer–oil interface, an acorn-like structure evolves, which comprises a solvent-rich droplet attached to part of the co-polymer bilayer. Solvent continues to evaporate from the attached solvent droplet, which can also break off the bilayer, until an aggregate containing excess BCP is left attached to the polymersome. Other BCP/solvent systems appear to form polymersomes in the absence of such a transition, *e.g.* poly(butyl acrylate)-*b*-poly(acrylic acid), dissolved in a mixture of toluene and tetrahydrofuran (THF).<sup>139</sup> Figure 4.17(c–f) shows the structure of PEG-*b*-PLA polymersomes with confocal microscopy (c), cryo-scanning electron microscope (cryo-SEM) (d) and SEM after freeze-drying (e, f). Polymersomes formed are typically spherical with thin shells, and those shown here encapsulate a PEG solution. The foam-like internal structure, typical of freeze-dried PEG solutions, is retained within the capsule and demonstrates that the self-assembled polymersome shells are mechanically robust. Investigation of solvent evaporation from microfluidic double emulsions containing poly(lactic-*co*-glycolic) acid (PLGA), with varying molar ratios of lactide to glycolide in the polymer, confirmed that surface activity of the polymer was required to induce a dewetting transition, *i.e.* an amphiphilic BCP is required for formation of a polymersome. This only occurred for PLGA with sufficient glycolide fraction and not for PLA homopolymers.<sup>140</sup> Instead, evaporation from W/O/W emulsions, where the middle phase comprised solely homopolymers, results in the formation of a thick polymer layer.

Microfluidic approaches enable the formation of hierarchical structures to form polymersome precursors. Figure 4.18(a, b) shows the encapsulation of multiple PEG-*b*-PLA polymersomes in the inner phase of W/O/W double emulsion droplets.<sup>141</sup> Confocal microscopy images with fluorescent dyes show that single polymersomes as well as polymersomes-in-polymersomes can be formed by this approach (c, d). Acrylic monomers can be dissolved in the aqueous core to further functionalise the microcapsules. Figure 4.18(d) shows the schematic formation of hydrogel core polymersomes by addition of PEGDA to the aqueous inner phase, and optical microscopy images of the resulting polymersomes (e, f). The hydrogel core is formed by UV photopolymerisation, following the dewetting transition. Hydrogels exhibit better retention of hydrophilic material upon rupture of the other polymersome bilayer.

Multi-compartment polymersomes with hydrogel cores can also be formed by incorporation of multiple aqueous droplets as the inner phase of a double emulsion.<sup>142</sup> For instance, Figure 4.18(g) shows a schematic of a dumbbell Janus hydrogel-core polymer formed from UV photopolymerisation of a polymersome comprising two distinct core droplets, from separate inlets within the capillary device. Bilayer formation prevents the coalescence of internal aqueous droplets. Figure 4.18(h) and (i) show confocal microscopy images of PEG-*b*-PLA polymersomes with hydrogel cores encapsulating different fluorescently tagged biomacromolecules (rhodamine tagged-bovine serum albumin and FITC-dextran).<sup>143</sup> Figure 4.18(j–q) shows the multi-compartment polymersomes formed from a double emulsification in a

capillary microfluidic device with 1–8 compartments. The number of compartments within the polymersome can be tuned through the number of aqueous droplets encapsulated as the inner phase of a W/O/W emulsion.

Tuning the structure and chemical composition of polymersomes offers improved stability and release properties. For example, hydrogel cores slow down the release of encapsulated hydrophilic material compared to entirely vesicular structures.<sup>142</sup> Polymersomes composed of double bilayer structures or polymersomes with additional homopolymer in the bilayer are more osmotically stable.<sup>141,144</sup> In combination with the formation of distinct multi-compartmental cores, this can be exploited to generate vesicular structures which can pre-mix internal compartments before release to the



external environment. Diffusion of small molecules through the outer membrane, which is more stable to rupture, can induce a triggered rupture of internal polymersomes, and mixing, before the outer membrane breaks down, *e.g.* for PEG-*b*-PLA polymersome(s)-in-polymersome structures.<sup>141</sup>

#### 4.4.3 Solvent Extraction of Polymer-containing Droplets

A versatile and ubiquitous approach for polymer microparticle formation involves the removal of solvent from a polymer solution droplet. In spray-drying, an atomising nozzle produces droplets that are subsequently dried in a tower, often with a counter-current of air at elevated temperature. Solvent extraction is the analogue of spray drying, where the ‘evaporation’ medium is now another solvent, and thus requires careful consideration of the solution thermodynamics, and inter-diffusion and solidification kinetics. The process is generally referred to as droplet ‘solvent extraction’, as well as ‘evaporation’. In a first step, droplets are formed by the emulsification of a polymer solution with an immiscible carrier phase, often employing microfluidics. Then the extraction solvent is introduced, to selectively remove the ‘good solvent’ from the droplet, and thus concentrate the solute until a particle is formed. Generally, three solvents are therefore required: the ‘good solvent’ contained within the polymer solution droplet, the ‘extraction’ or ‘bad’ or ‘non-solvent’ solvent, and the ‘carrier’ solvent phase, although this nomenclature can be somewhat ambiguous. The carrier solvent, must be immiscible with the ‘good’ solvent (to enable emulsification) and miscible with the ‘bad’ solvent, to enable the extraction process. The ‘extraction’ solvent must be partially miscible with the ‘good’ solvent in the droplet, to enable solvent exchange across the interface. This also implies that some of

**Figure 4.18** (a) Schematic of W/O/W emulsion formation in a capillary microfluidic flow-focussing device. The inner aqueous phase comprises a dispersion of PEG-*b*-PLA polymer-somes. (b) Optical microscopy image of injection of polymersomes into the inner phase of the W/O/W emulsion droplets to form multi-compartment polymersomes. (c, d) Confocal microscopy images of single polymersomes encapsulating dyes (c) and polymersome-in-polymersomes containing multiple dyed droplets. (d) Formation mechanism of hydrogel precursor core polymersome through a dewetting transition before UV polymerisation induces hydrogel formation in the core. (g) Schematic representation of the structure of the Janus dumbbell hydrogel core polymersome. (h, i) Confocal microscopy images of polymersomes with fluorescently tagged biomacromolecules in the hydrogel core. (j-q) Optical microscopy images of multi-compartment PEG-*b*-PLA polymersomes with (j) 1 (k) 2 (l) 3 (m) 4 (n) 5 (o) 6 (p) 7 (q) 8 compartments. Orientation of the compartments is not unique for each number of compartments. Scale bars are 30 µm. Adapted from ref. 141 with permission from American Chemical Society, Copyright 2013. (d-i) Reproduced from ref. 143 with permission from John Wiley and Sons, Copyright © 2011 WILEY-VCH Verlag GmbH & Co. KGaA, Weinheim.

the ‘bad’ or ‘extraction’ solvent, generally a small fraction, will ingress the droplet (providing numerous pathways for demixing). The solute, which can be a polymer, but also colloids or mixtures, is only miscible (or dispersible) within the ‘good’ solvent. In some conditions, the carrier and extraction solvent can be the same, which simplifies the process design. In that sense, the process is analogous to phase inversion or non-solvent induced phase separation (NIPS) extensively used in membrane fabrication,<sup>145,146</sup> albeit in a spherical geometry. Overall, this ternary or quaternary phase behaviour (or higher in the case of mixtures) can somewhat restrict the systems available for droplet extraction; nonetheless a significant number of combinations have been reported. Figures 4.19(a) and (b) illustrate two such approaches to droplet extraction: by addition of an extraction solvent stream in the microfluidic device (*in situ*), or by immersion of the outlet from the device into an extraction solvent bath,<sup>147</sup> analogous to the *ex-situ* ionic crosslinking approach. As depicted by the series of optical microscopy images in Figure 4.19(c), the process evolves through droplet shrinkage, internal demixing and ultimately kinetic arrest of the shrinking droplet, as the polymer precipitates (or the polymer-rich phase reaches the glassy state) and forms a skin. Figure 4.19(d) and (e) show SEM images of spherical homopolymer particles formed by solvent extraction from neutral polymer PLA and polyelectrolyte sodium poly(styrene sulfonate) (NaPSS), respectively. Consequently, the particle structures formed from hydrophobic polymers dissolved in the inner phase of O/W droplets are typically smooth and spherical.<sup>148–150</sup>

Microparticles formed by solvent extraction are generally out-of-equilibrium structures. The interplay of inter-diffusion and extraction kinetics, demixing and coarsening, and eventually solidification (precipitation, kinetic arrest or vitrification) of the solute-rich phase, alongside mechanical instabilities in the interfacial skin formed determine the internal microstructure and external particle morphologies. The skin results from the fact that extraction is a directional solidification process, which can lead to a stratified internal structure, and is generally influenced by internal droplet convection (driven by Marangoni flows and external fields surrounding the droplet). The internal demixing, caused by the increasing solute concentration within the droplet during extraction and/or ingress of the ‘bad’ solvent, is responsible for the heterogeneous microstructure within the resulting polymer capsules or particles.<sup>147,151</sup> Depending on initial polymer concentration and process parameters, a range of internally porous microparticles can be formed (requiring no porogens), as illustrated in Figure 4.19(f) which shows cross-sectioned NaPSS particles. Direct addition of a non-solvent into the polymer solution (which is insoluble in the carrier or extraction solvent), prior to droplet formation, can also be used to induce phase separation as the good solvent is removed. For example, perfluoroctyl bromide (PFOB) added into PLA/ethyl acetate (EA) droplets prior to solvent extraction, with an EA saturated aqueous carrier phase, leads to internal demixing and migration of droplets to the surface to create dimpled particles.<sup>151</sup>

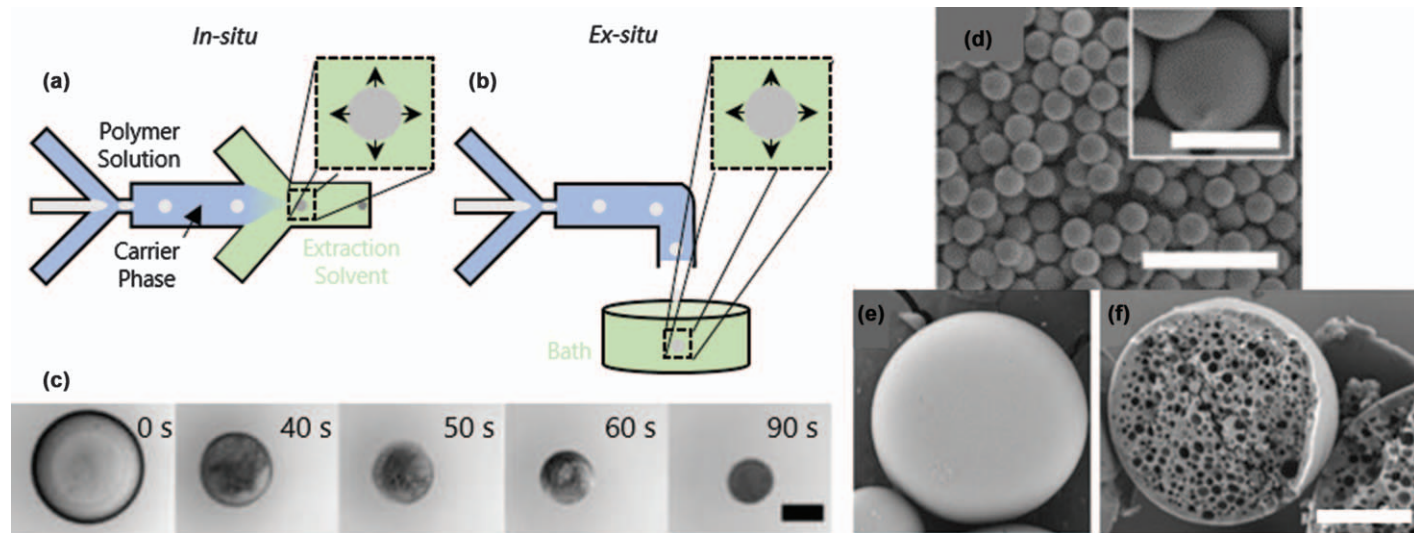


**Figure 4.19** (a, b) Schematics of microfluidic solvent extraction from polymer solution droplets with a partially miscible non-solvent. (a) *In-situ* precipitation of particles by addition of a non-solvent, miscible with the droplet carrier phase, downstream of droplet formation in the microfluidic device. (b) *Ex-situ* precipitation where droplets are immersed into a non-solvent bath. (c) Optical microscopy time series showing droplet shrinkage, internal demixing and eventual particle formation. Scale bar is 200 µm (d) SEM image of PLA particles formed by solvent extraction. Scale bars are 100 µm in main image and 20 µm in the inset. (e, f) Spherical NaPSS particle (e) and cross-section (f), revealing the presence of internal particle porosity. (c, e, f) Adapted from ref. 146, <https://doi.org/10.1021/acs.langmuir.6b01799>, under the terms of the CC BY 4.0 licence, <https://creativecommons.org/licenses/by/4.0/>. (d) Reproduced from ref. 152 with permission from The Royal Society of Chemistry.

The initial polymer solution composition and choice of extraction solvent set the droplet composition trajectory across the ternary (or higher) mixture phase space. This pathway has been modeled for planar interfaces relevant to membranes for separations, by several authors, including recently with field theory approaches.<sup>153</sup> In simple terms, the relative rate of solvent extraction with respect to solvent diffusion sets the Péclet number, which provides an indication for the possible formation of an interfacial skin and its associated timescale. It can be estimated by  $Pe \approx Ru/D$ , where  $R$  is the initial droplet radius,  $u$  the interfacial velocity (estimated by  $dR/dt$ ) and  $D$  is the solute diffusion coefficient. Evidently, solute concentration and morphology evolve over time and this estimate is used qualitatively to classify and compare various systems. The  $Pe$  can be readily tuned by the extraction solvent miscibility with the good solvent and, to a lesser degree, for a given system, with polymer concentration. Udo *et al.*<sup>146</sup> demonstrated the internal porosity of NaPSS particles could be increased by selecting an extraction solvent with relatively high partial miscibility (in this case, methyl ethyl ketone, MEK), and by decreasing the initial concentration of polymer in the precursor droplets. Interestingly, the higher the miscibility, the faster the extraction kinetics and thus the larger the  $Pe$ , resulting in *earlier* skin formation and thus larger, more porous particles. A range of extraction solvents was investigated, from toluene ( $T$ ) with vanishingly small miscibility to the relatively miscible MEK, and their role in the particle/capsule formation of polymer-colloid solutions. In the case of mixed solutes, both the system thermodynamics and the individual  $Pe$  numbers of the solutes must be considered for effective encapsulation and particle design. The variation of internal porosity with choice of extraction solvent and the corresponding release properties of encapsulated (silica) colloids within PSS particles was recently reported.<sup>154</sup> Figure 4.20(a-d) shows SEM images of particle cross-sections formed from 250  $\mu\text{m}$  droplets containing 1% w/v NaPSS (neat) following extraction in different solvents. Figure 4.20(e-h) shows optical microscopy images of the corresponding release of silica colloid clusters upon immersion of the composite NaPSS-SiO<sub>2</sub> particles, shown in Figure 4.20(a-d), in deionised water.

For an individual polymer solution droplet immersed in extraction solvent, the radius decreases monotonically over time before reaching a plateau in which the shrinkage is arrested by formation of a polymer-rich skin. Given the complexity of the several mechanism at play, the radial-time profile has been modelled descriptively by:

$$R(t) = (R_0 - R_\infty) \left(1 - \frac{t}{\tau}\right)^\alpha + R_\infty$$

where  $R_0$  is initial droplet radius,  $R_\infty$  the final particle radius,  $\tau$  characterises the extraction timescale and  $\alpha$  is a hyperbolicity parameter (of order 1). The latter arises from Epstein-Plesset models of droplet dissolution in a partially miscible solvent.<sup>156-158</sup> Describing the radius as a function of time

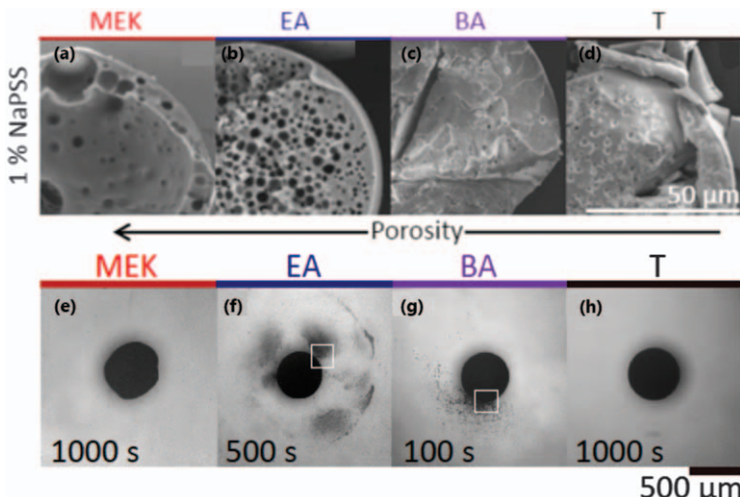


**Figure 4.20** (a-d) SEM images of microparticles formed by solvent extraction of 1% w/v NaPSS droplets ( $R_0 = 250 \mu\text{m}$ ) in a range of extraction solvents: methyl ethyl ketone (a), ethyl acetate (b), butyl acetate (c), toluene (d). (e-f) Optical microscopy images of the release of 10% w/v of SiO<sub>2</sub> colloids from the corresponding particles in (a-d) when immersed in deionised water. No discernible release of silica clusters is observed from MEK and T capsules (e) and (h), while pulsed release is observed from EA particles (f) and a slow, continuous release from BA particles (g). (a-d) Reproduced from ref. 154 with permission from The Royal Society of Chemistry. (e-h) Adapted from ref. 155, <http://dx.doi.org/10.1126/sciadv.aa03353>, under the terms of the CC BY 4.0 licence, <https://creativecommons.org/licenses/by/4.0/>.

in this way allows quantification of the effects of changes to the droplet composition, size and extraction solvent on the particle size and extraction kinetics. Extraction kinetics appear to follow the miscibility of the good solvent (often water) with the extraction solvents. Evidently, the less miscible, the longer the extraction and thus larger  $\tau$ , yielding more compact particles. Figure 4.21(a) shows the radial decrease of droplets, containing NaPSS/silica colloids and with  $R_0 \approx 250\text{--}270 \mu\text{m}$ , extracted in the different solvents. Kinetic arrest occurs (from slowest to faster) in the following order in this system: toluene (*T*)>butyl acetate (BA)>EA>MEK.<sup>154</sup> Additionally, bifurcation points in the particle formation, where shape deformations and deviations from sphericity occur, can be identified. This is expected as the liquid–liquid interfaces gives rise to a solid skin, which thus obeys different energy minimisation rules that replace reducing surface area of the liquid droplet. Figure 4.21(b) illustrates the bifurcation of major and minor radii for NaPSS/SiO<sub>2</sub> composite droplets as a folded non-spherical particle forms. Buckling, crumpling and folding can be observed depending on extraction conditions and droplet composition, giving rise to a rich morphology diagram for capsule formation.

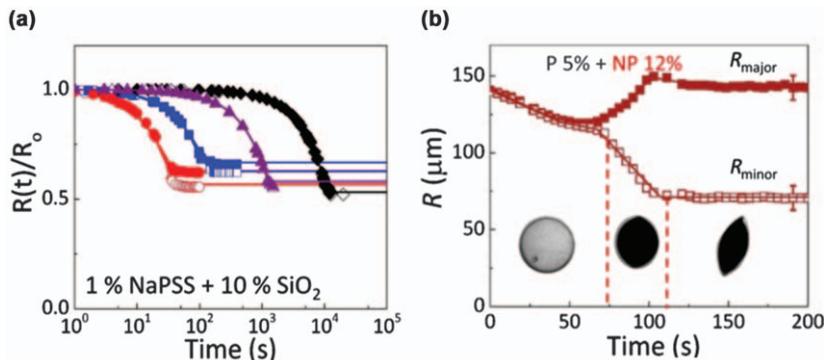


**Figure 4.21** (a) Particle formation kinetics for droplets containing 1 w/v% NaPSS + 10 w/v%  $\text{SiO}_2$  colloids and extracted in different solvents. Each colour represents a different extraction solvent: red = MEK, blue = EA, purple = BA, black = toluene. Radii are normalised to initial radius  $R_0$ . Open and closed circles represent the major and minor radii, accounting for deviations from sphericity. Lines show descriptive data fits with the equation given in the text. (b) Particle formation kinetics by solvent extraction for a 140  $\mu\text{m}$  droplet containing 5% (w/v) NaPSS + 12% (w/v)  $\text{SiO}_2$ . Optical microscopy insets and dashed lines illustrate the anisotropic particle shape formed and deformation points upon extraction. Two radial profiles are shown, corresponding to the major and minor radii of the droplet/particle.  
 (a) Reproduced from ref. 154 with permission from the Royal Society of Chemistry. (b) Adapted from ref. 155, <http://dx.doi.org/10.1126/sciadv.aa03353>, under the terms of the CC BY 4.0 licence, <https://creativecommons.org/licenses/by/4.0/>.

Control over the particle size can be exerted through a number of parameters: initial droplet size ( $R_0$ ), polymer concentration and choice of non-solvent.<sup>146</sup> Decreasing  $R_0$  has been shown, for a given mixture, to result in faster particle formation and smaller particle sizes, owing to the larger surface: volume ratio. Particle size  $R_\infty$  and formation timescale  $\tau$  both appear to depend linearly on  $R_0$ . The influence of  $R_0$  on both  $R_\infty$  and  $\tau$  can be tuned by the polymer (solute) concentration, whereby polymer precipitation and skin formation arrests the extraction earlier for higher polymer concentrations. Molecular parameters, such as molecular weight and chemical functionality (degree of hydrolysis), appear not to affect the solvent extraction process in one system (PVA) investigated systematically.<sup>159</sup> For a given polymer/solvent/extraction solvent combination, the particle size and extraction kinetics, and resulting morphology, appear to be rather dominated by the influence of droplet size and polymer concentration. Both the internal microstructure and external morphology can be effectively modulated by polymer concentration, as shown above. Further reducing polymer content (well below the overlap concentration  $c^*$ ) yields thin (sub-micron) polymeric skins that can become mechanically unstable and buckle to form non-spherical structures. Some of these morphologies are illustrated in Figure 4.22.

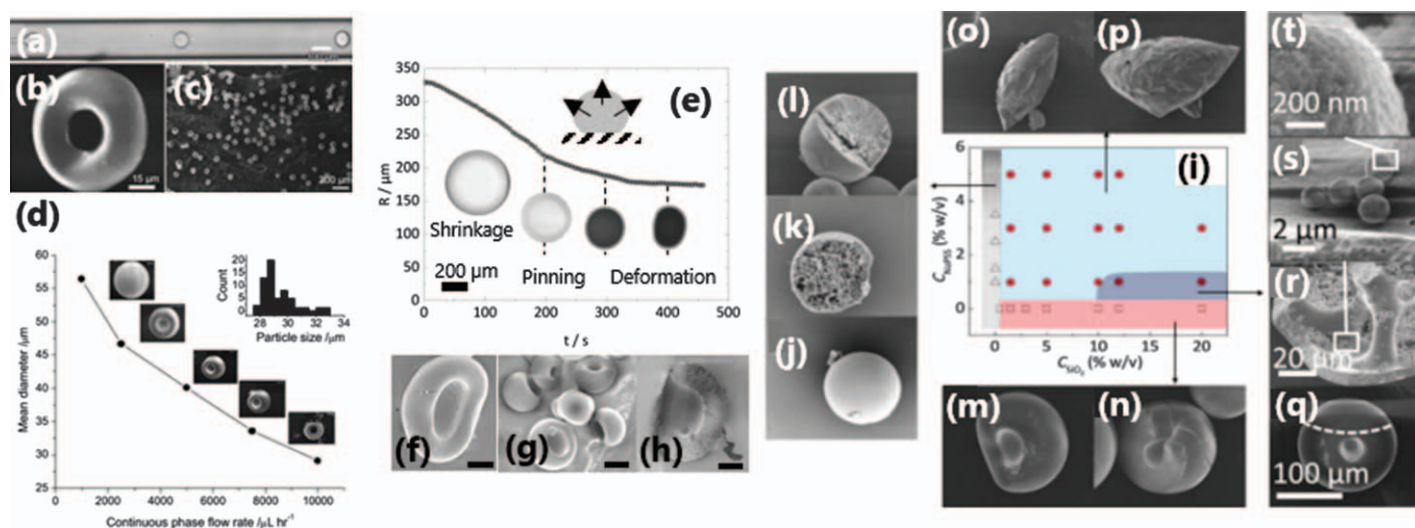


**Figure 4.22** (a) PES/dimethylformamide droplet formation in a silicone oil carrier phase within a capillary microfluidic device. (b, c) Optical microscopy images of a single toroidal particle (b) and multiple (c) microparticles. (d) Particle diameter and morphology as a function of silicone oil flow rate. (e) Radial-time profile for an aqueous PVA droplet extracted with EA whilst residing on a partially wetting substrate. Optical microscopy images illustrate the morphological transitions occurring as particles solidify. (f, g, h) SEM images of resulting particle morphologies, deformed (f) and invaginated (g) while retaining an internally porous microstructure (h). (i): Morphology diagram, and accompanying SEM images, of NaPSS/SiO<sub>2</sub> composite microcapsules generated by solvent extraction. Initial droplet size was fixed at 150  $\mu\text{m}$ . (j, k, l) show internally porous spherical particles formed from NaPSS alone (gray). (m, n) Compact and dimpled colloidal capsules in the absence of NaPSS (pink). (o, p) Tricorn and folded, pollen grain-like structures are found for most NaPSS/SiO<sub>2</sub> compositions (light blue). (q-t) Dimpled capsules with an internally bicontinuous structure are found within a small compositional envelope (dark blue). (a-d) Reprinted from B. Wang, H. C. Shum and D. A. Weitz, *Chemphyschem*, 2009, 10, 641–645. © 2009 Wiley VCH Verlag GmbH & Co. KGaA, Weinheim. (e-h) Reproduced from 159 with permission from The Royal Society of Chemistry. (i-t) Adapted from ref. 155, <http://dx.doi.org/10.1126/sciadv.aa03353>, under the terms of the CC BY 4.0 licence, <https://creativecommons.org/licenses/by/4.0/>.

Figure 4.22(a–c) shows the formation of poly(ether sulfone) (PES) toroidal microparticles from the solvent extraction of dimethylformamide (DMF) into silicone oil. Their shape emerges from the anisotropic extraction of droplets convected along the microchannel. Along the flow direction, stagnation points form in front and behind the droplets, which modulate the solvent (mixture) concentration profile around the droplet, which thus becomes anisotropic. Accumulation of good solvent near the stagnation points slows the rate of solvent removal. Solidification thus begins at the circumferential region and drives polymer from the centre of the droplet to the periphery, causing eventual toroid formation upon complete solidification. This anisotropy can be tuned by change the carrier phase/extraction solvent flow rate, shown in Figure 4.22(d). By reducing the flow rate the particle morphology could be varied from toroidal to dimpled to spherical. For *ex-situ* solvent extraction, *i.e.* taking place in an external bath, anisotropic extraction is also possible when the droplets reside on a partial wetting surface,<sup>159</sup> which breaks the symmetry of extraction kinetics, as well as due to contact line pinning of droplets resting on surfaces, illustrated in Figure 4.22(e). Invaginated and deformed structures (f–h) are thus readily formed. Finally, mixtures of polymers (or polyelectrolytes) and colloids offer more complex phase behaviour and mechanical instabilities upon solidification by solvent extraction. Figure 4.22(i–t) shows a morphology map of NaPSS-silica composite capsules. Polymer-only particles (j, k, l) show the expected spherical morphologies and internal porosity, arising from internal demixing. Dimpled particles are observed for neat colloid particles (m, n). Tricorn and folded pollen grain-like structures are observed, from mechanical instabilities during solidification, for moderate concentrations of both polymer and colloid ( $\simeq 5\%$  and 10% w/v respectively) (o, p). In a small compositional envelope, which appears to coincide with the spinodal region of ternary polymer-colloid solutions (so-called gas–liquid region), bicontinuous internal structures develop (q–t), which can exhibit the pulsed release of colloidal clusters described above. We note that other authors have reported similar bicontinuous structures, “bijel” particles and fibres, with a microfluidic solvent extraction approach.<sup>160</sup> Solvent extraction into the continuous phase, from a ternary O/W droplet or stream containing colloidal particles, induces a spinodal transition which is arrested in a bicontinuous structure through the jamming of the stabilising colloids.

## 4.5 Summary and Outlook

In this chapter, we have provided an overview of recent developments in the formation of polymeric microparticles and capsules *via* droplet microfluidics and flow lithography approaches. Through judicious choice of soft materials precursors (monomers, crosslinkable polymers and colloids), and corresponding solidification approaches, an exceptional range of particle and capsule structures, as well as microstructures, can be attained in both single and multi-phase microfluidics. The overview presented here is

inevitably not exhaustive and, for instance, supramolecular approaches<sup>161</sup> and particles formed from the extraction of BCP stabilised emulsions<sup>162</sup> have not been discussed. The field of polymer particle design and fabrication in microfluidics has reached a certain maturity but continues to evolve. A number of challenges remain to be addressed, and several research avenues provide opportunities that should, from our perspective, be explored.

#### 4.5.1 Particle Formation Strategies

Alternative strategies to induce solidification, from single or multi-phase, which further exploit the physical chemistry of complex fluids and/or microfluidic approaches offer potential for added functionality and ‘morphogenesis’ (the emergence of shape and morphology) of particles. The effect of complex flow fields during particle formation remains largely unexplored, and should enable modulation of the concentration field and deformation of emerging particles and capsules. While inertial microfluidics has been used to shape particles under continuous flow, with optofluidics, and shape fibres from multi-phase jets,<sup>81,82,163</sup> and toroidal particles templated from droplets in laminar channel flow,<sup>164</sup> the precise coupling of flow fields of prescribed type and magnitude has yet to be fully realised. A range of phase and dynamic transitions can be used to impart further structure and function into microparticles and capsules. The majority of phase transitions exploited currently are either solvent- or polymerisation/crosslinking induced. For instance, BCP ordering transitions used to template both nanoparticles and microparticles,<sup>162,165</sup> could be applied in combination with microfluidics and the use of external fields (thermal, electric, magnetic, gravity) in addition to flow and chemical fields, can undoubtedly provide functionality in both active and passive approaches, that appear to be largely unexplored.

#### 4.5.2 Scalability

So far, microfluidic approaches to particle formation are predominately used within an academic context. Whilst they offer unique possibilities for control of droplet and particle formation and mechanistic insights (which can inform scale-up), the throughput of these methods is relatively low. Single droplet generators achieve frequencies of the order of 1–10 kHz, and thus approximately 1 g h<sup>-1</sup>, corresponding to an annual production yield of around  $\frac{1}{100\,000}$  of industrial emulsification processes.<sup>49,166</sup> A recent review considers strategies to address the scale of microfluidic approaches.<sup>167</sup> A combination of parallelisation of droplet generator junctions, typically cross-flow or flow-focussing, and operation of multiple chips appears to be a promising scale-up route. For particles generated from single emulsion droplets, and from a single device, the production capability scales linearly (ignoring downtime, channel clogging and manifold control issues) with the

number of generators.<sup>168,169</sup> The throughput of more complex emulsions has also been vastly increased.<sup>170,171</sup> For example, Romanowsky *et al.* have integrated up to 15 parallel flow-focussing droplet generators in a 3D arrangement to generate up to 1 kg day<sup>-1</sup> with low coefficient of variation for inner and outer droplets. The approach is expected to scale to 9 tonnes per year from a device occupying only a litre of space. However, in spite of this progress, further work is needed to improve scalability, beyond research or high-value/low-volume manufacturing, to compete with the cost and yields from more traditional droplet generation processes and membrane emulsification.<sup>47</sup> After approximately 15 years of microfluidic polymer particle formation, and some industrial uptake, we expect a growing commercial presence of microfluidic approaches, at least in high-value products, assisted by improvements in throughput and tailored optimisation strategies discussed next.

#### 4.5.3 Full Process Integration, Feedback and Learning

The generation of emulsion droplets, prior to solidification, is not the only bottle-neck in particle production. Much of the research discussed in this chapter involves multiple ‘work-up’ steps that take place *off-chip*. These include washing, solvent or monomer removal, or drying of particles, which would be desirable to carry out *on-chip* instead. However, this also requires a precise reconciliation of timescales for each on-chip process (including particle solidification), in order to achieve truly integrated particle generators. Innovative chemical engineering solutions thus appear necessary. Further performance testing or function could be integrated *on-chip*, *e.g.* decoding of encoded particles for bio-medical assays<sup>84</sup> or particle dissolution/triggered release of encapsulants. With additional incorporation of feedback loops and automated optimisation routines,<sup>172,173</sup> we expect that particles can be designed *in situ* for desired properties and avoid laborious screening studies. Further, machine learning approaches can potentially elucidate design parameters (including particle shape, patchiness and microstructure) which appear otherwise challenging to map in detail, given the extensive parameter space available for particle design.

We believe it is only matter a time before these and other developments transform the mechanistic understanding, functionality and manufacturing of advanced polymeric particles, whose societal impact is expected to be significant, in areas ranging from food to precision medicine.

## References

1. R. K. Shah, H. C. Shum, A. C. Rowat, D. Lee, J. J. Agresti, A. S. Utada, L. Y. Chu, J. W. Kim, A. Fernandez-Nieves, C. J. Martinez and D. A. Weitz, *Mater. Today*, 2008, **11**, 18–27.
2. R. Langer and D. A. Tirrell, *Nature*, 2004, **428**, 487–492.
3. E. Amstad, *ACS Macro Lett.*, 2017, **6**, 841–847.

4. M. B. Oliveira and J. F. Mano, *Biotechnol. Prog.*, 2011, **27**, 897–912.
5. C. S. Ana, M. L. Carla, M. S. L. Josfffdffd and H. A. Maria, *Curr. Pharm. Biotechnol.*, 2015, **16**, 940–954.
6. Q.-S. Wang, G.-F. Wang, J. Zhou, L.-N. Gao and Y.-L. Cui, *Int. J. Pharm.*, 2016, **515**, 176–185.
7. B. J. Battersby, D. Bryant, W. Meutermans, D. Matthews, M. L. Smythe and M. Trau, *J. Am. Chem. Soc.*, 2000, **122**, 2138–2139.
8. X.-H. Ji, W. Cheng, F. Guo, W. Liu, S.-S. Guo, Z.-K. He and X.-Z. Zhao, *Lab Chip*, 2011, **11**, 2561–2568.
9. M. Oh and C. A. Mirkin, *Nature*, 2005, **438**, 651.
10. Y.-M. Jeon, G. S. Armatas, D. Kim, M. G. Kanatzidis and C. A. Mirkin, *Small*, 2008, **5**, 46–50.
11. F. Pignon, A. Magnin and J.-M. Piau, *J. Rheol.*, 1998, **42**, 1349–1373.
12. B. P. Binks, *Curr. Opin. Colloid Interface Sci.*, 2002, **7**, 21–41.
13. A. Kumar and J. J. L. Higdon, *J. Rheol.*, 2011, **55**, 581–626.
14. Y. Lu, Y. Yin and Y. Xia, *Adv. Mater.*, 2001, **13**, 415–420.
15. L. Skedung, M. Arvidsson, J. Y. Chung, C. M. Stafford, B. Berglund and M. W. Rutland, *Sci. Rep.*, 2013, **3**, 2617.
16. S. C. Glotzer, M. J. Solomon and N. A. Kotov, *AIChEJ*, 2004, **50**, 2978–2985.
17. S. Sacanna and D. J. Pine, *Curr. Opin. Colloid Interface Sci.*, 2011, **16**, 96–105.
18. S. C. Glotzer, *Chem. Eng. Sci.*, 2015, **121**, 3–9.
19. D. C. Duffy, J. C. McDonald, O. J. Schueller and G. M. Whitesides, *Anal. Chem.*, 1998, **70**, 4974–4984.
20. Calyxia, [www.calyxia.fr](http://www.calyxia.fr), (Accessed June 2019).
21. Capsum, <http://www.capsum.net/en/artisan/>, (Accessed June 2019).
22. B. Gale, A. Jafek, C. Lambert, B. Goenner, H. Moghimifam, U. Nze and S. Kamarapu, 2018, **3**, 60.
23. E. K. Sackmann, A. L. Fulton and D. J. Beebe, *Nature*, 2014, **507**, 181–189.
24. E. Kumacheva and P. Garstecki, *Microfluidic Reactors for Polymer Particles*, John Wiley Sons, Ltd, 2011.
25. S.-Y. Teh, R. Lin, L.-H. Hung and A. P. Lee, *Lab Chip*, 2008, **8**, 198–220.
26. R. Seemann, M. Brinkmann, T. Pfohl and S. Herminghaus, *Rep. Prog. Phys.*, 2012, **75**, 016601.
27. P. Zhu and L. Wang, *Lab Chip*, 2017, **17**, 34–75.
28. L. Shang, Y. Cheng and Y. Zhao, *Chem. Rev.*, 2017, **117**, 7964–8040.
29. K. Zhanxiao, K. Tiantian, L. Leyan, Z. Pingan, T. Xiaowei and W. Liqiu, *J. Micromech. Microeng.*, 2016, **26**, 075011.
30. S. Xu, Z. Nie, M. Seo, P. Lewis, E. Kumacheva, H. A. Stone, P. Garstecki, D. B. Weibel, I. Gitlin and G. M. Whitesides, *Ange. Chem., Int. Ed.*, 2005, **44**, 724–728.
31. J.-T. Wang, J. Wang and J.-J. Han, *Small*, 2011, **7**, 1728–1754.
32. H. C. Shum, A. R. Abate, D. Lee, A. R. Studart, B. Wang, C.-H. Chen, J. Thiele, R. K. Shah, A. Krummel and D. A. Weitz, *Macromol. Rapid Commun.*, 2010, **31**, 108–118.

33. T. Kong, J. Wu, M. To, K. Wai Kwok Yeung, H. Cheung Shum and L. Wang, *Biomicrofluidics*, 2012, **6**, 34104.
34. J. H. Kim, T. Y. Jeon, T. M. Choi, T. S. Shim, S.-H. Kim and S.-M. Yang, *Langmuir*, 2014, **30**, 1473–1488.
35. D. Dendukuri and P. S. Doyle, *Adv. Mater.*, 2009, **21**, 4071–4086.
36. P. W. Chen, R. M. Erb and A. R. Studart, *Langmuir*, 2012, **28**, 144–152.
37. T. Brugarolas, F. Q. Tu and D. Lee, *Soft Matter*, 2013, **9**, 9046–9058.
38. J. D. Tice, H. Song, A. D. Lyon and R. F. Ismagilov, *Langmuir*, 2003, **19**, 9127–9133.
39. Z. Z. Chong, S. H. Tan, A. M. Ganan-Calvo, S. B. Tor, N. H. Loh and N. T. Nguyen, *Lab Chip*, 2016, **16**, 35–58.
40. A. R. Abate and D. A. Weitz, *Small*, 2009, **5**, 2030–2032.
41. L. L. A. Adams, T. E. Kodger, S.-H. Kim, H. C. Shum, T. Franke and D. A. Weitz, *Soft Matter*, 2012, **8**, 10719.
42. S. L. Anna, N. Bontoux and H. A. Stone, *Appl. Phys. Lett.*, 2003, **82**, 364–366.
43. L. Martin-Banderas, M. Flores-Mosquera, P. Riesco-Chueca, A. Rodriguez-Gil, A. Cebolla, S. Chavez and A. M. Ganan-Calvo, *Small*, 2005, **1**, 688–692.
44. E. Castro-Hernandez, V. Gundabala, A. Fernandez-Nieves and J. M. Gordillo, *New J. Phys.*, 2009, **11**, 075021.
45. P. Garstecki, M. J. Fuerstman, H. A. Stone and G. M. Whitesides, *Lab Chip*, 2006, **6**, 437–446.
46. G. F. Christopher, N. N. Noharuddin, J. A. Taylor and S. L. Anna, *Phys. Rev. E*, 2008, **78**, 036317.
47. R. G. Holdich, M. M. Dragosavac, G. T. Vladisavljevic and S. R. Kosvintsev, *Ind. Eng. Chem. Res.*, 2010, **49**, 3810–3817.
48. E. Amstad, X. Chen, M. Eggersdorfer, N. Cohen, T. E. Kodger, C. L. Ren and D. A. Weitz, *Phys. Rev. E*, 2017, **95**, 043105.
49. H. Christian, *J. Phys. D: Appl. Phys.*, 2013, **46**, 114008.
50. J. C. McDonald and G. M. Whitesides, *Acc. Chem. Res.*, 2002, **35**, 491–499.
51. J. T. Cabral, S. D. Hudson, C. Harrison and J. F. Douglas, *Langmuir*, 2004, **20**, 10020–10029.
52. T.-F. Hong, W.-J. Ju, M.-C. Wu, C.-H. Tai, C.-H. Tsai and L.-M. Fu, *Microfluid. Nanofluid.*, 2010, **9**, 1125–1133.
53. D. J. Guckenberger, T. E. de Groot, A. M. D. Wan, D. J. Beebe and E. W. K. Young, *Lab Chip*, 2015, **15**, 2364–2378.
54. E. Sollier, C. Murray, P. Maoddi and D. Di Carlo, *Lab Chip*, 2011, **11**, 3752–3765.
55. A. S. Utada, E. Lorenceau, D. R. Link, P. D. Kaplan, H. A. Stone and D. A. Weitz, *Science*, 2005, **308**, 537–541.
56. Y. Wu, X. Qian, M. Zhang, Y. Dong, S. Sun and X. Wang, *Micromachines*, 2018, **9**, 139.
57. S. A. Nabavi, G. T. Vladisavljevic, S. Gu and E. E. Ekanem, *Chem. Eng. Sci.*, 2015, **130**, 183–196.

58. C. Tonhauser, A. Nataello, H. Lowe and H. Frey, *Macromolecules*, 2012, **45**, 9551–9570.
59. E. Quevedo, J. Steinbacher and D. T. McQuade, *J. Am. Chem. Soc.*, 2005, **127**, 10498–10499.
60. S. Takeuchi, P. Garstecki, D. B. Weibel and G. M. Whitesides, *Adv. Mater.*, 2005, **17**, 1067–1072.
61. Z. D. Liu, Y. C. Lu, B. D. Yang and G. S. Luo, *Ind. Eng. Chem. Res.*, 2011, **50**, 11853–11862.
62. M. Seo, Z. Nie, S. Xu, M. Mok, P. C. Lewis, R. Graham and E. Kumacheva, *Langmuir*, 2005, **21**, 11614–11622.
63. H. Chen, Y. Zhao, J. Li, M. Guo, J. Wan, D. A. Weitz and H. A. Stone, *Lab Chip*, 2011, **11**, 2312–2315.
64. C. H. Choi, J. H. Jung, D. W. Kim, Y. M. Chung and C. S. Lee, *Lab Chip*, 2008, **8**, 1544–1551.
65. E. Kumacheva and P. Garstecki, in *Microfluidic Reactors for Polymer Particles*, John Wiley Sons, Ltd, 2011, pp. 109–145.
66. Z. Nie, W. Li, M. Seo, S. Xu and E. Kumacheva, *J. Am. Chem. Soc.*, 2006, **128**, 9408–9412.
67. T. Nisisako, T. Torii, T. Takahashi and Y. Takizawa, *Adv. Mater.*, 2006, **18**, 1152–1156.
68. T. Nisisako and T. Hatsuzawa, *Sens. Actuators, B*, 2016, **223**, 209–216.
69. T. Nisisako and T. Hatsuzawa, *Microfluid. Nanofluid.*, 2009, **9**, 427–437.
70. T. Nisisako, T. Ando and T. Hatsuzawa, *Small*, 2014, **10**, 5116–5125.
71. M. J. Zhang, W. Wang, X. L. Yang, B. Ma, Y. M. Liu, R. Xie, X. J. Ju, Z. Liu and L. Y. Chu, *ACS Appl. Mater. Interfaces*, 2015, **7**, 13758–13767.
72. E. Loiseau, F. Niedermair, G. Albrecht, M. Frey, A. Hauser, P. A. Ruhs and A. R. Studart, *Langmuir*, 2017, **33**, 2402–2410.
73. X. Xie, W. Zhang, A. Abbaspourrad, J. Ahn, A. Bader, S. Bose, A. Vegas, J. Lin, J. Tao, T. Hang, H. Lee, N. Iverson, G. Bisker, L. Li, M. S. Strano, D. A. Weitz and D. G. Anderson, *Nano Lett.*, 2017, **17**, 2015–2020.
74. S. Guo, G. Kang, D. T. Phan, M. N. Hsu, Y. C. Por and C. H. Chen, *Sci. Rep.*, 2018, **8**, 2245.
75. D. Dendukuri, D. C. Pregibon, J. Collins, T. A. Hatton and P. S. Doyle, *Nat. Mater.*, 2006, **5**, 365–369.
76. N. Hakimi, S. S. Tsai, C. H. Cheng and D. K. Hwang, *Adv. Mater.*, 2014, **26**, 1393–1398.
77. D. Dendukuri, S. S. Gu, D. C. Pregibon, T. A. Hatton and P. S. Doyle, *Lab Chip*, 2007, **7**, 818–828.
78. J. H. Jang, D. Dendukuri, T. A. Hatton, E. L. Thomas and P. S. Doyle, *Angew. Chem., Int. Ed. Engl.*, 2007, **46**, 9027–9031.
79. K. W. Bong, D. C. Pregibon and P. S. Doyle, *Lab Chip*, 2009, **9**, 863–866.
80. K. W. Bong, J. Xu, J. H. Kim, S. C. Chapin, M. S. Strano, K. K. Gleason and P. S. Doyle, *Nat. Commun.*, 2012, **3**, 805.
81. K. S. Paulsen, D. Di Carlo and A. J. Chung, *Nat. Commun.*, 2015, **6**, 6976.
82. K. S. Paulsen and A. J. Chung, *Lab Chip*, 2016, **16**, 2987–2995.

83. G. C. Le Goff, R. L. Srinivas, W. A. Hill and P. S. Doyle, *Eur. Polym. J.*, 2015, **72**, 386–412.
84. D. C. Pregibon, M. Toner and P. S. Doyle, *Science*, 2007, **315**, 1393–1396.
85. S. C. Chapin, D. C. Appleyard, D. C. Pregibon and P. S. Doyle, *Angew. Chem., Int. Ed. Engl.*, 2011, **50**, 2289–2293.
86. N. W. Choi, J. Kim, S. C. Chapin, T. Duong, E. Donohue, P. Pandey, W. Broom, W. A. Hill and P. S. Doyle, *Anal. Chem.*, 2012, **84**, 9370–9378.
87. J. W. Kim, A. S. Utada, A. Fernandez-Nieves, Z. Hu and D. A. Weitz, *Angew. Chem., Int. Ed. Engl.*, 2007, **46**, 1819–1822.
88. S. Ghosh and P. Schurtenberger, *Colloids Surf., A*, 2019, **573**, 205–210.
89. S. Seiffert, M. B. Romanowsky and D. A. Weitz, *Langmuir*, 2010, **26**, 14842–14847.
90. S. Seiffert and D. A. Weitz, *Polymer*, 2010, **51**, 5883–5889.
91. S. Seiffert, J. Thiele, A. R. Abate and D. A. Weitz, *J. Am. Chem. Soc.*, 2010, **132**, 6606–6609.
92. C. L. Mou, X. J. Ju, L. Zhang, R. Xie, W. Wang, N. N. Deng, J. Wei, Q. Chen and L. Y. Chu, *Langmuir*, 2014, **30**, 1455–1464.
93. T. Rossow, J. A. Heyman, A. J. Ehrlicher, A. Langhoff, D. A. Weitz, R. Haag and S. Seiffert, *J. Am. Chem. Soc.*, 2012, **134**, 4983–4989.
94. J. Esquena, *Curr. Opin. Colloid Interface Sci.*, 2016, **25**, 109–119.
95. A. Sauret and H. C. Shum, *Appl. Phys. Lett.*, 2012, **100**, 154106.
96. I. Ziemecka, V. van Steijn, G. J. Koper, M. Rosso, A. M. Brizard, J. H. van Esch and M. T. Kreutzer, *Lab Chip*, 2011, **11**, 620–624.
97. T. Watanabe, I. Motohiro and T. Ono, *Langmuir*, 2019, **35**, 2358–2367.
98. S. Ma, J. Thiele, X. Liu, Y. Bai, C. Abell and W. T. Huck, *Small*, 2012, **8**, 2356–2360.
99. S. Sacanna, W. T. Irvine, P. M. Chaikin and D. J. Pine, *Nature*, 2010, **464**, 575–578.
100. F. T. Wall and J. W. Drenan, *J. Polym. Sci.*, 1951, **7**, 83–88.
101. I. Michaeli, *J. Polym. Sci.*, 1960, **48**, 291–299.
102. S. C. Nigam, I. F. Tsao, A. Sakoda and H. Y. Wang, *Biotechnol. Tech.*, 1988, **2**, 271–276.
103. K. A. Narh and A. Keller, *J. Polym. Sci., Part B: Polym. Phys.*, 1993, **31**, 231–234.
104. S. Sugiura, T. Oda, Y. Izumida, Y. Aoyagi, M. Satake, A. Ochiai, N. Ohkohchi and M. Nakajima, *Biomaterials*, 2005, **26**, 3327–3331.
105. K. Liu, H. J. Ding, J. Liu, Y. Chen and X. Z. Zhao, *Langmuir*, 2006, **22**, 9453–9457.
106. K. S. Huang, T. H. Lai and Y. C. Lin, *Lab Chip*, 2006, **6**, 954–957.
107. C.-H. Yang, K.-S. Huang, P.-W. Lin and Y.-C. Lin, *Sens. Actuators, B*, 2007, **124**, 510–516.
108. M. Marquis, J. Davy, A. Fang and D. Renard, *Biomacromolecules*, 2014, **15**, 1568–1578.
109. G. T. Grant, E. R. Morris, D. A. Rees, P. J. C. Smith and D. Thom, *FEBS Lett.*, 1973, **32**, 195–198.

*Design and Fabrication of Polymer Microparticles and Capsules Using Microfluidics* 145

110. E. R. Morris, D. A. Rees, D. Thom and J. Boyd, *Carbohydr. Res.*, 1978, **66**, 145–154.
111. H. Zhang, E. Tumarkin, R. M. A. Sullan, G. C. Walker and E. Kumacheva, *Macromol. Rapid Commun.*, 2007, **28**, 527–538.
112. T. Y. Lee, R. Praveenkumar, Y. K. Oh, K. Lee and S. H. Kim, *J. Mater. Chem. B*, 2016, **4**, 3232–3238.
113. L. Capretto, S. Mazzitelli, C. Balestra, A. Tosi and C. Nastruzzi, *Lab Chip*, 2008, **8**, 617–621.
114. T. D. Dang and S. W. Joo, *Colloids Surf. B*, 2013, **102**, 766–771.
115. Y. S. Lin, C. H. Yang, Y. Y. Hsu and C. L. Hsieh, *Electrophoresis*, 2013, **34**, 425–431.
116. Y. Hu, Q. Wang, J. Wang, J. Zhu, H. Wang and Y. Yang, *Biomicrofluidics*, 2012, **6**, 26502–265029.
117. C. S. Peyratout and L. Dahne, *Angew. Chem., Int. Ed. Engl.*, 2004, **43**, 3762–3783.
118. G. Kaufman, R. Boltynskiy, S. Nejati, A. R. Thiam, M. Loewenberg, E. R. Dufresne and C. O. Osuji, *Lab Chip*, 2014, **14**, 3494–3497.
119. G. Kaufman, S. Nejati, R. Sarfati, R. Boltynskiy, M. Loewenberg, E. R. Dufresne and C. O. Osuji, *Soft Matter*, 2015, **11**, 7478–7482.
120. L. Zhang, L. H. Cai, P. S. Lienemann, T. Rossow, I. Polenz, Q. Vallmajó-Martin, M. Ehrbar, H. Na, D. J. Mooney and D. A. Weitz, *Angew. Chem., Int. Ed. Engl.*, 2016, **55**, 13470–13474.
121. M. Kim, S. J. Yeo, C. B. Highley, J. A. Burdick, P. J. Yoo, J. Doh and D. Lee, *ACS Nano*, 2015, **9**, 8269–8278.
122. M. Kim, J. Doh and D. Lee, *ACS Macro Lett.*, 2016, **5**, 487–492.
123. G. Duan, M. F. Haase, K. J. Stebe and D. Lee, *Langmuir*, 2018, **34**, 847–853.
124. N. N. Deng and W. T. S. Huck, *Angew. Chem., Int. Ed. Engl.*, 2017, **56**, 9736–9740.
125. O. D. Velev, K. Furusawa and K. Nagayama, *Langmuir*, 1996, **12**, 2374–2384.
126. G.-R. Yi, V. Manoharan, S. Klein, K. Brzezinska, D. Pine, F. Lange and S.-M. Yang, *Adv. Mater.*, 2002, **14**, 1137–1140.
127. O. D. Velev, A. M. Lenhoff and E. W. Kaler, *Science*, 2000, **287**, 2240–2243.
128. A. D. Dinsmore, M. F. Hsu, M. G. Nikolaides, M. Marquez, A. R. Bausch and D. A. Weitz, *Science*, 2002, **298**, 1006–1009.
129. G. R. Yi, S. J. Jeon, T. Thorsen, V. N. Manoharan, S. R. Quake, D. J. Pine and S. M. Yang, *Synth. Met.*, 2003, **139**, 803–806.
130. S. H. Kim, S. J. Jeon, G. R. Yi, C. J. Heo, J. H. Choi and S. M. Yang, *Adv. Mater.*, 2008, **20**, 1649.
131. D. Lee and D. A. Weitz, *Adv. Mater.*, 2008, **20**, 3498–3503.
132. Y. D. Hu and J. Perez-Mercader, *ACS Appl. Nano Mater.*, 2018, **1**, 3346–3354.
133. J. W. Kim, A. Fernandez-Nieves, N. Dan, A. S. Utada, M. Marquez and D. A. Weitz, *Nano Lett.*, 2007, **7**, 2876–2880.

134. R. K. Shah, J. W. Kim and D. A. Weitz, *Langmuir*, 2010, **26**, 1561–1565.
135. S.-H. Kim, H. Hwang, C. H. Lim, J. W. Shim and S.-M. Yang, *Adv. Funct. Mater.*, 2011, **21**, 1608–1615.
136. D. E. Discher and A. Eisenberg, *Science*, 2002, **297**, 967–973.
137. H. C. Shum, J. W. Kim and D. A. Weitz, *J. Am. Chem. Soc.*, 2008, **130**, 9543–9549.
138. H. C. Shum, E. Santanach-Carreras, J. W. Kim, A. Ehrlicher, J. Bibette and D. A. Weitz, *J. Am. Chem. Soc.*, 2011, **133**, 4420–4426.
139. E. Lorenceau, A. S. Utada, D. R. Link, G. Cristobal, M. Joanicot and D. A. Weitz, *Langmuir*, 2005, **21**, 9183–9186.
140. M. H. Lee, K. C. Hribar, T. Brugarolas, N. P. Kamat, J. A. Burdick and D. Lee, *Adv. Funct. Mater.*, 2012, **22**, 131–138.
141. S. H. Kim, H. C. Shum, J. W. Kim, J. C. Cho and D. A. Weitz, *J. Am. Chem. Soc.*, 2011, **133**, 15165–15171.
142. S. H. Kim, J. W. Kim, D. H. Kim, S. H. Han and D. A. Weitz, *Small*, 2013, **9**, 124–131.
143. H. C. Shum, Y. J. Zhao, S. H. Kim and D. A. Weitz, *Angew. Chem., Int. Ed. Engl.*, 2011, **50**, 1648–1651.
144. S. H. Kim, J. Nam, J. W. Kim, D. H. Kim, S. H. Han and D. A. Weitz, *Lab Chip*, 2013, **13**, 1351–1356.
145. G. R. Guillen, Y. J. Pan, M. H. Li and E. M. V. Hoek, *Ind. Eng. Chem. Res.*, 2011, **50**, 3798–3817.
146. C. E. Udoeh, V. Garbin and J. T. Cabral, *Langmuir*, 2016, **32**, 8131–8140.
147. T. Watanabe, C. G. Lopez, J. F. Douglas, T. Ono and J. T. Cabral, *Langmuir*, 2014, **30**, 2470–2479.
148. Q. Xu, M. Hashimoto, T. T. Dang, T. Hoare, D. S. Kohane, G. M. Whitesides, R. Langer and D. G. Anderson, *Small*, 2009, **5**, 1575–1581.
149. L. H. Hung, S. Y. Teh, J. Jester and A. P. Lee, *Lab Chip*, 2010, **10**, 1820–1825.
150. G. T. Vladisavljevic, W. J. Duncanson, H. C. Shum and D. A. Weitz, *Langmuir*, 2012, **28**, 12948–12954.
151. T. Watanabe, Y. Kimura and T. Ono, *Langmuir*, 2013, **29**, 14082–14088.
152. T. Watanabe, T. Ono and Y. Kimura, *Soft Matter*, 2011, **7**, 9894–9897.
153. D. R. Tree, K. T. Delaney, H. D. Ceniceros, T. Iwama and G. H. Fredrickson, *Soft Matter*, 2017, **13**, 3013–3030.
154. C. E. Udoeh, V. Garbin and J. T. Cabral, *Soft Matter*, 2019, DOI: 10.1039/C9SM00708C.
155. C. E. Udoeh, J. T. Cabral and V. Garbin, *Sci. Adv.*, 2017, **3**, eaao3353.
156. P. S. Epstein and M. S. Plessset, *J. Chem. Phys.*, 1950, **18**, 1505–1509.
157. P. B. Duncan and D. Needham, *Langmuir*, 2006, **22**, 4190–4197.
158. D. L. Bitterfield, A. Utoft and D. Needham, *Langmuir*, 2016, **32**, 12749–12759.
159. W. N. Sharratt, A. Brooker, E. S. J. Robles and J. T. Cabral, *Soft Matter*, 2018, **14**, 4453–4463.
160. M. F. Haase, K. J. Stebe and D. Lee, *Adv. Mater.*, 2015, **27**, 7065–7071.

*Design and Fabrication of Polymer Microparticles and Capsules Using Microfluidics* 147

161. J. Liu, Y. Lan, Z. Yu, C. S. Tan, R. M. Parker, C. Abell and O. A. Scherman, *Acc. Chem. Res.*, 2017, **50**, 208–217.
162. K. H. Ku, J. M. Shin, H. Yun, G. R. Yi, S. G. Jang and B. J. Kim, *Adv. Funct. Mater.*, 2018, **28**, 1802961.
163. J. K. Nunes, C. Y. Wu, H. Amini, K. Owsley, D. Di Carlo and H. A. Stone, *Adv. Mater.*, 2014, **26**, 3712–3717.
164. B. Wang, H. C. Shum and D. A. Weitz, *ChemPhysChem*, 2009, **10**, 641–645.
165. L. S. Grundy, V. E. Lee, N. Li, C. Sosa, W. D. Mulhearn, R. Liu, R. A. Register, A. Nikoubashman, R. K. Prud'homme, A. Z. Panagiotopoulos and R. D. Priestley, *ACS Nano*, 2018, **12**, 4660–4668.
166. L. Yobas, S. Martens, W. L. Ong and N. Ranganathan, *Lab Chip*, 2006, **6**, 1073–1079.
167. G. T. Vladisavljevic, N. Khalid, M. A. Neves, T. Kuroiwa, M. Nakajima, K. Uemura, S. Ichikawa and I. Kobayashi, *Adv. Drug Delivery Rev.*, 2013, **65**, 1626–1663.
168. W. Li, J. Greener, D. Voicu and E. Kumacheva, *Lab Chip*, 2009, **9**, 2715–2721.
169. T. Nisisako and T. Torii, *Lab Chip*, 2008, **8**, 287–293.
170. T. Nisisako, T. Ando and T. Hatsuzawa, *Lab Chip*, 2012, **12**, 3426–3435.
171. M. B. Romanowsky, A. R. Abate, A. Rotem, C. Holtze and D. A. Weitz, *Lab Chip*, 2012, **12**, 802–807.
172. B. E. Walker, J. H. Bannock, A. M. Nightingale and J. C. deMello, *React. Chem. Eng.*, 2017, **2**, 785–798.
173. O. J. Dressler, P. D. Howes, J. Choo and A. J. deMello, *ACS Omega*, 2018, **3**, 10084–10091.

## CHAPTER 5

# *Recent Advances in Colloidal Polyelectrolyte Brushes*

QINGSONG YANG,<sup>a</sup> XIAOFENG NIU,<sup>a</sup> ZHINAN FU,<sup>a</sup> LI LI<sup>a</sup> AND XUHONG GUO<sup>\*a,b</sup>

<sup>a</sup> State Key Laboratory of Chemical Engineering, East China University of Science and Technology, 200237 Shanghai, China; <sup>b</sup> Engineering Research Center of Materials Chemical Engineering of Xinjiang Bingtuan, Shihezi University, 832000 Xinjiang, China

\*Email: guoxuhong@ecust.edu.cn; guoxuhong@hotmail.com

## 5.1 Introduction

Polymer brush refers to a macromolecular assembly which is formed by polymer chains densely attached by one end to a surface or an interface.<sup>1,2</sup> For a brush, the distance between neighboring grafting sites ( $D$ ) is much smaller than the gyration radius ( $R_g$ ) of free polymer chains (normally  $D$  should be at least smaller than  $2R_g$ ) so that the polymer chains stretch away from the interface into the solution.<sup>3</sup> Since the report that grafting polymer molecules to colloidal particles was an effective way to prevent flocculation in the 1950s,<sup>4,5</sup> polymer brushes have attracted considerable attention in protein immobilization,<sup>6</sup> catalysis,<sup>7</sup> nanoreactors,<sup>8</sup> environmental engineering,<sup>9</sup> disease diagnosis<sup>10,11</sup> and other fields.<sup>12</sup>

Polymer brushes can be generated by grafting polymer chains to either planar<sup>13</sup> or curved interfaces e.g. cylinders<sup>14</sup> or spheres.<sup>15</sup> If the polymer chains are polyelectrolytes and are densely grafted onto a spherical core, a spherical polyelectrolyte brush (SPB) is the result (Figure 5.1).

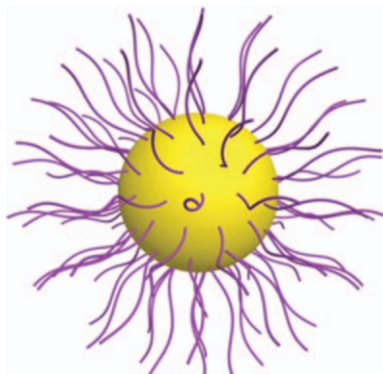


**Figure 5.1** Schematic diagram of spherical polyelectrolyte brushes (SPBs).

Generally, there are two methods used to prepare polymer brushes, physical adsorption and chemical attachment.<sup>16,17</sup> Chemical attachment attracts more attention because it overcomes the drawbacks of physical adsorption such as restricted grafting density and low stabilities. Chemical attachment can be divided into two techniques: “grafting to” and “grafting from”.<sup>18</sup> The “grafting to” strategy involves polyelectrolyte chains which are prefabricated and end-functionalized reacting with appropriate groups immobilized on the substrate to generate SPBs. Relatively low grafting density is obtained by this approach as the steric hindrance increases sharply with grafting density. “Grafting from” does not have these problems as the polymerization of polymer chains are directly polymerized onto the surface by an initiator that is chemically affixed to the surface of the particles. Grafting from methods include photo-emulsion polymerization,<sup>19</sup> thermo-controlled emulsion polymerization,<sup>20</sup> atom transfer radical polymerization (ATRP),<sup>21</sup> reversible addition–fragmentation chain transfer polymerization (RAFT),<sup>22</sup> and surface-initiated photo-iniferter-mediated polymerization (SI-PIMP).<sup>23</sup>

Photo-emulsion polymerization, as one of the most popular “grafting from” methods to prepare SPBs, was first reported by Guo *et al.*<sup>19</sup> It includes three main steps, as shown in Figure 5.2. In the first step, a polystyrene (PS) latex is generated by conventional emulsion polymerization. Then the PS core is covered by a thin layer of photo-initiator 2-[*p*-(2-hydroxy-2-methylpropiophenone)]-ethylene glycol-methacrylate (HMEM). In the third step, polyelectrolyte chains are grafted from the surface of the PS core under ultraviolet (UV) irradiation. The generated SPB consists of a PS core and densely-grafted polyelectrolyte chains.

Utilizing photo-emulsion polymerization to prepare SPBs has become popular as it has various advantages.<sup>24</sup> Firstly, the SPB particles synthesized by this method have well-defined morphologies and narrow size distributions. Secondly, the structure of SPBs can be easily controlled. The grafting density of polyelectrolyte chains can be tuned by changing the amount of photo-initiator and the contour length can be controlled by

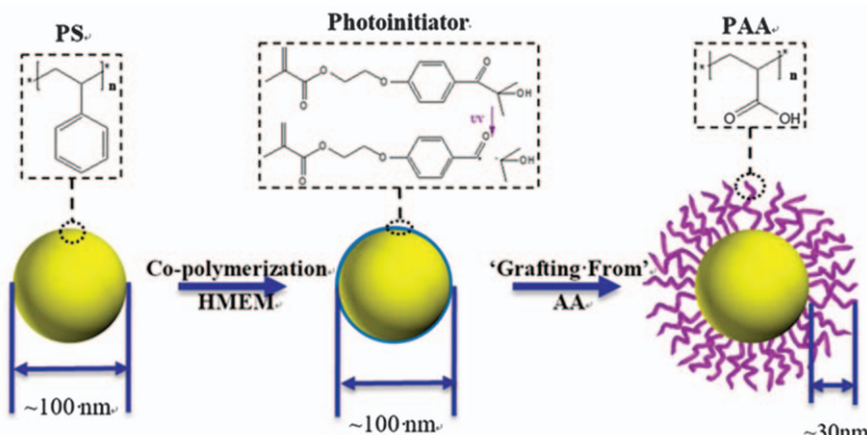


**Figure 5.2** Schematic representation of SPBs preparation by photo-emulsion polymerization.

Reproduced from ref. 106 with permission from American Chemical Society, Copyright 2017.

changing the mass of monomer. In addition, parameters including the grafting density and molecular weight of polyelectrolyte chains can be determined as the ester bond of HMEM molecules can be cleaved under strong base conditions. More importantly, almost all water-soluble monomers can be grafted onto colloidal core particles by this method, in theory.<sup>25</sup> Because of its well-defined core–shell structure, various techniques can be used for the characterization of SPBs, *e.g.*, dynamic light scattering (DLS),<sup>26</sup> small angle X-ray scattering (SAXS),<sup>27,28</sup> atomic force microscopy (AFM),<sup>29</sup> and cryogenic transmission electron microscopy (cryo-TEM).<sup>30</sup>

According to the type of charge carried by polyelectrolyte chains, SPBs can be divided into: cationic SPBs, such as poly(2-aminoethylmethacrylate hydrochloride) (PAEMH), anionic SPBs, such as poly(acrylic acid) (PAA), and zwitterionic SPBs.<sup>31</sup> Based on the difference in dissociation of the polyelectrolyte chains, SPBs can be further classified into two kinds: (1) quenched polyelectrolyte brushes, in which the grafted polymer chains are strong polyelectrolytes such as poly(sodium styrene sulfonate) (PNaSS) and the charge distribution does not depend on the external conditions; (2) annealed polyelectrolyte brushes, in which the grafted polymer chains are weak polyelectrolytes such as PAA, and the degree of dissociation is not fixed but can vary with external conditions such as pH and ionic strength (or salt concentration).<sup>26</sup> For both the quenched and the annealed brushes the electrostatic interactions between the polyelectrolyte chains can be tuned by changing the external conditions in the system.<sup>32</sup> Depending on the ionic strength, SPBs can be distinguished into three main regimes: the neutral brush regime (at very high added salt concentration), the salted brush regime (when the salt concentration in the solution becomes comparable to that inside the SPB), and the osmotic brush regime (at very low added salt concentration).<sup>24</sup>

The stretching of brush chains is affected by the steric hindrance and repulsion among polyelectrolytes with the same charge. A lot of theoretical studies have also been done to understand the polyelectrolyte brush. For instance, Pincus and Borisov *et al.* found that, as a very important behavior, most of the counterions in aqueous solution are confined within the brush layer because of the Donnan effect and electrostatic interactions.<sup>33,34</sup> Thus, the stretching of polyelectrolyte chains in SPB can be controlled by the osmotic pressure of the confined counterions.<sup>35,36</sup> The direct measurements of the osmotic pressure of dilute solutions of SPBs have shown that about 95% of counterions are confined inside the brush, resulting in a strong elongation of the grafted polyelectrolyte chains.<sup>37,38</sup>

SPBs have attracted considerable attention because of their unique features, *e.g.*, high grafting density, legible interface, narrow size distribution, and stimulus-responsive properties. More importantly, the behaviors of SPBs can be controlled by grafting different chains and embedding functional nanoparticles. Cang *et al.*<sup>39</sup> prepared two kinds of dual-responsive SPBs, the cores of which were composed of polystyrene with grafting from co-polymers of *N*-isopropyl acrylamide (NIPA) and acrylic acid (AA). They found that a change in charge distribution could lead to different responses toward pH, temperature, and ionic strength. Functional SPBs can also be prepared by embedding nanoparticles into a PS core. Chen *et al.*<sup>40</sup> successfully synthesized magnetic SPBs with embedded magnetite nanoparticles into the PS core. Similarly, fluorescent SPBs were prepared by embedding quantum dots (QDs) in the PS core.<sup>41</sup>

Owing to their unique structure and multifunctional properties, SPBs exhibit great potential for applications in many fields. They are ideal models for the investigation of emulsion and colloidal systems due to their narrow size distribution and excellent stability. They can be used as carriers for nanosized catalysis, proteins, and drugs.<sup>42,43</sup> When the confined metal ions within SPB layers are reduced *in situ*, metal nanoparticles can be generated and affixed in SPBs. In addition, the uniform morphology and facile control of surface functionality make SPBs ideal templates for the preparation of composite nanoparticles. Finally, interactions between SPBs and proteins can be modulated by changing pH and ionic strength, which is convenient for selective immobilization and purification of proteins, enzymes, and antibodies.<sup>32</sup>

In this chapter, the recent advances in SPBs prepared by photo-emulsion polymerization will be reviewed. We will highlight the applications of SPBs in catalysis, protein immobilization, and preparation of multifunctional composite nanoparticles.

## 5.2 Generation of Metallic Nanoparticles in SPBs

For many chemical reactions metallic nanoparticles (diameters around 1–100 nm) are ideal catalysts with large specific area, long-term stability, and high catalytic activity. With decrease in particle size, the specific surface area increases sharply.<sup>44,45</sup> However, the nanosized catalyst particles become

easier to aggregate with reducing size. To improve their stability, many carriers have been developed. Among these carriers, SPBs have come onto the stage and have attracted the interest of many researchers.<sup>45,46</sup> Polyelectrolyte brushes can modify the surface properties of colloidal particles, and improve their stability significantly because of the electrostatic repulsion and steric hindrance among SPB particles.<sup>47</sup>

Due to the enhanced Donnan effect of the polyelectrolyte chains in SPBs, the counterion concentration inside SPBs ( $C_s$ ) is essentially the same level as the external counterion concentration ( $C_a$ ) in a high salt concentration (which is normally higher than  $0.1 \text{ mol L}^{-1}$ , as shown in Figure 5.3). However, as the salt concentration decreases,  $C_s$  becomes increasingly higher than  $C_a$  in solution. The difference between the counterion concentrations inside and outside SPBs can be further enlarged by increasing SPB surface grafting density or reducing the thickness of the brush layer.<sup>26,48</sup> This phenomenon exists in both positive and negative SPBs, which can be applied in different situations.<sup>28,49</sup>

Therefore, with the aid of the electrostatic force and Donnan effect,<sup>34,49–51</sup> SPBs can effectively absorb counterions even at low concentrations in solution, which make them ideal nanoreactors for *in-situ* metallic ion reduction and immobilization of metallic nanoparticles. In other words, SPBs can act as excellent stabilizing agents and carriers for both metallic ions and particles. Metallic particles loaded in SPBs are well dispersed in water, which

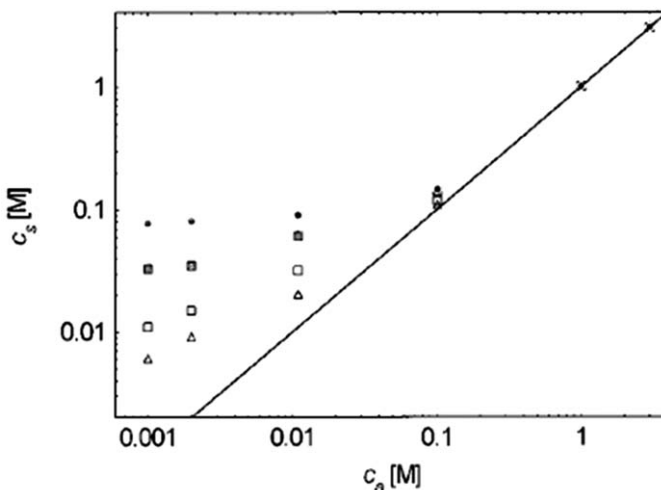


**Figure 5.3** Local ionic strength within the brush  $C_s$  as a function of the ionic strength of added KCl in bulk solution  $C_a$  in the case of an annealed spherical poly(acrylic acid) (PAA) brush. During the experiment  $10^{-3} \text{ M}$  NaOH was used to keep the pH value about 11. ( $\triangle$ ) core radius  $R = 66 \text{ nm}$ , PAA contour length  $L_c = 228 \text{ nm}$ , grafting density  $\sigma = 0.039 \text{ m}^{-2}$ ; ( $\square$ )  $R = 54 \text{ nm}$ ,  $L_c = 131 \text{ nm}$ ,  $\sigma = 0.025 \text{ m}^{-2}$ ; (+)  $R = 54 \text{ nm}$ ,  $L_c = 134 \text{ nm}$ ,  $\sigma = 0.050 \text{ m}^{-2}$ ; (●)  $R = 57 \text{ nm}$ ,  $L_c = 42 \text{ nm}$ ,  $\sigma = 0.038 \text{ m}^{-2}$ . Reproduced from ref. 26 with permission from American Chemical Society, Copyright 2000.

facilitates the catalysis of reactions in water.<sup>52</sup> Various kinds of metallic nanoparticles (such as Au,<sup>53</sup> Ag,<sup>30</sup> Pt,<sup>54,55</sup> Pd,<sup>56</sup> and Ni<sup>57</sup>) and metallic oxide nanoparticles (like TiO<sub>2</sub><sup>58</sup>) have been successfully prepared in SPBs.

### 5.2.1 Synthesis of Monometallic Nanoparticles

Ballauff *et al.*<sup>53</sup> prepared SPBs with PAEMH chains by photo-emulsion polymerization (Figure 5.4). AuCl<sub>4</sub><sup>-</sup> ions, as the counterions, were immobilized in SPBs and reduced *in situ* by sodium borohydride to Au nanoparticles. The Au nanoparticles were immobilized stably in SPBs and dispersed well in water. Similarly, Mei *et al.*<sup>54</sup> prepared Pt nanoparticles with a diameter around 2 nm by *in-situ* reduction of PtCl<sub>6</sub><sup>2-</sup> counterions inside SPBs.

Unlike the gold and platinum nanoparticles, the silver nanoparticles were generated in negatively charged SPBs. Lu *et al.*<sup>30</sup> synthesized Ag nanoparticles by *in-situ* reduction of the SPBs with PAA chains, where positively charged Ag<sup>+</sup> ions act as counterions (Figure 5.5). Firstly, PS cores were synthesized using convention emulsion polymerization. The photo initiator HMEM was coated onto the surface of the PS cores by polymerization. Then, the addition of a mixture of AgNO<sub>3</sub> and acrylate under UV radiation

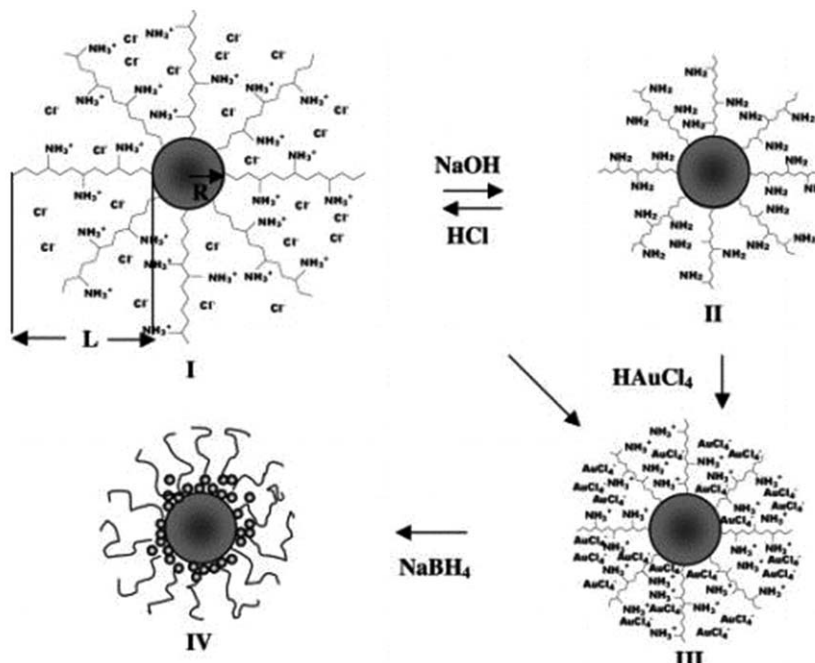


**Figure 5.4** Schematic representation of the formation of gold particles in cationic SPB layers.

Reproduced from ref. 53 with permission from John Wiley and Sons, Copyright © 2004 WILEY-VCH Verlag GmbH & Co. KGaA, Weinheim.

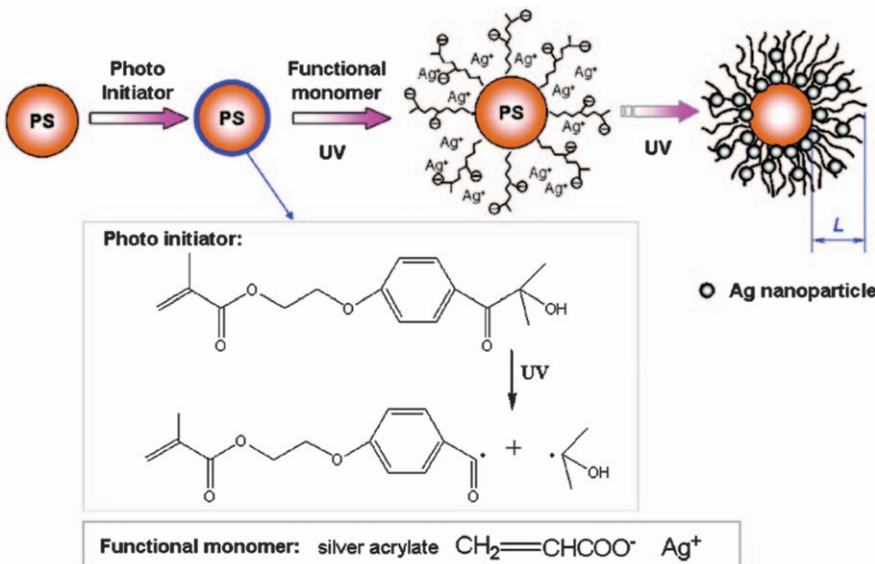


**Figure 5.5** Schematic representation of the preparation of silver nanoparticles *in situ* in PAA SPBs with polystyrene (PS) cores.  
Reproduced from ref. 30 with permission from American Chemical Society, Copyright 2007.

promoted the polymerization of silver acrylate on the surface of the PS cores and the reduction of Ag nanoparticles by UV. This method can synthesize both SPB and silver nanoparticles around 3 nm simultaneously without the addition of sodium borohydride.

Zhu *et al.* also prepared nickel nanoparticles in negatively charged PAA SPBs.<sup>57</sup>  $\text{Ni}^{2+}$  ions, as counterions, were absorbed on the SPB layer and reduced into nickel nanoparticles with an average diameter of 7.5 nm (Figure 5.6). Most importantly, they found that the nickel particle size and size distribution obtained can be controlled by changing reaction temperature.<sup>57</sup>

### 5.2.2 Synthesis of Bimetallic Nanoparticles

After successful generation of single metallic nanoparticles with narrow size distributions and outstanding stability in SPBs, bimetallic nanoparticles aroused the interest of researchers because bimetallic nanoparticles have better catalytic activity due to their synergistic effects.

Schrinner *et al.*<sup>59</sup> successfully prepared Au-Pt composite metallic nanoparticles loaded in SPBs, which proved to be better catalysts compared to either pure gold or platinum nanoparticles. As shown in Figure 5.7,  $\text{AuCl}_4^-$  replaced some of the chloride ions as counterions ions inside positively charged PAEMH SPBs. Then,  $\text{PtCl}_6^{2-}$  ions were added to the solution to replace the rest of the chloride ions inside the SPBs. The Au-Pt alloy nanoparticles were successfully prepared by addition of sodium borohydride.

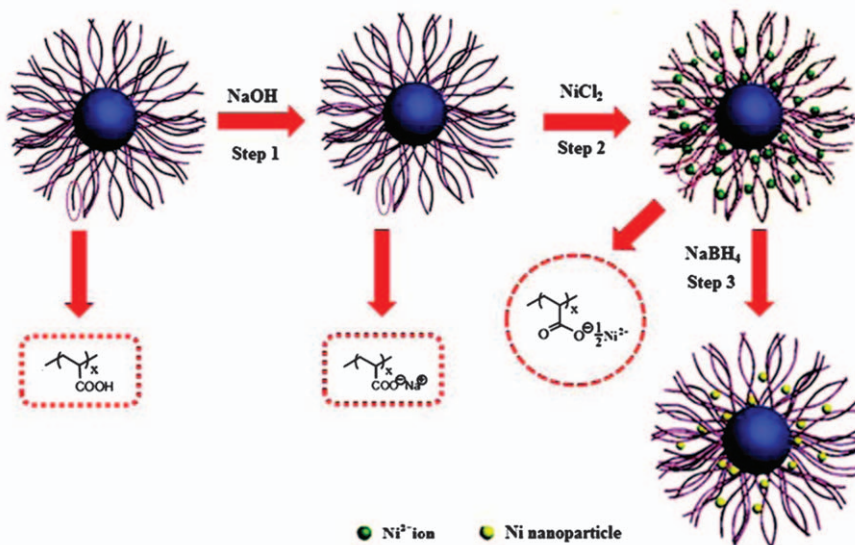


**Figure 5.6** Schematic representation of the formation of the Ni nanoparticles inside SPBs.

Reproduced from ref. 57 with permission from American Chemical Society, Copyright 2011.

The molar ratio between Au and Pt in the alloy could be tuned by the amount of  $\text{AuCl}_4^-$  and  $\text{PtCl}_6^{2-}$  added. The alloy structure of the metallic nanoparticles loaded into the SPBs was confirmed by EDX spectrum, where peaks of both Au and Pt could be identified, as shown in Figure 5.7.

Single crystals of platinum were obtained in SPBs after dissolving the gold, as reported by Schrinner *et al.*<sup>7</sup> The addition of NaCN solution to SPBs loaded with Au and Pt alloy under oxygen conditions facilitated the process of dissolving the gold, which further promoted the reorganization of platinum nanoparticles to form highly crystalline single crystals. The structure change from alloy to single crystal platinum could be observed by cryo-TEM.

Zhang *et al.* prepared Ag-Pd bimetallic nanoparticles in thermosensitive spherical brushes with crosslinked poly(*N*-isopropylacrylamide) (PNIPA) chains.<sup>60</sup> Aqueous PNIPA solutions show a reversible phase transition around 32 °C. PNIPA becomes hydrophobic above 32 °C and hydrophilic below 32 °C, which makes it sensitive to temperature. With increasing temperature, the shrunken brush layer forms a barrier to the diffusion of reactant and product, which can control the reaction rates. The bimetallic nanoparticles seemed mainly to locate in the inner layer of the SPB and their catalytic activity was sensitive to temperature, as observed by small angle X-ray scattering (SAXS).<sup>60</sup>

### 5.2.3 Catalytic Performance

To evaluate the catalytic activity of nanocatalysts immobilized in SPBs, the reduction of 4-nitrophenol to 4-aminophenol by borohydride ions in

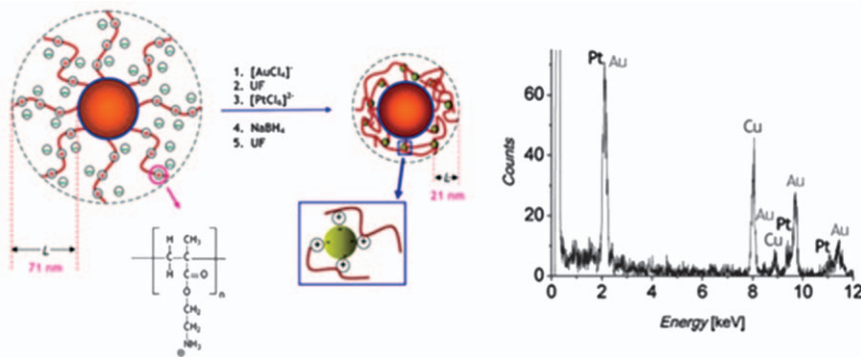


**Figure 5.7** (Left) SPB used as carriers for bimetallic Au–Pt nanoparticles (NPs). Linear cationic polyelectrolytes of poly(2-aminoethyl methacrylate) are densely grafted onto a solid polystyrene (PS) core with a radius of 45 nm. (Right) EDX spectrum of one single Au–Pt-NP on the surface of the carrier particle. The copper peaks are from the copper grid used as support in the measurements.

Reproduced from ref. 59 with permission from John Wiley and Sons, Copyright © 2008 WILEY-VCH Verlag GmbH & Co. KGaA, Weinheim.

aqueous solution is frequently used as a model reaction because of its facile and mild reaction conditions, convenient detection, and dynamic monitoring (Figure 5.8).<sup>61–64</sup>

The catalytic performance of metallic nanoparticles immobilized in SPBs can be studied quantitatively by the reduction of 4-nitrophenol to 4-aminophenol in water. Taking nickel nanoparticles as an example, there is almost no change in the UV characteristic absorption peak of 4-nitrophenol at 400 nm without the catalyst.<sup>57</sup> When SPB with nickel nanoparticles were added, the peak at 400 nm began to reduce immediately, and the peak of the product 4-aminophenol at 300 nm enhanced continuously.<sup>57</sup> The decay of intensity around 400 nm represents the consumption amount of 4-nitrophenol. The reaction rate constant was obtained by fitting quasi-first-order reaction kinetics, which increased with temperature. The activation energy of the catalytic reaction was estimated to be 41.7 kJ mol<sup>-1</sup>.<sup>57</sup>

Lu *et al.* summarized the catalytic activity of different metallic nanoparticles (Table 5.1).<sup>52</sup> The rate constants for the reduction of 4-nitrophenol to 4-aminophenol by borohydride ions reflect the catalytic performance of different nanoparticles. It can be seen from Table 5.1 that among the same kind of metallic nanoparticles, those generated and immobilized in SPBs show higher catalytic performance.<sup>30</sup>

### 5.2.4 Preparation of Metallic Compound Nanoparticles

The preparation of metallic compound nanoparticles in SPBs is also quite interesting for scientists. Lu *et al.* reported the synthesis of TiO<sub>2</sub> nanoparticles in SPBs.<sup>58</sup> XRD spectrum could confirm the highly crystalline

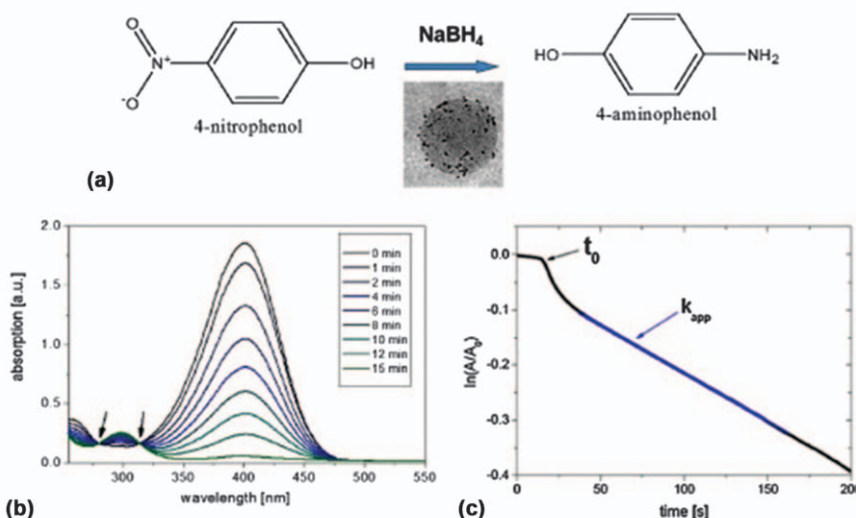


**Figure 5.8** Reduction of 4-nitrophenol by borohydride ions as a model reaction for testing the catalytic activity of nanoparticles. (a) Scheme of the reaction. (b) Absorption spectrum of 4-nitrophenol by sodium borohydride. The main peak at 400 nm (nitrophenolate ions) is decreasing with reaction time, whereas a second peak at 300 nm is slowly increasing. The two isosbestic points are visible at 280 and 314 nm, marked with arrows. (c) Typical time dependence of the absorption of 4-nitrophenolate ions at 400 nm. The blue portion of the line displays the linear section referring to the stationary state of the reaction. The rate constant  $k_{app}$  is taken from this portion of the plot. The induction period  $t_0$  is marked with the black arrow. Reproduced from ref. 64 with permission from American Chemical Society, Copyright 2010.

**Table 5.1** Catalytic activity of metal nanoparticles immobilized in different system. Reproduced from ref. 30 with permission from American Chemical Society, Copyright 2007.

Carrier	Nano-particles	Diameter/nm	$k/(s^{-1} m^{-2} L)$
Anionic SPB	Ag	$3.0 \pm 1.2$	$3.80 \times 10^{-2}$
Cationic SPB	Pt	$2.1 \pm 0.4$	0.55
Cationic SPB	Pd	$2.4 \pm 0.5$	1.50
Cationic SPB	Au	$1.25 \pm 0.25$	0.31
PS-NIPA core-shell microgel	Ag	$8.5 \pm 1.5$	$5.02 \times 10^{-2}$
Highly branched polymer brush	Ag	$7.5 \pm 2$	$7.27 \times 10^{-2}$
PVA polymer	Ag	$\sim 25$	$3.28 \times 10^{-7}$
PVA/PS-PEGMA composite hydrogel	Ag	$35 \pm 5$	$7.80 \times 10^{-5}$
PVA hydrogel	Ag	$45 \pm 5$	$7.31 \times 10^{-5}$

structure of TiO<sub>2</sub> loaded into SPBs. Zhu *et al.*<sup>65</sup> successfully synthesized magnetic nanoparticles with controllable size by using SPBs as nanoreactors. The obtained SPBs with magnetic response (MSPBs), containing magnetic

nanoparticles in the brush layer, showed excellent stability, and their behaviors under the effect of pH and ionic strength were almost unchanged after the introduction of magnetic nanoparticles.

Chen *et al.*<sup>40</sup> successfully introduced magnetic nanoparticles into PS cores to synthesize MSPBs. Firstly, nanosized magnetic particles modified with oleic acid on the surface were prepared by co-precipitation. Then they were mixed with styrene to synthesize polystyrene nanoparticles by mini-emulsion polymerization under continuous ultrasonication, and finally MSPBs were prepared by photo-emulsion polymerization. The obtained MSPBs were *ca.* 140 nm, and magnetic nanoparticles are successfully embedded inside the PS core with relatively high magnetic content. MSPBs can be collected by magnets and redispersed in the aqueous solution by slight shaking after removing the external magnetic field (Figure 5.9). MSPBs provided a novel method to recover SPBs and to deliver drugs guided by a magnetic field.

Wu *et al.*<sup>66</sup> prepared platinum nanoparticles by *in-situ* reduction using MSPBs as nanoreactors (Figure 5.10). The platinum nanocatalyst with magnetic response was obtained by using MSPBs as the carrier. The embedded ferric oxide magnetic nanoparticles were prepared by co-precipitation with a size of *ca.* 10 nm, and cationic poly(methacryloxyethyltrimethyl ammonium chloride) (PMATAC) SPBs were prepared by mini-emulsion polymerization and photo-emulsion polymerization. The obtained platinum nanoparticles

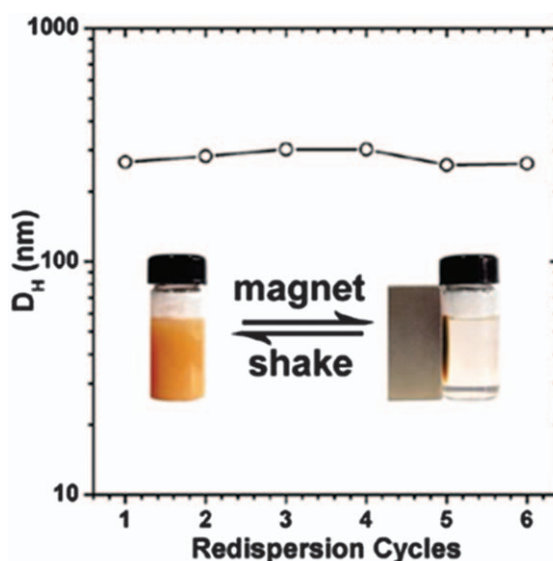


**Figure 5.9** Size of the magnetic SPBs (MSPBs) after several cycles of aggregation by magnet and redispersion as determined by dynamic light scattering (DLS). Inset photos show the aggregation and redispersion of MSPBs. Reproduced from ref. 40 with permission from American Chemical Society, Copyright 2011.

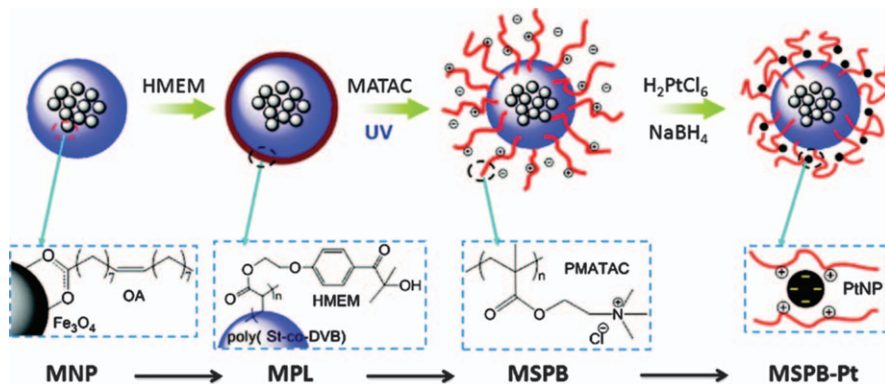


**Figure 5.10** Schematic representation of magnetically recoverable Pt nanocatalysts immobilized on magnetic spherical polyelectrolyte brushes (MSPBs). Reproduced from ref. 66 with permission from American Chemical Society, Copyright 2012.

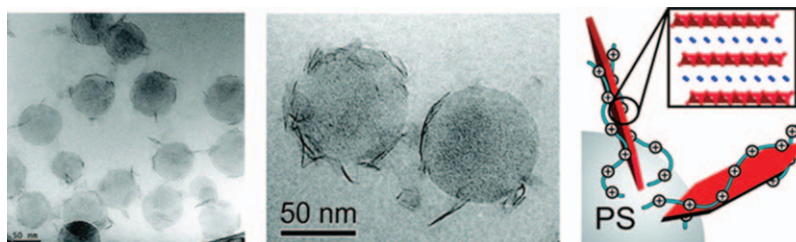


**Figure 5.11** (Left) (Middle) Cryo-TEM of the composite system SPB- $\text{MnO}_2$ . (Right) Schematic representation of the stabilization of the layered birnessite structure by the cationic PTMAEMC chains of SPBs. Reproduced from ref. 67 with permission from American Chemical Society, Copyright 2010.

not only showed excellent catalytic performance, but also could be recovered by controlling the external magnetic field.<sup>66</sup>

Ultrathin birnessite particles were also prepared in SPBs by a one-step method (Figure 5.11).<sup>67</sup> Cationic SPBs were mixed with  $\text{MnO}_4^-$  ions to produce birnessite platelets, which was confirmed on the cryo-TEM graph. These composite particles exhibited excellent colloidal stability and catalytic activity in aqueous systems.

Liu *et al.*<sup>68</sup> prepared fluorescent SPBs (FSPBs) (Figure 5.12), in which fluorescent quantum dots (QDs) were introduced onto the PS core of SPBs by hybrid emulsion polymerization.<sup>69</sup> Like QDs the FSPBs can emit fluorescence under UV light.<sup>70,71</sup> Fluorescence with different colors can be emitted under UV radiation by changing the size of the QDs in FSPBs. Cang *et al.* prepared *in-situ* water-dispersible quantum dots (QDs) including CdS, ZnS, and CdTe in PAA SPBs (Figure 5.13).<sup>41,72</sup> The fluorescent color of QDs depends on their size, which can be tuned by adjusting experimental conditions. The shrinkage

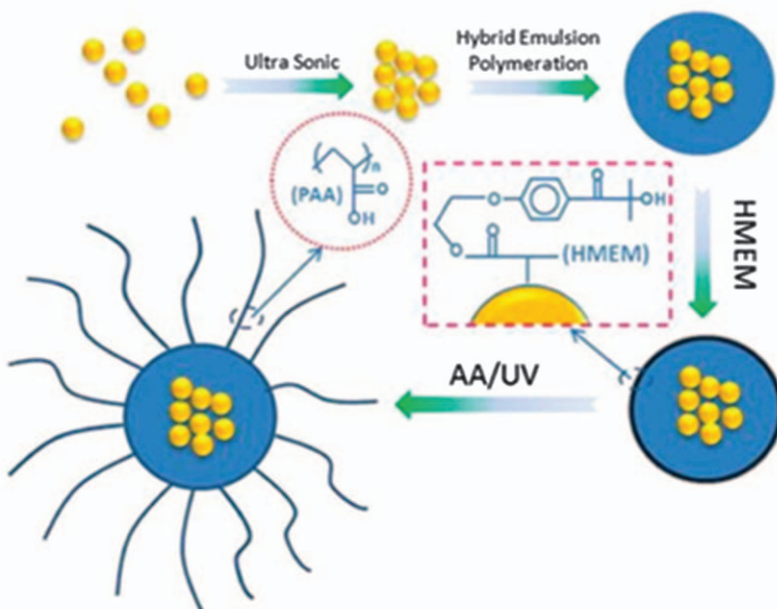


**Figure 5.12** Schematic representation of the synthetic procedure for fluorescent SPBs (FSPBs).

Reproduced from ref. 68 with permission from American Chemical Society, Copyright 2014.

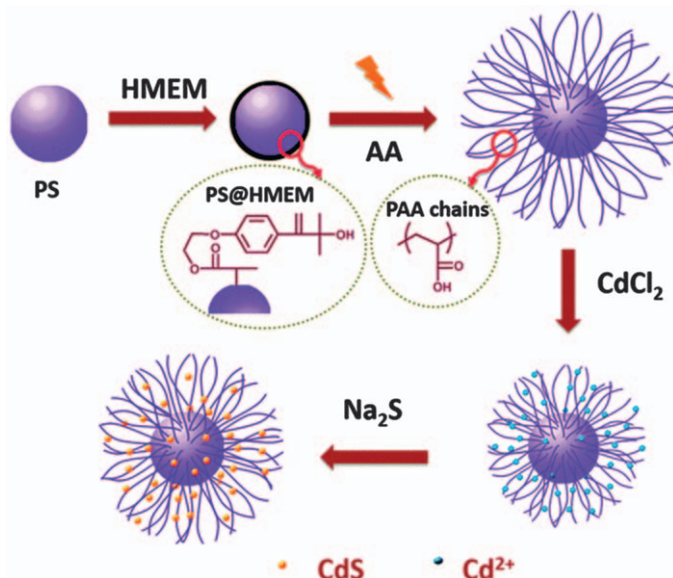


**Figure 5.13** Preparation of SPBs immobilized with CdS nanoparticles.

Reproduced from ref. 72 with permission from The Royal Society of Chemistry.

of SPB layers at low pH led to fluorescence quenching of packed QDs. When SPBs are swelled at high pH, the fluorescence was recovered. This process could be repeated many times without loss of the fluorescent properties.<sup>41,72</sup> These FSPBs should have broad applications as tracers in fields such as medical diagnosis, drug delivery, and oil exploration.

### 5.3 Preparation of Organic–Inorganic Hybrid Nanoparticles Tempered by SPBs

Organic–inorganic hybrid nanomaterials are homogeneous multiphase materials in which at least one phase, either organic or inorganic, is on the nanoscale, and the nanophase is normally combined with other phases by strong (chemical, ionic, or coordination bonds) or weak interactions (such as hydrogen bonding and van der Waals forces). They have shown interesting properties and great potential for applications in many fields. The sol–gel method is most commonly used to synthesize organic–inorganic hybrid nanomaterials, in which metal organic alkoxide or siloxane as precursor in a composite system is dissolved in water or organic solvent, and the nanoparticle network of silica or metal oxide is formed by hydrolysis or polycondensation; the polymer monomer is introduced as an organic constituent to form organic–inorganic hybrid nanomaterials by *in-situ* polymerization. The advantage of this method is that it can be processed under mild conditions, and the organic and inorganic phases are uniformly dispersed.<sup>73–78</sup>

Recently, organic–inorganic composite core–shell nanoparticles with organic nuclear and inorganic shell or *vice versa* have attracted much attention.<sup>79–82</sup> They have many advantages, such as high stability and large specific surface area, as well as ease of introducing surface charge and magnetic or specific optical properties, and are ideal candidates for applications in many fields such as drug delivery, catalysis, coating, tissue engineering, and biomaterials.<sup>79–82</sup> Among them, the core–shell silica nanoparticles demonstrate outstanding performance, such as low toxicity, high mechanical strength, and high thermal stability, and have been used widely in the fields of coating, medicine, catalysis, *etc.*<sup>83,84</sup>

Hollow nanoparticles are particularly interesting due to their high loading capacity, low density, and large specific area,<sup>85–89</sup> which make them especially useful as carriers and fillers.<sup>90</sup> Among them, hollow silica particles are relatively cheap, easy to prepare, with high loading capacities due to their cavity volume, large specific surface area, and abundant silicon hydroxyl groups.<sup>90–98</sup> Hollow silica nanoparticles are usually prepared by using polymeric templates which can be removed by either high temperature calcination or dissolution by adding specific solvent.<sup>79,99,100</sup> The structure of the obtained core–shell silica or hollow nanoparticles depends on the category of the template core and the formation method of the silica shell. The template is most commonly composed of polymer colloidal particles, polymeric microgels, and micelles.<sup>83,84,101–103</sup> The sol–gel method is always employed to generate the silica layers on the templates. Due to the Donnan effect, the

ammonium ion can be enriched in SPBs, which acts as the catalyst for sol-gel reactions to prepare silica layers. In this way, SPBs have been successfully used as templates to prepare core-shell silica and hollow silica particles.<sup>104</sup>

Huang *et al.*<sup>104</sup> reported the preparation of core-shell polystyrene-silica and hollow silica nanoparticles templated by SPBs. The carboxyl groups in PAA SPBs were extensively ionized by ammonium, which acted as the catalyst and the nucleation centre for the precipitation of silica precursor to form silica. The silica shell was generated within the brush layer of the template SPB. Finally, the silica hollow nanoparticles were obtained by removing the PS cores with organic solvent (Figure 5.14). These hollow silica nanoparticles worked very well for controlled drug delivery.<sup>105</sup>

Core-shell-corona silica/polyelectrolyte hybrid nanoparticles with narrow size distributions were prepared by Han *et al.* using SPBs with a shell of densely grafted long PAA chains as templates. Hollow silica nanoparticles with a PAA corona were obtained after dissolving the PS core in CHCl<sub>3</sub> (Figure 5.15).<sup>106</sup> As observed by small-angle X-ray scattering (SAXS), the silica shell showed a unique inner-loose outer-dense structure, the thickness of which was pH sensitive. These particles can be pH-triggered drug delivery carriers.

Han *et al.*<sup>107</sup> found that the density and thickness of generated silica layers in SPBs were tunable by crosslinking PAA brushes using *N,N'*-methylenebisacrylamide (BIS) with controlled crosslinking density in the

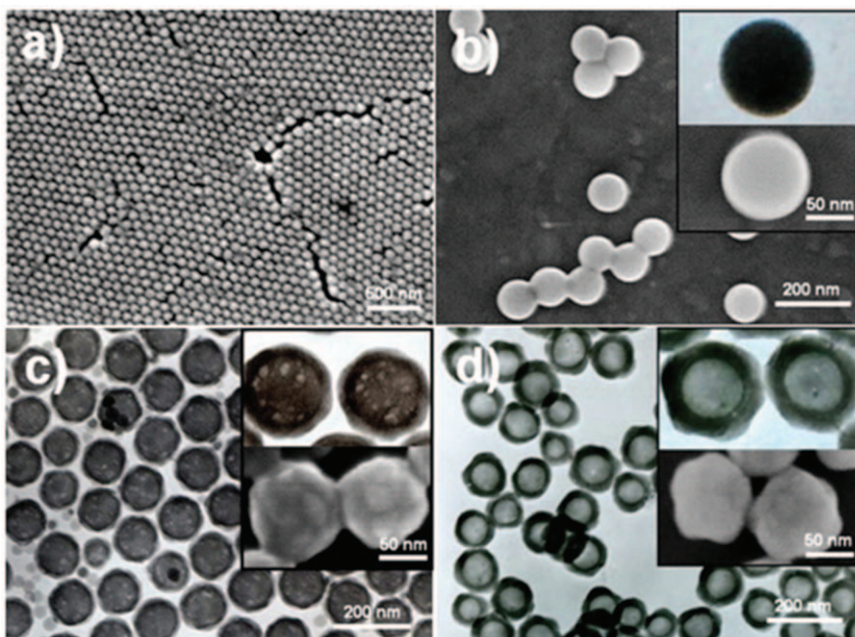


**Figure 5.14** TEM images of hollow microspheres.

Reproduced from ref. 104 with permission from Elsevier, Copyright 2012.

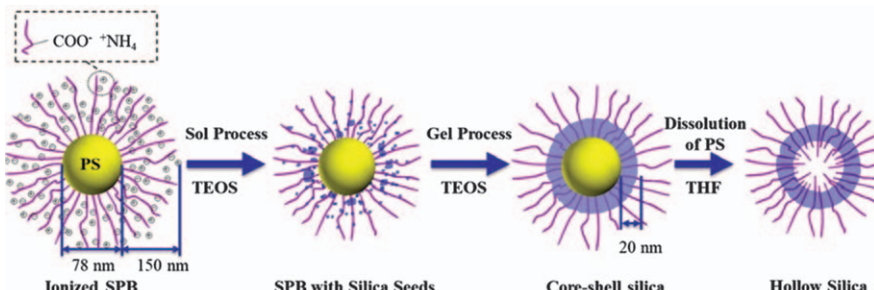


**Figure 5.15** Schematic illustration of the preparation of hollow silica-polyelectrolyte composite nanoparticles using SPBs as templates.  
Reproduced from ref. 106 with permission from American Chemical Society, Copyright 2017.

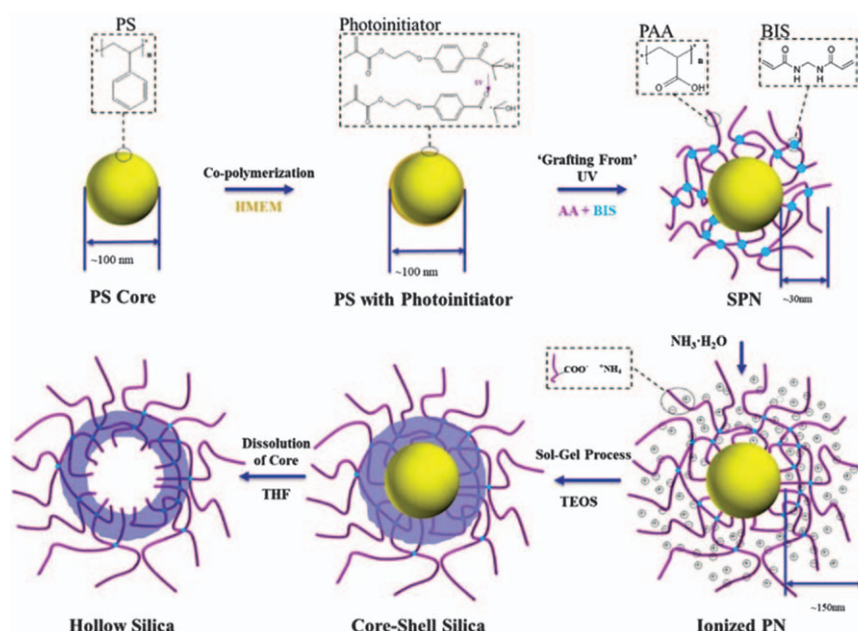


**Figure 5.16** Scheme for the preparation of hollow silica nanoparticles with templates of crosslinked SPBs.  
Reproduced from ref. 107 with permission from the Royal Society of Chemistry.

templates. Thus, hollow silica nanoparticles with designable wall density and wall thickness can be prepared by removing the PS core *via* solvent dissolution (Figure 5.16). The nucleation of silica occurred both inside the PAA SPBs and in the external solution. The diffusion of the initial nucleation silica particles in the external solution to the brush layer was hindered by the PAA network, which resulted in a looser silica layer by using crosslinked

SPBs as templates. This finding provides a novel way to prepare controllable hollow silica nanoparticles.<sup>109</sup>

Compared to other templates to prepare hollow silica nanoparticles, the advantages of SPBs are as follows: (1) the size and size distribution are easily controlled by tuning the size and size distribution of the SPBs; (2) pH and ionic strength response can be introduced by the preserved polyelectrolyte chains; (3) the wall density and thickness are controllable by crosslinking polyelectrolyte brushes.

## 5.4 Controlled Protein Immobilization in SPBs

Proteins account for *ca.* 45% of the dry weight of human body.<sup>108,109</sup> As complex organic macromolecules with rich biological contents, complex functions, and various types, proteins are the basis of living organisms and play an important role in the activities of life. In recent years, there has been significant demand for the separation and extraction of proteins for antigen and vaccine production,<sup>110</sup> food science,<sup>111</sup> drug metabolism,<sup>112</sup> and tissue engineering.<sup>113</sup>

The effective separation and purification of proteins usually depend on differences in biological activity, charge properties, affinity binding forces, hydrophobic degree, and molecular weights of proteins.<sup>114,115</sup> A variety of methods, such as high performance liquid chromatography, electrophoresis, dialysis, precipitation, and mass spectrometry have been developed for protein separation.<sup>116–118</sup> However, the application of these traditional methods is still limited because they usually require a relatively long operation time and pretreatment, as well as having low separation efficiencies and obtain a minimal amount of the proteins. Because of this, a more efficient method for the separation and purification of proteins is always highly anticipated.

The charge characteristics of polyelectrolytes<sup>119–126</sup> provide a new approach for protein purification by phase separation. This separation technique has many benefits, such as good selectivity, high purification capacity, high resolution, high speed, and simplicity with respect to instrumentation.<sup>127,128</sup> Compared to other traditional protein separation methods, phase separation by polyelectrolytes can offer selectivity without damage to protein redissolution and activity.<sup>129–131</sup> In this section, recent achievements of SPBs in the controlled immobilization and separation of proteins are summarized. Considering the rapid development of SPBs and their great application prospects, much more opportunity and potential exist in this field.

### 5.4.1 Interactions Between Protein and SPB

Interactions between proteins and polyelectrolytes are a common phenomenon in nature.<sup>33,132</sup> In principle, these interactions can be versatile and tunable because of the changeable charge density and charge distribution. Hence, many parameters can be used to modulate the interactions between proteins and polyelectrolytes in order to achieve controlled immobilization of proteins and thus the efficient purification and separation of proteins.

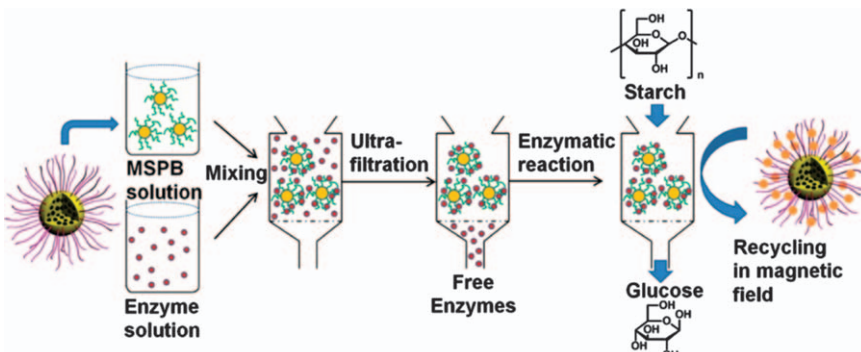


**Figure 5.17** The schematic representation of enzyme immobilization in SPBs and their operation as a biocatalyst.

Reproduced from ref. 131 with permission from American Chemical Society, Copyright 2014.

In general, the biological activity of proteins immobilized and separated by polyelectrolyte adsorption will not be changed.<sup>127,129</sup> For example, SPBs can be used as outstanding bioreactors after immobilization of enzymes (Figure 5.17).<sup>133</sup> Based on the selective adsorption of proteins by tuning the interactions between proteins and polyelectrolytes, this method should have many potential applications in protein separation and purification, as well as controlled release of proteins and biological sensors.<sup>133–135</sup>

The interactions between proteins and polyelectrolytes have been widely studied, and most of the literature suggests that proteins have charge patches because their local charge density can be significantly different from or completely opposite to the total net charge.<sup>136,137</sup> The electrostatic properties of polyelectrolyte–protein interactions are affected by the solution pH, polyelectrolyte charge density, and ionic strength.<sup>131</sup> The separation of proteins is mainly achieved through the modulation of electrostatic interactions between proteins and polyelectrolytes.

Protein adsorption on surfaces has been a key research topic in the field of biotechnology and biological material.<sup>138,139</sup> The adsorption dynamics and driving force of protein adsorption have laid a foundation for its application in many fields.<sup>140–143</sup> In recent years, quite a few articles based on protein adsorption by polyelectrolyte brush modified nanoparticles have been published. This research can help to semi-quantitatively predict the trend of protein adsorption in brushes, the core problem being how to analyze the driving force of adsorption and the theoretical model. The ultimate goal of this research is to estimate the change in composition of proteins adsorbed in brushes.

Chen and co-workers prepared gold nanoparticles modified by charged polymer brushes,<sup>144</sup> and the chemical structure of the polymer used to modify the gold nanoparticles is shown in Figure 5.18. The modified gold nanoparticles adsorbed bovine serum albumin (BSA) and  $\beta$ -lactoglobulin (BLG) selectively, as shown in Figure 5.19.<sup>144</sup> BLG bound to the modified

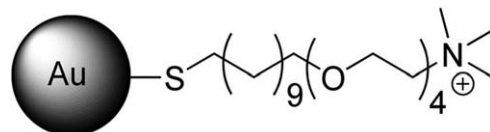


**Figure 5.18** Chemical structure of the polymers used to modify gold nanoparticles. Reproduced from ref. 144 with permission from American Chemical Society, Copyright 2011.

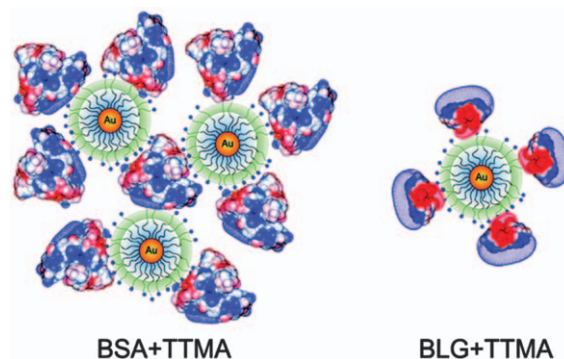


**Figure 5.19** The schematic representation of interactions between the modified gold nanoparticles and BSA/BLG. Reproduced from ref. 144 with permission from American Chemical Society, Copyright 2011.

cationic nanoparticle at pH well below the isoelectric point (pI) of the protein. The mechanism of binding was complex, with higher-order aggregation likely arising from charge neutralization. Chen *et al.* were able to show that the modified gold nanoparticles could be used for the separation and purification of the proteins, biological detection within the human body, *in vitro* biological sensors, and other applications.

Further exploration was reported by Chen *et al.* on optimizing the selective recognition of protein isoforms through tuning of nanoparticle hydrophobicity.<sup>145</sup> In this work functional gold nanoparticles with various end groups with different hydrophobicities were prepared in order to absorb two different  $\beta$ -lactoglobulin protein isoforms (BLGA and BLGB) (Figure 5.20). Through the experiments they found that the hydrophobicity of ligands could be used to increase affinity and selectivity of binding between  $\beta$ -lactoglobulin protein isoforms and the modified cationic gold nanoparticles. They demonstrated that both hydrophobic and electrostatic interactions can be employed to adjust the protein-SPB affinity. By using BLGA/BLGB protein isoforms in the test, they observed that thermodynamic parameters for complexation between the modified nanoparticles and BLGA/BLGB mainly depend on the relative hydrophobicities of the ligands of the prepared nanoparticles. The maximum binding affinity was achieved through proper

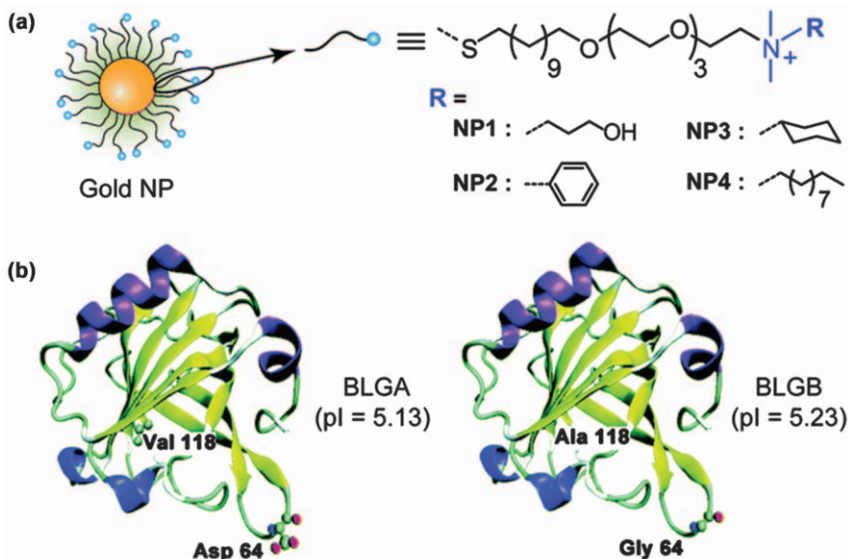


**Figure 5.20** Chemical structures of cationic gold nanoparticles with different hydrophobicities.

Reproduced from ref. 145 with permission from the Royal Society of Chemistry.

balance of electrostatics and hydrophobicity.<sup>145</sup> The ability of functionalized SPBs to achieve selective binding with subtly different proteins is the starting point for engineering particles required for applications such as biosensing.

The mechanism of protein adsorption and the energy change not only included the contribution of enthalpy (electrostatic interactions, hydrophobic association, Coulomb force, hydrogen bonding), but also that of entropy released by counterions and water molecules. The driving force for protein absorption is the counterions in the brush layer being replaced by charge clusters in the protein. A lot of counterions gathered in the brush layer makes the local charge of polyelectrolyte brushes neutral, and the amount of the counterions is equal to the charge number of the brushes. Due to the anisotropy of the charge within the protein, a protein with zero net charge can also be adsorbed by polyelectrolyte brushes. Welsch and co-workers<sup>146</sup> found that the adsorption of lysozyme by negatively charged SPBs with P(NIPA-*co*-AA) chains happened at a solution pH greater than the pI of the protein. Based on their experiments they put forward two hypotheses, one being that acidic protein contains a positively charged cluster, the other that there is so-called “charge adjustment”. Because of the surface of the anionic polyelectrolyte brush it has a potential field. When the pH of the system is greater than the pI of the protein, the net charge of the protein is negative, and at the same time, it has ability to adjust the charge of the protein. The anisotropy of the protein charge quantitatively explained why the protein combined with the anionic polyelectrolyte when pH > pI.

Kusomo and co-workers<sup>147</sup> prepared modified gold particles by grafting a poly(*N,N'*-dimethylaminoethyl methacrylate) (PDAEMA) brush on the surface. A large number of BSA molecules were adsorbed in these cationic PDSEMA SPBs, each occupying about 40 nm of the polyelectrolyte chain. They found that the amount of protein adsorbed increased significantly with grafting density or PDSAEMA chain length in SPBs. These results indicate that even if the net charge of BSA is positive at a pH below its pI (4.9), the proteins still have negative charge clusters and can combine with the cationic polyelectrolyte brushes. There exist many regulating methods to achieve optimum electrostatic interaction in the protein and SPB complex system.

#### 5.4.2 Characterization Methods for Protein Immobilization on SPBs

Several characterization methods have been employed to observe the adsorption of proteins and to detect the interaction between proteins and SPBs.

##### 5.4.2.1 Turbidimetric Titration

The earliest study of the association between proteins and polyelectrolytes by turbidimetry can be traced back to 1980, when Kokufuta *et al.* titrated protein into a polyelectrolyte solution and determined the stoichiometric ratio of the complex formed in aqueous solution by observing the turbidity of the system.<sup>148</sup> Turbidimetric titration can be used to determine the binding window of proteins to both cationic and anionic SPBs upon changing pH or ionic strength, as shown in Figure 5.21a and b.<sup>130,149,150</sup>

##### 5.4.2.2 Dynamic Light Scattering (DLS)

The hydrodynamic size and size distribution of nanoparticles including proteins, SPBs, and their complexes can be determined by DLS. By monitoring the change in size and size distribution during protein adsorption in SPBs, information on interaction between proteins and SPBs can be obtained. As shown in Figure 5.21c and d, DLS results are highly consistent with those of turbidity titration.<sup>130</sup>

In the pH range where interaction among SPB-protein complexes does not take place, the size of the SPB-protein complex is basically the same as that of the blank SPB. With the enhancement of interaction, aggregates were formed between the SPB-protein complexes and the particle size of the complexes increases rapidly. However, the particle size of the complexes is significantly reduced when the aggregates are decomposed with further pH changes.<sup>130,149,150</sup> Unfortunately, DLS cannot distinguish the small change in size of SPBs adsorbing proteins in the dynamic equilibrium region and see the distribution of proteins in SPBs.

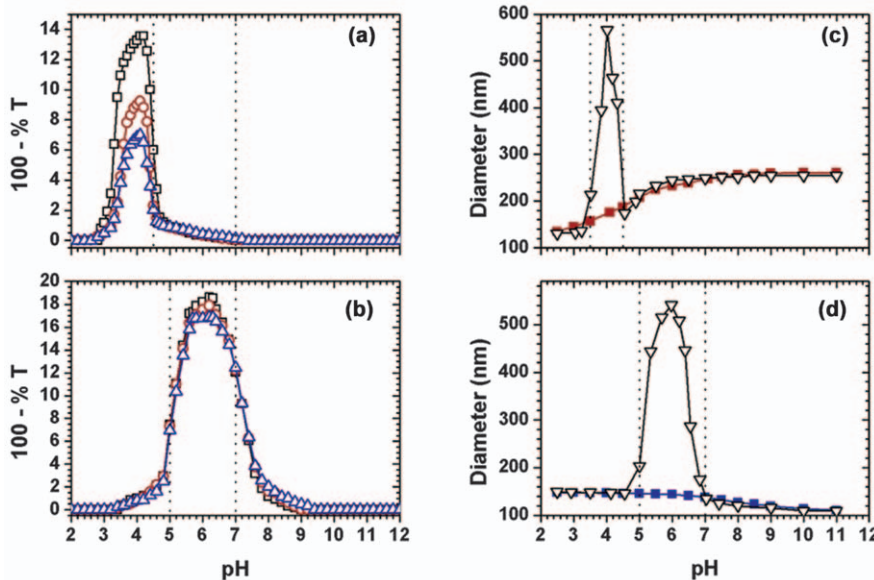


**Figure 5.21** (a) Turbidimetric titration for a mixture of BSA and PAA SPBs as a function of pH at various ionic strengths. (b) Turbidimetric titration for a mixture of BSA and PAEMH SPBs as a function of pH at various ionic strengths. Symbols denote: (□) 1 mM, (○) 5 mM, and (△) 10 mM. (c) Size of BSA and PAA SPBs complexes and free PAA SPBs as a function of pH in 1 mM NaCl solutions. (d) Size of BSA and PAEMH SPBs complexes and free PAEMH SPBs as a function of pH in 1 mM NaCl solutions. Symbols denote: (▽) BSA and SPBs complexes, (■) blank SPB<sub>PAA</sub>, (■) blank SPB<sub>PAEMH</sub>. BSA and SPB concentrations are 0.020 and 0.004 mg mL<sup>-1</sup>, respectively.

Reproduced from ref. 130 with permission from the Royal Society of Chemistry.

#### 5.4.2.3 Isothermal Titration Calorimetry (ITC)

ITC can quantitatively detect the thermodynamic change in the process of protein-SPB association, thus revealing the nature of the interaction.<sup>151</sup> By evaluating the binding isotherms of proteins and SPBs obtained by ITC, the structure and morphology of the complex can be analyzed. The original thermodynamic curves are drawn from the enthalpy change ( $\Delta H$ ) and the protein polyelectrolyte stoichiometry. The enthalpy changes ( $\Delta H$ ) whenever the ligand is injected into the matrix solution, and its change reflects the ability of proteins to bind with polyelectrolytes.<sup>152</sup> The binding constant ( $K_b$ ) and the number of proteins bound to each polyelectrolyte chain can be obtained by fitting the model.<sup>153</sup> The entropy change ( $\Delta S$ ) can be calculated from  $\Delta H$  and the free energy change ( $\Delta G$ ). By analyzing these thermodynamic parameters, we can estimate the driving forces of the protein-polyelectrolyte interaction process.<sup>130,131,149,150,154,155</sup>

As shown in Figure 5.22, an isothermal curve was obtained from ITC, corresponding to the critical point between the aggregation and releasing

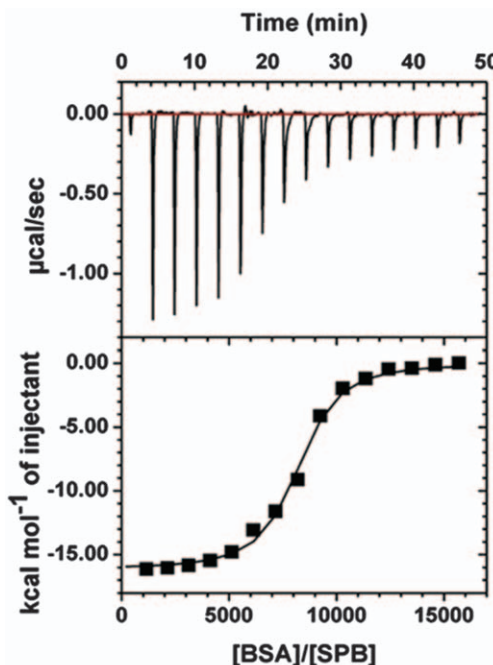


**Figure 5.22** Isothermal calorimetry titration data for the binding of BSA onto cationic SPBs in MES buffer at pH 7.1 and ionic strength of 5 mM. The upper panel shows the raw data of the ITC. The integrated heats of each injection (solid square) and one-site binding fitting (solid line) are shown in the lower panel.

Reproduced from ref. 150 with permission from American Chemical Society, Copyright 2013.

region. The binding heat is negative, indicating the complexation between BSA and cationic SPBs is exothermic, which corresponds to a dominant electrostatic attraction between the oppositely charged surfaces. The driving force for the protein adsorption is, therefore, enthalpic in origin.<sup>150</sup>

#### 5.4.2.4 Small Angle X-ray Scattering (SAXS)

When very fine X-rays pass through a material with nanosized electron inhomogeneity, X-ray scattering occurs at very small angle ( $3 \sim 5^\circ$ ) to the incident beam. This phenomenon is called small angle X-ray scattering (SAXS). SAXS is particularly sensitive and occurs in materials with nanoscale non-uniformity of electron density. This feature makes it an important tool for the study of SPBs around 100 nm. Qualitative and quantitative information such as size, shape, and internal structure can be obtained.<sup>27</sup>

Because of the strong SAXS signal and contrast in water, SAXS is especially suitable for characterization of protein adsorption in SPBs, which can

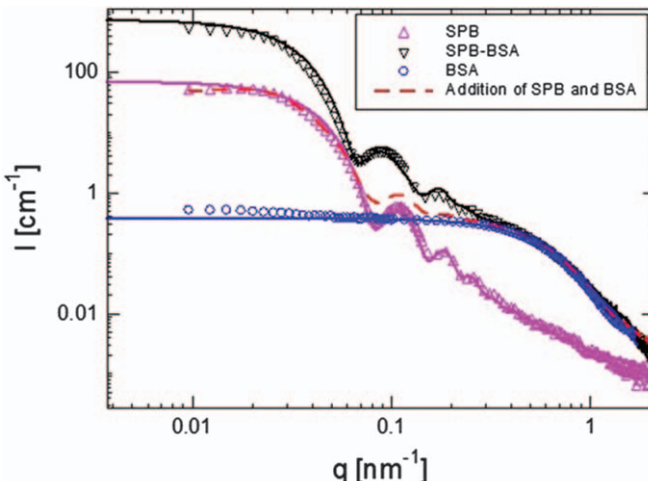


**Figure 5.23** SAXS curves of PAA SPBs loaded (SPB-BSA) and unloaded with BSA (pH = 6.1, ionic strength  $I = 7 \text{ mmol L}^{-1}$ , SPBs concentration 1 wt%, BSA concentration  $10 \text{ g L}^{-1}$ ).

Reproduced from ref. 50 with permission from Springer, Copyright 2015.

determine the interactions between proteins and SPBs as well as their position and distribution.<sup>28,50,156–159</sup>

When proteins are adsorbed in the brush layer, the electron density increases, and the overall scattering intensity will be affected.<sup>50</sup> As shown in Figure 5.23, The dashed line is the mathematical summation of the scattering intensity of PAA SPBs and BSA. In the small  $q$  region ( $q < 0.3 \text{ nm}^{-1}$ ), the mathematical summation of the scattering intensity of SPB and BSA is much lower than scattering intensity of BSA after adsorption of BSA, but it is almost the same in a large  $q$  range ( $q > 0.3 \text{ nm}^{-1}$ ). In the small  $q$  range, the enhancement of scattering intensity reflects that BSA enters the brush layer, and the electron density in the brush layer increases.

Rosenfeldt *et al.*<sup>156</sup> reported the SAXS scattering curves before and after bovine pancreatic ribonuclease A (RNase A) was absorbed on poly(styrene sulfonic acid) (PSS) SPBs (Figure 5.24). After protein adsorption, the scattering intensity of SPBs increased obviously, and the position of the first maximum moved towards smaller  $q$ , indicating that the electron density increased and the brush layer swelled significantly when proteins entered the brush layer. It shows that RNase A can enter the deep layer of PSS SPBs and disperse in the whole brush layer. A five-layer model was employed to describe the electron density distribution in the brush layer, which proved to be suitable to describe the change in electron density of the SPBs.<sup>156</sup>

Henzler *et al.*<sup>158</sup> observed the SAXS scattering curves before and after adsorption of bovine hemoglobin (BHb) in PSS SPBs (Figure 5.25) and confirmed that SPBs with adsorbed proteins contributed most of the scattering intensity in the small  $q$  range, while the scattering intensity of

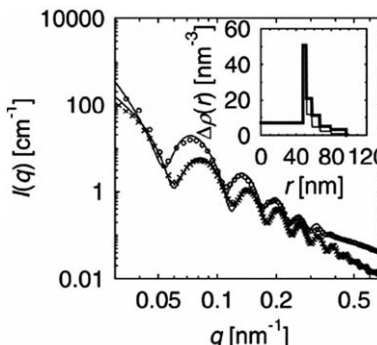


**Figure 5.24** Scattering intensity of PSS brush before and after RNase A adsorption ( $408 \text{ mg g}^{-1}$  SPB); the corresponding distribution of excess electron density (Inset).

Reproduced from ref. 156, <http://dx.doi.org/10.1103/PhysRevE.70.061403>, with permission from American Physical Society, Copyright 2004.

proteins played a major role in the large  $q$  range. The excess electron density profile (Figure 5.25b) shows that the proteins were distributed in the brush layer and mainly in the region near the core.

Recently, the dynamics of BSA adsorption onto cationic SPBs with PAEMH chains was observed by time-resolved SAXS.<sup>28</sup> The SAXS data were recorded at an interval of 0.05 s after the addition of BSA into SPBs with the help of a stopped-flow device, and the scattering intensity curves at different mixing times were obtained (Figure 5.26). The scattering intensity increased significantly right after the addition of BSA, and the scattering intensity at 0.01 s had already reached a similar level to the last measurement at 9.05 s, which reflected the fact that the adsorption of BSA onto PAEMH shell occurred very rapidly. However, the scattering curve immediately after mixing (0.01 s) showed less defined oscillations which is typical for colloids with a spherical structure (Figure 5.26c). Possibly aggregation of SPBs occurred by bridging through BSA. After about 1.57 s, the oscillations became well-defined, like pure SPBs, which means the aggregates were completely dissolved. The scattering curves remained unchanged until the last measurement, suggesting saturation of BSA adsorption into the SPB layer. Therefore, BSA adsorption into the cationic SPBs can be divided into two stages. In the first stage, within tens of milliseconds, the BSA bridges instantaneously caused the aggregation of SPBs. In the second stage (tens of seconds), the aggregated SPBs are redispersed into single SPB particles, and BSA penetrates into the brush layer driven by electrostatic attractions and reaches equilibrium.<sup>28</sup> Obviously, SAXS is a very powerful characterization method to see the structure of SPBs, to monitor the *in-situ* generation of nanoparticles or protein adsorption in SPBs, to observe the distribution of nanoparticles or proteins inside SPBs, and to detect interactions between SPBs or between SPBs and proteins.

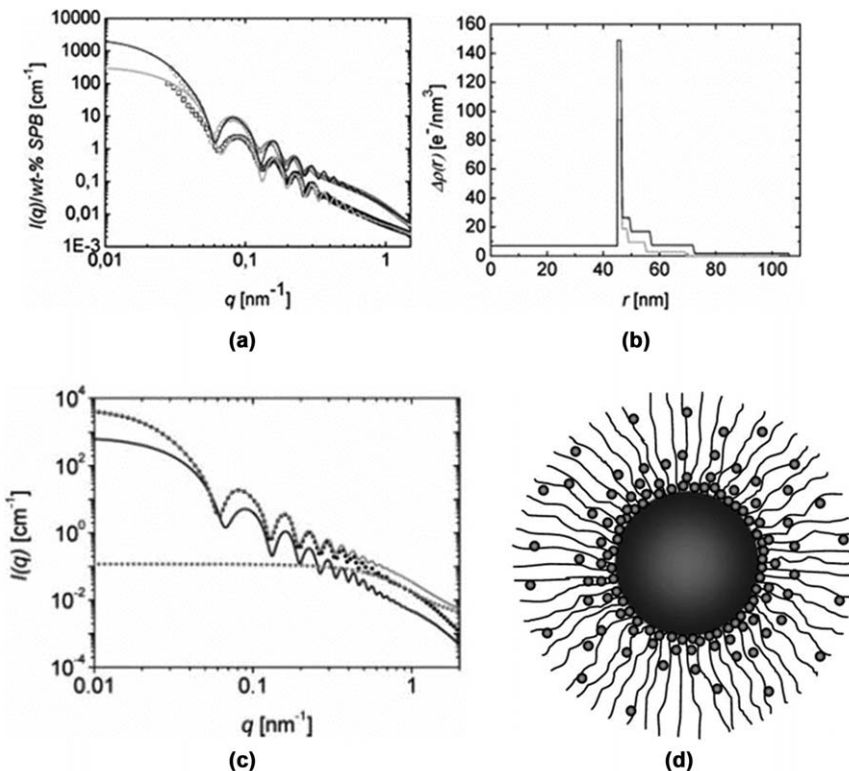


**Figure 5.25** (a) Scattering intensity of PSS brush before and after bovine hemoglobin (BHb) adsorption ( $648 \text{ mg g}^{-1}$  SPBs) and (b) the corresponding distribution of excess electron density; (c) the specific analysis and (d) schematic diagram of BHb adsorption onto PSS brush.  
Reproduced from ref. 158 with permission from American Chemical Society, Copyright 2007.

#### 5.4.3 Effect of SPB Structure on Protein Immobilization in SPBs

The type of charge in SPBs pays an important role in protein adsorption. Anionic SPBs are quite different from cationic SPBs in binding affinities, adsorption amounts, architectures, and phase states for proteins, which may arise from the different interaction modes between SPBs and protein “charge patches”<sup>160</sup> or “charge regulation”.<sup>161</sup>

Recently, we prepared both anionic PAA and cationic PAEMH SPBs, through photo-emulsion polymerization, consisting of a polystyrene core with a diameter of about 80 nm and a brush layer with a thickness from 10 to 50 nm (Figure 5.27), and observed the binding of BSA and  $\beta$ -lactoglobulin (BLG) to the SPBs.<sup>130,150</sup> For a particular protein, the binding stoichiometry, affinity, architecture, and phase state were significantly different between positively and negatively charged SPBs. Significantly larger binding affinity

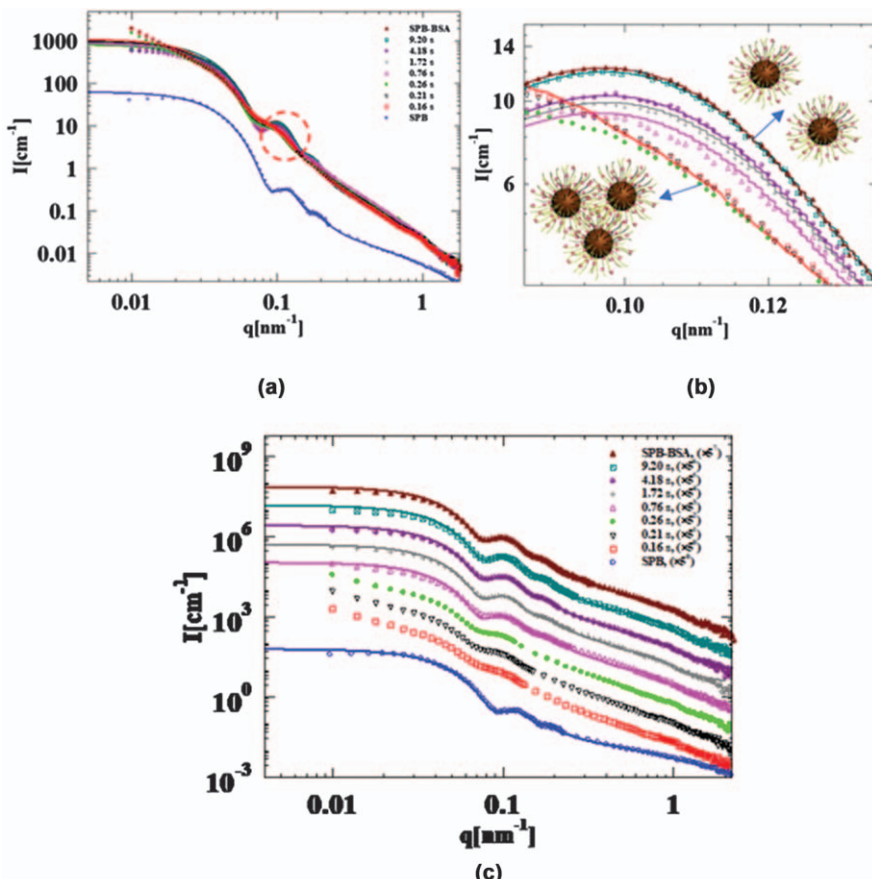


**Figure 5.26** (a) Time-resolved SAXS curves as a function of time after mixing SPBs and BSA (measured in ESRF); (b) the local enlarged SAXS curves in the region of first maximum; (c) curves multiplied by a factor listed in the inset for clarity. Solid lines represent the fits of the experimental data with  $S(q)=1$ . The concentration of cationic SPBs and protein after mixture are 1 wt% and  $10 \text{ g L}^{-1}$ , respectively. The samples were dispersed in MES buffer solution with pH 6.1 and ionic strength of 7 mM. Reproduced from ref. 28 with permission from American Chemical Society, Copyright 2017.

and amount were observed for BSA in anionic *versus* cationic SPBs, while the opposite was true for BLG, which was explained in terms of the different charge anisotropy of the proteins.<sup>130</sup>

The adsorption of BSA onto cationic and anionic SPBs was compared by SAXS.<sup>28</sup> The scattering intensities of both positively charged PAEMH SPBs and negatively charged PAA SPBs increased significantly, and their first maxima shifted to a lower  $q$  value after addition of BSA, indicating the adsorption of BSA in both SPBs (Figure 5.28a). The much higher scattering intensity of PAEMH SPBs with BSA at low  $q$  values ( $q < 0.2 \text{ nm}^{-1}$ ) compared to PAA SPBs

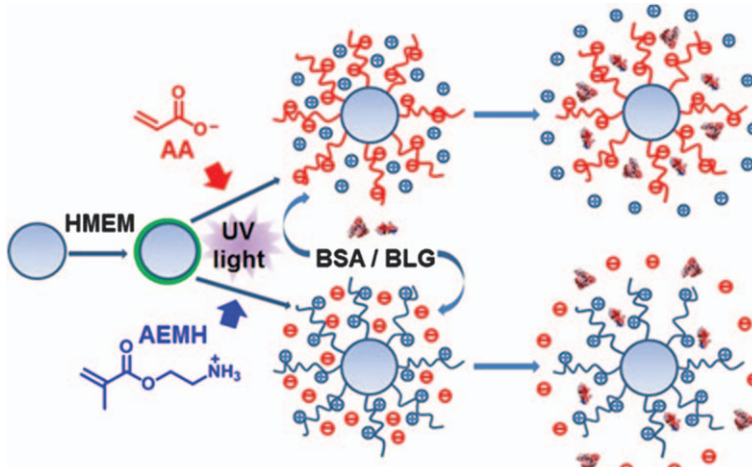


**Figure 5.27** Synthetic scheme of annealed anionic (upper)/cationic (bottom) SPBs and the consequent binding of proteins. (2-[*p*-(2-hydroxy-2-methylpropiophenone)]-ethyleneglycol-methacrylate) (HMEM) is a home-made photoinitiator, acrylic acid (AA) and 2-aminoethyl methacrylate hydrochloride (AEMH) are anionic and cationic monomers, respectively. Reproduced from ref. 130 with permission from the Royal Society of Chemistry.

with BSA reflects the fact that more BSA was adsorbed onto positively charged SPBs. This was confirmed by the larger area of excess electron density in the radial profile for cationic SPB after immobilization of BSA than that for anionic SPBs (Figure 5.28b). Obviously, the electrostatic interaction is the dominated driving force for protein adsorption in SPBs because under the experimental conditions ( $\text{pH } 6.1$  and ionic strength of  $7 \text{ mmol L}^{-1}$ ) the net charge of BSA is negative. The positively charged PAEMH SPBs showed stronger electrostatic attractions with BSA and provided high adsorption capacity for BSA compared to PAA SPBs with negative charges.<sup>28</sup>

#### 5.4.4 Effect of pH and Ionic Strength on Protein Immobilization in SPBs

The pH, ionic strength, and stoichiometry were found to have significant impact on the binding behaviors between proteins and SPBs. The protein binding amount in SPBs is especially tunable by controlling pH and ionic strength.<sup>150</sup>

##### 5.4.4.1 Effect of pH

Upon decreasing pH from 7.2 to 5.8, the adsorption amount of BSA in anionic PAA SPBs, determined at a wavelength of 278 nm by UV spectra, increased monotonically, while the adsorption amount increased at first and

reached saturation with increasing protein concentration (Figure 5.29).<sup>50</sup> When we observed the SAXS curves and radial distributions of excess electron density of PAA SPBs with BSA at a larger pH range (3 to 9), the change in immobilized protein amount became non-monotonic (Figure 5.30).

At pH 3, the scattering intensity over the whole  $q$  range and the excess electron density were the lowest, which meant a minimum amount of BSA was immobilized in PAA SPBs. In this case, most of the carboxyl groups in the PAA chains were unionized, the electrostatic attraction between BSA and PAA chains was very weak, and the SPBs were shrunken. When pH increased to 5, which is close to the pI of BSA (around 4.9), both the scattering intensity and the excess electron density reached a maximum due to the increased degree of dissociation of the carboxyl groups. Further increasing pH, the scattering

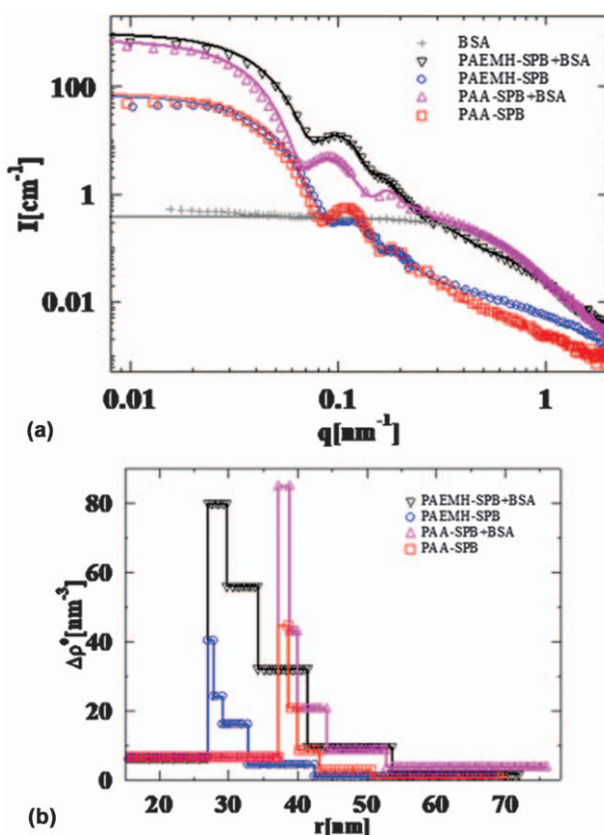


**Figure 5.28** SAXS curve of BSA adsorption onto cationic SPBs (PAEMH-SPBs) and anionic SPBs (PAA-SPBs) at  $\text{pH} = 6.1$ ,  $I = 7 \text{ mmol L}^{-1}$ . The Solid line represents the fitting curve. The excess electron density distributions of cationic and anionic SPBs are shown at the right corner (inset). The concentrations of SPBs and BSA are  $1 \text{ wt\%}$  and  $10 \text{ g L}^{-1}$ , respectively. Reproduced from ref. 28 with permission from American Chemical Society, Copyright 2017.

intensity decreased, especially at low  $q$  values ( $q < 0.25 \text{ nm}^{-1}$ ) and reached a minimum at pH 9 due to BSA partly moving out of the SPBs. The reduction of positively charged patches on the BSA surface with increasing pH above the pI weakened the electrostatic attraction between BSA and SPBs.<sup>50</sup>

For cationic PAEMH SPBs, the dissociation degree of PAEMH and the amount of positive charge in SPBs also strongly depends on the pH value, but the maximum degree of dissociation appears at different pH ranges with anionic SPBs.<sup>28</sup> Because the overall charge and charge patches of proteins change with pH, the attraction of proteins with cationic SPBs, which is attributed to the electrostatic interactions, also showed non-monotonic change with pH value.

As observed by SAXS, the scattering intensity and the excess electron density (Figure 5.31) as well as the amount of BSA adsorption in positively charged SPBs increased with pH, reached a maximum at pH 6.1, and reduced by further increasing pH to 9.0. At pH 6.1, most of the amino groups in PAEMH chains were positively charged and the net negative charges on the BSA surface increased greatly. The enhanced electrostatic attraction between SPBs and protein backed by almost fully swollen SPBs resulted in the most BSA immobilized in the brush layer.<sup>28</sup>

Interestingly, the binding region between proteins and SPBs can be controlled by modulating pH.<sup>150</sup> It becomes possible to separate proteins with various structures, sizes, and isoelectric points by SPBs at a selected pH window. For example, BSA, BLG, and papain were absorbed in cationic PAEMH SPBs and aggregated at clearly distinguishable pH regions (Figure 5.32).<sup>150</sup>

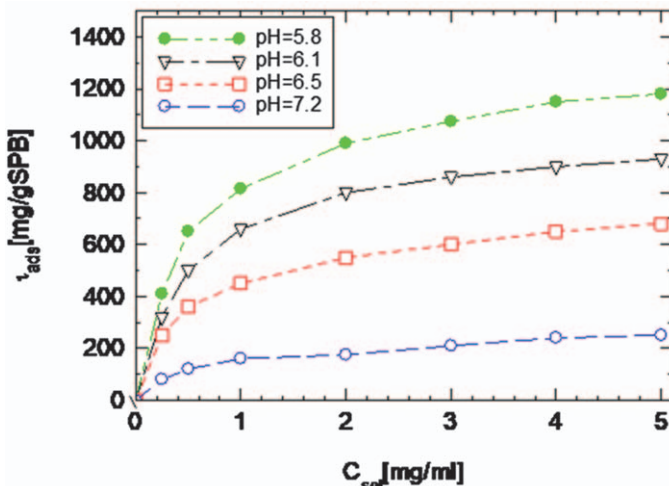


**Figure 5.29** Adsorption amount of BSA  $\tau_{\text{ads}}$  versus protein concentration in solution  $C_{\text{sol}}$  at various pH values. PAA SPBs concentration is  $2.5 \text{ mg mL}^{-1}$  and salt concentration is  $7 \text{ mmol L}^{-1}$ .

Reproduced from ref. 50 with permission from Springer Nature, Copyright 2015.

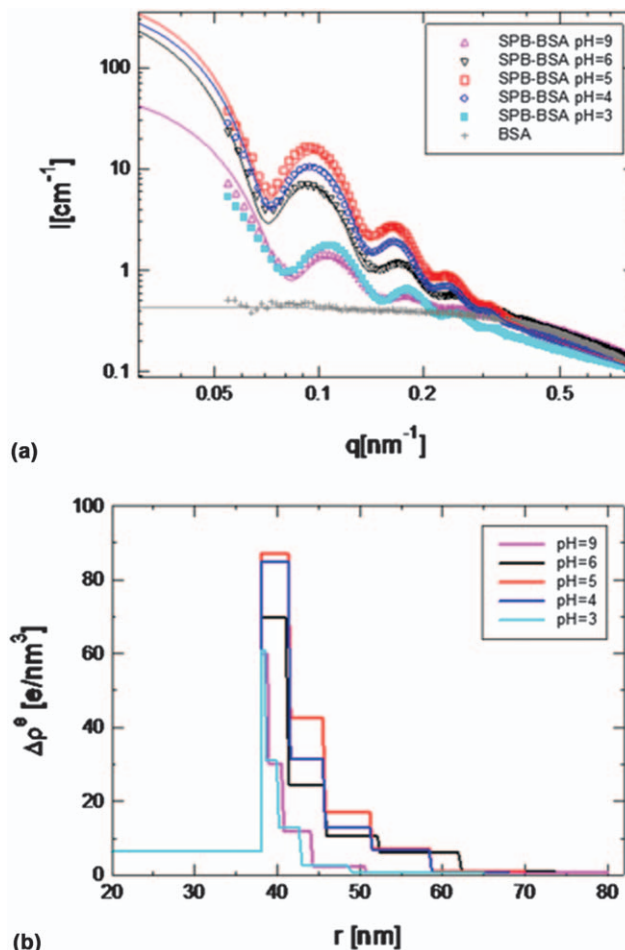


**Figure 5.30** (a) Normalized scattering intensity of SPB-BSA at different pH; (b) the radial excess electron density  $\Delta\rho^e$  distribution of SPB-BSA. The mass fraction of SPB is 1 wt%, BSA concentration is  $10 \text{ g L}^{-1}$ , and the salt strength is  $7 \text{ mmol L}^{-1}$ .

Reproduced from ref. 50 with permission from Springer Nature, Copyright right 2015.

#### 5.4.4.2 Effect of Ionic Strength

The immobilization of proteins in SPBs under the effect of ionic strength has been systematically investigated both qualitatively and quantitatively.<sup>28,50,150</sup> The adsorption amount of proteins in both negatively and positively charged SPBs reduced with increasing ionic strength, as determined by UV spectra and confirmed by turbidimetric titration (Figures 5.33 and 5.34). The capacity of protein adsorption for cationic PAEMH SPBs was higher than that for anionic PAA SPBs, and the impact of ionic strength on protein adsorption was also

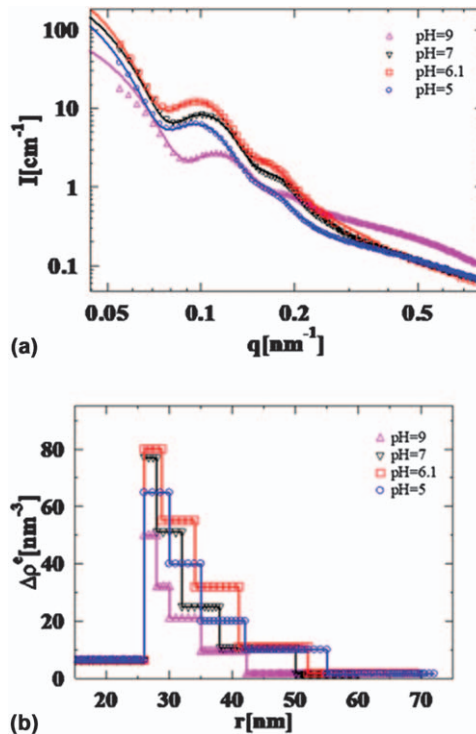


**Figure 5.31** The SAXS curves of SPB-BSA as a function of pH value. The radial distribution of excess electron density of SPB-BSA *versus* radius (inset). Solid lines represent fitting curves. The mass fraction of SPBs is 1 wt% and BSA concentration is  $10 \text{ g L}^{-1}$ .

Reproduced from ref. 28 with permission from American Chemical Society, Copyright 2017.

larger for cationic compared to anionic SPBs, especially at relatively low salt concentrations.<sup>50,150</sup>

As further observed by SAXS, the scattering intensity of cationic PAEMH SPBs with BSA and the excess electron density of the brush layer decreased with increasing ionic strength from 7 to 47 mM (Figure 5.35), which was caused by the loss of BSA in SPBs, replaced by increasing counterions. The enhanced screening effect of the addition of salt also led to the weakening of electrostatic attractions between BSA and SPBs.<sup>28</sup> Compared to the impact of pH on the protein immobilization of proteins in SPBs, the effect of ionic strength is relatively weaker, but monotonic.

## 5.5 Conclusion and Perspective

In summary, recent advances in utilizing SPBs as nanoreactors to prepare metallic and metallic compound nanoparticles, as templates to generate organic-inorganic functional nanomaterials, and as nanocarriers to

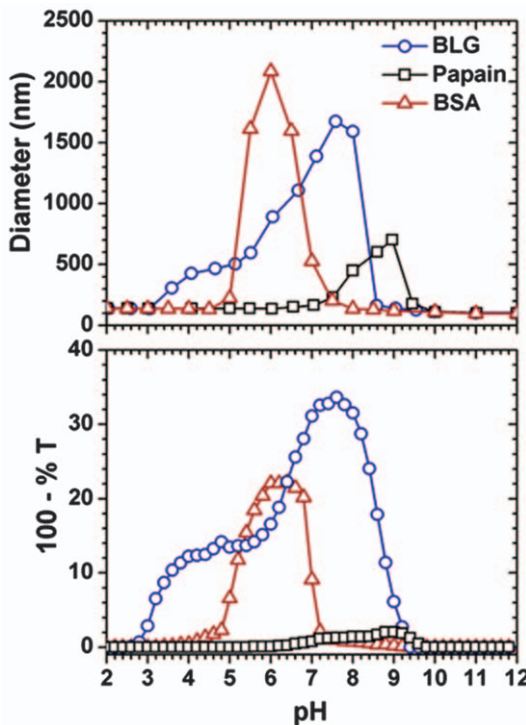


**Figure 5.32** Size and turbidity of complexes between various proteins and cationic SPBs (with 50 mol% dose of AEMH) as a function of pH in 1 mM NaCl solutions under same condition. Symbols denote: ( $\triangle$ ) BSA-SPB complexes, ( $\circ$ ) BLG-SPB complexes, and ( $\square$ ) papain-SPB complexes. Proteins and SPBs concentration are 0.020 and  $0.004 \text{ mg mL}^{-1}$  for turbidimetric titration, and 0.040 and  $0.008 \text{ mg mL}^{-1}$  for DLS, respectively. Bulk stoichiometry was set at 5 for protein/SPB (w/w). Reproduced from ref. 150 with permission from American Chemical Society, Copyright 2013.

selectively immobilize proteins were introduced in this chapter. SPBs are interesting functional colloids with a range of unique properties, in particular the confinement of counterions caused by an intensified Donnan effect and electrostatic interaction making SPBs excellent nanoreactors and carriers. Thus, SPBs open a new way to prepare nanosized metallic catalysts and organic-inorganic hybrid materials. In addition, because of the tuneable charge density and charge distribution in the densely grafted polyelectrolyte chains, SPBs have great potential in the controlled immobilization and separation of proteins. Using this method, the bioactivity and stability of proteins is not changed, which is especially suitable for enzyme immobilization to act as bioreactors.

Although great progress has been made, there are still some aspects of SPBs that need to be improved, especially from the perspective of applications.

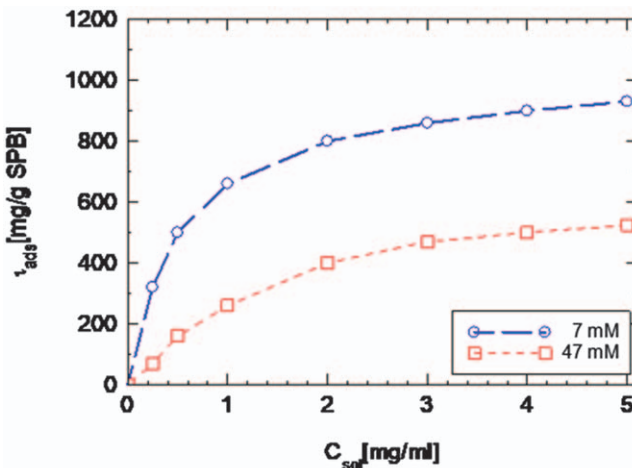


**Figure 5.33** The adsorption amount of BSA  $\tau_{ads}$  versus BSA concentration in solution  $C_{sol}$  for anionic PAA SPBs, at various ionic strengths. SPB concentration is  $2.5 \text{ mg mL}^{-1}$  and  $\text{pH} = 6.1$ . Reproduced from ref. 50 with permission from Springer Nature, Copyright right 2015.

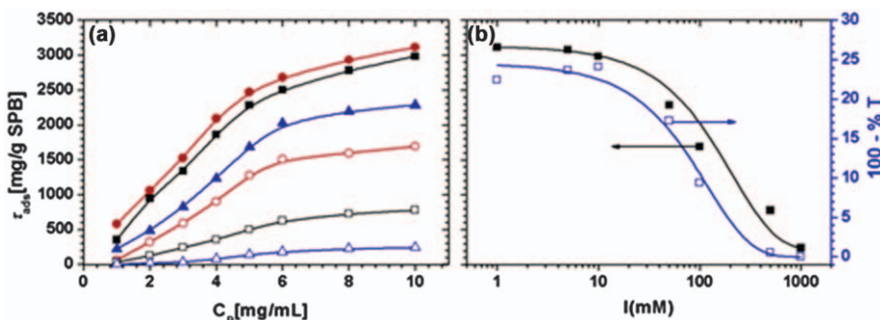


**Figure 5.34** (a) The binding amount of BSA  $\tau_{ads}$  per unit mass particles plotted against the original protein concentration in solution  $C_p$  for cationic PAEMH SPBs. The changing parameter is ionic strength: ( $\bullet$ ) 1, ( $\blacksquare$ ) 10, ( $\blacktriangle$ ) 50, ( $\circ$ ) 100, ( $\square$ ) 500, and ( $\triangle$ ) 1000 mM,  $\text{pH} = 6.0$ . (b) Turbidity ( $\square$ ) and saturation binding amount ( $\blacksquare$ ) for BSA-SPB complexes as a function of ionic strength at  $\text{pH} 6.0$ . SPB and BSA concentrations were  $0.004$  and  $0.020 \text{ mg mL}^{-1}$  for turbidimetric titration, respectively. Bulk stoichiometry was set at 5 for BSA/SPBs (w/w). The cationic SPBs were formed using 75 mol% doses of AEMH monomer. Reproduced from ref. 150 with permission from American Chemical Society, Copyright 2013.

For instance, preparing SPBs on a large scale at low cost, improving the preparation efficiency and catalytic activity of metallic nanoparticles in SPBs, generating more kinds of organic-inorganic hybrid nanoparticles with controlled

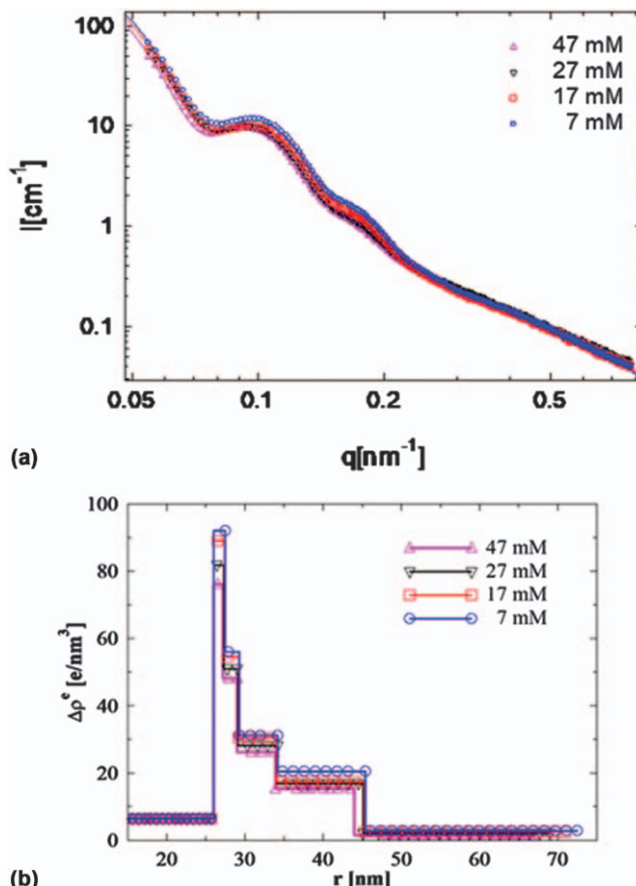


**Figure 5.35** (a) SAXS curves of PAEMH SPBs with BSA at various ionic strengths. Solid lines represent fitting curves. (b) The distribution of excess electron density ( $\Delta\rho^e$ ) of SPB-BSA *versus* radius as a function of ionic strength. BSA concentration is  $10 \text{ g L}^{-1}$  and  $\text{pH} = 6.1$ . Symbols denote: (○) 7 mM; (□) 17 mM; (▽) 27 mM; (△) 47 mM.  
Reproduced from ref. 28 with permission from American Chemical Society, Copyright 2017.

structures using SPBs as templates, and improving the selectivity of proteins immobilization in SPBs deserve further in-depth research.

More theoretical analysis or molecular simulations are especially expected to improve our understanding of the relationship between the structures and properties of SPBs, to reveal the reaction dynamics in SPBs, and to clarify the mechanism of interaction between SPBs and proteins. More powerful characterization techniques are needed to observe the behaviors of SPBs as nanoreactors, nanotemplates, and nanocarriers.

In addition, there has been much research on cationic and anionic SPBs, but very few reports on zwitterionic SPBs. Owing to their interesting

properties, including high resistance to non-specific protein adsorption and good biocompatibility, zwitterionic SPBs should draw more attention,<sup>162</sup> as they could have huge potential applications in bioscience, biological engineering, and drug delivery.

As for the applications of SPBs, efforts have mainly focused on catalysis and protein immobilization. Because SPBs show excellent confinement ability for counterions and good stability in aqueous solution, they should also be ideal candidates for removal of harmful metal ions and harmful microorganisms in the area of environmental protection. For example, introduction of functional groups, fluorescent molecules, drugs, enzymes, or bacteria to SPBs can endow them with more powerful capacities for applications in many fields.

In the future, more work can be done on the industrialization of nanomaterials based on SPBs. The focus of research will shift to preparing nanomaterials multifunctional properties utilizing SPBs as nanoreactors or templates. The applications of SPBs and SPB-based nanomaterials in catalysis, biomedicine, environmental engineering, and other fields will continue to draw a lot of attention. In fact, there are probably more new functional materials based on SPBs waiting for us to develop.

## References

1. S. T. Milner, *Science*, 1991, **251**(4996), 905.
2. B. Zhao and W. J. Brittain, *Prog. Polym. Sci.*, 2000, **25**(5), 677.
3. S. Minko, *Polym. Rev.*, 2006, **46**(4), 397.
4. M. V. Der Waarden, *J. Colloid Sci.*, 1950, **5**(4), 317.
5. M. V. Der Waarden, *J. Colloid Sci.*, 1951, **6**(5), 443.
6. A. L. Becker, N. Welsch, C. Schneider and M. Ballauff, *Biomacromolecules*, 2011, **12**(11), 3936.
7. M. Schrinner, M. Ballauff, Y. Talmon, Y. Kauffmann, J. Thun, M. Möller and J. Breu, *Science*, 2009, **323**(5914), 617.
8. Y. M. Wang, F. Versluis, S. Oldenhof, V. Lakshminarayanan, K. Zhang, Y. W. Wang, J. Wang, R. Eelkema, X. H. Guo and J. H. van Esch, *Adv. Mater.*, 2018, **30**(21), 7.
9. R. Zhang, Z. C. Yu, L. Wang, Q. Z. Shen, X. Y. Hou, X. H. Guo, J. W. Wang, X. D. Zhu and Y. Yao, *Chem. - Eur. J.*, 2017, **23**(55), 13696.
10. Q. Zhu, Z. Y. Yuan, W. Q. Qian, Y. Y. Li, Z. Q. Qiu, W. J. Tang, J. Wang, Y. Ding and A. G. Hu, *Adv. Healthcare Mater.*, 2017, **6**(12), 10.
11. W. Q. Qian, Q. Zhu, B. Duan, W. J. Tang, Y. Yuan and A. G. Hu, *Dalton Trans.*, 2018, **47**(23), 7663.
12. W. L. Chen, R. Cordero, H. Tran and C. K. Ober, *Macromolecules*, 2017, **50**(11), 4089.
13. O. Hollmann and C. Czeslik, *Langmuir*, 2006, **22**(7), 3300.
14. K. Tsubaki and K. Ishizu, *Polymer*, 2001, **42**(20), 8387.
15. S. Forster, E. Wenz and P. Lindner, *Phys. Rev. Lett.*, 1996, **77**(1), 95.

16. R. Barbey, L. Lavanant, D. Paripovic, N. Schuwer, C. Sugnaux, S. Tugulu and H. A. Klok, *Chem. Rev.*, 2009, **109**(11), 5437.
17. S. S. Sheiko, B. S. Sumerlin and K. Matyjaszewski, *Prog. Polym. Sci.*, 2008, **33**(7), 759.
18. K. M. Ho, W. Y. Li, C. H. Wong and P. Li, *Colloid Polym. Sci.*, 2010, **288**(16–17), 1503.
19. X. Guo, A. A. Weiss and M. Ballauff, *Macromolecules*, 1999, **32**(19), 6043.
20. X. Wang, J. Xu, L. Li, S. Wu, Q. Chen, Y. Lu, M. Ballauff and X. Guo, *Macromol. Rapid Commun.*, 2010, **31**(14), 1272.
21. L. Qin, Y. Xu, H. Han, M. Liu, K. Chen, S. Wang, J. Wang, J. Xu, L. Li and X. Guo, *J. Colloid Interface Sci.*, 2015, **460**, 221.
22. Z. Y. Qu, F. L. Hu, K. M. Chen, Z. Q. Duan, H. C. Gu and H. Xu, *J. Colloid Interface Sci.*, 2013, **398**, 82.
23. L. Cao, K. Chen, Y. Zhang, K. Li, X. Qin and X. Guo, *Mater. Lett.*, 2018, **223**, 116.
24. M. Ballauff, *Macromol. Chem. Phys.*, 2003, **204**(2), 220.
25. Y. Lu, A. Wittemann, M. Ballauff and M. Drechsler, *Macromol. Rapid Commun.*, 2006, **27**(14), 1137.
26. X. Guo and M. Ballauff, *Langmuir*, 2000, **16**(23), 8719.
27. M. Guo, M. Ballauff and T. Narayanan, *Macromolecules*, 2000, **33**(24), 9109.
28. W. Wang, L. Li, K. Henzler, Y. Lu, J. Wang, H. Han, Y. Tian, Y. Wang, Z. Zhou and G. Lotze, *Biomacromolecules*, 2017, **18**(5), 1574.
29. S. Huang, X. Guo, L. Li and Y. Dong, *J. Phys. Chem. B*, 2012, **116**(33), 10079.
30. Y. Lu, Y. Mei, M. Schrinner, M. Ballauff, M. W. Möller and J. Breu, *J. Phys. Chem. C*, 2007, **111**(21), 7676.
31. F. Polzer, J. Heigl, C. Schneider, M. Ballauff and O. V. Borisov, *Macromolecules*, 2011, **44**(6), 1654.
32. Y. Lu and M. Ballauff, *Prog. Polym. Sci.*, 2016, **59**, 86.
33. P. Pincus, *Macromolecules*, 1991, **24**, 8.
34. E. Zhulina, T. Birshtein and O. Borisov, *Macromolecules*, 1995, **28**(5), 1491.
35. Y. Mei and M. Ballauff, *Eur. Phys. J. E*, 2005, **16**(3), 341.
36. A. Jusufi, C. N. Likos and M. Ballauff, *Colloid Polym. Sci.*, 2004, **282**(8), 910.
37. B. Das, X. Guo and M. Ballauff, *Prog. Colloid Polym. Sci.*, 2002, **121**, 34.
38. D. J. Sandberg, J. M. Y. Carrillo and A. V. Dobrynin, *Langmuir*, 2007, **23**(25), 12716.
39. C. Yu, R. Zhang, D. Fang, X. Guo and X. Zhu, *Des. Monomers Polym.*, 2016, **19**(2), 145.
40. K. Chen, Y. Zhu, Y. Zhang, L. Li, Y. Lu and X. Guo, *Macromolecules*, 2011, **44**(3), 632.
41. C. Yu, R. Zhang, G. Shi, D. Fang and X. Guo, *Colloid Polym. Sci.*, 2015, **293**(10), 3043.
42. M. Ballauff, *Prog. Polym. Sci.*, 2007, **32**(10), 1135.

43. Z. Y. Qu, H. Xu and H. C. Gu, *ACS Appl. Mater. Interfaces*, 2015, **7**(27), 14537.
44. M. C. Daniel and D. Astruc, *Chem. Rev.*, 2004, **104**(1), 293.
45. P. Zhao, N. Li and D. Astruc, *Coord. Chem. Rev.*, 2013, **257**(3–4), 638.
46. G. J. Hutchings, *Dalton Trans.*, 2008, **41**, 5523.
47. J. Rühe, M. Ballauff, M. Biesalski, P. Dziezok, F. Gröhn, D. Johannsmann, N. Houbenov, N. Hugenberg, R. Konradi and S. Minko, *Polyelectrolyte brushes*, in *Polyelectrolytes with Defined Molecular Architecture I*, Springer, 2004, pp. 79–150.
48. X. Guo and M. Ballauff, *Phys. Rev. E*, 2001, **64**(5), 051406.
49. X. Liu, Y. Xu, X. Wang, M. Shao, J. Xu, J. Wang, L. Li, R. Zhang and X. Guo, *Colloid Surf., B*, 2015, **127**, 148.
50. W. Wang, L. Li, H. Han, Y. Tian, Z. Zhou and X. Guo, *Colloid Polym. Sci.*, 2015, **293**(10), 2789.
51. X. Guo, in *Synthesis and Study of the Colloidal Polyelectrolyte Brushes Prepared by Photo-emulsion Polymerization*, Logos Press Berlin, Berlin, 2001, p. 25.
52. S. Y. Lu and S. W. Chen, *J. Am. Ceram. Soc.*, 2000, **83**(4), 709.
53. G. Sharma and M. Ballauff, *Macromol. Rapid Commun.*, 2004, **25**(4), 547.
54. Y. Mei, G. Sharma, Y. Lu, M. Ballauff, M. Drechsler, T. Irrgang and R. Kempe, *Langmuir*, 2005, **21**(26), 12229.
55. G. Sharma, Y. Mei, Y. Lu, M. Ballauff, T. Irrgang, S. Proch and R. Kempe, *J. Catal.*, 2007, **246**(1), 10.
56. Y. Mei, Y. Lu, F. Polzer, M. Ballauff and M. Drechsler, *Chem. Mater.*, 2007, **19**(5), 1062.
57. Z. Zhu, X. Guo, S. Wu, R. Zhang, J. Wang and L. Li, *Ind. Eng. Chem. Res.*, 2011, **50**(24), 13848.
58. Y. Lu, M. Hoffmann, R. S. Yelamanchili, A. Terrenoire, M. Schrinner, M. Drechsler, M. W. Möller, J. Breu and M. Ballauff, *Macromol. Chem. Phys.*, 2009, **210**(5), 377.
59. M. Schrinner, S. Proch, Y. Mei, R. Kempe, N. Miyajima and M. Ballauff, *Adv. Mater.*, 2008, **20**(10), 1928.
60. T. Zhang, L. Li, Z. Ye, Q. Yang, Y. Tian and X. Guo, *RSC Adv.*, 2018, **8**(33), 18252.
61. P. Herves, M. Perez-Lorenzo, L. M. Liz-Marzan, J. Dzubiella, Y. Lu and M. Ballauff, *Chem. Soc. Rev.*, 2012, **41**(17), 5577.
62. T. Aditya, A. Pal and T. Pal, *Chem. Commun.*, 2015, **51**(46), 9410.
63. P. Zhao, X. Feng, D. Huang, G. Yang and D. Astruc, *Coord. Chem. Rev.*, 2015, **287**, 114.
64. S. Wunder, F. Polzer, Y. Lu, Y. Mei and M. Ballauff, *J. Phys. Chem. C*, 2010, **114**(19), 8814.
65. Y. Zhu, K. M. Chen, X. Wang and X. H. Guo, *Nanotechnology*, 2012, **23**(26), 9.
66. S. Wu, J. Kaiser, X. H. Guo, L. Li, Y. Lu and M. Ballauff, *Ind. Eng. Chem. Res.*, 2012, **51**(15), 5608.

67. F. Polzer, D. A. Kunz, J. Breu and M. Ballauff, *Chem. Mater.*, 2010, **22**(9), 2916.
68. X. C. Liu, Y. S. Xu, S. J. Ma, Y. F. Ma, A. Ahmad, Y. C. Tian, X. H. Zhong and X. H. Guo, *Ind. Eng. Chem. Res.*, 2014, **53**(28), 11326.
69. L. L. Cui, H. Xu, P. He, K. K. Sumitomo, Y. Yamaguchi and H. C. Gu, *J. Polym. Sci., Part A: Polym. Chem.*, 2007, **45**(22), 5285.
70. V. L. Colvin, M. C. Schlamp and A. P. Alivisatos, *Nature*, 1994, **370**(6488), 354.
71. B. O. Dabbousi, M. G. Bawendi, O. Onitsuka and M. F. Rubner, *Appl. Phys. Lett.*, 1995, **66**(11), 1316.
72. Y. Cang, R. Zhang, G. Shi, J. Zhang, L. Liu, X. Hou, Z. Yu, D. Fang and X. Guo, *J. Mater. Chem. C*, 2015, **3**(15), 3745.
73. J. Pyun and K. Matyjaszewski, *Chem. Mater.*, 2001, **13**(10), 3436–3448.
74. Z. L. Lei and S. X. Bi, *Mater. Lett.*, 2007, **61**(16), 3531.
75. Y. B. Sun, X. B. Ding, Z. H. Zheng, X. Cheng, X. H. Hu and Y. X. Peng, *Eur. Polym. J.*, 2007, **43**(3), 762.
76. Q. S. Wei, J. Ji and J. C. Shen, *Macromol. Rapid Commun.*, 2008, **29**(8), 645.
77. M. N. Tchoul, M. Dalton, L. S. Tan, H. C. Dong, C. M. Hui, K. Matyjaszewski and R. A. Vaia, *Polymer*, 2012, **53**(1), 79.
78. J. C. Daigle and J. P. Claverie, *J. Nanomater.*, 2008, 8.
79. F. Caruso, R. A. Caruso and H. Mohwald, *Science*, 1998, **282**(5391), 1111.
80. W. Schlee, *Nanoscale*, 2011, **3**(11), 4474.
81. J. S. Wang, Z. H. Shah, S. F. Zhang and R. W. Lu, *Nanoscale*, 2014, **6**(9), 4418.
82. W. Schartl, *Nanoscale*, 2010, **2**(6), 829.
83. A. Khanal, Y. Inoue, M. Yada and K. Nakashima, *J. Am. Chem. Soc.*, 2007, **129**(6), 1534.
84. M. Sasidharan and K. Nakashima, *Acc. Chem. Res.*, 2014, **47**(1), 157.
85. J. Hu, M. Chen, X. S. Fang and L. W. Wu, *Chem. Soc. Rev.*, 2011, **40**(11), 5472.
86. Y. Zhao and L. Jiang, *Adv. Mater.*, 2009, **21**(36), 3621.
87. Y. S. Si, M. Chen and L. M. Wu, *Chem. Soc. Rev.*, 2016, **45**(3), 690.
88. Y. S. Li and J. L. Shi, *Adv. Mater.*, 2014, **26**(20), 3176.
89. P. Podsiadlo, S. G. Kwon, B. Koo, B. Lee, V. B. Prakapenka, P. Dera, K. K. Zhuravlev, G. Krylova and E. V. Shevchenko, *J. Am. Chem. Soc.*, 2013, **135**(7), 2435.
90. F. Q. Tang, L. L. Li and D. Chen, *Adv. Mater.*, 2012, **24**(12), 1504.
91. Y. F. Zhu, J. L. Shi, W. H. Shen, X. P. Dong, J. W. Feng, M. L. Ruan and Y. S. Li, *Angew. Chem., Int. Ed.*, 2005, **44**(32), 5083.
92. Y. Zhang, B. Y. W. Hsu, C. L. Ren, X. Li and J. Wang, *Chem. Soc. Rev.*, 2015, **44**(1), 315.
93. C. Park, K. Oh, S. C. Lee and C. Kim, *Angew. Chem., Int. Ed.*, 2007, **46**(9), 1455.
94. A. Guerrero-Martinez, J. Perez-Juste and L. M. Liz-Marzan, *Adv. Mater.*, 2010, **22**(11), 1182.

95. S. S. Cao, Y. Zhang, L. L. Zhou, J. R. Chen, L. Fang, D. Fei, H. J. Zhu and Y. Ge, *J. Mater. Chem. B*, 2014, **2**(41), 7243.
96. E. Amstad and E. Reimhult, *Nanomedicine*, 2012, **7**(1), 145.
97. X. W. Lou, L. A. Archer and Z. C. Yang, *Adv. Mater.*, 2008, **20**(21), 3987.
98. Y. M. Wang, J. Wang, H. Y. Han, J. J. Liu, H. Q. Zhao, M. X. Shen, Y. S. Xu, J. Xu, L. Li and X. H. Guo, *J. Mater. Sci.*, 2016, **51**(3), 1591.
99. Z. W. Deng, M. Chen, S. X. Zhou, B. You and L. M. Wu, *Langmuir*, 2006, **22**(14), 6403.
100. I. Tissot, C. Novat, F. Lefebvre and E. Bourgeat-Lami, *Macromolecules*, 2001, **34**(17), 5737.
101. L. Li, J. Ding and J. M. Xue, *Chem. Mater.*, 2009, **21**(15), 3629.
102. A. Schmid, S. Fujii and S. P. Armes, *Langmuir*, 2006, **22**(11), 4923.
103. L. Han and S. N. Che, *Chem. Soc. Rev.*, 2013, **42**(9), 3740.
104. S. Huang, X. Yu, Y. Dong, L. Li and X. Guo, *Colloid Surf., A*, 2012, **415**, 22.
105. S.-b. Huang, Y.-m. Dong and X.-h. Guo, *J. East China Univ. Sci. Technol.*, 2011, **37**(6), 655.
106. H. Y. Han, L. Li, W. H. Wang, Y. C. Tian, Y. W. Wang, J. Y. Wang, R. von Klitzing and X. H. Guo, *Langmuir*, 2017, **33**(38), 9857.
107. H. Y. Han, L. Li, Y. C. Tian, Y. W. Wang, Z. S. Ye, Q. S. Yang, Y. M. Wang, R. von Klitzing and X. H. Guo, *RSC Adv.*, 2017, **7**(76), 47877.
108. A. Niemann, P. Berger and U. Suter, *NeuroMol. Med.*, 2006, **8**(1–2), 217.
109. F. Stirpe and R. Gilabert-Oriol, Ribosome-Inactivating Proteins: An Overview, in *Plant Toxins*, ed. C. R. Carlini and R. Ligabue-Braun, Springer Netherlands, Dordrecht, 2017, p. 153.
110. B. S. Powell, G. P. Andrews, J. T. Enama, S. Jendrek, C. Bolt, P. Worsham, J. K. Pullen, W. Ribot, H. Hines, L. Smith, D. G. Heath and J. J. Adamovicz, *Biotechnol. Prog.*, 2005, **21**(5), 1490.
111. H. N. Rabetafika, V. Van Remoortel, S. Danthine, M. Paquot and C. Blecker, *Int. J. Food Sci. Technol.*, 2011, **46**(2), 221.
112. M. J. de Groot, M. J. Ackland, V. A. Horne, A. A. Alex and B. C. Jones, *J. Med. Chem.*, 1999, **42**(9), 1515.
113. W. L. Murphy and D. J. Mooney, *J. Periodontal Res.*, 1999, **34**(7), 413.
114. J. Bao, W. Chen, T. T. Liu, Y. L. Zhu, P. Y. Jin, L. Y. Wang, J. F. Liu, Y. G. Wei and Y. D. Li, *ACS Nano*, 2007, **1**(4), 293.
115. H. Gu, K. Xu, C. Xu and B. Xu, *Chem. Commun.*, 2006, **9**, 941.
116. T. B. Tennikova, F. Svec and B. G. Belenkii, *J. Liq. Chromatogr.*, 1991, **13**(1), 63.
117. D. Armstrong, R. Menges and I. Wainer, *J. Liq. Chromatogr.*, 2016, **13**(18), 3571.
118. Y. H. Lin and H. S. Chan, *Biophys. J.*, 2017, **112**(10), 2043.
119. M. Antonietti, J. Conrad and A. Thuenemann, *Macromolecules*, 1994, **27**(21), 6007.
120. F. Bordi, S. Sennato and D. Truzzolillo, *J. Phys.: Condens. Matter*, 2009, **21**(20), 203102.
121. B. Y. Ha and D. Thirumalai, *Macromolecules*, 1995, **28**(2), 577.

122. M. Ballauff and O. Borisov, *Curr. Opin. Colloid Interface Sci.*, 2010, 11(6), 316.
123. A. F. Thunemann, M. Muller, H. Dautzenberg, J. F. O. Joanny and H. Lowen, Polyelectrolyte complexes, in *Polyelectrolytes with Defined Molecular Architecture II*, ed. M. Schmidt, Springer-Verlag Berlin, Berlin, 2004, pp. 113–171.
124. B. Wang, T. Jin, Q. Xu, H. Liu, Z. Ye and H. Chen, *Bioconjugate Chem.*, 2016, 27(5), 1305.
125. K. Tang and N. A. Besseling, *Soft Matter*, 2016, 12(4), 1032.
126. L. H. Tostanoski, Y. C. Chiu, J. I. Andorko, M. Guo, X. Zeng, P. Zhang, W. Royal, 3rd and C. M. Jewell, *ACS Nano*, 2016, 10(10), 9334.
127. Y. F. Wang, J. Y. Gao and P. L. Dubin, *Biotechnol. Prog.*, 1996, 12(3), 356.
128. A. B. Kayitmazer, H. B. Bohidar, K. W. Mattison, A. Bose, J. Sarkar, A. Hashidzume, P. S. Russo, W. Jaeger and P. L. Dubin, *Soft Matter*, 2007, 3(8), 1064.
129. P. L. Dubin, J. Gao and K. Mattison, *Sep. Purif. Methods*, 2006, 23(1), 1.
130. S. Y. Wang, K. M. Chen, Y. S. Xu, X. J. Yu, W. H. Wang, L. Li and X. H. Guo, *Soft Matter*, 2013, 9(47), 11276.
131. Y. S. Xu, S. Y. Wang, H. Y. Han, K. M. Chen, L. Qin, J. Xu, J. Wang, L. Li and X. H. Guo, *Langmuir*, 2014, 30(37), 11156.
132. A. Dobrynin and M. Rubinstein, *Prog. Polym. Sci.*, 2005, 30(11), 1049.
133. J. H. Fang, X. X. Guo, S. Harada, T. Watari, K. Tanaka, H. Kita and K. Okamoto, *Macromolecules*, 2002, 35(24), 9022.
134. A. Pinotti, A. Bevilacqua and N. Zaritzky, *J. Food Eng.*, 1997, 32(1), 69.
135. K. Lee, L. K. Povlich and J. Kim, *Adv. Funct. Mater.*, 2007, 17(14), 2580.
136. H. Schmal, P. Niemeyer, J. Zwingmann, F. Stoffel, N. P. Südkamp and A. T. Mehlhorn, *J. Food Sci.*, 1985, 50(2), 486.
137. K. Bradley, M. Briman, A. Star and G. Gruner, *Nano Lett.*, 2004, 4(2), 253.
138. A. E. Nel, L. Madler, D. Velegol, T. Xia, E. M. Hoek, P. Somasundaran, F. Klaessig, V. Castranova and M. Thompson, *Nat. Mater.*, 2009, 8(7), 543.
139. D. F. Moyano and V. M. Rotello, *Langmuir*, 2011, 27(17), 10376.
140. F. Fang and I. Szleifer, *Biophys. J.*, 2001, 80(6), 2568.
141. X. R. Xia, N. A. Monteiro-Riviere and J. E. Riviere, *Nat. Nanotechnol.*, 2010, 5(9), 671.
142. L. Treuel and G. U. Nienhaus, *Biophys. Rev.*, 2012, 4(2), 137.
143. M. Weber, A. Bujotzek, K. Andrae, M. Weinhart and R. Haag, *Mol. Simul.*, 2011, 37(11), 899.
144. K. Chen, Y. Xu, S. Rana, O. R. Miranda, P. L. Dubin, V. M. Rotello, L. Sun and X. Guo, *Biomacromolecules*, 2011, 12(7), 2552.
145. K. Chen, S. Rana, D. F. Moyano, Y. Xu, X. Guo and V. M. Rotello, *Nanoscale*, 2014, 6(12), 6492.
146. N. Welsch, A. L. Becker, J. Dzubiella and M. Ballauff, *Soft Matter*, 2012, 8(5), 1428.
147. A. Kusumo, L. Bombalski, Q. Lin, K. Matyjaszewski, J. W. Schneider and R. D. Tilton, *Langmuir*, 2007, 23(8), 4448.

148. E. Kokufuta, H. Shimizu and I. Nakamura, *Macromolecules*, 1982, 15(6), 1618.
149. S. Wang, K. Chen, A. B. Kayitmazer, L. Li and X. Guo, *Colloid Surf., B*, 2013, 107, 251.
150. S. Wang, K. Chen, L. Li and X. Guo, *Biomacromolecules*, 2013, 14(3), 818.
151. V. Ball and C. Maechling, *Int. J. Mol. Sci.*, 2009, 10(8), 3283.
152. H. Y. Lin, C. Y. Hsu, J. L. Thomas, S. E. Wang, H. C. Chen and T. C. Chou, *Biosens. Bioelectron.*, 2006, 22(4), 534.
153. G. Baier, C. Costa, A. Zeller, D. Baumann, C. Sayer, P. H. H. Araujo, V. Mailander, A. Musyanovych and K. Landfester, *Macromol. Biosci.*, 2011, 11(5), 628.
154. S. A. Tikhonenko, E. A. Saburova, E. N. Durdenko and B. I. Sukhorukov, *Russ. J. Phys. Chem. A*, 2009, 83(10), 1781.
155. X. H. Wang, S. Zhang, Y. S. Xu, X. T. Zhao and X. H. Guo, *Langmuir*, 2018, 34(28), 8264.
156. S. Rosenfeldt, A. Wittemann, M. Ballauff, E. Breininger, J. Bolze and N. Dingenaerts, *Phys. Rev. E*, 2004, 70(6), 10.
157. M. Ballauff, *Curr. Opin. Colloid Interface Sci.*, 2001, 6(2), 132.
158. K. Henzler, A. Wittemann, E. Breininger, M. Ballauff and S. Rosenfeldt, *Biomacromolecules*, 2007, 8(11), 3674.
159. Z. Ye, L. Li, F. Zhao, H. Han, Y. Tian, Y. Wang, Q. Yang, W. Fan and X. Guo, *J. Polym. Sci., Part B: Polym. Phys.*, 2018, DOI: 10.1002/polb. 24746.
160. A. B. Kayitmazer, D. Seeman, B. B. Minsky, P. L. Dubin and Y. S. Xu, *Soft Matter*, 2013, 9(9), 2553.
161. W. M. de Vos, F. A. M. Leermakers, A. de Keizer, M. A. C. Stuart and J. M. Kleijn, *Langmuir*, 2010, 26(1), 249.
162. O. Azzaroni, A. A. Brown and W. T. Huck, *Angew. Chem., Int. Ed.*, 2006, 45(11), 1770.



## **Section II: Recent Advances in Colloid Characterization**



## CHAPTER 6

# *The Advanced Microscopy of Colloids*

DANIEL G. GREGORY AND NAN YAO\*

Princeton University, New Jersey, USA

\*Email: nyao@princeton.edu

## 6.1 Introduction

Microscopy, in terms of its impact on modern society, has not only led to important discoveries but has inspired entire fields of modern science. The development of the microscope has revolutionized modern thought, spawned the field of cellular biology, guided development of the semiconductor, and provided visual evidence of a concept that was once termed “atomos”; *i.e.*, the classical era conceptualization of the atom, as originally proposed by the Greek philosopher Democritus. The ability of the microscope to resolve microscopic particles and colloids has provided humankind with direct, visible proof of scientific concepts and theories proposed by both early and modern scientists alike.

Today's microscope has evolved from a series of focused lenses into an advanced *in situ* laboratory which offers the resolution of individual atoms, imaging under environmentally controlled conditions, and both structural and elemental material analysis. The assortment of microscopes available to the modern researcher include optical instruments such as the visible light microscope, the fluorescence microscope, and the confocal microscope; an array of electron, ion, and X-ray microscopes; and the atomic force microscope.<sup>1</sup> This diverse range of instrumentation offers an arsenal of techniques

available for the characterization of materials which span broad lengths of scale. Yet, the resolution and information provided by each instrument varies; thus, it is essential to develop an understanding of the capabilities and limitations of each instrument for proper analysis of a specimen of given dimensions.

Colloids, or microscopic particles which range in size from 1 nanometer to 1 micron in diameter, offer a promising means of controlling fluid flow properties, drug delivery, gas separation, and catalytic performance, as noted by their increased use in products and emerging technologies. Modern synthetic routes towards colloid production now offer the size-tunable control of particle diameter over the entire length scale of the colloidal spectrum. Yet this particularly broad size range, which spans from the nanoscale to the microscale, requires the application of an advanced series of microscopic instrumentation for adequate material characterization. This chapter will provide a basis for the characterization of colloidal materials *via* microscopy.

## 6.2 A Brief History of Microscopy

Microscopy offers a glimpse into a world which remains unseen by the naked eye. While the heavens were the focus of early astronomers – who employed telescopic lenses to view neighboring planets in the 1500s – bacteria, cells, and fungi were the focus of study for early scientists and biologists in the 1600s. Utilizing early techniques in lens grinding, light harvesting, and empirical lens matching, scientists uncovered a microscopic living-world on the surface of every material. This area of research evolved into the field of microscopy, an area of study which has improved our understanding of the natural world by bridging the advances of engineering, science, and technology.

Since ancient times mankind has understood that curved glasses could bend light and magnify images.<sup>2</sup> However, the possibility of the microscope wasn't realized until Antonie van Leeuwenhoek, a lens grinder by trade, began using lenses to examine insects, plants, and inorganic materials. His discovery of the existence of microscopic organisms in common pond water not only sparked the field of microscopy but also microbiology, a field which is still evolving to this day. The modern visible light microscope, the instrument that allowed van Leeuwenhoek to view microbes in pond water, can now be engineered to offer a maximum resolution of roughly 250 nm.

The observations established during the scientific revolution ultimately provided the framework necessary for the development of the mathematics, engineering, and manufacturing which led to the standardization of early light microscopes during the industrial revolution. Economic competition drove industrially minded innovators, such as Carl Zeiss, to employ pioneering optical scientists to develop standard practices for the grinding and measurement of lenses. Ernst Abbe, a principle scientist in the field of

optics, rapidly improved the understanding and resolution of early compound microscopes by accurately measuring and documenting the dimensions of each lens produced by the Zeiss Optical Works Company. Through his research, Abbe was able to calculate the diffraction limit of the light microscope, formulate a standardized system of lens classification, and develop early methods of resolving common optical aberrations.

Soon however, manufacturers approached Abbe's proposed diffraction limit, as resolution is ultimately restricted by the wave-like diffraction of light around small particles and holes. Much like ripples on the surface of a pond, light is observed to travel in waves which can bend around topographical features, often interacting both constructively and destructively with neighboring waves to form striated interference patterns. Waves of a given length scale, as defined by their characteristic peak-to-peak dimension known as wavelength ( $\lambda$ ), are diffracted by features with dimensions roughly half the size of the wave (*i.e.*, particle diameter  $\sim\lambda/2$ ). Thus, visible light, which possesses an average wavelength of 550 nm, is diffracted by small features roughly 250 nm in size. This phenomenon ultimately poses a natural barrier to the analysis of small microscopic specimens such as colloids, which range in size from a few dozen angstroms to several hundred nanometers.

In the early 20th century, scientists hypothesized that nanoscale features could be resolved by the utilization of probes which possessed wavelengths shorter than that of visible light. Louis de Broglie theorized that the electron possessed both a particle and wave-like nature, with a wavelength vastly shorter than that of visible light. This led to the development of the first transmission electron microscope (TEM) by Ernst Ruska and Max Knoll in 1931 and allowed the observation of specimens smaller than that originally achieved with the light microscope.<sup>3</sup> In 1938 von Ardenne<sup>4</sup> added a series of scanning coils to the electron microscope to produce the first scanning transmission microscope (STEM). Shortly thereafter, Zworykin produced the first scanning electron microscope in 1942, which allowed examination of thick samples *via* the collection of backscattered and secondary electrons.

Over the course of the next few decades, improvements in accelerating voltage, vacuum systems, magnetic lenses, and the electron source greatly improved the resolution of the electron microscope (EM). Today's high-end EMs offer sub-angstrom resolution – allowing the observation of individual atoms. Additionally, researchers have extended the engineering of the electron microscope to develop advanced *in situ* sample holders which allow material observation under controlled environmental conditions including temperature control, atmospheric gas selection, pressure control, and even the incorporation of cryogenic sample holders. While great advances have been made in the resolution power of the microscope, today, broader technological development has been focused on engineering a diverse spectrum of microscopes including the atomic force microscope and the helium ion microscope.

Microscopy offers a unique method of characterizing colloids as it allows direct analysis of their size, morphology, and packing at length scales which encompass their full spectrum of size. Additionally, through proper instrumental selection, one can reveal not only the structure and morphology of colloids with sub-nanometer resolution, but perform simultaneous in-column analysis with various compositional techniques. However, with such a diverse selection of tools at the disposal of the modern researcher, an adequate review of the capabilities offered by each instrument is required. This chapter highlights the utilization of microscopy to characterize colloidal particles ranging in size from *ca.* 1 nm to 1  $\mu\text{m}$  and above.

### 6.3 Narrowing our Focus – The Specimen: Colloids

Colloids, along with solutions and suspensions, fall into the general classification of matter known as homogeneous mixtures. Homogeneous mixtures include any multiphase combination of matter which is suspended and well mixed. A homogeneous mixture is sub-classified as either a solution, a colloid, or a suspension based upon the size of the suspended phase and its degree of stability. Solutions, such as air and seawater, refer to well-mixed phases containing particles and ions less than 1 nm in size. Colloids including milk, clouds, and paints, refer to stable mixtures containing microscopic suspended particles which remain stable indefinitely. Lastly, suspensions are defined as mixtures with particles greater than 1 micron in size which often precipitate over time, gradually producing a two-phase heterogeneous mixture.

Colloidal suspensions are not solely defined as a solid in a liquid but also include any multiphase combination of matter which is suspended and well mixed. Common examples of colloids include clouds, latex polymer particles, silica ( $\text{SiO}_2$ ) colloids, natural opals, and oil emulsions. Colloids are often sub-classified based upon the phases which are contained within the colloidal mixture; these classifications include foams, which incorporate a gas dispersed in either a liquid or a solid; emulsions, which pertain to liquids dispersed in a liquid or solid; sols, which consist of solids dispersed in a liquid or solid; and finally aerosols, which can include either liquids or solids dispersed in a gas. The International Union of Pure and Applied Chemistry (IUPAC) defines a colloid as a stable, multiphase mixture in which one phase possesses a characteristic dimension ranging from 1 nm to 1  $\mu\text{m}$  in size.<sup>5</sup> However, the term colloid is more generally used by researchers to describe any microscopic particle which is either dispersed within a fluid medium or deposited as a quasi-crystalline dried colloidal powder.

Modern synthetic techniques allow chemists and engineers to tailor the size, concentration, and surface chemistry of a colloidal mixture on the microscopic scale as a means of tuning the macroscopic properties required for a given commercial application. Colloids have been manufactured for use in numerous products ranging from coatings to synthetic rubbers, paints, fabrics, inks, catalytic supports, cosmetics, and food additives.

Driven by the need for increasingly small nanotechnologies, researchers have recently extended the boundaries of colloidal synthesis to develop routes which facilitate the production of increasingly small, monodisperse colloidal suspensions and, more recently, colloidal crystal (CC) powders. Thus, microscopy has proven to be a vital characterization technique as it provides the modern colloidal scientist with direct analysis of the size, morphology, and packing of these microscopic particles.

## 6.4 Polymer Colloids

The synthetic production of polymer colloids provides the largest and most economically efficient route towards the mass production of commercial colloidal additives. Polymerization offers a versatile technique for colloid synthesis as it allows precise control of particle size by tuning stirring rates and solution parameters during the manufacture of large volumetric batches of colloids. Additionally, polymer colloids have been a primary area of research and development in recent decades as they offer an environmentally safe alternative to solvents as a means of tuning solution properties. These benign additives can be readily mixed into a system to alter parameters such as viscosity, dilatancy, elasticity, and storage moduli, while solvents are often costly and in some cases, caustic.

The most common technique utilized for the synthesis of polymer colloids is emulsion polymerization, in which suspended monomer colloids are polymerized *via* a free radical polymerization reaction under vigorous stirring. This technique is the basis for the commercial production of synthetic latexes such as styrenes, which are polymerized within an aqueous medium and provide a synthetic alternative to natural colloidal latex rubbers.<sup>6</sup> Emulsion polymerization offers a versatile approach to colloid synthesis as it provides several tunable handles for the precise control of particle size. These handles include variation of the relative concentrations of monomer, initiator, surfactant, and stabilizer. Conventional emulsions utilize low emulsifier concentrations (*i.e.*, 1–3%) to produce opaque latexes with particle sizes on the order of 1 µm and above. Similarly, mini-emulsion polymerization reactions form polymer colloids ranging in size from *ca.* 50 to 500 nm in diameter by employing moderate emulsifier concentrations (*i.e.*, 1–5%). Lastly, micro-emulsion techniques utilize high emulsifier concentrations (*i.e.*, 15–30%) to produce translucent colloidal mixtures with particles *ca.* 100 nm in diameter and below.<sup>7</sup>

Possibly the best demonstration of the mutual impact that can be achieved through collaboration between the fields of microscopy and colloidal science was the polymerization and application of emulsified colloidal space beads as calibration standards during the late 20th century.<sup>8</sup> The immense technological advancement achieved by the invention of the electron microscope (EM), and its rising application in the characterization of products for the growing semiconductor market, necessitated an innovative means of developing standard reference materials. As the electron

microscope market began to rapidly expand during the 1970s and 80s, new reference materials were required that could be used for instrument calibration and the correction of image distortions.

While mechanical techniques for the fabrication of calibration standards often provided significant errors, emulsified polymers offered a means of producing size-tunable spherical reference particles which could accurately meet the calibration needs of the growing microscope market.<sup>9</sup> However, slight variations in the morphology of terrestrial batches of emulsified colloids prevented their utilization as early calibration standards.<sup>10</sup> Thus, researchers took the field of colloidal science into outer space, employing low gravity as a means of synthesizing highly spherical, emulsified colloids on board Space Shuttle Columbia. These batch-sized quantities of mono-disperse polymer colloids, up to *ca.* 10 µm in diameter, became the first commercial product to be produced in space and have since been adopted by the National Bureau of Standards as a reference material for microscopic instrument calibration.<sup>11</sup>

This multidisciplinary interaction between industry, academia, and government institutions demonstrates the collaborative possibilities that can be achieved through interaction by combined efforts spanning multiple institutions. The value-added impact of emulsion polymerization will likely extend its use as a key method employed for the commercial synthesis of suspensions which span the entire colloidal spectrum as defined by the IUPAC. Additionally, microscopy will remain a key characterization technique in the analysis of colloidal nanoparticles as is demonstrated today through current research focused on the synthesis of emulsified colloids with unique anisotropic morphologies<sup>12–15</sup> and Janus particles<sup>16–21</sup> – which offer multimodal surface chemistries.

## 6.5 Natural Opals and Colloidal Silica

Colloids are not solely a synthetic commercial additive recently conceived by modern polymer chemists. Their development has been inspired by the natural formation of mineralogical opals which were once coveted by ancient civilizations and whose counterfeits continue to trick the eye of the modern gem collector. Natural opals, capable of the optical diffraction of light, quickly attracted the attention of early miners by their ability to scatter light and produce a brilliant rainbow effect.<sup>22</sup> While the phenomenon responsible for this remarkable coloration was originally debated in early literature, the application of a scanning electron microscope conclusively revealed this natural rainbow effect was a result of the optical diffraction of light along the digitated surface of naturally occurring ordered colloidal silica arrays (dia.  $\sim$ 150–400 nm).<sup>23,24</sup>

Inspired by these naturally occurring colloidal opals, researchers sought a means of developing laboratory-grown colloidal silica ( $\text{SiO}_2$ ) nanospheres. Colloidal silica provides an attractive synthetic alternative to

emulsified polymer colloids as it is a stable inorganic oxide capable of withstanding elevated temperatures. The first synthetic routes to colloidal silica were patented in 1951,<sup>25</sup> unfortunately, these unstable sols were highly susceptible to gelation upon drying but were gradually stabilized over the years through a series of synthetic alterations.<sup>26–28</sup> A synthetic route developed in 1968, commonly referred to today as the Stöber process, would eventually become recognized as a preferred method of synthesis.<sup>29</sup> This technique utilizes a modified sol-gel process – which employs an alkali buffer in a solution of water and alcohol – to control the hydrolysis and condensation of tetraethyl orthosilicate (TEOS) under vigorous stirring. The Stöber process facilitates the synthesis of monodisperse colloids which range in size from a few hundred nanometers to a few microns in diameter and has now been utilized for decades in diverse applications including catalysis, gas adsorption, photonics, and for the templating of porous materials.<sup>30</sup>

In recent decades researchers have pushed for the development of ever smaller inorganic silica colloids. This has been accomplished through modified Stöber techniques which utilize zwitterionic amino acid buffers in combination with TEOS to produce monodisperse silica colloids ranging in size from *ca.* 10–100 nm.<sup>31</sup> Much like emulsion polymerization, colloid size is tuned in these modified recipes through control of synthetic parameters including solution stir rates, SiO<sub>2</sub> precursor concentration, and pH control *via* the manipulation of buffer concentration.<sup>32</sup> Additional processing steps now allow surface decoration of the resulting colloids, the production of core-shell nanoparticles,<sup>33–35</sup> inverse opals, and even the production of hollow colloids,<sup>36–41</sup> as achieved through sacrificial colloidal templating and etching. These silica-derived colloidal nanoparticles have been the subject of increasing academic research in the study of material synthesis, particle packing, self-assembly, microfluidics, and rheology – through which microscopy has played an important role in analysis and characterization.

### 6.5.1 Colloidal Crystals

Both polymer<sup>42</sup> and silica colloids have been increasingly studied in recent years for the production of colloidal crystals (CCs)<sup>43</sup> through self-assembled drying processes.<sup>44</sup> Colloidal crystals are often fabricated into either three-dimensional bulk powder matrices or stacked on substrates as two-dimensional thin film arrays.<sup>45</sup> The resulting CC product can be engineered through manipulation of the drying rate, coating speed, solids content, and solvent parameters as a means of tuning CC product properties.<sup>46</sup> These promising synthetic opals have proven to be advantageous for use as adsorbents, photonic crystals, thin films, and as nano-molds for the replication of templated nanomaterials.<sup>47–49</sup> Once again, microscopic instrumentation, particularly confocal and electron microscopes, have proven vital to the study and characterization of the intricate nanoarchitecture presented by these colloidal crystal materials.

Colloidal crystals are prepared by drying an as-made colloid solution along a substrate in order to disperse the individual particles into a porous, three-dimensionally ordered crystalline matrix.<sup>50</sup> This process, often referred to as convective deposition or evaporative self-assembly, provides a rapid means of producing bulk quantities of colloidal crystal powder and thin CC films.<sup>51</sup> During evaporation of the colloidal suspension, the microscopic colloid particles are collected by surface tension along the meniscus of the advancing drying front and are pinned to the substrate to form ordered crystalline arrays.<sup>52</sup> Through synthetic manipulation of the diameter of these colloidal nanospheres, researchers are capable of tuning product properties including surface area, pore size, and packing structure of the CC product. A reduction in colloid diameter facilitates an astonishing increase in the surface area of the resulting powder, while increasing the colloidal dimension results in an enlargement of the interconnected pores, as demonstrated through electron microscopy.<sup>53–55</sup>

Extensive research is currently being conducted to optimize the self-assembly process of colloidal crystals in order to develop new methods of autonomously fabricating nanostructures. CCs can be engineered to pack in the hexagonally closed packed (HCP) arrangement,<sup>46</sup> face centered cubic (FCC) packing arrangement,<sup>56</sup> or in a quasicrystalline manner,<sup>57</sup> which is often rarely observed in nature. Researchers have also shown the ability to selectively engineer defects in arrays of thin, colloidal crystal films with potential applications in the photonic crystal industry.<sup>58–60</sup> In more recent studies, researchers have broadened the diversity of the CC materials palette by mixing colloidal solutions of varying diameter to produce interdigitated colloidal crystal assemblies which mimic the complex atomic packing patterns observed in nature.<sup>61–64</sup> Now, additional material processing even allows replication of the CC structure to produce inverse opals,<sup>65–68</sup> classified as either three-dimensionally ordered mesoporous (3DOM) or macroporous (3DOM) materials, through the application of CCs as sacrificial nanomolds.<sup>69–74</sup> This vast array of colloidal crystals is highly dependent upon the application of scanning and transmission electron microscopy as a means of characterizing their crystal structure, packing defects, and for the assessment of porosity.

### 6.5.2 Characterization of Colloids

After synthesis of a colloidal product, material characterization is required in order to evaluate the success of the synthetic process and the resulting packing arrangement. Colloid diameter, particle size distribution (PSD), morphology, particle aggregation, and packing provide key parameters which are vital to the assessment of a colloidal suspension. Microscopy offers a direct means of imaging the as-made colloidal products and facilitates accurate analysis of these key parameters, which often remain elusive to detection with alternative instruments and techniques. Additionally,

through the application of statistical image processing techniques, colloidal scientists can employ microscopy as a means of analyzing large numbers of colloids with statistical confidence.

While light scattering techniques offer potential routes toward the characterization of colloid size and PSD, they often lack the ability to differentiate between primary particles and secondary particle aggregates. Additional difficulties arise in the statistical analysis of light scattering data collected from colloids which contain broad size distributions. This is particularly problematic as most colloidal materials flocculate in solution, resulting in the formation of large particle aggregates which contain hundreds or thousands of colloids.<sup>75</sup> Furthermore, light scattering is generally unable to assess colloid morphology or resolve the dimensions of anisotropic colloidal particles.<sup>76</sup> Thus, the microscopic and nanoscopic nature of colloids and colloidal crystals necessitates the application of microscopy as an accurate means of characterizing colloid diameter, morphology, and flocculated colloidal aggregates.

Through application of an appropriate microscope and the use of statistical processing software (*e.g.* ImageJ), colloid diameter ( $d_i$ ), the number average diameter ( $d_n$ ), and standard deviation ( $\sigma$ ) – as defined as the root-mean-squared deviation from the mean value of a given colloidal specimen – can be calculated (see eqn (6.1) and (6.2)).<sup>77</sup> Additionally, the accurate characterization of colloids requires analysis of large numbers ( $n_i$ ) of individual particles, a task which is often best achieved through direct imaging *via* microscopy. However, each microscope offers variable degrees of resolution, environmental limitations, and operational restrictions which implores careful consideration to determine which instrument is best suited for the analysis of a given colloidal specimen.

$$d_n = \frac{\sum n_i d_i}{\sum n_i} \quad (6.1)$$

$$\sigma^2 = \frac{\sum n_i |d_i - d_n|^2}{(\sum n_i) - 1} \quad (6.2)$$

Colloid characterization can be accomplished through select use of a spectrum of microscopes including the visible light microscope, confocal microscope, electron microscope, ion microscope, and the atomic force microscope (see Figure 6.1). These instruments provide the modern colloid researcher with direct, visible images of colloids which can be used to assess particle size and morphology. However, as each instrument utilizes a unique series of probes, each with variable resolution, a review of modern microscopy is required to aid the colloidal researcher during characterization of a colloidal product. This process is preferably accompanied by hands on experience with an instrument and a general reflection of the artistic nature of microscopy.

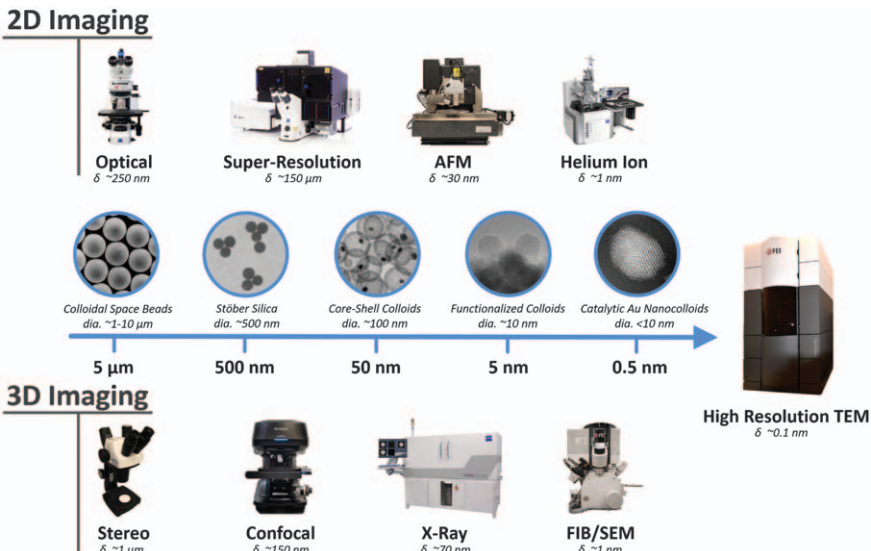


**Figure 6.1** The “spectrum” of microscopes facilitates imaging covering all microscopic length scales. Common instruments offering two-dimensional imaging include optical, super-resolution, AFM, and  $\text{He}^+$  ion microscopes. Three-dimensional microscopes include stereo, confocal, X-ray,  $\text{Ga}^+$  ion, and SEMs. Additionally, high resolution transmission electron microscopes offer advanced imaging capabilities which facilitate atomic scale resolution. Images include colloidal space beads,<sup>8</sup> Stöber silica,<sup>29</sup> hollow core-shell colloids,<sup>36</sup> functionalized  $\text{SiO}_2$  colloids decorated with  $\sim 10$  nm zirconia crystals,<sup>78</sup> and catalytic gold colloids demonstrating atomic fringes.<sup>79</sup> Stöber silica image reproduced from ref. 29 with permission from Elsevier, Copyright 1968. Hollow core-shell colloids image reproduced from ref. 36 with permission from the Royal Society of Chemistry. Catalytic Au Nanocolloids image reproduced from ref. 79 with permission from John Wiley and Sons, © 2017 Wiley-VCH Verlag GmbH & Co. KGaA, Weinheim. Super-Resolution image reproduced from [https://commons.wikimedia.org/wiki/File:ZEISS\\_ELYRA\\_PS.1\\_3D\\_Superresolution\\_Microscope.jpg](https://commons.wikimedia.org/wiki/File:ZEISS_ELYRA_PS.1_3D_Superresolution_Microscope.jpg), under the terms of the CC BY 2.0 licence, <https://creativecommons.org/licenses/by/2.0/deed.en>. X-Ray Microscope image reproduced from [https://commons.wikimedia.org/wiki/File:ZEISS\\_Xradia\\_520\\_Versa\\_X-ray\\_microscope\\_\(12286854824\)\\_\(2\).jpg](https://commons.wikimedia.org/wiki/File:ZEISS_Xradia_520_Versa_X-ray_microscope_(12286854824)_(2).jpg), and Helium Ion Microscope image reproduced from [https://commons.wikimedia.org/wiki/File:ORION\\_NanoFab\\_-\\_Helium\\_Ion\\_Microscope\\_\(8410606251\).jpg](https://commons.wikimedia.org/wiki/File:ORION_NanoFab_-_Helium_Ion_Microscope_(8410606251).jpg), under the terms of the CC BY 2.0 Share-Alike licence, <https://creativecommons.org/licenses/by-sa/2.0/deed.en>.

## 6.6 Basics of Microscopy

### 6.6.1 Microscope Probes

Microscopes employ focused incident probes which interact with a specimen of interest and subsequently collect the resulting signals emitted by this interaction. In more abstract terms, the characterization of a material

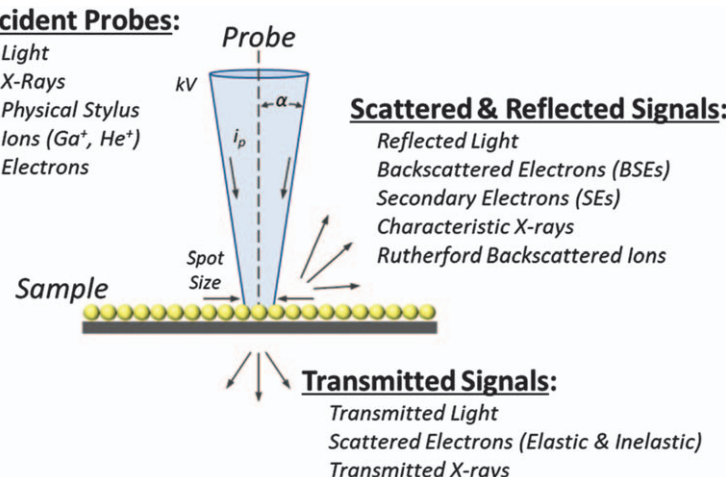


**Figure 6.2** Sample–probe interaction and common signals which can be generated during this interaction.

requires: (i) the selection and formation of an incident probe, (ii) interaction of the probe with a material under a controlled environment, and (iii) the collection and processing of the resulting signals generated by this interaction (see Figure 6.2). A diverse series of probes including infrared radiation, visible light, monochromatic lasers, X-rays, ions, and electrons have been utilized for the analysis of microscopic specimens. The wavelength and energy of each probe interacts uniquely with the atomistic and molecular components of the sample to yield information and characteristic material properties including images, elemental composition, atomic spatial distribution, atomic structure, and morphology.<sup>80</sup> However, in order to produce and obtain this information, the probe must first be generated and focused with a series of apertures, lenses, and optics in order to produce sharp, magnified images with limited aberrations.

### 6.6.2 The Wave-like Nature of Light, Electrons, and Electromagnetic Radiation

Visible light, the principle probe of early microscopes, encompasses only a small range of energies along a much larger electromagnetic spectrum (see Figure 6.3). This continuous spectrum of radiation includes radio waves, microwaves, and infrared radiation on one end, while gamma rays, X-rays, and UV radiation reside on the other end of the spectrum. Electromagnetic radiation can be harnessed as probes in many forms to image, detect, and characterize objects with dimensions extending over an enormously vast size range – as each probe interacts uniquely with various atomistic and molecular components of the object to yield characteristic information about the specimen of interest.

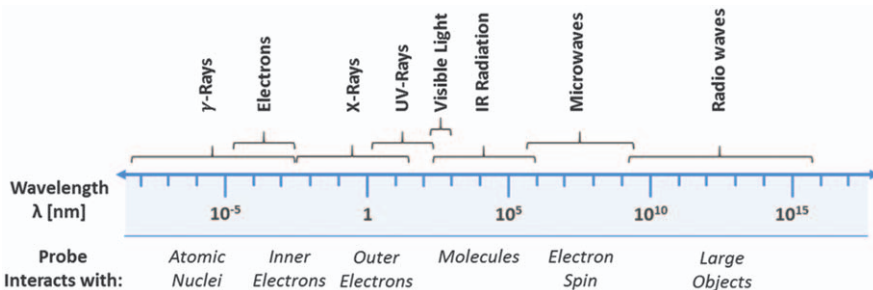


**Figure 6.3** The spectrum of wavelengths possessed by electromagnetic radiation and electrons.

When traversing the electromagnetic spectrum, radiation is found to have an inverse relationship between wavelength and energy. High energy radiation correlates to short wavelengths, while low energy radiation correlates to long wavelengths. This facilitates interaction with matter on both small and large length scales. Massive objects such as planets and stars (with dimensions on the order of  $\sim 10^9$  m) can be detected with radio telescopes, which harness radio waves with long wavelengths. Similarly, extremely small objects such as atoms, colloids, and nanocrystals (on the order of  $\sim 10^{-9}$  m) can be imaged and detected with probes possessing short wavelengths. Visible light, which possesses moderately long wavelengths ranging from  $\sim 400$ – $750$  nm, interacts with outer shell electrons to facilitate imaging of features as small as  $\sim 250$  nm. More energetic probes, such as X-rays and electrons, possess short wavelengths (*ca.* 0.01–1 nm) and can interact with the inner electrons of an atom to provide increased resolution.

In microscopy, the interaction of electromagnetic probes with matter can generally be classified into six categories: (i) absorption, (ii) transmission, (iii) reflection, (iv) refraction, (v) diffraction, and (vi) scattering. Absorption entails the conversion of an incident beam into internal energy which is retained by the sample. Transmission involves the transfer of an incident probe through a sample which is then re-emitted on the opposite side. Reflection occurs as the probe interacts with the surface of the sample and is redirected at a new characteristic angle. Refraction involves the transmission of the beam through the sample but is diverted at a characteristic angle upon interaction with the sample. Diffraction involves a wave-like redirection of a beam, often resulting in a constructive and destructive interference. Lastly, scattering entails the diffuse reflectance and dispersion of light in various directions upon interaction with the sample.

All six forms of light-matter interaction play a role during the microscopic analysis of a sample and can be used to obtain information about a specimen. In general, microscope operation is classified into two categories: transmission mode and reflection mode. Transmission mode places the sample in between the probe's source and the detector; sample information is then a result of the interaction of the probe with the sample as it transmits

through the material. Reflection mode involves the analysis of a probe which is redirected upon interaction with the sample. Both techniques require proper focusing and collection of the beam through a series of lenses in order to magnify an image. This is accomplished *via* refraction in the optical microscope and later achieved with electrostatic lenses in electron microscopes.

### 6.6.3 Lens Basics

The visible light microscope has traditionally utilized a series of curved glasses (*i.e.*, lenses), to refract or bend visible light and magnify an image; a concept which has inspired the development of the electrostatic lens for the electron microscope. When light transmits at an oblique angle (*i.e.*, an angle other than  $90^\circ$ ) from one medium to another, it refracts within the material at a characteristic angle related to the refractive index of each medium. This phenomenon was originally adapted in ancient times to ignite fires with the application of crude burning glasses and later used to harness light and magnify images with the application of finely engineered lenses.

Visible light microscopes employ curved lenses with either positive curvature, negative curvature, or a combination of both geometries to focus or disperse light *via* refraction. Collimated light, or parallel rays of light, can be focused to a given focal point as defined by  $f$ , with utilization of a convex lens. Convex lenses utilize positively curved surfaces, or surfaces which protrude outward, to bend light to a focal point opposite that of the light source (see Figure 6.4). Conversely, concave lenses utilize negatively curved surfaces, which are depressed inwards towards the lens.

The combination of multiple simple lenses aligned along a central optical axis is the basis for the compound lens, which is configured to harness visible light from a specimen using an objective lens and then magnify the image with an eyepiece lens (see Figure 6.5). These basic concepts are the central techniques employed in all modern visible light microscopes which, with proper engineering to avoid optical aberrations, can facilitate the

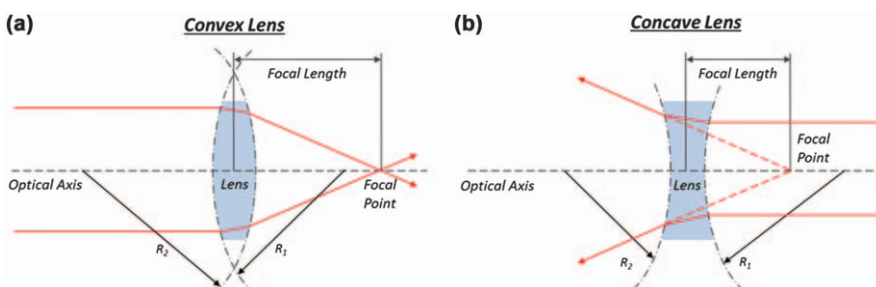


**Figure 6.4** Light refraction through (a) a convex lens *versus* (b) a concave lens.

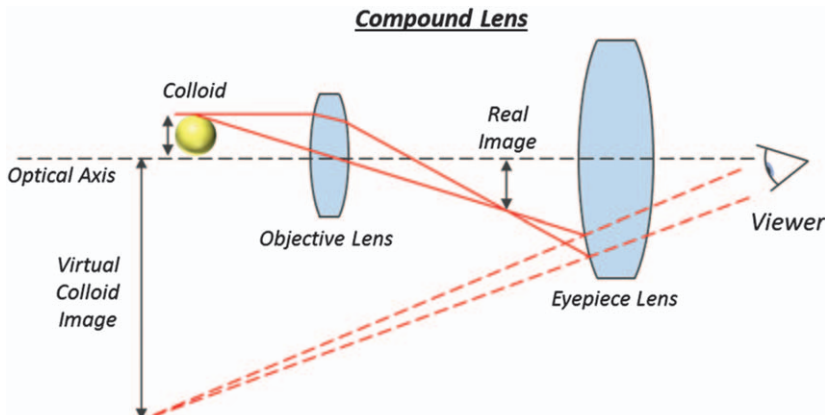


**Figure 6.5** A generalized depiction of the compound lens during characterization of a colloid.

resolution of features as small as  $\sim 250$  nm. However, this has only been accomplished through significant research and development to limit optical aberrations including spherical, chromatic, coma, and astigmatisms.

#### 6.6.4 Aberrations

Despite vast leaps in the knowledge and technology utilized to finely mill and grind lenses with precise curvature, aberrations – or optical defects associated with the interaction of the probe and lens – still hinder the performance of modern optical systems. Aberrations generally occur when individual rays are not focused to converge upon a single incident point, but rather come into focus at either different focal lengths or azimuthal angles about the optical axis. Common examples include spherical and chromatic aberrations, aperture diffraction, astigmatisms, and coma aberrations. Each aberration acts to distort the size and shape of the probe, ultimately limiting optical resolution.

In order to obtain high resolution of nanoscale features, small probe sizes are required. In the electron microscope, the probe size ( $d_p$ ) is a function of the Gaussian probe diameter ( $d_G$ ) and the size of each aberration disk including: the spherical aberration disk ( $d_s$ ), chromatic aberration disk ( $d_c$ ), and the diffraction disk ( $d_d$ ), as shown by eqn (6.3). Thus, it is necessary to engineer optical systems that incorporate measures which mitigate aberrations as much as possible.

$$d_p = (d_G^2 + d_s^2 + d_d^2 + d_c^2)^{\frac{1}{2}} \quad (6.3)$$

Spherical aberrations occur as incident light rays near the edge of the lens are refracted or bent at a much higher angle than those which are paraxial to the center point of the lens (see Figure 6.6a). This causes image distortion

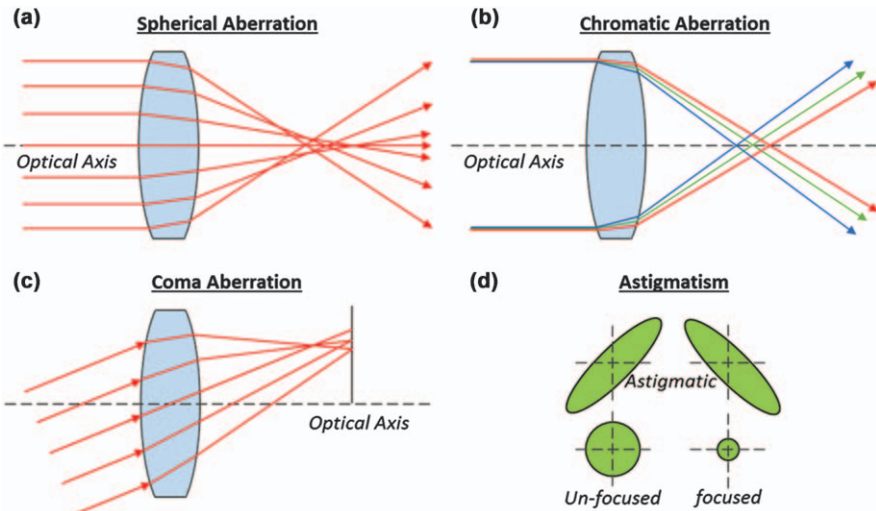


**Figure 6.6** Illustration of common optical aberrations including: (a) a spherical lens aberration; (b) a chromatic lens aberration; (c) a coma lens aberration; and (d) an optical astigmatism.

as the central, paraxial rays, are focused at a focal length which is greater than the focal length of the outer, more peripheral, rays – those that are focused by the edge of the lens. Spherical aberrations hinder both visible light microscopes and electron microscopes. The effect can be limited by reducing the diameter of the lens in visible light microscopes and by employing advanced spherical aberration correctors in transmission electron microscopes. In the electron microscope, the spherical aberration disk is related to the coefficient of spherical aberration ( $C_s$ ) and angle of deflection ( $\alpha$ ) of the outer electrons (see eqn (6.4)). Spherical aberrations still remain a challenging aberration to correct in practice.

$$d_s = \frac{1}{2} C_s \alpha^3 \quad (6.4)$$

Chromatic aberrations occur when incident probe rays of varying wavelengths and energies are focused at different focal lengths along the optical axis (see Figure 6.6b). This effect often causes a ring of distorted colors about a feature in visible light microscopes and is observed as a distorted blur around features imaged with an electron microscope. Chromatic aberrations are limited by incorporating monochromators or apochromatic lenses. Apochromatic lenses employ a series of materials of differing refractive indices to focus light rays of various energies to a single focal plane in the visible light microscope. Monochromators act to filter out probe rays with energies which significantly deviate from the selected probe energy in the electron microscope. The aberration disk associated with chromatic

aberration ( $d_c$ ) is related to the coefficient of chromatic aberration ( $C_c$ ), the angle of convergence ( $\alpha$ ), the incident electron energy ( $E_0$ ), and the electron energy spread ( $\Delta E$ ) as shown by eqn (6.5).

$$d_c = C_c \alpha \left( \frac{\Delta E}{E_0} \right) \quad (6.5)$$

Coma aberrations once plagued early optical instruments but are largely eliminated in today's microscopes. Coma aberrations occur when rays are incident upon a lens at an oblique angle relative to the optical axis (see Figure 6.6c). When directed at a lens at a high angle of incidence, the refracted rays are shifted in a linear fashion away from the optical axis. In optical instruments, coma aberrations are distinguished as a cone or tail shape which trails behind a given feature. Comas are mitigated by utilizing apertures and precision engineering to properly align the incident beam along the optical axis, perpendicular to the lens.

Astigmatisms present another common aberration in microscopic instruments. Astigmatisms occur when lenses unevenly bend an incident beam at varying azimuthal angles oriented perpendicular to the optical axis (see Figure 6.6d). This creates an elongated distortion of the image as if it were stretched in one dimension and compressed in another. Astigmatisms can be mitigated in the visible light microscope by properly milling the lens to a precise and uniform curvature, whereas the electron microscope employs a quadrupole lens, referred to as a stigmator, to correct for the astigmatism.

### 6.6.5 Apertures

In addition to lenses, microscopes utilize an aperture, or opening of select dimension, to collimate and regulate the amount of light collected by the lens system. Apertures control the depth-of-focus viewed by the microscope, provide a handle for image brightness, and can be used to mitigate optical aberrations. Aperture construction is typically achieved by either milling a series of circular holes of fixed dimensions into a monolithic plate, which can then be interchangeably positioned in the beam's pathway, or from a single size-variable diaphragm to facilitate continuous diameter adjustment. Alternatively, some optical systems lack a separate stand-alone aperture; in these systems, the aperture is effectively defined by the diameter of the lens and lens column, as these dimensions ultimately govern light collection and collimation.

Light collimation is achieved by restricting the amount of diffuse light which is collected by the microscope at large oblique angles relative to the lens. Small apertures act to collimate light by harvesting only paraxial and parallel light which is oriented at or near the central optical axis and by blocking light oriented at moderate-to-large angles relative to the optical axis. Small apertures offer large depths-of-focus and allow features spanning

a wide focal length to come into focus simultaneously; however, this is achieved at the cost of brightness and resolution. Conversely, by increasing the diameter of the aperture, additional light is collected and higher resolutions can be obtained; this is achieved at the expense of a reduced depth-of-focus and the introduction of additional optical aberrations. Therefore, a tradeoff exists between depth-of-focus, resolution, and overall image quality.

### 6.6.6 Magnification

Lenses facilitate the magnification or enlargement of features oriented along the focal plane; that is the plane of focus oriented perpendicular to the optical axis at a distance,  $f$ , from the lens. Magnification provides a quantitative measure which relates the apparent size of the features in an image to the actual size of the features within the specimen (see eqn (6.6)). The magnification ( $M$ ) of a single lens is given by the ratio between the lateral dimension of an imaged feature ( $d_i$ ) and the dimension of the actual colloidal feature ( $d_c$ ). When positive, magnification provides an enlargement of the image, while negative magnification values correlate to a reduction in the size of the image. While an image can be magnified or stretched to increasingly large dimensions, a point is reached at which no additional information is obtained and image sharpness is merely distorted by further magnification. Increasing magnification beyond the resolving power of the instrument is often termed empty or hollow magnification.

$$M = -\frac{d_i}{d_c} \quad (6.6)$$

### 6.6.7 Resolution

Resolution defines the smallest point-to-point lateral dimension that can be distinguished in an image and is often used to provide a quantifiable measure of the maximum optical performance that can be achieved by an instrument. While the human eye is capable of resolving features on the order of  $\sim 0.1$  mm (*i.e.*,  $100$   $\mu\text{m}$ ), colloids remain unobservable as even the largest of colloids (dia.  $\sim 1.0$   $\mu\text{m}$ ) are at least two orders of magnitude smaller than that resolved by the eye. However, modern versions of the visible light microscope, which has stemmed from the instrument that van Leeuwenhoek first used to view pond microbes, are now capable of resolving features on the order of a few hundred nanometers in size (*ca.*  $0.3$   $\mu\text{m}$ ). Thus, a magnification of approximately  $100\times$  allows researchers to distinguish large colloids from their neighbors (dia.  $\sim 1.0$   $\mu\text{m}$ ), whereas small colloids (dia.  $< 250$  nm) and colloidal surface features remain elusive to observation with the visible light microscope due to the diffraction barrier.

### 6.6.8 Diffraction Limit of Resolution

While modern visible light microscopes provide considerable image magnification and enhanced resolution of microscopic features, their resolution power is fundamentally restricted by the diffraction of visible light through apertures, small features, and holes. Diffraction occurs when a wave interacts with a narrow hole or slit, creating an interference wave pattern due to the constructive and destructive interaction of the emerging wave front (see Figure 6.7). When shining a light through a narrow aperture at a surface, the interference of diffracted light rays creates a ripple-like effect which forms a central bright disk surrounded by a series of alternating bright and dark concentric rings. This ripple effect, known as an Airy disk, was first explained by Sir George Airy when shining visible light through a lens and aperture system. The dimensions of a diffraction pattern are related to the geometry and operating parameters of a microscope and ultimately limit the maximum resolution that can be obtained by an optical instrument.

The size of the diffraction disk was first calculated by Ernst Abbe in 1873 (see eqn (6.7)).<sup>81</sup> Abbe theorized that a microscope magnifies a field of individual point-sources of light spread across the surface of a specimen to create an enlarged image. When magnified through a lens and aperture, each individual point-source projects a diffraction pattern with a central spot size ( $d_d$ ) governed by the wavelength of light ( $\lambda$ ), the refractive index of the projection medium ( $n$ ), and the aperture angle – which is defined as the half-angle subtended by the aperture ( $\theta$ ). The refractive index and aperture angle is often referred to as the numerical aperture, NA, when labeling objective lenses. Abbe demonstrated that in order to resolve neighboring features upon diffraction by the objective lens, the diffracting disk projected by each point-source of light must not overlap extensively. Therefore, optical resolution is improved by minimizing the size of the diffraction disk.

$$d_d = \frac{\lambda}{2n \sin \theta} = \frac{\lambda}{2NA} \quad (6.7)$$

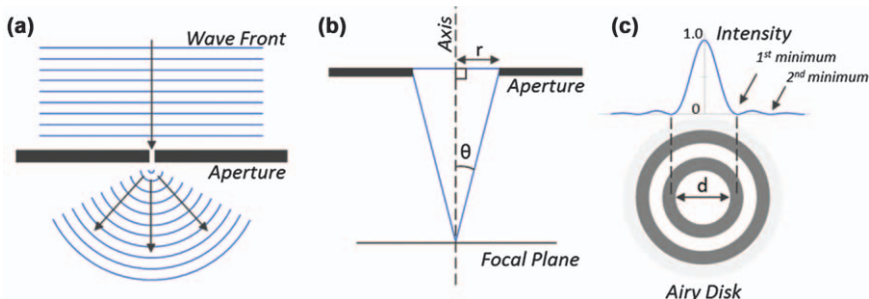


**Figure 6.7** Principles of probe diffraction through a narrow aperture, (a) diffraction of a wave through an aperture; (b) aperture geometry; (c) an Airy disk and simulated intensity pattern.

Abbe's diffraction limit computes the optimum diffraction spot size that can theoretically be achieved by employing a diffraction limited microscope equipped with a perfectly milled optical lens which lacks all aberrations. Engineering a microscope to operate at the diffraction barrier is desirable as it pushes the boundaries of the microscope to allow resolution of increasingly small features. This is accomplished in practice by reducing the wavelength of light ( $\lambda$ ), increasing the refractive index of the projection medium ( $n$ ), and by increasing the aperture angle ( $\theta$ ). In other words, the diffraction limit is achieved by using more energetic light sources and by increasing the numerical aperture ( $NA$ ).

The diffraction limit of a microscope is generally approximated as half of the wavelength of the illumination source (*i.e.*,  $d_d \sim \lambda/2$ ). This correlates to roughly 250 nm for a visible light microscope, as demonstrated through a simple back of the envelope calculation which utilizes an average wavelength for visible light of *ca.* 550 nm, a large aperture angle (*e.g.*  $\sin(\theta) \sim 1.0$ ), and a common immersion medium such as air ( $n \sim 1.0$ ) or oil ( $n \sim 1.5$ ). Thus, each point-source of light projected from the surface of a specimen produces a minimum diffracted disk approximately 250 nm in diameter. This presents a new question: what is the minimum allowable distance permitting two neighboring features (*e.g.* colloids), which lay in close proximity, to be differentiated as unique features when magnified at the diffraction limit of a microscope?

### 6.6.9 Resolution Criteria

Lord Rayleigh, a Nobel Prize-winning physicist, advanced Abbe's diffraction limitation theory to define the minimum point-to-point resolvable distance ( $\delta$ ) which allows the resolution of nearby points. Using the geometric definitions established by Ernst Abbe, Rayleigh was able to correlate the wavelength of light, refractive index, and aperture semi-angle to the minimum resolvable distance for two point-sources of light (see eqn (6.8)).<sup>82</sup> The Rayleigh criterion for resolution is satisfied when the center of a diffracted disk, as projected from a point-source of light, resides within the first minimum of a diffraction pattern from a neighboring point-source of light. This distance is  $\sim 22\%$  greater than the Abbe diffraction limit (*i.e.*,  $\delta \sim 1.22d$ ), as the magnified diffraction spots must be spaced adequately apart to be resolved.

$$\delta = \frac{0.61\lambda}{n \sin \theta} = \frac{0.61\lambda}{NA} \quad (6.8)$$

While the Abbe diffraction limit provides a measure for determining the size of the diffraction disk produced by a microscope, the Rayleigh resolution criterion defines the minimum point-to-point resolvable distance that is required to distinguish two overlapping diffraction patterns. Thus, for a standard visible light microscope, operating with a 250 nm diffraction limit

( $d_d$ ), the minimum resolvable distance between neighboring colloids is approximately 300 nm. This allows an observer to just begin to distinguish moderate-to-large colloids (*i.e.* 300–1000 nm) from their neighbors. Yet at this resolution, small colloids (dia.<300 nm) and surface features remain unresolved; thus, more advanced imaging techniques are required in order to resolve features closer to the atomic scale.

### 6.6.10 Inspiration for the Electron, Ion, and X-ray Microscope

As described by Abbe, the physical resolution limit imposed on the visible light microscope is a general phenomenon related to the wave-like diffraction of light upon small features. This phenomenon has driven scientists and engineers to develop optical instruments with alternative probes in order to reduce the optical diffraction limit and achieve higher resolutions. This can be accomplished by using probes with very short wavelengths and has inspired development of the X-ray, electron, and ion microscopes. These powerful instruments offer enhanced resolution capabilities in comparison to the visible light microscope and permit observation of features on the atomic scale.

The wave-like nature of electromagnetic radiation is also observed during the movement of physical matter, including ions and electrons. French physicist Louis de Broglie first proposed that matter travels as both a particle and wave in a similar fashion to that observed in the wave–particle duality of light. de Broglie connected Albert Einstein’s energy equation (*i.e.*,  $E=mc^2$ ) with Max Planck’s correlation between the energy ( $E$ ) and frequency ( $f$ ) of light (*i.e.*,  $E=hf$ ) to propose a new concept known as the de Broglie wavelength of matter (see eqn (6.9)). Using Planck’s constant ( $\hbar=6.626\times10^{-34}$  Js), de Broglie related the momentum ( $p$ ) of an electron to its wavelength, where the electron’s momentum is its mass ( $m$ ) multiplied by its velocity ( $v$ ).

$$\lambda = \frac{h}{p} = \frac{h}{mv} \quad (6.9)$$

de Broglie’s theory was later validated through a series of experimental studies which demonstrated the diffraction of electrons through narrow slits, a phenomenon previously demonstrated by Thomas Young with light waves. de Broglie’s “matter waves” as they were termed, would later provide a direct correlation between the movement of light and matter – offering a key conceptual link between the optics of the physical light microscope and that of the electron microscope.<sup>83</sup> This correlation would suggest that imaging could be accomplished not only with electromagnetic radiation including light, but with matter; hence, electrons and ions could theoretically be used to resolve increasingly small features – and even atoms!

Through application of de Broglie’s wavelength equation (eqn (6.9) and the Rayleigh criterion for resolution (eqn (6.8))), one can calculate an

approximate theoretical resolution that can be achieved by utilization of a probe of given wavelength, as depicted in Figure 6.3. The visible light microscope offers a maximum resolution of only  $\sim 250$  nm, while the application of lasers, as utilized by the confocal microscope, can achieve a resolution of  $\sim 150$  nm. In comparison, X-ray microscopes allow lateral resolutions on the order of a few dozen nanometers ( $\delta \sim 70$  nm) and ion microscopes offer resolutions on the order of  $\sim 10$  nm. Finally, the utilization of electron probes now allow the modern colloid researcher to distinguish atomic features on the order of  $\sim 0.1$  nm.

The application of electromagnetic radiation, electrons, and ions as analytical probes has culminated in the development of a variety of instruments which offer a broad spectrum of resolution capabilities. However, while the theoretical resolution of each probe can provide powerful resolving capabilities in principle, actual instrument performance is ultimately restricted by optical aberrations, engineering limitations, and physical phenomena. Yet through modern engineering, today's colloid scientists are now equipped with an array of powerful instruments for the advanced characterization of colloidal materials (see Figure 6.1).

## 6.7 The “Spectrum” of Microscopes

The spectrum of microscopes can generally be classified as optical microscopes, which consist of visible, fluorescence, and confocal microscopes; electron microscopes, which include scanning and transmission microscopes; ion microscopes, which now include gallium and helium ion microscopes; and alternative instruments such as the X-ray and atomic force microscopes. This wide array of instruments offers a unique set of tools which the modern colloid researcher can use for the characterization of a colloidal specimen. This section will now highlight each instrument and summarize their use for the analysis of colloids.

## 6.8 Optical Microscopes

### 6.8.1 The Visible Light Microscope

The conceptual design of the optical microscope has evolved only slightly from the original design that was improved upon by Ernst Abbe. Modern optical microscopes still employ a series of lenses which collect and refract light in order to magnify images. Today, these instruments are equipped with additional technological features, detectors, and software which aid the modern researcher in analysis. These technological advancements have led to the development of an array of economically priced instruments including the visible, fluorescence, and confocal microscopes, all of which are now readily accessible in most research institutions.

Optical microscopes offer several advantageous features which have contributed to their widespread application in diverse areas of research.

These advantages include comparatively low instrument and operational costs, limited instrument maintenance, operation under ambient conditions, limited sample damage, and operational ease of use. However, in comparison to other microscopic instrumentation, the optical microscope offers limited lateral resolution (*ca.* 250 nm), narrow depths-of-focus, and often requires sample thinning *via* sectioning to create optically transparent specimens. While optical microscopes remain incapable of resolving small colloids with diameters less than *ca.* 250 nm,<sup>84</sup> they provide a means of rapidly assessing large colloids and colloidal crystal features including primary and secondary particle size, film striations, large particle movements, and defects.<sup>85–87</sup>

Optical micrographs can be collected in either transmission<sup>88</sup> or reflective mode<sup>89</sup> (see Figure 6.8a) after performing the standard Köhler illumination protocol, which is used to optimize contrast and illumination. Sample preparation is typically executed by drop casting a small quantity of colloid suspension on a transparent microscope slide for analysis *via* transmission mode, whereas for reflection mode, convective deposition is often employed to deposit a film of stacked colloids along the surface of a gold coated microscope slide or a similar reflective substrate. These deposition techniques provide a rapid means of preparing samples for particle size analysis and for the analysis of CC deposition parameters. Additionally, oil immersion lenses are typically employed as a means of increasing the refractive index of the optical system for the observation of sub-micron colloids. As a result, optical microscopes have been used extensively as a quick means of assessing striation defects and patterning generated by inhomogeneous fluxes which arise during the convective deposition of CC films.<sup>90</sup>

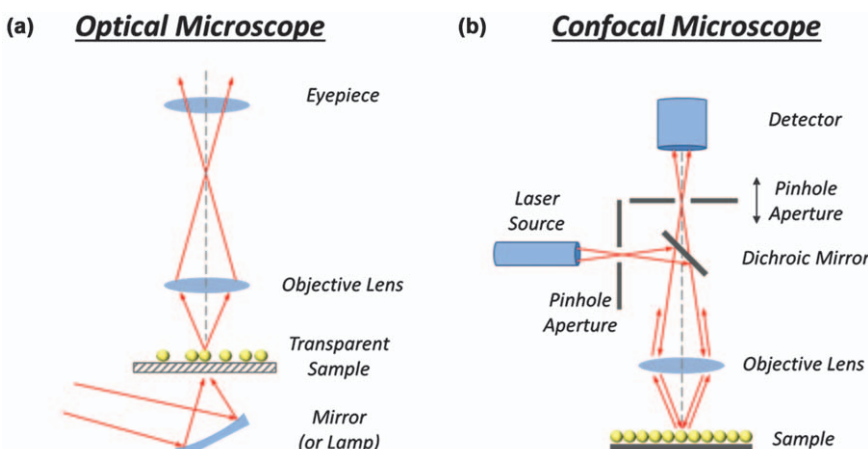


**Figure 6.8** Schematic diagrams of (a) an optical microscope configured to utilize visible light in transmission mode, and (b) a laser scanning confocal microscope (LSCM).

## 6.8.2 The Fluorescence Microscope

Fluorescence microscopy is an alternative optical technique to visible light microscopy and often widely employed by colloidal and biological researchers. The fluorescence microscope is configured in a similar manner to the visible light microscope, utilizing a series of lenses which refract and magnify light to facilitate imaging. However, fluorescence microscopes only utilize probes with select wavelengths of light which span a narrow region of the electromagnetic spectrum. Upon absorption of irradiated light by the sample, the microscope collects fluoresced photons which are re-emitted by the specimen. Through the application of fluorochrome dyes, researchers are able to selectively label colloids with a fluorescent molecular marker which makes them readily discernable for observation and particle tracing experiments.<sup>91</sup> This unique feature allows colloids and cellular organelles to be tagged and tracked within a given specimen or application.

The fluorescence microscope operates by irradiating the sample with high intensity light from the visible portion of the electromagnetic spectrum.<sup>92</sup> This highly energetic light, typically from the neighboring vicinity of the blue region, is reflected towards the sample with a dichroic mirror and focused into a probe using an objective lens. The fluorophore molecules contained within the dye are selectively excited by the absorption of these high-energy photons which act to elevate the dye's electrons to higher energy states. As the electrons begin to relax, the absorbed energy is subsequently re-emitted in the form of fluoresced light which is red shifted along the electromagnetic spectrum. The fluoresced photons, now possessing characteristic wavelengths longer than that of the incident probe, are then transmitted back through the dichromatic mirror to a detector for analysis.

Fluorescence microscopes are not limited to the analysis of samples which spontaneously autofluoresce under irradiation of the probe; non-fluorescent samples can be coated or stained with a fluorochrome dye for observation *via* fluorescence microscopy. Thus, most polymer and silica colloids are first soaked in a fluorescent chemical such as rhodamine-B prior to imaging.<sup>93</sup> Through the application of dyes and the employment of multispectral imaging, researchers can effectively track and locate the location of small particles which are deposited within a larger specimen.<sup>94,95</sup> These fluorescently stained colloids have been used to mark the location of select features within a larger cell,<sup>96</sup> biological tissue, or synthetic matrix including hydrogels.<sup>97</sup>

Similar to the visible light microscope, the fluorescence microscope is modestly priced, offers similar lateral resolution (*i.e.*, ~250 nm), requires minimal maintenance, and involves limited training. The added aspect of fluorescence imaging offers a unique method of highlighting select features for observation at the expense of an additional processing step required to stain the specimen of interest. While the traditional fluorescence microscope does not greatly improve optical resolution beyond that of the diffraction barrier of visible light, the advent of super-resolution microscopy now allows the resolution of individual fluorochromes well beyond the

visible diffraction limit – a technique which will likely continue to gain popularity in the future.<sup>98</sup>

### 6.8.3 The Confocal Microscope

The confocal microscope is widely used for the study of colloids, particularly colloidal assemblies, due to its ability to selectively image a sample at various focal planes which span the optical axis. In a similar fashion to its fluorescence counterpart, the laser scanning confocal microscope (LSCM) utilizes a high intensity laser to initiate fluorophore excitation and subsequently collects the fluoresced signals to produce an image. However, a key feature of the LSCM is its application of a pinhole aperture which is used to selectively block unfocused rays of light and collect only those rays which fluoresce from within the focal plane (see Figure 6.8b). This configuration allows two-dimensional image rendering at various points along a sample's optical axis and the ability to compile these serially collected images into a three-dimensional map of the sample's internal structure – an important concept which can be effectively used to assess packing structure in colloidal solutions and crystals.<sup>12,99</sup>

Confocal microscopes utilize either a light emitting diode (LED) or, more commonly, a monochromatic laser to illuminate and probe a specimen of interest. The light source is combined with a series of pinhole apertures, an objective lens, and a dichromatic mirror – all of which are employed to image thin slices of the sample along the optical z-axis.<sup>100</sup> The initial light beam is shaped into a narrow probe *via* a small aperture and reflected towards the sample using the dichromatic mirror. Utilizing the same techniques employed by the fluorescence microscope, the confocal microscope then focuses the light with an objective lens to probe the sample and subsequently collects the fluoresced signals after transmission through the dichromatic mirror. However, in the case of the confocal microscope, a narrow pinhole is placed between the dichromatic mirror and the detector to selectively filter out undesired rays. By shifting either the sample or the pinhole aperture along the z-axis, the instrument operator can shift the focal plane to selectively choose which rays remain in focus, while filtering out rays which project from undesired focal planes.

The confocal microscope offers many of the same appealing technical features which are offered by alternative microscopes. Similar to modern optical microscopes, the confocal microscope is widely available in most research facilities; they require low maintenance and upkeep, allow *in situ* operation under ambient conditions, require only limited training to obtain images, and their associated costs are generally moderate in comparison to that of both state-of-the-art optical and electron microscopes. LSCMs offer slightly improved resolution *versus* the visible light microscope due to their utilization of lasers with short wavelengths, yet their resolution is still less than that of the electron microscope as the LSCM is fundamentally limited by the diffraction barrier. This makes the LSCM an important instrument

which bridges the resolution capabilities that can be obtained by the optical and electron microscopes.

The LSCM has become particularly useful for the study of colloidal crystal materials and convectively deposited colloidal films.<sup>101</sup> The unique ability of the confocal microscope to selectively exclude unfocused rays of light from an image, while simultaneously imaging those concentrated at a given focal plane, makes the LSCM a preferred technique for internal analysis of colloid packing.<sup>43,102</sup> This technique affords a noninvasive method of assessing colloid solutions and films, without having to prepare optically transparent specimens *via* sectioning.<sup>21,103,104</sup> In fact, inverted confocal microscopes can even be positioned under convective deposition instruments for the *in situ* analysis of colloidal particles during deposition or when under an applied shear.<sup>105–109</sup> Much like in the case of the fluorescence microscope, colloids are typically stained with a fluorophore dye prior to confocal analysis.<sup>14</sup> This, in combination with particle tracking techniques such as the IDL method,<sup>110</sup> makes confocal microscopy a powerful tool for the *in situ* analysis of convectively deposited colloids – a process which is not observable in vacuum-based microscopes, including scanning and transmission electron microscopes.<sup>13</sup>

## 6.9 The X-ray and Atomic Force Microscopes

### 6.9.1 The X-ray Microscope

X-ray microscopes bridge the resolution gap between the optical and electron microscopes through the employment of short wavelength X-rays as microscopic probes. In comparison to the visible light microscope, these instruments offer enhanced resolution ( $\delta \sim 30\text{--}70\text{ nm}$ ) and the ability to operate under ambient conditions – unlike their electron microscope counterparts. While originally relegated to integration with high-energy synchrotron X-ray sources, X-ray microscopes are now stand-alone commercial instruments which have been brought to a larger research base. These high-energy instruments require little sample preparation, allowing them to probe the internal structure of colloidal specimens without tedious sample preparation procedures (see Figure 6.9a). Additionally, three-dimensional scanning techniques now allow multiangle scanning for the reconstruction of three-dimensional maps.

X-rays possess wavelengths ranging from  $\sim 0.01\text{--}10\text{ nm}$ , which is over an order of magnitude shorter than visible light, making them prime candidates for use as microscopic probes. This broad wavelength spectrum is sub-classified into hard X-rays, which are defined as X-rays with wavelengths less than 1 nm, and soft X-rays, which include X-rays with characteristic wavelengths ranging from 1–10 nm. Hard X-rays are primarily utilized for crystallographic X-ray diffraction studies (XRD) as they diffract along crystalline arrays of atoms *ca.* 1 nm in dimension. Soft X-rays are typically employed for the analysis of larger specimens, as is the case with the X-ray

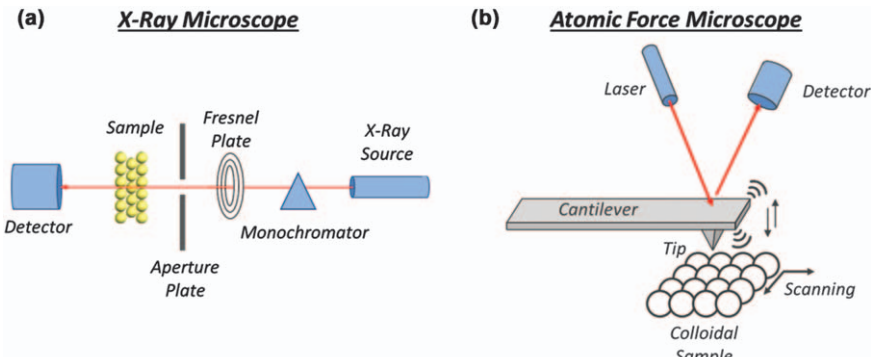


**Figure 6.9** Schematic diagrams depicting operation of (a) an X-ray microscope, and (b) an atomic force microscope (AFM) during tapping mode.

microscope, due to their interaction with particles on the order of tens of nanometers in diameter.<sup>111</sup>

The first X-ray microscopes were integrated in terminal endstations connected to large-scale synchrotrons and utilized the bremsstrahlung radiation emitted by the cyclical revolution of particles which circled within the synchrotron. Due to the inherently small wavelength of soft X-rays, they cannot be refracted by glass and thus cannot be focused in a similar fashion as employed by the optical microscope. Additionally, their lack of charge prevents their focusing *via* electrostatic lenses, typically employed in electron and ion microscopes. Therefore, X-rays must be focused by utilizing zone plates or gradually redirected with curved mirrors. Synchrotron based X-ray microscopes typically siphon off X-rays from the synchrotron and focus them within the beamline using a series of zone plates. These Fresnel lenses facilitate the focusing of X-rays *via* diffraction and direct them towards the sample. The X-rays then transmit through the specimen and are absorbed by either a photographic film or a charge coupled device (CCD). Image contrast is produced by the variable absorption of X-rays across the specimen.

Today's commercial X-ray microscope employs a sealed X-ray tube for the generation of soft X-rays. These instruments are readily integrated in traditional laboratories without the need for high-energy synchrotron radiation sources. Advances in computer technology now allow three-dimensional rotation of the specimen and the ability to reconstruct successive scans into a visual 3D map. These instruments are optimal for the noninvasive imaging and structural assessment of biological and colloidal specimens. Compact versions of the X-ray microscope will likely grow in application over the coming years, bridging the resolution gap between the optical and electron microscopes.

### 6.9.2 The Atomic Force Microscope (AFM)

The atomic force microscope (AFM) utilizes a physical stylus to probe the surface of a specimen and provide contour-based topographical information

about the sample (see Figure 6.9b). This physical means of sample analysis diverges from the traditional radiative and particle-based microscopic techniques employed by alternative instruments, yet nevertheless provides unique characteristic information which is particularly useful for the characterization of colloidal crystal films. The AFM was originally inspired by the scanning tunneling microscope (STM), for which the 1986 Nobel Prize was awarded to Gerd Binnig and Heinrich Rohrer.<sup>112</sup> These instruments, the AFM and STM, are more generally classified as scanning-probe microscopes (SPMs) due to their use of sharp-tipped styluses – a probe which is uniquely suited for the characterization of films.

The scanning tunneling microscope was the first instrument to employ a physical stylus to probe a specimen and conduct imaging. The STM operates by applying a voltage across the specimen and then rastering the probe along the sample in both the *x*- and *y*-directions. The instrument then records voltage-based intensity information associated with the position of the probe in relation to the specimen and correlates this information into a topographical map. By utilizing a precisely machined drive shaft and a piezoelectric crystal, the instrument is configured in a feedback loop that allows the instrument to raise or lower the stylus in order to maintain a constant voltage across the sample. If the stylus is brought closer to the specimen due to a protruding feature, the quantum-mechanical tunneling of electrons creates a feedback signal which causes the piezoelectric crystal to lift the probe and maintain a constant distance from the specimen. The resulting signals are recorded to produce a topographical map. While often challenging to use and requiring conductive specimens, this technique allows an impressive sub-angstrom resolution ( $\delta < 0.1$  nm) in all Cartesian coordinates (*i.e.*, *x*-, *y*-, and *z*-directions).

The atomic force microscope operates in a similar conceptual manner as the STM but utilizes a cantilevered tip to raster along a specimen and collect topographic data. Sample information is obtained using the AFM by either bringing the stylus into full contact with the specimen, a technique termed contact mode, or by iteratively tapping the surface of the specimen and scanning along the *x*- and *y*-coordinates of the surface; *i.e.*, tapping mode. These techniques provide characteristic *z*-based elevation data which is mapped in a three-dimensional graph to provide topographical surface information. Data collection is facilitated by a laser which is reflected off the end of the tip, towards a photodiode detector. As the cantilever is rastered along the specimen, slight elevation variations are detected by the photodiode and recorded as a topographic map. This technique offers a versatile approach to imaging and is achieved without the necessity of coating a specimen in conductive material, as required with the STM.

In comparison to alternate microscopes, commercial AFMs offer impressive lateral resolutions ( $\sim 30$  nm) at relatively moderate costs; additionally, more advanced AFM instruments now provide near atomic resolution of microscopic specimens. The major downside of the AFM is that it only provides topographic surface information and yields no underlying data

related to the internal composition or structure of a specimen; this limits the AFM's application to the study of films and flat specimens. Thus, the AFM has been widely employed for the characterization of convectively deposited CC films in order to assess striation defects.<sup>113</sup> Additionally, the quantitative  $z$ -coordinate data provided by the AFM offers a direct measure of slight deviations in film thickness – which often remains elusive to characterization with optical microscopes and difficult to quantify under an electron microscope. Atomic force microscopy will continue to remain a valuable tool in the spectrum of microscopes available to colloid researchers, as it offers an innovative technique for the analysis of convectively deposited colloids.<sup>114–118</sup>

## 6.10 Electron Microscopes

### 6.10.1 Electron Microscopy Background

The electron microscope has revolutionized the field of microscopy by facilitating imaging of increasingly small features. While visible light microscopes have a limited resolution of  $\delta \sim 250$  nm, electron microscopes offer sub-nanometer resolution. Electron microscopes are generally classified as either scanning or transmission electron microscopes (*i.e.*, SEM or TEM), and are termed scanning transmission electron microscopes (STEM) when combining the two techniques. These instruments excel in the observation of small colloids less than 250 nm in diameter and enable simultaneous elemental analysis through in-column characterization with techniques such as energy-dispersive X-ray spectroscopy (EDS). Additionally, the recent development of commercial *in situ* sample holders now allows the observation of colloidal specimens under environmentally controlled conditions and even colloids which remain suspended within solution.<sup>119</sup>

Both the SEM and TEM incorporate similar components in their construction. These consist of a series of stacked chambers which operate under vacuum including: (i) an electron gun used to emit a beam of electrons, (ii) an evacuated column which houses a series of electrostatic lenses and apertures, (iii) an evacuated sample port or chamber, (iv) a series of detectors and viewing monitors, and lastly, (v) a series of vacuum pumps which evacuate the instrument to create a stable environment for the electron beam (see Figure 6.10). The TEM probes a sample and collects the resulting transmitted signals from the opposite side of the specimen in an analogous fashion to the optical microscope when operated in transmission mode. Conversely, the SEM typically collects backscattered and secondary electrons which are ejected from the top of the specimen in a comparable manner to that utilized during reflection mode with an optical microscope.

In order to generate an electron beam, SEMs and TEMs employ either a thermionic emission gun or a field emission gun (FEG) under high voltage to overcome the work function barrier necessary for electron emission. Thermionic emission guns are generally cheaper and require less powerful vacuums than field emission guns; however, they lack the brightness, lifetime,

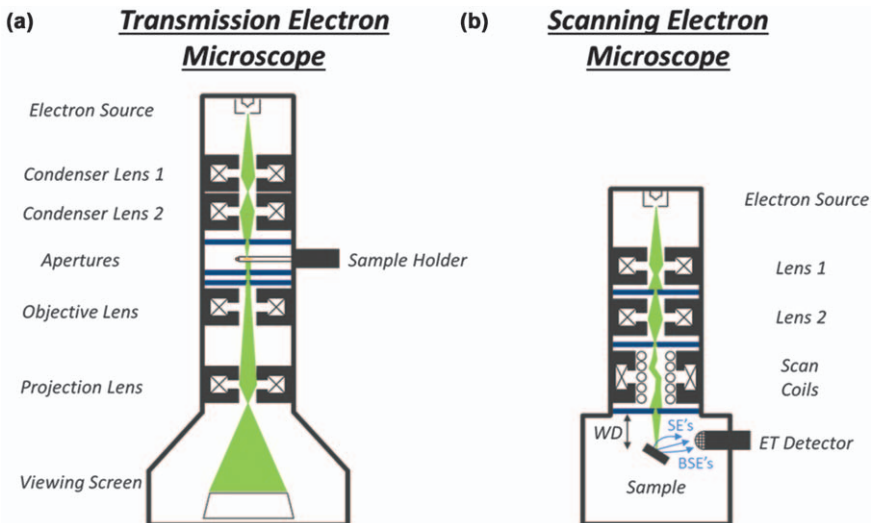


**Figure 6.10** Schematic depiction of the primary components which comprise (a) the transmission electron microscope and (b) the scanning electron microscope.

and resolution that can be achieved by utilization of a field emission gun. Thermionic guns consist of an evacuated chamber which houses a thermionic triode consisting of a filament, grid cap, and anode. The thermionic filament, often tungsten (W) or lanthanum hexaboride ( $\text{LaB}_6$ ), is first heated through the application of a high voltage which typically reaches as high as 300 kV. Thermionic emission is then achieved by flowing current through the heated filament, resulting in the emission of electrons into the grid gap. In order to harness and focus this cloud of emitted electrons, a bias voltage is applied to the grid cap – commonly referred to as a Wehnelt cylinder – which funnels the electrons through a narrow opening in the cylinder. Lastly, an anode is positioned below the cylinder to accelerate the beam upon entrance to the evacuated column of lenses.

Field emission guns utilize a selectively engineered tungsten single-crystal, which is highly sharpened to a fine tip and immersed in a strong electric field, in order to effectively strip electrons out of the filament. This is achieved by bringing the FEG tip in close proximity to a series of anode plates. As opposed to thermionic guns, which effectively boil off electrons from the tip of the filament, this design greatly reduces the work function barrier necessary for electron emission and allows the electrons to quantum-mechanically tunnel from the tip of the crystal into the evacuated electron column. FEGs are generally classified as either Schottky field emitters, which are heated to assist in electron emission, or cold field emitters, which employ highly pristine FEG crystals for low temperature operation. FEG microscopes are employed in both SEMs and TEMs and provide the high current densities necessary to resolve features on the atomic scale.

After initial formation of the electron beam, the electron probe is shaped by the operator using a series of electrostatic lenses, apertures, and multipole correctors housed within the evacuated column. These components each accomplish tasks necessary to focus the electron probe and are analogous to the components utilized in the optical microscope to focus light. The apertures are inserted in the beams' pathway in order to restrict current flow through the column, much like that employed in the visible light microscope to control illumination. Apertures also help define the diameter and convergence angle of the beam in order to produce either a narrow convergent probe, or a wider, more collimated beam. Similar to the visible light microscope, electron microscopes typically employ at least two lenses for probe formation; these include the condenser lens and the objective lens. Electrostatic lenses consist of copper windings encased in an iron housing and allow the operator to focus the beam along a specified optical axis, eliminate aberrations, and correct for astigmatisms.

The condenser lens, the first lens encountered by the beam, acts to demagnify the electron beam and ultimately governs both the probe diameter and current. The condenser lens can be strengthened or weakened through manipulation of the electromagnetic field surrounding the beam in order to control the amount of crossover and thus control the amount of electrons, or current, that remains aligned along the optical axis and permitted through the column. The objective lens is used to focus the beam in order to provide optical resolution when imaging the specimen. In the SEM, the objective lens is placed above the sample, whereas the TEM is typically configured with the objective lens positioned underneath the sample. The SEM utilizes an objective lens to converge the beam to a focal point located at a desired working distance (WD) from the final pole piece of the objective lens onto the surface of the sample. Conversely, the TEM uses the objective lens in order to magnify the beam for projection on either a fluorescent screen or electronic detector after transmitting through the sample.

Multipole correctors – including quadrupoles, sextupoles, and octupoles – are utilized for the correction of axial astigmatisms and lens aberrations. Multipoles are composed of a series of north and south magnetic dipoles, generated by a sequence of solenoid coils, and aligned along azimuthal angles perpendicular to the optical axis. Quadrupoles are commonly employed for the correction of astigmatisms, while sextupoles and octupoles are utilized for the correction of lens aberrations such as spherical aberrations ( $C_s$ ) and chromatic aberrations ( $C_c$ ).<sup>120</sup> Multipoles are often arranged in a stacked format along the optical axis allowing redirection of the beam's pathway. Scanning coils are also employed within EMs in order to deflect the electron beam; by altering the amount of current delivered to these coils, an operator can divert the beam and raster it along the surface of a specimen. This technique is a primary aspect of the SEM and is employed within most modern TEMs to offer operation *via* scanning transmission mode. While probing a specimen with the electron beam, information is collected *via* a series of detectors and the resulting images are projected on

either a monitor or a fluorescent screen. While both the SEM and TEM employ several similar components for the magnification and imaging of a specimen, there are several key features crucial to the understanding of the operator. The following sections will highlight the differences between the SEM and TEM during the characterization of colloid-based samples.

### 6.10.2 The Scanning Electron Microscope (SEM)

The scanning electron microscope operates by rastering a beam of electrons along the surface of a colloidal specimen and collecting ejected electrons, including backscattered and secondary electrons (*i.e.* BSEs and SEs), which are re-emitted from the sample to produce an image. The ejected electrons are collected by either an Everhart-Thornley (ET) detector or a solid-state detector (SSD) which are typically positioned above the sample. Imaging is accomplished by converting the relative number of electrons emitted from each point, or picture element (*i.e.*, pixel), located along the surface of the sample and converting this quantity into a numerical contrast value which is mapped on the viewing screen. The result is to provide a familiar and appealing depiction of the specimen that is easy to interpret.

Scanning electron microscopes offer many advantages *versus* the optical light microscope, yet also impart several limitations that a colloid researcher must consider. The scanning electron microscope offers improved resolution in comparison to optical microscopes, allowing colloidal features as small as *ca.* 1–10 nm to be resolved.<sup>16</sup> The SEM also facilitates imaging with a much larger depth-of-focus *versus* the visible light microscope; this allows features which are displaced by several microns along the optical axis to come into focus simultaneously. Additionally, the SEM is capable of analyzing thick samples which are not optically transparent, allowing the characterization of thick colloidal crystals without the need to perform delicate sectioning techniques.<sup>121</sup> However, the SEM also provides several limitations which are encountered during the characterization of colloids. Scanning electron microscopes operate under high vacuum conditions in order to generate a stable electron beam and achieve high optical resolutions. This prevents the observation of fluids and suspensions, requiring samples such as colloids to be dried from their native suspension prior to imaging under an electron microscope. Unfortunately, the SEM's incorporation of vacuum components translates into a substantial increase in instrument cost.

Colloid samples are readily prepared for SEM analysis by simply drop casting a small quantity of suspended colloid solution on the surface of an aluminum sample stub or by adhering a colloidal film to the stub using conductive tape. Non-conductive colloid specimens are then sputter coated with a thin layer of carbon, iridium, or gold prior to analysis in order to improve their conductivity. When imaging colloid samples with a SEM, several key operating parameters must be selected to optimize image quality and resolution. These parameters include accelerating voltage (kV), probe

current ( $i_p$ ) – or spot size – the working distance (WD), and the convergence angle ( $\alpha$ ). The optimal resolution of nano-colloids (dia. < 10 nm) and small surface features is best achieved by utilizing low accelerating voltages (~5 kV), small spot sizes (low current), high magnification, short working distances (WD < 10 mm), and large convergence angles (wide apertures). This allows the observation of small colloids which remain indistinguishable under an optical microscope. Conversely, large colloids are best observed by employing low magnification, larger working distances (WD > 10 mm), small convergence angles (small apertures), and moderate accelerating voltages.<sup>122</sup> These settings are best used when a large depth-of-field is desired in order to assess large expanses of colloids and for the analysis of particle packing and assembly.<sup>123–126</sup>

Common challenges often encountered during SEM imaging of colloidal specimens are the effects of sample charging and beam damage, which arise due to the use of the highly energetic electron probe to analyze non-conductive materials. Localized surface charging presents a common challenge during SEM imaging as many colloids consist of either a nonconductive polymer latex, or a semiconducting oxide material. Electron probes bombard the sample with a large quantity of negatively charged electrons which must be effectively dissipated from the surface of the specimen in order to obtain an image. Without proper charge dissipation, the electron beam is repelled from the surface of the sample and effectively blinds the detector. Additionally, the high energy electrons are typically accelerated by voltages on the order of 2–30 kV; this is relatively high in comparison to the chemical bonding strength of colloids, which only range on the order of a few eV per bond, and often damages the specimen. Beam damage is evidenced by time-resolved changes in the sample's appearance, while sample charging is noted by bright regions distributed along the sample's surface, which saturate the detector and prevent imaging.

Fortunately beam damage and surface charging can be mitigated by reducing the accelerating voltage of the electron gun (e.g. ~2–5 kV) and by sputter coating the sample in a highly conductive covering (~5 nm thick) often composed of carbon, gold, or iridium. A reduction in accelerating voltage effectively reduces sample damage while the metallic coating helps dissipate the accumulated surface charge. Furthermore, modern environmental scanning electron microscopes (ESEMs) now facilitate the addition of a low partial pressure gas, such as water vapor or CO<sub>2</sub>, which can be dispersed within the sample chamber to assist in the dissipation of surface charge.<sup>127</sup> These techniques can be utilized in combination to eliminate both sample charging and beam damage, allowing imaging of virtually all colloidal specimens.

### 6.10.3 The Transmission Electron Microscope (TEM)

The transmission electron microscope utilizes similar components as the SEM, employing a series of electrostatic lenses, multipole correctors, and

stigmators to generate an electron probe for specimen examination.<sup>128</sup> TEMs are constructed in a design that closely resembles that of the optical transmission microscope, yet employs the elastic and inelastic scattering of transmitted electrons to generate image contrast and project a magnified image. Advanced TEMs currently offer the highest resolution capabilities of all microscopes; this is achieved by the application of electrons, which possess short de Broglie wavelengths, as opposed to electromagnetic probes. For sample imaging, a specimen of interest is thinned to a few hundred nanometers or less – such that it remains electron transparent – and is subsequently inserted in the pathway of the beam for imaging. Electrons then bombard the sample, penetrating the specimen in thin areas, while being scattered in thicker areas. This generates a silhouette-like image which can be resolved by magnifying and projecting the beam onto a fluorescent screen or digital imaging device.<sup>129</sup>

As with all microscopes, TEMs offer several advantages and limitations. TEMs offer the highest resolution of all microscopes, provide elemental z-contrast due to the inelastic scattering of electrons, allow integration of in-column elemental analysis techniques, and now offer *in situ* analysis *via* the application of specially engineered environmental sample holders.<sup>130</sup> However, TEMs also have large associated costs, demand high vacuum conditions, and require substantial training and beam time to utilize these complex instruments at their optimal resolution limit. Yet, these limitations are only minor obstacles in comparison to the valuable information and atomic-level resolution that can be obtained with an advanced transmission electron microscope.

Colloid samples are readily prepared for TEM analysis by simply depositing a colloidal specimen on the surface of a TEM grid. Liquid specimens can be dried on the surface of the grid; while powdered, colloidal crystals are typically ground with a mortar and pestle before iteratively raking the grid within the powder. TEM grids generally consist of a metallic mesh, often composed of copper, nickel, or gold, which is used as a rigid frame to support an outstretched carbon film. This sub-nanometer thick carbon film is manufactured as either a solid film or a holey, web-like net that acts as a canvas to electrostatically capture colloid particles for analysis. After dispersion of the specimen, the grid is then clipped into place within a sample holder and inserted in the TEM for analysis.

TEMs typically operate at relatively high accelerating voltages (*i.e.*, 80–300 kV) in comparison to SEMs. This provides enhanced resolution and gives the electrons the energy necessary to transmit through the specimen. TEMs have been used to assess the packing of small colloidal crystals, validate the arrangement of binary colloid assemblies,<sup>61,131</sup> and identify catalytic surface moieties dispersed along the surface of colloidal supports and Janus particles.<sup>17,132,133</sup> Additionally, the variation in trajectories of electrons which are scattered by heavy *versus* light elements, a phenomenon which generates atomic z-contrast, offers a means of visually distinguishing heavy elements dispersed either on the surface or within the bulk portion of a colloid.<sup>134</sup>

#### 6.10.4 Scanning Transmission Electron Microscopy (STEM)

Many modern TEMs are now equipped with a series of scanning coils located above the specimen holder which can be used to raster the TEM's beam in a scanning-transmission process. This technique, termed scanning transmission electron microscopy, collects transmitted electrons which project through the sample during a rastering process which incorporates features similar to both SEM and TEM operation.<sup>135</sup> During STEM operation, the electron probe is shaped to converge to a narrow tip much like that utilized by SEMs; this is opposed to the larger, more collimated beam of electrons employed by TEMs. By utilizing a narrow electron probe, the STEM instrument is able to obtain high resolution images and perform EDS mapping.<sup>136</sup>

STEM instruments typically employ a series of high-angle annular dark-field (HAADF) detectors which are positioned below the sample in order to collect elastically scattered electrons.<sup>137</sup> These detectors create an inverse depiction of that obtained during TEM imaging and consist of a dark background with bright spots corresponding to electrons which were forward scattered by the sample. Imaging *via* STEM-HAADF offers optimum resolution and pronounced z-contrast,<sup>138</sup> excelling in the detection of small atomic clusters and catalytic moieties located on the surface of a larger colloidal particle.<sup>79</sup> Additionally, transmitted electrons can be simultaneously collected by detectors located below the sample to produce enhanced resolution images analogous to that collected during operation under TEM mode. Furthermore, the unique scanning and rastering STEM process allows simultaneous EDS characterization in order to generate atomically precise chemical maps of the specimen.<sup>139–141</sup> This remarkable in-column combination facilitates direct imaging of a specimen on the atomic scale, with point-by-point chemical mapping of atomic species.

#### 6.10.5 The Ion Microscope

Ion microscopes utilize a similar design to electron microscopes to image a specimen, but employ ions – as opposed to electrons – as a probing source. Ions are a fascinating probe option as they have substantially larger masses than electrons and thus possess considerably reduced de Broglie wavelengths. This makes ion microscopes, when operated at comparable energies, theoretically capable of resolving much smaller features than that possible with even the most advanced electron microscopes. Yet, despite the fact that ion microscopes have been in development for over 60 years, their maturation and commercialization has significantly lagged behind their electron-based counterparts; this is primarily due to technical difficulties related to the development of stable ion sources. However, with the advent of more recent technological developments, ion microscopes have achieved rapid advances in resolution and are now equipped with a variety of probes including gallium ( $\text{Ga}^+$ ), helium ( $\text{He}^+$ ), and neon ( $\text{Ne}^+$ ) ions.

Ion microscopes offer the unique ability to not only image a specimen, but perform nanofabrication *via* the precise deposition and removal of material to produce nanoscale structures. This concept has led to the development of several application-driven sample processing techniques which have rapidly matured through collaborative interaction between the EM and semiconductor industries. Ion beams are typically configured as either a dedicated ion microscope or integrated with an electron microscope (*i.e.*, E-beam), as a single stand-alone instrument, equipped with two distinct beam columns. These dual-beam (DB) nanofabrication instruments facilitate the precise additive and subtractive manufacturing of nanostructures well within the size range of even the smallest colloids. DB instruments typically employ an E-beam for imaging, while the ion beam is utilized for the addition and subtraction of material. These innovative tools are used for the precise milling of a sample to fabricate cross-sectional specimens for internal, depth-profiling-based analysis and for the preparation of lamellar specimens for subsequent TEM analysis.<sup>142</sup>

The principal ion microscopes which are currently available on the market include the gallium-based focused ion beam (FIB) instrument and the more recently commercialized helium ion microscope (HIM). These instruments employ either a liquid metal ion source (LMIS) to generate an ion beam, as is the case with the gallium-based FIB, or a gas field ion source (GFIS), as utilized by He<sup>+</sup> and Ne<sup>+</sup> instruments. While both probe sources offer similar imaging and nanofabrication applications, recent GFIS advances will likely lead to a shift in the application and marketplace of these two complementary ion microscopes. The following sections will highlight the application of ion microscopes for the analysis of colloidal specimens.

### 6.10.6 The Focused Ion Beam System

The Ga<sup>+</sup> focused ion beam system is currently the most widely used ion microscope available on the market. The FIB has evolved from a single-column instrument – which employed an ion beam for both imaging and nanofabrication – into a two-column (*i.e.*, dual-beam) instrument which employs both an E-beam and an ion beam for imaging and milling respectively. The first FIBs were primarily utilized for the preparation of thin TEM lamella and cross-sectional specimens. These instruments offered an astounding reduction in the time required to prepare TEM samples from bulk specimens; a process which could often take years of iterative polishing and etching steps to complete. Today the FIB is typically integrated with the SEM in a series of powerful stand-alone instruments, each of which function as complete characterization and nanofabrication laboratories.<sup>143</sup>

Dual beam FIB instruments employ both electron and ion beam columns which are strategically angled – with the ion beam typically rotated at a 52° angle in relation to the E-beam – such that each beam is coincident upon the same point on the specimen. After setting the eucentric height of the instrument so the sample does not shift upon tilting of the stage, the sample is

freely allowed to tilt towards each beam for observation and the precise addition or ablation of material. The electron beam is typically produced by a field emission gun while the ion beam is produced by a liquid metal ion source. In a process similar to that utilized by the electron microscope's FEG, the focused ion beam system utilizes an LMIS which is immersed within a strong electric field in order to generate an ionized beam of  $\text{Ga}^+$ . Gallium, which is a highly viscous metal near room temperature, is stored in a spring-like reservoir located atop the LMIS's tungsten filament. Upon resistive heating of the filament, the viscous gallium metal slowly flows downwards and forms an extended Taylor cone at the tip of the LMIS.  $\text{Ga}^+$  ions are then gradually stripped from the cone by the electric field and directed towards the sample *via* a series of electrostatic lenses and scanning coils which are configured in a similar arrangement to that found in the SEM.<sup>144</sup>

The  $\text{Ga}^+$  FIB instrument is generally a destructive technique, yet with proper operation this ion microscope can be used for imaging, material ablation, and material deposition. While the electron beam is primarily utilized for high resolution imaging, ion beam imaging is often used to quickly locate features and check coincidence in order to ensure precise nanofabrication. Upon irradiation of a sample by the  $\text{Ga}^+$  beam, a stream of secondary electrons, backscattered gallium species, and surface atoms are ejected from the sample. By varying the current of the ion beam, *i.e.* spot size, an operator can control the rate of material sputtering in order to gently image the sample or quickly sputter away large amounts of material. Low currents and fast scan rates offer imaging of the sample with minimal sputtering, while high currents and slower scan rates can be used to quickly etch away large portions of the sample. Imaging is achieved by either collecting the ejected secondary electrons with an ET detector or by utilizing a silicon drift detector (SiDD) to count the number of backscattered  $\text{Ga}^+$  ions emitted at each point along the specimen.

The FIB has been historically used for the preparation of TEM lamella (*i.e.*, coupons) and cross-sectional specimens which are prepared by a combination of material deposition and sputtering. Material deposition is executed by inserting a gas injection needle into the chamber and passing a low partial-pressure precursor gas over the sample. The ion beam is then used to decompose the precursor gas and deposit a layer of material (*e.g.* Pt, W, or C) of tailored thickness onto the sample in a process known as FIB-assisted chemical vapor deposition. This technique can be utilized to build small nanostructures, precisely edit semiconductor circuitry, or to deposit passivating layers for the preparation of TEM lamella. Thus, the dual-beam FIB's combination of both an electron beam and ion beam offers a complete suite of nanofabrication techniques, all housed within a single instrument.

While the FIB will continue to play a dominant role in the field of nanofabrication, particularly for the semiconductor industry, it also offers a powerful tool for the characterization of colloids. The FIB's remarkable sputtering and imaging capabilities can be used for the assessment of internal particle packing in colloidal films and CC powders. By tilting the stage

and sputtering away a quarry shaped cross-sectional pit, the underlying layers of the sample become readily observable by the E-beam. A cross-sectioned sample can then be carved even further and the resulting coupon, or lamellar slice, can be removed *via* the *in situ* lift-out process (*i.e.*, INLO) for subsequent TEM analysis.<sup>145</sup> Another potential colloidal application of the FIB is for the nanofabrication of custom-built microfluidic channels for the study of fluid flow in confined channels. These small interwoven waterways demonstrate unique flow properties not observed on the macroscale and have seen a surge of interest by colloid researchers in recent years.<sup>146,147</sup> Thus, the FIB offers a versatile in-house tool for the customized preparation of colloidal specimens and application-specific research components.

### 6.10.7 The Helium Ion Microscope

The helium ion microscope (HIM) has been in various stages of development for the past 60+ years, yet has only recently become a commercial reality. This unique instrument has evolved from the field ion microscope (FIM) which was first constructed by Erwin Müller in 1951.<sup>148</sup> Müller's FIM was a rather simple device but was able to resolve individual atoms for the first time in history! The original FIM operated by adding small doses of helium to an evacuated flask which contained a biased tungsten needle positioned near a counter electrode. Each tungsten atom protruding from the apex of the needle effectively ionized the He gas, emanating hundreds of He<sup>+</sup> beamlets. These low current density beams were each projected onto a fluorescent screen to form an image of the lattice of tungsten atoms located along the tip of the needle. Unfortunately, the FIM's tip lacked the stability required to make this instrument a viable commercial microscope, yet it remained an inspiration for the eventual development of the gas field ion source which has made the helium ion microscope a commercial reality today.<sup>149</sup>

The HIM operates in an analogous manner to both the FIM and SEM but employs a GFIS to generate a probe of He<sup>+</sup> ions. In order to produce a stable He<sup>+</sup> beam, the GFIS is shaped into an atomically sharp, three-pronged pyramidal tip. This pyramid structure maintains the prolonged stability necessary to make the HIM a viable commercial instrument. At the top of the pyramid rest just three atoms, each of which emit a beam of He<sup>+</sup> ions from the tip of the GFIS in the same process as that utilized by the FIM. Using an aperture, just a single He<sup>+</sup> beam is selected to pass through the column and probe a specimen of interest. This beam is focused and rastered across the sample using the same series of electrostatic lenses and scanning coils employed by the SEM. As each ion beam collides with the sample, multiple secondary electrons and occasional backscattered helium ions are released. Using an ET-detector, the resulting SEs can be collected in the same process as that employed by the SEM. Additionally, in a process termed Rutherford backscattering (RBS), the HIM allows imaging using a silicon drift detector (SiDD) to collect backscattered ions which are inelastically scattered by the

sample.<sup>150</sup> The RBS technique provides z-contrast and compositional information, as the incident ions are more effectively scattered by elements with higher atomic numbers, resulting in an intensity-based spatial image correlating to elemental composition.<sup>151</sup>

The helium ion microscope offers several remarkable image enhancements over the SEM including improved resolution, enhanced image contrast, larger depths-of-field, and increased brightness.<sup>152</sup> These superior imaging properties are achieved due to the use of the atomically sharp GFIS tip which allows a significant reduction in probe size. The GFIS achieves a high current density per spot size and affords nearly three times the resolution of a standard field emission SEM. Additionally, the mass of the He<sup>+</sup> ion far exceeds that of the electron, providing He<sup>+</sup> ions with a markedly reduced de Broglie wavelength (*i.e.*,  $\lambda_{\text{He}} \ll \lambda_{\text{e}^-}$ ) and minimal diffraction effects. This added mass also helps eject a substantially greater number of SEs from the sample upon irradiation, resulting in increased signal and brightness. In addition to these outstanding imaging properties, the application of positively charged ions results in limited sample charging and damage, eliminating the need to coat samples in a conductive material.<sup>153</sup> This makes He<sup>+</sup> ions a suitable choice for the characterization of sensitive materials including biological specimens and soft polymer colloids.

In the future, the HIM will likely see further applications development focused on nanofabrication and the employment of He<sup>+</sup> sputtering techniques to cut cross-sectional regions from delicate samples (*i.e.*, polymer colloids) for the assessment of internal composition and morphology. While the HIM is still an emerging technology, its use will undoubtedly become more widespread, particularly for colloid analysis, where its large depth-of-focus can assist in the characterization of particle packing arrangements. Additionally, as the application of the helium ion microscope broadens its user base, its substantial cost – which remains its largest downside – will likely drop significantly.

## 6.11 Instrument Selection for Colloid Analysis

The spectrum of microscopes available to the modern researcher offers a wide selection of capabilities and costs which must be considered prior to sample analysis. Additionally, with the ever-evolving field of research, one must constantly consider the potential of instrument reconfiguration for the combinatorial analysis of a specimen. While the resolution capabilities of the microscope have finally surpassed the diffraction barrier of the optical microscope, allowing imaging of the complete scale of colloids (*i.e.*, 1 nm to 1  $\mu\text{m}$ ), it is important to select the appropriate instrument for analysis of a sample in order to obtain the desired information (see Table 6.1).

The optical microscope, which employs visible light as a probe, can be used to study the surface morphology of colloidal films and larger striation defects. However, this instrument is ultimately limited to a lateral resolution of approximately 250 nm. Fluorescence and confocal microscopes offer

**Table 6.1** A list of common microscopic instruments and their *approximate* resolution capabilities.

Instrument	Probe	Lateral resolution (nm)	Notes
Optical	Visible light	250	Packing morphology, deposition defects
Confocal	Laser	150	Packing and 3D reconstruction
3D X-ray	X-rays	70	Packing and 3D reconstruction
AFM	Physical contact	30	Surface morphology and surface properties
Gallium ion	Ga <sup>+</sup> ions	15	Surface morphology, chemical analysis (EDS), fabrication (milling & deposition), 3D reconstruction
SEM	Electrons	2	Surface morphology, packing analysis, chemical analysis (EDS)
Helium ion	He <sup>+</sup> ions	0.5	Direct surface imaging, chemical analysis
TEM	Electrons	0.1	Morphology, structure, chemical analysis (EDS and EELS), 3D reconstruction

similar lateral resolution capabilities and the ability to detect colloids which are dispersed in a larger biological cell or synthetic matrix. These instruments offer the unique ability to dye a colloid with a fluorescent chemical marker and track its location in a given specimen. The X-ray microscope employs an electromagnetic X-ray probe to reduce the diffraction barrier and resolve smaller features than is possible with the optical microscope. Three-dimensional versions of the X-ray microscope are now commercially available as stand-alone instruments which offer resolutions on the order of ~70 nm and the ability to three-dimensionally reconstruct the internal structure of a colloidal specimen. Additionally, the atomic force microscope offers a versatile microscopic technique for the analysis of colloidal films *via* physical contact with a stylus. AFM offers resolution on the order of ~30 nm, with advanced instruments approaching atomic level resolution.

Scanning electron microscopes offer advanced analysis of surface morphology and simultaneous chemical analysis through the utilization of energy dispersive X-ray spectroscopy. These instruments now offer lateral resolutions on the order of a few nanometers. Similarly, their TEM counterparts offer the most powerful resolution capabilities of any microscope, with many instruments now capable of resolving sub-nanometer-sized features and the ability to distinguish individual atoms. TEMs offer additional in-column compositional capabilities, including EDS, cryo-EM, and even *in situ* analysis with the application of advanced sample holders. The application of cryo-TEM and *in situ* sample analysis will provide a rich field of research for the future characterization of colloids. Within the past few decades ion microscopes – including the Ga<sup>+</sup> FIB and the He<sup>+</sup> HIM – offer the ability to selectively mill and deposit material for the nanofabrication of specimens. These instruments now offer resolutions on the order of

~0.5–10 nm, with the He<sup>+</sup> microscope rapidly offering advanced imaging capabilities, without the need to coat or passivate the surface of the specimen. These instruments offer a versatile toolbox for the thorough analysis of colloidal specimens of all size scales.

## 6.12 The Microscopy of Colloids – A Summary

Colloids are defined by the IUPAC as any collection of suspended, microscopic particles which range in size from 1 nm to 1 μm. Today however, this designation has grown to more generally define any collection of microscopic particles which are dispersed in a continuous medium or deposited in a colloidal crystal matrix. Colloids have become essential for the industrial scale manufacturing of latex polymers; provide an inorganic support for the deposition of catalytic surface moieties; and have even been launched into space for the uniform synthesis of monodisperse calibration standards. These small microscopic particles were first coveted as natural opal rock specimens, consisting of multitudes of hydrated silicon dioxide spheres which are packed in ordered arrays and found within natural mineral deposits. Under natural light, these sub-micron particles produce a brilliant rainbow-like diffraction effect which is easily discernable and sought-after by gem hunters. Yet, the same principle of light diffraction which makes opals appealing to the eye, also provides a barrier to their analysis with the visible light microscope.

Optical microscopes employ a series of lenses which refract visible light in order to magnify and project an image. Early versions of the microscope permitted the observation of plant-based specimens and small biological cells; however, these still undeveloped instruments were fundamentally limited in performance due to optical aberrations and the diffraction barrier of visible light. As the microscope was standardized and improved upon by researchers including Ernst Abbe at the Zeiss Optical Works Company, many of the aberrations which plagued these early instruments were corrected for. Soon however, the diffraction barrier of visible light was reached and – as demonstrated by Lord Rayleigh – the resolution criterion for visible light would only allow the observation of specimens ~250 nm in diameter or larger, preventing the characterization of small colloids.

At the turn of the 19th century, scientists predicted that the lateral resolution of the microscope could be enhanced by utilizing microscopic probes which possessed smaller wavelengths than that of visible light. During this same time period Louis de Broglie predicted that matter travels as both a particle and a wave in a similar fashion to electromagnetic radiation. It was soon proposed that physical probes with extremely small de Broglie wavelengths, such as electrons and ions, could be used to resolve increasingly small features. This idea would spark a revolution in microscope design which ultimately resulted in the development of the X-ray, electron, and ion microscopes. Over the course of the next century, developments in vacuum technology, electron guns, lasers, and electrostatic lenses now allow the

characterization of even the smallest colloids, with resolutions on the atomic scale.

Modern microscopes now offer the best means of characterizing colloidal materials as they provide direct visible evidence of the size, morphology, aggregation, and polydispersity of a given colloidal specimen. While chemists have continually pushed the boundaries of colloid synthesis to produce ever smaller particles with monodisperse uniformity in size and shape; microscope designers have matched the resolution of these small nanoparticles with innovative means of instrument development. Today's microscopes now deliver a spectrum of resolution capabilities and also facilitate simultaneous in-column compositional techniques. In the future, colloid researchers will continue to benefit from the growing arsenal of *in situ* techniques which can be employed to observe colloids in their native suspensions and under controlled environmental conditions. These innovative techniques offer an exciting frontier for the field of colloid science, through which microscopes will continue to be utilized as primary tools for colloid characterization for many years to come.

## References

1. *Handbook of Microscopy for Nanotechnology*, ed. N. Yao and Z. L. Wang, Kluwer Academic, New York, 2005.
2. E. Hecht, in *Optics*, Pearson Education Limited, London, 2014, pp. 1–10.
3. M. Knoll and E. Ruska, *Z. Phys.*, 1932, **78**, 318–339.
4. M. von Ardenne, *Z. Phys.*, 1938, **109**, 553–572.
5. IUPAC, *Compendium of Chemical Terminology*, Blackwell Scientific Publications, Oxford, 2nd edn, 1997.
6. M. Rippel, C. Alberto, P. Leite and F. Galembeck, 2002, **74**, 2541–2546.
7. E. S. Daniels, E. D. Sudol and M. S. El-Aasser, in *Polymer Colloids*, 2002, pp. 1–12.
8. T. R. Lettieri, A. W. Hartman, G. G. Hembree and E. Marx, *J. Res. Natl. Inst. Stand. Technol.*, 1991, **96**, 669–691.
9. J. W. Vanderhoff, M. S. El-Aasser, F. J. Micale, E. D. Sudol, C. M. Tseng and A. Silwanowicz, *J. Dispersion Sci. Technol.*, 1984, **5**, 231–246.
10. G. Mulholland, G. Hembree and A. Hartman, *Sizing of Polystyrene Spheres Produced in Microgravity*, Gaithersburg, MD, 1985.
11. Microscopic Beads Made in Space Go on Sale, *The New York Times*, July 17, 1985.
12. A. A. Shah, B. Schultz, W. Zhang, S. C. Glotzer and M. J. Solomon, *Nat. Mater.*, 2014, **14**, 117–124.
13. L. C. Hsiao, B. A. Schultz, J. Glaser, M. Engel, M. E. Szakasits, S. C. Glotzer and M. J. Solomon, *Nat. Commun.*, 2015, DOI: 10.1038/ncomms9507.
14. L. Colón-Meléndez, D. J. Beltran-Villegas, G. van Anders, J. Liu, M. Spellings, S. Sacanna, D. J. Pine, S. C. Glotzer, R. G. Larson and M. J. Solomon, *J. Chem. Phys.*, 2015, DOI: 10.1063/1.4919299.

15. Y. Kang, M. Li, Y. Cai, M. Cargnello, R. E. Diaz, T. R. Gordon, N. L. Wieder, R. R. Adzic, R. J. Gorte, E. A. Stach and C. B. Murray, *J. Am. Chem. Soc.*, 2013, **135**, 2741–2747.
16. V. E. Lee, C. Sosa, R. Liu, R. K. Prud'homme and R. D. Priestley, *Langmuir*, 2017, **33**, 3444–3449.
17. C. Sosa, R. Liu, C. Tang, F. Qu, S. Niu, M. Z. Bazant, R. K. Prud'homme and R. D. Priestley, *Macromolecules*, 2016, **49**, 3580–3585.
18. L. C. Bradley, K. J. Stebe and D. Lee, *J. Am. Chem. Soc.*, 2016, **138**, 11437–11440.
19. J. Lenis, S. Razavi, K. D. Cao, B. Lin, K. Y. C. Lee, R. S. Tu and I. Kretzschmar, *J. Am. Chem. Soc.*, 2015, **137**, 15370–15373.
20. A. B. Pawar and I. Kretzschmar, *Macromol. Rapid Commun.*, 2010, **31**, 150–168.
21. O. Shemi and M. J. Solomon, *Langmuir*, 2014, **30**, 15408–15415.
22. R. K. Iler, *Nature*, 1965, **207**, 472–473.
23. J. V. Sanders, *Nature*, 1964, **201**, 1151–1153.
24. J. B. Jones, J. V. Sanders and E. R. Segnit, *Nature*, 1964, **204**, 990–991.
25. M. F. Bechtold and O. E. Snyder, *U. S. Pat. Off.*, 2,574,902, 1951, 1–9.
26. R. K. Iler, *U. S. Pat. Off.*, 2727008, 1955, 1–4.
27. G. B. Alexander, *U. S. Pat. Off.*, 2750345, 1956, 1–5.
28. R. C. Atkins, *U. S. Pat. Off.*, 3012973, 1961, 1–5.
29. W. Stöber, A. Fink and E. Bohn, *J. Colloid Interface Sci.*, 1968, **26**, 62–69.
30. Y. A. Vlasov, N. Yao and D. J. Norris, *Adv. Mater.*, 1999, **11**, 165–169.
31. T. M. Davis, M. A. Snyder, J. E. Krohn and M. Tsapatsis, *Chem. Mater.*, 2006, **18**, 5814–5816.
32. G. H. Bogush, M. A. Tracy and C. F. Zukoski, *J. Non-Cryst. Solids*, 1988, **104**, 95–106.
33. R. Liu and R. D. Priestley, *J. Mater. Chem. A*, 2016, **4**, 6680–6692.
34. P. M. Arnal, C. Weidenthaler and F. Schüth, *Chem. Mater.*, 2006, **18**, 2733–2739.
35. W. Stichert and F. Schüth, *Chem. Mater.*, 1998, **10**, 2020–2026.
36. R. Liu, Y.-W. Yeh, V. H. Tam, F. Qu, N. Yao and R. D. Priestley, *Chem. Commun.*, 2014, **50**, 9056–9059.
37. R. Liu, F. Qu, Y. Guo, N. Yao and R. D. Priestley, *Chem. Commun.*, 2014, **50**, 478–480.
38. N. C. Strandwitz and G. D. Stucky, *Chem. Mater.*, 2009, **21**, 4577–4582.
39. P. M. Arnal, M. Comotti and F. Schüth, *Angew. Chem., Int. Ed.*, 2006, **45**, 8224–8227.
40. P. M. Arnal, F. Schüth and F. Kleitz, *Chem. Commun.*, 2006, 1203–1205.
41. F. Schüth, *Angew. Chem., Int. Ed.*, 2003, **42**, 3604–3622.
42. P. N. Pusey, W. C. K. Poon, S. M. Ilett and P. Bartlett, *J. Phys.: Condens. Matter*, 1994, **6**, A29–A36.
43. A. van Blaaderen, R. Ruel and P. Wiltzius, *Nature*, 1997, **385**, 321–324.
44. M. A. Snyder, *MRS Bull.*, 2016, **41**, 683–688.
45. P. Kumnorkaew, A. L. Weldon and J. F. Gilchrist, *Langmuir*, 2010, **26**, 2401–2405.

46. Z. Tian and M. A. Snyder, *Langmuir*, 2014, **30**, 9828–9837.
47. O. D. Velev and A. M. Lenhoff, *Curr. Opin. Colloid Interface Sci.*, 2000, **5**, 56–63.
48. C. B. Murray, D. J. Norris and M. G. Bawendi, *J. Am. Chem. Soc.*, 1993, **115**, 8706–8715.
49. C. B. Murray, S. Sun, W. Gaschler, H. Doyle, T. A. Betley and C. R. Kagan, *IBM J. Res. Dev.*, 2001, **45**, 47–56.
50. O. D. Velev, T. A. Jede, R. F. Lobo and A. M. Lenhoff, *Nature*, 1997, **389**, 447–448.
51. T. Yokoi, Y. Sakamoto, O. Terasaki, Y. Kubota, T. Okubo and T. Tatsumi, *J. Am. Chem. Soc.*, 2006, **128**, 13664–13665.
52. D. D. Brewer, J. Allen, M. R. Miller, J. M. de Santos, S. Kumar, D. J. Norris, M. Tsapatsis and L. E. Scriven, *Langmuir*, 2008, **24**, 13683–13693.
53. W. Fan, M. A. Snyder, S. Kumar, P.-S. Lee, W. C. Yoo, A. V. McCormick, R. L. Penn, A. Stein and M. Tsapatsis, *Nat. Mater.*, 2008, **7**, 984–991.
54. S. G. Rudisill, S. Shaker, D. Terzic, R. Le Maire, B.-L. Su and A. Stein, *Inorg. Chem.*, 2014, **54**, 993–1002.
55. A. Stein, S. G. Rudisill and N. D. Petkovich, *Chem. Mater.*, 2014, **26**, 259–276.
56. M. Joy, T. Muangnapoh, M. A. Snyder and J. F. Gilchrist, *Soft Matter*, 2015, **11**, 7092–7100.
57. X. Ye, J. Chen, M. E. Irrgang, M. Engel, A. Dong, S. C. Glotzer and C. B. Murray, *Nat. Mater.*, 2016, **16**, 214–219.
58. A. L. Weldon, K. Joshi, A. F. Routh and J. F. Gilchrist, *J. Colloid Interface Sci.*, 2017, **487**, 80–87.
59. J. M. Boettcher, M. Joy, K. Joshi, T. Muangnapoh and J. F. Gilchrist, *Langmuir*, 2015, **31**, 10935–10938.
60. J.-H. Choi, H. Wang, S. J. O. Oh, T. Paik, P. S. Jo, J. Sung, X. Ye, T. Zhao, B. T. Diroll, C. B. Murray and C. R. Kagan, *Science*, 2016, **352**, 205–208.
61. S. C. Kung, C.-C. Chang, W. Fan and M. A. Snyder, *Langmuir*, 2014, **30**, 11802–11811.
62. E. V. Shevchenko, D. V. Talapin, N. A. Kotov, S. O'Brien and C. B. Murray, *Nature*, 2006, **439**, 55–59.
63. G. M. Whitesides and B. Grzybowski, *Science*, 2002, **295**, 2418–2422.
64. J. V. Sanders, *Philos. Mag. A*, 1980, **42**, 705–720.
65. R. C. Schrodern, M. Al-Daous and A. Stein, *Chem. Mater.*, 2001, **13**, 2945–2950.
66. A. Stein, F. Li and N. R. Denny, *Chem. Mater.*, 2008, **20**, 649–666.
67. D. P. Josephson, M. Miller and A. Stein, *Z. Anorg. Allg. Chem.*, 2014, **640**, 655–662.
68. A. Stein, B. E. Wilson and S. G. Rudisill, *Chem. Soc. Rev.*, 2013, **42**, 2763–2803.
69. O. D. Velev, P. M. Tessier, A. M. Lenhoff and E. W. Kaler, *Nature*, 1999, **401**, 548.
70. D. G. Gregory, Q. Guo, L. Lu, C. J. Kiely and M. A. Snyder, *Langmuir*, 2017, **33**, 6601–6610.

71. Z. Tian and M. A. Snyder, *Langmuir*, 2014, **30**, 12411–12420.
72. P. Yang, T. Deng, D. Zhao, P. Feng, D. Pine, B. F. Chmelka, G. M. Whitesides and G. D. Stucky, *Science*, 1998, **282**, 2244–2246.
73. Z. Wang, M. A. Al-Daous, E. R. Kiesel, F. Li and A. Stein, *Microporous Mesoporous Mater.*, 2009, **120**, 351–358.
74. F. Li, W. C. Yoo, M. B. Beernink and A. Stein, *J. Am. Chem. Soc.*, 2009, **131**, 18548–18555.
75. J. W. Vanderhoff, in *Emulsion Polymerization and Emulsion Polymers*, 1981, pp. 199–208.
76. F. Li, D. P. Josephson and A. Stein, *Angew. Chem. Int. Ed. Engl.*, 2011, **50**, 360–388.
77. E. A. Collins, in *Emulsion Polymerization and Emulsion Polymers*, 1997, pp. 385–436.
78. D. G. Gregory, *Stabilization of Metastable Oxides via Surface Modification*, PhD Thesis, Lehigh University, Bethlehem, PA, USA, 2016.
79. L. Abis, S. J. Freakley, G. Dodekatos, D. J. Morgan, M. Sankar, N. Dimitratos, Q. He, C. J. Kiely and G. J. Hutchings, *ChemCatChem*, 2017, **9**, 2914–2918.
80. B. Imelik and J. C. Vedrine, in *Catalyst Characterization: Physical Techniques for Solid Materials*, 1994, pp. 1–10.
81. E. Abbe, *Arch. Mikrosk. Anat.*, 1873, **9**, 413–418.
82. L. Rayleigh, *Philos. Mag.*, 1896, **42**, 167–195.
83. H. von Busch, *Ann. Phys.*, 1926, **386**, 974–993.
84. O. D. Velev, T. A. Jede, R. F. Lobo and A. M. Lenhoff, *Chem. Mater.*, 1998, **10**, 3597–3602.
85. M. Cavallarou Jr, M. A. Gharbi, D. A. Beller, S. Čopar, Z. Shi, R. D. Kamien, S. Yang, T. Baumgart and K. J. Stebe, *Soft Matter*, 2013, **9**, 9099–9102.
86. N. Li, N. Sharifi-Mood, F. Tu, D. Lee, R. Radhakrishnan, T. Baumgart and K. J. Stebe, *Langmuir*, 2016, **33**, 600–610.
87. M. S. Elliot and W. C. K. Poon, *Adv. Colloid Interface Sci.*, 2001, **92**, 133–194.
88. L. C. Bradley, W.-H. Chen, K. J. Stebe and D. Lee, *Curr. Opin. Colloid Interface Sci.*, 2017, **30**, 25–33.
89. I. B. Liu, G. Bigazzi, N. Sharifi-Mood, L. Yao and K. J. Stebe, Curvature Capillary Repulsion, *Phys. Rev. Fluids*, 2017, **2**, 100501.
90. M. Ghosh, F. Fan and K. J. Stebe, *Langmuir*, 2007, **23**, 2180–2183.
91. P. Kumnorkaew, Y. K. Ee, N. Tansu and J. F. Gilchrist, *Langmuir*, 2008, **24**, 12150–12157.
92. H. Deschout, F. C. Zanacchi, M. Mlodzianoski, A. Diaspro, J. Bewersdorf, S. T. Hess and K. Braeckmans, *Nat. Methods*, 2014, **11**, 253–266.
93. Z. Song, E. S. Daniels, E. D. Sudol, J. F. Gilchrist, A. Klein and M. S. El-aasser, *J. Appl. Polym. Sci.*, 2013, 2635–2640.
94. J. Cui, D. Long, P. Shapturenka, I. Kretzschmar, X. Chen and T. Wang, *Colloids Surf., A*, 2017, **513**, 452–462.
95. M. K. Klein, N. Klinkenberg, S. Schuetter, N. Saenger, P. Pfleiderer and A. Zumbusch, *Langmuir*, 2015, **31**, 2655–2661.

96. J. Shan, S. J. Budijono, G. Hu, N. Yao, Y. Kang, Y. Ju and R. K. Prud'Homme, *Adv. Funct. Mater.*, 2011, **21**, 2488–2495.
97. O. S. Wolfbeis, *Chem. Soc. Rev.*, 2015, **44**, 4743–4768.
98. E. Betzig, G. H. Patterson, R. Sougrat, O. W. Lindwasser, S. Olenych, J. S. Bonifacino, M. W. Davidson, J. Lippincott-Schwartz and H. F. Hess, *Science*, 2006, **313**, 1642–1645.
99. M. K. Klein, A. Zumbusch and P. Pfleiderer, *J. Mater. Chem. C*, 2013, **1**, 7228–7236.
100. V. Prasad, D. Semwogerere and E. R. Weeks, *J. Phys.: Condens. Matter*, 2007, DOI: 10.1088/0953-8984/19/11/113102.
101. T. Muangnapoh, A. L. Weldon and J. F. Gilchrist, *Appl. Phys. Lett.*, 2013, **103**, 181603.
102. A. Mohraz and M. J. Solomon, *Langmuir*, 2005, **21**, 5298–5306.
103. T. E. Kodger, R. E. Guerra and J. Sprakler, *Sci. Rep.*, 2015, DOI: 10.1038/srep14635.
104. A. A. Shah, B. Schultz, K. L. Kohlstedt, S. C. Glotzer and M. J. Solomon, *Langmuir*, 2013, **29**, 4688–4696.
105. M. Cavallaro Jr., M. A. Gharbi, D. A. Beller, S. Copar, Z. Shi, T. Baumgart, S. Yang, R. D. Kamien and K. J. Stebe, *Proc. Natl. Acad. Sci.*, 2013, **110**, 18804–18808.
106. L. T. Shereda, R. G. Larson and M. J. Solomon, *Phys. Rev. Lett.*, 2008, DOI: 10.1103/PhysRevLett.101.038301.
107. Y. Kim, A. A. Shah and M. J. Solomon, *Nat. Commun.*, 2014, **5**, 1–8.
108. L. C. Hsiao, R. S. Newman, S. C. G. Glotzer and M. J. Solomon, *Proc. Natl. Acad. Sci. U. S. A.*, 2012, **109**, 16029–16034.
109. L. T. Shereda, R. G. Larson and M. J. Solomon, *Phys. Rev. Lett.*, 2010, **105**, 1–4.
110. J. C. Crocker and D. G. Grier, *J. Colloid Interface Sci. U. S. A.*, 1996, **179**, 298–310.
111. R. F. Egerton, *Physical Principles of Electron Microscopy*, Springer International Publishing, Switzerland, 2016.
112. G. Binning, H. Rohrer, C. Gerber and E. Weibel, *Am. Phys. Soc.*, 1982, **49**, 57–61.
113. S. Suryajaya, A. Nabok, F. Davis, A. Hassan, S. P. J. Higson and J. Evans-Freeman, *Appl. Surf. Sci.*, 2008, **254**, 4891–4898.
114. E. Dokou, M. A. Bartheau, N. J. Wagner and A. M. Lenhoff, *J. Colloid Interface Sci.*, 2001, **240**, 9–16.
115. M. Raşa, B. W. M. Kuipers and A. P. Philipse, *J. Colloid Interface Sci.*, 2002, **250**, 303–315.
116. V. Komanicky, A. Barbour, M. Lackova, M. Zorko, C. Zhu and M. Pierce, *Nanoscale Res. Lett.*, 2014, **9**, 1–7.
117. G. Singh, K. E. Bremmell, H. J. Griesser and P. Kingshott, *Soft Matter*, 2015, **11**, 3188–3197.
118. Y. Qian, Y. Deng, X. Qiu, H. Li and D. Yang, *Green Chem.*, 2014, **16**, 21562163.

119. F. Wu and N. Yao, in *Microscopy and Analysis*, ed. S. G. Stanciu, InTech, 2016, pp. 267–297.
120. P. W. Hawkes, *Philos. Trans. R. Soc., A*, 2009, **367**, 3637–3664.
121. A. Nikoubashman, V. E. Lee, C. Sosa, R. K. Prud'homme, R. D. Priestley and A. Z. Panagiotopoulos, *ACS Nano*, 2016, **10**, 1425–1433.
122. R. C. Hayward, D. A. Saville and I. A. Aksay, *Nature*, 2000, **404**, 56–59.
123. P. Kumrnorkaew and J. F. Gilchrist, *Langmuir*, 2009, **25**, 6070–6075.
124. J.-Q. Cui and I. Kretzschmar, *Langmuir*, 2006, **22**, 8281–8284.
125. M. J. Solomon and P. T. Spicer, *Soft Matter*, 2010, **6**, 1391–1400.
126. F. Fan and K. J. Stebe, *Langmuir*, 2004, **20**, 3062–3067.
127. A. M. Donald, *Nat. Mater.*, 2003, **2**, 511–516.
128. D. B. Williams and C. B. Carter, *Transmission Electron Microscopy*, Springer, New York, 2009.
129. C. J. Kiely, J. Fink, M. Brust, D. Bethell and D. J. Schiffrin, *Nature*, 1998, **396**, 444–446.
130. R. Ristau, R. Tiruvalam, P. L. Clasen, E. P. Gorskowski, M. P. Harmer, C. J. Kiely, I. Hussain and M. Brust, *Gold Bull.*, 2009, **42**, 133–143.
131. T. Paik, B. T. Diroll, C. R. Kagan and C. B. Murray, *J. Am. Chem. Soc.*, 2015, **137**, 6662–6669.
132. R. Liu, C. Sosa, Y. Yeh, F. Qu, N. Yao, K. Prud'homme and R. D. Priestley, *J. Mater. Chem. A*, 2014, **2**, 17286–17290.
133. K. Elbert, D. Jishkariani, Y. Wu, J. D. Lee, B. Donnio and C. B. Murray, *Chem. Mater.*, 2017, **29**, 8737–8746.
134. Y. He, B. Wang, X. Hu, X. Zhang, L. Sun, R. D. Priestley and R. Liu, *Colloid Polym. Sci.*, 2017, **295**, 521–527.
135. R. J. Keyse, A. J. Garratt-Reed, P. J. Goodhew and G. W. Lorimer, *Introduction to Scanning Transmission Electron Microscopy*, BIOS Scientific Publishers, Oxford, UK, 1998.
136. J. L. Hutchison, J. M. Titchmarsh, D. J. H. Cockayne, R. C. Doole, C. J. D. Hetherington, A. I. Kirkland and H. Sawada, *Ultramicroscopy*, 2005, **103**, 7–15.
137. M. T. Otten, *J. Electron Microsc. Tech.*, 1991, **117**, 221–230.
138. C. J. Kiely, J. Fink, J. G. Zheng, M. Brust, D. Bethell and D. J. Schiffrin, *Adv. Mater.*, 2000, **12**, 640–643.
139. N. Dimitratos, C. Hammond, C. J. Kiely and G. J. Hutchings, *Appl. Petrochem. Res.*, 2014, **4**, 85–94.
140. M. Cargnello, A. C. Johnston-Peck, B. T. Diroll, E. Wong, B. Datta, D. Damodhar, V. V. T. Doan-Nguyen, A. A. Herzing, C. R. Kagan and C. B. Murray, *Nature*, 2015, **524**, 450–453.
141. D. Jishkariani, Y. Wu, D. Wang, Y. Liu, A. van Blaaderen and C. B. Murray, *ACS Nano*, 2017, **11**, 7958–7966.
142. N. Yao, in *Focused Ion Beam Systems Basics and Applications*, ed. N. Yao, Cambridge University Press, Cambridge UK, 2007, pp. 1–30.
143. L. A. Giannuzzi and F. A. Stevie, *Introduction to Focused Ion Beams Instrumentation, Theory, Techniques, and Practice*, Springer, New York, 2005.

144. D. C. Cox, *Introduction to Focused Ion Beam Nanometrology*, Morgan & Claypool, San Rafael, CA, 2015.
145. D. G. Gregory, L. Lu, C. J. Kiely and M. A. Snyder, *J. Phys. Chem. C*, 2017, **121**, 4434–4442.
146. J. Wang, M. Jin, T. He, G. Zhou and L. Shui, *Micromachines*, 2015, **6**, 1331–1345.
147. N. Ochiai, E. L. Kraft and J. S. Selker, *Water Resour. Res.*, 2006, **42**, 1–14.
148. E. W. Muller, *Z. Phys.*, 1951, **131**, 136–142.
149. N. P. Economou, J. A. Notte and W. B. Thompson, *Scanning*, 2012, **34**, 83–89.
150. S. Kostinski and N. Yao, *J. Appl. Phys.*, 2011, DOI: 10.1063/1.3549016.
151. D. C. Joy, *Helium Ion Microscopy Principles and Applications*, Springer, New York, 2013.
152. D. Cohen-Tanugi and N. Yao, *J. Appl. Phys.*, 2008, DOI: 10.1063/1.2976299.
153. J. Notte and J. Huang, in *Helium Ion Microscopy*, ed. G. Hlawacek and A. Gölzhäuser, Springer, 2016, pp. 3–30.

## CHAPTER 7

# *Simulations in Polymer Colloid Formation*

ARASH NIKOUBASHMAN

Institute of Physics, Johannes Gutenberg University Mainz, Staudingerweg 7, 55128 Mainz, Germany  
Email: anikouba@uni-mainz.de

## 7.1 Introduction

Polymeric nanoparticles (NPs) are increasingly sought after in various scientific and industrial areas, such as biomedical drug delivery,<sup>1,2</sup> cosmetics,<sup>3,4</sup> and interfacial property modifiers in enhanced oil recovery.<sup>5</sup> This broad scope of applications is achieved through the versatility of NP material properties and structures. One promising pathway for generating such tailored NPs in large quantities is flash nanoprecipitation (FNP).<sup>6</sup> Here, hydrophobic polymers in solution are rapidly mixed with a miscible aqueous antisolvent in a confined environment, inducing supersaturation and subsequent aggregation of the polymers. This technique stands out as a one-step continuous process that operates at room temperature, consumes little energy, and has the potential to scale up. Further, the FNP process allows for a wide range of feed materials, which in turn can be used to achieve various particle structures, including Janus, core-shell, patchy, and lamellar morphologies.

It is clear that the precipitation process and the properties of the resulting NPs strongly depend on the microscopic properties of the constituent polymers. However, it is experimentally challenging to determine the underlying mechanisms because the FNP process takes place on nanometer length scales and millisecond time scales. Furthermore, it is an expensive

and time-consuming task to systematically search and screen in the experiments all relevant process parameters, such as the feed ratio, feed concentration, flow rate, and molecular properties. Computer simulations can provide considerably more microscopic-level information than experiments and are therefore formidable tools in the study of complex mechanisms and morphologies. They also offer advantages in efficient parameter space searching.

FNP is an inherently multi-scale problem, as the solvent molecules typically have sizes of a few ångströms, the dissolved polymers are on the order of nanometers, while the precipitated NPs can have radii up to several hundred nanometers. Further, this process spans a wide range of time scales, *e.g.* the characteristic relaxation times of the polymers are on the order of nanoseconds, whereas typical mixing times lie in the millisecond regime. Models with atomistic detail quickly become computationally intractable, both in terms of the number of particles required for such a model and the number of simulation time steps that are necessary to access the time scales of interest. Thus, it is crucial to reduce the details of the model as much as possible, without sacrificing the essential aspects of the system. This procedure is one of the most challenging aspects of theoretical modeling and simulation, since it is often not clear *a priori* which contributions can be safely neglected. In this chapter, we will discuss in detail simulations in polymer colloid formation with a focus on the FNP technique. In Section 7.2, particle-based molecular dynamics (MD) simulations are presented, highlighting the thought process behind the modeling. In Section 7.3, we discuss how the microscopically detailed MD simulations can be extended to macroscopic length and time scales through the Kinetic Monte Carlo (KMC) approach.

## 7.2 Particle-based Modeling

### 7.2.1 General Considerations

The first step in developing a computational model consists in mapping out the experimental parameter space. Typically, FNP utilizes polymers with molecular weights in the order of  $M = 10\text{--}100 \text{ kg mol}^{-1}$  at feed concentrations in the range of  $\Phi = 0.01\text{--}1.0 \text{ mg ml}^{-1}$ . For these conditions, typical radii of the precipitated NPs vary between a few tens of nanometers and a few hundreds of nanometers. In order to establish a sense of scale for the problem, let us consider for example a polymeric NP with a radius of  $R = 100 \text{ nm}$ , consisting of polystyrene (PS) homopolymers with a molecular weight of  $M = 16.5 \text{ kg mol}^{-1}$ .<sup>7</sup> We can determine the approximate number of polymers in a single aggregate by dividing its volume by the volume of a single PS chain. In Table 7.1 we have summarized the relevant parameters for selected polymers, and using these data we find  $V_{\text{chain}} = M/\rho_{\text{PS}} \approx 28 \text{ nm}^3$ . Therefore, each NP contains roughly  $4/3\pi R^3/V_{\text{chain}} \approx 150\,000$  polymer chains. If we now take into account that each of these polymers consists of roughly

**Table 7.1** Molecular weight of the repeat unit  $M_0$ , molecular weight of the Kuhn segment  $M_K$ , Kuhn length  $b_K$ , and mass density  $\rho$  for atactic polystyrene (PS), *cis*-polyisoprene (PI), polymethylmethacrylate (PMMA) and *cis*-polybutadiene (PBd).

Polymer	$M_0$ [kg mol $^{-1}$ ]	$M_K$ [kg mol $^{-1}$ ]	$b_K$ [\mathring{A}]	$\rho$ [g cm $^{-3}$ ]	Ref.
PS	0.104	0.720	18	0.969	8, 9
PI	0.068	0.129	9.3	0.910	10
PMMA	0.100	0.598	15	1.13	10
PBd	0.054	0.091	8.3	0.900	10

$N = 160$  monomers, which in turn consist each of eight carbon and eight hydrogen atoms, then we find that roughly  $4 \times 10^8$  particles are needed to represent a *single* NP in atomistic detail. The situation becomes even worse if we consider the large number of solvent particles which is required due to the low feed concentrations of FNP. Another prohibitive constraint of such atomistic models is the small simulation time step on the order of femtoseconds required for resolving the fast vibrational modes of the molecules.

It is thus clear that atomistic simulations of the entire FNP process are computationally impossible and that reductions in model detail are inevitable. In united atom (UA) models the number of particles is reduced by representing a small group of adjacent atoms by one effective bead. For instance, in the transferable potentials for phase equilibria-united atom (TraPPE-UA) force fields,<sup>11</sup> hydrogen and carbon atoms in a methyl group are treated as a single interaction site. Such an approximation is reasonable for molecular systems where the intermolecular motion is much more important than the intramolecular one, and it can lead to a substantial performance increase compared to fully atomistic descriptions. Despite this reduction in detail, however, UA models are still too computationally taxing for simulating the FNP process. These models are rather applicable for studying the behavior of few macromolecules in solution on nanosecond time scales.<sup>12</sup>

The number of interaction sites can be further reduced by representing each monomer by a single (spherical) bead. This level of coarse-graining is suitable for many problems, where spatial resolution on the monomer level is desired, but atomistic details, *e.g.* the orientation of the phenyl groups in PS, are of minor importance. These models can accurately reproduce structural and thermodynamic properties of the specific experimental systems rather well, when the parametrization is performed carefully.<sup>13–15</sup> With this level of coarse-graining, roughly  $2.5 \times 10^7$  particles are needed to simulate a single polymeric NP, which is in the realm of feasibility for current supercomputers.<sup>16</sup> However, sampling many configurations or exploring parameter space will be challenging due to the high computational cost.

For sufficiently large intramolecular distances, the spatial correlation between bonded monomers has sufficiently decayed so that the chains follow the random walk model, where each step taken in a random direction is independent of the directions taken in the previous steps. The resulting

random coil consists of  $N_K$  segments with length  $b_K$ , and its radius of gyration,  $R_{g,id}$ , can be computed through:<sup>9</sup>

$$R_{g,id} = \frac{1}{\sqrt{6}} b_K N_K^{1/2}. \quad (7.1)$$

Values of  $b_K$  and  $N_K$  for typical polymers are listed in Table 7.1. In practice,  $N_K$  and  $b_K$  can be determined by equating the expressions for the radius of gyration,  $R_g$ , and for the contour length,  $L$ , from the actual chain and the equivalent chain with Kuhn segments. The Kuhn segment construction is useful in that it allows complicated polymers to be treated with simplified models as a (self-avoiding) random walk. For instance, a PS chain with  $M = 16.5 \text{ kg mol}^{-1}$  can be mapped to a chain with  $N_K = 23$  Kuhn segments, and it has a radius of gyration of  $R_{g,id} \approx 3.5 \text{ nm}$ . This mapping effectively reduces the number of particles per chain by two orders of magnitude compared to the fully atomistic description. This polymer representation strikes the balance between microscopic detail and computational efficiency, and therefore is the model of choice in several MD simulations of the FNP process.<sup>7,17-19</sup>

As the next step, the solvent needs to be modeled. In the experiments, the polymers are initially dissolved in a good solvent, for example tetrahydrofuran (THF) for PS. Under such good solvent conditions, the polymers attain a swollen coil-like configuration with a sizable amount of solvent located within the enclosed volume. In contrast, when the polymers are dispersed in a poor solvent, *e.g.* water for PS, the chains collapse into compact globules and aggregate to minimize the interface area with the surrounding liquid (see Figure 7.1 for a schematic representation). At intermediate solvent qualities, the intermolecular interactions between polymer chain segments and coordinated solvent molecules become similar ( $\Theta$ -condition), and the dispersed chains effectively act like ideal chains. In addition to these structural effects on the polymer conformation, the solvent also impacts the

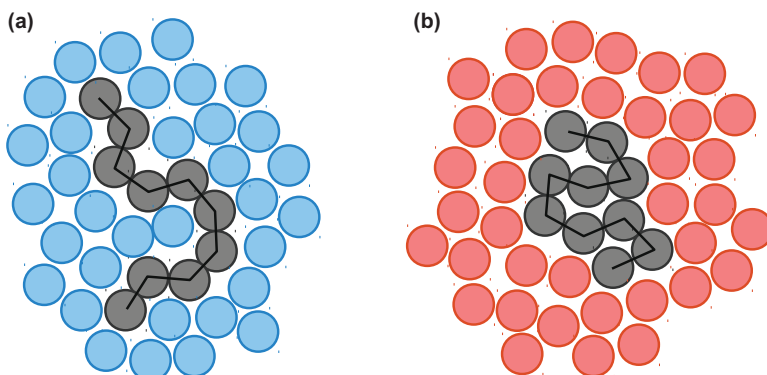


**Figure 7.1** Schematic illustration of a polymer with  $N=10$  segments in (a) good, and (b) poor solvents.

Published on 02 December 2019 on https://pubs.rsc.org | doi:10.1039/9781788016476-00240

polymer dynamics by exerting drag on the dispersed particles and mediating hydrodynamic interactions. There are numerous strategies for incorporating solvent-induced effects, for example by explicitly representing solvent particles,<sup>7,17–21</sup> by modeling the solvent implicitly using Langevin dynamics simulations,<sup>21</sup> or by coupling the simulations to a computational fluid dynamics solver.<sup>22</sup> An extensive discussion of the various methods goes beyond the scope of this contribution, and therefore we will focus on one model and discuss its advantages and disadvantages in detail.

In many simulation studies of the FNP process, the solvent is represented with an explicit-solvent model where the solvent particles are represented as spherical beads. This model captures thermal fluctuations, solvent displacement and hydrodynamic effects. For computational convenience, each solvent particle is chosen to have the same size and mass as a polymer Kuhn segment, *i.e.*  $\sim 1$  nm (*cf.* Table 7.1). In order to better understand the physical consequences of this choice, it is helpful to consider the structuring of the solvent molecules on the molecular level. Figure 7.2 shows the radial pair distribution functions,  $g(r)$ , between solvent molecules for THF–water mixtures at various water mole fractions,  $X_w$ , computed from simulations using an UA model.<sup>12</sup> The radial pair distribution between pairs of water molecules (see Figure 7.2a) has a clear first peak at an intermolecular distance of  $r \approx 3$  Å, irrespective of  $X_w$ . The  $g(r)$  data further indicate local clustering and layering of water molecules in the shell of nearest neighbors, which become more pronounced for decreasing  $X_w$ . This structuring vanishes for distances  $r \gtrsim 8$  Å, where the liquid is essentially homogeneous. The THF molecules exhibit a similar structuring (see Figure 7.2b), with a first peak at  $r \approx 5$  Å and a subsequent layering of THF molecules, which disappears for  $r \gtrsim 15$  Å. The  $g(r)$  data for pairs of water and THF molecules shown in Figure 7.2c reveals the presence of two pronounced solvation shells of water around THF molecules at  $r \approx 3$  Å and  $r \approx 5$  Å, respectively. For larger distances  $r \gtrsim 10$  Å, we find  $g(r) \approx 1$ , which indicates homogeneous mixing of the two liquids. (Similar results for  $g(r)$  were obtained in other UA<sup>23</sup> and fully atomistic<sup>24,25</sup> simulations of THF–water systems.) In summary, the solvent can be regarded as structureless in the spatial resolution of our simulation model, *i.e.*  $\sim 1$  nm.

There are various strategies for modeling the rapid mixing of good solvent and poor solvent in FNP. One possibility is to use distinct particle types for the good and poor solvent particles, as proposed in ref. 26. Initially, the polymers are dispersed in a good solvent. Then, at a certain time some of the solvent particles change their interactions with the polymers to those of poor solvent particles. These identity changes occur only for solvent particles beyond the interaction range with the dispersed polymers in order to avoid unphysical sudden changes. The effective fraction of poor solvent locally experienced by the polymer changes gradually as the solvent particles diffuse into the formerly protected volume. On the one hand, this model closely mimics the experiments and it is able to capture effects such as solvent trapping, which can play an important role in the structure formation in FNP.<sup>27</sup> On the other hand, this approach can quickly become computationally taxing when the

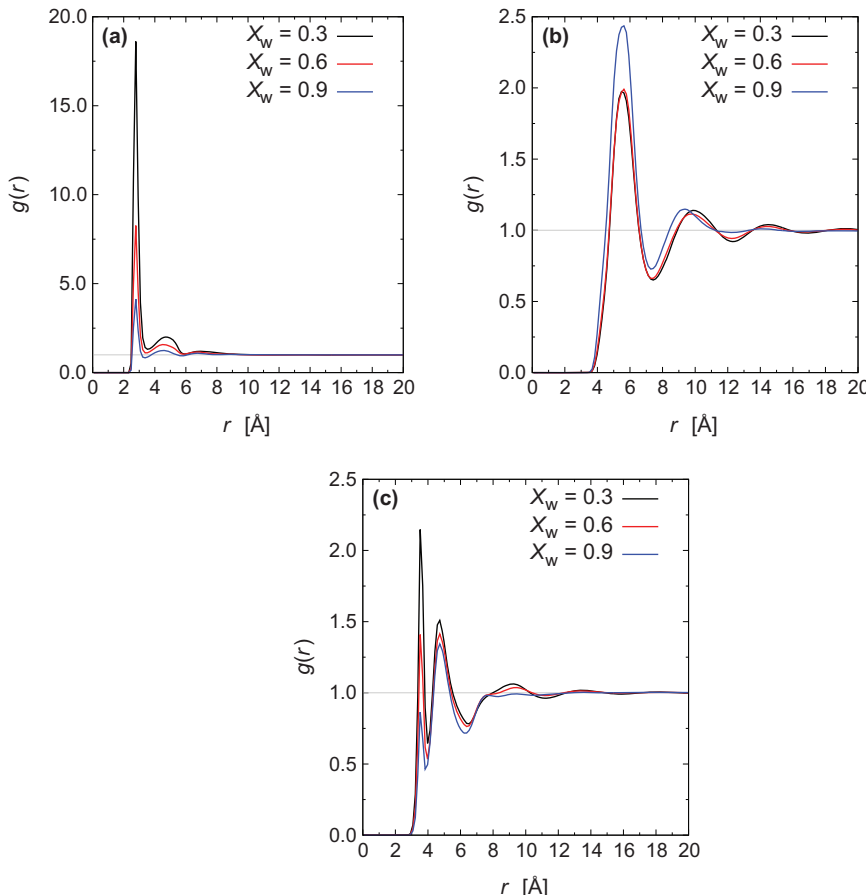


**Figure 7.2** Radial pair distribution function,  $g(r)$ , between the center of mass positions of (a) water–water, (b) THF–THF, and (c) water–THF molecules at various water mole fractions  $X_w$ .

Reproduced from ref. 12 with permission from American Chemical Society, Copyright 2018.

polymer concentration increases, due to the overhead of determining the protected volume around the individual polymers. (In fact, current studies using this model are limited to a single polymer in solution.<sup>26</sup>)

Alternatively, the solvent exchange can be mimicked by gradually changing over a fixed mixing time,  $\tau_{\text{mix}}$ , the interaction between the polymer beads and *all* solvent particles in the system. This strategy was employed in several simulation studies of the FNP process,<sup>7,17–21</sup> and can be motivated by the fact that the good and poor solvent particles are essentially homogeneously mixed on the spatial resolution of a solvent particle (*cf.* Figure 7.2c). However, it should be noted that such mean-field type models cannot capture the fractioning of good and poor solvent, which can occur when polymers are added to

the solvent mixture.<sup>12,27</sup> For example, recent UA simulations<sup>12</sup> of PS in THF–water mixtures have revealed a small mixing regime (water mole fraction  $X_w = 0.75$ ), where a sizable fraction of residual THF molecules was trapped inside the collapsed polymers, with an excess amount located at the globule–solvent interface, serving as a protective layer between the hydrophobic PS and the surrounding water-rich mixture. Nonetheless, this simplified model captures the essential aspects of the FNP process, and therefore we will focus on this model for the remainder of this work.

### 7.2.2 Model Details

In this section we will concentrate on the specific choices for the interaction potentials and the parameterization of the model. As discussed in Section 7.2.1, we represent the polymers on the level of Kuhn segments to expedite the simulations. In practice, this is achieved by using a bead–spring model, where each Kuhn segment is represented as an individual spherical bead with mass  $m$ . The nonbonded interactions between the beads are given by the standard Lennard–Jones (LJ) potential:

$$U_{MM}(r) = 4\epsilon \left[ \left( \frac{\sigma}{r} \right)^{12} - \left( \frac{\sigma}{r} \right)^6 \right], \quad (7.2)$$

with interparticle distance  $r = |\mathbf{r}_j - \mathbf{r}_i|$ . The prefactor  $\epsilon$  dictates the strength of the interaction, while the parameter  $\sigma$  corresponds to the diameter of the beads. (Note that the pair potential is usually truncated for distances beyond a predefined cutoff radius,  $r_{cut}$ , for computational efficiency.) If not stated otherwise,  $\sigma$ ,  $\epsilon$ , and  $m$  will be used as the units of length, energy, and mass respectively in the simulations. The LJ potential is chosen due to its functional simplicity and because it has been used extensively in prior studies,<sup>28–33</sup> but in general more complex interactions are also possible, such as the Morse or Mie potentials. Another advantage of the LJ potential is its generic nature, which helps to reveal the principal physical mechanisms behind the FNP process, instead of concentrating on a single specific monomer chemistry. It is also possible to use this model for simulating FNP of homopolymer blends<sup>17,18</sup> and block copolymers.<sup>19</sup> To this end, the parameter  $\epsilon$  in eqn (7.2) for the interspecies interactions needs to be adjusted to achieve the desired surface tension<sup>17,18</sup> or Flory–Huggins interaction parameter,  $\chi$ .<sup>19,33</sup>

Covalent bonds are mimicked *via* the finitely extensible nonlinear elastic (FENE) potential:<sup>34</sup>

$$U_{FENE}(r) = \begin{cases} -\frac{1}{2} kr_0^2 \ln \left[ 1 - \frac{r^2}{r_0^2} \right], & r \leq r_0 \\ \infty, & r > r_0 \end{cases}, \quad (7.3)$$

with spring constant  $k$  and maximum spring extension  $r_0$ . These parameters are set to  $k = 30\epsilon/\sigma^2$  and  $r_0 = 1.5\sigma$  to prevent unphysical bond crossing.<sup>35</sup> The resulting equilibrium bond length for this parameterization is  $b \approx 0.97\sigma$ .

The surrounding solvent is modeled explicitly as a liquid of LJ particles with the same size and mass as the polymer beads (see Figure 7.1). Following ref. 36 and 37, a reduced number density of  $\rho_s = 0.66\sigma^{-3}$  was used, and the solvent–solvent interaction strength was set to  $\varepsilon_{ss} = \varepsilon$ . For this choice of parameters, the Schmidt number of the LJ solvent is  $Sc \approx 10$ , which is sufficiently large for describing a liquid-like medium.<sup>36,38</sup> The solvent quality can be controlled by tuning the cross interaction between solvent particles and monomers:<sup>29</sup>

$$U_{MS}(r) = \gamma U_{WCA}(r) + (1 - \gamma) U_{MM}(r), \quad (7.4)$$

where  $U_{WCA}(r)$  is the purely repulsive Weeks–Chandler–Andersen (WCA) potential,<sup>39</sup> which is obtained by truncating eqn (7.2) at  $r = 2^{1/6}$  and shifting it by  $\varepsilon$ . The dimensionless parameter  $0 \leq \gamma \leq 1$  controls the solvent quality; for  $\gamma = 0$ , the solvent–monomer interaction becomes identical to the monomer–monomer interactions, resulting in good solvent conditions. For  $\gamma = 1$ , however,  $U_{MS}$  becomes purely repulsive so that the monomers want to minimize contact with the surrounding solvent particles, effectively mimicking poor solvent conditions.  $\Theta$ -conditions are achieved at  $\gamma \approx 0.05$  for the present parameterization.<sup>29</sup>

In ref. 7, 17–19, MD simulations of this model were performed using the HOOMD-blue software package<sup>16,40</sup> on graphics processing units (GPUs). Simulations were conducted in the *NVT* ensemble using a cubic simulation box (edge length  $L_{box}$ ) with periodic boundary conditions in all directions to mimic bulk conditions. A Nosé–Hoover thermostat using the Martyna–Tobias–Klein equations<sup>41,42</sup> was employed to fix the temperature at  $T = \varepsilon/k_B$  with  $k_B$  being Boltzmann's constant. This thermostat couples the system to an (implicit) external heat reservoir through a fictitious spring, allowing for heating as well as for dissipation of excess heat. The coupling strength can be tuned *via* the damping time of the spring,  $\tau_{NH}$ . Too large values of  $\tau_{NH}$  (loose coupling) may cause poor temperature control, whereas too small values (tight coupling) may cause high-frequency temperature oscillations. It was found that  $\tau_{NH} = 0.5$  leads to quick equilibration as well as good temperature stability and therefore this value was used in the simulations. The time step of the simulations was set to  $\Delta t = 0.005\tau$ , where  $\tau$  is the unit of time, which will be specified further below.

Before simulating the entire FNP process, let us first consider the behavior of a single polymer in a solvent of varying quality. Figure 7.3 shows the radius of gyration,  $R_g$ , and the diffusion coefficient,  $D$ , of a chain as a function of  $\gamma$ . For  $\gamma = 0$ , the polymer is well dispersed in the solvent and has an open coil-like conformation. As the solvent quality worsens for  $\gamma \rightarrow 1$ , the polymer collapses into a compact globule, which is reflected by the strong decay of  $R_g$ . At the same time,  $D$  increases by roughly the same factor, as expected from the Stokes–Einstein relationship  $D \propto R_g^{-1}$ . In ref. 7, 17–19, an upper bound of  $\gamma = 0.5$  was used to reproduce the 1:1 volume ratio of polymer solution to poor solvent, typically used in FNP experiments with a confined impinging jet mixer.<sup>19,27,43,44</sup>

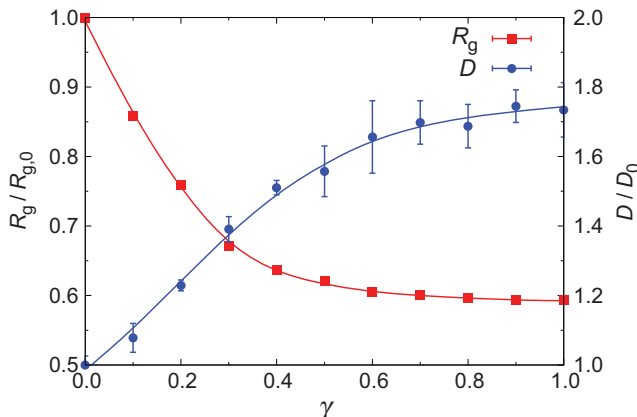


**Figure 7.3** Radius of gyration,  $R_g$ , and diffusion coefficient,  $D$ , of a single polymer ( $N=23$ ) in solution as a function of solvent quality, which worsens as  $\gamma \rightarrow 1$ . The data have been normalized by their values at good solvent conditions ( $\gamma = 0$ ),  $R_{g0}$  and  $D_0$ , respectively. The solid lines are guides to the eye.  
Reproduced from ref. 7 with permission from American Chemical Society, Copyright 2016.

The simulation results for a single polymer in solution can now be used to establish a connection between the units of energy, length, and time from simulations and experiments. The experimental reference system consists of PS homopolymers ( $M = 16.5 \text{ kg mol}^{-1}$ ) dissolved in THF, water is used as the poor solvent, and mixing is performed at room temperature ( $T_{\text{room}} = 298 \text{ K}$ ). The energy scale is given by the thermal energy  $\varepsilon = k_B T$ , which then is  $\varepsilon = 4.11 \times 10^{21} \text{ J}$ . For the length scale, eqn (7.1) is used to estimate the radius of gyration of a single PS chain in a  $\Theta$ -solvent, *i.e.*  $R_{g,\Theta}^{\text{PS}} = 3.5 \text{ nm}$ . Then the same quantity is computed for our bead-spring polymer model, *i.e.*  $R_{g,\Theta}^{\text{sim}} = 2.35 \sigma$ , leading to a conversion factor of  $\sigma = 1.5 \text{ nm}$ . To establish the time scale, the long-time diffusion coefficients in a dilute polymer solution are matched. The diffusion coefficients of various PS chains in THF were measured experimentally *via* laser light scattering spectrometry in ref. 45, and we extrapolated the value  $D_0^{\text{PS}} \approx 1.4 \times 10^6 \text{ cm}^2 \text{ s}^{-1}$  for a polymer with  $M = 16.5 \text{ kg mol}^{-1}$ . In the simulations, Nikoubashman *et al.* set  $\gamma = 0$  and computed  $D_0^{\text{sim}} = 0.019 \sigma^2 \tau^{-1}$  through the mean square displacement of the polymer's center of mass.<sup>7</sup> Matching  $D_0^{\text{PS}}$  with  $D_0^{\text{sim}}$  results in the time scale  $\tau = 3 \times 10^{-10} \text{ s}$ .

With these conversion factors at hand, it is possible to estimate how close the microscopic MD simulations can get to the characteristic processing parameters of FNP (see Section 7.2.1). Typical simulation boxes have edge lengths ranging from  $L_{\text{box}} = 120 \text{ nm} - 210 \text{ nm}$ , containing up to 2 000 000 particles. At a polymer concentration of  $\Phi = 0.1 \text{ mg ml}^{-1}$ , the entire simulation box would then only include between 6 and 30 polymers. Therefore, in the simulations polymer concentrations roughly 2 orders of magnitude higher than those in the experimental systems were used. Another consequence of the finite size of the simulation box is that there is an upper

bound for the size of the NPs that can form. For example, if there are 1024 polymers in the system, then the maximum NP radius is limited to  $R \approx 21$  nm.<sup>7</sup> Finally, simulation times of up to a few milliseconds can be achieved with this microscopic model,<sup>18</sup> whereas the experimentally relevant time scales can extend up to several months if particle stability is of interest. However, despite these approximations, the simulations successfully reproduce the experimental trends in a semiquantitative manner and provide valuable insights into the microscopic self-assembly mechanisms of FNP.<sup>7,17-19</sup>

One key element of the FNP process, which we have not discussed so far, is *particle stabilization*. To ensure a long shelf life of colloidal dispersions, a high stability against aggregation is desirable. There are two main mechanisms for achieving stability in colloidal dispersions, namely electrostatic stabilization<sup>46</sup> and steric stabilization.<sup>47-49</sup> The former is based on the mutual repulsion of like electrical charges on the NPs, while the latter is usually achieved by coating NPs with amphiphilic chains. It is rather straightforward to implement these effects in this microscopic model. For example, polymers with charged end groups can be simulated by assigning an electric charge to the last bead in a polymer chain, while amphiphilic polymers can be modeled by keeping the solvent-monomer interaction of the hydrophilic block fixed at  $\gamma = 0$  during the entire simulation.

Surprisingly, in several experimental works the precipitated NPs were found to be stable, even though the employed hydrophobic polymers were electroneutral and no external stabilizers were added.<sup>7,19,27,43,44</sup> Using electrophoretic light scattering, the  $\zeta$ -potential of homogeneous PS NPs precipitated in THF–water mixtures was determined as  $\zeta \approx -33$  mV, almost independent of the NP size (radii ranging from 45 to 135 nm).<sup>7</sup> The physical origin of this negative surface charge is still elusive, but previous experiments of air bubbles and oil droplets in water suggest that the measured  $\zeta$ -potential is closely related to the presence of water in the FNP experiments.<sup>50-56</sup> Due to the degree of coarse-graining in the present model it is impossible to simulate this stabilization mechanism on a molecular level. Instead, the charge stabilization of the NPs is modeled by placing a virtual particle at the center of each aggregate which carries the equivalent surface charge. Hydroxide ions (and water molecules) exhibit a considerably higher mobility compared to the free and aggregated polymer chains in the system,<sup>57</sup> and thus it is safe to assume that the surface charges build up instantaneously.

This description of electrostatic stabilization is inspired by the theory for colloids developed by Derjaguin, Landau, Verwey, and Overbeek,<sup>58,59</sup> with the difference that our model takes into account attractive van der Waals interactions on a microscopic level. Here, the screened electrostatic repulsion between two NPs  $i$  and  $j$  is given by

$$U_{\text{Yukawa}}(r) = \lambda_B \left( \frac{Z_i e^{\kappa R_i}}{1 + \kappa R_i} \right) \left( \frac{Z_j e^{\kappa R_j}}{1 + \kappa R_j} \right) \frac{e^{-\kappa r}}{r}, \quad (7.5)$$

where  $\lambda_B = e^2/(4\pi\varepsilon_0\varepsilon_r k_B T)$  is the Bjerrum length with elementary charge  $e$ ,  $\varepsilon_r$  is the relative dielectric constant, and  $\varepsilon_0$  is the vacuum permittivity. The parameters  $Z_i$  and  $Z_j$  denote the size-dependent charge of NPs  $i$  and  $j$ , respectively, and  $\kappa$  is the inverse of the Debye screening length  $\lambda_D$ . For water with pH 7 at room temperature,  $\lambda_B = 0.7$  nm and  $\lambda_D = 0.97$   $\mu$ m.

In order to identify precipitated NPs and to determine their size during simulation runtime, Nikoubashman *et al.* carried out the following three-step protocol at each time step: first, the center of mass of each polymer is calculated. Then, all neighboring polymers within a distance of  $r \leq 2R_{g,0}$  are grouped together. After all polymers have been assigned to a cluster, its center of mass position and its radius of gyration,  $R_g$ , are computed. The (hydrodynamic) radius of the NP is then set to:<sup>9</sup>

$$R = \sqrt{5/3}R_g \approx 1.3R_g. \quad (7.6)$$

Note that using  $R_g = \sqrt{I/M}$  in combination with the moment of inertia of a solid sphere  $I = 2MR^2/5$  leads to a slight overestimation of the NP radius. This discrepancy is due to the fact that the NPs do not have a homogeneous density, but rather consist of densely packed beads.

Finally, in order to evaluate  $U_{Yukawa}$ , the charge  $Z$  carried by each NP needs to be determined. For a spherically symmetric environment, this problem can be approached using Gauss's law, and the potential distribution can be solved analytically within linear-screening theory and at low colloid concentrations:<sup>60</sup>

$$\frac{Z_i \lambda_B}{R_i} = (1 + \kappa R_i) \frac{e\zeta}{k_B T}. \quad (7.7)$$

For example, an NP with radius  $R = 100$  nm and  $\zeta$ -potential  $\zeta = -33$  mV dispersed in water carries  $Z \approx 200$  unit charges.

The model now contains all the required elements for simulating FNP. Figure 7.4 shows snapshots of simulations with polymer concentration  $\Phi = 8.2$  mg ml<sup>-1</sup> and instantaneous mixing ( $\tau_{mix} = 0$ ) at three different stages of the FNP process. In Figure 7.4a the initial configuration of the simulation is shown when the polymers are still dispersed in a good solvent ( $\lambda = 0$ ). Figure 7.4b shows the simulations in poor solvent conditions ( $\lambda = 0.5$ ), where the polymers have collapsed into compact globules, and nearby globules have merged into small aggregates. Figure 7.4c shows the final simulation snapshots at  $t = 30$   $\mu$ s, where stable NPs with an average radius of  $R \approx 9.5$  nm have formed.

The particle-based nature of the employed model allows us to study the conformation of the polymers constituting the NP. In Figure 7.5,  $R_g$  is plotted as a function of the distance from the aggregate center, and it is clear that  $R_g$  remains close to  $R_{g,0}$  in the NP center, but then decays towards the particle-liquid interface. However, the polymers on the NP surface are not fully collapsed (*cf.* Figure 7.3), because they are only partially exposed to the poor

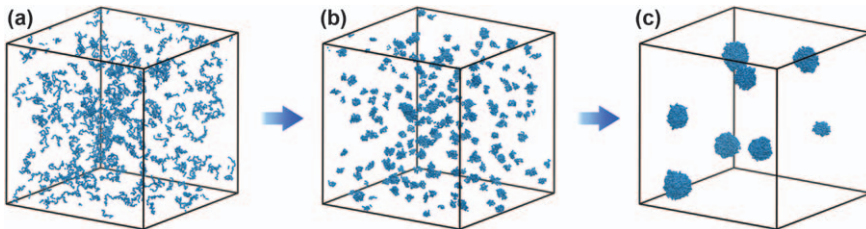


**Figure 7.4** Simulation snapshots at polymer concentration  $\Phi = 8.2 \text{ mg ml}^{-1}$  and instantaneous mixing ( $\tau_{\text{mix}} = 0$ ). Panel (a) shows the initial configuration in a good solvent, panel (b) shows the system after mixing with a poor solvent, and panel (c) shows the final NPs after  $t = 30 \mu\text{s}$ . Solvent particles have been omitted for the sake of clarity. Snapshots rendered using Visual Molecular Dynamics 1.9.2.<sup>61</sup>

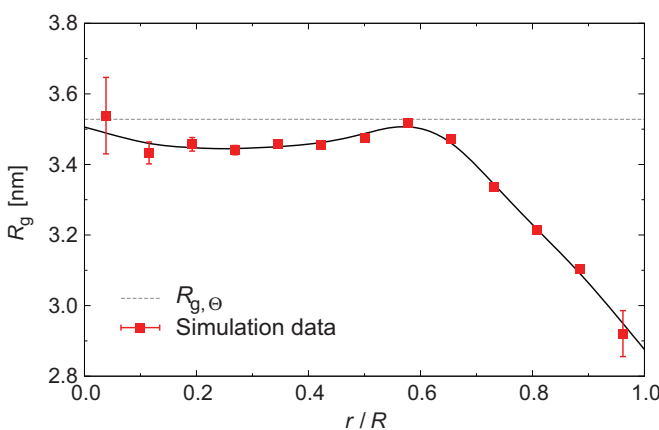


**Figure 7.5** Polymer radius of gyration  $R_g$  vs. distance from the NP center,  $r$ . The data were recorded from simulations of a single NP with radius  $R = 17 \text{ nm}$ . The dotted line shows the expected value in a melt,  $R_{g,\Theta}$ , and the solid line is a guide to the eye.

Reproduced from ref. 7 with permission from American Chemical Society, Copyright 2016.

solvent. Furthermore, the simulations revealed that the final polymer conformation is independent of mixing time, *i.e.* it is irrelevant for the internal structure of the homogeneous NP whether the polymers first collapse into globules and then merge, or *vice versa*. This behavior is most likely due to the disentangled nature and short relaxation times of the employed polymers.

The microscopic aspects of the FNP process can be studied with this model in even more detail, and we refer the interested reader to ref. 7 for simulation studies of FNP using homopolymers. In ref. 17 and 18, this particle-based model was employed to investigate the self-assembly of homopolymer blends into structured NPs, such as Janus and core-shell morphologies. Finally, the fabrication of NPs with internally structured

geometries through rapid precipitation of diblock copolymers was studied in ref. 19.

### 7.3 Kinetic Monte Carlo Simulations

In Section 7.2 it was shown how a particle-based model can be developed for MD simulations of the FNP process. This approach provides valuable insights into the directed self-assembly behavior on microscopic length scales, while it also helps to explore the effect of the various processing parameters. However, such microscopically detailed models are inherently limited to relatively small length scales ( $\sim$ nm) and short time scales ( $\mu$ s – ms), and are thus not suitable for providing quantitative predictions on experimental scales. To bridge this gap, Li *et al.*<sup>62</sup> developed a KMC model that can reach macroscopic length and time scales by solving stochastically the following system of ordinary differential equations:<sup>63</sup>

$$\frac{d\rho_j}{dt} = \frac{1}{2} \sum_{i=1}^{j-1} K_{i,j-i}\rho_i(t)\rho_{j-i}(t) - \sum_{i=1}^{N_p-j} K_{i,j}\rho_i(t)\rho_j(t), \quad (7.8)$$

where the first term represents all events that lead to particles of size  $n_j$ , and the second term corresponds to all events that particles of size  $n_j$  participate in. Further,  $K_{i,j}$  are the rate constants (specified further below),  $N_p$  is the total number of dispersed polymers in the system, and  $\rho_i$  and  $\rho_j$  are the number densities of particles with sizes  $n_i$  and  $n_j$ , respectively.

In order to solve eqn (7.8) numerically, Li *et al.* adapted the KMC algorithm outlined by Gillespie,<sup>64</sup> which has been applied extensively for studying the kinetics of chemical reactions and aggregation processes.<sup>65–69</sup> The KMC simulations can be summarized by the following cycle: (1) an event  $k$  is chosen to occur with probability  $P_k = A_k/A_T$ , where  $A_k$  is the rate of event  $k$ , and  $A_T$  is the sum of the rates of all possible events for the system at the current time, respectively; (2) the time of the system is advanced by  $\tau = \ln(u)/A_T$ , where  $u$  is a uniform random number in the interval (0, 1]; (3) the system and the rate database are updated.

The results from MD simulations have shown that the relevant events in FNP are particle aggregation due to Brownian diffusion.<sup>7</sup> Further, particle breakage essentially never occurs and hence can be neglected. Nucleation and growth are not included in this description because the aggregation process has been shown to be growth-controlled through both experiments<sup>7,46</sup> and simulations.<sup>7</sup> In addition to diffusion, turbulent shear can also cause particles to collide and aggregate. Using the turbulent shear kernel outlined by Saffman and Turner,<sup>70</sup> its magnitude only becomes comparable to that of Brownian aggregation for  $R \gtrsim 300$  nm. For the range of particle sizes studied here, the effect of turbulent shear is thus negligible and therefore has not been included in the description. Assuming that the particles are spherical and are uniformly distributed in the system, then the

rate constant for Brownian aggregation between particle  $i$  and particle  $j$ ,  $K_{i,j}$ , can be calculated as follows:<sup>71</sup>

$$K_{i,j} = \frac{4\pi}{W} (R_i + R_j)(D_i + D_j), \quad (7.9)$$

where  $R_i$  and  $R_j$  are the radii, and  $D_i$  and  $D_j$  are the diffusion coefficients of particles  $i$  and  $j$ , respectively.  $W$  is the Fuchs stability ratio which takes into account interparticle interactions:<sup>72</sup>

$$W = (R_i + R_j) \int_{R_i+R_j}^{\infty} \frac{e^{U/k_B T}}{r^2} dr, \quad (7.10)$$

where  $U$  is the total energy of interaction, and  $r$  is the center-to-center distance between the two particles.  $W=1$  when every collision leads to an aggregation event.

In practice, the KMC simulations were initialized with  $N_p$  dispersed polymer chains, *i.e.* particles with an aggregation number 1. Typical values of  $N_p$  employed in ref. 62 range from  $10^4$  to  $10^6$ , so that NPs with  $R \sim 100$  nm can be achieved (see discussion in Section 7.2.1). The system volume  $V$  is then set according to the desired polymer feed concentration,  $\rho = N_p/V$ . When an aggregation event is chosen to occur at a certain time, both the numbers of particles  $n_i$  and  $n_j$  decrease by  $K_{i,j}V\rho_i\rho_j$ , and the number of particles  $n_i + n_j$  increases by  $K_{i,j}V\rho_i\rho_j$ . This change triggers an update of the rate database. To speed up the calculation and to reduce the memory footprint of the program, the rate constants were grouped by particle size with a base ten logarithm, and intermediate values were determined through linear interpolation. For example, NPs with  $10 \leq n_i \leq 100$  polymers were split into ten groups with  $10 \leq n_i < 20$ ,  $20 \leq n_i < 30$ , and so forth.

To propagate the KMC simulations, it is required to determine  $R$ ,  $D$  and  $W$  in eqn (7.9), and how these properties change upon aggregation. To this end, the microscopic MD simulations developed in Section 7.2 are used to derive theoretically informed expressions. The particle radius,  $R$ , can be estimated through the radius of gyration [see eqn (6)]:

$$R_i \approx 1.3R_{g,i} \approx 1.3 \frac{\sigma}{c} (n_i N)^{\nu}, \quad (7.11)$$

where  $n_i \geq 1$  is the number of polymers in aggregate  $i$ ,  $N$  is the number of beads per polymer, and  $\sigma$  is the bead diameter ( $N=23$  and  $\sigma=1.5$  nm for the employed parametrization, see Section 7.2.1).  $\nu$  is the Flory exponent, which depends on the solvent quality ( $\nu=0.588$  for good solvents,  $\nu=1/2$  for  $\Theta$ -solvents,  $\nu=1/3$  for poor solvents). The parameter  $c$  ensures that eqn (7.11) reproduces the limiting cases, *i.e.*  $c=\sqrt{6}$  for good and  $\Theta$ -solvents [*cf.* eqn (7.1)], and  $c=2$  for poor solvents. For simplicity, Li *et al.* set  $c=2$  irrespective of solvent quality.<sup>62</sup> This approximation is of minor consequence, as precipitation occurs under poor solvent conditions, where  $c=2$ .

Under good solvent conditions, the dispersed polymers have a coil-like configuration and the pervaded volume is filled with solvent particles (see Figure 7.1a). According to Zimm theory,<sup>73</sup> the diffusion coefficient of a nondraining coil is given by:<sup>73–75</sup>

$$D_{\text{Zimm}} = \frac{D_m}{N} + \frac{k_B T}{6\pi\eta_0} \left\langle \frac{1}{R_h} \right\rangle, \quad (7.12)$$

where the first term reflects the random Brownian motion of the  $N$  constituent monomers with diffusivity  $D_m$ . The second term originates from the hydrodynamic interactions between monomers, where  $\eta_0$  is the viscosity of the solution and  $R_h$  is the hydrodynamic radius of the polymers. In the Gaussian chain limit,  $R_h$  can be determined from theory as  $R_h = (3/8)\pi^{1/2}R_g \approx 0.66 R_g$ .<sup>76</sup> In a poor solvent, the polymers collapse into compact globules, containing little or no solvent in their interiors (see Figure 7.1b). In this case, the polymers (and also the aggregates) can be essentially regarded as spherical particles with radius  $R$ , for which the diffusion is well-described by the Stokes–Einstein relationship:

$$D_{\text{SE}} = \frac{k_B T}{6\pi\eta_0 R}. \quad (7.13)$$

Hence, the polymer diffusion gradually goes from  $D_{\text{Zimm}}$  to  $D_{\text{SE}}$  as the solvent quality degrades. For the sake of simplicity, however, Li *et al.* solely used eqn (7.13) for computing the diffusion coefficients for the aggregation kernel, eqn (7.9).<sup>62</sup> This approximation has no significant impact on the accuracy of the KMC model, because under good solvent conditions the chains are effectively inert to one another and thus no aggregation events occur (see further below).

Having obtained expressions for the radius,  $R_i$ , and diffusion coefficient,  $D_i$ , we now discuss the interaction potentials between the particles, required for calculating  $W$  in eqn (7.10). Li *et al.* considered that  $U$  is the sum of the van der Waals attraction,  $U_{\text{VDW}}$ , the electrostatic repulsion,  $U_{\text{Yukawa}}$ , and the depletion interaction,  $U_{\text{AO}}$ .<sup>62</sup>

The electrostatic repulsion  $U_{\text{Yukawa}}$  is the same as eqn (7.5), and the charge of each NP is computed along the same lines as described in Section 7.2.2. To reproduce the attractive LJ interactions [see eqn (7.2)] between the precipitated NPs in the KMC simulations,  $U_{\text{VDW}}$  is represented as follows:<sup>77</sup>

$$U_{\text{VDW}}(r) = -\frac{H}{6} \left[ \frac{2R_i R_j}{r^2 - (R_i + R_j)^2} + \frac{2R_i R_j}{r^2 - (R_i - R_j)^2} + \ln \left( \frac{r^2 - (R_i + R_j)^2}{r^2 - (R_i - R_j)^2} \right) \right], \quad (7.14)$$

with  $H = 4\varepsilon\pi^2 = 1.6 \times 10^{-19}$  J being the Hamaker constant, where  $4\varepsilon$  is from the coefficient of the LJ interaction and  $\pi^2$  arises from integrating all the monomer–monomer interactions over the volumes of the interacting

particles. Values of  $H$  calculated for PS in water typically lie between  $10^{-20}$  J and  $10^{-19}$  J, depending on the specific calculation method.<sup>78</sup> For the FNP systems of interest here, Li *et al.* found that the radius of the precipitated NPs,  $R$ , is not strongly influenced by the magnitude of  $H$ :<sup>62</sup>  $R$  decreased by approximately 10 nm for a 40-fold decrease in  $H$  over a broad range of mixing times, while the qualitative behavior remained the same. Thus, the value of  $H$  directly derived from the LJ interaction was used in all simulations to be consistent with the MD model.

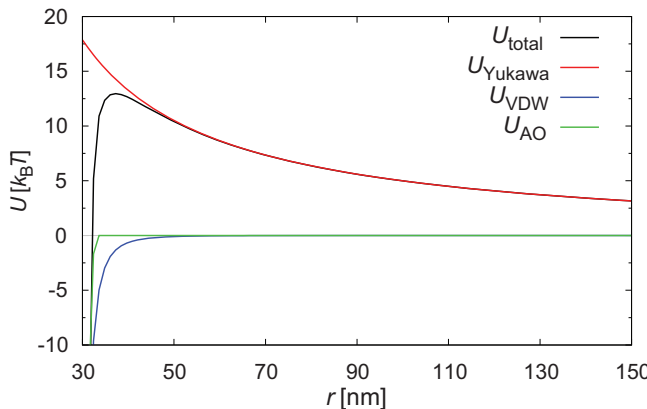
Depletion interactions between two spherical NPs  $i$  and  $j$  are approximated by the Asakura–Oosawa model:<sup>79</sup>

$$U_{AO}(r) = \begin{cases} \infty, & r \leq 2R_{avg} \\ -\frac{4}{3}P\pi(R_s + R_{avg})^3 \left[ 1 - \frac{3r}{4(R_s + R_{avg})} + \frac{r^3}{16(R_s + R_{avg})^3} \right], & 2R_{avg} < r < 2(R_{avg} + R_s) \\ 0, & 2(R_{avg} + R_s) \leq r \end{cases} \quad (7.15)$$

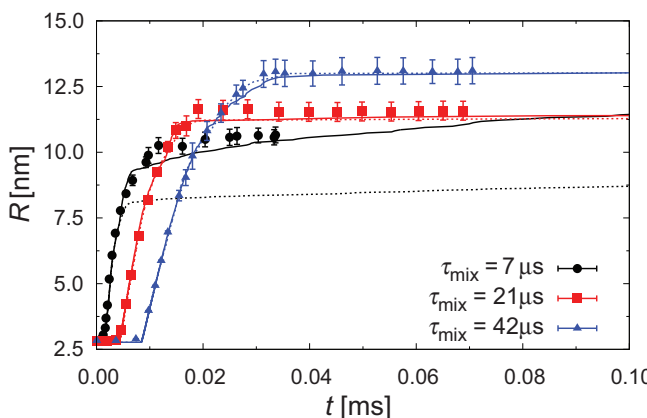
where  $R_s = \sigma/2 = 0.75$  nm is the radius of a solvent particle, and  $R_{avg} = (R_i + R_j)/2$  is the mean radius of NPs  $i$  and  $j$ . In eqn (7.15),  $P = \rho_s k_B T$  is the osmotic pressure, with solvent number density  $\rho_s = 0.2$  nm<sup>-3</sup> from our MD model.

Figure 7.6 shows the total interaction potential between two NPs with  $R_i = R_j = 15$  nm in water, together with the individual contributions  $U_{Yukawa}$ ,  $U_{VDW}$ , and  $U_{AO}$ . This plot highlights the strong and long-ranged electrostatic repulsion, which stabilizes the NPs against further aggregation: once the charges have fully built up, there is an energetic barrier of roughly  $12k_B T$ , and the attractive van der Waals forces outweigh the repulsive forces solely when the NP surfaces are within  $\approx 5$  nm. Depletion effects play only a secondary role, but have been included in the description nonetheless for the sake of completeness.

The effect of solvent displacement was accounted for in the KMC simulations in the following two aspects. First, the parameters for the electrostatic potential  $U_{Yukawa}$  were linearly varied during the mixing time between their values for good solvent conditions and poor solvent conditions. Second, the effect of solvent quality should also be reflected in the attractive contribution of the interaction potential. For example, in a  $\Theta$ -solvent ( $\lambda = 0.05$  for the employed MD model, see Section 7.2.2), the LJ interaction between monomers is identical to the monomer–solvent interaction, and the chains are effectively inert to one another. MD simulations of the particle-based model<sup>62</sup> showed that for  $\lambda \leq 0.08$  no aggregation occurred despite the presence of (weak) van der Waals attraction between polymer chains. The aggregation rate then increased gradually for increasing  $\lambda$  until it reached its



**Figure 7.6** Total interaction potential,  $U_{\text{total}}$ , and its individual contributions *vs.* center-to-center distance,  $r$ , of two NPs with  $R_i = R_j = 15$  nm and  $\zeta = -33$  mV in pure water.



**Figure 7.7** Average NP radius,  $R$ , *vs.* time,  $t$ , from MD (symbols) and KMC (lines) simulations for a polymer feed concentration of  $\Phi = 8.2 \text{ mg ml}^{-1}$  and  $\zeta$ -potential  $-33 \text{ mV}$  at various mixing times,  $\tau_{\text{mix}}$ , as indicated. Solid and dotted lines correspond to calculations with bounded and unbounded integration limits in eqn (7.10), respectively.

Reproduced from ref. 62 with permission from AIP Publishing, Copyright 2018.

full value for  $\lambda \geq 0.18$ . To account for this solvent effect in the KMC model, the aggregation rate constant,  $K_{ij}$ , was modified by a prefactor,  $f$ , so that  $f=0$  for  $\lambda \leq 0.08$ , and  $f=1$  for  $\lambda \geq 0.18$ . In the intermediate region for  $0.08 < \lambda < 0.18$ ,  $f$  increased linearly from 0 to 1.

In Figure 7.7 we compare the time evolution of the NP radius,  $R$ , computed from the MD and KMC simulations at  $\Phi = 8.2 \text{ mg ml}^{-1}$  and  $\zeta = -33 \text{ mV}$  for different mixing times,  $\tau_{\text{mix}}$ . There is good agreement between the KMC

and MD results in almost all cases, except for the shortest mixing time  $\tau_{\text{mix}} = 7 \mu\text{s}$ , where the KMC simulations underpredict the particle radius  $R$ . This discrepancy stems from the calculation of the stability ratio in eqn (7.10), which assumes that the NPs approach each other from infinity with zero interaction. However, there is a finite polymer concentration in the system, and thus the mean distance between particles is roughly  $l \approx \rho_p^{-1/3}$ , where  $\rho_p = N_p/V$  is the number density of polymers in solution ( $l = 15 \text{ nm}$  for  $\Phi = 8.2 \text{ mg ml}^{-1}$ ). Due to the long-ranged nature of the electrostatic interactions, the potential energy is nonzero at  $l$ . Hence, the potential energy barrier for aggregation (see Figure 7.6) effectively becomes smaller, which explains the larger NP sizes observed in the MD simulations. This effect is especially pronounced for large  $\Phi$  and short  $\tau_{\text{mix}}$ , because the mean distance decreases with increasing concentration and because high surface charge is built up when there are still many small particles in the system. It is possible to apply a correction to  $W$ , by bounding the integral in eqn (7.10) between  $[R_i + R_j, l]$ . The solid lines in Figure 7.7 show that better agreement can be achieved with this modification. However, such a correction to the KMC algorithm is only required for comparisons with the high  $\Phi$  and short  $\tau_{\text{mix}}$  employed in the previous MD simulations by Nikoubashman *et al.*<sup>7</sup> In contrast, typical FNP experiments operate in the range of much smaller  $\Phi \lesssim 1 \text{ mg ml}^{-1}$  and larger  $\tau_{\text{mix}} \gtrsim 100 \mu\text{s}$ . In these cases, the mean particle distance is sufficiently high, so that the particles approach each other essentially from infinity with zero interaction.

Having verified the agreement of the KMC model with the previous MD simulations, Li *et al.* explored the behavior at mixing times and polymer concentrations closer to typical experiment values (see Section 7.2.1), which are not accessible in the MD simulations.<sup>62</sup> Figure 7.8 shows the NP radius

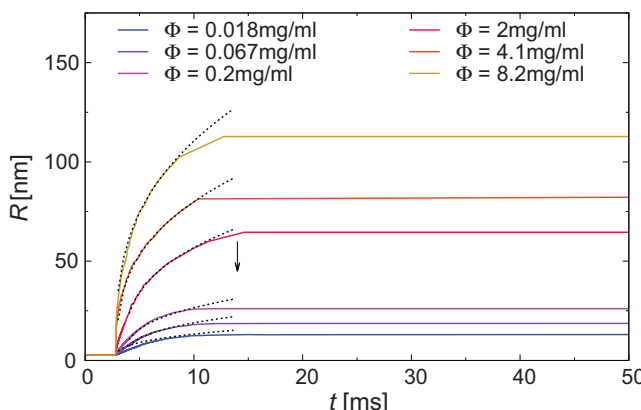


**Figure 7.8** Average NP radius,  $R$ , vs. time,  $t$ , for mixing time  $\tau_{\text{mix}} = 14 \text{ ms}$  and  $\zeta$ -potential  $-33 \text{ mV}$ . The dotted lines are fits to the DLA approximation, eqn (7.17). The arrow marks the completion of mixing.  
Reproduced from ref. 62 with permission from AIP Publishing, Copyright 2018.

$R$  as a function of time for  $\tau_{\text{mix}} = 14$  ms and  $\zeta = -33$  mV for  $0.018 \text{ mg ml}^{-1} \leq \Phi \leq 8.2 \text{ mg ml}^{-1}$ . For all  $\Phi$ , the polymers were initially well dispersed and started aggregating at  $t \approx 3$  ms, when the solvent quality had sufficiently degraded. The NPs grew faster with increasing polymer concentration, and growth stopped essentially when  $t \approx \tau_{\text{mix}}$  due to the electrostatic repulsion between the aggregates.

In order to describe the time evolution of  $R$  at short times, Li *et al.* considered diffusion-limited aggregation (DLA) dynamics.<sup>62,80</sup> This model gives the change in the average aggregation number,  $n$ , with respect to time,  $t$ , according to:

$$n = 1 + \frac{1}{2} K_{\text{DLA}} \Phi t, \quad (7.16)$$

where  $K_{\text{DLA}}$  is the rate kernel from the DLA approximation:

$$K_{\text{DLA}} = 16\pi R_1 D_1. \quad (7.17)$$

$R_1$  and  $D_1$  are the radius and diffusion coefficients of unimers, respectively. Eqn (7.17) assumes that  $W = 1$ , and that the rate kernel for aggregation is independent of particle size. This approximation is good for describing aggregation between particles  $i$  and  $j$  when  $1 < n_i/n_j < 2$ .

From Figure 7.8 it can be seen that at short times before mixing is complete, the time evolution of  $R$  can be well described by DLA. The reason is twofold. First, there is a large number of similarly sized particles in the early stage of aggregation, and the condition  $1 < n_i/n_j < 2$  can be satisfied for most of the aggregation events that take place. Therefore, the term  $(R_i + R_j)(D_i + D_j)$  in eqn (7.9) is approximately constant. Second, at the early stage of aggregation when the electrostatic repulsion is still small,  $W$  is also close to 1. The dynamics can thus be approximated by a constant  $K_{i,j}$ . Further the scaling relationship  $n \propto \Phi$  (or alternatively  $R \propto \Phi^{1/3}$ ) from DLA [see eqn (7.16)] is in good agreement with the results from KMC. DLA slightly overpredicts the NP size at the end of mixing because of the underlying assumption  $W = 1$ , which does not hold anymore for  $t \approx \tau_{\text{mix}}$  due to the electrostatic forces between the NPs.

After the rapid NP growth during the initial mixing, aggregation enters a slow-growth regime and deviates from the DLA approximation. In Figure 7.9,  $R$  is plotted against  $t$  up to macroscopic time scales for  $\Phi = 0.018 \text{ mg ml}^{-1}$ . These data show that small NPs are not yet fully stabilized, but continue to grow at a slow rate and gradually converge on a much larger time scale. To understand this behavior, it is helpful to consider the aggregation rate. Unlike the rate of aggregation in the DLA regime [eqn (7.16)], which is directly proportional to  $\Phi$  as  $K_{\text{DLA}}$  is constant, the rate of aggregation in the slow growth regime is largely determined by the magnitude of the stability ratio,  $W$ . Smaller particles experience weaker electrostatic repulsion, which leads to smaller  $W$  and thus a higher rate constant, and *vice versa*. Therefore, growth curves for different mixing times  $\tau_{\text{mix}}$  and  $\Phi$  in Figure 7.9 eventually converge when the systems are evolved in the slow growth regime for a

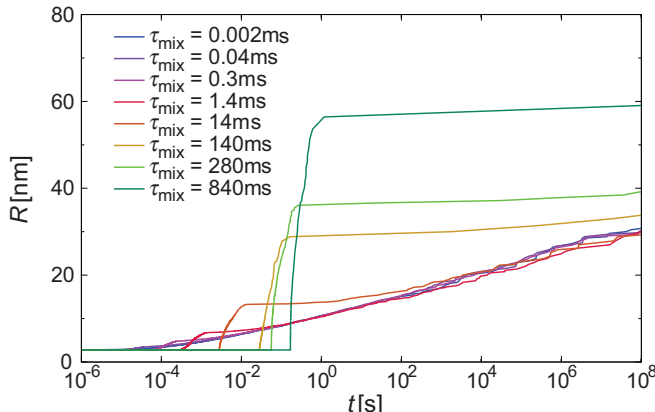


**Figure 7.9** Average NP radius,  $R$ , vs. time,  $t$ , for polymer concentration  $\Phi = 0.018 \text{ mg ml}^{-1}$  and  $\zeta$ -potential  $-33 \text{ mV}$  at various mixing times,  $\tau_{\text{mix}}$ , as indicated.

Reproduced from ref. 62 with permission from AIP Publishing, Copyright 2018.

sufficiently long time. In contrast, larger NPs are more strongly stabilized by charge, and their growth is less appreciable on macroscopic time scales up to  $10^8 \text{ s}$ .

The results presented here are just a subset of findings that can be achieved through this hybrid MD-KMC approach, and the interested reader is referred to ref. 62 for a more extensive discussion.

## Acknowledgements

A.N. thanks Nannan Li and Athanassios Z. Panagiotopoulos for many fruitful discussions. A.N. received support from the German Research Foundation under Project NI 1487/2-1.

## References

1. L. Wu, J. Zhang and W. Watanabe, *Adv. Drug Delivery Rev.*, 2011, **63**, 456.
2. M. Elsabahy and K. L. Wooley, *Chem. Soc. Rev.*, 2012, **41**, 2545.
3. R. Alvarez-Román, A. Naik, Y. N. Kalia, R. H. Guy and H. Fessi, *J. Controlled Release*, 2004, **99**, 53.
4. S. S. Guterres, M. P. Alves and A. R. Pohlmann, *Drug Target Insights*, 2007, **2**, 147.
5. H. ShamsiJazeyi, C. A. Miller, M. S. Wong, J. M. Tour and R. Verduzco, *J. Appl. Polym. Sci.*, 2014, **131**, 40576.
6. B. K. Johnson and R. K. Prud'homme, *AIChE J.*, 2003, **49**, 2264.
7. A. Nikoubashman, V. E. Lee, C. Sosa, R. K. Prudhomme, R. D. Priestley and A. Z. Panagiotopoulos, *ACS Nano*, 2015, **10**, 1425.
8. M. Rawiso, R. Duplessix and C. Picot, *Macromolecules*, 1987, **20**, 630.

9. M. Rubinstein and R. H. Colby, *Polymer Physics*, Oxford University Press, USA, 1st edn, 2003.
10. L. J. Fetters, D. J. Lohse and R. H. Colby, in *Physical Properties of Polymers Handbook*, Springer, New York, 2007, p. 447.
11. C. D. Wick, M. G. Martin and J. I. Siepmann, *J. Phys. Chem. B*, 2000, **104**, 8008.
12. T. I. Morozova and A. Nikoubashman, *J. Phys. Chem. B*, 2018, **122**, 2130.
13. Q. Sun and R. Faller, *J. Chem. Phys.*, 2007, **126**, 144908.
14. T. Spyriouni, C. Tzoumanekas, D. Theodorou, F. Müller-Plathe and G. Milano, *Macromolecules*, 2007, **40**, 3876.
15. H.-J. Qian, P. Carbone, X. Chen, H. A. Karimi-Varzaneh, C. C. Liew and F. Müller-Plathe, *Macromolecules*, 2008, **41**, 9919.
16. J. Glaser, T. D. Nguyen, J. A. Anderson, P. Lui, F. Spiga, J. A. Millan, D. C. Morse and S. C. Glotzer, *Comput. Phys. Commun.*, 2015, **192**, 97.
17. N. Li, A. Z. Panagiotopoulos and A. Nikoubashman, *Langmuir*, 2017, **33**, 6021.
18. N. Li, A. Nikoubashman and A. Z. Panagiotopoulos, *Soft Matter*, 2017, **13**, 8433.
19. L. S. Grundy, V. E. Lee, N. Li, C. Sosa, W. D. Mulhern, R. Liu, R. A. Register, A. Nikoubashman, R. K. Prud'homme, A. Z. Panagiotopoulos and R. D. Priestley, *ACS Nano*, 2018, **12**, 4660.
20. J. R. Spaeth, I. G. Kevrekidis and A. Z. Panagiotopoulos, *J. Chem. Phys.*, 2011, **134**, 164902.
21. J. R. Spaeth, I. G. Kevrekidis and A. Z. Panagiotopoulos, *J. Chem. Phys.*, 2011, **135**, 184903.
22. J. C. Cheng and R. O. Fox, *Ind. Eng. Chem. Res.*, 2010, **49**, 10651.
23. I. A. Sedov and T. I. Magsumov, *J. Phys. Chem. B*, 2015, **119**, 8773.
24. M. D. Smith, B. Mostofian, L. Petridis, X. Cheng and J. C. Smith, *J. Phys. Chem. B*, 2016, **120**, 740.
25. V. Vasudevan and S. H. Mushrif, *RSC Adv.*, 2015, **5**, 20756.
26. J. Schneider, A. Z. Panagiotopoulos and F. Müller-Plathe, *J. Phys. Chem. C*, 2017, **121**, 27664.
27. C. Sosa, V. Lee, L. Grundy, M. J. Burroughs, R. Liu, R. K. Prud'Homme and R. D. Priestley, *Langmuir*, 2017, **33**, 5835.
28. J. K. Johnson, E. A. Mueller and K. E. Gubbins, *J. Phys. Chem.*, 1994, **98**, 6413.
29. J. M. Polson and N. E. Moore, *J. Chem. Phys.*, 2005, **122**, 024905.
30. F. J. Blas, L. G. MacDowell, E. de Miguel and G. Jackson, *J. Chem. Phys.*, 2008, **129**, 144703.
31. A. Chremos, P. M. Chaikin, R. A. Register and A. Z. Panagiotopoulos, *Soft Matter*, 2012, **8**, 7803.
32. A. Chremos, P. M. Chaikin, R. A. Register and A. Z. Panagiotopoulos, *Macromolecules*, 2012, **45**, 4406.
33. A. Chremos, A. Nikoubashman and A. Z. Panagiotopoulos, *J. Chem. Phys.*, 2014, **140**, 054909.
34. M. Bishop, M. H. Kalos and H. L. Frisch, *J. Chem. Phys.*, 1979, **70**, 1299.

35. G. S. Grest and K. Kremer, *Phys. Rev. A*, 1986, **33**, 3628.
36. M. K. Petersen, J. B. Lechman, S. J. Plimpton, G. S. Grest, P. J. in't Veld and P. R. Schunk, *Chem. Phys.*, 2010, **132**, 174106.
37. D. S. Bolintineanu, G. S. Grest, J. B. Lechman, F. Pierce, S. J. Plimpton and P. R. Schunk, *Comput. Part. Mech.*, 2014, **1**, 321.
38. K. Meier, A. Laeseke and S. Kabelac, *J. Chem. Phys.*, 2004, **121**, 9526.
39. J. D. Weeks, D. Chandler and H. C. Andersen, *J. Chem. Phys.*, 1971, **54**, 5237.
40. J. A. Anderson, C. D. Lorenz and A. Travesset, *J. Comput. Phys.*, 2008, **227**, 5342.
41. G. J. Martyna, D. J. Tobias and M. L. Klein, *J. Chem. Phys.*, 1994, **101**, 4177.
42. J. Cao and G. J. Martyna, *J. Chem. Phys.*, 1996, **104**, 2028.
43. C. Sosa, R. Liu, C. Tang, F. Qu, R. K. Prud'homme and R. D. Priestley, *Macromolecules*, 2016, **49**, 3580.
44. V. Lee, C. Sosa, R. Liu, R. K. Prud'homme and R. D. Priestley, *Langmuir*, 2017, **33**, 3444.
45. W. Mandema and H. Zeldenrust, *Polymer*, 1977, **18**, 835–839.
46. C. Zhang, V. J. Pansare, R. K. Prud'homme and R. D. Priestley, *Soft Matter*, 2012, **8**, 86.
47. M. Gindy, A. Z. Panagiotopoulos and R. K. Prud'Homme, *Langmuir*, 2008, **24**, 83.
48. R. F. Pagels, J. Edelstein, C. Tang and R. K. Prud'Homme, *Nano Lett.*, 2018, **18**, 1139.
49. C. Tian, J. Feng, H. J. Cho, S. S. Datta and R. K. Prud'Homme, *Nano Lett.*, 2018, **18**, 4854.
50. J. K. Beattie and A. M. Djerdjev, *Angew. Chem., Int. Ed.*, 2004, **43**, 3568–3571.
51. J. K. Beattie, A. M. Djerdjev and G. G. Warr, *Faraday Discuss.*, 2009, **141**, 31–39.
52. R. Vácha, S. W. Rick, P. Jungwirth, A. G. F. de Beer, H. B. de Aguiar, J.-S. Samson and S. Roke, *J. Am. Chem. Soc.*, 2011, **133**, 10204–10210.
53. R. Vácha, O. Marsalek, A. P. Willard, D. J. Bonthuis, R. R. Netz and P. Jungwirth, *J. Phys. Chem. Lett.*, 2012, **3**, 107–111.
54. J. K. Beattie and A. Gray-Weale, *Angew. Chem., Int. Ed.*, 2012, **51**, 12941–12942.
55. K. Roger and B. Cabane, *Angew. Chem., Int. Ed.*, 2012, **51**, 5625–5628.
56. J. K. Beattie, A. M. Djerdjev, A. Gray-Weale, N. Kallay, J. Lützenkirchen, T. Preocanin and A. Selmani, *J. Colloid Interface Sci.*, 2014, **422**, 54–57.
57. M. E. Tuckerman, D. Marx and M. Parrinello, *Nature*, 2002, **417**, 925–929.
58. B. V. Derjaguin and L. V. Landau, *Acta Physicochim. USSR*, 1941, **14**, 633.
59. E. J. W. Verwey and J. T. G. Overbeek, *Theory of the Stability of Lyophobic Colloids: The Interaction of Sol Particles Having an Electric Double Layer*, Elsevier, New York, 1st edn, 1948.
60. F. Smallenburg, N. Boon, M. Kater, M. Dijkstra and R. van Roij, *J. Chem. Phys.*, 2011, **134**, 074505.

61. W. Humphrey, A. Dalke and K. Schulten, *J. Mol. Graphics*, 1996, **14**, 33–38.
62. N. Li, A. Nikoubashman and A. Z. Panagiotopoulos, *J. Chem. Phys.*, 2018, **149**, 084904.
63. M. V. Smoluchowski, *Z. Phys. Chem.*, 1917, **92**, 129.
64. D. T. Gillespie, *J. Comput. Phys.*, 1967, **22**, 403.
65. M. Thorn, H.-P. Breuer, F. Petruccione and J. Honerkamp, *Macromol. Theory Simul.*, 1994, **3**, 585.
66. G. Odriozola, A. Moncho-Jordá, A. Schmitt, J. Callejas-Fernández, R. Martínez-García and R. Hidalgo-Álvarez, *Europhys. Lett.*, 2001, **53**, 797.
67. D. Mukherjee, C. G. Sonwane and M. R. Zachariah, *J. Chem. Phys.*, 2003, **119**, 3391–3404.
68. M. H. Flamm, T. Sinno and S. L. Diamond, *J. Chem. Phys.*, 2011, **134**, 034905.
69. N. S. Tiwari and P. van der Schoot, *J. Chem. Phys.*, 2016, **144**, 235101.
70. P. G. Saffman and J. S. Turner, *J. Fluid Mech.*, 1956, **1**, 16.
71. M. V. Smoluchowski, *Ann. Phys.*, 1906, **326**, 756.
72. N. Fuchs, *Z. Phys.*, 1934, **89**, 736.
73. M. Doi and S. F. Edwards, *The Theory of Polymer Dynamics*, Clarendon Press, Oxford, 1st edn, 1986.
74. J. G. Kirkwood and J. Riseman, *J. Chem. Phys.*, 1948, **16**, 565.
75. B. Liu and B. Dünweg, *J. Chem. Phys.*, 2003, **118**, 8061.
76. I. Teraoka, *Polymer Solutions: An Introduction to Physical Properties*, John Wiley & Sons, 1st edn, 2002.
77. H. C. Hamaker, *Physica*, 1937, **4**, 1058.
78. J. Visser, *Adv. Colloid Interface Sci.*, 1972, **3**, 331.
79. S. Asakura and F. Oosawa, *J. Chem. Phys.*, 1954, **22**, 1255.
80. K. J. Ives, *The Scientific Basis of Flocculation*, Springer Netherlands, 1st edn, 1978.

## CHAPTER 8

# *Glass Transition and Crystallization in Colloidal Polymer Nanoparticles*

DANIELE CANGIALOSI<sup>\*a,b</sup> AND AURORA NOGALES<sup>c</sup>

<sup>a</sup> Centro de Física de Materiales (CSIC-UPV/EHU), Paseo Manuel de Lardizabal 5, 20018 San Sebastián, Spain; <sup>b</sup> Donostia International Physics Center, Paseo Manuel de Lardizabal 4, 20018 San Sebastián, Spain;

<sup>c</sup> Instituto de Estructura de la Materia, IEM-CSIC, Serrano 121, Madrid 28006, Spain

\*Email: daniele.cangialosi@ehu.eus

## 8.1 Introduction

Colloidal polymer nanoparticles have recently attracted great interest as a result of their use in a wide range of applications including drug delivery,<sup>1</sup> biolabeling,<sup>2</sup> advanced biological sensors,<sup>3</sup> photonic crystals,<sup>4</sup> etc. The large interfacial area of nanoparticles may induce profound changes in the properties of the polymers, a fact which is of utmost importance from both technological and fundamental viewpoints.

The aim of this chapter is to emphasize the role of 3D confinement, a hallmark of colloidal polymer nanoparticles, in affecting glassy dynamics and crystallization kinetics. In doing so, we highlight two main aspects of confining polymers in 3D. One is the existence of an interface, which can be either free or based on a contact with an attractive or repulsive substrate. This aspect is general for any kind of confinement. The second aspect originates from the fact that 3D confinement entails the presence of a geometrical

Published on 02 December 2019 on https://pubs.rsc.org | doi:10.1039/9781788016476-00263

curvature at the polymer/external world interface. As can be seen, both aspects are critical in determining both glassy dynamics and crystallization behavior in colloidal polymer nanoparticles. Furthermore, these two features of polymer physics are intimately connected. In particular, crystallization kinetics depends on both the thermodynamic driving force – that is, the amount of supercooling, which determines the kinetics of formation of crystalline nuclei – and the kinetics of crystal growth, which basically depends on the polymer molecular mobility and, thereby, its glassy dynamics.<sup>5–10</sup>

Starting from these premises, the chapter is organized into two main sections. The Section 8.2 reviews the recent activity on how glassy dynamics is modified in colloidal polymer nanoparticles with respect to the bulk. We first introduce different aspects of glassy dynamics, including the glass transition and physical aging in the glassy state, and emphasize how these phenomena are related to the molecular mobility of the glass former. Subsequently, we provide a general overview regarding investigations in the last couple of decades on how glassy dynamics is modified by confinement. Special attention is dedicated to thin polymer films, which is by far the most investigated confinement geometry. In the subsequent subsection of this part, we show how colloidal polymer nanoparticles have seen increasing attention in the last few years. Experimental efforts in this area have shown analogies with other kinds of confinement. At the same time, we also discuss the peculiarity of colloidal polymer nanoparticles, essentially related to the curvature at the polymer/external world interface.

The Section 8.3 of the chapter is focused on the way crystallization kinetics are modified in colloidal polymer nanoparticles. Firstly, the way crystallizable nanoparticles are generated is introduced. Similarly to the previous section, parallelism with other kinds of confinement, in particular thin polymer films, is drawn. Furthermore, the way conformational disorder, which can be affected by the curvature of polymer nanoparticles, plays a role in crystallization kinetics will be discussed.

## 8.2 Glassy Dynamics in Colloidal Polymer Nanoparticles

The aim of this section is to provide an overview of recent activity on the characterization of how glassy dynamics are modified in colloidal polymer nanoparticles with respect to their bulk counterparts. To do so, we first provide some conceptual guidelines on the main features of glassy dynamics, in particular the connection between the vitrification kinetics (the so-called glass transition) and the way equilibrium is recovered in the glassy state on the one hand, and the polymer molecular mobility on the other. Subsequently, we review the experimental effort carried out on how glassy dynamics are modified by geometrical confinement. Before providing details of the results on polymer nanoparticles, we first introduce a general overview of this topic with special reference to polymer thin films, which are to date the most explored confinement geometry. In the last part of this section, we

provide a detailed overview of the investigation of glassy dynamics in colloidal nanoparticles, highlighting the analogies with other types of confinement, in particular thin polymer films, but also the peculiarities of 3D confinement, a hallmark of colloidal nanoparticles.<sup>63</sup>

### 8.2.1 The Glass Transition

Liquids can be supercooled below their melting temperature ( $T_M$ ) when cooled down at rates greater than those relevant for crystallization.<sup>11,12</sup> A class of supercooled liquids, called glass-forming liquids, can be characterized in the amorphous state below  $T_M$  if the crystallization rate exceeds the time scale required to carry out the experimental observation. A wide variety of polymers generally belong to the class of glass-forming liquids. In this case, crystallization is generally hampered by chain connectivity and, in some cases, conformational disorder. Further temperature decrease generally results in the vitrification of the supercooled liquid, that is, its transformation to a glass. This is a system in non-equilibrium not only with respect to the crystal but also to the supercooled liquid state. As a natural consequence, the thermodynamic state of glasses spontaneously evolves towards equilibrium, a phenomenon known as structural recovery<sup>13</sup> or physical aging.<sup>14</sup> The temperature at which vitrification takes place is named the glass transition temperature ( $T_g$ ). The thermodynamic signature of the glass transition is a step in second-order thermodynamic properties, for instance, the specific heat, the coefficient of thermal expansion, and the compressibility or, equivalently, a kink in a first-order thermodynamic property, for instance, the enthalpy, the entropy, or the specific volume (see Figure 8.1).<sup>15</sup> A glass formed by cooling a supercooled liquid below its  $T_g$  exhibits a thermodynamic state defined by its enthalpy level. A common way to identify such a state is based on the concept of fictive temperature ( $T_f$ ) introduced by Tool.<sup>16</sup> This is the temperature at which a given glass will be at equilibrium and is determined by the intersection of the glass line, drawn from the thermodynamic state of a given glass, with the extrapolated supercooled liquid line. This is schematically shown in Figure 8.1.

When observing the thermodynamic plot of Figure 8.1, the glass transition might be seen as a second-order thermodynamic transformation within the Ehrenfest classification.<sup>12</sup> However, there are other observations that highlight the kinetic nature of the glass transition. Among them, likely the most straightforward is its dependence on the cooling rate applied for the transformation. In particular, supercooled liquids cooled at high rates transform into glasses at high temperatures, which implies high  $T_g$ . The opposite occurs when low cooling rates are applied. The cooling rate dependence of  $T_g$  originates from its intimate link with the molecular mobility of the glass former. According to this connection, the glass transition takes place when the time scale of the experiment, related to the inverse of the cooling rate, is of the order of the typical time scale  $\tau$  of molecular fluctuations.<sup>17–21</sup> In line with this connection, several reports exist showing that the temperature dependence of

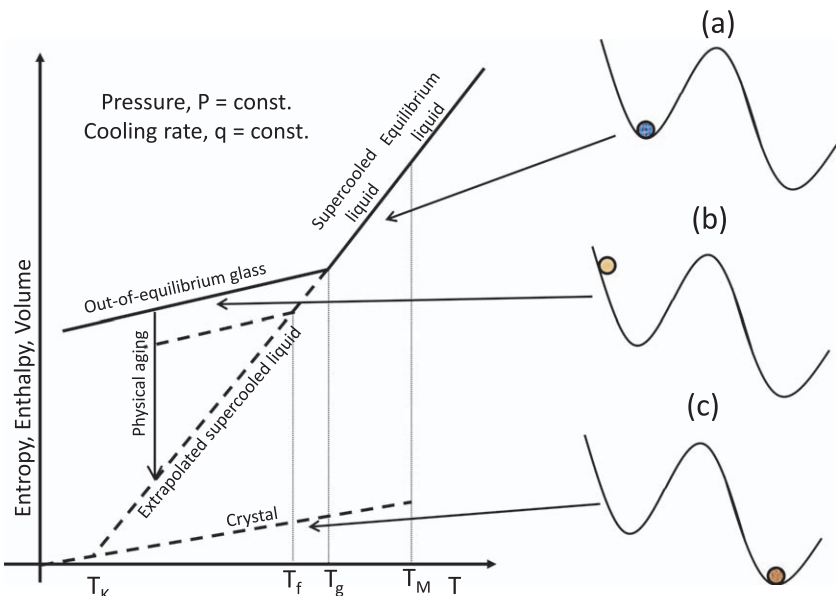


**Figure 8.1** Left side: Schematic representation of the temperature dependence of thermodynamic properties in glass-forming systems at constant pressure. Right side: Stability plots for (a) the metastable supercooled liquid, (b) the non-equilibrium glass, and (c) the stable crystal.

$\tau$  and the cooling-rate-dependent  $T_g$  exhibit the same trend. This is generally described by the Vogel–Fulcher–Tammann (VFT) equation<sup>22–24</sup> (or equivalently the Williams–Landel– Ferry (WLF) equation<sup>25</sup>):

$$X = X_0 \exp\left(-\frac{B}{T - T_0}\right) \quad (8.1)$$

where  $X$  can equivalently be  $\tau^{-1}$  or the cooling rate  $q$  (in which case  $T$  is replaced by  $T_g$ ).

Despite the intimate connection between the vitrification and molecular mobility, it is of great importance to point out that these two aspects are different from a conceptual viewpoint and, thereby, there is no *a priori* reason why a one-to-one connection should be found in all conditions.<sup>26</sup> Probing the molecular mobility requires the application of small perturbations, in particular smaller than the amplitude of spontaneous fluctuations. In this way, the fluctuation dissipation theorem (FDT)<sup>27,28</sup> is fulfilled and the measurement is conducted in the so-called linear regime. In contrast, characterizing the way in which vitrification takes place entails the application of a cooling ramp, that is, a perturbation well beyond the linear regime. The same applies to the physical aging regime where the deviations from equilibrium quantify the degree of non-linearity. For this reason, in the rest of the chapter vitrification and physical aging will be addressed as non-equilibrium glassy dynamics.

While the mentioned difference is in most cases (though with some noticeable exceptions<sup>29</sup>) of no relevance when the glassy dynamics of bulk systems are characterized,<sup>21,30</sup> as will be shown in the following parts of this section, there exist numerous examples of polymeric glasses subjected to geometrical confinement showing a decoupling between non-equilibrium dynamics and molecular mobility.

### 8.2.2 Glass Transition in Geometrical Confinement

Reducing the size of a polymer by geometrically confining it at sub-micrometer length scales results in a general alteration of properties. Regarding modification of glassy dynamics, the first observations in this sense date back the mid 90s. Keddie *et al.*<sup>31</sup> investigating how film thickness modifies vitrification, found that polystyrene (PS) films supported on top of silicon wafers exhibited a  $T_g$  suppression with respect to the bulk for thicknesses less than 40 nm. Such suppression was as large as 25 K for sub-10 nm thick films. Interestingly, a subsequent study by the same authors<sup>32</sup> showed that, while behavior analogous to that of PS supported on top of silicon wafers was found for poly(methyl methacrylate) (PMMA) supported on gold, the same polymer, when deposited on top of native silicon oxide, exhibited a  $T_g$  increase with decreasing film thickness. These results highlighted the importance of the interface in determining the sign and magnitude of  $T_g$  deviations in thin polymer films. As an example, taken from ref. 33, in Figure 8.2, the thickness dependence of  $T_g$  is shown for different polymer films supported on top of

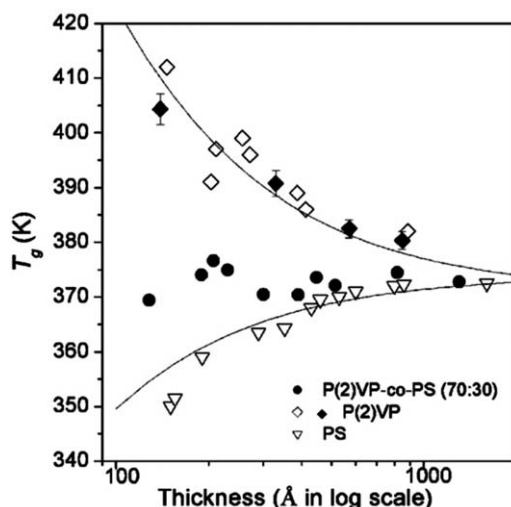


**Figure 8.2** Thickness dependence of  $T_g$  for PS, poly(2-vinyl pyridine) (P2VP), and P2VP-PS copolymer.

Reproduced from ref. 33 with permission from Elsevier, Copyright 2004.

silicon-based substrates. As can be seen, a variety of situations can be found including decrease, increase, or no change in  $T_g$ .

The utmost importance of the interface was highlighted by Forrest *et al.*<sup>34</sup>, who showed that freestanding PS films exhibit a massive  $T_g$  reduction. This can be as large as 70 K for films with a thickness of 30 nm. Similar results were obtained by Boucher *et al.*<sup>35</sup> on stacked PS films, that is, systems resembling those in the freestanding configuration – given the fact that the interaction among films is essentially neutral and no interpenetration among chains of different films takes place in experiments where the temperature never exceeds  $T_g$  by more than 20 K. In this case, as well as in more recent work,<sup>36,37</sup> apart from the role of the interface, that of the cooling rate was highlighted, showing that  $T_g$  reductions are more pronounced at lower cooling rates. Similar results were presented by others for supported PS films using ellipsometry.<sup>38</sup>

Since the work of Keddie *et al.*<sup>31,32</sup> a wide variety of results have been presented showing either a decrease, increase, or no change in  $T_g$  for thin polymer films. This activity is reviewed in several recent papers.<sup>39–43</sup> Generally speaking, negative deviations from bulk  $T_g$  are observed when the polymer and the substrate are weakly interacting, whereas the opposite is observed when the polymer is deposited on top of attractive surfaces (see Figure 8.2 as an example). In this context, it is very important to emphasize the crucial role of polymer adsorption onto the substrate<sup>44</sup> in determining the magnitude and sign of  $T_g$  deviations. Activity in this area was promoted by the finding that thin polymer films annealed well above  $T_g$  exhibit time-dependent recovery of bulk  $T_g$ .<sup>45</sup> This finding provided evidence for the first time that  $T_g$  deviations from the bulk value must be attributed to polymer chain adsorption onto the substrate. Subsequent work showed that, rather than the amount of adsorbed polymer chains, the crucial parameter determining the  $T_g$  of polymer film supported on a substrate is the amount of interfacial free volume, that is, the portion of interface where adsorption has not taken place yet.<sup>46–48</sup> For supported or capped films, this can be tuned by adsorbing polymer chains *via* thermal protocols based on prolonged annealing well above  $T_g$  and/or using the appropriate substrate and preparation conditions.<sup>43</sup>

### 8.2.3 Specific Features of the Glass Transition in Colloidal Polymer Nanoparticles

Colloidal polymer nanoparticles bear the analogy with thin polymer films of exhibiting a large amount of free interface. At the same time, the specificity of colloidal nanoparticles lies in the fact that in this case the confining interface exhibits a curvature. In other words, 3D confinement is the hallmark of colloidal polymer nanoparticles in contrast to 1D confinement in thin polymer films. This marks an important difference between these two kinds of confinement, which, as will be seen in this section, may be of importance in some conditions.

Historically the first report on the glass transition of colloidal PS nanoparticles was provided by Gaur and Wunderlich<sup>49</sup> in the early 80s, using

differential scanning calorimetry (DSC). While these authors found no significant deviations in  $T_g$ , taken as the temperature corresponding to half of the specific heat, a number of observations indicated that the calorimetric response of these colloidal systems was markedly different from that of bulk PS. These differences consist of a much broader glass transition range – encompassing 80 K – and a reduced step in the specific heat.

Subsequently a wide variety of studies were presented showing either a decrease, an increase, or no change in  $T_g$  in colloidal polymer nanoparticles. In the first case, this was shown by Zhang *et al.*<sup>50</sup> on PS nanoparticles with diameters ranging from 100 to 700 nm in aqueous suspension. The main outcome of this study was a pronounced deviation from bulk  $T_g$  for particles with diameters smaller than 400 nm. The same PS nanoparticles employed in ref. 50 were characterized by capacitive dilatometry,<sup>51</sup> a dielectric technique delivering information on the temperature variation of the density.<sup>52</sup> In this case, PS nanoparticles were surrounded by nitrogen gas during the measurement. The results, shown in Figure 8.3 together with those of ref. 50, indicate that the decrease in  $T_g$  with the diameter was independent of the medium surrounding the nanospheres. Other studies reported negative  $T_g$  deviations in colloidal nanoparticles of PS<sup>53</sup> and PMMA<sup>54</sup> suspended in water or measured in atmospheric air.<sup>55</sup> However, the latter works showed that if the surface of the nanoparticles contains a certain kind of surfactant,  $T_g$  deviations can be suppressed. This is the case for PS<sup>53</sup> and PMMA<sup>54</sup> nanoparticles surrounded by an anionic surfactant.

The presence of a specific modification on the surface of the colloidal nanoparticle may profoundly affect the kind of  $T_g$  deviations from bulk behavior. One case was highlighted by capping colloidal polymer nanoparticles

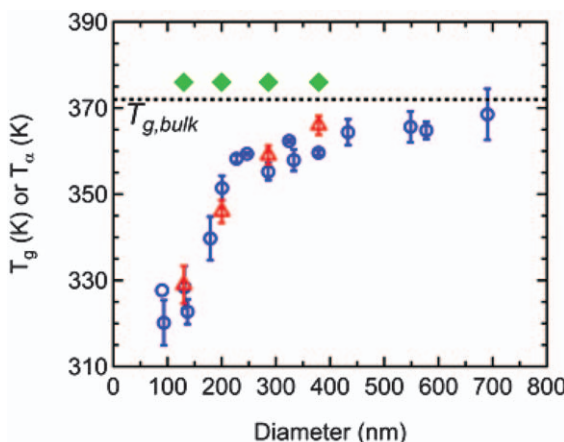


**Figure 8.3**  $T_g$  versus PS nanoparticles diameter measured by CD (red triangles) and modulated-DSC (blue circles). The dynamic  $T_g$ , taken from measurements of the molecular mobility by BDS, is also plotted as a function of nanoparticle diameter (green diamonds).

Reproduced from ref. 51 with permission from Elsevier, Copyright 2013.

with silica. This was done on PS nanoparticles, which exhibited small reductions of  $T_g$ ,<sup>56</sup> if any,<sup>50</sup> when decreasing the diameter. Interestingly, in both PS in aqueous solution and capped by silica, a marked reduction in the so-called dynamic fragility<sup>57</sup> was observed with decreasing nanoparticle diameter.<sup>58</sup> Another case is that of PS nanoparticles in aqueous solution surrounded by a surfactant.<sup>59</sup> In this case, and similarly to the results reported by Feng *et al.*,<sup>53</sup> no measurable deviations from bulk  $T_g$  were observed by DSC. However the same work showed reduced specific heat in PS nanoparticles in comparison to the bulk polymer. The presence of surfactants at the surface of the colloidal polymer nanoparticle may also induce an increase in  $T_g$ , as shown in PMMA<sup>60,61</sup> and PS.<sup>62</sup> A systematic study on the effect of the medium surrounding the nanoparticles was recently carried out by Priestley and co-workers.<sup>63</sup> They showed that, depending on the interfacial energy of the polymer/surrounding medium, the  $T_g$  of PS colloidal nanoparticles could be tuned from a large depression in water, to a mild reduction in glycerol, and no change with respect to the bulk in an ionic liquid. This result is depicted in Figure 8.4,<sup>63</sup> showing the  $T_g$  sensitivity to the presence of a given surrounding liquid.

In the context of purely size effects, it is important to point out that there exist several reports showing positive  $T_g$  deviations on polymer nanoparticles with no surfactant and surrounded by a gas.<sup>64–66</sup> This result challenges the idea that an interface with non-attractive interactions can explain all  $T_g$  effects. Given the fact that results by Martinez-Tong *et al.*<sup>64,65</sup> were obtained in sub-100 nm diameter nanoparticles, it was argued that restrictions to molecular motions due to the curved polymer/surrounding

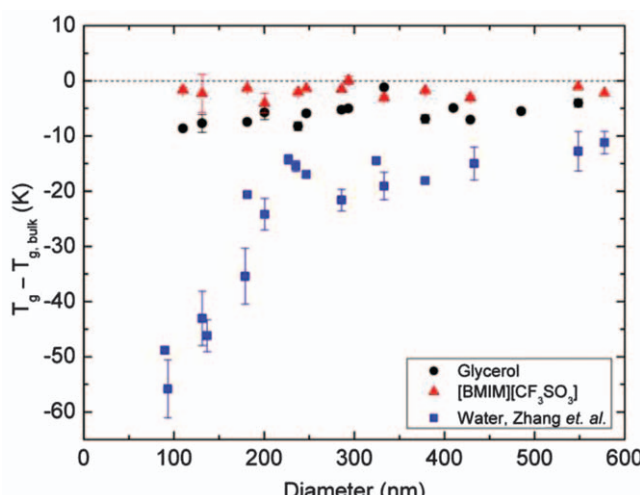


**Figure 8.4**  $T_g$  deviation from bulk behavior for PS nanoparticles suspended in glycerol,  $[\text{BMIM}][\text{CF}_3\text{SO}_3]$ , and water.  
Reproduced from ref. 63 with permission from John Wiley and Sons, © 2016 Wiley Periodicals, Inc.

medium interface was responsible for the  $T_g$  increase. Given this premise, Martinez-Tong *et al.*<sup>64,65</sup> developed an entropic model based on the removal of configurational degrees of freedom to explain the  $T_g$  increase.

### 8.2.4 Specific Features of Physical Aging in Colloidal Polymer Nanoparticles

The glass transition implies the transformation from a supercooled liquid in metastable equilibrium to a glass. As discussed, the non-equilibrium nature of the latter results in the slow evolution of its thermodynamic state towards equilibrium in the physical aging regime. This marks an intimate connection between  $T_g$  and physical aging.<sup>15,42,67</sup> As a result, it is possible to foresee whether physical aging is accelerated or retarded in colloidal polymer nanoparticles from the sign of  $T_g$  deviations from bulk behavior. Studies on colloidal polymer nanoparticles, although so far relatively scarce, have seen growing interest in recent years. The first report providing a systematic study of physical aging in colloidal polymer nanoparticles was presented by Guo *et al.*<sup>68</sup> using DSC, allowing the amount of enthalpy recovered during physical aging to be assessed. This study showed that, at a given aging temperature, PS nanoparticles suspended in water exhibit a faster approach to equilibrium with respect to bulk PS. This result is consistent with the negative  $T_g$  deviations observed for these nanoparticles.<sup>50,51</sup> At the same time, the study by Guo *et al.*<sup>68</sup> showed that silica-capped PS nanospheres, exhibiting essentially bulk-like  $T_g$ , also display recovery of equilibrium in the physical aging regime analogous to that of bulk PS.

More recently, similar results have been obtained by Perez-de-Eulate and Cangialosi<sup>69</sup> for colloidal PS nanoparticles obtained by flash nanoprecipitation,<sup>70</sup> and suspended in a silicon oil. They assessed the thermodynamic state of these systems employing fast scanning calorimetry (FSC) using the concept of  $T_f$ . Apart from the acceleration of physical aging<sup>68</sup> in proximity to  $T_f$ , in this work the existence of multiple steps of equilibrium recovery was shown. As an example, Figure 8.5 shows the aging time-dependent decrease in  $T_f$  for PS nanoparticles with diameter 230 nm. The disclosure of multiple steps during physical aging experiments – already observed in a variety of glass-forming systems, including bulk polymers,<sup>71–73</sup> thin polymer films,<sup>74,75</sup> polymers with reduced dimensionality,<sup>76</sup> metallic glasses,<sup>77–80</sup> glycerol,<sup>81</sup> and chalcogenide glasses,<sup>82,83</sup> – implies that equilibrium recovery is triggered by different molecular mechanisms. Importantly, as demonstrated in some of these works,<sup>74–76</sup> the time scale of observation of different steps of equilibrium recovery can be significantly shortened in systems with a large amount of free interfacial area. Thus, employing colloidal polymer nanoparticles suspended in non-attractive media constitutes a formidable route to explore these phenomena, circumventing the large time scales normally required in bulk systems. This can deliver insights into fundamental problems of extraordinary importance in the topic of the glass transition, such as the existence of a true thermodynamic transition, the so-called “ideal” glass transition, at a finite temperature<sup>84</sup> long ago theorized by Gibbs and

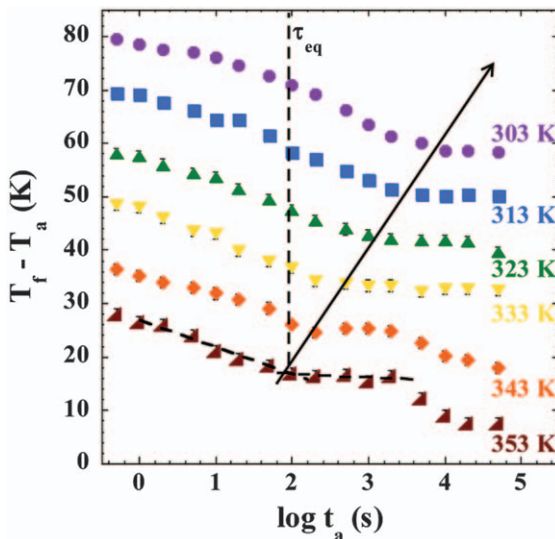


**Figure 8.5** Aging time evolution of  $T_f$ , shown as its difference with the aging temperature  $T_a$ , for PS nanoparticles with diameter 230 nm.  
Reproduced from ref. 69 with permission from American Chemical Society, Copyright 2016.

DiMarzio.<sup>85</sup> Its existence has been recently demonstrated for the first time in 30 nm thick PS films.<sup>74</sup> We anticipate that colloidal polymer nanoparticles can be successfully exploited to obtain glasses undergoing the ideal glass transition in experimentally accessible time scales.<sup>76</sup>

### 8.2.5 Connection with Molecular Mobility

As discussed in Section 8.2.1, although in the vast majority of cases the one-to-one connection between the glass transition and physical aging, on the one hand, and the molecular mobility, on the other, is fulfilled in bulk glasses, the two aspects of glassy dynamics are not equivalent. Hence, after presenting results on the glass transition and physical aging of colloidal polymer nanoparticles, the natural question to be posed is: Does the connection of the glass transition and physical aging with molecular mobility hold in colloidal polymer nanoparticles?

In order to provide an exhaustive answer, it is important to recall the analogy between 3D confinement, a hallmark of colloidal polymer nanoparticles, and other kinds of confinement. We begin our discussion by pointing out that when positive  $T_g$  deviations and/or enhanced time scales for approaching equilibrium in glasses are observed, these are generally associated with a slowing-down of the molecular mobility. Few examples regard a specific case of confinement, that is, polymer nanocomposites exhibiting attractive interactions with polymer/nanofillers.<sup>86–89</sup> In all these cases, a direct correlation between the slowing-down of molecular mobility

and a concomitant  $T_g$  increase was shown. Hence, it is expected that this kind of behavior would also be found in colloidal polymer nanospheres exhibiting positive  $T_g$  deviations from bulk behavior. These experiments are at present lacking and effort in this area is warranted in the future.

The connection of the glass transition and physical aging with molecular mobility is less trivial in confined polymer glasses exhibiting negative  $T_g$  deviations with respect to the bulk material. In this case, several works on thin polymer films point towards a decoupling between  $T_g$  and molecular mobility. This was the case of polymer nanocomposites<sup>90–92</sup> and thin polymer films,<sup>93–95</sup> which exhibited  $T_g$  depression and bulk-like molecular mobility. For those colloidal polymer nanospheres exhibiting negative  $T_g$  deviations, the first result indicating this decoupling was shown by Zhang *et al.*<sup>51</sup> in PS nanoparticles. In this work, the  $T_g$  was characterized by capacitive dilatometry,<sup>52,96,97</sup> a technique based on measurements of the high frequency dielectric permittivity, which is directly related to the sample density. This technique is based on broadband dielectric spectroscopy (BDS), which also allows characterization of the molecular mobility. The results of Zhang *et al.*<sup>51</sup> are summarized in Figure 8.3. As can be observed, the previously described  $T_g$  decrease with decreasing the nanoparticle diameter is *not* accompanied by a concomitant enhancement of molecular mobility, which, in contrast, remains bulk-like. Similar results were reported by Rharbi and co-workers,<sup>98</sup> who measured the  $T_g$  by DSC and, in the same experiments, the kinetics of coalescence of colloidal PS nanoparticles, related to the polymer molecular mobility. They showed that – while the step in the specific heat, marking the glass transition, progressively shifted towards lower temperatures with decreasing nanoparticle diameter – the temperature at which coalescence among nanoparticles takes place is insensitive to changes in nanoparticle size. This result indicates that on changing the nanoparticle diameter the molecular mobility remained bulk-like.

Compelling arguments in favor of decoupling between vitrification and molecular mobility were provided by Perez-de-Eulate *et al.*<sup>99</sup> for PS nanoparticles. By employing fast scanning calorimetry (FSC), they were able to obtain information on the vitrification kinetics, from the temperature dependence of the total specific heat, and the molecular mobility, from the frequency and temperature dependence of the complex specific heat. The latter was obtained by employing a step-response analysis originally developed by Schick and co-workers,<sup>100</sup> and later extended to FSC.<sup>101</sup> Figure 8.6, showing information on both the temperature dependence of the total specific heat on cooling at  $20\text{ K s}^{-1}$  and the real part of the complex specific heat at 20 Hz, indicates that vitrification on cooling is delayed when decreasing the nanoparticle diameter, signifying a  $T_g$  decrease. In contrast, the real parts of the complex permittivity of all samples collapse on each other, indicating that molecular mobility remains bulk-like when the nanoparticle size is decreased. Importantly, in this case vitrification kinetics and molecular mobility results have been obtained on identical samples and employing the same perturbation, that is, a temperature change.

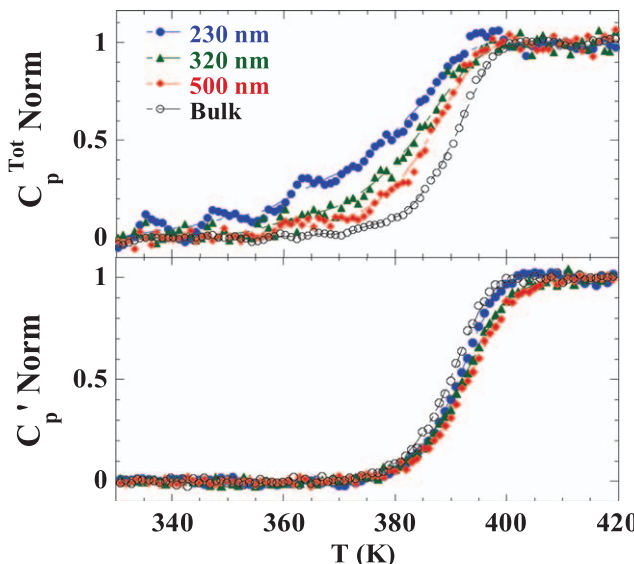


**Figure 8.6** Total specific heat (upper panel), obtained at  $20 \text{ K s}^{-1}$ , and real part of the complex specific heat at  $20 \text{ Hz}$  (lower panel) as a function of temperature. Reproduced from ref. 99 with permission from American Chemical Society.

Altogether these results indicate that, while in colloidal polymer nanoparticles exhibiting positive  $T_g$  deviations the molecular mobility is expected to be slowed down, there are numerous examples showing simultaneously negative  $T_g$  deviations and essentially bulk-like molecular mobility. The decoupling between these two aspects of glassy dynamics urges the development of a suitable framework able to catch the physics behind such decoupling. In this area, recent efforts have aimed to describe equilibration of polymers exhibiting a large amount of free interface via a model based on free volume hole diffusion.<sup>47,90,102–106</sup> This model describes the equilibration of a glass former on the basis of diffusion of free volume holes in the amorphous system and their exchange at the free interface. Hence, when two glass-forming liquids with different amounts of free interface, for instance two colloidal polymer nanoparticles surrounded by a gas with different diameters, are cooled, the one with the larger amount of free interface will vitrify at a lower temperature, provided that the two systems have identical molecular mobilities. Similarly, once in the glassy state, systems with a large free interface will exhibit accelerated physical aging. Hence, this model is compatible with experimental results showing  $T_g$  depression and accelerated physical aging, and bulk-like molecular mobility.

### 8.3 Semicrystalline Colloidal Particles

Some polymers may crystallize under particular circumstances. In general, due to topology hindrances associated with chain connectivity and

entanglements of the chains in the melt, polymer crystallization is only partial, and therefore, polymers in this configuration are always addressed as “semi-crystalline”. It is impossible to overcome the large free energy barriers necessary to achieve the most stable conformation for all the chains that leads to a complete ordered state. For this reason, in these polymers there are a variety of hierarchically organized phases, including crystalline lamellae, crystal-amorphous interphases, stacks of crystalline lamellae, liquid pockets, rigid amorphous phases, and fringed micellar crystals. How these structural elements are arranged depends on different variables like chemical structure, steric hindrances, chain flexibility, thermal history, or processing.<sup>107–109</sup>

As anticipated in the Introduction, crystallization kinetics bears a strong relation to polymer molecular mobility and nucleation kinetics.<sup>5,6,9,10</sup> The latter is associated with the thermodynamic driving force of crystallization, which basically scales with the degree of supercooling, that is, the distance from the melting temperature. Hence, nucleation kinetics is independent of the system molecular mobility. This implies that the nucleation rate is zero at the melting temperature and progressively increases with decreasing temperature. In contrast, the intimate link between glassy dynamics and the kinetics of crystal growth have been widely established. Hence, the slowdown of glassy dynamics with decreasing temperature also applies to the kinetics of crystal growth. The interplay between nucleation rate and kinetics of crystal growth, that is, two factors with opposing dependences on temperature, gives rise to the well-known bell-shaped temperature dependence of the crystallization rate<sup>110</sup> (see for instance Figure 8.9). As discussed in Section 8.2, glassy dynamics may be profoundly affected in confinement and, thereby, in reviewing recent activity on the way crystallization is modified in polymer nanoparticles with respect to the bulk, we will show how such modifications can be related to those of glassy dynamics.

Semicrystalline polymers exhibit characteristic features on different length scales. In highly crystalline polymers, such as polyethylene (PE)<sup>111</sup> and in polymers with intermediate crystallinity, such as aromatic polyesters,<sup>112–114</sup> or poly(ether-ketones),<sup>115</sup> there is a periodic arrangement of crystalline regions (lamellar crystals) and amorphous regions (inter-lamellar amorphous regions) forming lamellar stacks. The typical periodicity of such an arrangement is in the range of a few tens of nanometers. With the exception of highly crystalline polymers, lamellar stacks do not extend to the whole volume of the sample.<sup>112</sup> The lamellae are packed into stacks which are separated by broad amorphous regions. The stacks can assemble themselves into superstructures, generally with spherical symmetry (spherulites) which can reach microns or even several millimeters.

Considering this hierarchy of structures whose size spans through several orders of length scale, it is obvious that confinement at such scales has an impact on polymer crystallization. Besides the technological interest in understanding polymer properties under confinement, from a fundamental viewpoint, different geometries of confinement have been studied. They can be classified on the basis of the number of space dimensions confined; in

thin films, only one of the dimensions is confined, and therefore, crystals are forced to grow in two dimensions. Intensive work on 1D crystallization of polymers has been performed, studying morphologies,<sup>116–119</sup> kinetics and interfacial effects<sup>120–122</sup> among others. The reader is directed to excellent reviews and dedicated book chapters.<sup>123,124</sup>

When two dimensions are confined (crystallization in cylindrical nanopores, for example), crystals have a preferential orientation, that will be perpendicular or parallel to the unconfined dimension, depending on the crystallization conditions.<sup>125–130</sup> In these geometries, besides pure size effects, an enhanced role of interfacial interactions is found.<sup>42,43</sup> On one side, sample thickness becomes a crucial parameter controlling crystallization,<sup>131</sup> while surface effects mostly lead to a competition between adsorption on the solid surface and nucleation of polymer crystals.<sup>120,131–134</sup>

Finally, the case of crystallization under 3D nanoconfinement has been less studied. 3D confinement can be understood as a case where all dimensions are confined, as in the case of droplets<sup>135</sup> (generally with micron sizes), or nanodroplets prepared by polymer dewetting on substrates, where, again, the role of the interface is very important, since it plays a key role in the conformation, orientation, and absorption of the chains with respect to the substrate.<sup>136</sup> In a different approach, Loo *et al.*<sup>137</sup> studied the crystallization of a block in a copolymer melt with strong interblock segregation, where a cubic packing on nanospheres of the crystallizable segment were immersed in a matrix of the other block of the copolymer. In this case the authors observed that, upon 3D confinement, crystallization followed first-order kinetics, compared to the typical sigmoidal kinetics of bulk polymers. However, the role of chain connectivity with non-crystallizable blocks was not addressed. Therefore, polymer nanoparticles, prepared from suspensions of preformed crystallizable polymers in water, constitute an ideal geometry to study polymer crystallization under 3D nanoconfinement, where the role of solid interfaces is minimized. In this section we present recent advances in the study of the crystallization behavior of polymers in nanoparticle geometries.

### 8.3.1 Methods for Generation of Nanoparticles from Preformed Semicrystalline Polymers

In general, polymer nanoparticles can be prepared from several heterophase methods. One of the most well-known methods, developed extensively Landfester *et al.*<sup>138,139</sup> at the beginning of this century, is the so-called *mini-emulsion method*. Briefly, the method consists in mixing a polymer solution in an organic solvent, with a surfactant solution in water. The mixture is ultrasonicated, forming a miniemulsion of polymer solution in water, with nanometer-sized polymer solution droplets stabilized by the surfactant. The solvent is subsequently allowed to evaporate, provided it has a boiling point lower than water and, in this way, a dispersion of polymer nanoparticles in water is obtained. Excess of surfactant is removed by dialysis. Figure 8.7 shows some

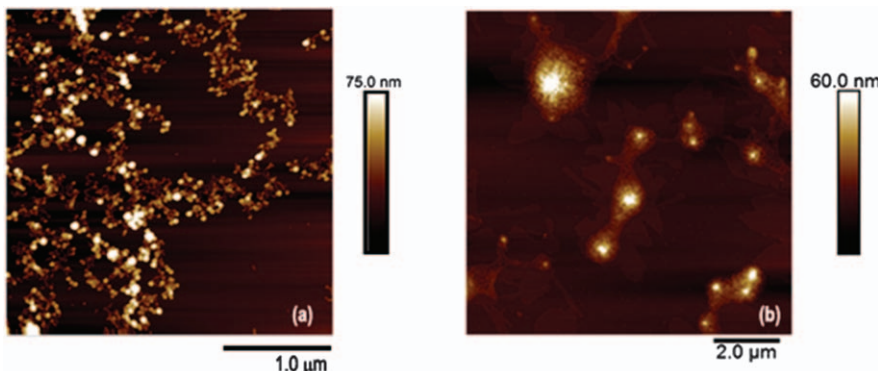


**Figure 8.7** AFM topography images for (a) PLLA and (b) P3HT nanoparticles prepared from the miniemulsion method.

Reproduced from ref. 140 and 141 with permission from Daniel E. Martínez-Tong, PhD (a) and from Edgar Gutiérrez-Fernández (b).

examples of crystallizable polymer nanoparticles, that is, poly(L-lactic acid) (PLLA) and poly(3-hethylthiophene) (P3HT), obtained by this method.<sup>140,141</sup>

The miniemulsion method requires polymer solvents with boiling points below that of water and that are immiscible with water. For polymers soluble in solvents with higher boiling points or that are water-miscible several other approaches can be pursued. These methods are based on solvent-displacement. *Dialysis nanoprecipitation* is a method by which a polymer solution is prepared in a water-miscible solvent. The polymer solution is placed in a dialysis membrane with appropriate pore size, and is immersed in a large water volume. To restore chemical equilibrium, solvent flows outwards through the membrane walls, and water flows inwards. During this process, a controlled precipitation of the polymer occurs in the dialysis membrane to form polymer nanoparticles.<sup>142</sup> This method has been used for preparing nanoparticles of poly(vinylidene fluoride-co-trifluoroethylene) P(VDF-TrFE)<sup>143</sup> and polycaprolactone (PCL).<sup>144</sup>

The principle of solvent displacement is also used in the so-called *reprecipitation* or *flash precipitation* method.<sup>70,145</sup> In this method a filtered polymer solution is rapidly injected into a given volume of distilled water, resulting in an emulsion of polymer in the water-solvent mixture. The emulsion is stirred at a given temperature (below the boiling point of water) to allow complete evaporation of the solvent. The final state is a dispersion of polymer nanospheres in water. This method, again, requires solvents with boiling points below that of water. A modification of the method can be used, where the solvent in the water-solvent mixture is removed by dialysis.<sup>140</sup> By this method, particles of P(VDF-TrFE) can also be obtained.<sup>141</sup> The sizes of the obtained nanoparticles depend on several factors, the solvent used being a key one. An alternative method for preparing polymer nanoparticles is based on pulsed laser ablation of liquid media (PLAL).<sup>146</sup> Although preparation of nanoparticles of semicrystalline polymers by this

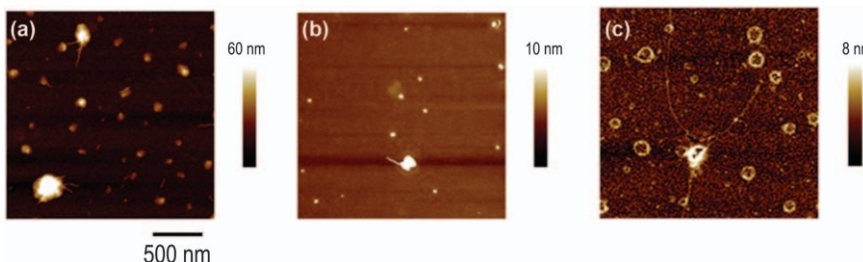


**Figure 8.8** AFM topography images for poly(bisphenol-A-carbonate) nanoparticles obtained by pulsed laser ablation in different liquids (a) carbon tetroxide, (b) hexane and (c) ethylene glycol.

Reproduced from ref. 140 with permission from Daniel E. Martínez-Tong, PhD.

method has been only marginally reported,<sup>147</sup> polycarbonate particles prepared by PLAL in different liquids has been documented. Very different morphologies were found depending on the liquid properties. In particular, the size of the obtained nanoparticles depended on the thermal conductivity of the liquid medium. Figure 8.8 shows an example of poly(bisphenol-A-carbonate) nanoparticles obtained by PLAL in different solvents.<sup>140,146</sup>

The PLAL method for obtaining polymer nanoparticles is experimentally similar to Matrix Assisted Pulsed Laser Evaporation (MAPLE), where a frozen polymer solution is ablated and the solvent acts as a sacrificial matrix. The chains in the solvent are ejected and the solvent avoids degradation.<sup>148</sup> Individual polymer droplets are obtained. Recently, the effect of confinement in crystallization has been studied in films deposited by MAPLE.<sup>149</sup> The described methods arise from very different physico-chemical principles. Therefore, particles from each method are expected to have their own singularities when polymer crystallization is studied. However, several common aspects might be considered, such as the role of confinement size and curvature, among others.

### 8.3.2 Chain Conformation by Confinement of Polymers in Nanoparticles

The driving force for crystallization in glass-forming systems at constant pressure is associated with the difference in the contributions to the Gibbs free energy between liquid and crystal per unit volume of the crystal phase,<sup>150</sup> which can be described by eqn (8.2):

$$\Delta G(T) = -T\Delta S(T) \quad (8.2)$$

where  $\Delta S$  is the difference in specific entropy between both phases, and is given by:

$$\Delta S = S_{\text{liquid}} - S_{\text{crystal}} \quad (8.3)$$

In polymers, the entropic contribution arises from the number of available conformations for the polymer chains. The entropy of a polymer chain is

provided by the Boltzmann relation  $S = k \cdot \ln \Omega$  where  $\Omega$  is the number of conformations. The latter can be calculated from the relation:

$$\Omega \approx \mu^{n_u} \quad (8.4)$$

where  $\mu \approx 2 - 6$  is the number of rotational isomers, determined by the type of monomer, and  $n_u$  is the number of repeating units in a single chain. Therefore, the main factor controlling the number of conformations in a chain is the total number of repeating units. Since nanoparticles may contain just a few chains, it is possible to estimate the number of monomers included in a particle to obtain, in a first approximation, the number of possible conformations of the chains in the nanoparticles. In the case of an ensemble of a small number  $n_c$  of chains, as is the case in a polymer nanoparticle, the number of conformation can be described by:<sup>151</sup>

$$\Omega \approx \mu^{n_u \cdot n_c} \quad (8.5)$$

From eqn (8.3) and (8.5) it can therefore be concluded that, in the limited volume imposed by the nanoparticle geometry, the driving force for crystallization is weaker than in bulk. This might imply that crystallinity can be inhibited when compared to bulk systems.

Another aspect of crystallization that can be modified upon confinement is kinetics. Crystallization from the glass, *i.e.*, cold crystallization, occurs when a glassy crystallizable polymer that has been quenched is brought to temperatures above its  $T_g$ . The kinetics of crystallization in this regime, which is well below the maximum in nucleation, is governed mainly by the molecular mobility of the system, since nuclei have already been preformed at lower temperatures and crystallization proceeds through the transport of chains with the correct conformation to the crystal front. It has been reported that at temperatures slightly above the glass transition, the kinetics of crystallization is governed by segmental dynamics.<sup>6,114</sup> Crystallization in confined polymer systems is modified with respect to that of the bulk, and sometimes even inhibited.<sup>117,120,152,153</sup>

In confinement, heterogeneous nucleation is highly suppressed. Therefore, crystallization is governed by homogeneous nucleation. Floudas *et al.*<sup>154,155</sup> suggested that at large undercoolings, close to the  $T_g$ , crystallization is strongly linked to the local viscosity and therefore, to segmental dynamics. Any modification in the dynamics due to confinement should be reflected in the kinetics of crystallization. Taking this aspect into account, in the next sections, we review the observed modifications in crystallization kinetics and the shape of the developed crystals in semicrystalline polymer nanoparticles.

### 8.3.3 Modification of Crystallization in Polymer Nanoparticles

In the case of crystallization in polymer nanoparticles, slight variations in the temperature dependence of the crystallization kinetics with respect to the bulk

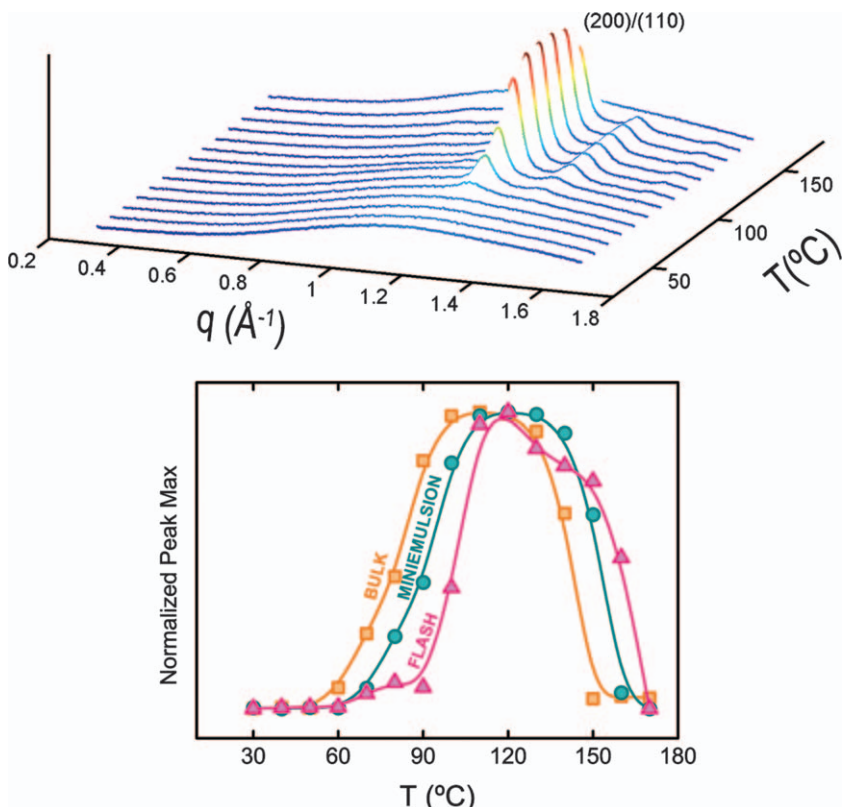


**Figure 8.9** (Top) Evolution of wide angle X-ray scattering patterns of initially amorphous PLLA nanoparticles prepared by miniemulsion. The diameter of the nanoparticles is around 100 nm. The crystalline diffraction pattern corresponds to that of the  $\alpha$  phase of PLLA. (Bottom) Normalized intensity of the maximum peak as a function of temperature for bulk PLLA, nanoparticles prepared by miniemulsion and nanoparticles prepared by flash precipitation.

Reproduced from ref. 140 with permission from Daniel E. Martínez-Tong, PhD.

have been observed. Figure 8.9 shows the evolution of diffraction patterns with temperature from initially amorphous polymer nanoparticles of PLLA. As observed, the cold crystallization in the nanoparticles occurs at temperatures slightly higher than for the bulk. Recalling the intimate connection between crystallization rate and glassy dynamics, this may be associated with slight positive deviations in  $T_g$ . As detailed in Section 8.2, this is actually found in some studies<sup>64,65</sup> for amorphous nanoparticles prepared by the same technique. Though in these studies the investigated nanoparticles were acrylate-based, one could hypothesize a similar effect for PLLA nanoparticles. To clarify this aspect, further investigation is warranted since, as discussed, reducing the nanoparticle diameter can also have the opposite effect, that is, a reduction in  $T_g$ .<sup>42</sup>

In the case of polymers that are semicrystalline at room temperature under normal processing conditions, it has been shown that confinement into nanoparticles decreases crystallinity. Ferroelectric polymer nanoparticles prepared by dialysis nanoprecipitation exhibit a ferroelectric-to-paraelectric transition associated with the crystalline phase of the ferroelectric polymer at lower temperatures compared with the bulk, confirming the lower crystallinity of the nanoparticles.<sup>156</sup>

### 8.3.4 Polymer Nanocrystals from Crystallizable Nanoparticles

In terms of morphology, nanoparticles offer an elegant framework to obtain polymer nanocrystals, or even single crystals. The size of the nanoparticles is often very similar to that of the polymer crystal in bulk, and therefore, confinement might affect the morphology of the obtained crystals. Monitoring crystallization of polymer nanoparticles by atomic force microscopy reveals the mechanism by which, after a certain time, the nanoparticles collapse and form small droplets from which crystallization proceeds. Besides starting from almost pure 3D confinement (particles with spherical shape) after collapsing, their form changes to a pancake-like shape, and the role of the substrate is enhanced. As has been shown by simulations,<sup>157</sup> competition appears between interfacial and geometrical effects. The flatness of the surface imposes a deformation of the polymer chains so that they tend to align parallel to the surface. This effect would promote flat-on lamella orientation.

However, if the interaction of the polymer with the flat substrate surface is strong, a slowing down of the molecular mobility is induced, impeding the reorganization of polymer chains. In this situation, the preferred growth orientation for crystalline lamella is edge on. This is exemplified in Figure 8.10 where three snapshots of an isothermal crystallization experiment on initially amorphous PLLA particles are shown.<sup>140,158</sup> After several minutes, the collapse of the nanoparticles into droplets is observed. After that, the droplets evolve into crystals, with flat-on and edge-on lamella observed, demonstrating the balance between the two different effects.

## 8.4 Conclusions

The aim of this chapter is to review recent experimental activity dedicated to the comprehension of how two fundamental aspects of polymer physics, that is, the glass transition and the crystallization kinetics, are modified when colloidal polymer nanoparticles are investigated. Attention is also devoted on how the interplay between crystallization and glass transition intervenes in these systems. In doing so, special emphasis is devoted to the presence of a large amount of interface, a common feature to all polymer materials geometrically confined at the nanoscale. In addition, the specific features of colloidal polymer nanoparticles are discussed. These originate from the

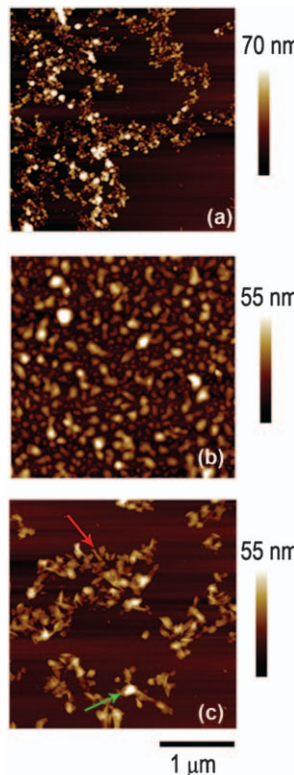


**Figure 8.10** PLLA nanoparticles obtained by miniemulsion, at  $T = 75\text{ }^{\circ}\text{C}$  at (a) 0 min, (b) 5 min and (c) 1200 min. The red arrow points to a edge-on lamella, and the green arrow points to a flat-on lamella.  
Adapted from ref. 158 with permission of Springer Nature, Copyright 2016.

presence of geometrical curvature at the polymer surface and, differently from 1D confinement typical of thin polymer films, may result in positive  $T_g$  deviations from bulk behavior. The same effect is discussed in relation to the experimental evidence of a slowing-down of the crystallization rate observed in several experiments. Entropic effects, arising from the suppression of degrees of freedom at the curved polymer surface, are recalled and discussed in detail to explain these results.

## Acknowledgements

DC acknowledges financial support from the project MAT2015-63704-P, (MINECO/FEDER, UE) and PGC2018-094548-B-I00 (MICINN-Spain and FEDER-UE), and the Basque Government (Grant No. IT-654-13 (GV)). AN acknowledges financial support from the Spanish Ministry of Economy (Grant No. MAT2014-59187-R).

## References

1. W. Abdelwahed, G. Degobert, S. Stainmesse and H. Fessi, *Adv. Drug Delivery Rev.*, 2006, **58**, 1688–1713.
2. F. Zhang, E. Lees, F. Amin, P. Rivera\_Gil, F. Yang, P. Mulvaney and W. J. Parak, *Small*, 2011, **7**, 3113–3127.
3. P. D. Howes, R. Chandrawati and M. M. Stevens, *Science*, 2014, **346**, 1247390.
4. Y. Zhao, L. Shang, Y. Cheng and Z. Gu, *Acc. Chem. Res.*, 2014, **47**, 3632–3642.
5. A. Nogales, T. A. Ezquerra, Z. Denchev and F. J. Balta-Calleja, *Polymer*, 2001, **42**, 5711–5715.
6. A. Sanz, A. Nogales and T. A. Ezquerra, *Macromolecules*, 2010, **43**, 29–32.
7. K. Kaminski, K. Adrjanowicz, Z. Wojnarowska, M. Dulski, R. Wrzalik, M. Paluch, E. Kaminska and A. Kasprzycka, *J. Phys. Chem. B*, 2011, **115**, 11537–11547.
8. A. Sanz and K. Niss, *Cryst. Growth Des.*, 2017, **17**, 4628–4636.
9. R. Androsch, E. Zhuravlev, J. W. Schmelzer and C. Schick, *Eur. Polym. J.*, 2018, **102**, 195–208.
10. S. Vyazovkin, *Macromol. Rapid Commun.*, 2019, **40**, 1800334.
11. P. G. Debenedetti, *Metastable Liquids: Concepts and Principles*, Princeton University Press, Princeton, 1996.
12. J. W. P. Schmelzer and I. S. Gutzow, *Glasses and the Glass Transition*, Wiley-VCH, Weinheim, 2011.
13. A. J. Kovacs, *Fortsch. Hochpolym. Forsch.*, 1963, **3**, 394–508.
14. L. C. E. Struik, *Physical Aging in Amorphous Polymers and Other Materials*, Technische Hogeschool Delft., 1977.
15. D. Cangialosi, *J. Phys.: Condens. Matter*, 2014, **26**, 153101.
16. A. Tool, *J. Am. Ceram. Soc.*, 1946, **29**, 240–253.
17. I. M. Hodge, *J. Non-Cryst. Solids*, 1994, **169**, 211–266.
18. E. Donth, J. Korus, E. Hempel and M. Beiner, *Thermochim. Acta*, 1997, **304**, 239–249.
19. I. Gallino, J. Schroers and R. Busch, *J. Appl. Phys.*, 2010, **108**, 063501.
20. J. W. P. Schmelzer and T. V. Tropin, *J. Chem. Phys.*, 2013, **138**, 034507.
21. J. E. K. Schawe, *J. Chem. Phys.*, 2014, **141**, 184905.
22. H. Vogel, *Phys. Z.*, 1921, **22**, 645–646.
23. G. S. Fulcher, *J. Am. Ceram. Soc.*, 1925, **8**, 339–355.
24. G. Tammann and W. Hesse, *Z. Anorg. Allg. Chem.*, 1926, **156**, 245.
25. M. L. Williams, R. F. Landel and J. D. Ferry, *J. Am. Chem. Soc.*, 1955, **77**, 3701–3707.
26. G. Johari, *Thermochim. Acta*, 2011, **523**, 97–104.
27. H. Nyquist, *Phys. Rev.*, 1928, **32**, 110–113.
28. H. Callen and R. Greene, *Phys. Rev.*, 1952, **86**, 702–710.
29. C. G. Robertson, P. G. Santangelo and C. M. Roland, *J. Non-Cryst. Solids*, 2000, **275**, 153–159.

30. M. K. Saini, X. Jin, T. Wu, Y. Liu and L.-M. Wang, *J. Chem. Phys.*, 2018, **148**, 124504.
31. J. L. Keddie, R. A. L. Jones and R. A. Cory, *Europhys. Lett.*, 1994, **27**, 59.
32. J. L. Keddie, R. A. L. Jones and R. A. Cory, *Faraday Discuss.*, 1994, **98**, 219–230.
33. C. H. Park, J. H. Kim, M. Ree, B.-H. Sohn, J. C. Jung and W.-C. Zin, *Polymer*, 2004, **45**, 4507–4513.
34. J. A. Forrest, K. Dalnoki-Veress, J. R. Stevens and J. R. Dutcher, *Phys. Rev. Lett.*, 1996, **77**, 2002–2005.
35. V. M. Boucher, D. Cangialosi, A. Alegría and J. Colmenero, *Macromolecules*, 2012, **45**, 5296–5306.
36. S. Gao, Y. P. Koh and S. L. Simon, *Macromolecules*, 2013, **46**, 562–570.
37. D. Cangialosi, A. Alegría and J. Colmenero, in *Cooling Rate Dependent Glass Transition in Thin Polymer Films and in Bulk*, ed. C. Schick and V. Mathot, Springer International Publishing, Cham, 2016, pp. 403–431.
38. Z. Fakhraai and J. A. Forrest, *Phys. Rev. Lett.*, 2005, **95**, 025701.
39. M. D. Ediger and J. A. Forrest, *Macromolecules*, 2014, **47**, 471–478.
40. R. D. Priestley, D. Cangialosi and S. Napolitano, *J. Non-Cryst. Solids*, 2015, **407**, 288–295.
41. F. Kremer, M. Tress and E. U. Mapesa, *J. Non-Cryst. Solids*, 2015, **407**, 277–283.
42. D. Cangialosi, A. Alegría and J. Colmenero, *Prog. Polym. Sci.*, 2016, **54** 55, 128–147.
43. S. Napolitano, E. Glynnos and N. B. Tito, *Rep. Prog. Phys.*, 2017, **80**, 036602.
44. G. Fleer, M. C. Stuart, J. M. Scheutjens, T. Cosgrove and B. Vincent, *Polymers at Interfaces*, Springer Science & Business Media, 1993.
45. S. Napolitano and M. Wübbenhurst, *Nat. Commun.*, 2011, **2**, 260.
46. S. Napolitano, C. Rotella and M. Wubbenhorst, *ACS Macro Lett.*, 2012, **1**, 1189–1193.
47. M. J. Burroughs, S. Napolitano, D. Cangialosi and R. D. Priestley, *Macromolecules*, 2016, **49**, 4647–4655.
48. N. G. Perez-de Eulate, M. Sferrazza, D. Cangialosi and S. Napolitano, *ACS Macro Lett.*, 2017, **6**, 354–358.
49. U. Gaur and B. Wunderlich, *Macromolecules*, 1980, **13**, 1618–1625.
50. C. Zhang, Y. Guo and R. D. Priestley, *Macromolecules*, 2011, **44**, 4001–4006.
51. C. Zhang, V. M. Boucher, D. Cangialosi and R. D. Priestley, *Polymer*, 2013, **54**, 230–235.
52. C. Bauer, R. Böhmer, S. Moreno-Flores, R. Richert, H. Sillescu and D. Neher, *Phys. Rev. E*, 2000, **61**, 1755.
53. S. Feng, Z. Li, R. Liu, B. Mai, Q. Wu, G. Liang, H. Gao and F. Zhu, *Soft Matter*, 2013, **9**, 4614–4620.
54. S. Feng, Y. Chen, B. Mai, W. Wei, C. Zheng, Q. Wu, G. Liang, H. Gao and F. Zhu, *Phys. Chem. Chem. Phys.*, 2014, **16**, 15941–15947.
55. J. Ding, G. Xue, Q. Dai and R. Cheng, *Polymer*, 1993, **34**, 3325–3327.
56. C. Zhang, Y. Guo, K. B. Shepard and R. D. Priestley, *J. Phys. Chem. Lett.*, 2013, **4**, 431–436.

57. C. Angell, *J. Non-Cryst. Solids*, 1991, **131**, 13–31.
58. C. Zhang and R. D. Priestley, *Soft Matter*, 2013, **9**, 7076–7085.
59. C. T. Thurau and M. D. Ediger, *J. Chem. Phys.*, 2003, **118**, 1996–2004.
60. S. C. Pilcher and W. T. Ford, *Macromolecules*, 1998, **31**, 3454–3460.
61. L. Li, B. Li, J. Chen, D. Zhou, G. Xue and X. Liu, *Polymer*, 2004, **45**, 2813–2816.
62. W. Ming, J. Zhao, X. Lu, C. Wang and S. Fu, *Macromolecules*, 1996, **29**, 7678–7682.
63. D. Christie, C. Zhang, J. Fu, B. Koel and R. D. Priestley, *J. Polym. Sci., Part B: Polym. Phys.*, 2016, **54**, 1776–1783.
64. D. E. Martnez-Tong, M. Soccio, A. Sanz, C. Garca, T. A. Ezquerra and A. Nogales, *Macromolecules*, 2013, **46**, 4698–4705.
65. D. E. Martnez-Tong, J. Cui, M. Soccio, C. Garca, T. A. Ezquerra and A. Nogales, *Mater. Chem. Phys.*, 2014, **215**, 1620–1624.
66. Y. Mi, G. Xue and X. Wang, *Polymer*, 2002, **43**, 6701–6705.
67. D. Cangialosi, V. M. Boucher, A. Alegria and J. Colmenero, *Soft Matter*, 2013, **9**, 8619–8630.
68. Y. Guo, C. Zhang, C. Lai, R. D. Priestley, M. DÁcunzi and G. Fytas, *ACS Nano*, 2011, **5**, 5365–5373.
69. N. G. Perez-De-Eulate and D. Cangialosi, *Macromolecules*, 2018, **51**, 3299–3307.
70. C. Zhang, V. J. Pansare, R. K. Prud'Homme and R. D. Priestley, *Soft Matter*, 2012, **8**, 86–93.
71. D. Cangialosi, V. M. Boucher, A. Alegra and J. Colmenero, *Phys. Rev. Lett.*, 2013, **111**, 095701.
72. M. Chowdhury and R. D. Priestley, *Proc. Natl. Acad. Sci. U. S. A.*, 2017, **114**, 4854–4856.
73. N. G. Perez-De Eulate and D. Cangialosi, *Phys. Chem. Chem. Phys.*, 2018, **20**, 12356–12361.
74. V. M. Boucher, D. Cangialosi, A. Alegria and J. Colmenero, *Phys. Chem. Chem. Phys.*, 2017, **19**, 961–965.
75. V. M. Boucher, D. Cangialosi, A. Alegria and J. Colmenero, *J. Chem. Phys.*, 2017, **146**, 203312.
76. X. Monnier and D. Cangialosi, *Phys. Rev. Lett.*, 2018, **121**, 137801.
77. D. V. Louzguine-Luzgin, I. Seki, T. Yamamoto, H. Kawaji, C. Suryanarayana and A. Inoue, *Phys. Rev. B*, 2010, **81**, 144202.
78. I. Gallino, D. Cangialosi, Z. Evenson, L. Schmitt, S. Hechler, M. Stolpe and B. Ruta, *Acta Mater.*, 2018, **144**, 400–410.
79. Y. P. Mitrofanov, N. Kobelev and V. Khonik, *J. Non-Cryst. Solids*, 2018, **497**, 48–55.
80. L. Song, W. Xu, J. Huo, J.-Q. Wang, X. Wang and R. Li, *Intermetallics*, 2018, **93**, 101–105.
81. A. A. Miller, *Macromolecules*, 1970, **3**, 674–677.
82. R. Golovchak, A. Kozdras, V. Balitska and O. Shpotyuk, *J. Phys.: Cond. Matter*, 2012, **24**, 505106.

83. O. Shpotyuk, A. Kozdras, V. Balitska and R. Golovchak, *J. Non-Cryst. Solids*, 2016, **437**, 1–5.
84. W. Kauzmann, *Chem. Rev.*, 1948, **43**, 219–256.
85. J. H. Gibbs and E. A. DiMarzio, *J. Chem. Phys.*, 1958, **28**, 373–383.
86. P. Rittigstein, R. D. Priestley, L. J. Broadbelt and J. M. Torkelson, *Nat. Mater.*, 2007, **6**, 278–282.
87. A. Lee and J. D. Lichtenhan, *Macromolecules*, 1998, **31**, 4970–4974.
88. V. Pryamitsyn and V. Ganesan, *Macromolecules*, 2010, **43**, 5851–5862.
89. L. Zhu, X. Wang, Q. Gu, W. Chen, P. Sun and G. Xue, *Macromolecules*, 2013, **46**, 2292–2297.
90. V. M. Boucher, D. Cangialosi, A. Alegria, J. Colmenero, I. Pastoriza-Santos and L. M. Liz-Marzan, *Soft Matter*, 2011, **7**, 3607–3620.
91. D. Cangialosi, V. M. Boucher, A. Alegria and J. Colmenero, *Polymer*, 2012, **53**, 1362–1372.
92. V. Ramakrishnan, S. Harsiny, J. G. P. Goossens, T. L. Hoeks and G. W. M. Peters, *J. Polym. Sci., Part B: Polym. Phys.*, 2016, **54**, 2069–2081.
93. V. M. Boucher, D. Cangialosi, H. Yin, A. Schoenhals, A. Alegria and J. Colmenero, *Soft Matter*, 2012, **8**, 5119–5122.
94. H. Yin, D. Cangialosi and A. Schoenhals, *Thermochim. Acta*, 2013, **566**, 186–192.
95. W. Zhang, J. F. Douglas and F. W. Starr, *Proc. Natl. Acad. Sci. U. S. A.*, 2018, **115**, 5641–5646.
96. D. Cangialosi, V. M. Boucher, A. Alegria and J. Colmenero, *J. Polym. Sci., Part B: Polym. Phys.*, 2013, **51**, 847–853.
97. K. Niss, *Phys. Rev. Lett.*, 2017, **119**, 115703.
98. Y. Rharbi, F. Boué and Q. Nawaz, *Macromolecules*, 2013, **46**, 7812–7817.
99. N. G. Perez-de Eulate, V. Di Lisio and D. Cangialosi, *ACS Macro Lett.*, 2017, **6**, 859–863.
100. M. Merzlyakov and C. Schick, *Thermochim. Acta*, 2001, **380**, 5–12.
101. E. Shoifet, G. Schulz and C. Schick, *Thermochim. Acta*, 2015, **603**, 227–236.
102. M. S. McCaig, D. R. Paul and J. W. Barlow, *Polymer*, 2000, **41**, 639–648.
103. D. Cangialosi, M. Wübbenhorst, J. Groenewold, E. Mendes, H. Schut, A. van Veen and S. J. Picken, *Phys. Rev. B*, 2004, **70**, 224213.
104. D. Cangialosi, V. M. Boucher, A. Alegria and J. Colmenero, *J. Chem. Phys.*, 2011, **135**, 014901.
105. S. Napolitano and D. Cangialosi, *Macromolecules*, 2013, **46**, 8051–8053.
106. A. W. Thornton and A. J. Hill, *Ind. Eng. Chem. Res.*, 2010, **49**, 12119–12124.
107. R. W. Cahn, P. Haasen, E. J. Kramer and P. J. Barham, *Crystallization and Morphology of Semicrystalline Polymers*, Wiley-Vch Verlag GmbH & Co KGaA, Weinheim, 2006.
108. A. Toda, K. Taguchi and H. Kajioka, *Macromolecules*, 2008, **41**, 7505–7512.
109. B. Lotz, T. Miyoshi and S. Z. D. Cheng, *Macromolecules*, 2017, **50**, 5995–6025.
110. G. R. Strobl and G. R. Strobl, *The Physics of Polymers*, Springer, vol. 2, 1997.
111. B. Wunderlich, *Macromolecular Physics, Volume 1: Crystal Structure, Morphology, Defects*, Academic Press, 1973.

112. C. Santa Cruz, N. Stribeck, H. G. Zachmann and F. J. Balta Calleja, *Macromolecules*, 1991, **24**, 5980–5990.
113. A. Nogales, Z. Denchev, I. Sics and T. A. Ezquerra, *Macromolecules*, 2000, **33**, 9367–9375.
114. A. Nogales, T. A. Ezquerra, Z. Denchev, I. Sics, F. J. B. Calleja and B. S. Hsiao, *J. Chem. Phys.*, 2001, **115**, 3804–3813.
115. D. C. Bassett, R. H. Olley and I. A. M. Al Raheil, *Polymer*, 1988, **29**, 1745–1754.
116. Y. Wang, S. Ge, M. Rafailovich, J. Sokolov, Y. Zou, H. Ade, J. Lüning, A. Lustiger and G. Maron, *Macromolecules*, 2004, **37**, 3319–3327.
117. D. E. Martínez-Tong, B. Vanroy, M. Wübbenhurst, A. Nogales and S. Napolitano, *Macromolecules*, 2014, **47**, 2354–2360.
118. J. Balko, A. Rinscheid, A. Wurm, C. Schick, R. H. Lohwasser, M. Thelakkat and T. Thurn-Albrecht, *J. Polym. Sci., Part B: Polym. Phys.*, 2016, **54**, 1791–1801.
119. B. Zhang, J. Chen, B. Liu, B. Wang, C. Shen, R. Reiter, J. Chen and G. Reiter, *Macromolecules*, 2017, **50**, 6210–6217.
120. S. Napolitano and M. Wübbenhurst, *J. Phys.: Condens. Matter*, 2007, **19**, 205121.
121. S. Luo, X. Kui, E. Xing, X. Wang, G. Xue, C. Schick, W. Hu, E. Zhuravlev and D. Zhou, *Macromolecules*, 2018, **51**, 5209–5218.
122. J. Xu, Y. Li, X. Wu, B. Zuo, X. Wang, W. Zhang and O. K. C. Tsui, *Macromolecules*, 2018, **51**, 3423–3432.
123. G. Reiter and G. Strobl, *Progress in Understanding of Polymer Crystallization*, Springer, Berlin, 2007, vol. 714.
124. Y.-X. Liu and E.-Q. Chen, *Coord. Chem. Rev.*, 2010, **254**, 1011–1037.
125. M. Steinhart, P. Güring, H. Dernaika, M. Prabhukaran, U. Güsele, E. Hempel and T. Thurn-Albrecht, *Phys. Rev. Lett.*, 2006, **97**, 027801.
126. J. Martín, A. Nogales and C. Mijangos, *Macromolecules*, 2013, **46**, 7415–7422.
127. J. Martin, A. D. Scaccabarozzi, A. Nogales, R. Li, D.-M. Smilgies and N. Stingelin, *Eur. Polym. J.*, 2016, **81**, 650–660.
128. J. Martín, A. Iturrospe, A. Cavallaro, A. Arbe, N. Stingelin, T. A. Ezquerra, C. Mijangos and A. Nogales, *Chem. Mater.*, 2017, **29**, 3515–3525.
129. Y. Yao, T. Sakai, M. Steinhart, H.-J. Butt and G. Floudas, *Macromolecules*, 2016, **49**, 5945–5954.
130. X. Dai, H. Li, Z. Ren, T. P. Russell, S. Yan and X. Sun, *Macromolecules*, 2018, **51**, 5732–5741.
131. B. Vanroy, M. Wübbenhurst and S. Napolitano, *ACS Macro Lett.*, 2013, **2**, 168–172.
132. G. Reiter and J.-U. Sommer, *Phys. Rev. Lett.*, 1998, **80**, 3771.
133. M. Bertoldo, M. Labardi, C. Rotella and S. Capaccioli, *Polymer*, 2010, **51**, 3660–3668.
134. M. Asada, N. Jiang, L. Sendogdular, P. Gin, Y. Wang, M. K. Endoh, T. Koga, M. Fukuto, D. Schultz, M. Lee, X. Li, J. Wang, M. Kikuchi and A. Takahara, *Macromolecules*, 2012, **45**, 7098–7106.
135. J. L. Carvalho and K. Dalnoki-Veress, *Eur. Phys. J. E*, 2011, **34**, 6.

136. J.-c. Zhao, B. Xing, Z. Peng and J.-m. Zhang, *Chin. J. Polym. Sci.*, 2013, **31**, 1310–1320.
137. Y.-L. Loo, R. A. Register and A. J. Ryan, *Phys. Rev. Lett.*, 2000, **84**, 4120–4123.
138. K. Landfester, *Adv. Mater.*, 2001, **13**, 765–768.
139. T. Kietzke, D. Neher, M. Kumke, O. Ghazy, U. Ziener and K. Landfester, *Small*, 2007, **3**, 1041–1048.
140. D. E. Martínez-Tong, PhD thesis, Universidad Complutense de Madrid, 2014.
141. E. Gutiérrez-Fernández, PhD thesis, Universidad Complutense de Madrid, 2019.
142. C. Zhang, J. W. Chung and R. D. Priestley, *Macromol. Rapid Commun.*, 2012, **33**, 1798–1803.
143. D. E. Martínez-Tong, M. Soccio, A. Sanz, C. García, T. A. Ezquerra and A. Nogales, *Polymer*, 2015, **56**, 428–434.
144. S. Feng, Y. Chen, C. Meng, B. Mai, Q. Wu, H. Gao, G. Liang and F. Zhu, *J. Colloid Interface Sci.*, 2015, **450**, 264–271.
145. Z. Hu and A. J. Gesquiere, *Chem. Phys. Lett.*, 2009, **476**, 51–55.
146. D. E. Martínez-Tong, M. Sanz, T. A. Ezquerra, A. Nogales, J. F. Marco, M. Castillejo and E. Rebollar, *Appl. Surf. Sci.*, 2017, **418**, 522–529.
147. I. Elaboudi, S. Lazare, C. Belin, J. L. Bruneel and L. Servant, *Appl. Surf. Sci.*, 2007, **253**, 7835–7839.
148. D. B. Chrisey, A. Piquü, R. A. McGill, J. S. Horwitz, B. R. Ringeisen, D. M. Bubb and P. K. Wu, *Chem. Rev.*, 2003, **103**, 553–576.
149. H. Jeong, M. Chowdhury, Y. Wang, M. Sezen-Edmonds, Y.-L. Loo, R. A. Register, C. B. Arnold and R. D. Priestley, *Macromolecules*, 2018, **51**, 512–519.
150. J. W. P. Schmelzer and A. S. Abyzov, *J. Non-Cryst. Solids*, 2016, **449**, 41–49.
151. D. E. Martínez-Tong, M. Soccio, A. Sanz, C. García, T. A. Ezquerra and A. Nogales, *Macromolecules*, 2013, **46**, 4698–4705.
152. M. J. Capitán, D. R. Rueda and T. A. Ezquerra, *Macromolecules*, 2004, **37**, 5653–5659.
153. J. Martín, C. Mijangos, A. Sanz, T. A. Ezquerra and A. Nogales, *Macromolecules*, 2009, **42**, 5395–5401.
154. Y. Suzuki, H. Duran, W. Akram, M. Steinhart, G. Floudas and H.-J. Butt, *Soft Matter*, 2013, **9**, 9189–9198.
155. Y. Suzuki, H. Duran, M. Steinhart, H.-J. Butt and G. Floudas, *Soft Matter*, 2013, **9**, 2621–2628.
156. D. E. Martínez-Tong, M. Soccio, A. Sanz, C. García, T. A. Ezquerra and A. Nogales, *Polymer*, 2015, **56**, 428–434.
157. W. Hu, T. Cai, Y. Ma, J. K. Hobbs, O. Farrance and G. Reiter, *Faraday Discuss.*, 2009, **143**, 129–141.
158. A. Nogales and D. E. Martínez-Tong, Crystallization in Nanoparticles, in *Controlling the Morphology of Polymers*, ed. G. R. Mitchell and A. Tojeira, Springer International Publishing, Cham, 2016, pp. 163–180.

## CHAPTER 9

# *Transport of Polymer Colloids in Porous Media*

NAVID BIZMARK,<sup>a,b</sup> JOANNA SCHNEIDER,<sup>b</sup> EMILY DE JONG<sup>b</sup>  
AND SUJIT S. DATTA\*<sup>b</sup>

<sup>a</sup> Princeton Institute for the Science and Technology of Materials (PRISM),  
Princeton University, Princeton, NJ 08540, USA; <sup>b</sup> Department of Chemical  
and Biological Engineering, Princeton University, Princeton, NJ 08540, USA  
\*Email: ssdatta@princeton.edu

## 9.1 Introduction

Colloidal particle transport in porous media is of practical interest in various engineering applications including wastewater treatment,<sup>1,2</sup> colloid-associated pollutant transport,<sup>3–5</sup> enhanced oil recovery,<sup>6,7</sup> and filtration of microorganisms.<sup>8–10</sup> These applications typically involve the transport of colloidal particles ranging from tens of nanometers to a few micrometers in size, including inorganic particles (e.g., metals and metal oxides), organic particles (e.g., humic substances and polymers), and biological materials (e.g., viruses and bacteria).<sup>11</sup> Moreover, such particles can have dramatically different physicochemical properties; as a result, their interactions with each other and with the solid matrix of the porous medium differ considerably, ultimately impacting transport behavior.

In some cases, the presence of these particles can enhance transport of other compounds. For example, field studies at hazardous waste sites have shown enhanced transport of radionuclides and metal ions due to the presence of colloids,<sup>12–14</sup> in agreement with laboratory experiments showing accelerated colloid-facilitated transport of ionic metals through a model

porous medium.<sup>15,16</sup> Frequently, nanometer- to micrometer-sized inorganic colloids such as clays, metal oxides, and carbonates appear to be responsible for enhanced contaminant transport in aquifers. Other works show the ability of natural and synthetic organic colloids to enhance transport of metallic<sup>17,18</sup> and hydrophobic<sup>19–22</sup> contaminants.

In other cases, the presence of colloids can suppress transport. Often, colloids are deposited as they are transported through the pore space, reducing pore space permeability and potentially leading to clogging.<sup>23</sup> This process can be desirable for waste isolation, in which colloidal clogging can hinder the spread of waste materials.<sup>3</sup> Conversely, clogging poses a significant problem for energy and environmental processes, such as enhanced oil recovery and contaminant removal from groundwater aquifers, which rely on unimpeded transport of fluids through the pore space. For example, an emerging approach for enhanced oil recovery is to inject surface-active particles into a reservoir to reduce the oil–water interfacial tension and thereby promote oil mobilization. However, in some cases, these particles can clog the reservoir prior to reaching the oil zone, decreasing recovery and potentially damaging the reservoir. Similarly, clogging of groundwater aquifers by naturally occurring colloidal particles poses a key challenge to aquifer remediation, because it limits the ability to recover trapped contaminants.

To control these processes, it is necessary to develop a deeper understanding of the pore-scale and macro-scale physical principles that govern colloidal transport in porous media. Figure 9.1 shows typical pore-scale events that control the transport of colloids in a porous medium. Particles introduced to a saturated porous medium—one that is already filled with the carrier fluid—may behave in a variety of ways. These particles may adsorb at the surface of the porous medium matrix—and thus, each matrix particle is often referred to as a

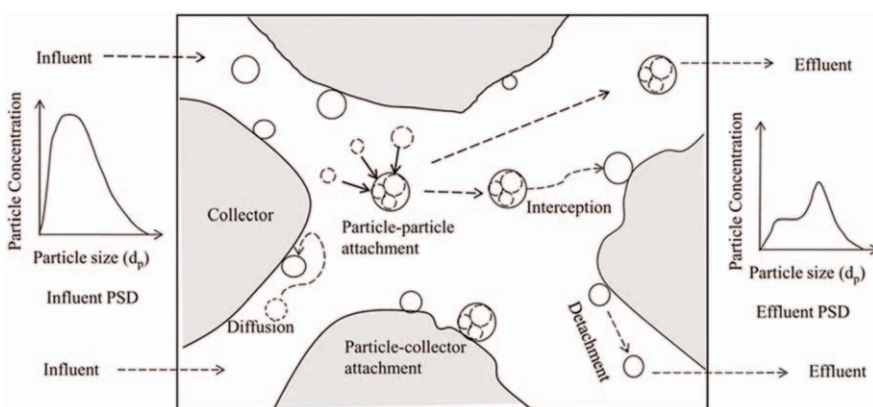


**Figure 9.1** Schematic of pore-scale events during particle transport in a porous medium: particle deposition on a porous medium matrix particle, or collector, via diffusion and interception, particle detachment from the collector, and particle aggregation.

Reproduced from ref. 24 with permission from Elsevier, Copyright 2012.

“collector”—*via* different mechanisms, such as diffusion or advection, often referred to as interception. They can also attach to other particles and form aggregates, detach from the surfaces of collectors after adsorption, or move through tight channels in the pore space, termed pore throats. These pore-scale events have clear macroscopic consequences: they lead directly to colloid concentration variations between the influent and the effluent.

This chapter will provide essential knowledge of the multiscale aspects of colloidal particle transport in saturated porous media. Specifically, we will review and derive models that describe the physical principles of colloidal transport at the pore scale and at the macro scale. We will discuss experimental findings that highlight advancements in our understanding of colloid transport. A review of these publications will therefore allow us to make connections between recent experimental findings and established theoretical results, and to describe the advantages and challenges of various experimental approaches. While in some cases these studies focus on non-polymeric colloids, the governing principles are relevant to polymeric colloids as well. Moreover, the use of polymers enables precise control over colloid morphology and surface properties. This precision provides exciting opportunities for the use of polymer colloids to control flow and transport in porous media for wastewater treatment, contaminant containment, enhanced oil recovery, and filtration.

## 9.2 Mathematical Modeling

### 9.2.1 Macro-scale Modelling: 1D Continuum Advection-dispersion Equation (ADE)

Typical applications involve fluid Reynolds numbers much smaller than one. Consequently, the steady-state flowrate  $Q$  of a fluid moving unidirectionally through a porous medium is directly proportional to the pressure drop  $\Delta P$  and inversely proportional to the fluid viscosity  $\mu$ . This behavior is quantified by Darcy's law:

$$Q = \frac{KA}{\mu} \left| \frac{\Delta P}{L} \right| \quad (9.1)$$

where  $A$  and  $L$  are the medium cross-sectional area and length, respectively, and  $K$  is an empirical descriptor known as the fluid permeability. This parameter is a strong function of a porous medium's properties, such as its porosity and the pore size distribution, which can be complex and difficult to quantify. As a result, the permeability is often determined by fitting experimental data.

Over the course of particle transport in porous media, permeability may change due to pore-scale events such as particle deposition, which dynamically alter the pore space geometry.<sup>25,26</sup> Continuum models describe this complex behavior by considering the advection and diffusion of particles through the pore space. Assuming one-dimensional (1D) flow along  $x$

through a saturated porous medium, mass conservation for the colloidal particles yields the relation<sup>25,27–29</sup>

$$\frac{\partial C}{\partial t} = \frac{\partial^2 (DC)}{\partial x^2} - \frac{\partial(vC)}{\partial x} - f \quad (9.2)$$

where  $C$  is the particle concentration,  $D$  is the particle diffusivity,  $f$  is the rate of particle deposition per unit volume, and  $v = Q/(A\phi)$  is the interstitial fluid velocity with porosity  $\phi$ ; for simplicity, the particles are assumed to move with the fluid.<sup>30</sup> Assuming the flow is uniform along  $x$ , eqn (9.2) can be written in non-dimensional form:

$$\frac{\partial \bar{C}}{\partial \bar{t}} = \frac{\partial^2 \bar{C}}{\partial \bar{x}^2} - \text{Pe} \frac{\partial \bar{C}}{\partial \bar{x}} - \bar{f} \quad (9.3)$$

Here,  $\bar{C} \equiv C/C_0$ , where  $C_0$  is the particle concentration entering the porous medium,  $\bar{x} \equiv x/L$ ,  $\bar{t} \equiv Dt/L^2$ , and  $\text{Pe} \equiv vL/D$ . The latter is one form of the Pécelt number, which compares advection-dominated particle transport to diffusion-dominated transport. At low Pécelt numbers ( $\text{Pe} < 1$ ), diffusion is dominant, whereas at large Pécelt numbers ( $\text{Pe} \gg 1$ ), advection becomes the main mechanism of colloidal transport. When modeling the transport of colloids in a porous medium, the diffusion of particles is typically modified to include an effective diffusion coefficient that takes into account the tortuosity ( $\tau$ ) of the medium, where tortuosity refers to the longer path that a particle must travel due to the geometry of the porous medium. This effective diffusion coefficient is known as the hydrodynamic dispersion coefficient,  $D_h$ , which can be estimated from  $D_h = D + \tau v$ . Substituting the diffusion coefficient with a dispersion coefficient in eqn (9.2) yields the advection-dispersion equation (ADE).

The particle volumetric deposition rate  $f$  can be written in terms of the fraction of the collector's surface covered by colloidal particles, or surface coverage ( $\Theta$ ).<sup>28,31</sup> In this approach, two deposition regimes with different kinetics are considered: (i) the deposition of colloidal particles on bare collectors, or single-layer deposition, and (ii) deposition on collectors that are already covered by particles, also called multilayer deposition. Assuming first-order kinetics, this rate can be written as  $f = k_{\text{dep}}C$ , where  $k_{\text{dep}}$  is the deposition rate constant. This constant can be determined empirically through what is known as filtration theory, described in Section 9.2.2. Alternatively, it can be written as  $k_{\text{dep}} = k' B(\Theta) + k'' \Theta$ , where  $k'$  and  $k''$  are the deposition rate constants for single-layer and multilayer deposits, respectively,<sup>31</sup> and  $B(\Theta)$  is the blocking function, which indicates how deposited particles influence the deposition of new particles. This function can be computed from Langmuirian adsorption or random sequential adsorption models.<sup>31,32</sup>

### 9.2.2 Pore-scale Events: Filtration Theory

When particles travel through a saturated porous medium, they often collide and deposit onto collectors' surfaces. The conceptual explanation of this phenomenon is given by filtration theory,<sup>26,29,33,34</sup> sometimes referred to as

deep-bed filtration theory,<sup>2,35,36</sup> which yields a simple expression for the particle deposition rate per unit volume,  $f$ .<sup>25,29</sup> Specifically, for a porous medium comprised of spherical collectors of equal size,  $k_{\text{dep}}$  can be computed as

$$k_{\text{dep}} = \frac{3}{2} \frac{(1 - \phi)}{d_c} v\eta \quad (9.4)$$

where  $d_c$  is the average collector diameter and  $\eta \equiv \alpha\eta_0$  is known as the single-collector efficiency.<sup>33,37</sup> Here,  $\alpha$  is the empirical collision or attachment efficiency and  $\eta_0$  is the rate at which particles strike the collector divided by the rate at which particles flow toward the collector.<sup>33,37</sup> This quantity is thus controlled by hydrodynamic driving forces, including particle Brownian motion, advection/interception, and gravity.<sup>29,33</sup> To include the effects of these mechanisms in the pair interaction between a colloidal particle and a single collector, it is postulated that  $\eta_0 = \eta_D + \eta_I + \eta_G$ , where  $\eta_D$ ,  $\eta_I$ , and  $\eta_G$  are the single-collector efficiencies due solely to diffusion, interception, and gravity, respectively.<sup>33,38,39</sup> These efficiencies may be formulated in terms of dimensionless parameters that reflect hydrodynamic forces, such as the Péclet number and the particle-to-collector size ratio.<sup>26,38,40–43</sup> Figure 9.2(a) shows a typical trend for these efficiencies as a function of colloidal particle size.<sup>33,37,44</sup> For particles smaller than 1  $\mu\text{m}$ , diffusion dominates in the determination of  $\eta_0$ ; for larger particles, interception and gravity begin to play a more appreciable role.<sup>45</sup>

While hydrodynamic forces are crucial in the determination of  $\eta_0$ , the empirical collision efficiency,  $\alpha$ , is determined largely by physicochemical forces, namely Derjaguin–Landau–Verwey–Overbeek (DLVO) forces.<sup>29,46–50</sup> DLVO forces, which account for van der Waals attractive forces and electrostatic repulsive forces, govern particle surface interactions in the near-surface domain.<sup>51</sup> The collision efficiency therefore varies from zero to unity, where  $\alpha < 1$  is known as the unfavorable deposition regime and  $\alpha = 1$  is known as favorable deposition. Under favorable conditions, all transported particles will be deposited onto the collector. However, when a net repulsion exists between a particle and a collector, deposition is unfavorable. Under these conditions, as particles approach the near-surface domain, the repulsion between the particle and the collector kinetically controls deposition.<sup>52,53</sup> As a result, only some particles will deposit onto the collector's surface [see Figure 9.2(a)].<sup>23,54</sup> When deposition is unfavorable, this process can be considered in two steps. Far from the collector, particles are transported by hydrodynamic driving forces, but as they approach the near-surface domain in the presence of a net repulsion, they may still deposit onto the collector's surface. In this two-step model,  $\eta$  represents the likelihood of colloidal particles entering the near-surface domain.

To use filtration theory for larger systems, the single-collector efficiency must be scaled up to account for multiple collectors. The upscaling approach depends on whether deposition is favorable or unfavorable.<sup>51</sup> Figure 9.2(c) shows a simple upscaling from a single-collector model to a multicollector model under favorable deposition conditions. Starting from

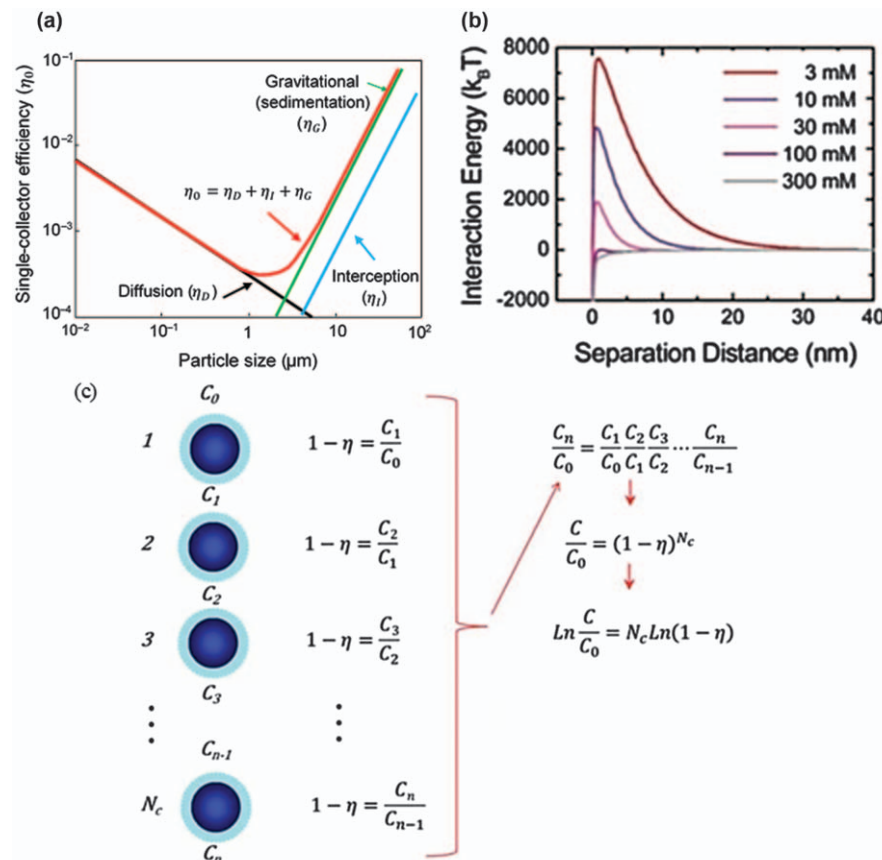


**Figure 9.2** (a) Numerical computation of  $\eta_0$ ,  $\eta_D$ ,  $\eta_I$ , and  $\eta_G$  for a column filled with 0.5 mm spherical glass beads as a function of colloidal particle concentration injected at a velocity of  $\sim 5 \text{ m h}^{-1}$ . (b) Pair interaction energy profiles between 3  $\mu\text{m}$  fluorescent carboxyl-modified polystyrene latex colloids and spherical glass beads with a mean size of 328  $\mu\text{m}$  separated by a known distance at various ionic strengths. (c) Upscaling from a single collector to an array of  $N_c$  collectors assuming the same single-collector efficiency ( $\eta$ ) for every collector.

(a) Reproduced from ref. 54 with permission from American Chemical Society, Copyright 2004. (b) Reproduced from ref. 33 with permission from American Chemical Society, Copyright 1971. (c) Reproduced from 51 with permission from John Wiley and Sons, ©2013. American Geophysical Union. All Rights Reserved.

an initial concentration of colloidal particles,  $C_0$ , an arbitrary number of collectors,  $N_c$ , and assuming all collectors share the same single-collector efficiency, one may expect the colloidal particle concentration to drop down to  $C = C_0(1 - \eta)^{N_c}$  [see Figure 9.2(c)].

Despite this existing upscaling approach, there are conditions under which the assumption of similar  $\eta$  for all collectors becomes inadequate. The

assumption that all collectors to have the same single-collector efficiency implies that collector efficiency is uniform across the whole porous medium and that deposition is independent of transport history. In direct contrast with the single-collector efficiency assumption, under unfavorable deposition conditions where interception and gravity dominate, the efficiency of the first collector is the highest. Computational fluid dynamics (CFD) simulations reveal a non-exponential particle deposition profile under these conditions. The efficiency decreases to an asymptotic value along the collector array, confirming that a simple upscaling method does not suffice for unfavorable deposition conditions.<sup>55</sup>

By combining the ADE with filtration theory, one can explore various aspects of colloidal transport in a porous medium. In a study that investigated the effects of heterogeneity in packed columns on carboxylated polystyrene particles under constant flowrate,<sup>56</sup> experiments showed that spatial heterogeneity in a porous medium does not have a significant impact on deposition kinetics for an advection-dominated process. To quantify this phenomenon,  $k_{\text{dep}}$  was computed using the ADE as a fitting parameter. In the regime of high Péclet number, experimental and computational results agree. However, when advection is not dominant, computational results are contrary to experiment results, and more fine-grained computational tools, such as the Lattice–Boltzmann method (LBM), become necessary.<sup>56</sup>

While geometry and ill-defined parameters often limit large-scale continuum models, a continuum description of concentration and permeability can still prove useful. The ability to non-dimensionalize the continuum equations of mass conservation and motion makes these models robust and generalizable to all length and time scales where the underlying assumptions hold. However, complex computational methods may be able to delve deeper into smaller systems, providing fine-grained information in complex, heterogeneous systems.

### 9.2.3 The Lattice–Boltzmann Method (LBM) and Pore Network Modeling (PNM)

Though continuum models provide meaningful coarse-grained information based on advection and diffusion with modified transport coefficients, they are incapable of integrating the role of heterogeneous structure into the determination of particle transport in porous media, which may be a dominant factor in some cases. Among different computational methods, the Lattice–Boltzmann method (LBM) is a rigorous computational algorithm that can account for structural heterogeneities in sufficiently small systems, up to a few pores in size.<sup>57</sup> The LBM has been successfully used to model the rearrangement of flow patterns and migration of fine particles in two-dimensional (2D) porous media.<sup>58</sup> Further, the LBM has been leveraged to uncover the two primary behaviors of clogging and channelization in porous media, as well as the physical mechanism of erosive bursting: a sufficient pressure drop results in the dissolution of a strained colloidal aggregate.<sup>59,60</sup> Unfortunately,

simulations employing the LBM are still sufficiently complex that they can only be used to study very limited system sizes, and even then, they rely on parallel computing. This complexity makes the LBM ideal for uncovering pore-scale physics, but too computationally expensive to be applied to real mesoscale systems, such as permeable shale formations. Instead, simplified pore-network models aid in more efficient coarse-grained studies of porous media.

Recent works have demonstrated that the transport of a material through a pore network is highly dependent on the pore size distribution and the coordination number.<sup>61</sup> Pore network models (PNMs) propose a compromise between continuum models and the LBM that involves tessellating the porous medium into a simplified system of pore bodies and narrow connecting pore throats,<sup>62</sup> or employing a branched network morphology<sup>63</sup> to eliminate the role of pore bodies. A variety of imaging and mathematical techniques have been established to connect pore geometries in geological formations with PNMs, such as sphere-packing, statistical matching, and Delaunay tessellation.<sup>62</sup> Pore network modeling has a strong community and is widely used to determine macroscopic Darcy transport coefficients,<sup>64</sup> percolation, adsorption, and reactive transport.<sup>65,66</sup> Some complex PNMs are able to track individual nanoparticles in a network of spherical pores and conical frustum throats.<sup>67</sup> However, these models do not drive the system to a fully clogged state, and the representation of individual particles is computationally expensive compared to a continuum concentration abstraction.

There exist a variety of open-source PNM codes with the capacity to generate networks, such as OpenPNM,<sup>68</sup> which can perform reactive transport calculations. However, available open-source models currently do not have an efficient capacity to modify network geometry throughout a simulation to account for changes in the pore radii due to deposition and erosion of nanoparticles. In a hybrid approach, an existing network model generator can be used to stochastically generate a pore network system that matches the key geometric parameters of a physical pore dataset. Then, the particle concentration, pore constriction, and a new flow field are computed at each time step using 1D continuum model equations. Using this approach, pore structure changes due to precipitation and dissolving rock formations could be modeled.<sup>66</sup> Continued studies of complex pore networks using this simulation framework could yield exciting insights about the role of heterogeneous structure and flow path rearrangement in porous media. After a 1D continuum model, PNMs are the next step in upscaling a simple set of parameters to a more realistic but slightly more computationally expensive simulation.

## 9.3 Experiments on Colloidal Particle Transport in Porous Media

### 9.3.1 Macro-scale Studies

As discussed in Section 9.2, the combination of the ADE and filtration theory is widely used to study the transport of particles in a porous medium. With

this macroscopic empirical approach, the computed concentration of particles in the effluent from a porous medium is compared to experimental results. UV-vis spectroscopy has been used extensively to measure the concentration of spherical<sup>69–74</sup> and non-spherical<sup>75,76</sup> surface-functionalized polystyrene colloids at the effluent with sizes ranging from 30 nm to 6  $\mu\text{m}$ . When colloidal particles are fluorescently-tagged, a fluorometer measures the effluent particle concentration,  $C_e$ .<sup>77</sup> The effluent particle concentration is measured over time and normalized by the inlet concentration,  $C_0$ , to obtain a breakthrough concentration profile [see Figure 9.3(a)]. Breakthrough curves provide macroscopic information that describes how colloidal transport in porous media progresses temporally under various conditions for particle size, ionic strength, pH, flowrate, particle concentration, and particle shape.<sup>75,76,78–82</sup>

For example, the collision efficiency,  $\alpha$ , is one piece of macroscopic information that can be obtained using breakthrough curves. To calculate  $\alpha$  under known operating conditions,  $\eta_0$  is computed from empirical equations<sup>37</sup> and  $\alpha$  is found by fitting the ADE to experimentally obtained breakthrough curves. When advection is the dominant mechanism of particle transport,  $\alpha$  can be computed from the following equation at steady-state conditions.<sup>37,46</sup>

$$\alpha = - \frac{2d_c}{3(1-\phi)\eta_0 L} \ln(C_e/C_0) \quad (9.5)$$

Further, in lieu of direct microscopic observations, various studies have sought to establish a connection between processes at the pore and macro scales. The Péclet number can be computed from fitting the ADE to the breakthrough curves without any need for direct visualization of pore-scale events. When  $\text{Pe} < 1$ , diffusion is the dominant mechanism of transport in porous media. Under these conditions, particles can move from one pore body to an adjacent one, resulting in a more complete sweep of the entire porous medium [see Figure 9.3(b)]. As Pe becomes larger, advection starts to contribute more to the transport process, and at  $\text{Pe} > 400$ , advection is dominant and particles move predominantly along the flow direction [compare longitudinal dispersion,  $D_L$ , to transverse dispersion,  $D_T$ , in Figure 9.3(b)-i and (b)-ii].<sup>83–88</sup>

While diffusion and advection are two main mechanisms of particle transport in porous media, analyses of breakthrough curves using the ADE do not capture other possible pore-scale behaviors. For example, experiments using model silica colloids showed a slow decrease in colloid concentration over the elution time, as compared to the sharp drop in outlet concentration for chloride tracer particles [see Figure 9.3(c)].<sup>89</sup> This observation, termed tailing,<sup>89–91</sup> is thought to be due to the detachment of already deposited particles from the solid matrix. Whereas the physical origin of this phenomenon is not well understood, mathematical models have been developed to capture the tailing effect.<sup>92</sup>

Breakthrough curves have also been measured for particles with different sizes and aspect ratios. Figure 9.3(a) shows the breakthrough profiles of micron-sized spherical sulfate-modified polystyrene latex particles with

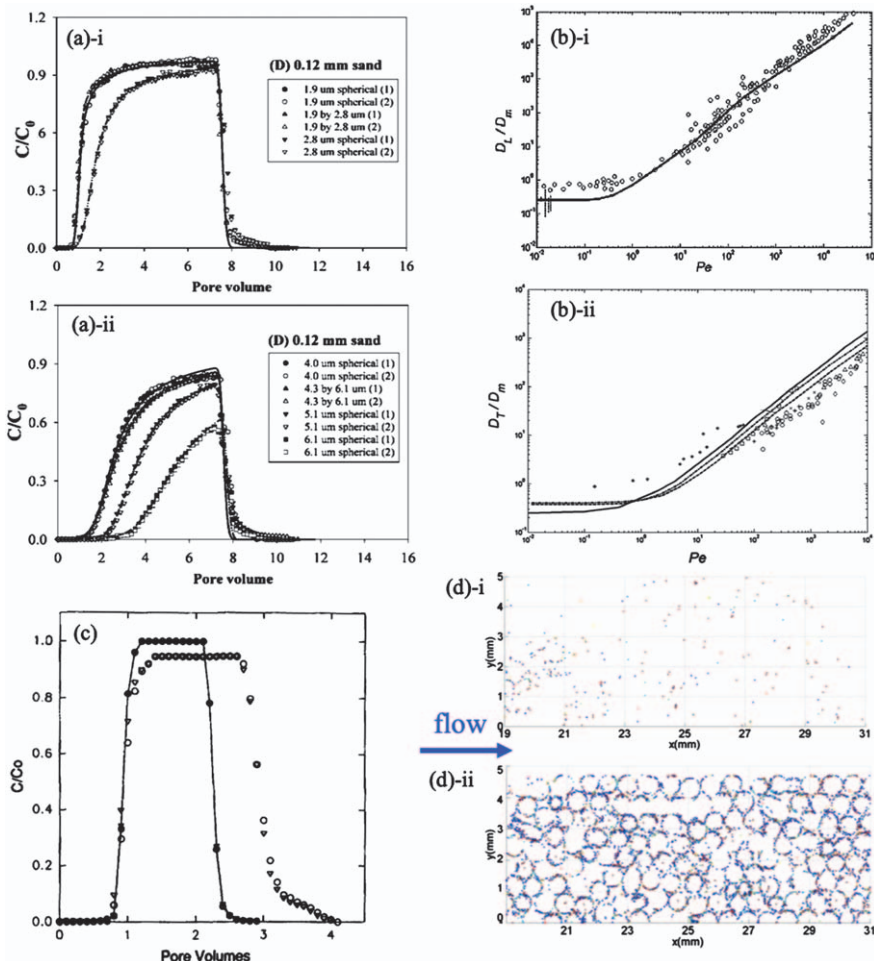


**Figure 9.3** (a) Breakthrough curves for spherical (i) and peanut (ii) shaped particles ranging from  $1.9\text{ }\mu\text{m}$  to  $6.1\text{ }\mu\text{m}$  injected into a porous medium made with  $0.12\text{ mm}$  quartz sand. Here, the variable  $C$  represents the effluent concentration  $C_e$ . (b)-i Longitudinal and (b)-ii transverse dispersion coefficients normalized by molecular diffusion coefficient ( $D_m$ ) as a function of Pécelt number. (c) Concentration breakthrough curves of chloride tracer (filled symbols) and  $91\text{ nm}$  colloidal silica particles (empty symbols) for columns packed with  $300\text{--}400\text{ }\mu\text{m}$  quartz sand. (d) Distribution of deposited  $210\text{ nm}$  spherical (i) and  $235.8\text{ nm}$  per  $100\text{ nm}$  (2:1) rod-shaped fluorescent carboxyl-modified polystyrene nanoparticles (ii) after the injection of  $40$  pore volumes into a porous medium comprised of  $600\text{--}710\text{ }\mu\text{m}$  glass beads.

(a) Reproduced from ref. 75 with permission from American Chemical Society, Copyright 2008. (b)-i Reproduced from ref. 88 with permission from John Wiley and Sons, Copyright 2006 by the American Geophysical Union. (b)-ii Reproduced from ref. 84 with permission from John Wiley and Sons, Copyright 2007 by the American Geophysical Union. (c) Reproduced from ref. 89 with permission from Elsevier, Copyright 1994. (d) Reproduced from ref. 93 with permission from American Chemical Society, Copyright 2013.

radius  $r_p$  to those of peanut-shaped, or rod-shaped particles with an aspect ratio of major axis radius to secondary axis radius  $a/b < 1$ .<sup>75</sup> When  $r_p = a$ , breakthrough curves [Figure 9.3(a)] for spherical and peanut-shaped particles are not significantly different and show similar percentages of retained colloids, but they are easily distinguishable otherwise. Even though the breakthrough curves look similar for these cases, the mechanism of retention may be different for spherical and rod-shaped particles.<sup>76</sup> Moreover, different deposition profiles arise for nanometer-sized spherical and rod-shaped particles [see Figure 9.3(d)].<sup>93</sup>

While Pe provides an intuitive understanding of the interplay between the advection and diffusion of particles during transport at the pore scale, it fails to capture the effects of other pore-scale transport mechanisms. Mechanisms such as interparticle interactions, interception, and sedimentation<sup>37</sup> are not distinguishable using Pe alone. As a result, classic colloid filtration theory and breakthrough curves often fail to represent the true physics of colloidal transport in porous media under conditions where these phenomena are significant.<sup>23,54,94,95</sup> It is thus of significant importance to have quantification methods for the transport of colloidal particles at the pore scale.

### 9.3.2 Indirect Pore-scale Assessments

Indirect pore-scale measurement techniques, such as nuclear magnetic resonance (NMR) and X-ray computed tomography (CT) scanning, are two non-invasive methods that have been widely used in investigating transport processes in porous media. By scanning the porous medium from outside, these powerful techniques gain information about the inside of the medium. The information provided by NMR and CT can then be used to successfully reconstruct a three-dimensional (3D) configuration of a porous medium [see Figure 9.4(a)],<sup>80</sup> but these techniques are still limited in their ability to provide information about pore-scale events in naturally occurring systems. Recent works have employed such indirect non-invasive techniques to shed light on the dynamics of particle deposition, pore clogging, or erosion in 3D porous media during the course of colloidal particle transport.

NMR spectroscopy works by collecting temporal and spatial signal profiles during the transport of particles in a porous medium. Using calibration curves, these profiles are then converted into concentration profiles of suspended particles.<sup>96–99</sup> These concentration profiles can be compared to the predictions of the ADE continuum model coupled with filtration theory. However, one weakness of the NMR technique is that the collected signals are influenced by the presence of both suspended and deposited particles. One way to distinguish these two effects is by injecting colloidal particles into the porous medium followed by particle-free carrier until steady-state NMR signals are recorded.<sup>97</sup> These steady-state signals correspond only to deposited particles. As new suspended particles are introduced to the porous medium containing deposited particles, the presence of suspended particles results in a decreased NMR signal. As this pulse moves along the porous

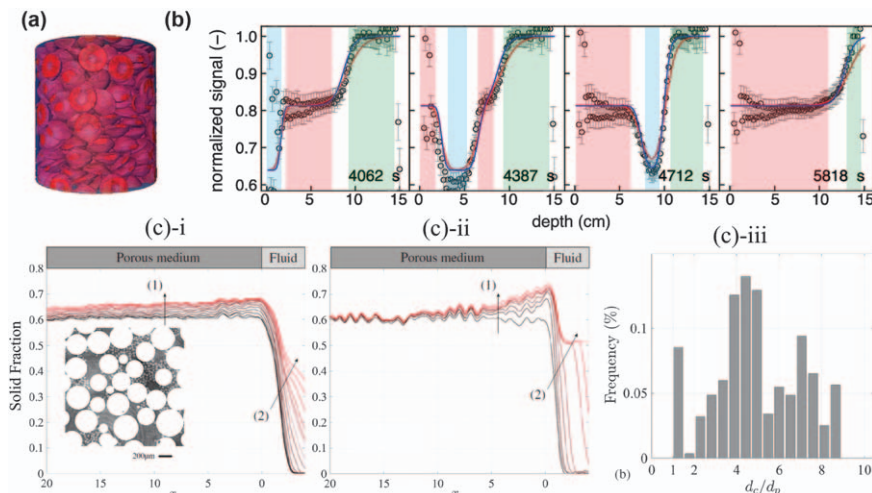


**Figure 9.4** (a) 3D constructed X-ray CT scanned images of a porous medium made with non-spherical beads (shown in red) with a shape of approximate half spheres. (b) Selected NMR signal profiles along a porous medium made with sand during four successive injections of 35 nm iron oxide nanoparticles. The blue-shaded section represents the suspended nanoparticles injected into the porous medium (far left picture) that moves as time progresses, the red-shaded section represents the deposited particle region inside the porous medium, and the green-shaded section shows the particle-free region. (c) Successive injections of 41  $\mu\text{m}$  polystyrene particles through bead packing for  $\bar{r} = 0.11$  and  $\bar{r} = 0.13$  in (c)-i and (c)-ii, respectively. The inset in (c)-i shows the X-ray CT scanned image of the internal structure of porous medium ( $\bar{r} = 0.11$ ): white spheres are the glass beads and the grey spheres are deposited particles. (c)-iii Size distribution of clusters within a porous medium with  $\bar{r} = 0.067$ .

(a) Reproduced from ref. 80 with permission from Elsevier, Copyright 2010. (b) Reproduced from ref. 97 with permission from Elsevier, Copyright 2017. (c) Reproduced from ref. 100, <https://doi.org/10.1103/PhysRevLett.120.148001>, with permission from American Physical Society, Copyright 2018.

medium, the NMR signals return to the baseline signal created by the previously deposited particles [see Figure 9.4(b)]. These profiles for deposited and moving particles in porous media provide more accurate estimates for deposition kinetics, which have been used for further development of continuum modelling.<sup>97</sup>

In a study of polystyrene particle transport under constant flowrate in a porous medium comprised of spherical glass beads, particle-to-bead size ratio,  $\bar{r}$ , was found to control the deposition profile across the length of the porous medium.<sup>100</sup> When  $\bar{r} < 0.05$ , no clogging is observed. As  $\bar{r}$  increases, in-depth deposition or surface deposition, frequently referred to as “caking,” occurs [see Figure 9.4(c)-i and ii]. These regimes were analyzed by X-ray CT images obtained at a desired distance away from the porous medium entrance.

Further from the porous medium inlet, clusters of nanoparticles form deposits with an effective diameter,  $d_c$ , trapped within pore bodies or pore throats [see Figure 9.4(c)-i inset]. For  $\bar{r}=0.067$ , the effective diameter of deposits ranges up to nine times the size of one particle [see Figure 9.4 (c)-ii]. Some hypotheses suggest that the formation of these clusters is a matter of probability. However, this probability is not defined based on the interaction between individual particles and the collector. Instead, it is defined based on the size exclusion of clusters at different distances away from the entrance of the porous medium. In this model, any individual particle has the same probability of depositing,  $p$ , on a clean collector's surface or on an already deposited cluster. When the cluster is as large as the pore size, it stops growing and diverts the flow path toward other pores. In this model,  $p$  is a function of  $\bar{r}$  with a critical value of  $p(\bar{r}=0.153)=1$ .

Understanding the transport of colloidal particles in porous media using NMR is limited by the challenge of interpreting NMR signals, while the utility of CT scanning is limited by spatial and temporal resolution. Therefore, it is of practical interest to develop techniques that are sensitive to pore-scale events, yet simple to analyze.

A recent work<sup>101</sup> detects particle deposition and erosion by measuring the pressure drop along the porous medium. Jumps in pressure drop readings can be connected to the clogging, or pore closing, and erosion, or pore opening. Mechanisms of pore clogging are discussed later in this section. In this approach, hypotheses suggest that erosion is promoted by two phenomena: (i) when the shear stress exerted by the fluid is large enough to detach a particle from a collector, termed shear erosion, and (ii) when the pressure drop along the porous medium exceeds a threshold, referred to as hydraulic erosion. These two mechanisms are formulated using two dimensionless parameters: shear erosion,  $T_c$ , and hydraulic erosion,  $F_c$ . Figure 9.5(a) shows that pressure jumps happen only for a specific range of  $F_c$  at a given  $T_c$ . In region I,  $F_c$  is small, so no jumps are observed in the pressure readings, and no clogging occurs. At the opposite extreme, in region III,  $F_c$  is large enough that hydraulic erosion becomes negligible and again no jumps are observed. Between these two regions, in region II, we observe substantial jumps in pressure. Figure 9.5(b)-i shows typical pressure readings for the transport of quartz particles in a porous medium made of glass beads.<sup>101</sup> Pressure readings show that when there is a pressure jump due to erosion, both flowrate and particle volume fraction increase—an indication of pore opening [see Figure 9.5(b)-ii]. All the possible regimes (non-clogging, clogging, and an intermediate between non-clogging and clogging) are mapped as a function of flowrate and particle volume fraction [see Figure 9.5(c)].<sup>101</sup> According to these findings, particle volume fraction is the parameter controlling the clogging regime at steady state.

Another study of the pressure evolution during particle transport in a porous medium corroborates the existence of three regions with distinct deposition and erosion characteristics.<sup>102</sup> Here, the transport of an aqueous suspension of silica powder with a diameter of 25  $\mu\text{m}$  was measured under constant flowrate through a column packed with soda lime glass beads. In

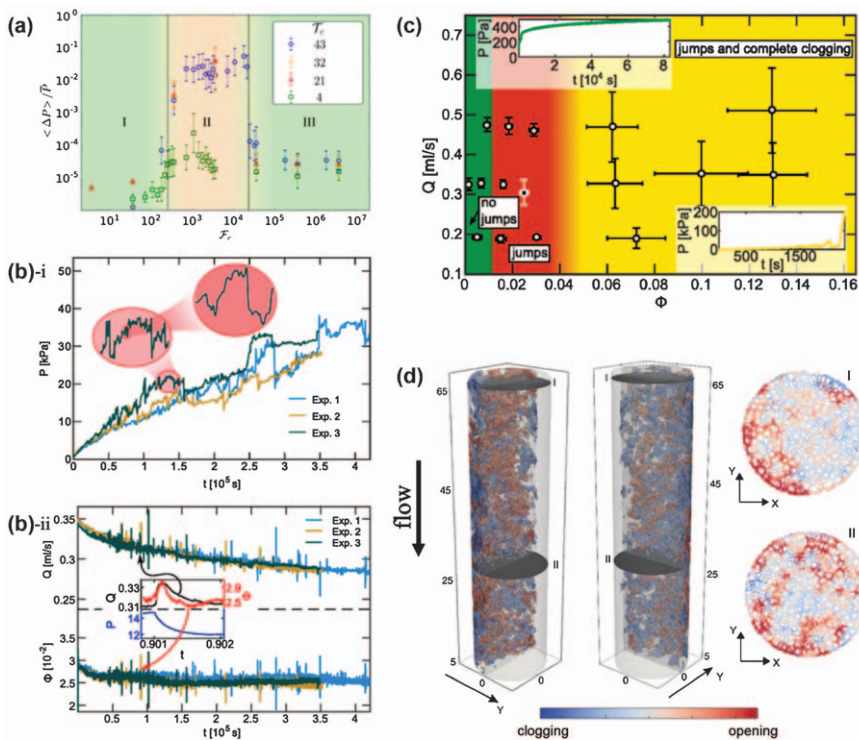


**Figure 9.5** (a) The average jumps normalized by the average pressure,  $\bar{P}$ , is shown for different values of  $F_c$  and  $T_c$ . In regions I and III, no jumps are detected, but for region II significant jumps are recorded. Three replicates of time evolution of pressure loss (b)-i, flowrate,  $Q$ , and the particle volume fraction,  $\Phi$ , (b)-ii during the transport of quartz particles through a porous medium made of glass beads. The inset in (b)-ii shows [with the same units as in (b)] the temporal evolution of  $Q$  and  $\Phi$  during a single jump. (c) Phase diagram of non-clogging, clogging, and the transition between these two regimes as a function of  $Q$  and  $\Phi$ . The insets show the typical temporal evolution of pressure loss for two regimes: the non-clogging (green) and clogging (yellow). (d) The cross-sectional deposition profile of 25  $\mu\text{m}$  silica particles at two locations: at the column entrance (I) and somewhere in the middle of the column (II). (a) Reproduced from ref. 60, <https://doi.org/10.1103/PhysRevLett.119.124501>, with permission from American Physical Society, Copyright 2017. (b) and (c) Reproduced from ref. 101, <https://doi.org/10.1103/PhysRevLett.120.034503>, with permission from American Physical Society, Copyright 2018. (d) Reproduced from ref. 102 with permission from Springer Nature, Copyright 2018.

these experiments, the identified regions are: (i) a smooth increase in the pressure corresponding to particle deposition along the porous medium, (ii) a “jumping period” at which continuous erosion and redeposition takes place, and (iii) complete clogging, where the maximum pressure supplied by the pump is achieved. In this study, pressure profiles were translated into a particle deposition profile by neutron tomography imaging and rigorous 3D

image processing [see Figure 9.5(d)]. Under set operating conditions, deposition and erosion events at a given distance from the column entrance vary over time. Pore clogging tends to be more likely near to the column inlet, while the pores in the rest of column remain relatively unclogged over time.

Indirect assessments of pore-scale events have led us to a better understanding of the dominant mechanisms controlling the transport of colloidal particles in 3D systems with conditions close to real applications. However, most of these techniques are limited to specific types of particle with an essential need for secondary justification by direct pore-scale assessments, such as X-ray CT scanning or microscopy, or by rigorous numerical computations. To acquire more details about pore-scale events, we look to direct pore-scale measurements.

### 9.3.3 Direct Pore-scale Assessments

#### 9.3.3.1 Studies in 2D

Transparent micromodels are suitable for direct observation of pore-scale events, such as particle deposition, pore clogging, and erosion of single particles or clusters of particles in 2D porous media. Colloidal suspensions are first pumped into a device made of glass or polydimethylsiloxane (PDMS) under known conditions for pH, ionic strength, particle size, and particle concentration. Then, one can directly monitor pore-scale events using either a conventional or epifluorescence microscope.<sup>103,104</sup> A survey of experimental setups for visualization of different classes of colloidal particles in micromodels can be found in ref. 104.

Using advanced fabrication methods, micromodels can contain a single collector, a single pore or pore throat, or a combination of multiple pores and channels with uniform or random shapes and connectivity. One single-collector study observed deposition of spherical sulfate-modified polystyrene particles with diameters of 1.04 µm or 3.6 µm on a single cylindrical PDMS collector with a diameter of 200 µm centered within a rectilinear channel.<sup>105</sup> Particles were introduced to the channel at a constant inlet concentration and an ionic strength above the critical coagulation concentration (CCC). At these conditions, no repulsion is expected between particles or between the particles and the PDMS device. Figure 9.6 shows the particle deposition profiles of particles for a wide range of Pe, varying from  $O(10^{-1})$  to  $O(10^3)$ , which was achieved experimentally by changing the flowrate. Since diffusion dominates at  $Pe < 1$ , uniform deposition around the collector surface is observed [see Figure 9.6(a)-i and (a)-ii]. However, when Pe increases, hydrodynamic forces start to compete with diffusion, resulting in angular anisotropic profiles of the deposits, as expected from theory.<sup>106</sup> Under these conditions, deposits grow on the side of collector facing the incoming flow. When Pe becomes even larger ( $Pe > 1000$ ), particles can be deposited at the rear of the collector due to vortex formation. This phenomenon has also been observed in the presence of multiple collectors [see Figure 9.6(c)].<sup>107</sup>

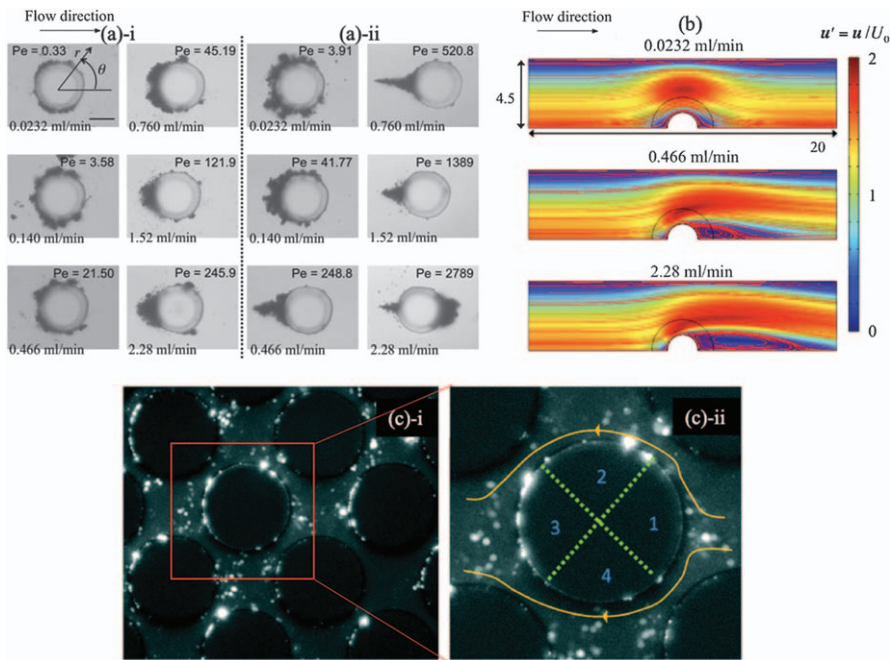


**Figure 9.6** Snapshots of spherical polystyrene sulfate latex particles deposit morphologies with diameters of  $1.04\text{ }\mu\text{m}$  [(a)-i] and  $3.6\text{ }\mu\text{m}$  [(a)-ii] at various values of Pe. Deposits were generated in a  $1.5\text{ M KCl}$  solution at  $\text{pH} \approx 6.9$ . Scale bar is  $100\text{ }\mu\text{m}$ . (b) Contour plot of velocity field and flow streamlines around a pillar (a) at three indicated flowrates. (c) Fluorescent latex colloidal particle deposits on an array of silicon collectors. Experiments were conducted at  $\text{pH} = 4$  at a flowrate of  $1\text{ }\mu\text{L h}^{-1}$  and a concentration of  $10^8$  particles per mL.  
 (a) and (b) Reproduced from ref. 105 with permission from American Chemical Society, Copyright 2010. (c) Reproduced from ref. 107 with permission from the Royal Society of Chemistry.

The deposition of particles on collectors' surfaces, as discussed in filtration theory, is connected to hydrodynamic forces and physicochemical forces that arise in the near-surface domain.<sup>23,37,54</sup> As an alternative to filtration theory, a probabilistic model<sup>108</sup> assuming a sticking region with a thickness of  $\varepsilon$  around each spherical collector has been proposed [see Figure 9.7(a)]. If particles enter this region, they experience a net attractive force to the collector and irreversibly adsorb at the collector's surface. The probability of sticking is then defined as the fraction of particles that go through the sticking region over the total number of particles. When  $\varepsilon$  is small enough, approximately 10 nm,  $N^*$  is independent of operating conditions (particle volume fraction, flowrate, etc.) and can be estimated from the geometry of pores alone.<sup>109</sup>

Particle deposition can be further categorized into four different cases of surface coverage. The fraction of injected particles that are deposited on a

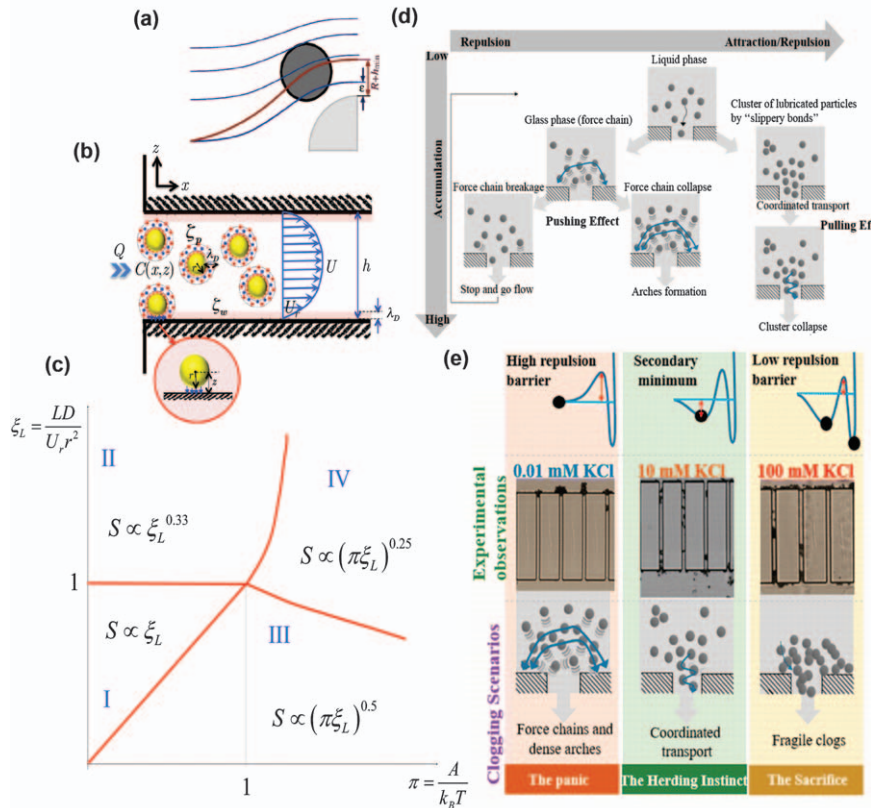


**Figure 9.7** (a) Schematic of sticking region around a spherical collector. (b) Schematic of transport of particles with a radius  $r$  through a rectangular microchannel with a height of  $h$ .  $\zeta_p$  and  $\zeta_w$  are the zeta potentials of the particles and wall, respectively. (c) Phase diagram of surface coverage,  $S$ , of channel wall shown in (b) as a function of dimensionless hydrodynamic,  $\xi_L$ , and van der Waals,  $\pi$ , forces. I, II, III, and IV show four different scenarios of particle deposition on the wall. (d) and (e) Proposed mechanisms of particle transport through a channel tuning the interplay between hydrodynamic forces and interparticle interactions.  
 (a) Reproduced from ref. 109, <https://doi.org/10.1103/PhysRevE.74.061402>, with permission from American Physical Society, Copyright 2006. (b) and (c) Reproduced from ref. 110, <https://doi.org/10.1103/PhysRevE.98.062606>, with permission from American Physical Society, Copyright 2018. (d) and (e) Reproduced from ref. 113 with permission from American Chemical Society, Copyright 2016.

capillary channel wall,  $S$ , is a function of dimensionless hydrodynamic forces,  $\xi_L$ , and van der Waals forces,  $\pi$  [see Figure 9.7(b)].<sup>110</sup> When diffusion dominates, particles close to the sticking boundary can diffuse through it to the wall (I). Particles in the bulk, sufficiently far away from the sticking boundary, may also diffuse to the wall (II). Either of these events can happen

for a given time  $t$  only if the travel distance due to diffusion,  $\sqrt{Dt}$ , is comparable to that for advection,  $Ut$ , where  $U$  is superficial velocity. When diffusion is not dominant, colloidal particles may deposit on channel walls due to strong van der Waals attractive forces. When van der Waals forces are dominant, particles are transported from the bulk to the sticking region (III). They are then deposited onto the wall by attractive van der Waals forces *via* a perfect sink condition (IV) [see Figure 9.7(c)].

Even though studying the transport of colloidal particles around a single collector can reveal the kinetics of particle deposition, such studies fail to address the complexities of particle transport in an array of collectors and pores. Multicollector events are controlled by hydrodynamic parameters such as particle flowrate, pressure drop, carrier fluid viscosity, and density as well as physical properties of the transported colloidal particles and porous medium.<sup>108</sup> When transported particles deposit continuously on multiple collectors' surfaces or on a channel wall, they may block the cross-sectional area of the pore, preventing suspended particles from subsequently flowing through. This is known as pore clogging. Clogging mechanisms may have either steric or electrostatic origins.<sup>108,109,111–116</sup> Steric origins include straining, which is a phenomenon that describes the trapping of particles in pore throats that are too small to let the particles move through, and arch formation. Experiments have revealed that straining becomes important when the pore throat to particle size ratio is smaller than 2.5.<sup>116</sup> Electrostatic origins may include phenomena like particle aggregation and deposition within a pore.

To understand the effects of interparticle interactions and hydrodynamic forces on pore clogging, the transport of aqueous suspensions of 5  $\mu\text{m}$  sulfate-modified polystyrene particles through a 2D microfluidic device fabricated with OSTEmerX 322 crystal clear polymer was studied.<sup>113</sup> Particles were injected under either constant pressure drop or constant flowrate at various ionic strengths adjusted using potassium chloride. From experimental observations, pushing and pulling effects are the primary mechanisms used to address the interplay between hydrodynamic and interparticle forces [see Figure 9.7(d)]. Pushing effects arise when colloidal particles repel each other in a constriction. Due to the osmotic pressure exhibited by concentrated repulsive particles, a lateral force component pushes particles toward bottlenecks, leading to the formation of force chains between particles. When the hydrodynamic force is large enough, the force chain is broken down by the flow. Otherwise, a new force chain can be created, leading to an arch formation at the entrance of channel. This mechanism is more likely to occur at low ionic strengths where there is a strong barrier against particle coagulation [see Figure 9.7(e)]. When ionic strength is large enough to observe a secondary energy minimum in the energy profile [see Figure 9.7(e)], arches do not form due to attractive forces between particles. Attraction between colloids results in a pulling effect that enhances transport through the pore [see Figure 9.7(d)]. If the ionic strength is very large, the energy barrier against coagulation of particles disappears

completely, resulting in a favorable deposition condition, and instead of a pulling effect, particles deposit at the channel wall [see Figure 9.7(e)].

For a given array of channels [see Figure 9.8(a)], because deposition is a stochastic process, a minimum number of particles,  $N^*$ , must pass through a channel before clogging happens.<sup>109</sup>  $N^*$  is found to be independent of the flowrate and initial volume fraction of particles in the carrier fluid.<sup>109,114</sup> However, the average clogging time is a strong function of particle volume fraction, flowrate, and pressure drop along the porous medium [see Figure 9.8(b)].<sup>109,111</sup> A Poisson distribution is typically enough to capture the fluctuations in particle concentration and can explain the distribution of clogging time intervals in an array of microchannels [see Figure 9.8(b)-iii].<sup>111</sup>

In addition to hydrodynamic parameters, physical properties of the colloidal particles and porous medium influence the deposition kinetics of particles and pore clogging.<sup>109,111,114,115</sup> Under a constant flowrate, it is shown that deposition of colloidal particles in a pore throat results in pore clogging if the length of the channel,  $L_{\text{flat}}$ , is at least 1.5 times the particle diameter [see Figure 9.8(c)].<sup>114</sup> While the deposit grows in the pore throat linearly with increasing  $L_{\text{flat}}$  until a critical value,  $N^*$  decreases exponentially to a constant value. Figure 9.8(d) shows the pore-scale events that lead to clogging. First, deposition initiates from the two corners of the pore entrance or at the flat part of the pore for longer pores. The deposit then grows toward the center of the pore until it blocks the flow path.

Clogging in porous media is a dynamic process during which clogged pores redirect the flow path. Microfluidic studies reveal not only the physical mechanisms of pore-scale events, such as particle deposition and pore clogging, but also provide a direct approach to compute the particle deposition rate. However, while 2D studies provide important intuition, how these effects translate to 3D porous media is unclear. For example, the pore space of a 3D medium is more connected, and the threshold solid fraction at which pores can percolate through the medium is lower, than in a 2D medium. As a result, particles have more paths available to them in 3D. Because of this fundamental difference, studies of particle transport in 3D porous media are critical.

### 9.3.3.2 Studies in 3D

Transport of colloidal particles in 3D porous media is typically studied in lab-scale columns. Columns range in size from tens of centimeters to several meters. Unfortunately, in these experiments, individual particles and pores often cannot be monitored due to light scattering from different layers of the medium.<sup>117,118</sup> Instead, hypotheses are made to connect pore-scale events to experimentally obtained breakthrough curves.<sup>74,77,118–120</sup> To overcome this visualization challenge, refractive index matching has been used to render 3D porous media transparent.<sup>121,122</sup> This technique has been successfully used in 3D fluidic devices<sup>123–126</sup> and is increasingly being used in studies of particle flow.<sup>127</sup>

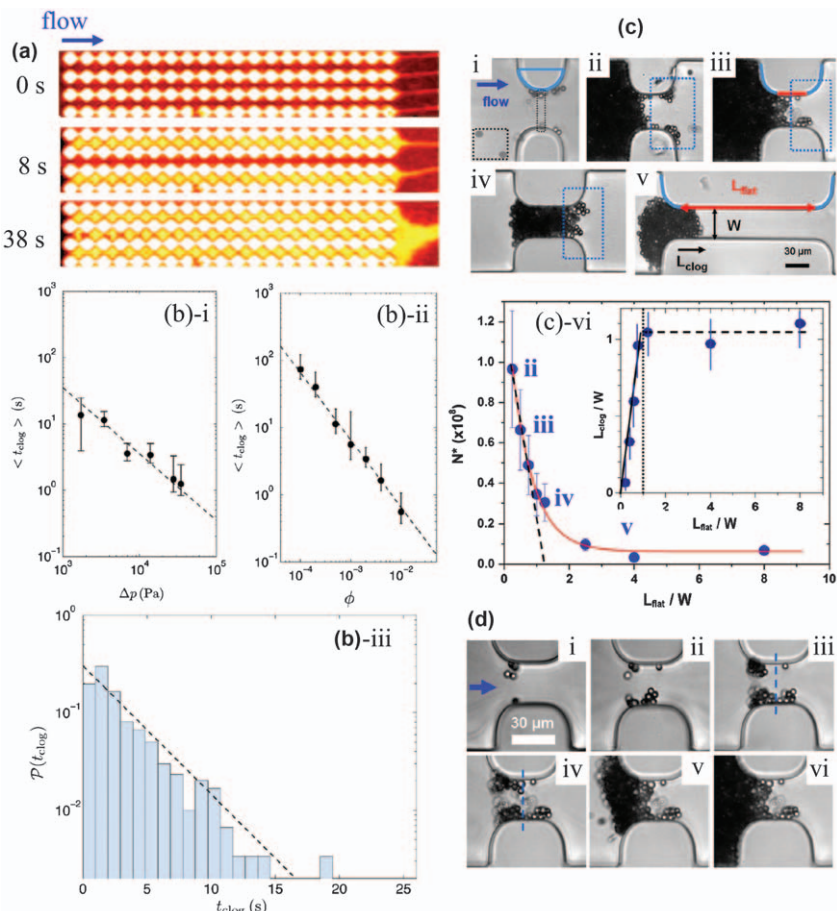


**Figure 9.8** (a) Microscope image of a microfluidic device with 1.2 mm channels at three time points (0 s, 8 s, and 38 s) during the flow of 2.9  $\mu\text{m}$  sulfate/carboxyl-functionalized polystyrene particles under a constant pressure drop of 2 psi. Dark red indicates regions where particles are deposited, yellow shows particle-free fluid and white represents the side walls of channel. (b) Average clogging time ( $\langle t_{\text{clog}} \rangle$ ) (i) as a function of pressure drop across the porous medium at a constant particle fraction ( $\phi = 2 \times 10^{-3}$ ) and (ii) as a function of particle fraction at a constant pressure drop ( $\Delta P = 13.8$  kPa). (iii) Distribution of clogging time intervals for  $\phi = 2 \times 10^{-3}$  and  $\Delta P = 13.8$  kPa. The dashed line is the best fit assuming a Poisson distribution with  $\langle t_{\text{clog}} \rangle = 3.3$  s. (c) Images of pores with different lengths (i to v), clogged by 4  $\mu\text{m}$  sulfate-functionalized polystyrene particles under a constant flowrate of 1.6  $\mu\text{l min}^{-1}$ . (iv)  $N^*$  as a function of  $L_{\text{flat}}/W$ . The width ( $W$ ) is kept constant at 30  $\mu\text{m}$  for all cases. Labels correspond to images, and the continuous line is an exponential fit of the data. Inset evolution of the rescaled clog length with  $L_{\text{flat}}/W$ . (d) Images of clogging of a pore by particles at 4 (i), 9 (ii), 12 (iii), 16 (iv), 22.5 (v), and 24 (iv) min.

(a) Reproduced from ref. 109, <https://doi.org/10.1103/PhysRevE.74.061402>, with permission from American Physical Society, Copyright 2006. (b) Reproduced from ref. 111 with permission from AIP Publishing, Copyright 2014. (c) and (d) Reproduced from ref. 114 with permission from Springer Nature, Copyright 2015.

To study the transport of particles in transparent porous media, 1 mm polyacrylamide hydrogels under constant pressure drop were injected into a packed-bed column made with 10–30 mm polyacrylamide hydrogels [see Figure 9.9(a)].<sup>127</sup> By choosing water as the carrier fluid, the optically-transparent column allows for particles to be tracked inside the porous medium. Similar to 2D studies, the average clogging time in this 3D model decreases as the volume fraction of particles increases following a power law or an exponential function [see Figure 9.9(b)].<sup>109</sup> Dividing the porous medium into three subsections, no significant difference exists between the number of deposited particles in each subsection at the beginning of process.<sup>127</sup> However, due to pressure buildup, particles are eventually removed from the top section of the column and redeposited in lower sections. This can be seen in the fluctuations shown in Figure 9.9(c). When the volume fraction of particles is large enough ( $>2.02\%$ ), deposition profiles plateau in the middle and lower sections but they grow in the upper section due to filter cake formation. Then, when clogging begins to develop, colloidal particles find new paths to move through the porous medium, resulting in more transverse motion.<sup>109</sup> Statistically, when the volume fraction of particles is low, there are fewer flow redirections due to less clogging. Therefore, fewer transverse motions are expected at low concentrations,

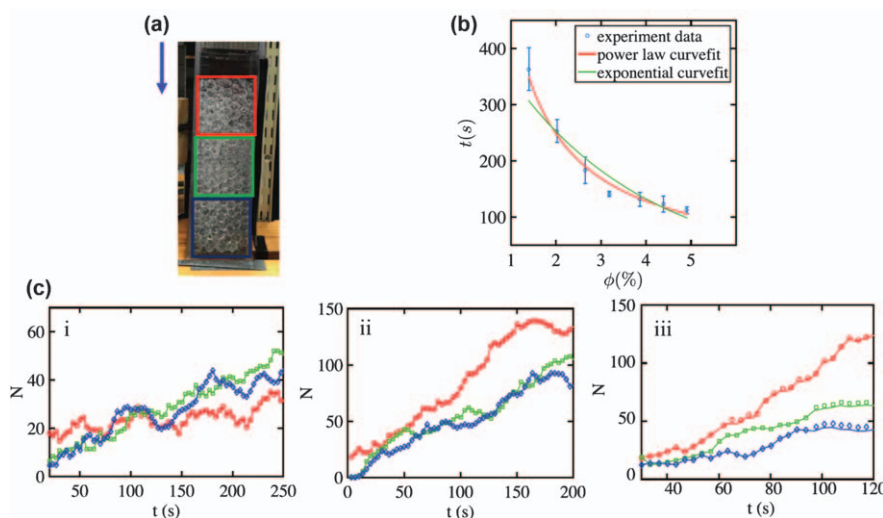


**Figure 9.9** (a) Actual picture of the packed-bed column made with 10–30 mm polyacrylamide hydrogels. Three subsections along the flow direction (arrow) are shown in different colors. (b) Clogging time ( $t$ ) as a function of particle fraction at a constant pressure drop with power law and exponential fittings. (c) Deposited number concentration at each subsection in corresponding colors to (a) at three different particle volume fractions: 2.02% (i), 2.65% (ii), and 4.39% (iii).

Reproduced from ref. 127 with permission from John Wiley and Sons, © 2017. American Geophysical Union. All Rights Reserved.

leading to slower clogging dynamics as opposed to that for higher concentrations where more transverse motions are detected. The discovery of this transverse motion is a key finding that could not be visualized without the use of a 3D system.

In systems where refractive index matching may not be possible, studies of colloidal deposition at the periphery of the medium can still be valuable. This approach is exemplified in a recent study<sup>128</sup> in which solute is used to controllably destabilize and deposit particles within a porous medium. The authors use humic acid-coated goethite nanoparticles, which exhibit significant contrast against a medium made of quartz sand [see Figure 9.10(a)]. The particles and a destabilizing cationic solution are injected into the porous medium in the same direction as pulses. The cationic solution, either calcium chloride or magnesium chloride, runs through the porous medium that is already saturated in the cationic solution at some time  $t_c$ . Then, a pulse of ultrapure water is injected at  $\Delta t$ , followed by the injection of colloidal particles at time  $t_p$  (*i.e.*,  $t_p = t_c + \Delta t$ ). Intriguingly, the colloidal particles move faster than cations inside the saturated porous medium [see Figure 9.10(b)]. Using this sequential injection technique, the transport of particles can be controlled by overlapping fronts of colloids and solute. This combination results in clogging the middle of the column [see Figure 9.10(a) and (b)]. The validity of this approach has been examined in different delivery conditions to deposit goethite nanoparticles in the middle of the model porous medium [see Figure 9.10(c)].

## 9.4 Conclusions and Outlook

In this chapter, we have reviewed the physical principles of colloidal particle transport in porous media. Importantly, colloid- and pore-scale behaviors, such as diffusion, interception, deposition, aggregation, and erosion, can strongly impact macro-scale transport; thus, investigations at multiple length and time scales are crucial.

At the pore scale, 2D and 3D models provide important visualization of colloidal interactions, and how these impact transport and deposition within the pore space. Computational simulations are able to capture some of this behavior; for example, Lattice-Boltzmann models provide detailed information about the particle interactions in porous media, but are often limited to small scales due to large computational costs. At the macroscopic scale, breakthrough curves, NMR/X-ray CT, and pressure measurements provide essential information on the dynamics of overall particle transport and deposition. These experimental techniques are often combined with simple continuum models, such as filtration theory, which provide a meaningful description of bulk transport—but in many cases, cannot capture complex pore-scale processes or the effects of pore-space heterogeneity. An important direction for future work is to bridge this gap and thereby enable accurate prediction and control of colloidal transport in more complex cases. Indeed, researchers have begun to explore the transport of deformable,<sup>129,130</sup>

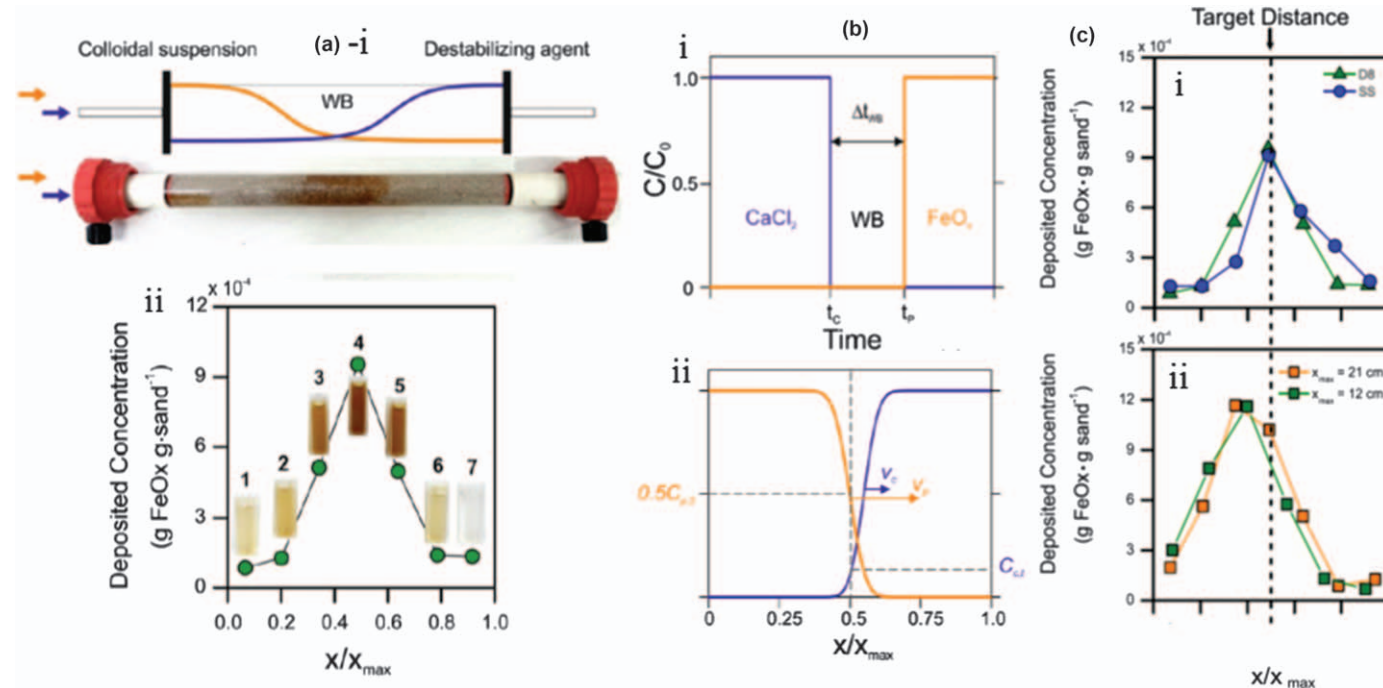


**Figure 9.10** (a) Deposition of humic acid-coated goethite colloidal nanoparticles in a model column (i) and the concentration profile of deposited colloids after the sequential injection of cation solution, ultrapure water, and nanoparticle suspension (ii). (b)-i The cycle and corresponding time intervals for injecting cation solution, ultrapure water, and nanoparticle suspension. (b)-ii Overlapping the cation solution and the colloidal nanoparticle fronts for depositing the particles at the center of column. (c) Controlled deposition of goethite nanoparticles at the center of column in (i) two different sandy media: Dorsilit n.8 (D8) and Sibelco S1 (SS) and at (ii) two different column lengths (21 cm and 12 cm).

Reproduced from ref. 128, <https://doi.org/10.1038/s41598-017-13423-y>, under the terms of the CC BY 4.0 licence, <https://creativecommons.org/licenses/by/4.0/>.

biological,<sup>131,132</sup> stimulus-responsive,<sup>133</sup> and surface-active particles<sup>134,135</sup> through typical rigid porous media or through deformable porous media,<sup>136–138</sup> which pose additional challenges to our understanding.

Some of the studies described in this chapter focused on non-polymeric colloids. However, the underlying physical principles are still relevant to polymeric colloids. Therefore, there exists an exciting opportunity to combine fabrication and characterization techniques established in polymer science with experimental and modeling tools used to generally describe colloids in porous media. One attractive feature is that the use of polymers enables precise control over colloid morphology and surface properties. An example is given by the development of polystyrene–polysisoprene (PS/PI) Janus colloids, which have been successfully fabricated *via* flash nanoprecipitation. These polymer colloids can be produced with a wide array of end group functionality, surface decoration, and internal structure.<sup>139,140</sup> Such capabilities can provide fundamental insights in the study of colloidal particle transport through porous media, by enabling systematic studies of the influence of particle morphology, interparticle interactions, and particle–medium interactions on transport. These capabilities can also provide a means to develop novel technologies capable of controlling flow and transport in fields ranging from water/soil remediation and enhanced oil recovery to drug delivery.

## References

1. J. E. Tobiason and C. R. O'Melia, Physicochemical aspects of particle removal in depth filtration, *J. Am. Water Works Assoc.*, 1988, **80**, 54–64.
2. C. Tien and A. C. Payatakes, Advances in deep bed filtration, *AIChE J.*, 1979, **25**, 737–759.
3. L. M. McDowell-Boyer, J. R. Hunt and N. Sitar, Particle transport through porous media, *Water Resour. Res.*, 1986, **22**, 1901–1921.
4. J. John, M. McCarthy and J. M. Zachara, Subsurface transport of contaminants, *Environ. Sci. Technol.*, 1989, **23**, 496–502.
5. J. N. Ryan and M. Elimelech, Colloid mobilization and transport in groundwater, *Colloids and Surface A: Physicochemical and Engineering Aspects*, 1996, **107**, 1–56.
6. H. Zhang, A. Nikolov and D. Wasan, Enhanced oil recovery (EOR) using nanoparticle dispersions: Underlying mechanism and imbibition experiments, *Energy Fuels*, 2014, **28**, 3002–3009.
7. H. ShamsiJazeyi, C. A. Miller, M. S. Wong, J. M. Tour and R. Verduzco, Polymer-coated nanoparticles for enhanced oil recovery, *J. Appl. Polym. Sci.*, 2014, **131**, 40576.
8. R. W. Harvey and S. P. Garabedian, Use of colloid filtration theory in modeling movement of bacteria through a contaminated sandy aquifer, *Environ. Sci. Technol.*, 1991, **25**, 178–185.
9. J. F. Schijven, H. A. M. De Bruin, S. M. Hassanzadeh and A. M. De Roda Husman, Bacteriophages and clostridium spores as

- indicator organisms for removal of pathogens by passage through saturated dune sand, *Water Res.*, 2003, **37**, 2186–2194.
- 10. N. Tufenkji, J. N. Ryan and M. Elimelech, The Promise of bank filtration, *Environ. Sci. Technol.*, 2002, **36**, 422A–428A.
  - 11. J. F. McCarthy and L. D. McKay, Colloid transport in the subsurface, *Vadose Zone J.*, 2004, **3**, 326–337.
  - 12. R. W. Buddemeier and J. R. Hunt, Transport of colloidal contaminants in groundwater: Radionuclide migration at the Nevada test site, *Appl. Geochem.*, 1988, **3**, 535–548.
  - 13. A. B. Kersting, D. W. Efurd, D. L. Finnegan, D. J. Rokop, D. K. Smith and J. L. Thompson, Migration of plutonium in ground water at the Nevada Test Site, *Nature*, 1999, **397**, 56–59.
  - 14. D. R. Champ, J. L. Young, D. E. Robertson and K. H. Abel, Chemical speciation of long-lived radionuclides in a shallow ground water flow system, *Water Qual. Res. J.*, 1984, **19**, 35–54.
  - 15. R. W. Puls and R. M. Powell, Transport of inorganic colloids through natural aquifer material: Implications for contaminant transport, *Environ. Sci. Technol.*, 1992, **26**, 614–621.
  - 16. J. B. F. Champlin, The physics of fine-particle movement through permeable aquifers, *Soc. Pet. Eng. J.*, 1971, **11**, 367–373.
  - 17. R. W. D. Killey, J. O. McHugh, D. R. Champ, E. L. Cooper and J. L. Young, Subsurface cobalt-60 migration from a low-level waste disposal site, *Environ. Sci. Technol.*, 1984, **18**, 148–157.
  - 18. W. I. Oden, G. L. Amy and M. Conklin, Subsurface interactions of humic substances with Cu(II) in saturated media, *Environ. Sci. Technol.*, 1993, **27**, 1045–1051.
  - 19. F. M. Dunnivant, P. M. Jardine, D. L. Taylor and J. F. McCarthy, Co-transport of cadmium and hexachlorobiphenyl by dissolved organic carbon through columns containing aquifer material, *Environ. Sci. Technol.*, 1992, **26**, 360–368.
  - 20. A. S. Abdul, T. L. Gibson and D. N. Rai, Use of humic acid solution to remove organic contaminants from hydrogeologic systems, *Environ. Sci. Technol.*, 1990, **24**, 328–333.
  - 21. B. R. Magee, L. W. Lion and A. T. Lemley, Transport of dissolved organic macromolecules and their effect on the transport of phenanthrene in porous media, *Environ. Sci. Technol.*, 1991, **25**, 323–331.
  - 22. L. R. Johnson-Logan, R. E. Broshears and S. J. Klalne, Partitioning behavior and the mobility of chlordane in groundwater, *Environ. Sci. Technol.*, 1992, **26**, 2234–2239.
  - 23. N. Tufenkji and M. Elimelech, Breakdown of colloid filtration theory: Role of the secondary energy minimum and surface charge heterogeneities, *Langmuir*, 2005, **21**, 841–852.
  - 24. T. Raychoudhury, N. Tufenkji and S. Ghoshal, Aggregation and deposition kinetics of carboxymethyl cellulose-modified zero-valent iron nanoparticles in porous media, *Water Res.*, 2012, **46**, 1735–1744.

25. P. Babakhani, J. Bridge, R. Doong and T. Phenrat, Continuum-based models and concepts for the transport of nanoparticles in saturated porous media: A state-of-the-science review, *Adv. Colloid Interface Sci.*, 2017, **246**, 75–104.
26. I. L. Molnar, W. P. Johnson, J. I. Gerhard, C. S. Willson and D. M. O'Carroll, Predicting colloid transport through saturated porous media: A critical review, *Water Resour. Res.*, 2015, **51**, 6804–6845.
27. Y. Ouyang, D. Shinde, R. S. Mansell and W. Harris, Colloid-enhanced transport of chemicals in subsurface environments: A review, *Crit. Rev. Environ. Sci. Technol.*, 1996, **26**, 189–204.
28. P. R. Johnson and M. Elimelech, Dynamics of colloid deposition in porous media: Blocking based on random sequential adsorption, *Langmuir*, 1995, **11**, 801–812.
29. I. L. Molnar, E. Pensini, M. A. Asad, C. A. Mitchell, L. C. Nitsche, L. J. Pyrak-Nolte, G. L. Miño and M. M. Krol, Colloid transport in porous media: A review of classical mechanisms and emerging topics, *Transp. Porous Media*, 2019, DOI: 10.1007/s11242-019-01270-6.
30. E. A. DiMarzio and C. M. Guttman, Separation by flow, *Macromolecules*, 1970, **3**, 131–146.
31. F. Kuhnen, K. Barmettler, S. Bhattacharjee, M. Elimelech and R. Kretzschmar, Transport of iron oxide colloids in packed quartz sand media: Monolayer and multilayer deposition, *J. Colloid Interface Sci.*, 2000, **231**, 32–41.
32. Z. Adamczyk, Particle adsorption and deposition: Role of electrostatic interactions, *Adv. Colloid Interface Sci.*, 2003, **100–102**, 267–347.
33. K.-M. Yao, M. T. Habibian and C. R. O'Melia, Water and waste water filtration: Concepts and applications, *Environ. Sci. Technol.*, 1971, **5**, 1105–1112.
34. Y. S. Kim and A. J. Whittle, Filtration in a porous granular medium: 1. Simulation of pore-scale particle deposition and clogging, *Transp. Porous Media*, 2006, **65**, 53–87.
35. V. Jegatheesan and S. Vigneswaran, Deep bed filtration: Mathematical models and observations, *Crit. Rev. Environ. Sci. Technol.*, 2005, **35**, 515–569.
36. J. P. Herzig, D. M. Leclerc and P. L. Goff, Flow of suspensions through porous media—Application to deep filtration, *Ind. Eng. Chem.*, 1970, **62**, 8–35.
37. N. Tufenkji and M. Elimelech, Correlation equation for predicting single-collector efficiency in physicochemical filtration in saturated porous media, *Environ. Sci. Technol.*, 2004, **38**, 529–536.
38. R. Rajagopalan and C. Tien, Trajectory analysis of deep-bed filtration with the sphere-in-cell porous media model, *AICHE J.*, 1976, **22**, 523–533.
39. W. Long and M. Hilpert, A correlation for the collector efficiency of Brownian particles in clean-bed filtration in sphere packings by a Lattice-Boltzmann method, *Environ. Sci. Technol.*, 2009, **43**, 4419–4424.

40. K. Li and H. Ma, Deposition dynamics of rod-shaped colloids during transport in porous media under favorable conditions, *Langmuir*, 2018, **34**, 2967–2980.
41. K. E. Nelson and T. R. Ginn, Colloid filtration theory and the Happel sphere-in-cell model revisited with direct numerical simulation of colloids, *Langmuir*, 2005, **21**, 2173–2184.
42. S. Torkzaban, S. A. Bradford and S. L. Walker, Resolving the coupled effects of hydrodynamics and DLVO forces on colloid attachment in porous media, *Langmuir*, 2007, **23**, 9652–9660.
43. C. Shen, Y. Huang, B. Li and Y. Jin, Predicting attachment efficiency of colloid deposition under unfavorable attachment conditions, *Water Resour. Res.*, 2010, **46**, W11526.
44. E. Pazmino, J. Trauscht, B. Dame and W. P. Johnson, Power law size-distributed heterogeneity explains colloid retention on soda lime glass in the presence of energy barriers, *Langmuir*, 2014, **30**, 5412–5421.
45. A. Melling, Tracer particles and seeding for particle image velocimetry, *Meas. Sci. Technol.*, 1997, **8**, 1406–1416.
46. A. R. Petosa, D. P. Jaisi, I. R. Quevedo, M. Elimelech and N. Tufenkji, Aggregation and deposition of engineered nanomaterials in aquatic environments: Role of physicochemical interactions, *Environ. Sci. Technol.*, 2010, **44**, 6532–6549.
47. J. N. Israelachvili, Van der Waals Forces between Particles and Surfaces, in *Intermolecular and Surface Forces*, Academic Press, Burlington, MA, USA, 3rd edn, ch. 13, 2011, pp. 253–289.
48. J. N. Israelachvili, Electrostatic Forces between Surfaces in Liquids, in *Intermolecular and Surface Forces*, Academic Press, Burlington, MA, USA, 3rd edn, ch. 14, 2011, pp. 291–340.
49. J. N. Israelachvili, Solvation, Structural, and Hydration Forces, in *Intermolecular and Surface Forces*, Academic Press, Burlington, MA, USA, 3rd edn, ch. 15, 2011, pp. 341–380.
50. J. N. Israelachvili, Steric (Polymer-Mediated) and Thermal Fluctuation Forces, in *Intermolecular and Surface Forces*, Academic Press, Burlington, MA, USA, 3rd edn, ch. 16, 2011, pp. 381–413.
51. W. P. Johnson and M. Hilpert, Upscaling colloid transport and retention under unfavorable conditions: Linking mass transfer to pore and grain topology, *Water Resour. Res.*, 2013, **49**, 5328–5341.
52. N. Tufenkji and M. Elimelech, Spatial distributions of cryptosporidium oocysts in porous media: Evidence for dual mode deposition, *Environ. Sci. Technol.*, 2005, **39**, 3620–3629.
53. C. Shen, B. Li, Y. Huang and Y. Jin, Kinetics of coupled primary- and secondary-minimum deposition of colloids under unfavorable chemical conditions, *Environ. Sci. Technol.*, 2007, **41**, 6976–6982.
54. N. Tufenkji and M. Elimelech, Deviation from the classical colloid filtration theory in the presence of repulsive DLVO interactions, *Langmuir*, 2004, **20**, 10818–10828.

55. F. Messina, T. Tosco and R. Sethi, On the failure of upscaling the single-collector efficiency to the transport of colloids in an array of collectors, *Water Resour. Res.*, 2016, **52**, 5492–5505.
56. J. Y. Chen, C.-H. Ko, S. Bhattacharjee and M. Elimelech, Role of spatial distribution of porous medium surface charge heterogeneity in colloid transport, *Colloids Surf. A*, 2001, **191**, 3–15.
57. N. H. Pham and D. V. Papavassiliou, Effect of spatial distribution of porous matrix surface charge heterogeneity on nanoparticle attachment in a packed bed, *Phys. Fluids*, 2017, **29**, 82007.
58. Q. Li and V. Prigobbe, Numerical simulations of the migration of fine particles through porous media, *Transp. Porous Media*, 2018, **122**, 745–759.
59. R. Jäger, M. Mendoza and H. J. Herrmann, Channelization in porous media driven by erosion and deposition, *Phys. Rev. E*, 2017, **95**, 13110.
60. R. Jäger, M. Mendoza and H. J. Herrmann, Mechanism behind erosive bursts in porous media, *Phys. Rev. Lett.*, 2017, **119**, 124501.
61. B. Ding, C. Li, M. Zhang, F. Ji and X. Dong, Effects of pore size distribution and coordination number on the prediction of filtration coefficients for straining from percolation theory, *Chem. Eng. Sci.*, 2015, **127**, 40–51.
62. Q. Xiong, T. G. Baychev and A. P. Jivkov, Review of pore network modelling of porous media: Experimental characterisations, network constructions and applications to reactive transport, *J. Contam. Hydrol.*, 2016, **192**, 101–117.
63. P. Sanaei and L. J. Cummings, Membrane filtration with complex branching pore morphology, *Phys. Rev. Fluids*, 2018, **3**, 94305.
64. N. Seetha, A. Raoof, M. S. Mohan Kumar and S. Majid Hassanzadeh, Upscaling of nanoparticle transport in porous media under unfavorable conditions: Pore scale to Darcy scale, *J. Contam. Hydrol.*, 2017, **200**, 1–14.
65. P. Meakin and A. M. Tartakovsky, Modeling and simulation of pore-scale multiphase fluid flow and reactive transport in fractured and porous media, *Rev. Geophys.*, 2009, **47**, RG3002.
66. L. Algive, S. Békri, F. H. Nader, O. Lerat and O. Vizika, Impact of diagenetic alterations on the petrophysical and multiphase flow properties of carbonate rocks using a reactive pore network modeling approach, *Oil Gas Sci. Technol.*, 2012, **67**, 147–160.
67. H. Yang and M. T. Balhoff, Pore-network modeling of particle retention in porous media, *AIChE J.*, 2017, **63**, 3118–3131.
68. J. Gostick, M. Aghighi, J. Hinebaugh, T. Tranter, M. A. Hoeh, H. Day, B. Spellacy, M. H. Sharqawy, A. Bazylak, A. Burns, W. Lehnert and A. Putz, OpenPNM: A pore network modeling package, *Comput. Sci. Eng.*, 2016, **18**, 60–74.
69. C. Shen, V. Lazouskaya, Y. Jin, B. Li, Z. Ma, W. Zheng and Y. Huang, Coupled factors influencing detachment of nano- and micro-sized particles from primary minima, *J. Contam. Hydrol.*, 2012, **134–135**, 1–11.
70. W. Zhang, V. L. Morales, M. E. Cakmak, A. E. Salvucci, L. D. Geohring, A. G. Hay, J.-Y. Parlange and T. S. Steenhuis, Colloid transport and

- retention in unsaturated porous media: Effect of colloid input concentration, *Environ. Sci. Technol.*, 2010, **44**, 4965–4972.
71. C. Shen, Y. Jin, B. Li, W. Zheng and Y. Huang, Facilitated attachment of nanoparticles at primary minima by nanoscale roughness is susceptible to hydrodynamic drag under unfavorable chemical conditions, *Sci. Total Environ.*, 2014, **466–467**, 1094–1102.
72. W. Sang, V. L. Morales, W. Zhang, C. R. Stoof, B. Gao, A. L. Schatz, Y. Zhang and T. S. Steenhuis, Quantification of colloid retention and release by straining and energy minima in variably saturated porous media, *Environ. Sci. Technol.*, 2013, **47**, 8256–8264.
73. D. Grolimund, M. Elimelech, M. Borkovec, K. Barmettler, R. Kretzschmar and H. Sticher, Transport of *in situ* mobilized colloidal particles in packed soil columns, *Environ. Sci. Technol.*, 1998, **32**, 3562–3569.
74. T. Tosco, A. Tiraferri and R. Sethi, Ionic strength dependent transport of microparticles in saturated porous media: Modeling mobilization and immobilization phenomena under transient chemical conditions, *Environ. Sci. Technol.*, 2009, **43**, 4425–4431.
75. S. Xu, Q. Liao and J. E. Saiers, Straining of nonspherical colloids in saturated porous media, *Environ. Sci. Technol.*, 2008, **42**, 771–778.
76. Q. Liu, V. Lazouskaya, Q. He and Y. Jin, Effect of particle shape on colloid retention and release in saturated porous media, *J. Environ. Qual.*, 2010, **39**, 500–508.
77. S. A. Bradford, S. R. Yates, M. Bettahar and J. Simunek, Physical factors affecting the transport and fate of colloids in saturated porous media, *Water Resour. Res.*, 2002, **38**, 12–63.
78. S. B. Roy and D. A. Dzombak, Chemical factors influencing colloid-facilitated transport of contaminants in porous media, *Environ. Sci. Technol.*, 1997, **31**, 656–664.
79. D. Liu, P. R. Johnson and M. Elimelech, Colloid deposition dynamics in flow-through porous media: Role of electrolyte concentration, *Environ. Sci. Technol.*, 1995, **29**, 2963–2973.
80. W. Long, H. Huang, J. Serlemitsos, E. Liu, A. H. Reed and M. Hilpert, Pore-scale study of the collector efficiency of nanoparticles in packings of nonspherical collectors, *Colloids Surf., A*, 2010, **358**, 163–171.
81. C. Shen, Y. Huang, B. Li and Y. Jin, Effects of solution chemistry on straining of colloids in porous media under unfavorable conditions, *Water Resour. Res.*, 2008, **44**, W05419.
82. J. Zhuang, J. Qi and Y. Jin, Retention and transport of amphiphilic colloids under unsaturated flow conditions: Effect of particle size and surface property, *Environ. Sci. Technol.*, 2005, **39**, 7853–7859.
83. B. Bijeljic, A. H. Muggeridge and M. J. Blunt, Pore-scale modeling of longitudinal dispersion, *Water Resour. Res.*, 2004, **40**, W11501.
84. B. Bijeljic and M. J. Blunt, Pore-scale modeling of transverse dispersion in porous media, *Water Resour. Res.*, 2007, **43**, W12S11.

85. T. K. Perkins and O. C. Johnston, A review of diffusion and dispersion in porous media, *J. Soc. Pet. Eng.*, 1963, **3**, 70–84.
86. J. M. P. Q. Delgado, Longitudinal and transverse dispersion in porous media, *Chem. Eng. Res. Des.*, 2007, **85**, 1245–1252.
87. S. B. Chen, Driven transport of particles in 3D ordered porous media, *J. Chem. Phys.*, 2013, **139**, 74904.
88. B. Bijeljic and M. J. Blunt, Pore-scale modeling and continuous time random walk analysis of dispersion in porous media, *Water Resour. Res.*, 2006, **42**, W01202.
89. J. E. Saiers, G. M. Hornberger and C. Harvey, Colloidal silica transport through structured, heterogeneous porous media, *J. Hydrol.*, 1994, **163**, 271–288.
90. J. E. Saiers, G. M. Hornberger and L. Liang, First- and second-order kinetics approaches for modeling the transport of colloidal particles in porous media, *Water Resour. Res.*, 1994, **30**, 2499–2506.
91. F. Compère, G. Porel and F. Delay, Transport and retention of clay particles in saturated porous media: Influence of ionic strength and pore velocity, *J. Contam. Hydrol.*, 2001, **49**, 1–21.
92. D. Pedretti and M. Bianchi, Reproducing tailing in breakthrough curves: Are statistical models equally representative and predictive?, *Adv. Water Resour.*, 2018, **113**, 236–248.
93. M. B. Seymour, G. Chen, C. Su and Y. Li, Transport and retention of colloids in porous media: Does shape really matter?, *Environ. Sci. Technol.*, 2013, **47**, 8391–8398.
94. J. C. Knox, A. D. Ebner, M. D. LeVan, R. F. Coker and J. A. Ritter, Limitations of breakthrough curve analysis in fixed-bed adsorption, *Ind. Eng. Chem. Res.*, 2016, **55**, 4734–4748.
95. W. P. Johnson and X. Li, Comment on breakdown of colloid filtration theory: Role of the secondary energy minimum and surface charge heterogeneities, *Langmuir*, 2005, **21**, 10895.
96. T. Baumann and C. J. Werth, Visualization of colloid transport through heterogeneous porous media using magnetic resonance imaging, *Colloids Surf., A*, 2005, **265**, 2–10.
97. A. P. Lehoux, A. P. Lehoux, P. Faure, F. Lafolie, S. Rodts, D. Courtier-Murias, P. Coussot and E. Michel, Combined time-lapse magnetic resonance imaging and modeling to investigate colloid deposition and transport in porous media, *Water Res.*, 2017, **123**, 12–20.
98. L. Cuny, M. P. Herrling, G. Guthausen, H. Horn and M. Delay, Magnetic resonance imaging reveals detailed spatial and temporal distribution of iron-based nanoparticles transported through water-saturated porous media, *J. Contam. Hydrol.*, 2015, **182**, 51–62.
99. B. Ramanan, W. M. Holmes, W. T. Sloan and V. R. Phoenix, Investigation of nanoparticle transport inside coarse-grained geological media using magnetic resonance imaging, *Environ. Sci. Technol.*, 2012, **46**, 360–366.

- Published on 02 December 2019 on https://pubs.rsc.org | doi:10.1039/9781788016476-00289
100. G. Gerber, S. Rodts, P. Aimedieu, P. Faure and P. Coussot, Particle-size-exclusion clogging regimes in porous media, *Phys. Rev. Lett.*, 2018, **120**, 148001.
  101. F. Bianchi, M. Thielmann, L. de Arcangelis and H. J. Herrmann, Critical bursts in filtration, *Phys. Rev. Lett.*, 2018, **120**, 34503.
  102. F. Bianchi, F. K. Wittel, M. Thielmann, P. Trtik and H. J. Herrmann, Tomographic study of internal erosion of particle flows in porous media, *Transp. Porous Media*, 2018, **122**, 169–184.
  103. T. Baumann and C. J. Werth, Visualization and modeling of polystyrol colloid transport in a silicon micromodel, *Vadose Zone J.*, 2004, **3**, 434–443.
  104. N. Ochiai, E. L. Kraft and J. S. Selker, Methods for colloid transport visualization in pore networks, *Water Resour. Res.*, 2006, **42**, W12S06.
  105. Y. Kusaka, J. F. L. Duval and Y. Adachi, Morphology and breaking of latex particle deposits at a cylindrical collector in a microfluidic chamber, *Environ. Sci. Technol.*, 2010, **44**, 9413–9418.
  106. L. Song and M. Elimelech, Dynamics of colloid deposition in porous media: Modeling the role of retained particles, *Colloids Surf., A*, 1993, **73**, 49–63.
  107. C. Chen, T. Waller and S. L. Walker, Visualization of transport and fate of nano and micro-scale particles in porous media: Modeling coupled effects of ionic strength and size, *Environ. Sci.: Nano*, 2017, **4**, 1025–1036.
  108. E. Dressaire and A. Sauret, Clogging of microfluidic systems, *Soft Matter*, 2017, **13**, 37–48.
  109. H. M. Wyss, D. L. Blair, J. F. Morris, H. A. Stone and D. A. Weitz, Mechanism for clogging of microchannels, *Phys. Rev. E*, 2006, **74**, 61402.
  110. C. M. Cejas, F. Monti, M. Truchet, J.-P. Burnouf and P. Tabeling, Universal diagram for the kinetics of particle deposition in micro-channels, *Phys. Rev. E*, 2018, **98**, 62606.
  111. A. Sauret, A. Sauret, E. C. Barney, A. Perro, E. Villermaux, H. A. Stone and E. Dressaire, Clogging by sieving in microchannels: Application to the detection of contaminants in colloidal suspensions, *Appl. Phys. Lett.*, 2014, **105**, 74101.
  112. B. Dersoir, A. B. Schofield and H. Tabuteau, Clogging transition induced by self filtration in a slit pore, *Soft Matter*, 2017, **13**, 2054–2066.
  113. Z. B. Sendekie and P. Bacchin, Colloidal Jamming dynamics in microchannel bottlenecks, *Langmuir*, 2016, **32**, 1478–1488.
  114. B. Dersoir, M. R. de Saint Vincent, M. Abkarian and H. Tabuteau, Clogging of a single pore by colloidal particles, *Microfluid. Nanofluid.*, 2015, **19**, 953–961.
  115. B. Mustin and B. Stoeber, Deposition of particles from polydisperse suspensions in microfluidic systems, *Microfluid. Nanofluid.*, 2010, **9**, 905–913.
  116. M. Auset and A. A. Keller, Pore-scale visualization of colloid straining and filtration in saturated porous media using micromodels, *Water Resour. Res.*, 2006, **42**, W12S02.

117. C. Q. Qiu, H. Gao, L.-P. Wang, J. Han and Y. Jin, Pore-scale numerical and experimental investigation of colloid retention at the secondary energy minimum, *Vadose Zone J.*, 2012, **11**, DOI: 10.2136/vzj2011.0071.
118. S. A. Bradford, J. Simunek, M. Bettahar, Y. F. Tadassa, M. T. van Genuchten and S. R. Yates, Straining of colloids at textural interfaces, *Water Resour. Res.*, 2005, **41**, W10404.
119. S. A. Bradford, S. Torkzaban and S. L. Walker, Coupling of physical and chemical mechanisms of colloid straining in saturated porous media, *Water Res.*, 2007, **41**, 3012–3024.
120. W. Fu, L. Hua and W. Zhang, Experimental and modeling assessment of the roles of hydrophobicity and zeta potential in chemically modified poly(ether sulfone) membrane fouling kinetics, *Ind. Eng. Chem. Res.*, 2017, **56**, 8580–8589.
121. J. A. Dijksman, F. Rietz, K. A. Lörincz, M. van Hecke and W. Losert, Invited Article: Refractive index matched scanning of dense granular materials, *Rev. Sci. Instrum.*, 2012, **83**, 11301.
122. S. Wiederseiner, N. Andreini, G. Epely-Chauvin and C. Ancey, Refractive-index and density matching in concentrated particle suspensions: A review, *Exp. Fluids*, 2011, **50**, 1183–1206.
123. S. S. Datta, H. Chiang, T. S. Ramakrishnan and D. A. Weitz, Spatial fluctuations of fluid velocities in flow through a three-dimensional porous medium, *Phys. Rev. Lett.*, 2013, **111**, 64501.
124. S. S. Datta, J.-B. Dupin and D. A. Weitz, Fluid breakup during simultaneous two-phase flow through a three-dimensional porous medium, *Phys. Fluids*, 2014, **26**, 62004.
125. S. S. Datta, T. S. Ramakrishnan and D. A. Weitz, Mobilization of a trapped non-wetting fluid from a three-dimensional porous medium, *Phys. Fluids*, 2014, **26**, 22002.
126. M. Carrel, V. L. Morales, M. Dentz, N. Derlon, E. Morgenroth and M. Holzner, Pore-scale hydrodynamics in a progressively bioclogged three-dimensional porous medium: 3-D particle tracking experiments and stochastic transport modeling, *Water Resour. Res.*, 2018, **54**, 2183–2198.
127. J. Shen and R. Ni, Experimental investigation of clogging dynamics in homogeneous porous medium, *Water Resour. Res.*, 2017, **53**, 1879–1890.
128. C. Bianco, J. E. Patiño Higuera, T. Tosco, A. Tiraferri and R. Sethi, Controlled deposition of particles in porous media for effective aquifer nanoremediation, *Sci. Rep.*, 2017, **7**, 12992.
129. M. G. O'Connell, N. B. Lu, C. A. Browne and S. S. Datta, Cooperative size sorting of deformable particles in porous media, *Soft Matter*, 2019, **15**, 3620–3626.
130. E. Benet, G. Lostec, J. Pellegrino and F. Vernerey, Mechanical instability and percolation of deformable particles through porous networks, *Phys. Rev. E*, 2018, **97**, 42607.
131. T. Bhattacharjee and S. S. Datta, Bacterial hopping and trapping in porous media, *Nat. Commun.*, 2019, **10**, 2075.

132. T. Bhattacharjee and T. E. Angelini, 3D T cell motility in jammed microgels, *J. Phys. D: Appl. Phys.*, 2018, **52**, 24006.
133. S. Ganta, H. Devalapally, A. Shahiwala and M. Amiji, A review of stimuli-responsive nanocarriers for drug and gene delivery, *J. Controlled Release*, 2008, **126**, 187–204.
134. K. Panthi and K. K. Mohanty, pH-insensitive polymeric particles for enhanced oil recovery in reservoirs with fractures, *SPE J.*, 2018, **23**, 34–47.
135. D. Luo, F. Wang, J. Zhu, F. Cao, Y. Liu, X. Li, R. C. Willson, Z. Yang, C.-W. Chu and Z. Ren, Nanofluid of graphene-based amphiphilic Janus nanosheets for tertiary or enhanced oil recovery: High performance at low concentration, *Proc. Natl. Acad. Sci. U. S. A.*, 2016, **113**, 7711–7716.
136. Z. Li, Z. Zhou, Y. Dai and B. Dai, Contaminant transport in a largely-deformed aquitard affected by delayed drainage, *J. Contam. Hydrol.*, 2019, **221**, 118–126.
137. M. Shilo, M. Motiei, P. Hana and R. Popovtzer, Transport of nanoparticles through the blood–brain barrier for imaging and therapeutic applications, *Nanoscale*, 2014, **6**, 2146–2152.
138. M. Zhang, L. Wei, H. Chen, Z. Du, B. P. Binks and H. Yang, Compartmentalized droplets for continuous flow liquid–liquid interface catalysis, *J. Am. Chem. Soc.*, 2016, **138**, 10173–10183.
139. V. E. Lee, C. Sosa, R. Liu, R. K. Prud'homme and R. D. Priestley, Scalable platform for structured and hybrid soft nanocolloids by continuous precipitation in a confined environment, *Langmuir*, 2017, **33**, 3444–3449.
140. L. S. Grundy, V. E. Lee, N. Li, C. Sosa, W. D. Mulhearn, R. Liu, R. A. Register, A. Nikoubashman, R. K. Prud'homme, A. Z. Panagiotopoulos and R. D. Priestley, Rapid production of internally structured colloids by flash nanoprecipitation of block copolymer blends, *ACS Nano*, 2018, **12**, 4660–4668.



## **Section III: Advanced Applications of Polymer Colloids**



## CHAPTER 10

# *Pickering Emulsions Stabilized by Polymer Colloids*

YANG LAN, YANKAI JIA AND DAEYEON LEE\*

Department of Chemical and Biomolecular Engineering,  
University of Pennsylvania, Philadelphia, PA 19104, USA

\*Email: daeyeon@seas.upenn.edu

## 10.1 Introduction

### 10.1.1 Emulsions

Emulsions are ubiquitous in our daily lives and are widely encountered in a variety of industries.<sup>1</sup> Emulsions are mixtures of two or more immiscible fluids, one being dispersed in the other, in the presence of surface-active agents.<sup>2</sup> Based on the nature of the dispersed phase, emulsions are classified into oil-in-water (O/W), water-in-oil (W/O) and multiple emulsions such as water-in-oil-in-water (W/O/W) emulsions. When pure oil and water are mixed, the system favors the state with the minimum area between the two liquid phases, leading to macroscopic phase separation. Thus, surface-active agents such as surfactants are added to lower the interfacial tension and stabilize emulsion droplets. Traditional surfactants include amphiphilic small molecules and polymers which preferentially adsorb to oil-water interfaces. The other role of surfactants is to form kinetic barriers that prevent destabilization of emulsions and to facilitate formation of smaller emulsion droplets. The surface activity of surfactants strongly depends on their molecular structures. The Bancroft rule states that “the phase in which an emulsifier is more soluble constitutes the continuous phase”.<sup>3</sup>

The hydrophile–lipophile balance (HLB) number of surfactants can be employed to quantitatively describe the Bancroft rule.<sup>4</sup> For example, surfactants with HLB values larger than 10 stabilize O/W emulsions whereas those with HLB lower than 10 stabilize W/O emulsions.

Even though conventional surfactants can substantially lower the interfacial tension, surfactant-stabilized emulsions are in general thermodynamically unstable. The thermodynamics of emulsion stabilization can be calculated by the change in free energy during emulsion formation, which contains an interfacial energy term ( $\Delta G_i$ ) and a configuration entropy term ( $T\Delta S_{\text{config}}$ ):<sup>5</sup>

$$\Delta G_{\text{formation}} = \Delta G_i - T\Delta S_{\text{config}} \quad (10.1)$$

Under constant temperature and pressure, the interfacial energy term ( $\Delta G_i$ ) is equal to the product of the oil–water interfacial tension ( $\gamma_{\text{ow}}$ ) and the increase in the interfacial area between oil and aqueous phases ( $\Delta A$ ).  $\Delta G_i$  is thus always larger than 0, and opposes emulsion formation.

$$\Delta G_i = \gamma_{\text{ow}} \Delta A \quad (10.2)$$

The configuration entropic term can be expressed as:

$$\Delta S_{\text{config}} = -\frac{nk}{\phi} (\phi \ln \phi + (1 - \phi) \ln(1 - \phi)) \quad (10.3)$$

where  $k$  is Boltzmann's constant,  $n$  is the number of droplets in the emulsion, and  $\phi$  is the volume fraction of the dispersed phase.  $\Delta S_{\text{config}}$  represents an increase in the number of possible configurations upon emulsification and is always larger than 0: thus, it favors emulsion formation. For most of the emulsion systems stabilized by traditional surfactants,  $\Delta G_i$  is much larger than  $T\Delta S_{\text{config}}$ : thus, the free energy of emulsion formation ( $\Delta G_{\text{formation}}$ ) is positive.<sup>5</sup> In other words, emulsions stabilized by traditional surfactants are typically thermodynamically unstable. An exception to this rule is the so-called microemulsions which, by definition, are thermodynamically stable emulsions.<sup>5</sup> The stability of microemulsions results from an optimum droplet size, at which point an ultralow interfacial tension is achieved.<sup>5</sup>

### 10.1.2 Pickering Emulsions

In 1903, Ramsden showed that colloidal particles can act as stabilizers for emulsion droplets.<sup>6</sup> Subsequently, Pickering reported a systematic study on colloid-stabilized emulsions in 1907, and hence these colloid-stabilized emulsions are often referred as ‘Pickering emulsions’.<sup>7</sup> Over the past two decades, a large number of publications have been reported on Pickering emulsions because of their potential applications in food, cosmetics and pharmaceuticals.<sup>8</sup>

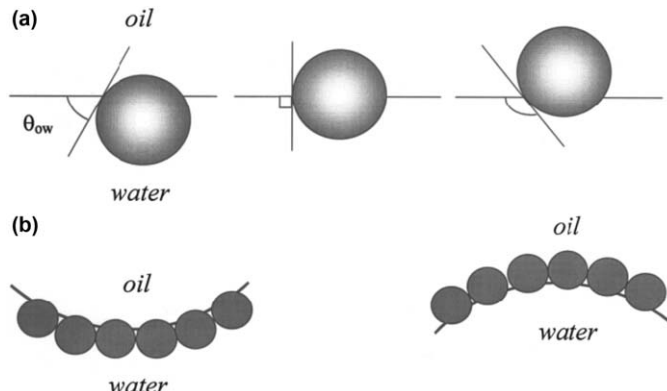


**Figure 10.1** (a) Position of a small spherical particle at a planar oil–water interface for a contact angle (measured through the aqueous phase) less than  $90^\circ$  (left), equal to  $90^\circ$  (centre) and greater than  $90^\circ$  (right). (b) Corresponding probable positioning of particles at a curved interface. For  $\theta < 90^\circ$ , O/W Pickering emulsions may form (left). For  $\theta > 90^\circ$ , W/O Pickering emulsions may form (right).

Reproduced from ref. 10 with permission from Elsevier, Copyright 2003.

In Pickering emulsions, colloids adsorb to the interface to stabilize emulsion droplets.<sup>9</sup> The stability of Pickering emulsions results from the reduction in the liquid–liquid interface area whose magnitude depends on the wettability and radius of colloids (Figure 10.1a).<sup>10</sup> The free energy of adsorption of a colloid to the interface, which can be calculated based on the free energy required for detachment of the colloid from the interface, depends on the contact angle as well as the interfacial tension:

$$\Delta G_{de} = \pi r^2 \gamma_{ow} (1 \pm \cos \theta)^2 \quad (10.4)$$

where  $r$  is the radius of colloids,  $\gamma_{ow}$  is the interfacial tension and  $\theta$  is the contact angle of colloids at the interface.  $1 + \cos \theta$  is used to describe particle removal into the oil phase, whereas  $1 - \cos \theta$  is used for the opposite case. The adsorption of a colloid at the oil–water interface is very strong. For example, for a colloid with a radius of 100 nm and neutral wetting ( $\theta = 90^\circ$ ) at the oil–water interface with an interfacial tension of  $0.036 \text{ N m}^{-1}$ , the adsorption/detachment energy is  $2.75 \times 10^5 \text{ kT}$  which is several orders of magnitude higher than thermal fluctuation ( $kT$ ), indicating irreversible adsorption of the colloid at the interface; this strong adsorption of particles to the liquid–liquid interface is often cited as one of the main reasons for the high stability of Pickering emulsions.

Similar to traditional surfactants, the wettability of colloids also determine the types of emulsions they stabilize. A useful rule developed by Finkle *et al.*<sup>11</sup> states that “in an emulsion containing solid particles, one of the liquids would probably wet the solid more than the other liquid, with the more poorly wetting liquid becoming the dispersed phase”. In other words, when the contact angle ( $\theta$ ) of colloids is smaller than  $90^\circ$ , it favors the

formation of O/W Pickering emulsions whereas when  $\theta > 90^\circ$ , such particles tend to stabilize W/O Pickering emulsions (Figure 10.1b).

For homogeneous spherical colloids, substantially high detachment energy leads to high stability of Pickering emulsions. However, Pickering emulsions stabilized by homogenous colloids, similar to emulsions stabilized by traditional surfactants, are also thermodynamically unstable.<sup>12,13</sup> The free energy change for formation of Pickering emulsions can be given by

$$\Delta G_{\text{formation}} = n_d A_{\text{ow}} \gamma_{\text{ow}} + n_d n_p (\Delta_a G - T \Delta_a S) - T \Delta S_{\text{config}} \quad (10.5)$$

where  $n_d$  and  $n_p$  are the number of droplets in the emulsion and the number of colloids adsorbed at the interface of a droplet, respectively,  $A_{\text{ow}}$  represents the surface area of a bare drop without colloids,  $\Delta_a G$  is the free energy of adsorption of colloids to the droplet interface excluding the entropy changes,  $\Delta_a S$  is the entropy change due to adsorption of colloids to the interface. The configuration entropy term ( $T \Delta S_{\text{config}}$ ) is rather small and can be ignored.<sup>12,13</sup> For Pickering emulsion stabilized by homogeneous colloids,  $\Delta G_{\text{formation}}$  is typically larger than 0 because the first term ( $n_d A_{\text{ow}} \gamma_{\text{ow}}$ ) is significantly larger than the last two terms, meaning they are thermodynamically unstable.<sup>12</sup> Thus despite their high stability, Pickering emulsions stabilized by homogeneous colloids in general are only kinetically stable. An exception was reported by Sacanna *et al.*<sup>14</sup> The thermodynamic stability of this Pickering emulsion was attributed to asymmetrically distributed surface charges on two sides of the oil–water interface which leads to preferred interfacial curvature.

Pickering emulsions can be stabilized by many different types of colloids including inorganic and organic colloids. This chapter will focus on Pickering emulsions stabilized by polymer colloids. In particular, we will highlight Pickering emulsions stabilized by nontraditional polymer colloids such as colloids with complex/inhomogeneous structures and composition (anisotropic particles, Janus particles, microgels, polymer-grafted colloids) as well as biopolymer-based colloids. To learn more about Pickering emulsions stabilized by homogeneous polymer colloids, we refer our readers to an excellent book on this topic.<sup>15</sup>

## 10.2 Pickering Emulsions Stabilized by Anisotropic Homogeneous Particles

The most unique property of polymer colloids is that they can be reshaped and molded into anisotropic structures such as polymer ellipsoids, microrods and thin sheets. Similar to spherical homogeneous particles, anisotropic homogeneous particles that do not have extreme wetting properties adsorb strongly to liquid–liquid interfaces to reduce the interfacial area between the two immiscible fluid phases. Different from spherical homogeneous particles, the configurations of anisotropic particles at the liquid interface are not only determined by the wettability

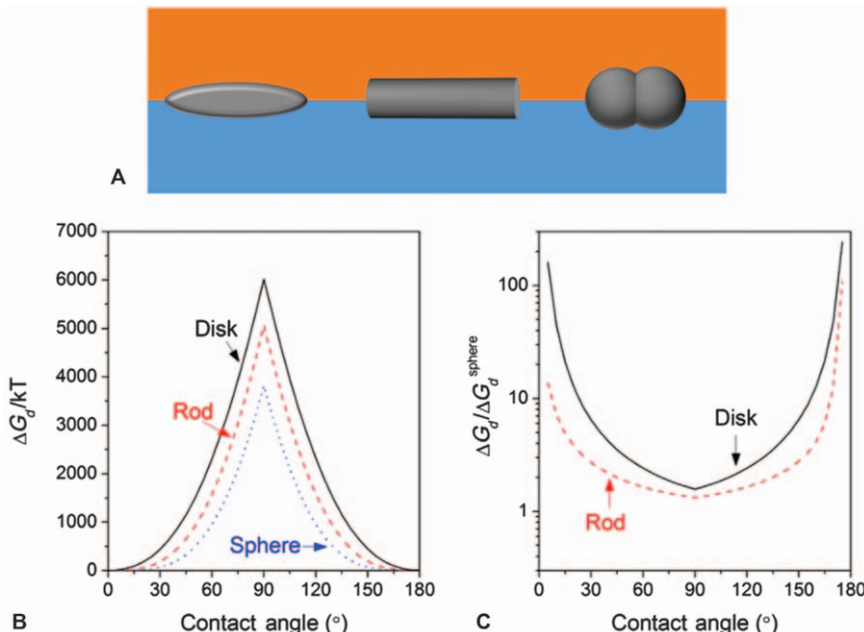


**Figure 10.2** (A) Schematic of ellipsoid, cylinder and dumbbell adsorbed to a fluid interface with the major axes in the plane of the interface. (B) Free energy of detachment as a function of contact angle for a disk, cylinder and sphere. (C) Ratio of the free energy of geometrically anisotropic particles with respect to spheres. Volume of all particles was constant at  $4.19 \times 10^3 \text{ nm}^3$  and the aspect ratio of the anisotropic particles was 2.5. Reproduced from ref. 18 with permission from Elsevier, Copyright 2018.

(indicated by the three-phase contact angle  $\theta$ , Figure 10.1), but also dependent on their geometry. In general, geometrically anisotropic particles (*i.e.* particles with large aspect ratios) tend to adsorb at liquid–liquid interfaces with their major axes in the plane to remove the largest fluid–fluid area (Figure 10.2)<sup>16</sup>

The detachment energy for anisotropic particles can be calculated using the same procedure as that for spherical particles. For example, the free energy required for the detachment of a microrod particle with an aspect ratio of  $a/b$  from the liquid interface is given by:<sup>17,18</sup>

$$\Delta G_{dw}^{\text{rod}} = \gamma_{ow} \pi b^2 (1 - \cos \theta)^2 \left[ 1 + \frac{4 \left( \frac{a}{b} - 1 \right) (\sin \theta - \theta \cos \theta)}{\pi (1 - \cos \theta)^2} \right] \quad (10.6)$$

$$\Delta G_{do}^{\text{rod}} = \Delta G_{dw}^{\text{rod}} + 4\pi \gamma_{ow} b^2 \cos \theta \left( \frac{a}{b} \right) \quad (10.7)$$

where  $\Delta G_{\text{dw}}^{\text{rod}}$  and  $\Delta G_{\text{do}}^{\text{rod}}$  are the free energies for the detachment of microrod particles into the aqueous and oil phases, respectively.

Similarly, the detachment energy of a round disk with an aspect ratio of  $a/b$  from the liquid interfaces can be expressed as:<sup>18,19</sup>

$$\Delta G_{\text{dw}}^{\text{disk}} = \gamma_{\text{ow}} \pi b^2 (1 - \cos \theta)^2 \left[ 1 + \frac{\left(\frac{a}{b} - 1\right)^2}{1 - \cos \theta} + \frac{2\left(\frac{a}{b} - 1\right)(\sin \theta - \theta \cos \theta)}{(1 - \cos \theta)^2} \right] \quad (10.8)$$

$$\Delta G_{\text{do}}^{\text{disk}} = \Delta G_{\text{dw}}^{\text{disk}} + 2\pi\gamma_{\text{ow}} b^2 \cos \theta \left[ \left(\frac{a}{b} - 1\right)^2 + \pi\left(\frac{a}{b} - 1\right) + 2 \right] \quad (10.9)$$

where  $\Delta G_{\text{dw}}^{\text{disk}}$  and  $\Delta G_{\text{do}}^{\text{disk}}$  are the free energies for the detachment of thin disks into the aqueous and oil phases, respectively.

Provided that the radius of the disk is much larger than the thickness, the desorption energy of the disk into its energetically favourable phase can be simplified as:

$$\Delta G^{\text{thin disk}} = \pi r^2 \gamma_{\text{ow}} (1 \pm \cos \theta) \quad (10.10)$$

Due to the difference in the power of the  $(1 \pm \cos \theta)$  term, it is clear that it requires higher energy to detach thin disks from the liquid interface than that for spherical particles. At a constant particle volume, the detachment energy scales as disks > microrods > spheres.<sup>18</sup> The anisotropic geometry results in enhanced particle stability at the liquid interface.

The high detachment energies of anisotropic particles from liquid interfaces potentially make them effective solid surfactants for emulsions or foams.<sup>20–23</sup> Velev *et al.*<sup>21</sup> reported water-in-oil emulsions and water-in-air foams stabilized by anisotropic particles of hypromellose phthalate (HP) formed *in situ*. Anisotropic HP particles with rod-like, fiber-like and/or thin sheet structures were obtained by shearing a stock solution of HP in aqueous media, which consequently adsorbed onto the water-oil or water-air interfaces, resulting in highly stable emulsions/foams (Figure 10.3).

Moreover, Velev *et al.*<sup>22</sup> also reported ‘hairy’ water-in-oil (W/O) emulsions stabilized by SU-8 microrods. The W/O emulsion was stable even at 70 °C due to steric obstruction resulting from the densely adsorbed layer of SU-8 microrods. A SEM image of the gel-trapped SU-8 microrods at the interfaces showed that the microrods laid horizontally with their major axes parallel to the fluid interface. Colloidosomes with shells of polymer micro-rods can be obtained after transferring the stable W/O emulsion into an aqueous environment.

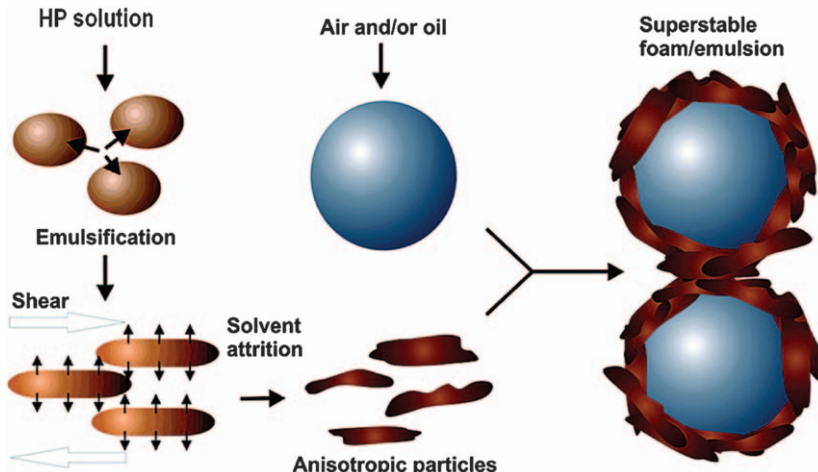


**Figure 10.3** Schematics of the mechanism of forming Pickering emulsions and foams stabilized by HP anisotropic particles (microrods, fiber and thin sheets) formed *in situ*. Structures are not drawn to scale.  
Reproduced from ref. 21 with permission from American Chemical Society, Copyright 2008.

### 10.3 Janus-particle Stabilized Pickering Emulsions

In 1991, in his Nobel lecture, Pierre-Gilles de Gennes broadly introduced the concept of 'Janus particles' named after the two faced Roman god Janus. Janus particles are special types of anisotropic colloids that have two regions with distinct physical properties such as polarity and wettability.<sup>24,25</sup> It is, thus, expected that Janus particles with polar and apolar regions will adsorb at a liquid–liquid interface with their hydrophobic side facing the oil phase and the hydrophilic side facing the aqueous phase. According to de Gennes, Janus particle-adsorbed interfaces should share the characteristics of an interface covered by surfactant molecules and homogeneous particles. On one hand, Janus particles resemble surfactant molecules when they assemble at a fluid–fluid interface because of their intrinsic amphiphilicity (Figure 10.4). On the other hand, the large interstices between Janus particles at the interface allow material exchange to occur between the two phases. This 'breathable skin' property, along with many others, motivated the development of Janus particles as stabilizers of Pickering emulsions.<sup>26–33</sup>

During the past two decades, a number of synthetic techniques have been developed for the preparation of Janus particles with diverse morphologies and functionalities.<sup>34–44</sup> Excellent review articles that highlight the recent developments on the synthesis of Janus particles can be found in ref. 29–32. Moreover, de Gennes' vision of breathable skin made of a Janus particle monolayer at a fluid–fluid interface has been realized recently. Faria and co-workers exploited Janus particles as solid surfactants to stabilize oil-in-water emulsions in which a biofuel refining process was enhanced on

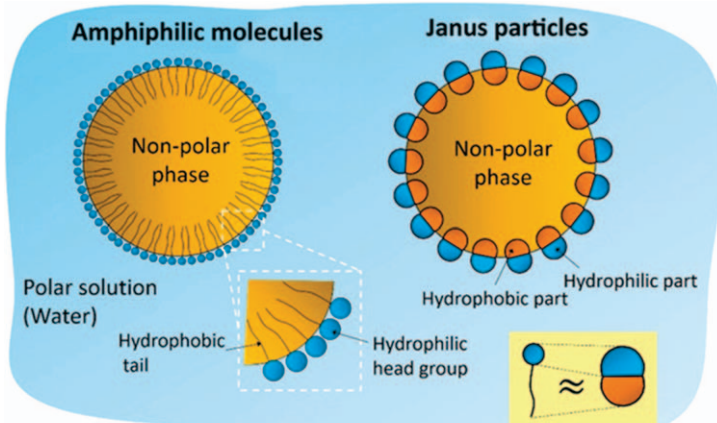


**Figure 10.4** Schematic illustrations of emulsion droplets stabilized by amphiphilic molecules and Janus particles.

Reproduced from ref. 16 with permission from Cambridge University Press, Copyright 2014.

account of fast mass transfer between the two phases during catalysis.<sup>45</sup> Recent reports have demonstrated that some of these Janus particles function as excellent solid stabilizers for Pickering emulsions.<sup>26,27,30,46–48</sup> For example, it has shown that Janus particles could stabilize and maintain water-in-toluene emulsions for weeks, much more effectively than their homogeneous counterparts (Figure 10.5).<sup>43</sup> Therefore, many research groups have investigated the interfacial activities of amphiphilic Janus particles, both theoretically and experimentally.

### 10.3.1 Janus Particles at Liquid–Liquid Interfaces

The enhanced stability of Janus particle-stabilized Pickering emulsions is credited to the strong attachment of Janus particles to the liquid–liquid interfaces.<sup>26</sup> Detachment energy, calculated from the energy required to transfer a Janus particle from the liquid–liquid interface into one of the bulk phases, is used to characterize the interfacial activity of a Janus particle. The energy of detachment is therefore a function of fluid–fluid and fluid–solid interfacial tensions [represented by the contact angles of the polar ( $\theta_p$ ) and apolar ( $\theta_a$ ) components] as well as the corresponding interfacial areas dictated by the particle position with respect to the interface.

Based on the model Janus particle shown in Figure 10.6, the detachment energy of Janus particles can be calculated as a function of angle  $\beta$  and Janus boundary ( $\alpha$ ):<sup>26</sup>

$$\text{For } \beta \leq \alpha: \Delta G_A(\beta) = 2\pi R^2 \left[ \gamma_{AO}(1 + \cos \alpha) + \gamma_{PO}(\cos \beta - \cos \alpha) + \gamma_{PW}(1 - \cos \beta) - \frac{1}{2}\gamma_{OW}(\sin^2 \beta) \right] \quad (10.11)$$

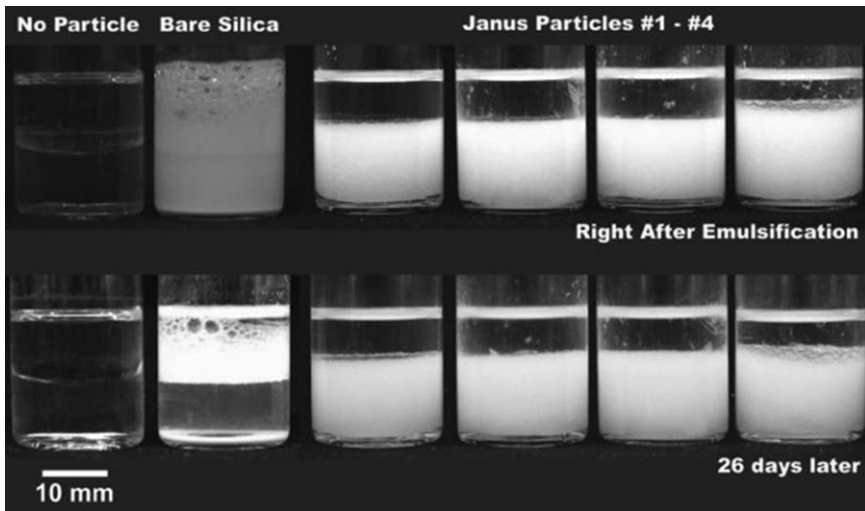


**Figure 10.5** Emulsion stability of water-in-toluene emulsions stabilized without particles (column 1), with homogeneous silica particles (column 2), and with amphiphilic Janus particles of varying Janus boundaries (columns 3–6). Janus particle-stabilized emulsions are stable after 26 days.

Reproduced from ref. 43 with permission from John Wiley and Sons, Copyright © 2010 WILEY-VCH Verlag GmbH & Co. KGaA, Weinheim.

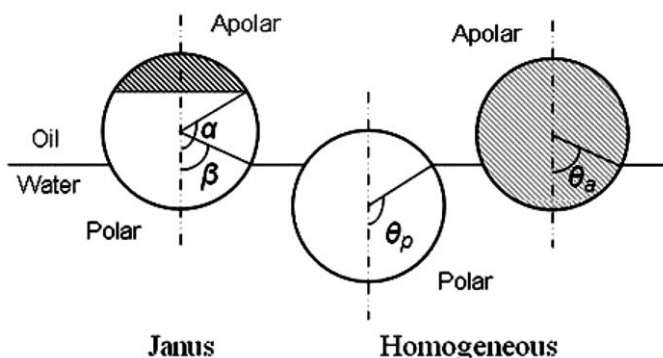


**Figure 10.6** Schematics of the geometry of a Janus particle at liquid interfaces.  $\alpha$  indicates the Janus boundary and  $\beta$  represent positions of the interfaces.  $\theta_p$  and  $\theta_a$  are the contact angles of polar and apolar components of the Janus particles.

Reproduced from ref. 47 with permission from AIP Publishing, Copyright 2007.

$$\text{For } \beta \geq \alpha: \Delta G_P(\beta) = 2\pi R^2 \left[ \gamma_{AO}(1 + \cos \beta) + \gamma_{AW}(\cos \alpha - \cos \beta) + \gamma_{PW}(1 - \cos \alpha) - \frac{1}{2}\gamma_{OW}(\sin^2 \beta) \right] \quad (10.12)$$

where  $R$  is the particle radius and  $\gamma$  is the interfacial tension between phases. For Janus particles that have the maximum wetting difference between the two sides, the maximum detachment energy can be approximated as:<sup>49,50</sup>

$$\Delta G_{de} \approx 3\pi R^2 \gamma_{ow} \quad (10.13)$$

The detachment energy of a Janus particle can be up to three times higher than that of a homogeneous particle, which has a significant implication in the thermodynamics of emulsion stabilization with Janus particles.

### 10.3.2 Thermodynamically Stable Pickering Emulsions Stabilized by Janus Particles

In contrast to emulsions stabilized by homogeneous colloids, thermodynamically stable Pickering emulsions can be prepared using Janus particles as stabilizers. Aveyard *et al.*<sup>49</sup> showed that the free energy of formation of emulsions stabilized by spherical Janus particles can be negative when the interface coverage of Janus particles is sufficiently high (Figure 10.7a). The high detachment energy of Janus particles and the lateral interactions between densely packed Janus particles attribute to the formation of thermodynamically stable Pickering emulsions. Similarly, Lee *et al.*,<sup>51</sup> demonstrated that emulsions stabilized by dumbbell-like Janus particles can also give rise to a negative free energy under certain conditions, leading to thermodynamically stable Pickering emulsions (Figure 10.7b).

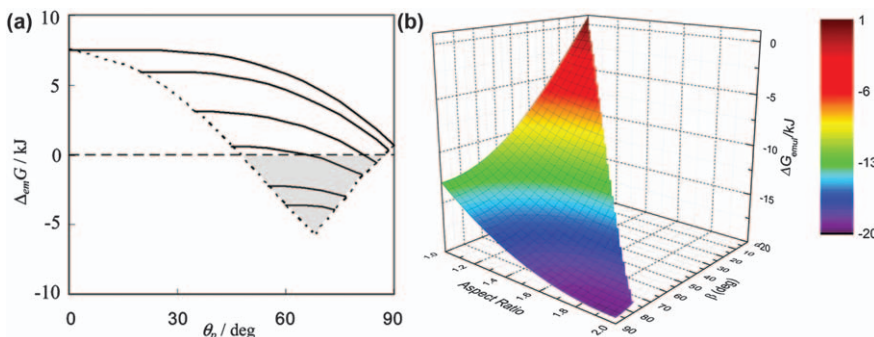


**Figure 10.7** (a) Free energy of formation of monodisperse Pickering emulsion stabilized by Janus particles as a function of contact angle of polar region of the Janus particle ( $\theta_p$ ). Volume = 1 m<sup>3</sup> (with  $\phi_o, \phi_w = 0.5$ ). The curves are for, from top,  $\alpha = 0^\circ, 20^\circ, 35^\circ, 45^\circ, 55^\circ$  and  $60^\circ$  and are truncated at  $\alpha$  at low angles and at  $\theta_p$  at high angles, as indicated by the dashed lines. Reproduced with permission from ref. 49 (b) Free energy of emulsion formation as a function of the amphiphilicity and the aspect ratio of Janus dumbbells. The emulsions modeled in this calculation consist of oil droplets of a radius of 10 μm and have a 0.5 m<sup>3</sup> aqueous phase and a 0.5 m<sup>3</sup> oil phase. Reproduced from ref. 51 with permission from American Chemical Society, Copyright 2013.

### 10.3.3 Janus Balance

Just like molecular amphiphiles, the geometry and wetting properties have a significant impact on the surfactancy of Janus particles, as indicated in eqn (10.11) and (10.12). In analogy to the hydrophilic–lipophilic balance (HLB), the Janus balance ( $J$ ), combining the geometry and wetting properties, was introduced to quantify the capability and efficiency of Janus particles as solid surfactants.<sup>47</sup> It is defined as the relative work required to move a Janus particle at the liquid–liquid interface to the hydrophobic phase compared to the hydrophilic phase:

$$J = \frac{\sin^2 \alpha + 2 \cos \theta_P (\cos \alpha - 1)}{\sin^2 \alpha + 2 \cos \theta_A (\cos \alpha + 1)} \quad (10.14)$$

The  $J$  value highly depends on the Janus boundary ( $\alpha$ ) and wetting properties of the two sides of the Janus particles (Figure 10.6). When the  $J$  value is close to 1, a larger detachment energy is required to transfer Janus particles into the bulk solvent, and thus very stable Pickering emulsions would be formed with such particles. Therefore,  $J$  could potentially be used to predict how Janus particles behave as solid surfactants.

### 10.3.4 Stimuli-responsive Pickering Emulsion Stabilized by Janus Particles

Both experimental and theoretical results have demonstrated that Janus particles exhibit superior surfactancy for Pickering emulsions compared to their homogenous counterparts. Recent progress has expanded to developing stimuli-responsive Janus particles for tunable emulsion structure and functionality.<sup>44,52–55</sup> For example, dual-responsive Janus particles bearing pH-responsiveness and a lower critical solution temperature (LCST) have been developed.<sup>54,55</sup> Changes in the pH and temperature induce changes in the wettability as well as the geometry of Janus particles, resulting in destabilization of the Pickering emulsions. Moreover, phase inversion of Pickering emulsions from W/O to O/W emulsions has been demonstrated by changing the Janus balance of a pH-responsive Janus particle (Figure 10.8).<sup>44</sup>

## 10.4 Microgel-stabilized Pickering Emulsions

### 10.4.1 Microgels

Microgels are colloidal particles that are composed of crosslinked hydrophilic polymer networks and contain significant amounts of solvents (typically water) inside the networks.<sup>56</sup> The crosslinked network of microgels provides the structural integrity of a gel “particle”; at the same time the presence of a significant amount solvents facilitates mass

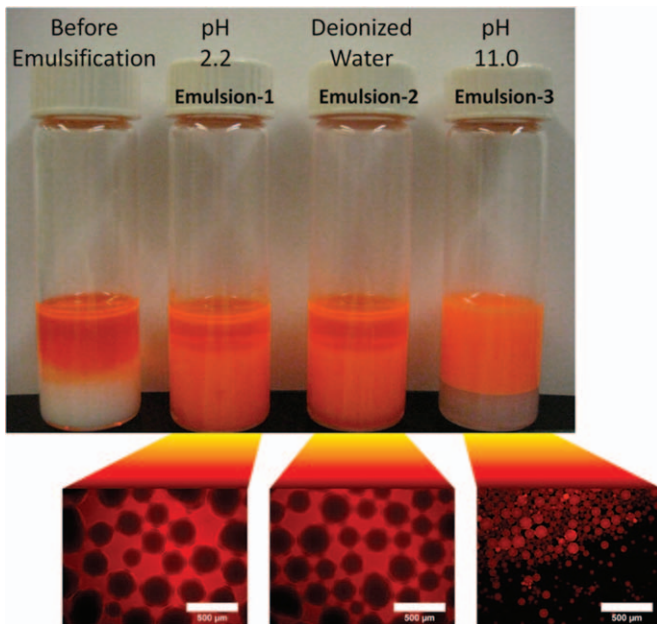


**Figure 10.8** Macroscopic (top) and fluorescence (bottom) microscopy images of emulsions made with an aqueous phase of pH 2.2, deionized water (water-in-oil emulsion) and an aqueous phase of pH 11.0 (oil-in-water emulsion). The volume ratio of oil and water phases is kept 50:50 in all cases, and the oil phase contains 0.01 wt% Nile Red. Scale bar = 500  $\mu\text{m}$ .

Reproduced from ref. 44 with permission from American Chemical Society, Copyright 2014.

exchange between the hydrophilic polymer network and the surroundings. These properties enable deformation of microgels, and also allows swollen and collapsed states of the polymer network. In their collapsed state, microgels resemble solid colloids. In contrast, in the swollen state microgels possess soft open structures with fuzzy surfaces and dangling chains.

The most interesting feature of microgels is their capability to adjust both their shape and volume in response to external stimuli such as temperature, pH, ionic strength, electrochemical stimulus, pressure and light. For example, poly(*N*-isopropylacrylamide) (PNIPAM)-based microgels display a drastic change in size at around the volume phase transition temperature (VPTT). Below the VPTT, the microgels are fully swollen due to the hydrophilic nature of PNIPAM. Upon temperature increase, PNIPAM become hydrophobic and the microgels collapse into smaller colloidal particles. Similarly, when ionizable functional groups such as methacrylic acid (MAA) are introduced into microgels, the resulting microgels become pH-responsive.

### 10.4.2 Stimuli-responsive Pickering Emulsions Stabilized by Microgels

The stability of Pickering emulsions can be tuned by taking advantage of the stimuli-responsive property of microgels, leading to stimuli-responsive emulsions. For example, thermal and pH-responsive poly(NIPAM-*co*-MAA) microgels were employed as stabilizers for octanol-in-water (O/W) emulsions.<sup>57</sup> The O/W emulsions were stable when the microgels were at their swollen state under high pH and low temperature (below VPTT). Freeze fracture scanning electron microscopy (SEM) images showed that the microgels were densely packed at the liquid-liquid interface (Figure 10.9). When the pH was decreased or the temperature was raised above the VPTT of the microgels, the O/W emulsions became unstable and complete phase separation of

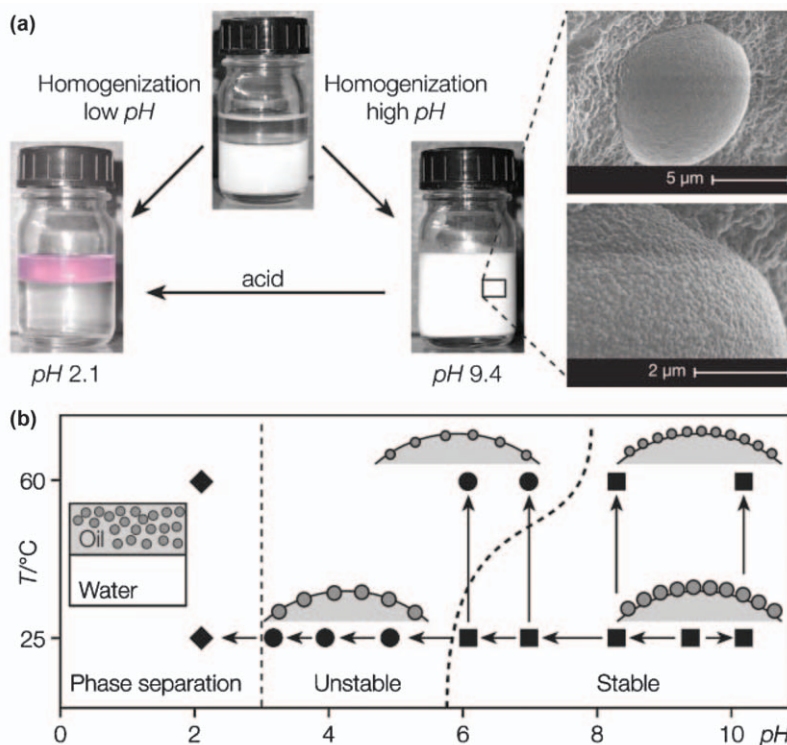


**Figure 10.9** (a), Influence of pH on the stability of octanol-in-water emulsions stabilized by poly(NIPAM-*co*-MAA) microgels. The inset shows the SEM image of microgels at the interface. (b), Summary of effects of temperature and pH on the behavior of the poly(NIPAM-*co*-MAA) microgels at the interface as well as on the stability of the octanol-in-water emulsions.

Reproduced from ref. 57 with permission from the Royal Society of Chemistry.

octanol and water was observed (Figure 10.9a). The effects of temperature and pH on behavior of the microgels and the Pickering emulsions are summarized in Figure 10.9b. The destabilization of poly(NIPAM-*co*-MAA) microgel-stabilized emulsions was attributed to reduced coverage of microgels at the oil–water interface due to the coalescence of microgels. Since the initial report on stimuli-responsive Pickering emulsions stabilized by poly(NIPAM-*co*-MAA) microgels, many research groups have developed other microgel-stabilized emulsion systems that are responsive to environmental stimuli such as temperature, pH, ionic strength or magnetic field.<sup>58</sup>

### 10.4.3 Microgels at Liquid–Liquid Interfaces

Similar to solid colloids, microgels adsorb at the liquid–liquid interface efficiently, enabling stabilization of emulsions. Yet, unlike solid colloids, microgels deform and flatten at the liquid–liquid interface because they are soft and porous in their swollen state. Schmitt *et al.*,<sup>59</sup> studied the packing of PNIPAM microgels with different degrees of crosslinking density at the interface of a heptane-in-water emulsion droplet by means of cryo-SEM. Microgels were significantly stretched at the interface, linked by filaments (Figure 10.10). This result agrees well with the observation of stretched pH-sensitive microgels at a flat heptane–water interface reported by Geisel *et al.*<sup>60</sup>

Upon changes in the environmental conditions such as temperature, microgels at interfaces can transform to the collapsed state. Even though the collapsed microgels can still remain at the interface, the phase transformation of microgels can trigger the destabilization of the emulsion. Richtering *et al.*<sup>61</sup> suggested that the destabilization is likely attributed to the change in the viscoelastic properties of the interface. In the swollen state, microgels form a partially interconnected structure, leading to an elastic and soft gel-like interface. In the collapsed state, however, microgels pack into brittle colloidal clusters which are not strong enough to withstand the collisions between emulsion droplets and eventually result in the destabilization of Pickering emulsions.

Unlike hard colloids, the surface charge density of microgels is not critical for the stabilization of emulsions. Schmidt *et al.*<sup>62</sup> designed two different types of core–shell microgels as stabilizers for emulsions: one had a core–shell structure with a neutral PNIPAM core and a charged PMAA shell, the other had a PMMA core and a PNIPAM shell. The results showed that the location of charges was not relevant to the stability of microgel-stabilized Pickering emulsions. In other words, the stability of these emulsions does not solely depend on the surface charge of the microgels. They also demonstrated that the deformation of microgels at the liquid–liquid interface is the key phenomenon for stabilization of emulsions.

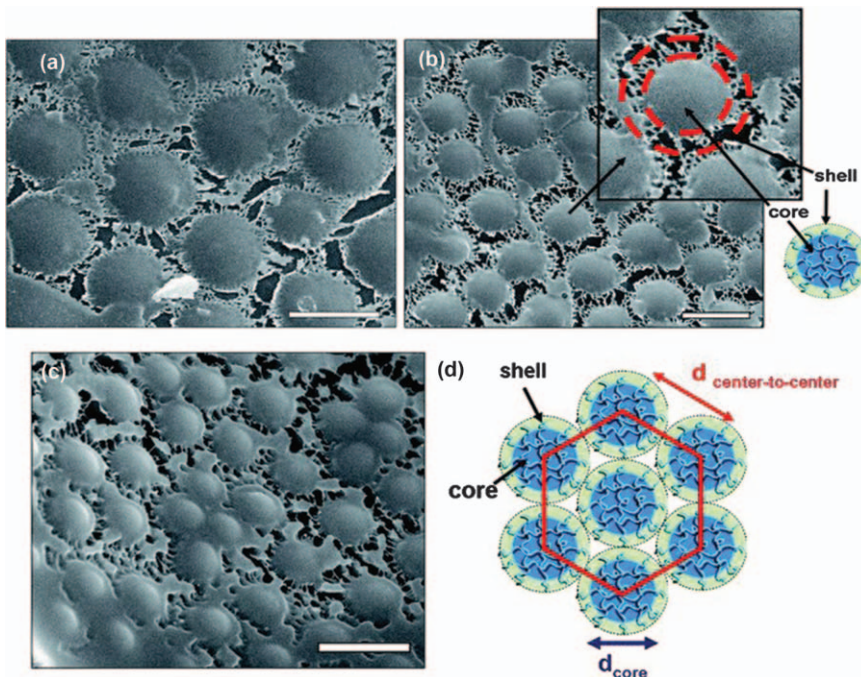


**Figure 10.10** Cryo-SEM image of the interface of a heptane-in-water Pickering emulsion covered by: (a) and (b) 2.5 mol% BIS cross-linked microgels after sublimation (front view), (c) 5 mol% BIS cross-linked microgels particles after sublimation (side view), scale bars are 1  $\mu\text{m}$ ; (d) scheme of the particle structure and arrangement at the interface.

Reproduced from ref. 59 with permission from the Royal Society of Chemistry.

#### 10.4.4 High Internal Phase Emulsions Stabilized by Microgels

The high stability of Pickering emulsions stabilized by swollen microgels has been utilized to prepare high internal phase emulsions (HIPEs). HIPEs are defined as concentrated emulsions with a volume fraction of the dispersed phase over 74%. HIPEs are useful as templates for highly porous materials. Ngai *et al.*<sup>63</sup> developed hexane-in-water (O/W) HIPEs using poly(NIPAM-*co*-MAA) microgels (Figure 10.11). In this work, the microgels were adsorbed and deformed at the liquid–liquid interface and employed as stabilizers for HIPEs. Moreover, in the aqueous phase, excessive poly(NIPAM-*co*-MAA) microgels simultaneously formed a gel matrix in the bulk phase which enhanced the stability of HIPEs by trapping the poly(NIPAM-*co*-MAA) microgel-stabilized emulsions in the matrix.

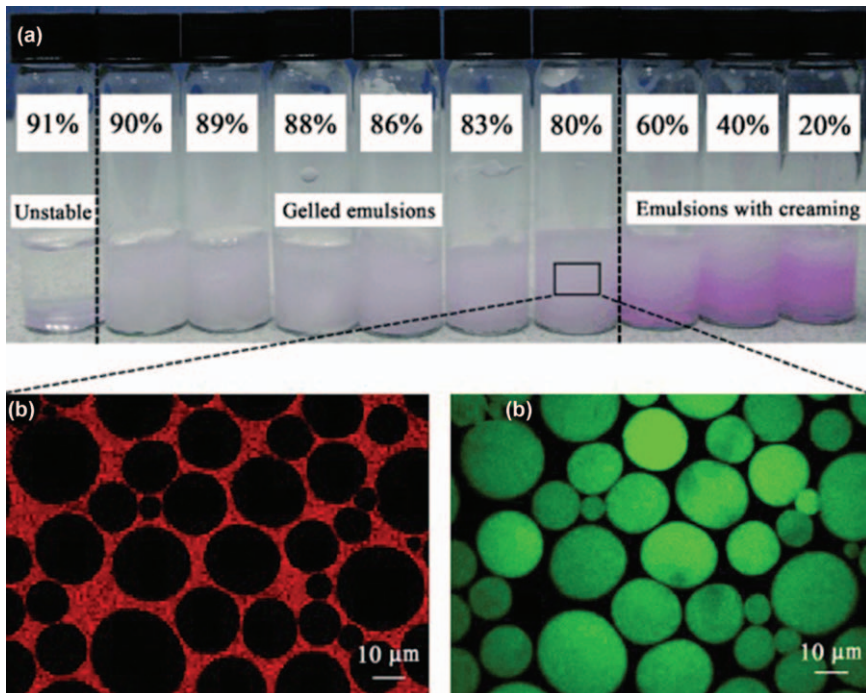


**Figure 10.11** (a) Photograph of microgel-stabilized emulsions having an internal oil phase volume from 20 to 91% at room temperature, where the continuous phases of all mixtures consist of 2 wt% microgels in the initial dispersion with a solution pH 6. (b) and (c) Confocal images of the emulsion with 80 vol% hexane oil stabilized by 2 wt% microgels excited by lasers with wavelengths of 408 and 543 nm, respectively.

Reproduced from ref. 63 with permission from John Wiley and Sons, Copyright © 2009 WILEY-VCH Verlag GmbH & Co. KGaA, Weinheim.

## 10.5 Pickering Emulsions Stabilized by Polymer-grafted Particles

The surface chemistry and wetting properties of colloids are key parameters that determine the type and stability of Pickering emulsions. The wetting properties and the ability of conventional colloids to stabilize emulsions can be significantly enhanced by grafting polymer chains onto these particles. In particular, major advances have been made in precisely controlling the density and length of polymer chains that can be grafted onto various particles *via* living polymerization. Excellent reviews on this topic can be found in ref. 64–66.

Amalvy *et al.*<sup>67</sup> reported polymer-grafted latex colloids as solid stabilizers for Pickering emulsions. Poly[2-(dimethylamino) ethyl methacrylate-*block*-methyl

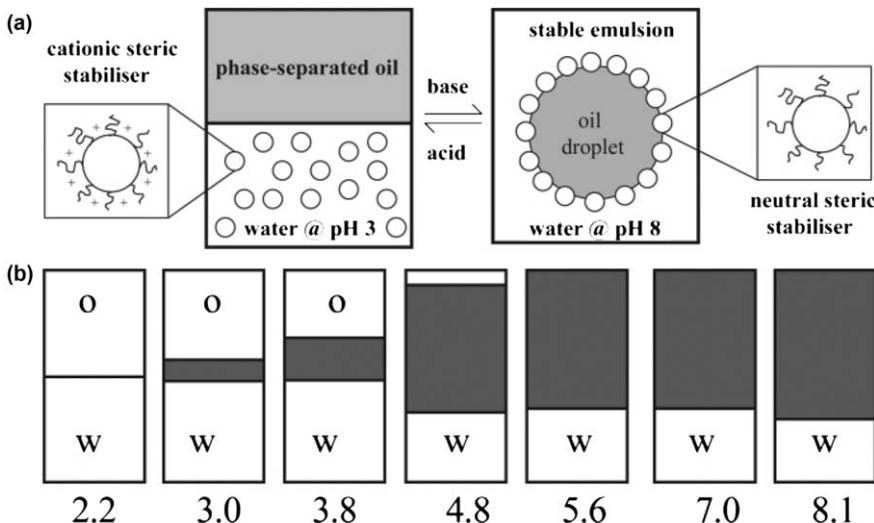


**Figure 10.12** (a) Schematic of the formation of an oil-in-water emulsion using pH-responsive sterically stabilized latex particles. (b) Effect of varying the solution pH on the appearance of the emulsion after standing for 24 h at room temperature.

Reproduced from ref. 67 with permission from the Royal Society of Chemistry.

methacrylate] ( $\text{P}(\text{DMA}-b\text{-MMA})$ ), whose hydrophilicity can be adjusted by controlling the solution pH, was grafted onto the surfaces of polystyrene (PS) particles, forming sterically stabilized latex particles ( $\text{PS@P}(\text{DMA}-b\text{-PMMA})$ ) (Figure 10.12a). pH-responsive hexadecane-in-water (O/W) Pickering emulsions were prepared using the  $\text{PS@P}(\text{DMA}-b\text{-PMMA})$  particles as stabilizers. Between pH 8.1 and 5.6, stable O/W Pickering emulsions were obtained as the hydrophilic PDMA residues were only weakly charged (Figure 10.12b). On lowering the pH of the aqueous phase from 5.6 to 2.2, the PDMA residues became fully protonated and hydrophilic which led to their desorption from the oil–water interface. Thus, the Pickering emulsions became unstable and macroscopic phase separation was observed (Figure 10.12b).

The same  $\text{P}(\text{DMA}-b\text{-PMMA})$  grafted PS colloids were utilized to prepare temperature-responsive Pickering emulsions as the PDMA residues also exhibit volume phase transition temperatures (VPTTs) between 35 °C and 45 °C, depending on the length of PDMA.<sup>68</sup> Phase inversion of Pickering emulsions from O/W to W/O was realized by changing the temperature of  $\text{P}(\text{DMA}-b\text{-PMMA})$ -grafted PS colloid-stabilized hexadecane/water emulsions. It was argued that the phase inversion resulted from the change in wettability of PDMA residues to the oil phase upon temperature change.

## 10.6 Biopolymer Colloid-stabilized Pickering Emulsions

### 10.6.1 Cellulose Nanocrystal-stabilized Pickering Emulsions

Cellulose is the most abundant renewable polymer in the world, produced by and available in plants, algae, fungi and bacteria. Cellulose is a tough and water-insoluble fibrous material that maintains the structure of plant cell walls. Cellulose nanocrystals (CNs), firstly reported in the 1950s,<sup>69</sup> are a type of needle-shaped colloidal particle prepared through the degradation of cellulose fibers. Recent work has shown that these needle-shaped cellulose nanocrystals can be used to stabilize oil-in-water emulsions by forming a 2D interfacial network of CNs (Figure 10.13).<sup>70</sup> Small angle neutron scattering (SANS) measurement of the Pickering emulsions showed that the CN particles organized as a monolayer at the oil–water interface, with only the (2 0 0) crystalline plane of the CNs contacting the oil phase without CN themselves immersing in the oil phase.<sup>71</sup> The 2D network structures of CNs at the oil–water interface can also facilitate the formation of high internal phase Pickering emulsions with deformed emulsion droplets.<sup>72</sup>

CNs have a large number of hydroxyl groups at the surface, which can be utilized to modify the surface properties of CNs *via* different chemical reactions such as esterification, etherification, oxidation and silylation.<sup>73</sup> Tam *et al.*<sup>74</sup> covalently introduced a weak polyelectrolyte of poly[2-(dimethylamino)ethyl methacrylate] (PDMAEMA) onto the surface of CNs *via* free radical polymerization. The PDMAEMA-modified CNs can significantly reduce the interfacial tensions between oil and water, forming highly stable emulsions compared to the pristine CNs. Moreover, the PDMAEMA polymers are both thermal and pH responsive. Thus, destabilization of Pickering emulsions stabilized by the PDMAEMA modified CNs can be triggered by varying the temperature or the pH of the emulsion.

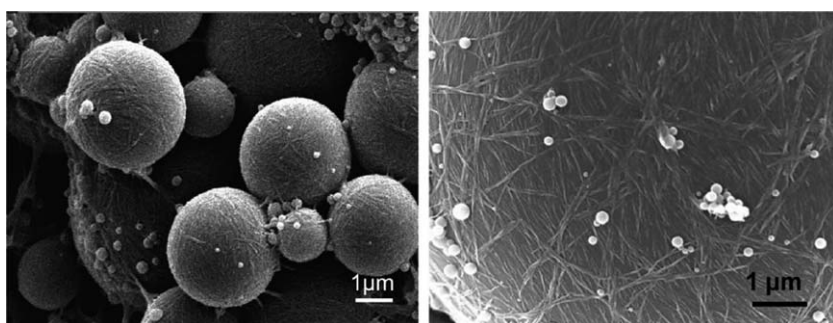


**Figure 10.13** Scanning electron micrographs of Pickering emulsion stabilized by CNs.

Reproduced from ref. 70 with permission from American Chemical Society, Copyright 2011.

### 10.6.2 Protein-stabilized Pickering Emulsions

Proteins are an important class of natural polymers and have been extensively employed as stabilizers in the food industry to prepare oil-in-water emulsions. For example, Decker *et al.*<sup>75</sup> have demonstrated that whey proteins such as whey protein isolate (WPI), sweet whey (SW),  $\beta$ -lactoglobulin ( $\beta$ -Lg), or  $\alpha$ -lactalbumin ( $\alpha$ -La) can stabilize salmon oil-in-water (O/W) emulsions. Moreover, protein-stabilized emulsions increased the oxidative stability of salmon oil thus eliminating or reducing the need for exogenous food antioxidants.

Taking advantage of strong hydrogen bonding between proteins, Ngai *et al.*<sup>76</sup> prepared O/W types of high internal phase emulsions using gelatin nanoparticles as solid stabilizers (Figure 10.14). In the system, gelatin nanoparticles can be crosslinked spontaneously at the interface and in the aqueous continuous phase, leading to the formation of stable three-dimensional (3D) hierarchical protein scaffolds after the evaporation of both oil and water.

### 10.6.3 Fat Crystal-stabilized Pickering Emulsions

Fat crystals have long been utilized to prepare edible Pickering emulsions because of their potential application in food texture modification, and bioactive compound encapsulation and delivery.<sup>77</sup> Due to the hydrophobic nature of fat crystals, water-in-oil (W/O) types of emulsion such as butter and margarines can be readily prepared.<sup>78</sup> Because fat has a melting temperature near body temperature, emulsions stabilized by fat crystals stay stable during

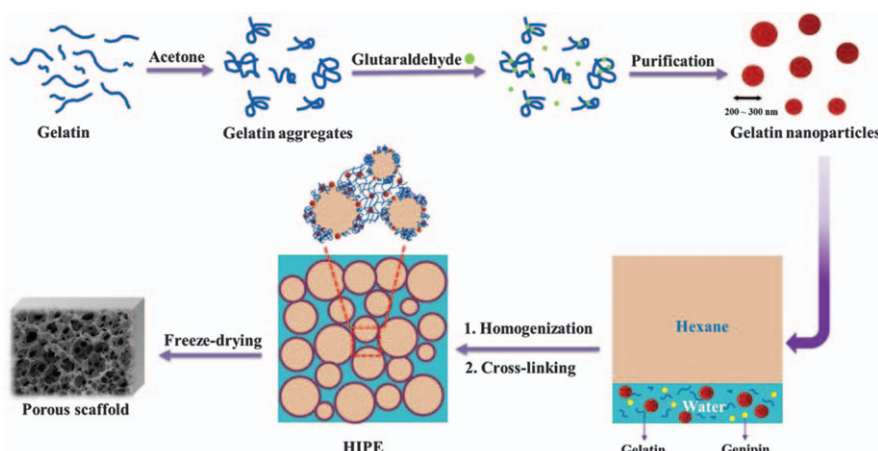


**Figure 10.14** Schematic preparation of a hierarchical protein scaffold *via* a high internal phase Pickering emulsion stabilized by gelatin nanoparticles. Reproduced from ref. 76 with permission from American Chemical Society, Copyright 2018.

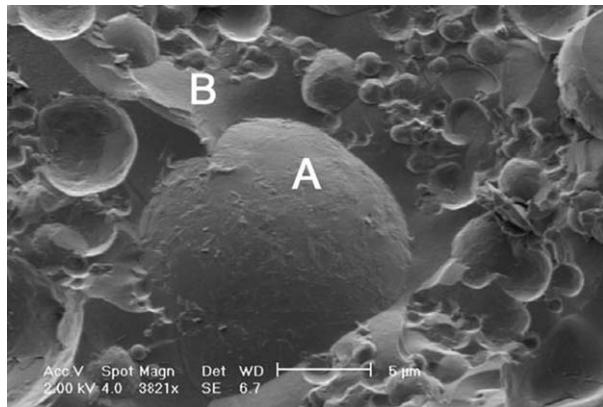


**Figure 10.15** SEM image of an W/O Pickering emulsion stabilized by tripalmitin crystals (A) and surrounding fat crystals (B).

Reproduced from ref. 80 with permission from Elsevier, Copyright 2010.

storage at ambient temperature but rapidly melt and consequently undergo phase separation at temperatures found within the mouth.<sup>79</sup> The structural stability of fat crystal-stabilized emulsions takes advantage of the fact that fat crystals are present in the continuous oil phase as a fine network (Figure 10.15).<sup>80</sup> The synergistic effects of fat crystals as both Pickering and network stabilizers prevent coalescence of water droplets, leading to long-term stability of W/O emulsions.

## 10.7 Conclusions and Outlook

In this chapter, we have highlighted recent developments of Pickering emulsions stabilized by polymer colloids with unique structures (anisotropic colloids, Janus particles, microgels and polymer-grafted colloids) and compositions (synthetic polymers and biopolymers). Compared with chemically homogeneous spherical colloids, these advanced colloids provide significantly improved surfactancy due to better control of wettability and surface chemistry. Moreover, the structural complexity of nontraditional polymer colloids enables the preparation of stimuli-responsive Pickering emulsions with tunable structures and functionalities. Thus one of the important future directions in the field is to establish the relationship between the structure of polymer colloids and the properties of resulting Pickering emulsions through experiments and theoretical calculations. In particular, more efforts toward connecting the microscale phenomena and interactions of particles at interfaces to the stability and behavior of bulk emulsions would significantly advance our understanding. For example, although there is exciting research on the lateral interactions between polymer colloids at the liquid–liquid interface, the connection between such interactions and emulsion stabilization has not been established. Polymer colloids with

advanced structures such as core–shell, raspberry-like and hollow polymer colloids could also represent new colloidal particles for effective preparation of Pickering emulsions with advanced structures and functionalities.

Pickering emulsions stabilized by polymer colloids are attractive to industry, in food, cosmetic and pharmaceutical applications, because of their high stability and functionality. Given that broad bans on use of polymer colloids made from petrochemical-based polymers (plastic microbeads) are expanding worldwide, one of the future development in the field must focus on the discovery of polymer colloids made from bio-derived and/or biodegradable materials. Natural biopolymers such as polysaccharides and peptides/proteins are ideal candidates as building blocks for such polymer colloids. Moreover, another key challenge in the application of polymer colloid-stabilized Pickering emulsions is manufacturability of polymer colloids that are both effective and acceptable for use in products (such as Janus particles made with biodegradable polymers) on the commercial scale. Thus, it is important to develop scalable processes for the synthesis of polymer colloids with complex structures and compositions.

## References

1. P. B. Bernard, *Modern Aspects of Emulsion Science*, 1998.
2. T. F. Tadros, *Emulsion Science and Technology: A General Introduction*, 2009.
3. J. Sjöblom, *Encyclopedic Handbook of Emulsion Technology*, CRC Press, 2001.
4. J. N. Israelachvili, *Intermolecular and Surface Forces*, 2011.
5. D. J. McClements, *Soft Matter*, 2012, **8**, 1719–1729.
6. W. Ramsden, *Proc. R. Soc. London*, 1903, **72**, 156–164.
7. S. U. Pickering, *J. Chem. Soc., Trans.*, 1907, **91**, 2001–2021.
8. Y. Chevalier and M.-A. Bolzinger, *Colloids Surf. A*, 2013, **439**, 23–34.
9. B. P. Binks, *Curr. Opin. Colloid Interface Sci.*, 2002, **7**, 21–41.
10. R. Aveyard, B. P. Binks and J. H. Clint, *Adv. Colloid Interface Sci.*, 2003, **100–102**, 503–546.
11. P. Finkle, H. D. Draper and J. H. Hildebrand, *J. Am. Chem. Soc.*, 1923, **45**, 2780–2788.
12. R. Aveyard, *Soft Matter*, 2012, **8**, 5233–5240.
13. T. F. Tadros, *Encyclopedia of Emulsion Technology*, 1983, vol. 1, p. 129.
14. S. Sacanna, W. K. Kegel and A. P. Philipse, *Phys. Rev. Lett.*, 2007, **98**, 158301.
15. B. Binks and T. S. Horozov, *Colloidal Particles at Liquid Interfaces*, Cambridge University Press, 2006.
16. B. J. Park and D. Lee, *MRS Bull.*, 2014, **39**, 1089–1098.
17. E. P. Lewandowski, M. Cavallaro Jr., L. Botto, J. C. Bernate, V. Garbin and K. J. Stebe, *Langmuir*, 2010, **26**, 15142–15154.
18. L. C. Bradley, W.-H. Chen and D. Lee, in *Anisotropic Particle Assemblies*, ed. N. Wu, D. Lee and A. Striolo, Elsevier, Amsterdam, 2018, pp. 201–231.

19. M. A. Creighton, Y. Ohata, J. Miyawaki, A. Bose and R. H. Hurt, *Langmuir*, 2014, **30**, 3687–3696.
20. B. Madivala, S. Vandebril, J. Fransaer and J. Vermant, *Soft Matter*, 2009, **5**, 1717–1727.
21. H. A. Wege, S. Kim, V. N. Paunov, Q. Zhong and O. D. Velev, *Langmuir*, 2008, **24**, 9245–9253.
22. P. F. Noble, O. J. Cayre, R. G. Alargova, O. D. Velev and V. N. Paunov, *J. Am. Chem. Soc.*, 2004, **126**, 8092–8093.
23. R. G. Alargova, D. S. Warhadpande, V. N. Paunov and O. D. Velev, *Langmuir*, 2004, **20**, 10371–10374.
24. A. Walther and A. H. E. Müller, *Chem. Rev.*, 2013, **113**, 5194–5261.
25. J. Hu, S. Zhou, Y. Sun, X. Fang and L. Wu, *Chem. Soc. Rev.*, 2012, **41**, 4356–4378.
26. B. P. Binks and P. D. I. Fletcher, *Langmuir*, 2001, **17**, 4708–4710.
27. A. Kumar, B. J. Park, F. Tu and D. Lee, *Soft Matter*, 2013, **9**, 6604–6615.
28. R. Aveyard, B. P. Binks and J. H. Clint, *Adv. Colloid Interface Sci.*, 2003, **100**, 503–546.
29. F. Wurm and A. F. M. Kilbinger, *Angew. Chem., Int. Ed.*, 2009, **48**, 8412–8421.
30. A. Walther and A. H. E. Müller, *Chem. Rev.*, 2013, **113**, 5194–5261.
31. A. Walther and A. H. E. Müller, *Soft Matter*, 2008, **4**, 663–666.
32. J. Hu, S. Zhou, Y. Sun, X. Fang and L. Wu, *Chem. Soc. Rev.*, 2012, **41**, 4356–4378.
33. L. C. Bradley, W.-H. Chen, K. J. Stebe and D. Lee, *Curr. Opin. Colloid Interface Sci.*, 2017, **30**, 25–33.
34. C. Casagrande, P. Fabre, E. Raphaël and M. Veyssié, *Europhys. Lett.*, 1989, **9**, 251–255.
35. S. C. Glotzer and M. J. Solomon, *Nat. Mater.*, 2007, **6**, 557–562.
36. Z. Nie, W. Li, M. Seo, S. Xu and E. Kumacheva, *J. Am. Chem. Soc.*, 2006, **128**, 9408–9412.
37. S. Jiang, M. J. Schultz, Q. Chen, J. S. Moore and S. Granick, *Langmuir*, 2008, **24**, 10073–10077.
38. C. Tang, C. Zhang, J. Liu, X. Qu, J. Li and Z. Yang, *Macromolecules*, 2010, **43**, 5114–5120.
39. G. Loget and A. Kuhn, *J. Mater. Chem.*, 2012, **22**, 15457–15474.
40. A. B. Pawar and I. Kretzschmar, *Macromol. Rapid Commun.*, 2010, **31**, 150–168.
41. A. Perro, S. Reculusa, S. Ravaine, E. Bourgeat-Lami and E. Duguet, *J. Mater. Chem.*, 2005, **15**, 3745–3760.
42. V. N. Paunov and O. J. Cayre, *Adv. Mater.*, 2004, **16**, 788–791.
43. S. Jiang, Q. Chen, M. Tripathy, E. Luijten, K. S. Schweizer and S. Granick, *Adv. Mater.*, 2010, **22**, 1060–1071.
44. F. Tu and D. Lee, *J. Am. Chem. Soc.*, 2014, **136**, 9999–10006.
45. J. Faria, M. P. Ruiz and D. E. Resasco, *Adv. Synth. Catal.*, 2010, **352**, 2359–2364.

46. T. M. Ruhland, A. H. Gröschel, N. Ballard, T. S. Skelhon, A. Walther, A. H. E. Müller and S. A. F. Bon, *Langmuir*, 2013, **29**, 1388–1394.
47. S. Jiang and S. Granick, *J. Chem. Phys.*, 2007, **127**, 161102–161105.
48. N. Glaser, D. J. Adams, A. Böker and G. Krausch, *Langmuir*, 2006, **22**, 5227–5229.
49. R. Aveyard, *Soft Matter*, 2012, **8**, 5233–5240.
50. P. Pieranski, *Phys. Rev. Lett.*, 1980, **45**, 569–572.
51. F. Tu, B. J. Park and D. Lee, *Langmuir*, 2013, **29**, 12679–12687.
52. D. Wu, J. W. Chew and A. Honciuc, *Langmuir*, 2016, **32**, 6376–6386.
53. T. Tanaka, M. Okayama, H. Minami and M. Okubo, *Langmuir*, 2010, **26**, 11732–11736.
54. C. Lu and M. W. Urban, *ACS Macro Lett.*, 2014, **3**, 346–352.
55. T. Yamagami, Y. Kitayama and M. Okubo, *Langmuir*, 2014, **30**, 7823–7832.
56. F. A. Plamper and W. Richtering, *Acc. Chem. Res.*, 2017, **50**, 131–140.
57. T. Ngai, S. H. Behrens and H. Auweter, *Chem. Commun.*, 2005, 331–333.
58. Z. Li and T. Ngai, *Nanoscale*, 2013, **5**, 1399–1410.
59. M. Destribats, V. Lapeyre, M. Wolfs, E. Sellier, F. Leal-Calderon, V. Ravaine and V. Schmitt, *Soft Matter*, 2011, **7**, 7689–7698.
60. K. Geisel, L. Isa and W. Richtering, *Langmuir*, 2012, **28**, 15770–15776.
61. B. Brugger, J. Vermant and W. Richtering, *Phys. Chem. Chem. Phys.*, 2010, **12**, 14573–14578.
62. S. Schmidt, T. Liu, S. Rütten, K.-H. Phan, M. Möller and W. Richtering, *Langmuir*, 2011, **27**, 9801–9806.
63. Z. Li, T. Ming, J. Wang and T. Ngai, *Angew. Chem., Int. Ed.*, 2009, **48**, 8490–8493.
64. H. Zou, S. Wu and J. Shen, *Chem. Rev.*, 2008, **108**, 3893–3957.
65. R. Barbey, L. Lavanant, D. Paripovic, N. Schüwer, C. Sugnaux, S. Tugulu and H.-A. Klok, *Chem. Rev.*, 2009, **109**, 5437–5527.
66. E. Ruckenstein and Z. F. Li, *Adv. Colloid Interface Sci.*, 2005, **113**, 43–63.
67. J. I. Amalyv, S. P. Armes, B. P. Binks, J. A. Rodrigues and G.-F. Unali, *Chem. Commun.*, 2003, 1826–1827.
68. B. P. Binks, R. Murakami, S. P. Armes and S. Fujii, *Angew. Chem., Int. Ed.*, 2005, **44**, 4795–4798.
69. B. G. Rånby, *Discuss. Faraday Soc.*, 1951, **11**, 158–164.
70. I. Kalashnikova, H. Bizot, B. Cathala and I. Capron, *Langmuir*, 2011, **27**, 7471–7479.
71. F. Cherhal, F. Cousin and I. Capron, *Biomacromolecules*, 2016, **17**, 496–502.
72. I. Capron and B. Cathala, *Biomacromolecules*, 2013, **14**, 291–296.
73. Y. Habibi, L. A. Lucia and O. J. Rojas, *Chem. Rev.*, 2010, **110**, 3479–3500.
74. J. Tang, M. F. X. Lee, W. Zhang, B. Zhao, R. M. Berry and K. C. Tam, *Biomacromolecules*, 2014, **15**, 3052–3060.
75. M. Hu, D. J. McClements and E. A. Decker, *J. Agric. Food Chem.*, 2003, **51**, 1435–1439.

76. H. Tan, Z. Tu, H. Jia, X. Gou and T. Ngai, *Langmuir*, 2018, **34**, 4820–4829.
77. D. Rousseau, *Curr. Opin. Colloid Interface Sci.*, 2013, **18**, 283–291.
78. S. Ghosh and D. Rousseau, *Curr. Opin. Colloid Interface Sci.*, 2011, **16**, 421–431.
79. D. Rousseau, *Food Res. Int.*, 2000, **33**, 3–14.
80. S. Frasch-Melnik, I. T. Norton and F. Spyropoulos, *J. Food Eng.*, 2010, **98**, 437–442.

## CHAPTER 11

# *Latexes for Advanced Coatings*

J. KLIER,\* S. TREVENEN AND P. J. BELTRAMO

University of Massachusetts Amherst, Department of Chemical Engineering, 686 North Pleasant Street, 159 Goessmann Laboratory, Amherst, MA 01003-9303, USA

\*Email: klier@umass.edu

## 11.1 Evolution of Latexes for Advanced Coatings

### 11.1.1 Background

Polymer dispersions based on vinyl addition, epoxy, polyurethane, alkyd, polyester and other chemistries, represent a very large and growing coating materials segment. Vinyl addition emulsion polymers based on acrylics, styrene acrylics and vinyl acrylic chemistries represent the single largest polymer dispersion category employed in coating applications and are most commonly used as binders in coating formulations along with pigments, rheology modifiers, dispersants and other ingredients. These materials are so ubiquitous because they combine performance with low cost and environmentally friendly “low VOC” low solvent or solvent-free coating capability. Emulsion polymer technology has evolved rapidly in the past decades to meet increasingly stringent VOC regulations and customer expectations, provide unique and valuable customer and consumer features and provide an environmentally friendly water-based option for demanding industrial, aftermarket, and maintenance and packaging applications.

### 11.1.2 Architectural Coatings

Key technical advances in emulsion polymers include morphological control, such as multilobal structures developed in the 1980s to enhance rheological properties for improved coating film formation (Figure 11.1). Multiphase emulsion polymers with higher glass transition temperature ( $T_g$ ) inclusions were introduced in the 1980s and 1990s to enable the enhanced performance of low VOC (low solvent) water-based coatings. These materials allow film formation along with enhanced coating mechanical properties without the need for excessive solvent levels. Hollow sphere emulsion polymers were developed and introduced in the 1980s. These highly engineered particles contain hydrated hydrophilic polymer cores with resilient polymer shells. Upon incorporation into a coating formulation and water evaporation, the core dehydrates to a hollow void in the coating film. These voided structures scatter light and greatly enhance the opacity of coating formulations. Similar emulsion polymer structures have recently been employed in consumer product sunscreen formulations and as enabling components of thermal printing paper – where the hollow voids collapse under the effect of heat, eliminating the scattering effect and allowing the substrate color to penetrate through the coating film.

New functional monomers were incorporated into emulsion polymers to provide enhanced properties of the resulting coatings. For example, functional monomers such as low-viscosity copolymers of poly(acrylic acid) allow emulsion polymers to tightly bind to metal substrates,<sup>1</sup> enhancing corrosion protection. They also enable spontaneous pigment encapsulation during paint formulation to enhance mechanical properties, enhance water and stain resistance, and improve scattering and opacity. Other functional polymers enable scavenging of potentially harmful pollutants in the indoor environment, contributing to indoor air quality and quality of life.<sup>2,3</sup>

Advanced crosslinking technologies, including self-crosslinking emulsion polymer chemistries, provide enhanced coating mechanical and barrier properties while still allowing stable, water-based low VOC emulsion polymers/dispersions. These chemistries address environmental pressures,

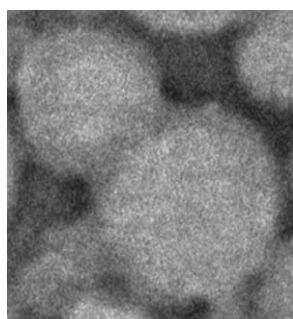


**Figure 11.1** Electron micrograph of latex with lobe structure.  
Courtesy of A. Brouillard, UMass Amherst Chemical Engineering.

allowing use of soft film-forming emulsion polymers with reduced VOC and Hazardous Air Pollutant (HAP) levels while providing development of excellent properties including mechanical strength,  $T_g$ , block, chemical and solvent resistant properties<sup>4,5</sup> after film formation. Alkyd chemistries, for example, provide an oxidative cure and enable one pack coating formulations that crosslink under ambient conditions.<sup>6,7</sup>

### 11.1.3 Industrial Coatings

New functional monomer chemistries also provide enhanced properties to emulsion polymer-based coatings in industrial applications. Recently introduced advanced hybrid latex technologies combine the stable, UV resistant attributes of acrylic emulsion polymers with the superior corrosion resistance of traditional thermoset chemistries to achieve the best of both worlds – low VOC water-based coatings with very high performance for industrial or highly demanding architectural applications. Vinyl emulsion polymers have also been hybridized with a host of other chemistries such as urethane, alkyd, polyester *etc.* to provide specific performance enhancements.

Water-based coatings have also found application in demanding applications such as road markings. Here water-based formulations provide reduced VOC and HAP content *versus* solvent-borne alternatives. The industry has successfully developed quick setting latex systems that rapidly build up physical properties, resist rain washoff and withstand traffic while developing final film properties (Figure 11.2). These systems may be based on “coacervate” type physical associations where amine-containing polymers are combined with ammonia neutralized carboxylated latexes. Application and ammonia evaporation results in rapid set *via* electrostatic interactions. Subsequent film formation takes place *via* traditional polymer interdiffusion driven by capillary actions.<sup>8</sup>

Advanced emulsion polymer coatings have also recently been employed to suppress vibration and resulting noise in transportation and industrial

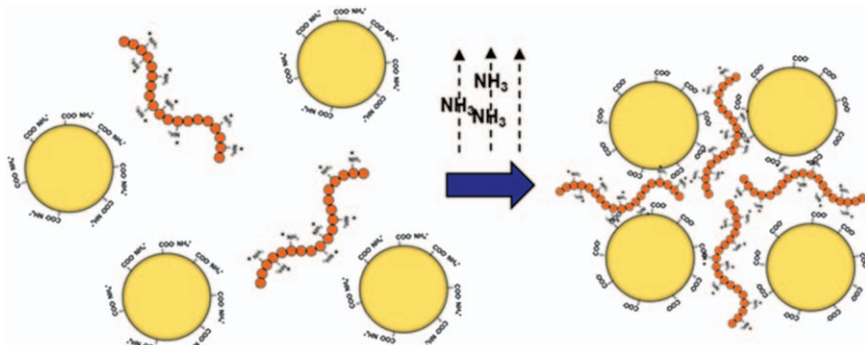


**Figure 11.2** Schematic of quick setting latex systems for traffic marking.

applications. These emulsion copolymers, employed in “liquid applied sound damping” formulations, may be robotically applied to automotive frames. The coatings are engineered to dampen vibrations in certain frequency ranges (typically 200 Hz) and ambient temperatures. New sophisticated emulsion polymers contain associative functional groups that interact with pigments to greatly enhance sound damping efficiency.<sup>9</sup>

Demanding vehicle and transportation equipment applications have also necessitated the development of advanced emulsion polymer based coating systems. Fully 60 to 70 percent of automotive basecoats in North America and Europe may be water-borne with a continuing trend in this direction. The base coat formulations provide color and optical effects and may contain high performance organic pigments, metal flakes, carbon black and special grades of titanium dioxide. Acrylic emulsion polymers may be blended with polyester-based polyurethane dispersions to enhance mechanical properties such as toughness. Water removal from these coatings prior to clearcoat application may take place at elevated but not full curing temperatures to accelerate process throughput and line speed.<sup>10</sup>

### 11.1.4 New Technological Applications of Anisotropic Latexes

While colloid chemistry has made significant advances, utilizing a multitude of functional groups and chemical processing advances to motivate an ever expanding list of uses, the physical shape of colloids has remained mainly spherical. Spherical geometries are by definition isotropic and produce isotropic material properties in applications such as coatings, nanofluids, and thin films. In nature, however, we see a variety of material properties defined not by their unique chemistries, but instead by their unique, and asymmetric structural design. From the iridescent wings of butterflies<sup>11</sup> to the changing color of chameleon skin<sup>12</sup> to the birefringence of calcite,<sup>13</sup> nature takes advantage of anisotropic micro-material design to achieve macro-material properties. This brings additional challenges when fabricating advanced coatings from anisotropic polymer colloids. First, efficient synthetic routes towards size- and shape-controlled microparticles must be established. Second, since the coating material properties are dependent on the particle microstructure, the creation of such surfaces requires control over the particle alignment before and during the process. This is in addition to all of the considerations for coatings from spherical particles. However, the additional applications of anisotropic particle-based coatings makes accomplishing such materials a worthy aim. In the remainder of this chapter, we revisit the synthesis of polymer ellipsoids by mechanical stretching above their glass transition temperature. In the future, the use of external fields (convective, capillary, electric, magnetic) to control alignment and microstructure in the fabrication of coatings based on these particles will be explored.

An efficient and scalable route to anisotropic colloids is the mechanical stretching of spherical polymer colloids into ellipsoids above the glass transition temperature of the polymer. While this method has been well studied,<sup>14</sup> and a device designed to continuously produce ellipsoidal polymer particles,<sup>15</sup> crucial variables such as the stretch time and temperature as well as the polymer film properties have not been systematically investigated. Published procedures use polymer films that vary extensively in molecular weight and perform the mechanical stretching at widely varying temperatures as well,<sup>14,15</sup> all of which can have important effects on the microstructural environment around the embedded polymer particles, affecting their monodispersity and size. In order to address these opportunities more fully, we are developing a systematic understanding of the effects of process variables on control of anisotropic colloid shape and uniformity. This in depth understanding will ultimately contribute to scalable processes for new categories of high technology coatings based on anisotropic polymer colloids.

## 11.2 Experimental

### 11.2.1 Film Formation

250 microliters of the 10 wt%, 1.0 micron diameter, sulfate-modified polystyrene spheres (Sigma-Aldrich), were added to 40 mL of 5 wt% poly(vinyl alcohol) (PVOH, 85 000–120 000 g mol<sup>-1</sup>, 88% hydrolysis), previously dissolved in Milli-Q water (Milli-Q, resistivity > 18.2 MΩ cm), and thoroughly mixed for 30 mins by rotomixer (30 rpm). 200 mL of PVOH from the same batch was then added to a Teflon cast measuring 23.5" × 3.5" × 0.18" (Length × Width × Depth). The thoroughly mixed solution of spheres in PVOH was then added to the central point of the cast and allowed to spread naturally through the liquid solution. This solution was then allowed to dry naturally until it was solid enough to be taken out of the cast as one whole film. The edges ( $\frac{1}{4}$ " width) along the entire rectangular film was cut to avoid inconsistencies due to adhesion to the sides of the cast. The film was then dried flat for two days. It is important to thoroughly dry the cast film to remove all trapped water since plasticization can cause glass transition point depression in the embedding film.

### 11.2.2 Sample Preparation

#### 11.2.2.1 Film Stretching

The film was marked with  $\frac{1}{2}"$  lines along its length, in order to have a reference for the stretched film. The film was then added to a custom-built stretching machine and dipped in a bath of silicone oil raised to a specified temperature undergoing mild mechanical agitation (180 rpm). The film was then stretched after a five-minute period of thermal equilibration, with a

decreasing portion of the film staying in the oil bath as the stretching occurs. The film was raised out of the hot oil bath after 30 mins all the while maintaining its final strained amount. After about 30 mins of drip drying and air-cooling the film was removed. The film thickness was re-measured and the length between each of the previously  $\frac{1}{2}$ " sections was measured in three places along the width of the film (in the center,  $\frac{1}{2}$ " from both edges).

#### 11.2.2.2 Sample Resuspension and Purification

Samples were cut at specific  $\frac{1}{4}$ " or  $\frac{1}{2}$ " strips along the length (pre-stretching) and separately cleaned in mildly agitated isopropyl alcohol to remove adhered silicone oil from the surface of the films. The film strips were then dissolved overnight in 10 mL of Milli-Q water. Each sample was then centrifuged for 1 hour at  $8000\times g$ . The centrifuged samples then had 9 mL of supernatant removed followed by an addition of 10 mL of water. The samples were then sonicated for an equal amount of time to resuspend the particles and break up any aggregates. This procedure was carried out twice with the second removal of supernatant being 10 mL. The next four dilution cycles were carried out with the same basic procedure as the second cycle step except as noted. On the 3rd and 4th cycles, the centrifugation was for 30 mins at  $4000\times g$  with a 30 min sonication step after each centrifugation. The 5th and 6th dilution cycles were centrifuged for 10 mins at  $4000\times g$  with 10 min sonication after each cycle. When complete, the samples were sonicated for an additional hour. The resultant particles are analyzed by scanning electron microscope after being drop cast and sputter coated with 2 nm of gold.

### 11.3 Results and Discussion

In order to understand how the aspect ratio of monodispersed polymer colloids could be precisely controlled, the crucial variables such as the stretch time and temperature, as well as the polymer film properties were systematically investigated. We highlight here the importance of stretching temperature, while other variables are still being examined. The stretching temperature relative to the glass transition temperature of the particles had a very strong influence on the resulting aspect ratio, as shown in Figure 11.3. In this set of experiments, the draw ratio of the film was kept constant at approximately 3 : 1, as determined by monitoring the stretching of the  $\frac{1}{2}$ " markings on the film; however, large differences in the resultant ellipsoids were observed. Polystyrene spheres of initial diameter 1  $\mu\text{m}$  stretched at temperatures above their glass transition ( $>107^\circ\text{C}$ ) were readily deformed into controlled, nearly monodispersed asymmetric polymer colloids. However, below  $T_g$  of the film, the deformation of the PVOH film did not translate to the embedded particles, and the particles largely remained spherical. A summary of the ellipsoid dimensions is given in Figure 11.4A.

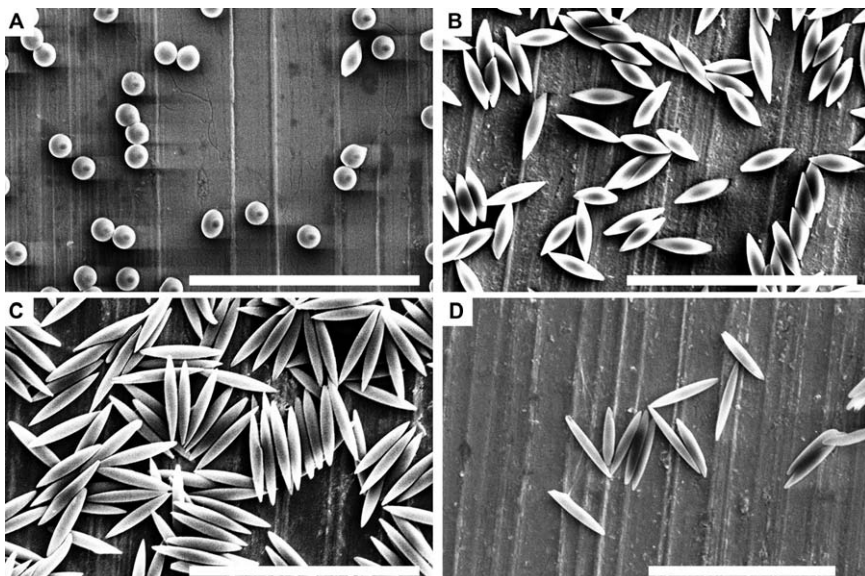


**Figure 11.3** SEM images of ellipsoids stretched at (A) 102 °C (B) 108 °C (C) 114 °C and (D) 128 °C. The scale bar represents 10 µm.

Although the draw ratio of the film was only 3 : 1, particle aspect ratios up to approximately 6 : 1 were realized when the stretching was carried out at elevated temperatures (Figure 11.4B). This was due to the particles simultaneously elongating and narrowing as the stretching occurs (Figure 11.4A). Above  $T_g$ , the stretching in the longitudinal (long axis) direction of the particle corresponds nicely with the 3 : 1 draw ratio. As Figure 11.4B shows, the transition in stretching behavior aligns with the glass transition temperature of the particles, confirming that this is a key parameter for the successful control of anisotropic particle synthesis. Controlling the precursor emulsion polymer and polymer dispersion size further allows control of both aspect ratio and absolute size, and these investigations are underway. Particularly for optical applications, modification of polymer colloid composition allows tuning of refractive index. These new materials are being employed for a new type of optical coating and results exemplified here are helping identify critical process parameters for scalable production of these coatings.

## 11.4 Conclusion

Emulsion polymer technology has evolved rapidly in the past decades to meet increasingly stringent VOC regulations and allow environmentally friendly water-based emulsion polymers to successfully compete in demanding architectural, industrial, aftermarket, maintenance and packaging applications. Increasing demands for green and sustainable coatings are

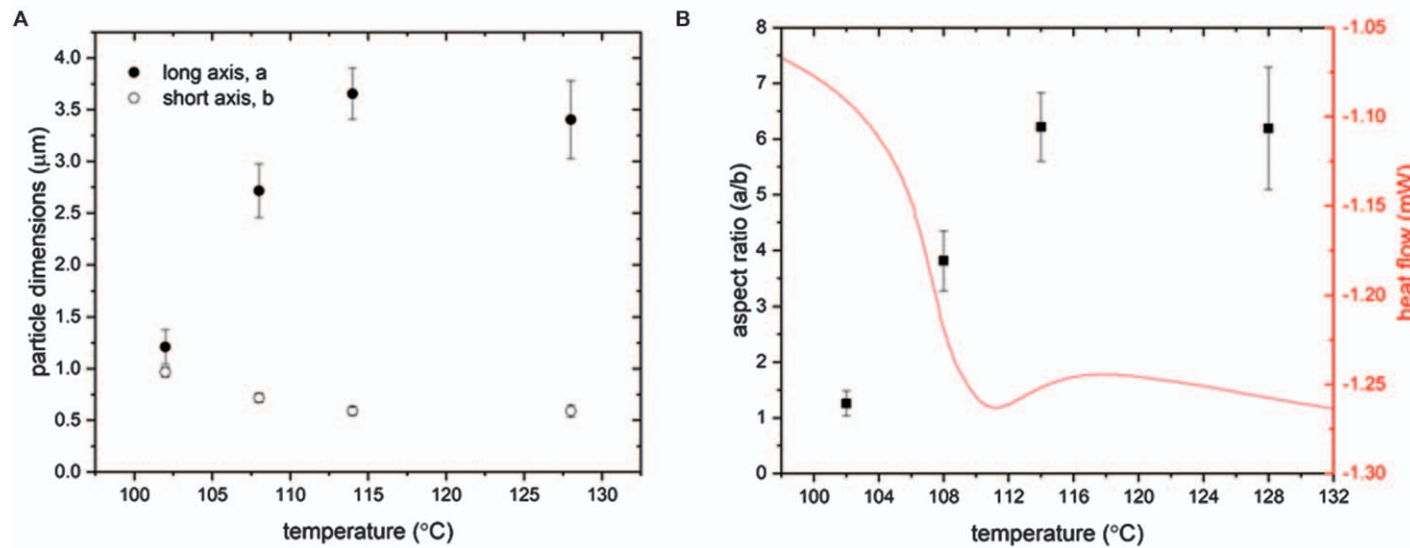


**Figure 11.4** (A) The long and short axis of 1 μm diameter polystyrene spheres stretched at a 3:1 draw ratio at the given temperatures. (B) Aspect ratio of the particles drawn along with a heat flow diagram of the seed spheres showing the  $T_g$  of approximately 107 °C.

especially driving adoption of latex-based coatings based on vinyl addition chemistries. Key technical advances include morphological control to enhance rheological and film-forming properties, new crosslinking chemistries to enhance physical properties, functional monomers to enhance adhesive and surface properties, and hybrid chemistries to provide corrosion resistance, toughness and a host of other property benefits.

Examples of advanced emulsion polymers include association behavior for hiding and performance, functionality for cleaner air, hybrid chemistry for improved chemical resistance and adhesion, crosslinking for improved physical properties and low VOC levels, complexation for quick setting performance and new monomers for new modes of emulsion polymerization. In addition, emulsion polymers have been successfully exploited in a host of new applications from medical diagnostics to optical applications. For example, anisotropic latexes and polymer colloids are being exploited for advanced optical applications. Synthesis conditions provide control over chemical composition and important properties such as refractive index and glass transition temperature. Tuning of process parameters such as temperature and deformation provides precise control over shapes and aspect ratios.

## References

1. B. Escaig, Binding metals to polymers. A short review of basic physical mechanisms, *J. Phys. IV, Colloq.*, 1993, **3**, 753–761.
2. J. Klier, J. Bohling and M. Keefe, *AICHE J.*, 2016, **62**(7), 2238–2247.
3. <http://coatings.dow.com/en/products/formashield>.
4. N. Kessel, D. R. Illsley and J. Keddie, *J. Coat. Technol. Res.*, 2008, **5**, 285–297.
5. W. Want, Z. Lu, Y. Cao, J. Chen, J. Wang and Q. Zheng, *J. Appl. Polym. Sci.*, 2012, **123**(3), 1822–1832.
6. R. N. Patil, B. V. Sharma and P. A. Mahanwar, *Chem. Sin.*, 2012, **3**(2), 458–467.
7. Paint and Coatings Industry, <http://www.pcimag.com/articles/101064-let-there-be-day-light>, 2015.
8. F. Landy, A. Mercurio and R. Flynn, *U. S. Pat.* 5,527,853, 1996.
9. A. R. Hermes, A. J. Swartz and D. E. Williams, *U. S. Pat. Appl.* 20080153969A1, 2008.
10. N. K. Akafuah, S. Poozesh, A. Salaimeh, G. Patrick, K. Lawler and K. Saito, *Coatings*, 2016, **6**(2), 24.
11. H. Ghiradella, *Appl. Opt.*, 1991, **30**, 3492–3500.
12. J. Teyssier, S. V. Saenko, D. Van Der Marel and M. C. Mlinkovitch, *Nat. Commun.*, 2015, **6**, 1–7.
13. R. N. Smartt and W. H. Steel, *J. Opt. Soc. Am.*, 1959, **49**, 710.
14. C. Ho, A. Keller, J. Odell and R. H. Ottewill, *Polym. Int.*, 1993, **30**, 207–211.
15. J. A. Ferrar, L. Pavlovsky, E. Viges, Y. Liu and M. J. Solomon, *AICHE J.*, 2018, **64**, 697–707.

## CHAPTER 12

# *Polymer Colloids Enable Medical Applications*

CHRISTINA TANG,<sup>\*a</sup> SHANI LEVIT,<sup>a</sup> MICHAEL ZEEVI,<sup>a</sup>  
CHRIS VASEY<sup>a</sup> AND CATHERINE FROMEN<sup>b</sup>

<sup>a</sup>Virginia Commonwealth University, Department of Chemical and Life Science Engineering, 601 West. Main Street, Richmond, VA 23284-3028, USA; <sup>b</sup>University of Delaware, Department of Chemical and Biomolecular Engineering, 150 Academy St., Newark, DE 19716, USA

\*Email: ctang2@vcu.edu

## 12.1 Introduction

Polymers are widely used in pharmaceutical formulations and drug delivery systems across length scales (macro-, micro-, and nano-systems). Miniaturization of such systems could enable on-demand, targeted delivery of therapeutic drugs to organs and cells, as well as cell substructures of interest. For example, active pharmaceutical ingredient (API)-loaded polymer micro-particles act as drug delivery depots. Such particles are approved by the United States Food and Drug Administration (FDA) for clinical applications such as delivery of chemotherapies or hormones over days to weeks. Nanoscale systems, *i.e.* polymer colloids, have demonstrated abilities to affect pharmacokinetic properties of traditional formulations.<sup>1</sup>

The concept of nanomedicine began in the early 20th century by Paul Ehrlich with the idea of a ‘magic bullet’ that selectively kill the ‘bad’ and spare the ‘good’. Rather than administering a free API directly to the body, encapsulation of that same molecule within a larger nanoparticle platform simultaneously protected the body from the API and the API from the body.

The first generation of nanomedicine (1950–1980) focused on such drug formulations, *e.g.* liposomes, to achieve controlled release (Figure 12.1).<sup>2</sup> Nanoscale drug encapsulation using liposome formulations (80–300 nm spherical vesicles with a phospholipid bilayer barrier) increased drug efficacy<sup>2,3</sup> and was approved by the United States FDA in 1995. Doxil, a liposomal formulation of doxorubicin (a chemotherapeutic agent), reduced cardiotoxicity improving patient morbidity compared to the conventional free-drug formulation.<sup>2,4,5</sup>

While reformulation of small molecule APIs into larger physical nanoparticle constructs yielded promising results to overcome biological barriers during circulation, the change in length scale also introduced new challenges. The second generation of nanomedicine (1980–2010), focused on “smart delivery systems” to overcome biological barriers of the circulatory system, such as nanoparticle clearance by opsonisation in order to capitalize on the Enhanced Permeability and Retention (EPR) effect. According to the EPR effect, nanoparticles delivered intravenously (IV) preferentially accumulate at the site of diseased tissue due to its leaky vasculature, occurring most notably in solid tumors. Key technologies from this era included: smart polymers and hydrogels, PEGylation, and widespread use of solid polymer nanoparticles. Surface functionalization with polyethylene glycol (PEG), *i.e.* PEGylation, enhances drug stability *in vivo* by preventing enzymatic attack and recognition by the immune system, which increases circulation time.

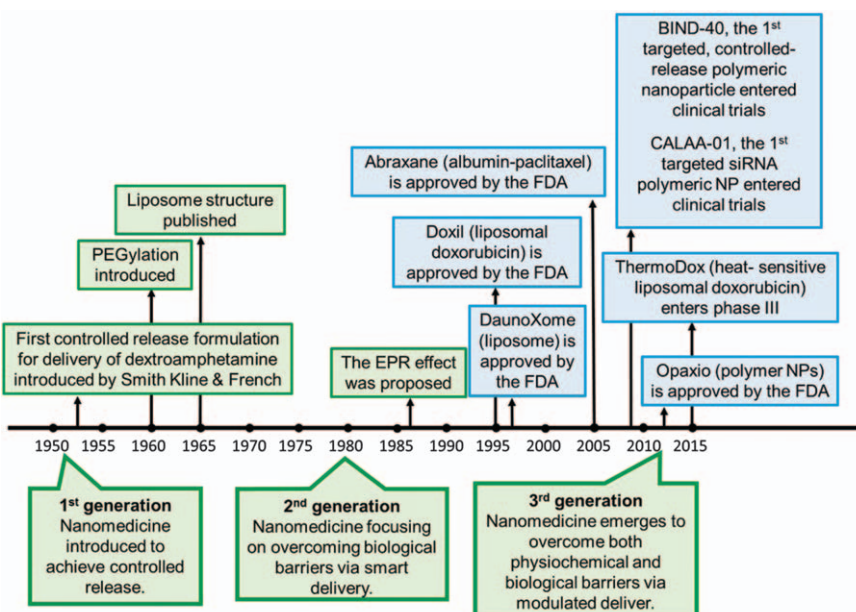


**Figure 12.1** Timeline outlining the evolution (green) and clinical milestones (blue) of nanomedicine.

This increased circulation time is especially important for passive targeting to disease sites using the EPR effect.<sup>2,3,6</sup>

The field of nanomedicine has continued to grow exponentially to develop systems that overcome biological barriers of every route of administration and can interface directly with the immune system. The current generation of nanomedicine (2010–present) seeks to create nanoparticle systems that can further overcome physiochemical and biological barriers by controlling nanoparticle morphology, implementing active targeting to improve therapeutic efficiency, achieving stimuli-responsiveness to enhance specificity, and delivering payloads over long-time periods (*e.g.* weeks to months).<sup>2,3,6</sup> As the field expands to increasingly complicated biological systems, technical advances stemming from polymer colloids and fundamental understanding of colloidal interactions with biological systems will continue to drive translational advances towards the ‘magic bullet’ promise of nanomedicine.

This chapter provides an overview of the use of polymer colloids in nanomedicine for API delivery applications. Material selection and nanomedicine processing are addressed. The effect of colloid properties on performance are explored. Emerging applications and regulatory considerations for clinical translation are briefly discussed.

## 12.2 Material Selection

Polymer selection is an important consideration when designing nanocarriers for therapeutic agents. Both natural and synthetic polymer systems have been explored.<sup>7</sup> For both classes of materials, polymer properties such as molecular weight, glass transition temperature, crystallinity, and hydrophobicity are important parameters that affect drug release.<sup>8</sup> The biocompatibility of the material must also be considered.

For nanomedicines, the biocompatibility of the polymer material is crucial. Traditionally, a biocompatible material minimizes inflammatory response and immunogenicity to avoid a foreign body reaction that would be characterized by severe inflammation, opsonization, and fibrosis and is clearly harmful to the patient.<sup>9,10</sup> The term ‘biocompatible’ has been primarily used for implanted devices and is applied to materials that produce normal tissue surrounding the device. Recently, the definition of biocompatibility in the context of nanomedicine has been further specified with the term of ‘biotolerable’ materials. Biotolerable materials can still produce some aspects of a foreign body reaction but do not secrete toxins and result in stable, long-term circulation. Therefore, biotolerable materials are not necessarily biocompatible.<sup>11</sup> Furthermore, biodegradable materials decompose into building blocks that are ubiquitous components occurring naturally in the body. To determine the biocompatibility or biotolerance of materials or materials in new applications, the bioresponse needs to be evaluated. Typically, the biocompatibility of materials can be assessed by evaluating the cytotoxicity, hemocompatibility, irritation, sensitization, systemic toxicity, cytokine production, and pyrogen formation.<sup>12</sup> This must

be assessed for each new polymer formulation early in development to establish clinical feasibility.

Many biocompatible, biotolerable, and biodegradable polymeric nanoparticle systems have been evaluated. Natural polymers include proteins and polysaccharides.<sup>13–15</sup> Although natural polymers are biodegradable, they can have active and unwanted biological function, or can be recognized by cells leading to immunogenicity. Properties of natural polymers such as mechanical strength and hydrophobicity can suffer from batch to batch variability affecting their reliability.<sup>16,17</sup> Synthetic polymer properties are reproducible between batches and their mechanical, chemical, and degradable properties can be tuned. However, without proper consideration, many synthetic polymers can induce inflammation or opsonization by the immune system. The immune response can be reduced with proper coatings.<sup>10</sup> We provide a brief overview of both natural and synthetic polymers that have been used in nanomedicine. More extensive reviews are available elsewhere.<sup>18,19</sup>

### 12.2.1 Natural Polymers

Initial work on the formation of particles using natural polymers included protein-based systems, which have been considered for delivery of hydrophilic and hydrophobic active ingredients.<sup>20,21</sup> For example, albumin has been used as a nanoparticle drug carrier due to its high endogenous abundance,<sup>21</sup> relative stability,<sup>21</sup> and ability to reversibly bind hydrophobic APIs. Commercially, Abraxane is an albumin bound paclitaxel formulation (*nab-paclitaxel*) that has been FDA approved for treating breast cancer.<sup>20,22</sup>

Other proteins used for nanoparticle delivery include gelatin, a protein derived from collagen. Gelatin is often modified, *e.g.* crosslinking with glutaraldehyde, to increase stability and circulation time or binding ligands to the surface.<sup>21</sup> Zein, a corn protein, has also been used to stabilize colloidal particles for medical applications. For example, zein nanoparticles were made by Flash NanoPrecipitation (FNP) as a biodegradable alternative to polymer stabilizers; zein self-assembled onto a precipitating core of the active ingredients.<sup>23</sup> Other proteins that have been considered are milk, soy, whey, and gluten proteins.<sup>21</sup> Drugs can be encapsulated in protein nanoparticles by electrostatic interactions, kinetic stabilization, natural affinity, or chemical reaction. The release of APIs from the nanoparticles can be induced by biodegradation and diffusion, as well as triggered by pH or reducing environments.<sup>24</sup>

Two commonly used polysaccharides in nanoparticle formulation have been chitosan and hyaluronic acid (HA) (Figure 12.2). Chitosan is derived from chitin found in crustaceans. Its positive charge makes it a useful carrier for gene and RNA therapies<sup>25,26</sup> and its low solubility allows for long *in vivo* circulation.<sup>27</sup> The rate of its degradation is dependent on the degree of crystallinity, which can be tuned with deacetylation of chitin or addition of side groups.<sup>28</sup> In contrast, HA is a highly water-soluble linear polysaccharide.

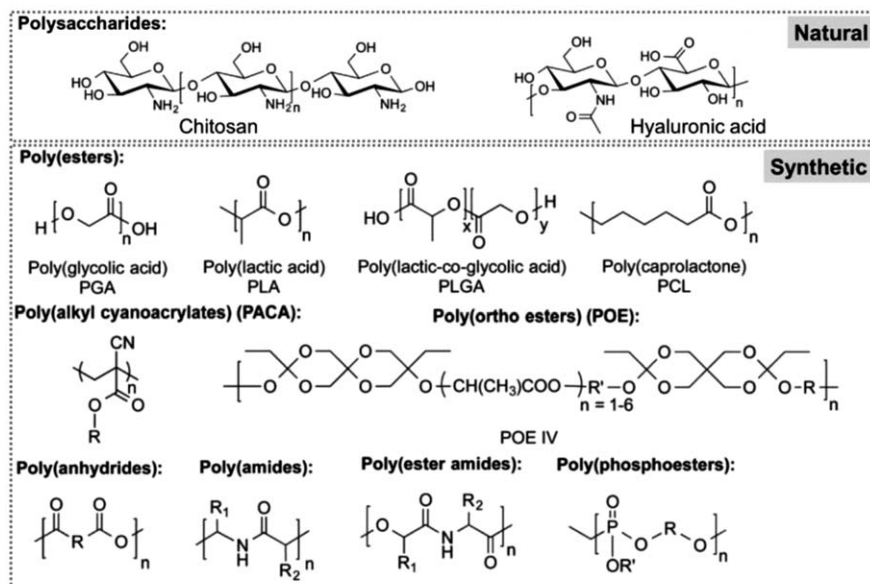


**Figure 12.2** Structures of polysaccharides and degradable synthetic polymers used in drug delivery.

Reproduced from ref. 19 with permission from American Chemical Society, Copyright 2016.

For drug delivery, therapeutics are either encapsulated within hydrogel systems or directed conjugated to the HA.<sup>14</sup> Conjugation has been found to improve API solubility and pharmacokinetics.<sup>14,29</sup> HA also has interesting binding properties to glycoproteins that are highly upregulated in many solid tumors<sup>30</sup> resulting in differential targeting to tumor cells.<sup>14,31,32</sup>

### 12.2.2 Synthetic Polymers

A wide range of synthetic polymers have been proposed as drug delivery carrier materials. Ideally, polymeric nanoparticle components would degrade and be easily eliminated from the body without producing harmful byproducts.<sup>19,33</sup> The degradation rate of the polymer is an important design criteria and is associated with the hydrophobicity of the material. Generally, more hydrophobic materials degrade at slower rates due to low affinity with water.<sup>34-36</sup> Polymer properties including molecular weight and crystallinity in addition to hydrophobicity can greatly impact degradation rate and are often interrelated.<sup>37,38</sup>

Crystallinity, *i.e.* the internal molecular organization, is an important factor because it affects water permeability.<sup>39</sup> Most polymers are considered semicrystalline and contain varying degrees of crystalline and amorphous (non-crystalline) regions.<sup>39,40</sup> The glass transition temperature ( $T_g$ ) and ratio of amorphous to crystalline region dictate the degradation rates, pore

formation, and the resulting API release rate.<sup>39</sup> Polymer molecular weight affects hydrophobicity, crystallinity, and  $T_g$ .<sup>19,37,41</sup> The overall effect is that lower molecular weight polymers tend to have a faster degradation rate when compared to the same polymer of higher molecular weight.<sup>42,43</sup>

Polymer degradation determines the drug release mechanism(s). In systems of non-degradable polymers, drug molecules release *via* diffusion driven by concentration gradients.<sup>44</sup> For systems of degradable polymers, drug molecules are released due to diffusion as well as surface erosion or bulk erosion.<sup>45,46</sup> Surface erosion occurs when the rate of polymer degradation is greater than water penetration, whereas bulk erosion occurs when water penetration is greater than polymer degradation. Achieving surface erosion is desirable because the drug release is more predictable than bulk erosion.<sup>19</sup> Hydrophobic polymers such as polylactic acid (PLA), polyglycolide (PGA), and poly(lactic-co-glycolic acid) (PLGA) typically exhibit bulk erosion, while polymers such as poly(ethylene oxide) (PEO) and polyanhydrides degrade *via* surface erosion. Polycaprolactone (PCL) degrades *via* both bulk and surface erosion.<sup>47</sup>

The release mechanism affects drug release kinetics. Zero-order release or sustained release maintains therapeutic dose, but is difficult to achieve in practice (Figure 12.3). Typical drug release is triphasic or biphasic. There is often an initial burst release due to release of surface-bound drug molecules. This phase is followed by sustained release due to diffusion. A second burst release may occur due to bulk erosion.<sup>48</sup> The degradation rates can be slowed by adding coatings to prevent burst release.<sup>35,48,49</sup>

The most commonly used polymers for nanomedicine have been aliphatic polyesters, as these systems are biodegradable and breakdown into lactic and glycolic acids,<sup>19</sup> which are ubiquitous in physiological systems. For example, poly(glycolic acid) (PGA) is a highly crystalline polymer that is poorly soluble with a fast degradation rate.<sup>51</sup> Polylactic acid (PLA) is a tunable system; its crystallinity, mechanical rates and degradation rate can be modulated by varying the relative amounts of the D- and L-lactic acids in the chain.<sup>51</sup> The D-lactic acid is amorphous while L-lactic acid has a high degree of crystallinity. Thus, the degree of crystallization and related properties of PLA can be tuned by varying the stereochemistry of the monomers. Alternatively, PLA can be combined with highly crystalline PGA to achieve PLGA with a desired intermediate crystallinity (Table 12.1).<sup>41</sup> Decreasing the ratio of lactide to glycolide in PLGA decreases the degradation rate.<sup>51</sup> These polymers can be modified to include a hydrophilic chain such as polyethylene glycol (PEG) to improve solubility.<sup>52</sup> Another commonly used polyester is polycaprolactone (PCL); however, it is less common in nanoparticle drug delivery than PLA and PLGA due to slow degradation and low solubility.<sup>53</sup>

Another class of polymers colloids used for nanomedicine are polyalkyl cyanoacrylates (PACAs). PACAs are biodegradable, release API *via* surface erosion, and can be completely eliminated from the body.<sup>51,54</sup> One type of PACA with lactic or glycolic monomers is type IV polyortho ester (POE),

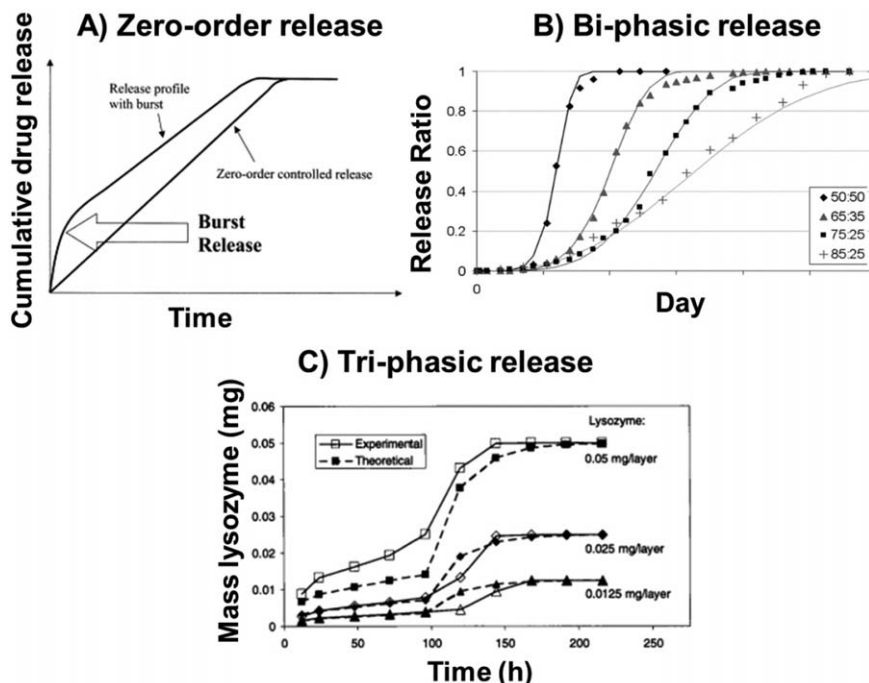


**Figure 12.3** Release profiles of (A) zero-order release with and without burst release,<sup>49</sup> (B) biphasic drug release due to hydrolytic degradation exhibiting bulk degradation, (C) triphasic degradation with an initial burst release followed by diffusion-controlled and degradation-controlled release.<sup>50</sup>

(A) Reproduced from ref. 50 with permission from Elsevier, Copyright 2001. (B) Reproduced from ref. 41, <http://dx.doi.org/10.3390/polym3031377>, under the terms of the CC BY 3.0 licence, <https://creativecommons.org/licenses/by/3.0/>. (C) Reproduced from ref. 50 with permission from Taylor and Francis, Copyright 2001.

**Table 12.1** Properties of commonly used synthetic polymers.

Polymers	Crystallinity	Glass transition ( $T_g$ )	Degradation	Hydrophobicity
PGA	Highly	35–40	Fast	Hydrophobic
PLA				Hydrophobic
PLLA	Semicrystalline	53	Slow	
PDLA	Amorphous	55	Slow (cryst)	
PLGA (50 : 50)			1–2 months (88)	
PLGA (75 : 25)			4–5 months	
PLGA (85 : 15)			5–6 months	
PCL		–60	2–3 years	Hydrophobic

which can be used for drug delivery. The degradation of such PACAs can be tuned by the monomer groups in the polymer chain.<sup>55</sup> Polyamino acids are another type of PACA that have been investigated for nanoparticle drug

delivery of low molecular weight drugs. Polyamino acids are soluble and biodegradable. Their rate of degradation depends on the amino acid constituents. For example, poly(L-lysine) has been commonly used for gene or RNA delivery due to its positive charge. Polyphosphoesters are another class of PACA. Their structure is similar to nucleic acids and facilitates conjugation to therapeutic agents. Polyphosphoesters are broken down by hydrolysis and enzymatic degradation.<sup>56</sup> Water-soluble polymers such as polyethylene glycol (PEG) are commonly used for stabilization and discussed further with regards to the effect of surface chemistry (Section 12.5.4.2).

## 12.3 Responsive Nanoparticle Platforms

One of the goals of the current generation of nanomedicines is stimuli-responsive systems to enhance specificity. Polymer systems that enable triggered release in response to the external environment such as pH or temperature have been investigated (Figure 12.4) and are discussed here.

### 12.3.1 pH Responsive

Responsive nanoparticle systems sensitive to pH are of interest due to naturally occurring pH changes within the body, *e.g.* acidic solid tumors,

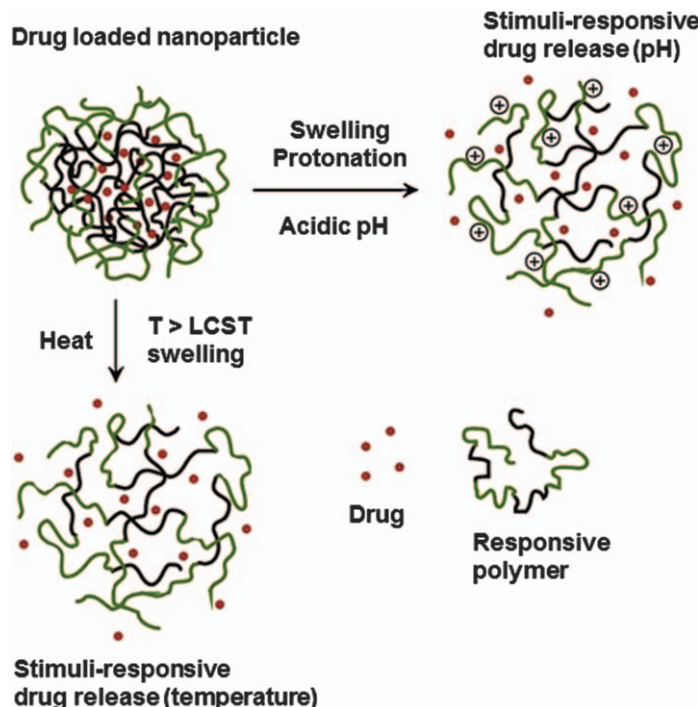


**Figure 12.4** Schematic of stimuli-responsive drug release.

Adapted from ref. 57 with permission from Elsevier, Copyright 2013.

endosomal compartments within the cell, and the gastrointestinal tract. Physiological pH is often considered to be 7.4, where the tumor and/or endosomal pH can range from 6 to 4. Therefore, pH-sensitive polymeric systems could selectively release their cargo in tumor microenvironments or within intracellular compartments. Such pH-responsive nanoparticles can be achieved either with a pH-responsive polymer or by including pH-responsive materials in the particle core to trigger disassembly.<sup>58,59</sup>

Responsiveness is due to pH-dependent polymer solubility. There is a switch between a hydrophobic (insoluble, collapsed state) and a hydrophilic (increased solubility, swollen) state as the functional groups protonate and deprotonate. Generally, particles are designed so that the expected decrease in pH at the site of interest causes an increase in polymer solubility and hydrophilicity leading to particle disassembly and release of payload. Examples of pH-responsive polymers include PEI,<sup>60,61</sup>  $\beta$ -carboxylic amides,<sup>62</sup> and polymers containing acid-cleavable functional groups such as acetal, orthoester, hydrazine, oxime, and boronic acid.<sup>19,63,64</sup> Alternatively, coordination complexes such as tannic acid-iron (TA-Fe<sup>3+</sup>)<sup>59,65,66</sup> and layer-by-layer assemblies of weak polyelectrolytes can also serve as the basis for pH-responsive systems.<sup>67,68</sup>

### 12.3.2 Temperature Responsive

Thermo-responsive polymers whose physical and chemical properties change when heated have been investigated for drug release triggered by a hyperthermic stimulus at the site of interest. Generally, thermo-responsive polymers have temperature-dependent conformations and are hydrophilic below a lower critical solution temperature (LCST) and hydrophobic above the transition temperature.<sup>69</sup> The change in hydration state triggered by heating leads to release of the therapeutic payload. Ideally, the transition temperature is between 37 and 42 °C. Such temperatures can be achieved therapeutically by local irradiation and/or co-delivery of light-to-heat generating agents. The transition temperature can be tuned by varying the composition of the polymer (Table 12.2). The transition temperature is dictated by the relative amount of hydrophilic and hydrophobic moieties of the polymer. Since the response to the change in temperature is sharp, spatiotemporal control over payload delivery can be achieved.<sup>69,70</sup> Examples of thermo-responsive systems include poly(N-isopropylacrylamide)

**Table 12.2** Transition temperatures of thermoresponsive polymers.

Polymers	LCST (°C)
PolyNIPAAm	32
PolyNVCL	32–50
PCL	30–50
Polycarbonates	36–53

(polyNIPAAm),<sup>71</sup> poly(*N*-vinylcaprolactam) (polyNVCL),<sup>72,73</sup> and oligoethylene glycol (OEG)-based polymers.<sup>74</sup> However, their fate *in vivo* is a concern because the hydrocarbon chains are not easily eliminated.<sup>75</sup> Alternatively, temperature-responsive derivatives of aliphatic polyesters, polycarbonates, polysaccharides, and polyamides are of interest due to their degradable nature.<sup>76–78</sup> Other approaches to thermo-responsive nanocarriers have been based on pluronic or poloxamers. Poloxamers or pluronic are ABA block copolymers of poly(ethylene oxide) (PEO, A) and hydrophobic, thermo-responsive poly(propylene oxide) (PPO, B) with LCSTs near physiological temperature.<sup>19</sup>

### 12.3.3 Chemoresponsive Polymer Systems

Polymeric systems that can trigger drug release in response to chemical or biochemical stimuli are of considerable interest. For example, triggered release of multiple APIs has been achieved using aptamer functionalized hydrogels. In such systems, functional aptamers are incorporated into hydrogels to entrap protein therapeutics. Release of the therapeutic protein is triggered by complementary oligonucleotides, which hybridize with the aptamers to cause aptamer–protein dissociation. The release kinetics can be tailored by aptamer design considering both aptamer affinity and structure.<sup>79–81</sup>

Injectable microgels have also been developed for glucose-responsive release of insulin. The microgels consist of enzyme nanocapsules containing glucose oxidase, catalase, and insulin in a physically crosslinked, pH-responsive polymeric matrix. In response to glucose, glucose oxidase generates a pH change, which causes the matrix to swell and triggers insulin release. This swelling is reversible and at normal glucose levels, the particles shrink so that insulin is no longer released. The catalase regenerates oxygen to consume hydrogen peroxide produced by the glucose oxidase. Using this system, dynamic regulation of blood glucose was possible *in vivo*.<sup>82</sup>

## 12.4 Processing Methods

Formulation of nanomedicines to encapsulate APIs within polymeric carriers can be achieved using various methods (Figure 12.5). Bottom-up methods are reliable, simple, and cost-effective. However, controlling the shape and polydispersity can present challenges. Top-down approaches have enabled a range of shapes with low polydispersity.

### 12.4.1 Bottom-up Methods

Bottom-up methods involve molecular self-assembly driven by non-covalent interactions. Specifically, nanocarrier assembly occurs due to aggregation and microphase separation of amphiphilic macromolecules. Controlling self-assembly is the key to achieving well-defined nanostructures.<sup>86</sup>

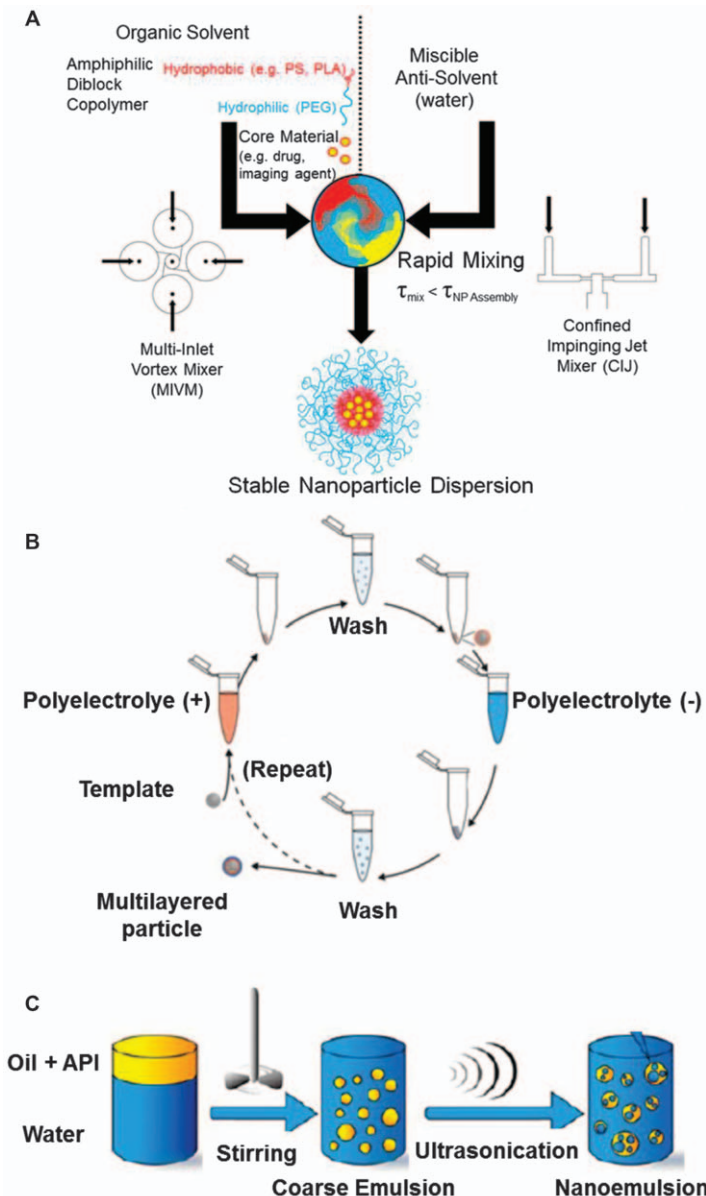


**Figure 12.5** Overview of nanomedicine production *via* bottom-up and top-down methods. (A) Solvent displacement *via* Flash Nanoprecipitation.<sup>83</sup> Reproduced from ref. 83 with permission from Springer Nature, Copyright 2016. (B) Layer-by-layer assembly is a bottom-up method.<sup>84</sup> Reproduced from ref. 84, <http://dx.doi.org/10.1021/cm402126n>, with permission from American Chemical Society, Copyright 2014. In contrast, (C) nanoemulsions are produced using top-down processing.<sup>85</sup> Reproduced from ref. 85 with permission from American Chemical Society, Copyright 2013.

We provide a brief overview of production methods to control self-assembly as well as self-assembly methods that involve electrostatic interactions.

### 12.4.1.1 Solvent Displacement

Using solvent displacement methods, polymeric nanoparticles are formed by precipitation of a molecularly dissolved polymer (in a water-miscible, organic solvent) supersaturated in aqueous media. The particle size is dictated by kinetics of nucleation and growth, which are affected by process parameters. The nucleation kinetics are affected by local supersaturation and temperature; nucleation ends when the solute is no longer supersaturated due to growth of earlier nuclei. Growth continues until the solute concentration reaches the equilibrium value.

Since control of nucleation is challenging, hydrophobic co-precipitants can be included in the formulation to promote nanoparticle formation at lower supersaturation. The co-precipitant is analogous to “seed” crystals traditionally used to achieve heterogeneous crystallization. To limit particle aggregation and maintain size, amphiphilic polymer dispersants are often used.<sup>83,87</sup>

Using anti-solvent precipitation, uniform particles are achieved when the time scale of mixing is less than the time scale of nucleation so that the nucleation rate is spatially uniform.<sup>88,89</sup> Therefore, processes with short characteristic mixing times are needed.<sup>87,90</sup> Several methods of anti-solvent precipitation for production of nanomedicines have been reported including confined impinging jet mixers and multiple inlet vortex mixers.<sup>87,90</sup> The use of such mixers enables anti-solvent precipitation in batch or continuous modes.<sup>87,90</sup> Based on these methods, several structures of nanoparticles can be achieved from amphiphilic molecules, *e.g.* vesicles and micelles, that are described here.

#### 12.4.1.1.1 Polymersomes.

Polymersomes, inspired by liposomes, are typically constructed from amphiphilic di- or triblock copolymers. These spherical vesicles have an aqueous core stabilized by a block copolymer bilayer. Because the block copolymers have higher molecular weight than lipids, polymersomes tend to have thicker membranes and be more resilient than liposomes.<sup>91</sup> The copolymer constituents are generally biocompatible derivatives of PEG or poly(ethylene oxide) (PEO). In order to achieve the bilayer for polymersome stabilization, the fraction of PEG in the block copolymer must be between 20% and 42%.<sup>92</sup> For drug delivery, hydrophilic APIs can be loaded in the polymersome core and lipophilic APIs can be loaded in the bilayer.

API-loaded polymersomes can be fabricated by adding water to the copolymer and drug(s) dissolved in an organic solvent to induce self-assembly of the block copolymer into vesicles. The polymersome properties are affected by both the characteristics of the block copolymer and processing parameters. Polymersome size is affected by the molecular weight of the polymer; the bilayer thickness is affected by the molecular weight of the

hydrophobic block. Polymersome size is further affected by the hydration level and processing (*e.g.* sonication, extrusion, presence of additives such as detergents and salts<sup>93</sup>). Alternatively, polymersomes can be made using microfluidic devices or micromixers. When made using microfluidics or micromixers, the flow rate affects the resulting size of the polymersome.<sup>94,95</sup>

**12.4.1.1.2 Core–Shell Nanoparticles/Micelles.** To encapsulate hydrophobic therapeutics, self-assembled core–shell nanoparticles are often used and stabilized by amphiphilic block copolymer shells. Flash NanoPrecipitation (FNP) enables rapid, scalable, and continuous processing of such core–shell nanoparticles with tunable size and composition. Flash NanoPrecipitation uses confined impinging jet mixers to achieve mixing time on the order of milliseconds. With such short characteristic mixing times (shorter than the time scale of nucleation and growth), nanoparticles assemble by diffusion-limited growth.<sup>96,97</sup> The kinetically trapped structures are stabilized by dense PEG brushes. Kinetically trapped nanoparticles enable drug loadings (>50%) that are significantly higher than the thermodynamic limit (~10%).<sup>98,99</sup> In practice, the nanoparticle size can be tuned by varying the process parameters, *e.g.* total solids concentration or concentration of the stabilizer.<sup>100</sup> Selection of materials is vital; typically, FNP can be used to encapsulate hydrophobic compounds with a calculated octanol–water partition coefficient greater than 6. Other molecules can be encapsulated by conjugation to a poorly soluble hydrophobic compound to reduce water solubility. The API of interest can also be complexed with an oppositely charged hydrophobic molecule *via* electrostatic interactions.<sup>83</sup>

#### 12.4.1.2 Layer-by-layer (LBL) Assembly

Multifunctional nanocarriers can be achieved by layer-by-layer (LbL) assembly. In this approach, functional materials are sequentially adsorbed onto an inner core *via* molecular interactions (electrostatic, guest–host, stereocomplexation). The inner core can be any particle system manipulated to have charge, so that different polyelectrolytes can be introduced in alternating layers. The alternating layers result in a shell with tunable properties that can enable active targeting, triggered release, stealth properties, and incorporation of multiple therapeutics. The coating can also be used to tune the release kinetics. LbL particle stability is affected by the number of layers; additional layers increase the stability.<sup>101</sup> In batch processing, each layer requires 5 minutes per layer.<sup>102</sup> Scalable, spray methods that combine LbL and top-down roll-to-roll approaches have also been reported.<sup>103</sup>

#### 12.4.1.3 Complex Coacervates

Coacervation based on electrostatic interactions is also promising for nanomedicine formulation. It is driven by electrostatic association of

oppositely charged macroions leading to phase separation of a dense, polyelectrolyte-rich liquid phase in equilibrium with a macromolecule-poor supernatant. Generally, coacervation is performed directly from aqueous solutions of the macroions and is controlled through changes in ionic strength or pH.<sup>90</sup> One of the most important parameters involved with coacervation is the ratio between the number of positive and negative charges in the formulation to achieve electroneutrality within a given phase. Addition of salt expands the range of compositions over which coacervation occurs through extrinsic charge compensation and partitioning of the salt. Properties of the macroion, *i.e.* molecular weight, chirality, and branching, affect coacervate formation and resulting structure. Block copolymer structures of macroions can result in hierarchical structures such as micelles (coacervate-corona or coacervate-core), coacervate-core vesicles, or hexagonal rods.<sup>90</sup>

Encapsulation is achieved by including the desired cargo with the coacervate components through specific interactions or preferential partitioning. Since encapsulation occurs in an entirely aqueous environment, this method is especially promising for encapsulation of biomacromolecules, *e.g.* DNA, RNA, DNA or RNA; complexation with a positively charged carrier polymer, surfactant, or lipid protects it from nucleases. Coacervate systems have been used for the delivery of plasmid DNA, microRNA, and/or siRNA with applications in atherosclerosis and cancer. Encapsulation of proteins can be achieved by conjugation with succinic anhydride to supplement the charge. This method has proven effective at improving protein thermal stability, which is important for long-term storage.<sup>90</sup>

### 12.4.2 Top-down Methods

In contrast to bottom-up methods, top-down methods involve processing macroscopic materials to create micro- or nanoscale particles. Examples of top-down methods include milling, grinding, and emulsion processing. Inspired by the photoelectronics industry, photolithography and molding technology for selective removal of excess bulk material to generate controlled particle features have recently been used for fabrication of nanomedicines. Leveraging photolithography and selective etching, soft lithographic templating and molding methods are especially useful for generating polymeric nanoparticles of controlled shapes. In this section, we will introduce a few prevalent techniques for polymer nanoparticle fabrication using top-down approaches; these techniques have been reviewed extensively elsewhere.<sup>104,105</sup>

#### 12.4.2.1 Emulsification

Emulsification methods are a versatile approach for drug delivery formulations. Oil-in-water emulsions in which lipophilic APIs are dissolved in the nanosized oil droplets (20 to 200 nm) dispersed in water are especially

promising. Nanoemulsification often involves multiple steps: application of external shear (high speed homogenization or ultrasonication) to emulsify the system, solvent removal *via* evaporation, then application of high pressure homogenization that uses cavitation forces, turbulence, and shear to reduce the size of the droplets to the nanoscale.<sup>106,107</sup> Continuous fabrication in flow has been reported.<sup>108</sup> Due to the high energy processing methods used, kinetically stable systems are achieved.<sup>109</sup> The size of the nanoemulsion is affected by the applied shear rate, interfacial tension, surfactant selection, and the relative viscosity of the two phases. For stability, the aqueous solubility of the oil phase is important to prevent Ostwald ripening and droplet growth. Incorporation of a hydrophobic polymer, amphiphilic block copolymers, or a charged surfactant can also improve nanoemulsion stability.<sup>109</sup> Depending on the oil selection, solid lipid nanoparticles (SLN) encapsulating hydrophobic APIs can be formed from nanoemulsions upon cooling and lipid crystallization. Similar to nanoemulsions, emulsifier selection and concentration affect SLN size and stability.<sup>110</sup>

Emulsification can also be combined with polymerization to produce drug-loaded polymer nanoparticles. In emulsion polymerization, surfactant, water-soluble initiator, poorly water-soluble monomer are combined in water. Phase separation can occur before or after the polymerization reaction. After termination of the reaction, polymer nanoparticles are typically ~100 nm. Surfactant-free methods in which nucleation and growth leads to nanoparticle formation have also been used. Hydrophobic API species can be encapsulated by including the API in the hydrophobic phase.<sup>111</sup> In these methods, the monomer concentration affects the size and stability of the resulting nanoparticle.<sup>112</sup>

#### 12.4.2.2 Continuous Particle Generation via Fluid Flows

Microfluidic devices have been used to achieve emulsions with uniform droplets as well as continuous processing of polymeric nanoparticles.<sup>113,114</sup> Confining the emulsion process to a microfluidic channel affords uniform laminar flow regimes for scalable, precise particle generation with high potential throughput. Initial “microfluidic flow-focusing devices” (MFFDs) combine traditional single and double emulsions with confined microfluidic geometries to generate solidified polymer particles of controlled composition and particle shape.<sup>115–118</sup> Further adaptation of this approach has yielded multicompartment polymeric particles, asymmetric polymer solidification, arrested coalescence, and clustering of inner droplets.<sup>114</sup> The microfluidic approaches have also been combined with lithographic masks to selectively expose flowing monomers within a microfluidic channel to UV light to control particle shape. Variations of these techniques include continuous flow lithography (CFL), stop-flow, and stop-flow interference lithography (SFL and SFIL), which yield particles of controlled geometries from a range of photocurable polymers.<sup>119–123</sup>

Electrodynamic co-jetting is another method which can create well-defined nanoparticles by harnessing fluid flows.<sup>124,125</sup> An electric field is applied to a laminar flow of polymeric solutions to generate a spray droplet, induce nano-precipitation, and generate solid particles on the counter electrode. The laminar flow conditions and the rapid precipitation supports generation of uniform multicompartiment particles.<sup>124</sup> Such multi-component particles can be selectively loaded and/or functionalized, producing Janus nanoparticles for medical applications.<sup>126–130</sup>

#### 12.4.2.3 Soft-lithography Templating

Top-down nanofabrication technology used in semiconductors can be applied to the production of particle-based nanomedicines. In traditional photolithography, geometric patterns are encoded in photomasks are applied to a substrate using light-sensitive materials (photoresists). While rigid templates of epoxy (SU8) and quartz have been employed as templates for many drug delivery applications, traditional photolithography is integrated with a soft template and was pioneered by Whitesides and colleagues.<sup>131–133</sup> For fabrication of the soft template, precursor polymer (*e.g.* polydimethyl siloxane (PDMS), gelatin, *etc.*) is flowed onto a patterned wafer and solidified to impart features inverted from the pattern on the wafer.<sup>134–137</sup> Then, the soft template is used to mold polymer nanoparticles through either mold filling or stamping. Often sacrificial polymer layers are employed to transfer templated particles; the sacrificial polymers are selectively dissolved in appropriate solvents to collect the particles. Template-based approaches provide a number of advantages, including high uniformity and precise composition. However, these approaches are often limited by throughput and scalability, and the feature sizes are dictated by the lithographic processes.<sup>104,105</sup>

The Particle Replication in Non-wetting Templates (PRINT) process, created by DeSimone and colleagues,<sup>138</sup> and scaled to a continuous roll-to-roll fabrication system by Liquidia Technologies, enables good manufacturing practice (GMP) top-down nanoparticle manufacturing (Figure 12.6).<sup>139</sup> The PRINT process utilizes templates made of perfluoropolyether (PFPE), which minimizes template swelling observed in PDMS-based approaches and enables fabrication of uniform nanoparticles with tunable composition and feature sizes as small as 55 nm. Patterned mold cavities are filled *via* capillary forces. Excess material is removed by laminating the mold during filling against a higher-surface-energy film, producing highly monodisperse particles. The pre-particle liquid is converted to a solid (photocuring, vitrification, or solvent evaporation) within the mold. Then, the solid particles are removed *via* contact with a sacrificial adhesive to pull the particles from the low-surface-energy mold. The gentle processing enables incorporation of a wide range of particle compositions, including biologics. Examples include cross-linked PEG, PLA, PLGA, proteins (insulin and albumin), small molecules (sugars and drugs), and siRNA.<sup>140–144</sup> Multicomponent particles can also be achieved using PRINT by selective evaporation of solvent within the

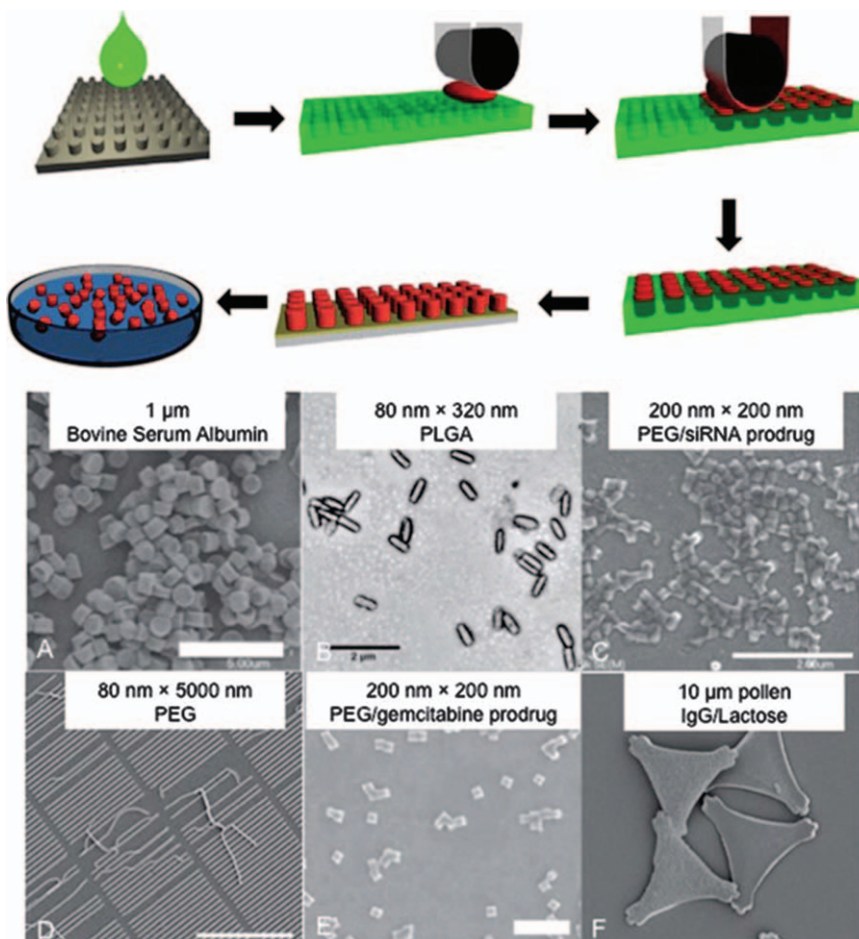


**Figure 12.6** Preparation of PRINT mold and fabrication of PRINT particles (top). A liquid PFPE precursor (green) completely wets the silicon and is photocured to generate a mold. The cavities are filled with a liquid pre-particle material (red) without wetting the land area surrounding the cavities using a roll-to-roll process against a high-surface-energy polyethylene terephthalate (PET) counter sheet. The liquid is then converted into a solid (photocuring, vitrification, or solvent evaporation). Once solidified, the array of particles (red) can be removed by bringing the mold into contact with an adhesive layer (yellow) to pull the particles from the low-surface-energy mold. The particles are recovered by dissolving the adhesive layer. Examples of particles of different shapes, sizes, and composition fabricated using PRINT in B (a-f), (a),<sup>147</sup> (b),<sup>148</sup> (c),<sup>142</sup> (d),<sup>149</sup> (e),<sup>150</sup> (f),<sup>139</sup>

Parts 6A and 6B-F reproduced from ref. 139, <http://dx.doi.org/10.1155/2012/941243>, under the terms of the CC BY 3.0 licence, <https://creativecommons.org/licenses/by/3.0/>. Parts 6B-A to 6B-E reproduced from ref. 142, 147–150 with permission from American Chemical Society, Copyright 2012.

mold and sequential backfilling with a secondary material.<sup>145</sup> In addition to control of the composition, size, and shape, the formulation of the matrix can be designed to tune the porosity, texture, and mechanical properties of the particles.<sup>139,146</sup>

## 12.5 Effect of Physiochemical Properties

For any fabrication method, the resulting physiochemical properties are important for application of the formulation. The major challenge of nanoparticle-based drug delivery systems has been non-specific uptake of nanoparticles in healthy tissue that prevents therapeutic levels of API from accumulating at the site of disease. To overcome the sequential barriers that nanoparticles face, several nanoparticle design parameters need to be considered and are discussed here.<sup>5</sup>

### 12.5.1 Size

Following intravenous administration, nanoparticle size is one of the greatest determining factors of the fate and biodistribution of the nanoparticle population (Figure 12.7). For example, small nanoparticles (less than 5 nm in diameter) are rapidly cleared by the kidneys upon IV administration. Larger nanoparticles tend to accumulate in the liver and spleen, the major organs of the mononuclear phagocyte system (MPS). Micrometer (2–5 micron) particles accumulate in the capillaries of the lung.<sup>5</sup> *In vivo*, elevated accumulation of long-circulating macromolecules and nanoparticles has been observed *via* extravasation through fenestrated blood vessels present in solid tumors, *i.e.* the EPR effect. There is growing evidence

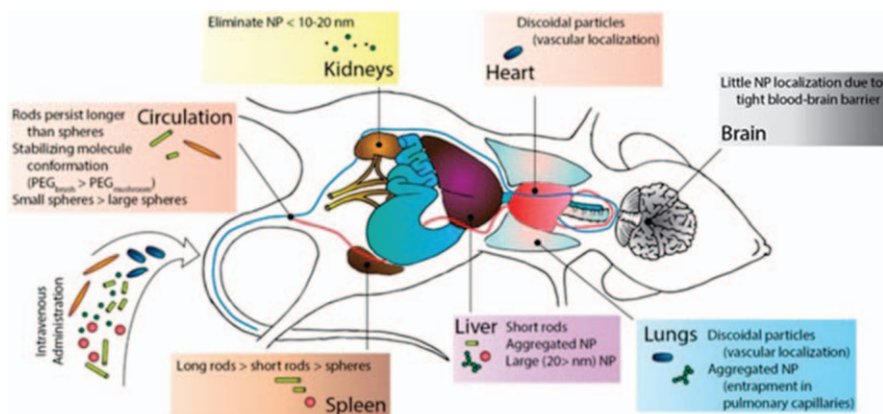


**Figure 12.7** Overview of the effect of particle size and shape on biodistribution. Reproduced from ref. 166 with permission from American Chemical Society, Copyright 2017.

that the EPR effect can be present in other diseases such as infection and heart failure. Therefore, nanoparticle formulations may be a powerful approach to affect a multitude of conditions, and particle size can be tailored to direct particle distribution *in vivo*.<sup>5,151–155</sup> Nanoparticles ~100 nm in diameter are generally considered most promising for passive targeting to disease sites *via* the EPR effect as they have relatively long circulation times and are smaller than the fenestrations present in tumors, which are several hundred nanometers. Nanoparticle transport into the tumor depends on nanoparticle size with 30–60 nm diameter particles resulting in optimal tissue penetration due to an intricate balance of internalization and diffusion.<sup>5,151–155</sup>

Particle size affects distribution within blood flow. Nanoparticles less than ~500 nm remain in the core of red blood cells within the center of flow in larger blood vessels. Conversely, 1–2 micron size particles can marginate to the “cell-free layer” and interact with the vasculature.<sup>156–159</sup> Nanoparticle size also affects cell internalization, impacting uptake efficiency, kinetics, and the biological mechanism of internalization. Phagocytic cells internalize large particles through phagocytosis.<sup>160</sup> For nanoparticles with diameters less than 200 nm, internalization involves endocytosis through clathrin-coated pits. With increasing size, caveolae-mediated internalization has been observed. Particle sizes of 30–50 nm are thought to optimize cell uptake depending on cell type and nanoparticle surface properties.<sup>152</sup> Such internalization can occur within the tissue or in blood flow.<sup>161,162</sup>

### 12.5.2 Shape

Nanoparticle shape is also an important design consideration. Based on experimental and computational analyses, particle shape affects particle transport and binding efficiency. In blood flow, spheres tend to accumulate in the core of a vessel, whereas non-spherical particles are more likely to marginate to vessel walls. The increase in margination enhances interactions with the vessel walls. At equivalent internal volumes, rod-shaped particles showed at least twofold higher binding affinity compared to spherical particles under various shear rates. This increase in affinity was attributed to larger surface area, increased probability of adhesion, and increased intermolecular bonds.<sup>5,160,163–168</sup>

Particle shape also affects circulation time. For example, filamentous micelles showed significantly longer circulation times when compared to spheres of the same composition. Initial lengths of ~8 µm had the longest circulation times, which is approximately the diameter of red blood cells. The longer circulating non-spherical geometries tend to have increased accumulation in the tumor and spleen *in vivo*.<sup>5,160,163–168</sup>

Cellular internalization is also significantly affected by particle shape. High aspect ratio particles have been observed to be internalized *via* actin-cup and ring formations with increasing kinetics at higher aspect ratios. In contrast, low aspect ratio has resulted in cell spreading rather than internalization.<sup>160,168</sup> The effect of particle shape on cell viability has also

been considered. In human lung fibroblasts and mouse alveolar macrophages, lower aspect ratio particles resulted in a greater degree of apoptosis and production of reactive oxygen species. Very high aspect ratio particles have also been found to mediate pro-inflammatory and cytotoxic effects similar to high aspect ratio asbestos. Such findings are highly dependent on the cell type and material.<sup>166</sup>

Elucidating the exact role of particle geometry on drug delivery has been confounded by a number of interdependent factors (*e.g.* particle size, surface chemistry, *etc.*). Multivariate analysis, thus far, indicates that particle shape has less of an effect on tumor accumulation when compared to other factors such as cancer type, materials, size, *etc.*<sup>166</sup> A full understanding of how shape affects biological processes and particle degradation may lead to a new class of drug delivery systems with enhanced clinical efficacy.

### 12.5.3 Mechanical Properties

Mechanical properties also affect performance of nanoparticle-based drug delivery systems.<sup>156,157</sup> Generally, flexible nanoparticles have shown decreased cell uptake compared to rigid particles of comparable size and surface chemistry. *In vivo*, flexible particles have longer circulation times than comparable rigid particles.<sup>166,169</sup> Flexible micro- and nanoparticles have been designed with a modulus ~10–25 kPa to mimic the elasticity of red blood cells, and demonstrated improved circulation times compared to geometrically equivalent rigid particles.<sup>126,146,170</sup> These flexible particles have been fabricated with lightly crosslinked PEG hydrogels to achieve the desired mechanical properties.

### 12.5.4 Surface Chemistry

In addition to particle geometry and flexibility, surface chemistry is also an important consideration that significantly influences nanoparticle interactions with cells *in vitro* and *in vivo*.<sup>166</sup> Upon administration, nanoparticles undergo rapid modification due to contact with the biological environment and ensuing nanoparticle–protein interactions. The resulting protein–particle coating, called the protein corona, affects the pharmacological and toxicological profile of the nanoparticle.<sup>171–174</sup> The corona is thought to be comprised of “hard” and “soft” layers in which the “hard” layer consists of protein tightly bound due to high affinity for the nanoparticle surface and the “soft” layer contains loosely bound proteins (Figure 12.8). The equilibrium binding and kinetics depends on the nanoparticle surface, size, particle material, surface roughness, and shape, as well as the protein composition of the biological environment. The protein composition of the corona, in turn, can dramatically impact the clearance rate of the particle, as the adsorbed opsonin proteins enhance particle cellular uptake. Thus, particle surface charge and composition are especially important considerations in controlling the adsorbed protein corona needed to control the

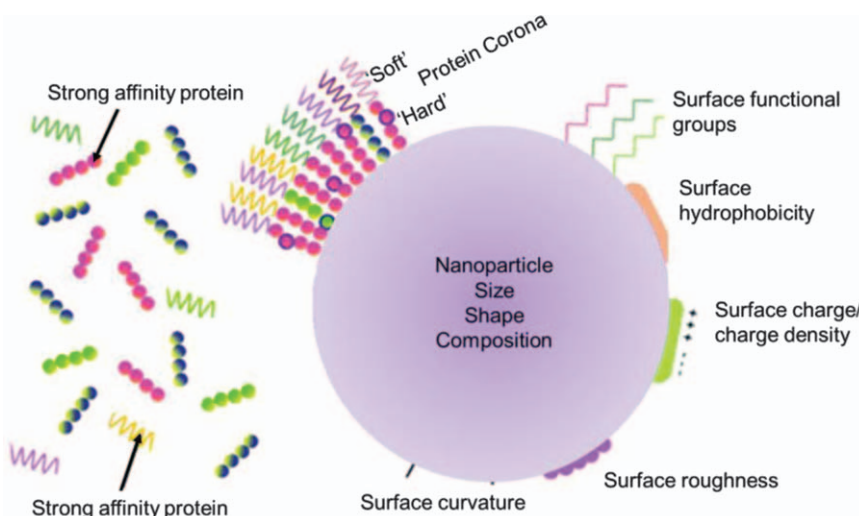


**Figure 12.8** Overview of how nanoparticle properties affect nanoparticle–protein corona that influence performance of nanomedicine.  
Adapted from ref. 174 with permission from the Royal Society of Chemistry.

overall fate and biodistribution.<sup>171–174</sup> Despite the known importance, characterization of the protein corona *in vivo* (including composition, kinetics, equilibrium binding) to predict performance of nanomedicines remains a significant challenge.<sup>171–174</sup>

#### 12.5.4.1 Surface Charge

Surface charge greatly affects protein adsorption and the resulting pharmacokinetics and biodistribution that depends on the route of administration. When injected intravenously, nanoparticles with high positive surface charge (cationic) are cleared more rapidly than nanoparticles with highly negative surface charge (anionic), whereas nanoparticles with neutral or slight negative charge demonstrate relatively long circulation times. This effect has been attributed to reduced adsorption of serum proteins<sup>5</sup> and non-specific uptake by macrophages for neutral or slightly negatively charged particles.<sup>175</sup> Nanoparticle surface charge can also impact toxicity; cationic particles have been observed to be more toxic than anionic nanoparticles due to interactions with the cell membrane<sup>176</sup> which can destabilize the cell membrane and cause cell lysis.<sup>177</sup> *In vivo*, it has been observed that cationic surfaces are more likely to cause hemolysis as well as aggregation of platelets compared to anionic or neutral surfaces.<sup>178</sup>

However, cationic particles are employed to drive endosomal escape within the cell and are commonly used as gene delivery carriers, as the cargo must be released into the cell cytosol.<sup>179</sup> Thus, nanoparticles with switchable

surface charge are promising for a number of applications. Initially, a neutral or slightly negative surface charge is desired to promote nanoparticle circulation. Upon localization to the target site, switching to a positive surface charge would promote nanoparticle transport within the tumor microenvironment,<sup>180</sup> cellular internalization,<sup>5</sup> endosomal escape,<sup>179</sup> and can even induce cell death signaling cascades.<sup>178</sup>

For alternative routes of administration, cationic particles can be beneficial. For example, when delivered to the lungs, cationic nanoparticles associated with dendritic cells whereas anionic nanoparticles were more readily internalized by alveolar macrophages and cleared. Therefore, cationic particles are advantageous for persisting on mucosal surfaces which may be particularly important in delivery of pulmonary vaccines.<sup>143,181</sup>

#### 12.5.4.2 PEGylation

To achieve long circulation times associated with particles with neutral or slightly negative surface charge, nanoparticles are often coated with inert polymers that minimize interaction with components found in the blood stream to provide “stealth” properties. PEG coatings sterically stabilize the particles and this hydration layer prevents particle aggregation, opsonization, and phagocytosis. The “stealth” properties are affected by PEG molecular weight and surface density since the PEG coating must be sufficiently thick. Due to the flexibility of the PEG chain, interpenetration of the PEG corona is thermodynamically unfavorable. When PEG chains overlap with increasing surface density, the PEG chains stretch away from the surface forming a brush layer. Dense brush layers are required for providing effective “stealth” properties.<sup>169</sup>

For intravenous administration, it has been generally found that PEG molecular weights greater than 5 kDa reduce protein adsorption depending on the surface density. The exact density required has been observed to depend on the PEG molecular weight, particle size, and particle flexibility.<sup>169</sup> The PEG density and molecular weight affect the extent of protein adsorption as well as the composition of the protein corona which ultimately determine *in vivo* fate (Figure 12.9).

Dense PEG brushes have also been effective coatings for achieving mucus-penetrating particles for delivery *via* mucosal routes (ocular, nasal, pulmonary, *etc.*) in which nanoparticles must diffuse through the mucus gel layer. PEG reduces mucoadhesion *via* hydrophobic or electrostatic interactions and enables the nanoparticles to slip through the mucus layer.<sup>169,182–184</sup> Overall, PEG coatings are commonly used to minimize protein adsorption and achieve mucus penetration. Alternatives to PEG include poly(2-alkyl-2-oxazolines), synthetic polypeptides, and zwitterionic polymers. Such materials are not FDA approved, but they are contained in formulations in clinical trials.<sup>169</sup>

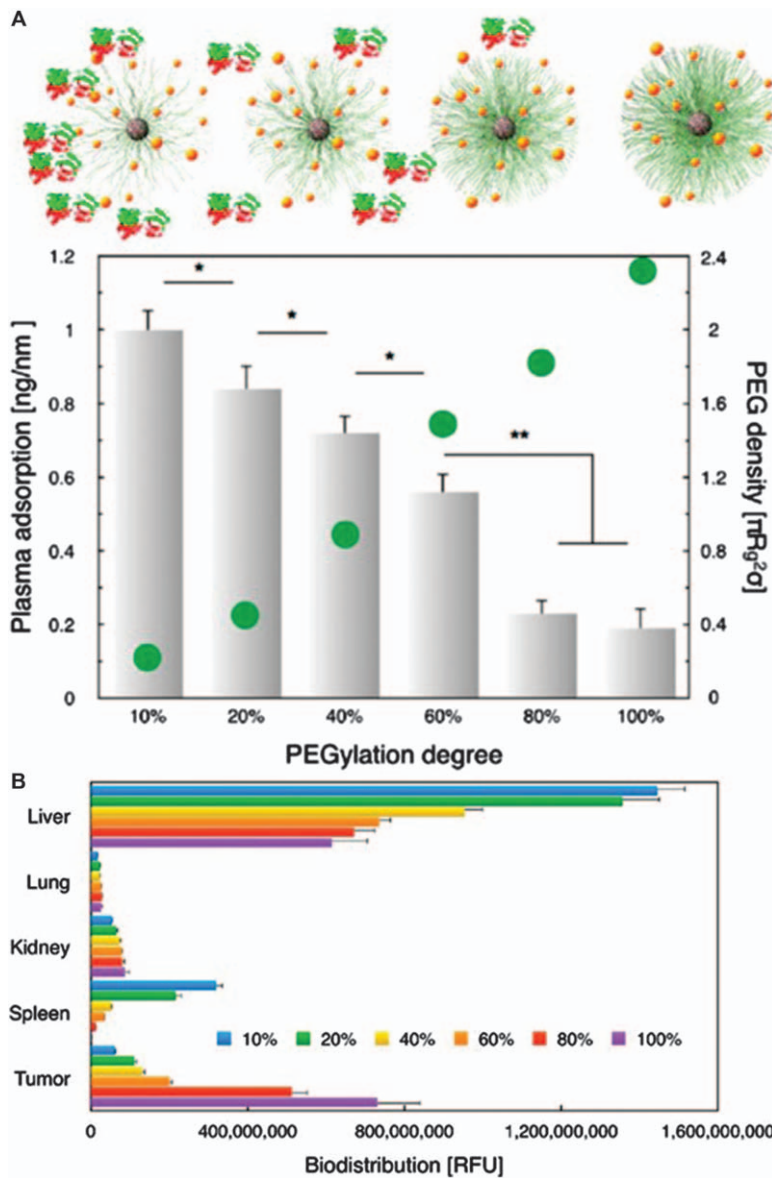


**Figure 12.9** Effect of PEG density on protein adsorption and biodistribution. Reproduced from ref. 184 with permission from American Chemical Society, Copyright 2017.

#### 12.5.4.3 Targeting Ligands

Active targeting using ligands (small molecule and biomolecule) have been widely used to increase nanomedicine accumulation at the diseased tissue of interest over levels achieved with passive accumulation. Small molecules or

biomolecule ligands are attached to the surface of the particle and search for their cognate receptor, often a molecule over-expressed in the diseased area, employing a “lock and key” strategy. A fundamental challenge is that the presence of the targeting ligands affects the stealth properties of the nanoparticles and can accelerate the clearance of the nanoparticles. The density of the ligand is an important consideration. For example, a fivefold increase in folic acid ligands produced a 68-fold increase in binding avidity.<sup>185</sup> In some cases, intermediate ligand densities led to optimal binding<sup>186,187</sup> due to steric limitations when the adjacent ligands were too close together. Ligands can also be used to affect cell internalization.<sup>185</sup> Combinations of ligands also can improve nanoparticle binding.<sup>188–190</sup>

## 12.6 Emerging Applications

### 12.6.1 Multifunctional Particles

Multifunctional nanoparticles incorporating multiple moieties (therapeutics and/or imaging agents) are under widespread development. For example, formulations of drug combinations can improve therapeutic efficacy,<sup>185</sup> which are especially promising for cancer,<sup>191,192</sup> anti-viral treatments (*e.g.* HIV AIDS),<sup>193</sup> and immunomodulation.<sup>194</sup> Advances in understanding of cancer biology, chemo-resistance, and metastasis will be important for developing nanomedicine-based combination therapies as valuable tools in precision medicine.<sup>191,192</sup>

Nanoparticles for *in vivo* quantification of biomarkers *via* imaging are important for diagnosis and determination of disease severity. For example, nanomedicines that incorporate MRI active inorganic nanoparticles, or probes (*e.g.* gold nanoparticles or near-infrared dyes) that enable photo-acoustic imaging (based on laser-generated ultrasound), or radioactive tracers to enable positron emission tomography (PET)<sup>195,196</sup> have utility as “theranostics”. Such theranostic nanoparticles that combine drug delivery and imaging agents have potential application to advance precision medicine. However, design of such nanoparticles is difficult because there is often a trade-off between the ideal features for drug delivery and imaging.<sup>185</sup> Despite the technical challenges, these materials are promising for treating chemotherapy-resistant cancers.<sup>185</sup>

### 12.6.2 Encapsulation of Biologics

Biologics, or biologically-derived molecules, are a rapidly growing class of therapeutics due to their high potency and improved safety profiles. Biologics are water soluble and more complex than small molecule APIs. Successful administration is challenging because they are rapidly cleared from the blood stream and can be degraded in the gastrointestinal tract. Thus, biologics are often administered by frequent injections. Formulations that achieve sustained release are highly desired. Approaches have often

involved double emulsions, hydrogel systems, and hydrophobic, degradable polymer particles (*e.g.* PLGA). Alternative methods for encapsulation of biologics under development are of considerable interest.<sup>197,198</sup>

### 12.6.3 Alternative Routes of Administration

Historically, nanoparticles have been designed primarily for systemic delivery *via* intravenous administration, where nanoparticles are applied directly to the blood stream. Thus, much of conventional nanomedicine understanding is related to biological barriers of the systemic vasculature. Since polymer nanoparticles are especially flexible in terms of material and API selection, as well as achievable physiochemical properties, applications of nanomedicine to additional routes of administration, including respiratory, ocular, and oral administration, *etc.* are of growing interest. Here, we further discuss respiratory and oral administration.

For these routes of delivery, transport across mucosal membranes is required. Mucus is a viscoelastic gel layer that coats mucosal membranes including the lung, gastrointestinal tract, nose, and eyes. Due to its continuous secretion and shedding, mucus can quickly eliminate foreign particulates and pathogens. Therefore, sustained drug delivery at mucosal surfaces remains an important challenge. Nanoparticles of small size are able to directly penetrate many mucosal membranes; however, larger and highly charged particles are readily entrapped by the adhesive mucin network.<sup>199</sup> Nanoparticles with dense PEG layers have been observed to rapidly diffuse through mucus.<sup>200</sup> This mucus penetration facilitates sustained and targeted mucosal drug delivery.<sup>200–203</sup> To achieve mucus-penetrating behavior, the PEG ( $\leq 5$  kDa) coating should be non-mucoadhesive and small compared to the average mesh spacing of mucus. Although PEG remains the gold standard, alternative mucus-penetrating coatings include neutral hydrophilic polymers *e.g.* poly(2-oxazoline), and *N*-(2-hydroxypropyl) methacrylamide and zwitterionic lipids.<sup>201,204</sup>

In addition to penetrating the mucosal membrane in the intestine,<sup>204</sup> oral delivery of nanoparticles is challenging due to the highly variable pH as well as high protease and enzymatic content within the GI tract.<sup>205</sup> Therefore, nanoparticle formulations to protect medications that are susceptible to degradation in the GI tract and improve bioavailability are promising. Oral administration may also reduce nanomedicine toxicity concerns as nanoparticle components that remain in the GI tract can be easily excreted as waste and avoid clearance by the mononuclear phagocyte system.<sup>206</sup> Specialized nanoparticle formulations targeting delivery to the stomach are in pre-clinical development; mucus-penetrating formulations for the treatment of *H. pylori* infections are of particular interest. Nanoparticles with enteric polymers that target delivery to the intestine are also being developed. Specifically, formulations for oral administration of insulin and vaccines with sustained release are actively being pursued.<sup>205,207–209</sup>

Particles administered *via* aerosol are able to deliver enhanced local API concentrations within the lung. Additionally, due to the large surface area and thin epithelial membrane in the alveoli, particles can also gain access to systemic circulation. However, polymer nanoparticles administered directly to the lung *via* inhalation must navigate the highly branched airspace as an aerosol before depositing onto a mucus or surfactant coating at the air-tissue interface. Particle size is an important consideration; optimal aerosol delivery occurs for particles between 1 and 5 microns.<sup>210,211</sup> However, as shown in Figure 12.10, nanoparticles less than 1 micron are able to penetrate to the furthest region of the lung, the alveoli, and increasing deposition is observed for nanoparticles below 100 nm.<sup>212–214</sup> Nanoparticles smaller than ~6 nm are able to diffuse across the epithelium into circulation, while anionic nanoparticles ~30 nm can diffuse to the lymphatic system.<sup>215</sup> While these size limitations prevent most nanoparticles directly crossing into systemic circulation, nanoparticles can be vehicles for sustained and controlled release of a therapeutic payload for both local and systemic action.<sup>212</sup>

Upon deposition, nanoparticles must penetrate the mucus membrane in the upper airways, whereas in the lower airways, nanoparticles must avoid internalization by resident alveolar macrophages. Two common approaches to avoid macrophage internalization are to generate particles smaller than 100 nm or larger than 5 microns. Larger particles are often achieved by spray drying a polymer (*e.g.*, PLGA, chitosan, hydroxypropyl cellulose) which creates geometrically large particles of high porosity and low density with aerodynamics similar to that of a solid, geometrically smaller nanoparticle.<sup>218–221</sup> Importantly, this spray drying approach has been used to encapsulate a wide range of therapeutic payloads including pre-formed polymeric nanoparticle formulations.<sup>15,222–226</sup> Nanoparticles are agglomerated into larger porous microparticles with optimized aerosol features and de-agglomerate upon deposition to diffuse through the tissue and/or release their cargo. Pulmonary applications for such particles include local delivery of vaccines and other proteins,<sup>139,144,181,226–228</sup> antibiotics against pulmonary infections,<sup>216,223,229–234</sup> chemotherapeutics for lung cancer,<sup>235</sup> and systemic delivery of insulin,<sup>219,236</sup> amongst many others.

#### 12.6.4 Immune Engineering

As the nanomedicine field evolves, immunological responses to drug delivery systems are receiving increasing attention. When delivered systemically, nanomedicines are cleared through phagocytic cells that directly interface with the immune system. Thus, there has been a recent shift from delivery of API payloads to sophisticated immunologically regulated molecules that can provide a controlled immune response, *i.e.* “immunoengineering”.<sup>237</sup> For example, polymeric nanoparticles are being developed as prophylactic vaccines against a wide range of infectious diseases,<sup>181,228,229,238</sup> and therapeutic nanoparticles are being developed as cancer vaccines.<sup>239,240</sup> In both cases, polymeric nanoparticles simultaneously deliver an antigen, *i.e.* a

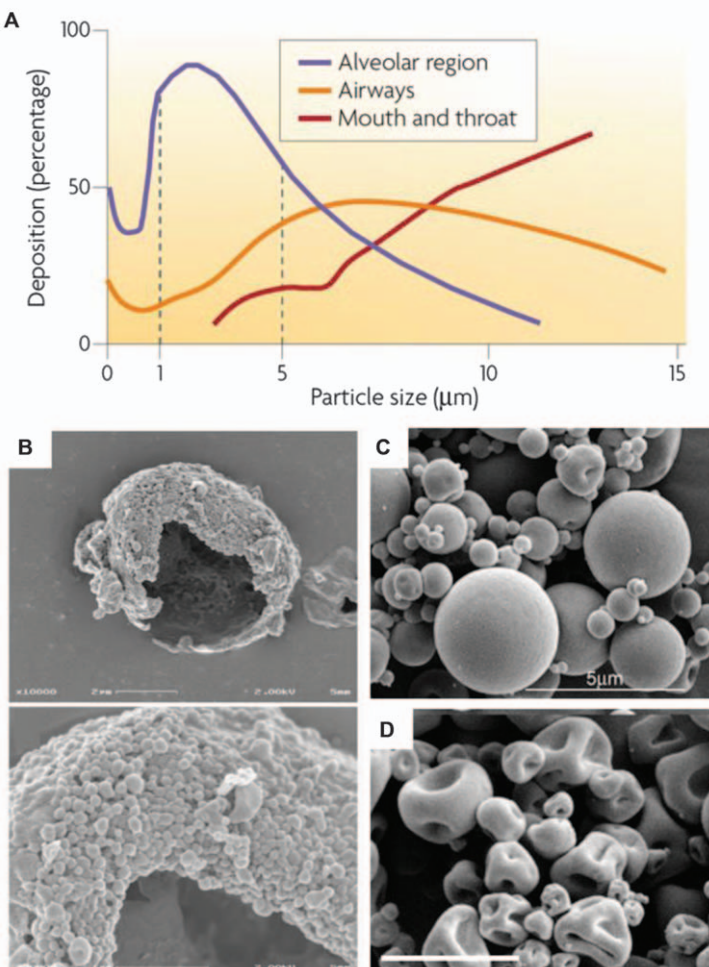


**Figure 12.10** Pulmonary delivery of polymeric particles. (A) Location of particle deposition in the lung as a function of aerosol size. (B–D) Examples of polymeric micro- and nanoparticles for pulmonary delivery.<sup>210</sup> Reproduced from ref. 210 with permission from Springer Nature, Copyright 2017. (B) Spray dried core shell rifampicin porous microparticle composed of PLGA nanoparticle aggregates, scale bars top 2  $\mu\text{m}$ , bottom 1  $\mu\text{m}$ .<sup>216</sup> Reproduced from ref. 216 with permission from Springer Nature, Copyright 2009. (C) and (D) Hydroxypropyl cellulose spray dried microparticles, scale bar 5  $\mu\text{m}$  and 2  $\mu\text{m}$ , respectively. Reproduced from ref. 217 with permission from Elsevier, Copyright 2008.

protein/peptide that the adaptive immune response will be directed against, and an adjuvant, a molecule that can direct the type of immune response.<sup>238,241</sup> Simultaneous co-delivery of these two signals to antigen-presenting cells provides superior immune response.<sup>238</sup> Polymer

nanoparticles provide facile co-delivery of these molecules through co-encapsulation or surface functionalization.<sup>229,238</sup> Single nanoparticle delivery of either the antigen or adjuvant alone can provide development of antigen-specific tolerance,<sup>242–245</sup> or stimulated immune phenotypes,<sup>246</sup> respectively.

In addition to delivering immune-directing molecules, polymeric nanoparticles themselves have been increasingly studied for their immune-modulating properties. Certain polymeric systems can have adjuvant-like properties providing a pro- or anti-inflammatory simulation to phagocytic cells.<sup>181,247,248</sup> Thus, polymer nanoparticles themselves can have therapeutic effects when delivered systemically. For example, circulating cells of the mononuclear phagocyte system (MPS) system, including inflammatory monocytes<sup>162</sup> and neutrophils,<sup>161</sup> have been shown to internalize inert, negatively charged polymer nanoparticles within the vasculature. Once internalized, cells continue to clear the foreign object in the liver or spleen, which “distracts” from aspects of their normal immune function. This approach can be used as treatment for multiple sclerosis and acute lung injury.<sup>161,162</sup> Moving forward, polymer nanoparticles are anticipated to have increasing utility in the emerging field of immunoengineering.

## 12.7 Clinical Translation

In 2014, the BCC Research firm estimated the value of the global market of nanopharmaceuticals to be \$209 billion with anticipated growth to \$412 by 2019.<sup>249</sup> Growth in nanoparticle-based systems, including polymeric formulations, is especially promising. However, clinical translation of nanoparticle-based drug delivery remains a significant challenge.<sup>5</sup> Despite significant effort in pre-clinical development, most nanomedicine products fail to achieve sufficiently high or improved therapeutic efficacy and/or safety in clinical trials and are never commercialized. Failure of nanomedicines in clinical settings have been attributed to numerous factors, including reproducible and scalable manufacturing, limited stability *in vivo*, and regulatory barriers.<sup>250</sup> Production of large-scale batches of nanomedicines under GMP conditions has been identified as a bottleneck for translation. Subtle deviations in manufacturing processes impact the resulting physiochemical properties (*e.g.* size, shape, crystallinity, drug loading, drug release, surface chemistry, *etc.*) of the nanomedicine, which greatly influence the therapeutic performance of the product. Many aspects of scalable manufacturing processes require significant advances, including growth of nanomedicine manufacturing infrastructure, storage processes, and real-time characterization. Freeze drying is often used to avoid cold-chain storage<sup>251</sup> and prolong stability, but can affect the physiochemical properties of the product and promote aggregation.<sup>249,250</sup> Process analytical techniques to monitor the manufacturing process in real-time as well as streamlined and standardized pre-clinical characterization assays (*i.e.* drug release rates, biodegradation) are needed. The environment for characterization should effectively mimic

the complex biophysical *in vivo* environment to establish predictive *in-vitro-in-vivo* correlations that are currently lacking.<sup>250</sup>

Regulatory agencies (e.g. U.S. Food and Drug Administration, European Medicines Agency) do not have standardized requirements for the pre-clinical and clinical testing of nanomedicines. Thus far, the evaluation of nanoparticle-based drug delivery systems is similar for small molecule APIs in which each nanoparticle product requires individual approval. The process approval includes pre-clinical testing, Investigational New Drug (IND) application, three phases of clinical trials, a New Drug Application (NDA), and market authorization. Pre-clinical evaluation includes detailed chemistry, manufacturing, and quality specifications as well as *in vitro* and *in vivo* evaluations to determine if the product is reasonably safe for humans, and demonstrates therapeutic efficacy that warrants commercialization.<sup>249,250</sup> The next stage involves large-scale manufacturing (grams to kilograms), animal toxicology and pharmacology data, and the proposed clinical trial protocols based on the pre-clinical data.<sup>249</sup> In Phase I clinical trials, the maximum tolerable dose, the recommended dose for Phase II, and any adverse effects are determined. In Phase II, therapeutic efficacy is assessed on a limited, homogeneous patient population to determine appropriate patient pre-selection criteria and endpoint(s) for the larger-scale phase III trials. While approximately 70% of drugs move from Phase I to Phase II, only 33% move from Phase II to Phase III, generally due to lack of efficacy. Due to disease heterogeneity in humans, patient selection criteria can be an important consideration.<sup>250,252</sup> Phase III (randomized and double blinded) involves a large, representative patient population to assess risk benefit, long-term safety data, and identification of potential rare side effects. Of Phase III trials, 25–30% of drugs tested result in an NDA. The cost of clinical trials (Phase I to III) in the United States is \$20M–\$70M.<sup>249</sup> Thus, new polymeric formulations face a rigorous and time-intensive barrier to achieve clinical translation.

## 12.8 Outlook

Advances in colloid synthesis has enabled significant progress in nanomedicine. Key examples to highlight include on-off switchable, glucose-sensitive insulin delivery, and targeted delivery of anti-cancer agents to tumors.<sup>3</sup> To impact human health, improving scalable synthesis, colloidal stability and characterization *in vivo*, as well as improved *in-vitro-in-vivo* correlations are necessary. While clinical translation is a challenging obstacle, the future at the interface of polymer colloids and biological interfaces is ripe with opportunity for enhancing fundamental understanding as well as *in vivo* performance.

## Acknowledgements

This work was partially supported by startup funding at Virginia Commonwealth University and NSF (Award number 1651957) (CT).

## References

1. D. Delcassian, A. K. Patel, A. B. Cortinas and R. Langer, *J. Drug Targeting*, 2018, **0**, 1–15.
2. D. S. Williams, I. A. B. Pijpers, R. Ridolfo and J. C. M. van Hest, *J. Controlled Release*, 2017, **259**, 29–39.
3. K. Park, *J. Controlled Release*, 2014, **190**, 3–8.
4. S. Tinkle, S. E. Mcneil, S. Mühlbach, R. Bawa, G. Borchard, Y. C. Barenholz, L. Tamarkin and N. Desai, *Ann. N. Y. Acad. Sci.*, 2014, **1313**, 35–56.
5. E. Blanco, H. Shen and M. Ferrari, *Nat. Biotechnol.*, 2015, **33**, 941–951.
6. R. Duncan and M. J. Vicent, *Adv. Drug Delivery Rev.*, 2013, **65**, 60–70.
7. E. Marin, M. I. Briceño and C. Caballero-George, *Int. J. Nanomed.*, 2013, **8**, 3071–3091.
8. D. W. van Krevelen and K. te Nijenhuis, *Properties of Polymers: Their Correlation with Chemical Structure; Their Numerical Estimation and Prediction from Additive Group Contributions*, Elsevier, 2009.
9. J. M. Anderson, in *Principles of Regenerative Medicine*, ed. A. Atala, R. Lanza, J. A. Thomson and R. Nerem, Academic Press, San Diego, 2nd edn, 2011, pp. 693–716.
10. D. E. Owens III and N. A. Peppas, *Int. J. Pharm.*, 2006, **307**, 93–102.
11. L. Mertz, *IEEE Pulse*, 2013, **4**, 14–15.
12. A. Pizzoferrato, G. Ciapetti, S. Stea, E. Cenni, C. R. Arciola, D. Granchi and L. Savarino, *Clin. Mater.*, 1994, **15**, 173–190.
13. M. S. El-Samaligy and P. Rohdewald, *J. Pharm. Pharmacol.*, 1983, **35**, 537–539.
14. K. Young Choi, K. Hyun Min, J. Hee Na, K. Choi, K. Kim, J. Hyung Park, I. Chan Kwon and S. Young Jeong, *J. Mater. Chem.*, 2009, **19**, 4102–4107.
15. J. J. Wang, Z. W. Zeng, R. Z. Xiao, T. Xie, G. L. Zhou, X. R. Zhan and S. L. Wang, *Int. J. Nanomed.*, 2011, **6**, 765–774.
16. P. X. Ma and R. Zhang, *J. Biomed. Mater. Res.*, 1999, **46**, 60–72.
17. O. Pillai and R. Panchagnula, *Curr. Opin. Chem. Biol.*, 2001, **5**, 447–451.
18. J. K. Kim, H. J. Kim, J.-Y. Chung, J.-H. Lee, S.-B. Young and Y.-H. Kim, *Arch. Pharmacal Res.*, 2014, **37**, 60–68.
19. N. Kamaly, B. Yameen, J. Wu and O. C. Farokhzad, *Chem. Rev.*, 2016, **116**, 2602–2663.
20. M. J. Hawkins, P. Soon-Shiong and N. Desai, *Adv. Drug Delivery Rev.*, 2008, **60**, 876–885.
21. W. Lohcharoenkal, L. Wang, Y. C. Chen and Y. Rojanasakul, *Biomed. Res. Int.*, 2014, **2014**, 180549.
22. X. Wan, X. Zheng, X. Pang, Z. Zhang, T. Jing, W. Xu and Q. Zhang, *Int. J. Pharm.*, 2015, **484**, 16–28.
23. K. K. Li, X. Zhang, Q. Huang, S. W. Yin, X. Q. Yang, Q. B. Wen, C. H. Tang and F. R. Lai, *J. Food Eng.*, 2014, **127**, 103–110.

24. N. M. Molino and S.-W. Wang, *Curr. Opin. Biotechnol.*, 2014, **28**, 75–82.
25. R. Jayakumar, K. P. Chennazhi, R. A. A. Muzzarelli, H. Tamura, S. V. Nair and N. Selvamurugan, *Carbohydr. Polym.*, 2010, **79**, 1–8.
26. H. Katas and H. O. Alpar, *J. Controlled Release*, 2006, **115**, 216–225.
27. S. K. Shukla, A. K. Mishra, O. A. Arotiba and B. B. Mamba, *Int. J. Biol. Macromol.*, 2013, **59**, 46–58.
28. I. Y. Kim, M. K. Yoo, J. H. Seo, S. S. Park, H. S. Na, H. C. Lee, S. K. Kim and C. S. Cho, *Int. J. Pharm.*, 2007, **341**, 35–43.
29. M. Hamidi, A. Azadi and P. Rafiei, *Adv. Drug Delivery Rev.*, 2008, **60**, 1638–1649.
30. G. Mattheolabakis, L. Milane, A. Singh and M. M. Amiji, *J. Drug Targeting*, 2015, **23**, 605–618.
31. S. Chono, S.-D. Li, C. C. Conwell and L. Huang, *J. Controlled Release*, 2008, **131**, 64–69.
32. H. Y. Yoon, H. Koo, K. Y. Choi, S. J. Lee, K. Kim, I. C. Kwon, J. F. Leary, K. Park, S. H. Yuk, J. H. Park and K. Choi, *Biomaterials*, 2012, **33**, 3980–3989.
33. M. Vert, Y. Doi, K.-H. Hellwich, M. Hess, P. Hodge, P. Kubisa, M. Rinaudo and F. Schué, *Pure Appl. Chem.*, 2012, **84**, 377–410.
34. B. Eling, S. Gogolewski and A. J. Pennings, *Polymer*, 1982, **23**, 1587–1593.
35. P. X. Ma, *Mater. Today*, 2004, **7**, 30–40.
36. P. X. Ma and R. Langer, in *Symposium Z – Polymers in Medicine and Pharmacy*, 1995, vol. 394.
37. S. Dumitriu, *Polymeric Biomaterials, Revised and Expanded*, CRC Press, 2001.
38. S. H. Bhang, J. S. Lim, C. Y. Choi, Y. K. Kwon and B.-S. Kim, *J. Biomater. Sci., Polym. Ed.*, 2007, **18**, 223–239.
39. P. C. Hiemenz and T. P. Lodge, *Polymer Chemistry*, CRC Press, 2nd edn, 2007.
40. W. B. Liechty, D. R. Kryscio, B. V. Slaughter and N. A. Peppas, *Annu. Rev. Chem. Biomol. Eng.*, 2010, **1**, 149–173.
41. H. K. Makadia and S. J. Siegel, *Polymers*, 2011, **3**, 1377–1397.
42. M. M. Knopp, N. E. Olesen, P. Holm, P. Langguth, R. Holm and T. Rades, *J. Pharm. Sci.*, 2015, **104**, 2905–2912.
43. M. F. Zambaux, F. Bonneaux, R. Gref, E. Dellacherie and C. Vigneron, *J. Controlled Release*, 1999, **60**, 179–188.
44. P. Blasi, S. S. D’Souza, F. Selmin and P. P. DeLuca, *J. Controlled Release*, 2005, **108**, 1–9.
45. K. E. Uhrich, S. M. Cannizzaro, R. S. Langer and K. M. Shakesheff, *Chem. Rev.*, 1999, **99**, 3181–3198.
46. H. Park, K. Park and W. S. W. Shalaby, *Biodegradable Hydrogels for Drug Delivery*, CRC Press, 2011.
47. D. W. Hutmacher, *Biomaterials*, 2000, **21**, 2529–2543.
48. S. Fredenberg, M. Wahlgren, M. Reslow and A. Axelsson, *Int. J. Pharm.*, 2011, **415**, 34–52.

49. X. Huang and C. S. Brazel, *J. Controlled Release*, 2001, **73**, 121–136.
50. A. T. Raiche and D. A. Puleo, *J. Drug Targeting*, 2001, **9**, 449–460.
51. B. D. Ulery, L. S. Nair and C. T. Laurencin, *J. Polym. Sci., Part B: Polym. Phys.*, 2011, **49**, 832–864.
52. K. Knop, R. Hoogenboom, D. Fischer and U. S. Schubert, *Angew. Chem., Int. Ed.*, 2010, **49**, 6288–6308.
53. T. K. Dash and V. B. Konkimalla, *Mol. Pharmaceutics*, 2012, **9**, 2365–2379.
54. A. Graf, A. McDowell and T. Rades, *Expert Opin. Drug Delivery*, 2009, **6**, 371–387.
55. K. W. Leong, B. C. Brott and R. Langer, *J. Biomed. Mater. Res.*, 1985, **19**, 941–955.
56. Y. Zhao, B. G. Trewyn, I. I. Slowing and V. S.-Y. Lin, *J. Am. Chem. Soc.*, 2009, **131**, 8398–8400.
57. A. Wang, H. Gao, Y. Sun, Y. L. Sun, Y. W. Yang, G. Wu, Y. Wang, Y. Fan and J. Ma, *Int. J. Pharm.*, 2013, **441**, 30–39.
58. W. Gao, J. M. Chan and O. C. Farokhzad, *Mol. Pharmaceutics*, 2010, **7**, 1913–1920.
59. C. Tang, D. Amin, P. B. Messersmith, J. E. Anthony and R. K. Prud'homme, *Langmuir*, 2015, **31**, 3612–3620.
60. W. T. Godbey, K. K. Wu and A. G. Mikos, *J. Controlled Release*, 1999, **60**, 149–160.
61. M. Ogris, S. Brunner, S. Schüller, R. Kircheis and E. Wagner, *Gene Ther.*, 1999, **6**, 595–605.
62. M. Kanamala, W. R. Wilson, M. Yang, B. D. Palmer and Z. Wu, *Biomaterials*, 2016, **85**, 152–167.
63. E. N. Guidry, J. Farand, A. Soheili, C. A. Parish, N. J. Kevin, B. Pipik, K. B. Calati, N. Ikemoto, J. H. Waldman, A. H. Latham, B. J. Howell, A. Leone, R. M. Garbaccio, S. E. Barrett, R. G. Parmar, Q. T. Truong, B. Mao, I. W. Davies, S. L. Colletti and L. Sepp-Lorenzino, *Bioconjugate Chem.*, 2014, **25**, 296–307.
64. X. Huang, S. Shen, Z. Zhang and J. Zhuang, *Int. J. Nanomed.*, 2014, **9**, 4785–4794.
65. J. Guo, Y. Ping, H. Ejima, K. Alt, M. Meissner, J. J. Richardson, Y. Yan, K. Peter, D. Von Elverfeldt, C. E. Hagemeyer and F. Caruso, *Angew. Chem., Int. Ed.*, 2014, **53**, 5546–5551.
66. H. Ejima, J. J. Richardson, K. Liang, J. P. Best, M. P. Van Koeverden, G. K. Such, J. Cui and F. Caruso, *Science*, 2013, **341**, 154–157.
67. B. M. Wohl and J. F. J. Engbersen, *J. Controlled Release*, 2012, **158**, 2–14.
68. S. W. Morton, Z. Poon and P. T. Hammond, *Biomaterials*, 2013, **34**, 5328–5335.
69. E. G. Kelley, J. N. L. Albert, M. O. Sullivan and T. H. Epps III, *Chem. Soc. Rev.*, 2013, **42**, 7057–7071.
70. M. A. Ward and T. K. Georgiou, *Polymers*, 2011, **3**, 1215–1242.

71. J. Ramos, A. Imaz and J. Forcada, *Polym. Chem.*, 2012, **3**, 852–856.
72. C. de las Heras Alarcón, S. Pennadam and C. Alexander, *Chem. Soc. Rev.*, 2005, **34**, 276–285.
73. S. Mura, J. Nicolas and P. Couvreur, *Nat. Mater.*, 2013, **12**, 991–1003.
74. J. Liu, A. Debuigne, C. Detrembleur and C. Jérôme, *Adv. Healthcare Mater.*, 2014, **3**, 1941–1968.
75. J.-F. Lutz, *Adv. Mater.*, 2011, **23**, 2237–2243.
76. E. A. Rainbolt, K. E. Washington, M. C. Biewer and M. C. Stefan, *J. Mater. Chem. B*, 2013, **1**, 6532–6537.
77. S. Xu, W. Wang, X. Li, J. Liu, A. Dong and L. Deng, *Eur. J. Pharm. Sci.*, 2014, **62**, 267–273.
78. S. H. Kim, J. P. K. Tan, K. Fukushima, F. Nederberg, Y. Y. Yang, R. M. Waymouth and J. L. Hedrick, *Biomaterials*, 2011, **32**, 5505–5514.
79. M. R. Battig, B. Soontornworajit and Y. Wang, *J. Am. Chem. Soc.*, 2012, **134**, 12410–12413.
80. B. Soontornworajit, J. Zhou, Z. Zhang and Y. Wang, *Biomacromolecules*, 2010, **11**, 2724–2730.
81. B. Soontornworajit, J. Zhou, M. P. Snipes, M. R. Battig and Y. Wang, *Biomaterials*, 2011, **32**, 6839–6849.
82. Z. Gu, T. T. Dang, M. Ma, B. C. Tang, H. Cheng, S. Jiang, Y. Dong, Y. Zhang and D. G. Anderson, *ACS Nano*, 2013, **7**, 6758–6766.
83. C. Tang and R. K. Prud'homme, in *Polymer Nanoparticles for Nanomedicines*, Springer International Publishing, Cham, 2016, pp. 55–85.
84. Y. Yan, M. Björnalm and F. Caruso, *Chem. Mater.*, 2014, **26**, 452–460.
85. S. H. Wu, Y. Hung and C. Y. Mou, *Chem. Mater.*, 2013, **25**, 352–364.
86. S. M. D'Addio and R. K. Prud'homme, *Adv. Drug Delivery Rev.*, 2011, **63**, 417–426.
87. S. M. D'Addio and R. K. Prud'homme, *Adv. Drug Delivery Rev.*, 2011, **63**, 417–426.
88. H. K. Chan and P. C. L. Kwok, *Adv. Drug Delivery Rev.*, 2011, **63**, 406–416.
89. C. I. C. Cruchó and M. T. Barros, *Mater. Sci. Eng., C*, 2017, **80**, 771–784.
90. D. Liu, H. Zhang, F. Fontana, J. T. Hirvonen and H. A. Santos, *Adv. Drug Delivery Rev.*, 2017, **128**, 54–83.
91. F. Meng, Z. Zhong and J. Feijen, *Biomacromolecules*, 2009, **10**, 197–209.
92. K. Letchford and H. Burt, *Eur. J. Pharm. Biopharm.*, 2007, **65**, 259–269.
93. C. E. Mora-Huertas, H. Fessi and A. Elaissari, *Int. J. Pharm.*, 2010, **385**, 113–142.
94. R. Bleul, R. Thiermann and M. Maskos, *Macromolecules*, 2015, **48**, 7396–7409.
95. Y. Men, F. Peng, Y. Tu, J. C. M. Van Hest and D. A. Wilson, *Polym. Chem.*, 2016, **7**, 3977–3982.

96. R. F. Pagels, J. Edelstein, C. Tang and R. K. Prud'homme, *Nano Lett.*, 2018, **18**, 1139–1144.
97. M. Akbulut, S. M. D'Addio and R. K. Prud'homme, *ACS Symp. Ser.*, 2010, **1053**, 25–45.
98. V. Kumar and R. K. Prud'homme, *J. Pharm. Sci.*, 2008, **97**, 4904–4914.
99. K. M. Pustulka, A. R. Wohl, H. S. Lee, A. R. Michel, J. Han, T. R. Hoye, A. V. McCormick, J. Panyam and C. W. Macosko, *Mol. Pharmaceutics*, 2013, **10**, 4367–4377.
100. W. S. Saad and R. K. Prud'homme, *Nano Today*, 2016, **11**, 212–227.
101. Z. Poon, J. B. Lee, S. W. Morton and P. T. Hammond, *Nano Lett.*, 2011, **11**, 2096–2103.
102. T. Ramasamy, Z. S. Haidar, T. H. Tran, J. Y. Choi, J. H. Jeong, B. S. Shin, H. G. Choi, C. S. Yong and J. O. Kim, *Acta Biomater.*, 2014, **10**, 5116–5127.
103. S. W. Morton, K. P. Herlihy, K. E. Shopsowitz, Z. J. Deng, K. S. Chu, C. J. Bowerman, J. M. DeSimone and P. T. Hammond, *Adv. Mater.*, 2013, **25**, 4706.
104. X. Fu, J. Cai, X. Zhang, W.-D. Li, H. Ge and Y. Hu, *Adv. Drug Delivery Rev.*, 2018, **132**, 169–187.
105. T. J. Merkel, K. P. Herlihy, J. Nunes, R. M. Orgel, J. P. Rolland and J. M. DeSimone, *Langmuir*, 2010, **26**, 13086–13096.
106. M. Kumar, A. Misra, A. K. Babbar, A. K. Mishra, P. Mishra and K. Pathak, *Int. J. Pharm.*, 2008, **358**, 285–291.
107. C. Lovelyn and A. A. Attama, *J. Biomater. Nanobiotechnol.*, 2011, **2**, 626–639.
108. K. Mitri, C. Vauthier, N. Huang, A. Menas, C. Ringard-Lefebvre, C. Anselmi, M. Stambouli, V. Rosilio, J. J. Vachon and K. Bouchemal, *J. Pharm. Sci.*, 2012, **101**, 4240–4247.
109. F. U. Rehman, K. U. Shah, S. U. Shah, I. U. Khan, G. M. Khan and A. Khan, *Expert Opin. Drug Delivery*, 2017, **14**, 1325–1340.
110. R. H. Müller, K. Mäder and S. Gohla, *Eur. J. Pharm. Biopharm.*, 2000, **50**, 161–177.
111. P. R. Lockman, R. J. Mumper, M. A. Khan and D. D. Allen, *Drug Dev. Ind. Pharm.*, 2002, **28**, 1–13.
112. K. M. El-Sawy and H. S. El-Sawy, *Int. J. Pharm.*, 2017, **528**, 675–691.
113. K. Sheets, J. Wang, S. Meehan, P. Sharma, C. Ng, M. Khan, B. Koons, B. Behkam and A. S. Nain, *J. Biomater. Tissue Eng.*, 2013, **3**, 355–368.
114. H. C. Shum, A. R. Abate, D. Lee, A. R. Studart, B. Wang, C.-H. Chen, J. Thiele, R. K. Shah, A. Krummel and D. A. Weitz, *Macromol. Rapid Commun.*, 2010, **31**, 108–118.
115. T. Thorsen, R. W. Roberts, F. H. Arnold and S. R. Quake, *Phys. Rev. Lett.*, 2001, **86**, 4163–4166.
116. S. L. Anna, N. Bontoux and H. A. Stone, *Appl. Phys. Lett.*, 2003, **82**, 364–366.

117. A. S. Utada, E. Lorenceau, D. R. Link, P. D. Kaplan, H. A. Stone and D. A. Weitz, *Science*, 2005, **308**, 537–541.
118. S. Xu, Z. Nie, M. Seo, P. Lewis, E. Kumacheva, H. A. Stone, P. Garstecki, D. B. Weibel, I. Gitlin and G. M. Whitesides, *Angew. Chem., Int. Ed. Engl.*, 2005, **44**, 724–728.
119. J.-H. Jang, D. Dendukuri, T. A. Hatton, E. L. Thomas and P. S. Doyle, *Angew. Chem., Int. Ed. Engl.*, 2007, **46**, 9027–9031.
120. A. Gupta, H. B. Eral, T. A. Hatton and P. S. Doyle, *Soft Matter*, 2016, **12**, 2826–2841.
121. M. E. Helgeson, S. C. Chapin and P. S. Doyle, *Curr. Opin. Colloid Interface Sci.*, 2011, **16**, 106–117.
122. D. Dendukuri, S. S. Gu, D. C. Pregibon, T. A. Hatton and P. S. Doyle, *Lab Chip*, 2007, **7**, 818–828.
123. D. Dendukuri, D. C. Pregibon, J. Collins, T. A. Hatton and P. S. Doyle, *Nat. Mater.*, 2006, **5**, 365.
124. K.-H. Roh, D. C. Martin and J. Lahann, *Nat. Mater.*, 2005, **4**, 759.
125. J. Lahann, *Small*, 2011, **7**, 1149–1156.
126. N. Doshi, A. S. Zahr, S. Bhaskar, J. Lahann and S. Mitragotri, *Proc. Natl. Acad. Sci. U. S. A.*, 2009, **106**, 21495–21499.
127. A. C. Misra and J. Lahann, *Adv. Healthcare Mater.*, 2018, **7**, 1701319.
128. J. S. Brenner, D. C. Pan, J. W. Myerson, O. A. Marcos-Contreras, C. H. Villa, P. Patel, H. Hekierski, S. Chatterjee, J.-Q. Tao, H. Parhiz, K. Bhamidipati, T. G. Uhler, E. D. Hood, R. Y. Kiseleva, V. S. Shuvaev, T. Shuvaeva, M. Khoshnejad, I. Johnston, J. V Gregory, J. Lahann, T. Wang, E. Cantu, W. M. Armstead, S. Mitragotri and V. Muzykantov, *Nat. Commun.*, 2018, **9**, 2684.
129. A. M. Ross, S. Rahmani, D. M. Prieskorn, A. F. Dishman, J. M. Miller, J. Lahann and R. A. Altschuler, *J. Biomed. Mater. Res., Part A*, 2016, **104**, 1510–1522.
130. J. Hao, K. C. K. Cheng, L. G. Kruger, L. Larsson, J. V Sugai, J. Lahann and W. V Giannobile, *Adv. Mater.*, 2016, **28**, 3145–3151.
131. S. K. Sia and G. M. Whitesides, *Electrophoresis*, 2003, **24**, 3563–3576.
132. E. Kim, Y. Xia and G. M. Whitesides, *Nature*, 1995, **376**, 581.
133. E. King, Y. Xia, X.-M. Zhao and G. M. Whitesides, *Adv. Mater.*, 2004, **9**, 651–654.
134. L. Tao, X. M. Zhao, J. M. Gao and W. Hu, *Nanotechnology*, 2010, **21**, 95301.
135. F. Buyukserin, M. Aryal, J. Gao and W. Hu, *Small*, 2009, **5**, 1632–1636.
136. L. C. Glangchai, M. Calderera-Moore, L. Shi and K. Roy, *J. Controlled Release*, 2008, **125**, 263–272.
137. G. Acharya, C. S. Shin, M. McDermott, H. Mishra, H. Park, I. C. Kwon and K. Park, *J. Controlled Release*, 2010, **141**, 314–319.
138. J. P. Rolland, B. W. Maynor, L. E. Euliss, A. E. Exner, G. M. Denison and J. M. DeSimone, *J. Am. Chem. Soc.*, 2005, **127**, 10096–10100.

139. A. Garcia, P. Mack, S. Williams, C. Fromen, T. Shen, J. Tully, J. Pillai, P. Kuehl, M. Napier, J. M. DeSimone and B. W. Maynor, *J. Drug Delivery*, 2012, **2012**, 1–10.
140. J. L. Perry, K. P. Herlihy, M. E. Napier and J. M. Desimone, *Acc. Chem. Res.*, 2011, **44**, 990–998.
141. J. Xu, D. H. C. Wong, J. D. Byrne, K. Chen, C. Bowerman and J. M. Desimone, *Angew. Chem., Int. Ed.*, 2013, **52**, 6580–6589.
142. S. S. Dunn, S. Tian, S. Blake, J. Wang, A. L. Galloway, A. Murphy, P. D. Pohlhaus, J. P. Rolland, M. E. Napier and J. M. Desimone, *J. Am. Chem. Soc.*, 2012, 300174.
143. C. A. Fromen, T. B. Rahhal, G. R. Robbins, M. P. Kai, T. W. Shen, J. C. Luft and J. M. DeSimone, *Nanomed. Nanotechnol.*, 2016, **12**, 677–687.
144. T. B. Rahhal, C. A. Fromen, E. M. Wilson, M. P. Kai, T. W. Shen, J. C. Luft and J. M. DeSimone, *Mol. Pharmaceutics*, 2016, **13**, 1626–1635.
145. J.-Y. Wang, Y. Wang, S. S. Sheiko, D. E. Betts and J. M. DeSimone, *J. Am. Chem. Soc.*, 2012, **134**, 5801–5806.
146. T. J. Merkel, S. W. Jones, K. P. Herlihy, F. R. Kersey, A. R. Shields, M. Napier, J. C. Luft, H. Wu, W. C. Zamboni, A. Z. Wang, J. E. Bear and J. M. DeSimone, *Proc. Natl. Acad. Sci. U. S. A.*, 2011, **108**, 586–591.
147. J. Xu, J. Wang, J. C. Luft, S. Tian, G. Owens, A. A. Pandya, P. Berglund, P. Pohlhaus, B. W. Maynor, J. Smith, B. Hubby, M. E. Napier and J. M. DeSimone, *J. Am. Chem. Soc.*, 2012, **134**, 8774–8777.
148. W. Hasan, K. Chu, A. Gullapalli, S. S. Dunn, E. M. Enlow, J. C. Luft, S. Tian, M. E. Napier, P. D. Pohlhaus, J. P. Rolland and J. M. DeSimone, *Nano Lett.*, 2012, **12**, 287–292.
149. F. R. Kersey, T. J. Merkel, J. L. Perry, M. E. Napier and J. M. DeSimone, *Langmuir*, 2012, **28**, 8773–8781.
150. M. C. Parrott, M. Finniss, J. C. Luft, A. Pandya, A. Gullapalli, M. E. Napier and J. M. DeSimone, *J. Am. Chem. Soc.*, 2012, **134**, 7978–7982.
151. J. W. Hickey, J. L. Santos, J. M. Williford and H. Q. Mao, *J. Controlled Release*, 2015, **219**, 535–547.
152. L. Shang, K. Nienhaus and G. U. Nienhaus, *J. Nanobiotechnol.*, 2014, **12**, 1–11.
153. E. A. Sykes, J. Chen and G. Zheng, *ACS Nano*, 2014, **8**, 5696–5706.
154. H. Cabral, Y. Matsumoto, K. Mizuno, Q. Chen, M. Murakami, M. Kimura, Y. Terada, M. R. Kano, K. Miyazono, M. Uesaka, N. Nishiyama and K. Kataoka, *Nat. Nanotechnol.*, 2011, **6**, 815–823.
155. N. Hoshyar, S. Gray, H. Han and G. Bao, *Nanomedicine*, 2016, **11**, 673–692.
156. M. B. Fish, C. A. Fromen, G. Lopez-Cazares, A. W. Golinski, T. F. Scott, R. Adili, M. Holinstat and O. Eniola-Adefeso, *Biomaterials*, 2017, **124**, 169–179.

157. A. Coclite, G. Pascazio, M. D. de Tullio and P. Decuzzi, *J. Fluid. Struct.*, 2018, **82**, 638–650.
158. E. Carboni, K. Tschudi, J. Nam, X. Lu and A. W. K. Ma, *AAPS PharmSciTech*, 2014, **15**, 762–771.
159. F. Gentile, A. Curcio, C. Indolfi, M. Ferrari and P. Decuzzi, *J. Nanobiotechnol.*, 2008, **6**, 9.
160. J. A. Champion, Y. K. Katare and S. Mitragotri, *J. Controlled Release*, 2007, **121**, 3–9.
161. C. A. Fromen, W. J. Kelley, M. B. Fish, R. Adili, J. Noble, M. J. Hoenerhoff, M. Holinstat and O. Eniola-Adefeso, *ACS Nano*, 2017, **11**, 10797–10807.
162. D. R. Getts, R. L. Terry, M. T. Getts, C. Deffrasnes, M. Müller, C. van Vreden, T. M. Ashhurst, B. Chami, D. McCarthy, H. Wu, J. Ma, A. Martin, L. D. Shae, P. Witting, G. S. Kansas, J. Kühn, W. Hafezi, I. L. Campbell, D. Reilly, J. Say, L. Brown, M. Y. White, S. J. Cordwell, S. J. Chadban, E. B. Thorp, S. Bao, S. D. Miller and N. J. C. King, *Sci. Transl. Med.*, 2014, **6**, 219ra7.
163. N. P. Truong, M. R. Whittaker, C. W. Mak and T. P. Davis, *Expert Opin. Drug Delivery*, 2015, **12**, 129–142.
164. C. Jordan, V. V Shuvaev, M. Bailey, V. R. Muzykantov and T. D. Dziubla, *Curr. Pharm. Des.*, 2016, **22**, 1259–1273.
165. R. Toy, P. M. Peiris, K. B. Ghaghada and E. Karathanasis, *Nanomedicine*, 2014, **9**, 121–134.
166. C. Kinnear, T. L. Moore, L. Rodriguez-Lorenzo, B. Rothen-Rutishauser and A. Petri-Fink, *Chem. Rev.*, 2017, **117**, 11476–11521.
167. J. Chen, N. E. Clay, N. hyung Park and H. Kong, *Chem. Eng. Sci.*, 2015, **125**, 20–24.
168. S. Venkataraman, J. L. Hedrick, Z. Y. Ong, C. Yang, P. L. R. Ee, P. T. Hammond and Y. Y. Yang, *Adv. Drug Delivery Rev.*, 2011, **63**, 1228–1246.
169. J. S. Suk, Q. Xu, N. Kim, J. Hanes and L. M. Ensign, *Adv. Drug Delivery Rev.*, 2016, **99**, 28–51.
170. A. C. Anselmo, M. Zhang, S. Kumar, D. R. Vogus, S. Menegatti, M. E. Helgeson and S. Mitragotri, *ACS Nano*, 2015, **9**, 3169–3177.
171. J. Lazarovits, Y. Y. Chen, E. A. Sykes and W. C. W. Chan, *Chem. Commun.*, 2015, **51**, 2756–2767.
172. M. Hadjidemetriou and K. Kostarelos, *Nat. Nanotechnol.*, 2017, **12**, 288–290.
173. R. García-Álvarez, M. Hadjidemetriou, A. Sánchez-Iglesias, L. M. Liz-Marzán and K. Kostarelos, *Nanoscale*, 2018, **10**, 1256–1264.
174. C. Gunawan, M. Lim, C. P. Marquis and R. Amal, *J. Mater. Chem. B*, 2014, **2**, 2060–2083.
175. K. Xiao, Y. Li, J. Luo, J. S. Lee, W. Xiao, A. M. Gonik, R. G. Agarwal and K. S. Lam, *Biomaterials*, 2011, **32**, 3435–3446.

176. S. Hirn, M. Semmler-Behnke, C. Schleh, A. Wenk, J. Lipka, M. Schäffler, S. Takenaka, W. Möller, G. Schmid, U. Simon and W. G. Kreyling, *Eur. J. Pharm. Biopharm.*, 2011, **77**, 407–416.
177. K. L. Aillon, Y. Xie, N. El-Gendy, C. J. Berkland and M. L. Forrest, *Adv. Drug Delivery Rev.*, 2009, **61**, 457–466.
178. S. Sharifi, S. Behzadi, S. Laurent, F. Ml, P. Stroeve and M. Mahmoudi, *Chem. Soc. Rev.*, 2012, **41**, 2323–2343.
179. L. Huang and S. Guo, *J. Nanomater.*, 2011, 742895.
180. R. K. Jain and T. Stylianopoulos, *Nat. Rev. Clin. Oncol.*, 2010, **7**, 653–664.
181. C. A. Fromen, G. R. Robbins, T. W. Shen, M. P. Kai, J. P. Y. Ting and J. M. DeSimone, *Proc. Natl. Acad. Sci. U. S. A.*, 2015, **112**, 488–493.
182. C. D. Walkey, J. B. Olsen, H. Guo, A. Emili and W. C. W. Chan, *J. Am. Chem. Soc.*, 2012, **134**, 2139–2147.
183. Q. Yang, S. W. Jones, C. L. Parker, W. C. Zamboni, J. E. Bear and S. K. Lai, *Mol. Pharmaceutics.*, 2014, **11**, 1250–1258.
184. X. Yang, Q. Chen, J. Yang, S. Wu, J. Liu, Z. Li, D. Liu, X. Chen and Y. Qiu, *ACS Appl. Mater. Interfaces*, 2017, **9**, 44045–44052.
185. Z. Cheng, A. Al Zaki, J. Z. Hui, V. R. Muzykantov and A. Tsourkas, *Nature*, 2012, **338**, 903–910.
186. D. R. Elias, A. Poloukhtine, V. Popik and A. Tsourkas, *Nanomed. Nanotechnol.*, 2013, **9**, 194–201.
187. S. M. D'Addio, S. Baldassano, L. Shi, L. Cheung, D. H. Adamson, M. Bruzek, J. E. Anthony, D. L. Laskin, P. J. Sinko and R. K. Prud'homme, *J. Controlled Release*, 2013, **168**, 41–49.
188. Q. S. Xia, H. M. Ding and Y. Q. Ma, *Nanoscale*, 2017, **9**, 8982–8989.
189. J. A. Loureiro, B. Gomes, G. Fricker, I. Cardoso, C. A. Ribeiro, C. Gaiteiro, M. A. N. Coelho, C. Pereira Mdo and S. Rocha, *Colloids Surf., B*, 2015, **134**, 213–219.
190. C. A. Fromen, M. B. Fish, A. Zimmerman, R. Adili, M. Holinstat and O. Eniola-Adefeso, *Bioeng. Transl. Med.*, 2016, **1**, 103–115.
191. L. Miao, S. Guo, C. M. Lin, Q. Liu and L. Huang, *Adv. Drug Delivery Rev.*, 2017, **115**, 3–22.
192. D. B. Pacardo, F. S. Ligler and Z. Gu, *Nanoscale*, 2015, **7**, 3381–3391.
193. T. Mamo, E. A. Moseman, N. Kolishetti, C. Salvador-Morales, J. Shi, D. R. Kuritzkes, R. Langer, U. von Andrian and O. C. Farokhzad, *Nanomedicine*, 2010, **5**, 269–285.
194. J. M. Stewart and B. G. Keselowsky, *Adv. Drug Delivery Rev.*, 2017, **114**, 161–174.
195. G. Bao, S. Mitragotri and S. Tong, *Annu. Rev. Biomed. Eng.*, 2013, **15**, 253–282.
196. M. J. Mitchell, R. K. Jain and R. Langer, *Nat. Rev. Cancer*, 2017, **17**, 659–675.
197. C. E. Markwalter and R. K. Prud'homme, in *Control of Amphiphile Self-Assembling at the Molecular Level: Supra-Molecular Assemblies with*

- Tuned Physicochemical Properties for Delivery Applications*, ed. M. A. Ilies, Oxford University Press, 2017, pp. 275–296.
- 198. R. F. Pagels and R. K. Prud'Homme, *J. Controlled Release*, 2015, **219**, 519–535.
  - 199. S. K. Lai, Y.-Y. Wang and J. Hanes, *Adv. Drug Delivery Rev.*, 2009, **61**, 158–171.
  - 200. S. K. Lai, D. E. O'Hanlon, S. Harrold, S. T. Man, Y.-Y. Wang, R. Cone and J. Hanes, *Proc. Natl. Acad. Sci. U. S. A.*, 2007, **104**, 1482–1487.
  - 201. J. T. Huckaby and S. K. Lai, *Adv. Drug Delivery Rev.*, 2017, **124**, 125–139.
  - 202. B. S. Schuster, J. S. Suk, G. F. Woodworth and J. Hanes, *Biomaterials*, 2013, **34**, 3439–3446.
  - 203. T. W. Shen, C. A. Fromen, M. P. Kai, J. C. Luft, T. B. Rahhal, G. R. Robbins and J. M. DeSimone, *Pharm. Res.*, 2015, **32**, 3248–3260.
  - 204. L. M. Ensign, C. Schneider, J. S. Suk, R. Cone and J. Hanes, *Adv. Mater.*, 2012, **24**, 3887–3894.
  - 205. Y. J. Yamanaka and K. W. Leong, *J. Biomater. Sci., Polym. Ed.*, 2008, **19**, 1549–1570.
  - 206. A. A. Date, J. Hanes and L. M. Ensign, *J. Controlled Release*, 2016, **240**, 504–526.
  - 207. E. M. Pridgen, F. Alexis, T. T. Kuo, E. Levy-Nissenbaum, R. Karnik, R. S. Blumberg, R. Langer and O. C. Farokhzad, *Sci. Transl. Med.*, 2013, **5**, 213ra167.
  - 208. K. B. Chalasani, G. J. Russell-Jones, A. K. Jain, P. V. Diwan and S. K. Jain, *J. Controlled Release*, 2007, **122**, 141–150.
  - 209. K. Whitehead, Z. Shen and S. Mitragotri, *J. Controlled Release*, 2004, **98**, 37–45.
  - 210. J. S. Patton and P. R. Byron, *Nat. Rev. Drug Discovery*, 2007, **6**, 67.
  - 211. S. P. Newman, *Ther. Delivery*, 2017, **8**, 647–661.
  - 212. H. M. Mansour, Y.-S. Rhee and X. Wu, *Int. J. Nanomed.*, 2009, **4**, 299–319.
  - 213. W. Yang, J. I. Peters and R. O. Williams, *Int. J. Pharm.*, 2008, **356**, 239–247.
  - 214. J. C. Sung, B. L. Pulliam and D. A. Edwards, *Trends Biotechnol.*, 2007, **25**, 563–570.
  - 215. H. S. Choi, Y. Ashitate, J. H. Lee, S. H. Kim, A. Matsui, N. Insin, M. G. Bawendi, M. Semmler-Behnke, J. V Frangioni and A. Tsuda, *Nat. Biotechnol.*, 2010, **28**, 1300–1303.
  - 216. J. C. Sung, D. J. Padilla, L. Garcia-Contreras, J. L. VerBerkmoes, D. Durbin, C. A. Peloquin, K. J. Elbert, A. J. Hickey and D. A. Edwards, *Pharm. Res.*, 2009, **26**, 1847–1855.
  - 217. N. Sivadas, D. O'Rourke, A. Tobin, V. Buckley, Z. Ramtoola, J. G. Kelly, A. J. Hickey and S.-A. Cryan, *Int. J. Pharm.*, 2008, **358**, 159–167.
  - 218. R. Vanbever, J. D. Mintzes, J. Wang, J. Nice, D. Chen, R. Batycky, R. Langer and D. A. Edwards, *Pharm. Res.*, 1999, **16**, 1735–1742.
  - 219. D. A. Edwards, J. Hanes, G. Caponetti, J. Hrkach, A. Ben-Jebria, M. Lou Eskew, J. Mintzes, D. Deaver, N. Lotan and R. Langer, *Science*, 1997, **276**, 1868–1872.

220. J. O.-H. Sham, Y. Zhang, W. H. Finlay, W. H. Roa and R. Löbenberg, *Int. J. Pharm.*, 2004, **269**, 457–467.
221. R. Vehring, *Pharm. Res.*, 2008, **25**, 999–1022.
222. C. Loira-Pastoriza, J. Todoroff and R. Vanbever, *Adv. Drug Delivery Rev.*, 2014, **75**, 81–91.
223. F. Ungaro, I. d'Angelo, A. Miro, M. I. La Rotonda and F. Quaglia, *J. Pharm. Pharmacol.*, 2012, **64**, 1217–1235.
224. A. Grenha, B. Seijo and C. Remuñán-López, *Eur. J. Pharm. Sci.*, 2005, **25**, 427–437.
225. S. Al-Qadi, A. Grenha, D. Carrión-Recio, B. Seijo and C. Remuñán-López, *J. Controlled Release*, 2012, **157**, 383–390.
226. A. Vila, A. Sánchez, K. Janes, I. Behrens, T. Kissel, J. L. V. Jato and M. J. Alonso, *Eur. J. Pharm. Biopharm.*, 2004, **57**, 123–131.
227. B. Pulliam, J. C. Sung and D. A. Edwards, *Expert Opin. Drug Delivery*, 2007, **4**, 651–663.
228. C. Nembrini, A. Stano, K. Y. Dane, M. Ballester, A. J. van der Vlies, B. J. Marsland, M. A. Swartz and J. A. Hubbell, *Proc. Natl. Acad. Sci. U. S. A.*, 2011, **108**, E989–E997.
229. H. Zazo, C. I. Colino and J. M. Lanao, *J. Controlled. Release*, 2016, **224**, 86–102.
230. S. Gelperina, K. Kisich, M. D. Iseman and L. Heifets, *Am. J. Respir. Crit. Care Med.*, 2005, **172**, 1487–1490.
231. S. Azarmi, W. H. Roa and R. Löbenberg, *Adv. Drug Delivery Rev.*, 2008, **60**, 863–875.
232. K. Kho, W. S. Cheow, R. H. Lie and K. Hadinoto, *Powder Technol.*, 2010, **203**, 432–439.
233. W. S. Cheow, M. W. Chang and K. Hadinoto, *Pharm. Res.*, 2010, **27**, 1597–1609.
234. G. Pilcer, R. Rosière, K. Traina, T. Sebti, F. Vanderbist and K. Amighi, *J. Pharm. Sci.*, 2013, **102**, 1836–1846.
235. F. Gagnadoux, J. Hureaux, L. Vecellio, T. Urban, A. Le Pape, I. Valo, J. Montharu, V. Leblond, M. Boisdran-Celle, S. Lerondel, C. Majoral, P. Diot, J. L. Racineux and E. Lemarie, *J. Aerosol Med. Pulm. Drug Delivery*, 2008, **21**, 61–70.
236. Y. Zhang, J. Zhu, Y. Tang, X. Chen and Y. Yang, *Drug Dev. Ind. Pharm.*, 2009, **35**, 1059–1065.
237. J. J. Moon, B. Huang and D. J. Irvine, *Adv. Mater.*, 2012, **24**, 3724–3746.
238. T. J. Moyer, A. C. Zmolek and D. J. Irvine, *J. Clin. Invest.*, 2016, **126**, 799–808.
239. K. Shao, S. Singha, X. Clemente-Casares, S. Tsai, Y. Yang and P. Santamaria, *ACS Nano*, 2015, **9**, 16–30.
240. L. Zhao, A. Seth, N. Wibowo, C.-X. Zhao, N. Mitter, C. Yu and A. P. J. Middelberg, *Vaccine*, 2014, **32**, 327–337.
241. S. L. Demento, W. Cui, J. M. Criscione, E. Stern, J. Tulipan, S. M. Kaech and T. M. Fahmy, *Biomaterials*, 2012, **33**, 4957–4964.

242. C. B. Smarr, W. T. Yap, T. P. Neef, R. M. Pearson, Z. N. Hunter, I. Ifergan, D. R. Getts, P. J. Bryce, L. D. Shea and S. D. Miller, *Proc. Natl. Acad. Sci. U. S. A.*, 2016, 5059–5064.
243. R. M. Pearson, L. M. Casey, K. R. Hughes, L. Z. Wang, M. G. North, D. R. Getts, S. D. Miller and L. D. Shea, *Mol. Ther.*, 2017, 25, 1655–1664.
244. R. M. Pearson, L. M. Casey, K. R. Hughes, S. D. Miller and L. D. Shea, *Adv. Drug Delivery Rev.*, 2017, 114, 240–255.
245. D. R. Getts, A. J. Martin, D. P. McCarthy, R. L. Terry, Z. N. Hunter, W. T. Yap, M. T. Getts, M. Pleiss, X. Luo, N. J. C. King, L. D. Shea and S. D. Miller, *Nat. Biotechnol.*, 2012, 30, 1217.
246. J. Noble, A. Zimmerman and C. A. Fromen, *ACS Biomater. Sci. Eng.*, 2017, 3, 560–571.
247. R. P. Allen, A. Bolandparvaz, J. A. Ma, V. A. Manickam and J. S. Lewis, *ACS Biomater. Sci. Eng.*, 2018, 4, 900–918.
248. J. I. Andorko, K. G. Pineault and C. M. Jewell, *J. Biomed. Mater. Res., Part A*, 2016, 105, 1219–1229.
249. H. Ragelle, F. Danhier, V. Préat, R. Langer and D. G. Anderson, *Expert Opin. Drug Delivery*, 2017, 14, 851–864.
250. V. Agrahari and V. Agrahari, *Drug Discovery Today*, 2018, 23, 974–991.
251. S. L. Levit, R. M. Stwodah and C. Tang, *J. Pharm. Sci.*, 2018, 107, 807–813.
252. A. C. Anselmo and S. Mitragotri, *Bioeng. Transl. Med.*, 2016, 1, 10–29.

## CHAPTER 13

# *Polymer Colloids for Cosmetics and Personal Care*

LIANGCHEN XU, YAO ZHOU AND SAMIUL AMIN\*

Department of Chemical Engineering, Manhattan College, Riverdale,  
NY 10471, USA

\*Email: samin01@manhattan.edu

### 13.1 Introduction

Polymer colloids can be defined as a heterogeneous two-phase system with at least one macromolecule component.<sup>1</sup> The versatile properties and modifiable structures make polymer colloids an attractive material for multiple different applications. The use of polymer colloids has been growing increasingly in various industries, such as food, pharmaceuticals, coatings, and cosmetics and personal care.

Prior to the use of commercial polymer colloids, natural ingredients were historically utilized in cosmetics and beauty products. Before the use of polymer colloids as we now know it, early humans started to mix naturally presented polymers, such as beeswax, honey, and milk, with different minerals to create face cream and other makeup products to intensify their beauty and demonstrate their wealth. Looking back at the ancient Egyptians' obsession with makeup products, they mixed different minerals with various oils, beeswax and honey to create creams and ointments, as well as eyeshadow, eyeliner, lipsticks, and other cosmetic products. Beeswax, which is a highly crystalline polymer in its natural form, can be considered to be one of the earliest polymer colloids to be used in a cosmetic product.<sup>2</sup> According to

the definition, these products are recognized as some of the earliest cosmetic products incorporating polymer colloids.

The historical application of polymer colloids in cosmetic products is not limited to ancient Egypt. Dating back to around 600 BC, ancient Chinese in the Tang dynasty already knew how to use a mixture of beeswax, egg white, gelatin, gum arabic, and plant-based dye to color their nails. This practice can be traced back to 3000 BC based on evidence found in literature.<sup>3</sup>

The cosmetic industry has been exhibiting high growth since the early 20th century.<sup>4</sup> Since then, a wide range of polymers has been introduced into cosmetic and personal care products to achieve better application, smoother texture, better water resistance, and long-lasting appearance. To date, different types of polymers have been put into use in cosmetic formulations.

A range of polymers have been utilized and further modified for use in the cosmetic industry as thickeners or film formers due to their high performance. The use of polymer colloids has encountered a recent development, where polymer latexes have played an increasingly important role as film formers, thickeners, moisturizers, conditioning agents, dispersing agents, waterproofing agents, exfoliating agents, micropore sponges, etc.<sup>4</sup>

## 13.2 Key Polymer Colloid Properties

The key properties of polymer colloids that are essential for performance in cosmetic products include particle size, size distribution, film formation, adhesion, and chemical modification such as hydrophobicity and hydrophilicity.

### 13.2.1 Particle Size, Particle Size Distribution

Polymer colloid size and size distribution can range from 20 nm,<sup>5</sup> when used as film forming polymer latexes in nanoemulsions, up to 2200 µm when they are utilized as microspheres.<sup>6</sup> In foundation, the spherical silicone resin particles can range from 0.05 to 100 microns,<sup>7</sup> while in nail polish and sunscreen formulations, polymer latexes typically have a size range from 40 nm to 1000 nm.<sup>8,9</sup> Choosing the appropriate size range and distribution for specific applications is very important. Particle size and size distribution directly affect the film-formation mechanism which can ultimately impact the final product efficacy significantly.<sup>10</sup> The impact of latex particle size and size distribution on the chemical,<sup>11,12</sup> physical,<sup>13,14</sup> and mechanical properties<sup>15,16</sup> of the final polymeric film has been the primary objective in many recent research investigations.<sup>10–16</sup> According to Ugur *et al.*,<sup>10</sup> nanosize polymer latexes can enhance the glossiness, smoothness, solvent resistance, and adhesion of the final polymeric film.<sup>10</sup> The nanoscale particle size and polydispersity facilitated the packing step of film formation by affecting the number of defects.<sup>17</sup> When the polymeric film was under mechanical shear, these defects serve as fracture initiators.<sup>15</sup> Ultimately, good packing of polymer latexes is vital for the performance of the final polymeric film.<sup>18</sup>

### 13.2.2 Film Formation

The ability to form a continuous film on a substrate of interest is critical for the cosmetic and personal care industry. Foundation, mascara, lipstick, sunscreen, and nail polish are some of the products that require the addition of film-forming polymer colloids, also known as “polymer latexes”.<sup>19</sup> Polymeric film formation is a simple process when the polymer is fully dissolved in the solvent. As shown in Figure 13.1, the polymeric solution spreads onto the substrate surface in the form of small droplets.<sup>20</sup> When the volatile solvent starts drying, the polymer chains start to interpenetrate and transition through a gel state. Upon further drying, a polymeric film begins to form on the substrate surface.

Bauer *et al.*<sup>21</sup> indicated that when the polymeric solution concentration reaches the reciprocal of its intrinsic viscosity, polymer chains begin to entangle and interpenetrate. When the end-to-end distance of a random coil polymer chain increases, the adhesion of the final film will improve due to the increase in polymer chain interaction with the substrate surface.<sup>22</sup> The rate of solvent evaporation is a key aspect in the film-formation process for both polymer dispersions and solutions. In extreme cases, the substrate becomes oversaturated with solvent and starts to dissolve when the rate of evaporation is too slow. This extreme situation should be completely avoided in cosmetics and personal care products. With the exception of some products, like nail polish, most are eliminating the usage of organic solvents. Fast evaporation of solvent from a substrate can lead to uneven spreading and the impinging of polymer solution droplets on a substrate surface therefore should be avoided. The solvent evaporation rate can be affected by temperature, pressure, relative humidity, and air movement.<sup>20</sup>

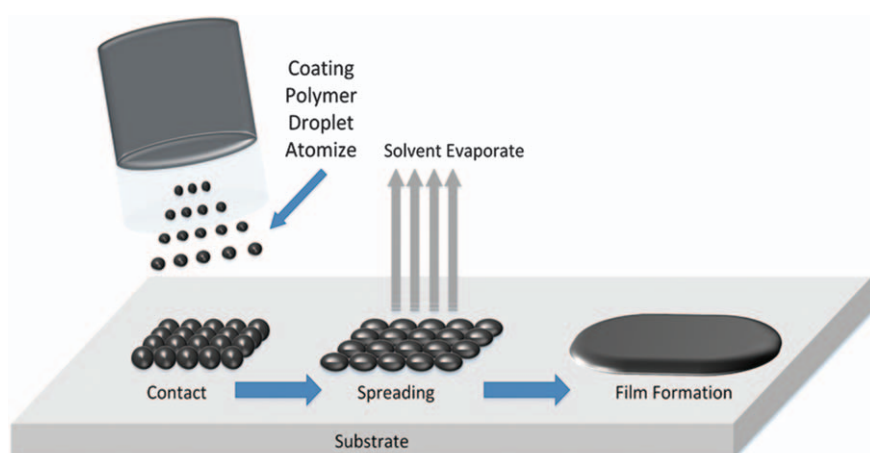


**Figure 13.1** Simple schematic of film formation from a solvent-based polymeric solution.

Considering the potential environmental and health hazards associated with organic-based polymer solutions, cosmetics and personal care products are all gearing towards the aqueous-based polymer colloids and polymer latex dispersion systems. The film-formation mechanism of aqueous-based polymeric dispersions is similar to that of non-aqueous ones. Polymer latexes are tightly packed on the substrate surface as water evaporates. Steward *et al.*<sup>18</sup> considered the water evaporation rate to be constant at the preliminary drying stage.<sup>18</sup> The vacated spaces left by water evaporation are filled by deformed polymer spheres. Upon further drying, the polymer spheres continuously merge together while polymer chains interpenetrate and entangle to form the polymeric film. This process is referred to as coalescence.<sup>20</sup>

### 13.2.3 Adhesion

One of the growing trends in the cosmetic industry is long wear. When applying cosmetic products, such as foundation or lipstick, they must have the ability to withstand certain environmental stresses such as humidity, temperature, and mechanical stress (eating, rubbing). These stresses all have a strong effect on the long-lasting property of the product. In order to ensure long wear of makeup, the adhesive properties of polymers need to be strong enough and adequate testing needs to be carried out in order to ensure this. There is a wide range of testing that could be used depending upon the application. These include peel test, lab shear test, pull out test, scratch test, etc.<sup>23</sup> During a peel test, for example, adhesive tape is attached and pressed on the surface with the ink or sample on top. Pressure is added to the tape using a rubber cylinder to apply a constant force over a period of time. After that, the tape is peeled off quickly. The adhesiveness can be described as the difference between amount of remaining sample compared to the amount of sample before testing.<sup>23</sup> Other peel tests are described by Awaja and Firas, *et al.*,<sup>23</sup> There is a trend for looking at natural adhesives and how they can be applied to polymer colloids. These natural adhesives can come from various sources, such as mussels.<sup>24</sup>

### 13.2.4 Waterproofing

In order to enhance the long-lasting property, waterproofing has become an essential component. There is a strong drive to find a polymer latex or modified polymer latex that has water-resistant properties built into the product. In this regard, there is lots of exploration in potentially applying amphiphilic particles and Janus particles<sup>25</sup> into cosmetic formulations. Most of these novel particles will be discussed in Section 13.4.

### 13.2.5 Chemistry Modification

In order to achieve an even dispersion in different solution environments and better compatibility with the polymer matrix, various functional groups

can be introduced into polymer colloids. These include new structures and functional groups which allow the hydrophobicity of the polymer colloids to be altered. This could potentially provide additional adhesiveness to the skin and hair substrate.<sup>26</sup>

### 13.2.6 Lubrication and Tribology

Tribology is derived from the Greek word “tribos” and can be literally translated as “the science of rubbing”. It studies the friction and motion between the interacting surfaces.<sup>27</sup> The hands are one of the most sensitive parts of the human body with numerous receptors including mechano-receptors, thermoreceptors, etc.<sup>28</sup> When people apply cosmetic products, such as face creams or foundations with their hands, the sensory feeling during rubbing is one of the factors that attracts consumers to purchase the product. Therefore, tribology has become a very useful tool when formulating a product.

There are three lubrication regimes that occur during product application: hydrodynamic, mixed, and boundary. These regimes can be described through a Stribeck curve, as shown in Figure 13.2. In the hydrodynamic regime, properties of the bulk fluid film, such as viscosity, play a key role in the lubrication. As the fluid layer gets thinner, the elastohydrodynamic lubrication regime or mixed regime starts. On further reduction in film thickness, the two surfaces start come in contact with each other. At this point, boundary lubrication starts to take place. Adding a boundary lubricant which adheres to the substrate can improve the after feel sensory performance.<sup>27</sup> Polymer colloids can be modified to either impact rheology and therefore the hydrodynamic/mix lubrication regimes or they can be functionalized to adhere to the skin and give rise to boundary lubrication effects, thereby impacting the entire sensory experience of consumers for product application to after feel.<sup>29</sup>

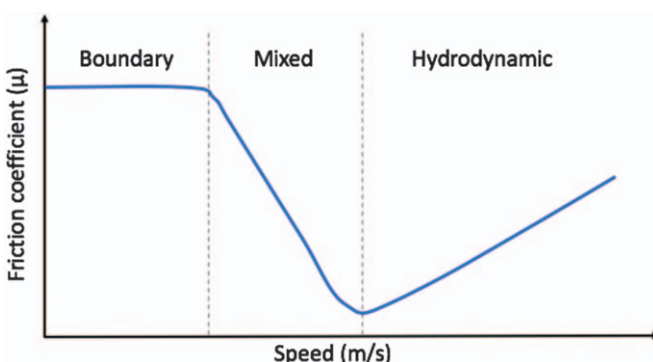


**Figure 13.2** A Stribeck curve describing three lubrication regimes.

### 13.3 Applications of Polymer Colloids

Applications of polymer colloids in cosmetic and personal care are very broad and they have been utilized in facial makeup, sunscreen, mascara, lipsticks, nail polish, *etc.*

#### 13.3.1 Facial Makeup

Facial makeup products are one of the most effective ways to perfect the appearance of skin. The two most common types of facial makeup are foundations and concealers. Foundation can create a uniform skin color with low to medium coverage. To fulfill consumer needs, a wide range of foundation colors have been developed with the aim of matching all skin tones while giving the consumers the choice of low to high coverage. Concealers are applied to areas of concern to hide minor skin problems like acne scars. Concealers appear to be thicker due to higher concentrations of pigments in the formulation. Other multifunctional facial makeups such as Beauty Balm creams (BB creams) and Color Correcting creams (CC creams) combine cosmetics and skin care benefits and have been growing in demand. From a consumer perspective, a facial makeup should have guaranteed evenness in color, concealment of flaws, and most importantly provide a final homogeneous, unifying, and long-lasting film that is matt and has a smooth finish. These requirements need to be reflected in the formulation considerations, which results in the extensive utilization of polymer colloids with the right physical properties.

Polymer colloids, also known as synthetic latexes,<sup>19</sup> are able to form a continuous film on a substrate. However, appropriate polymer colloids need to be chosen for different foundation formulations. The three most common types of emulsions for liquid and semi-solid foundations are oil-in-water (O/W), water-in-oil (W/O) and water-in-silicone (W/Si) emulsions. Among the W/O and W/Si formulations, some common silicon resin film formers such as cyclopentasiloxane and trimethylsiloxysilicate, dimethicone and trimethylsiloxysilicate,<sup>30</sup> and polymethylsilsesquioxane are utilized.<sup>7</sup> They are able to create a smooth, lubricating film which increases the skin's ability to repel water. The size of the spherical, fine particle silicone resin can range from 0.05 to 100 microns and can impart anti-caking and slip properties to the skin.<sup>7</sup> Other common film formers are polyvinylacetate/polyvinyl alcohol resins, PVP [Poly(vinyl pyrrolidone)], PVP/VA copolymers, and methyl methacrylate crosspolymer.<sup>31</sup> Methyl methacrylate crosspolymer is a porous polymer that absorbs excess sebum or acne-producing oils which is ideal for consumers with oily skin. Natural polymeric fill formers that are utilized in cosmetics can include pullulan, methyl ricinoleate, ethylcellulose, and polyhydroxystearic acid. Natural polymer latexes have been utilized in mostly water-based formulations, in which pullulan is not only an effective film former but also a good water-binding agent, thickening agent, and antioxidant.<sup>32</sup> Furthermore, polymer colloids can be utilized as emollients,

occlusive agents, emulsifiers, fillers, rheology modifiers, and opacifying agents based on the characteristics of the individual polymer latex.

### 13.3.2 Sunscreen

The basic function of sunscreen is to provide broad-spectrum protection against UVA and UVB, due to the known harmful effects on the human skin. However, as sunscreen is worn usually during outdoor activities, there is a requirement to have some additional benefits built in to a sunscreen product. These benefits include moisturization and require that the product be sweatproof and waterproof. The role of film-forming polymer latex is further emphasized while additional considerations are required when formulating sunscreens. An even and uniform film on the skin allows higher SPF which is crucial for an effective sunscreen. To ensure water resistance, most sunscreens are oil-in-water emulsions. Hydrophobic polymers such as acrylates/octylacrylamide copolymer, PVP/eicosene copolymer, and tri-acontanyl PVP are added to the oil phase in powder, flake, or wax form. These film formers and waterproofing agents can also enhance pigment dispersion which ultimately improves the sunscreen SPF.

The usage of both physical sunblocks like zinc oxide and chemical sunscreens such as octylcrylene, avobenzone, and octinoxate are heavily regulated by the FDA. Most research is focusing on improving uniform film formation by modify zinc oxide geometry, surface chemistry, or changing the polymer latex combination. In patent US20180280280,<sup>9</sup> they describe a combination of phosphorus-based copolymer and voided latex particles and their capability to enhance the efficacy of inorganic metal oxides while also improving the aesthetic qualities. The voided latex particle has a core–shell structure which is derived from monoethylenically unsaturated monomers and polyethylenically unsaturated monomers with a particle size from 50 nm to 1000 nm.<sup>9</sup>

### 13.3.3 Mascara

Mainstream mascaras enhance the overall appearance of eyes by thickening, lengthening, darkening, curling, and volumizing eyelashes. Some common formulations of mascaras are oil-in-water or water-in-oil emulsions and anhydrous formulations. The lamellar gel network-based oil-in-water emulsion is by far the most common type of mascara formulation in the market.<sup>33</sup> Water-resistant, waterproof, non-flaking, and long-wear properties of mascara are often optimized by forming resilient yet flexible films and adding waterproofing agents. Similar to the film formers in sunscreen and foundation, PVP, polyethylene, acrylate copolymer, and VP/eicosene copolymer are often utilized. Polyethylene can also be added as a wax to increase the film thickness which achieves the volumizing properties.

Polymer latexes are also added into the mascara formulation according to patent US20120156153A1.<sup>34</sup> This patent describes a natural film former and

plasticizer combination instead of a traditional petroleum-derived synthetic film former. The ratio of the film-forming system to plasticizer is preferably 1.2 : 1.<sup>34</sup> A combination of polymeric film formers consists of pullulan and a candelilla wax resin which is able to form a resilient and tough film around the wax structures.<sup>35</sup> Pullulan is a water-soluble polysaccharide with maltotriose as a primary structure linked by 1,6-glycosidic bonds. Because pullulan has a relatively linear structure compared to other natural polysaccharides, it can form a clear, tough film with good adhesion properties.<sup>34</sup> A pullulan with a degree of polymerization from 10–10 000 is sufficient for the film-forming system to perform.<sup>34</sup> Candelilla is added to the oil phase of the emulsion. It can increase volume and decrease smudging and flaking.<sup>34</sup> Moreover, candelilla resin is malleable and provides good adhesion to human hair.<sup>34,36</sup> A plasticizer system, consisting of a rosin and a sebacic acid/hydrogenated castor oil copolymer is used as reinforcement for the film and enhancement of the curvature of eyelashes. Rosin that has a number average molecular weight of less or equal to 10 000 is required. Both of these ingredients are added in the oil phase of the emulsion.<sup>34</sup>

### 13.3.4 Nail Polish

Nail polish has become a staple of colored cosmetics ever since its debut dating back to 3000 BC in China.<sup>3,37</sup> Colored nail polish first emerged onto the market and quickly became popular in the 1920s. Currently, nail polishes can be categorized into 17 principle finishes with the main ones being crème, matte, opalescent, and glitter. The formulation of this organic coating includes four building blocks: binders, solvents, pigments, and additives, according to M. Schlossman *et al.*<sup>38</sup> Based on the ratio between binder/solvent and content, nail polish formulation can be categorized into solvent-borne, water-borne, and latex dispersions. For a solvent-borne formulation, the builder usually consists of a low content of a film-forming polymer like nitrocellulose dissolved in a high content of volatile organic solvent such as butyl acetate, ethyl acetate, or toluene. Water-based nail polishes started to gain increasing popularity due to health concerns with solvent-based nail polishes as a result of their use of toluene and other similar harmful organic solvents.<sup>39</sup> Most water-borne nail polishes are aqueous polymer latex dispersions, since formulating nail polish with water-soluble polymers is far more challenging than latex dispersions due to the water sensitivity of the final crossed-linked product. According to patent US5965111A,<sup>40</sup> a water-borne nail polish formulation design comprises a topcoat, a midcoat, and a base coat, in which, both top coat and base coat are dispersions of film-forming polymer latexes such as polyurethanes, polyacryls, polymethacrylates, or styrene-acryl copolymers. At least one nanoparticle dispersion is required in a water-based formulation.<sup>8</sup> The polymer latexes used in this patent are acrylic polymers that have a size range from 40 to 80 nm.<sup>40</sup>

For all nail polish formulations, additional polymer colloid additives such as plasticizers, adhesive polymers, and rheology modifiers are crucial.

Plasticizers such as phthalates, dibutyl phthalate, and camphor are employed to strengthen films, and avoid chipping and cracking of the final coating. Tosylamide/formaldehyde resin are utilized as adhesive polymers in solvent-borne formulations, while acrylic acid and methacrylic acid are utilized in water-borne formulations to ensure the final film does not peel off the nail bed.<sup>38</sup> Just like regular paints, rheology modifiers that exhibit thixotropy like stearalkonium hectorite, are critical for nail polish formulations. They not only improve the overall aesthetics in the bottle but also help with easy application, and give the final nail enamel a smooth and seamless finish.

### 13.3.5 Lipstick, Liquid Lipstick

Traditional lipstick is designed to provide color, moisturization, and protection and usually contains pigments, emollients, oils, and waxes.<sup>41</sup> Usually, lipsticks are not transfer-proof, waterproof, and the color payoff is not pigmented or vivid enough for consumers. Liquid lipsticks emerged on the market in the early 2000s. The formulation is fairly simple with isododecane as the volatile solvent. Polymeric film formers like trimethylsiloxy silicate are added to the oil phase to ensure the liquid lipstick is transfer-proof. Dimethicone is an emollient that has waterproofing and film-forming characteristics which are utilized extensively in these formulations. To enhance velvet matte texture, silica and nylon-12 microspheres with diameters of 12 µm is added to the formulation. The ball-bearing lubrication effect of the microspheres not only gives the lipstick a luxurious silky texture but also increases product payoff and reduces contact friction by enhancing slip which improves the product blendability on the skin. It is also able to bring about beneficial optical effects through scattering light to reduce the look of fine lines on the skin, while letting through enough light to enhance the natural appearance of the skin.<sup>42</sup>

### 13.3.6 Shampoo and Conditioner

Polymer latexes are generally not utilized in shampoo or body wash formulations. There is a strong drive currently to avoid synthetic polymer latexes in these rinse-off products due to new environmental regulations on the prohibition of microparticles. This is covered in more detail in Section 13.5. Although they are not being utilized in shampoos and body washes, there are complex surfactant polyelectrolyte coacervates which can be considered as a naturally occurring polymer colloids, formed as a result of phase separation in the system. Unlike cleansing shampoos, conditioning shampoos are formulated with anionic surfactants, amphoteric surfactants, cationic polymers, and silicone.<sup>43</sup> These shampoos are formulated at a concentration much above the critical micelle concentration (CMC). When above the CMC, surfactants form micelles or hemi-micelles along the polyion chain. The polyion/surfactant is solubilized. Upon dilution, the

concentration of the conditioning shampoo is close to the CMC which leads to complex coacervate phase separation.<sup>43</sup> Engineering and optimizing polymer-surfactant interactions are the key aspects of shampoo formulation design. The formation of polymer-surfactant complexes starts at a critical surfactant concentration (CAC). Changing the polymer concentration will change the CAC of the surfactant-polymer complex. At the CAC, the surfactant micelles start to link or decorate the polymer chain. This process stops at a second critical surfactant concentration known as the polymer saturation point (PSP). At the PSP, the polymer chain becomes saturated by the micelles which leads to complex coacervation.<sup>44</sup> The phase-separated coacervates which are positively charged deposit on the negatively charged hair during rinsing. Silicones, anti-dandruff agents, and other additives can be co-deposited onto the hair with the coacervates.

Hair conditioners are usually based upon lamellar gels formed by cationic surfactants such as behentrimonium chloride (BTAC) and fatty alcohols. Cationic polymers such as polyquaternium 10, cationic hydroxyethylcellulose, and chitosan can improve wet combability and ameliorate electrostatic charging of hair which reduces flyaway effects.<sup>43</sup> The only application of polymer colloids in hair conditioners is the addition of silicone droplets/ PDMS particles for enhancement of dry lubrication.<sup>27</sup>

## 13.4 Novel Polymer Particles

### 13.4.1 Janus Particle

Janus particles are special synthetic colloids with two distinguishing chemistries or polarities. The size of the Janus particles can range from the microscale to the nanoscale.<sup>45</sup> The term Janus beads was first used by C. Casagrande<sup>46</sup> to describe a spherical glass particle which has one hydrophilic hemisphere with the other half being hydrophobic.<sup>46</sup> The potential of glass beads to stabilize emulsification has been evaluated by Casagrande *et al.*<sup>47</sup> After almost 30 years of development, various Janus particles with different sizes, shapes, and properties have been reported. Walther *et al.*<sup>48</sup> applied Janus particles to emulsion polymerization of different monomers for the first time. Shepard *et al.*<sup>49</sup> has utilized Matrix Assisted Pulsed Laser Evaporation (MAPLE) to produce patchy Janus particles with tunable roughness and composition.<sup>49</sup> Kumar *et al.*<sup>50</sup> investigated how the shape of the Janus particle impacts their interfacial behavior.<sup>50</sup> The challenge is to produce Janus particles which are robust, low-cost, and can be produced on a large scale. Additionally, the ability to create a wide range of functionality through changing chemistry on two hemispheres in a cost-effective way is critical to enhance further application within the cosmetic industry. There are three major ways to produce Janus polymer particles, masking, self-assembly, and phase separation.<sup>51</sup> The modified structure of Janus particles gives them unique properties in solution. The self-assembly of Janus

particles in solution was observed by Muller *et al.*,<sup>52</sup> where Janus particles successfully formed supramicelles in a water solution.<sup>52</sup> Other properties of Janus particles include but are not limited to reversible cluster formation, amphiphilic properties, and stabilizing emulsions.<sup>51</sup>

### 13.4.2 Amphiphilic Particles

Unlike Janus particles, amphiphilic particles consist of a hybrid structure and potentially exhibit amphiphilic properties. Protein–polymer particles are a good example of amphiphilic particles, considered to have potential applications in biomedicine, biotechnology, and nanotechnology. The combination of polymers and proteins can bring beneficial performance such as self-assembly and phase-separation. A diverse range of protein and polymer conjugate particles have been reported.<sup>53</sup>

### 13.4.3 Sustainable Particles

The strong demand for biodegradable products is driving cosmetic companies to search for new renewable and sustainable materials, replacing traditional petroleum-derived polymers.<sup>54</sup> Starch, collagen, polysaccharide, chitin, and lipid-based polymers are good alternatives due to their good biodegradability, low cost, positive environmental footprint, and good biocompatibility.<sup>55</sup>

Sustainable particles can be generated from different resources and methods. The choice of sustainable particles varies depends on the application. For example, keratin protein is a cationic biopolymer which has versatile application, due to its biodegradability and non-toxic nature.<sup>56</sup> It can be extracted from various sources, such as hair, nails, and wood fibers.<sup>57</sup> It can also be modified into different forms, ranging from nanoparticles to films.<sup>56</sup> In cosmetic applications, modified keratin-based materials can be added to hair care products to increase toughness,<sup>58</sup> it can also be applied to makeup products as a film-forming agent.<sup>59,60</sup>

### 13.4.4 Smart Particles – Stimuli-responsive Polymers

With the inclusion of stimuli-responsive polymers, cosmetic products can exhibit unique properties which can change in different physical environments. The smart response of this type of polymer has been drawing a lot of recent attention. The triggers for stimuli-responsive polymers can be temperature, pH, ionic strength, pressure, strain, *etc.* Modification of these stimuli-responsive polymers allows them to have a variety of changes in properties and performance and this has been shown with a range of novel stimuli. The following are two examples of stimuli-responsive polymers.<sup>61</sup>

#### 13.4.4.1 pH-sensitive Polymer

The pH of human skin depends on the position in the body. The skin surface pH generally ranges between 5.4 and 5.9 (forearm of healthy adult white male).<sup>62</sup> This pH range variability in different parts of the body allows a pH-sensitive polymer to potentially be applied in cosmetic products. Eunmi Lee and Bumsang Kim<sup>63</sup> reported a pH-triggered delivery system with P(MAA-*co*-EGMA) hydrogel to deliver cosmetics actives, including arbutin, adenosine, and niacinamide. The hydrogel microparticles swell significantly at a pH close to that of skin. At pH 4, almost none of the actives permeated into the skin. At pH 6, the actives achieved a high skin permeation rate.<sup>63</sup>

#### 13.4.4.2 Light-triggered Microcapsules

The light-triggered microcapsules provide a novel delivery system for active delivery and fragrance release. Bartosz Tylkowski *et al.*<sup>64</sup> reported a method of producing a microcapsule system that can be activated by visible light. In their research, the polyamide microcapsule shells containing visible-light-sensitive ortho-substituted azobenzene was incorporated in the main chain of the polymer. The length of the modified polymer decreased during exposure to light, allowing the encapsulated perfume oil to be released from the shell.

### 13.5 Environmental and Safety Concerns of Polymer Colloids

The remarkable properties of polymer colloids allow their use in various cosmetic products, ranging from lipstick and mascara to toothpaste and hair products. However, there are specific considerations that must be taken into account which are preventing the further wide-scale adoption of polymer colloids in cosmetic products. Some of these factors are determined by the size of the particle, the toxicity to humans and animals, and the impact on the environment. The environmental and safety influence is strongly dependent on the type of the particle and the size range of the particle. The following section highlights the details that need to be considered for both environmental and health and safety concerns.

#### 13.5.1 Health and Safety

##### 13.5.1.1 Nanotechnology and Nanomaterial

Nanosize particles less than 100 nm have gained wide-scale publicity from both consumers and regulatory bodies due to their potential impact on both environmental and human health and safety. The U.S. Food and Drug Administration (FDA) has now established an official definition of nanotechnology and nanomaterials. These are usually used to describe material

that has a size of 1 nm to 100 nm in at least one dimension.<sup>65</sup> In June 2014, “Guidance for Industry: Safety of Nanomaterials in Cosmetic Products” was issued by the FDA. It split FDA-regulated products that involved the application of nanotechnology into two categories: (1) the particle has an external and/or internal size which falls in between 1 nm to 100 nm in at least one dimension, (2) the material or end product is designed to exhibit properties that are attributable to its size(s), no matter whether the size falls in the nanoscale range or not (~1000 nm).<sup>66</sup>

While nanotechnology draws much attention due to its versatile application and high performance, there is still a lot of concern around applying this technology to cosmetic and personal care products. Although the toxicity of the nanoparticles to humans has not been well established, some *in vivo* and *in vitro* testing has revealed a correlation between nanoparticles and toxicity. They are considered to increase the intracellular reactive oxygen species (ROS) level and/or cause inflammation due to the high surface activity of the nanoparticles.<sup>67</sup> The application of nanotechnology could lead to an increase in biological interactions, and change the uptake, absorption, and biodistribution of the material in the consumer.<sup>66</sup>

The FDA suggested that the safety of the product can be evaluated by reliance on existing toxicological test data or the performance of any additional data through new toxicology tests. The general principle is still applicable to nanotechnology-based products. Considering the size effect of nanomaterials, additional tests are still recommended to evaluate the impact on the safety of the material and final products. Although the FDA is also giving guidance to toxicology test cosmetic products with nanotechnology, all the guidance is instructional, not mandatory.

### 13.5.1.2 Allergies

Plastics are a common cause of occupational skin disorders through irritation or allergic contact dermatitis (ACD). These generally occur during the plastic fabrication process and are rarely due to the end product itself.<sup>68</sup> However, there are a lot of cases of allergic reactions involving cosmetic products which contain certain polymers, such as natural rubber latex and acrylates.

### 13.5.1.3 Natural Rubber Latex

Natural rubber latex is primarily extracted from plants, such as the *H. brasiliensis* rubber tree.<sup>69</sup> It is added to the cosmetic product as a film former and opacity agent and is commonly seen in cosmetic products which require adhesiveness, such as hair styling products, face and body color products, and eyelash glues.

However, according to FDA estimations,<sup>69</sup> there might be one to six out of one hundred people allergic to natural rubber latex. Natural rubber latex can cause a series of allergic reactions ranging from minor skin irritation to

severe anaphylactic shock. According to the FDA website, there were 30 cases of an allergic reaction related to cosmetic products containing natural rubber latex reported between January 2015 and September 2017.<sup>69</sup> Since there is no current regulatory requirement for companies to report cosmetic-related cases, the actual number of the allergic reactions is potentially higher.

These allergic reactions may be triggered by the antigenic proteins occurring in natural rubber latex. The allergic reaction might not appear at first exposure, but the sensitivity could be established over time. It is commonly seen in people who are frequently exposed to natural rubber latex products.<sup>70</sup>

#### 13.5.1.4 Acrylates

Acrylate is an ingredient that is frequently used in cosmetic products, especially in nail cosmetics. The use of acrylate and its derivatives can increase the adhesiveness and long-lasting effects of nail polish application. However, acrylates are an allergen that can cause minor to severe allergic reactions, ranging from mild itchiness in the nail bed to permanent nail loss.<sup>71</sup>

In the 1950s, the first case of acrylate allergic contact dermatitis (ACD) was reported.<sup>72</sup> The reports of ACD with acrylates became more frequent recently because of the invention of new nail cosmetic techniques, such as “gel nails” and new long-lasting or semi-long-lasting nail polish.<sup>73</sup> Although there are many dermatological studies on the underlying causes of acrylate allergy in consumers and beauticians, the mechanism is still not well understood. Some factors could be the nature of the acrylate molecules, the potential reaction of acrylate with other molecules, the method of exposure to acrylates, and the length of time before polymer is cured.<sup>73</sup>

#### 13.5.2 Environmental Safety

Besides toxicity to humans, low biodegradability gives the polymer a long-term environmental footprint. Rising concerns have driven a lot of NGOs, governments, and companies to take action to monetize, regulate, and improve the use of polymer colloids in cosmetic and personal care products.

#### 13.5.2.1 Microbeads

The process of manufacturing microbeads was first discovered by Dr. John Ugelstad in the 1970s.<sup>74</sup> Microbeads are now manufactured in many cosmetic and personal care products, including but not limited to exfoliating face washes, toothpaste, shower gels, scrubs, and face cream. The chemical composition, shape, and the density of the microbeads vary depending on the application. In general, the size of the microbeads is above 1 µm and less than or equal to 5 mm.<sup>75</sup> The regulated size of microbeads in cosmetic products depends on the country.

**Table 13.1** List of effective ban date of microbeads in different countries.<sup>76</sup>

Country	Ban effective date	Summary
Netherland	End of 2016	Prohibit import, production, and retail of microbeads in rinse-off cosmetics.
USA	7/1/17	Prohibit production of rinse-off cosmetics microbeads at the federal level.
France	1/1/18	Prohibit import, production, and retail of rinse-off products.
Canada	1/1/18	Prohibit microbeads with a size less than 5 mm.
New Zealand	6/7/18	Prohibit import, production, and retail of microbeads in rinse-off cosmetics.
Taiwan	7/1/18	Prohibit import and production of microbeads in rinse-off cosmetics.
UK	10/1/18	Prohibit the application of microbeads in rinse-off cosmetics and personal care products nationwide.
Sweden	1/1/19	Prohibit import, production, and retail of microbeads in rinse-off cosmetics.
Italy	1/1/20	Prohibit microbeads existing in rinse-off cosmetics.
India	1/1/20	Prohibit microbeads existing in rinse-off cosmetics.

Microbeads in cosmetic products are usually rinsed off and go down the drain. Due to the size of these microbeads, it is difficult to filter them out in the wastewater treatment plants, which allows them to be released into the aquatic environment. Depending on the physical and chemical properties of the microbeads, they may interact with chemicals either in the water or sediment and therefore threaten aquatic life. The impact of microbeads includes uptake by aquatic life, translocation, food-web transfer, long-term or direct impact on the behavior of organisms, cellular or sub-cellular effects, and transport of pollutants.<sup>75</sup>

Governments in different countries are starting to discuss and ban the use of microbeads in cosmetics, based on rising concerns about the impact of microbeads on the local environment. The Table 13.1 summarizes regulations on microbeads based on country.

Due to government regulations and high demand for more sustainable products from the consumer, companies are starting to phase out the use of microbeads in personal care products. The Johnson & Johnson Family of Consumer Companies decided to phase out microbeads in 2013 and remove microbeads from their products globally by the end of 2017.<sup>77</sup> L'Oréal finished reformulation and eliminated microbeads in their rinse-off products in 2017.<sup>78</sup> However, although there is a clear ban on the use of synthetic polymer microbeads, the use and development of sustainable and natural microbeads are still active areas of research.

## 13.6 Conclusion

Polymer colloids have been utilized extensively in the cosmetic and personal care industry. This has been primarily due to their spectacular performance

in film formation, adhesiveness, optical properties, and water-repelling properties. This gives rise to consumer-conceivable benefits, in a wide range of cosmetic products, such as facial makeup, lipsticks, skin care products, shampoo, conditioner, etc. This technology landscape is, however, rapidly changing with wide-scale adoption of environmental regulation and consumer preference for more sustainable and greener products. In addition, the consumer requirement for novel sensory and functional benefits, and the highly competitive nature of the beauty industry requires adoption and development of a wide range of novel, sustainable, smart polymer colloids. These novel particles will play a key role for the future in the cosmetic industry.

## References

1. R. L. Rowell, in *An Introduction to Polymer Colloids*, ed. F. Candau and R. H. Ottewill, Kluwer Academic Publishers, ch. 7, 1990, p. 187.
2. A. A. Attama and C. C. Müller-Goymann, *Colloids Surf., A*, 2008, **315**, 189–195.
3. J. Toedt, D. Koza and K. Van Cleef-Toedt, in *Chemical Composition of Everyday Products*, Greenwood Publishing Group, CT, USA, 2005, pp. 49–50.
4. F. M. Winnik, in *Principles of Polymer Science and Technology in Cosmetics and Personal Care*, ed. E. D. Goddard and J. V. Gruber, Marcel Dekker, Inc., 1st edn, ch. 1, 1999, pp. 1–2.
5. B. W. Brooks, in *Nanoscience: Colloidal and Interfacial Aspects*, ed. V. M. Starov, 2010, pp. 717–745.
6. L. Weng, J. Golzarian and O. Souresrafil, *U. S. Pat.*, 20170273888A1, 2017.
7. J. J. Wang and J. L. Hung, *U. S. Pat.*, 4892726A, 1990.
8. A. Malnou, *U. S. Pat.*, 8883126B2, 2014.
9. K. Joshi, F. Zeng and B. Cooper, *U. S. Pat.*, 20180280280A1, 2018.
10. S. Ugur and M. S. Sunay, *Colloids Surf., A*, 2016, **510**, 283–292.
11. P. Zakaria, J. P. Hutchinson, N. Avdalovic, Y. Liu and P. R. Haddad, *Anal. Chem.*, 2005, **77**, 417–423.
12. J. Ramos, A. Martín-Molina, M. P. Sanz-Izquierdo, A. Rus, L. Borque, R. Hidalgo-Álvarez, F. Galisteo-González and J. Forcada, *J. Polym. Sci., Part A: Polym. Chem.*, 2003, **41**, 2404–2411.
13. J. Rottstegge, P. Kindervater, M. Wilhelm, K. Landfester, C. Heldmann, J. P. Fischer and H. W. Spiess, *Colloid Polym. Sci.*, 2003, **281**, 1111.
14. M. Do Amaral, A. Roos, J. M. Asua and C. Creton, *J. Colloid Interface Sci.*, 2005, **281**, 325–338.
15. Y. Mai, S. Wong and X. Chen, in *Polymer Blends*, ed. D. R. Paul and C. B. Bucknall, John Wiley & Sons, New York, vol. 2, ch. 20, 2000, pp. 17–58.
16. D. I. Lee, *Polymer*, 2005, **46**, 1287–1293.
17. K. te Nijenhuis, in *Encyclopedia of Surface and Colloid Science*, 2nd edn, Taylor & Francis, 2006, pp. 6326–6339.

18. P. A. Steward, J. Hearn and M. C. Wilkinson, *Adv. Colloid Interface Sci.*, 2000, **86**, 195–267.
19. R. M. Fitch, in *Polymer Colloids*, ed. and R. M. Fitch, Academic Press, London, 1st edn, ch. 1, 1997, pp. 1–5.
20. L. A. Felton, *Int. J. Pharm.*, 2013, **457**, 423–427.
21. K. H. Bauer, *Coated Pharmaceutical Dosage Forms: Fundamentals, Manufacturing Techniques, Biopharmaceutical Aspects, Test Methods, and Raw Materials*, Medpharm scientific, 1998.
22. L. A. Felton and J. W. McGinity, *Eur. J. Pharm. Biopharm.*, 1999, **47**, 3–14.
23. F. Awaja, M. Gilbert, G. Kelly, B. Fox and P. J. Pigram, *Prog. Polym. Sci.*, 2009, **34**, 948–968.
24. J. H. Waite, N. H. Andersen, S. Jewhurst and C. Sun, *J. Adhes.*, 2005, **81**, 297–317.
25. S.-H. Kim, S. Y. Lee and S.-M. Yang, *Angew. Chem., Int. Ed.*, 2010, **49**, 2535–2538.
26. B. T. Hoang and I. Popa, *H&PC Today*, 2014, **9**, 35–39.
27. B. Bhushan, *Introduction to Tribology*, John Wiley & Sons, 2013.
28. L. A. Jones and S. J. Lederman, *Human Hand Function*, Oxford University Press, 2006.
29. J. R. Stokes, M. W. Boehm and S. K. Baier, *Curr. Opin. Colloid Interface Sci.*, 2013, **18**, 349–359.
30. V. Ferrari, W. Yu, S. X. Lu, X. Blin, J. Mondet, I. Hansenne, A. Shah, A. Galdi and F. Tournilhac, *U. S. Pat.*, 20040170586A1, 2004.
31. K.-H. Lee, J.-H. Kim and S.-H. Chung, *U. S. Pat.*, 7879346, 2011.
32. D. O'Halloran and Y. Zolotarsky, *U. S. Pat.*, 20030082221A1, 2003.
33. G. Deckner, Lashing Out: Contemporary Mascara Formulations, <https://knowledge.ulprospector.com/7463/pcc-lashing-contemporary-mascara-formulation/>, (accessed Feburatry 2019).
34. S. R. Fogg, D. Patel and C. L. Orr, *U. S. Pat.*, 20120156153A1, 2012.
35. Y. Sakata and M. Otsuka, *Int. J. Pharm.*, 2009, **374**, 33–38.
36. D. Schlossman, E. Bartholomey and Y. Shao, *U. S. Pat.*, 20090257966A1, 2009.
37. V. Sherrow, *For Appearance' Sake: The Historical Encyclopedia of Good Looks, Beauty, and Grooming*, Greenwood Publishing Group, Canada, 2001.
38. M. Schlossman, *J. Cosmet. Sci.*, 1999, **50**, 105–110.
39. L. Kopelovich, A. L. Perez, N. Jacobs, E. Mendelsohn and J. J. Keenan, *Food Chem. Toxicol.*, 2015, **81**, 46–53.
40. P. C. Ellingson, A. J. Michels and E. D. Smith, III, *U. S. Pat.*, 5965111A, 1999.
41. C. G. Mercado and A. M. Krog, *U. S. Pat.*, 4996044A, 1991.
42. E. H. Robinson, *WO Pat.*, 2015167659 A1, 2015.
43. R. Y. Lochhead, in *Cosmetic Nanotechnology*, American Chemical Society, vol. 961, ch. 1, 2007, pp. 3–56.
44. A. El Aferni, M. Guettari and T. Tajouri, *Colloid Polym. Sci.*, 2016, **294**, 1097–1106.

45. A. Walther and A. H. E. Müller, *Soft Matter*, 2008, **4**, 663–668.
46. C. Casagrande, *C. R. Acad. Sci., Ser. II*, 1998, **306**, 1423–1425.
47. C. Casagrande, P. Fabre, E. Raphaël and M. Veyssié, *Europhys. Lett.*, 1989, **9**, 251–255.
48. A. Walther, M. Hoffmann and A. H. E. Müller, *Angew. Chem., Int. Ed.*, 2008, **47**, 711–714.
49. K. B. Shepard, D. A. Christie, C. L. Sosa, C. B. Arnold and R. D. Priestley, *Appl. Phys. Lett.*, 2015, **106**, 093104.
50. A. Kumar, B. J. Park, F. Tu and D. Lee, *Soft Matter*, 2013, **9**, 6604–6617.
51. M. Lattuada and T. A. Hatton, *Nano Today*, 2011, **6**, 286–308.
52. R. Erhardt, M. Zhang, A. Böker, H. Zettl, C. Abetz, P. Frederik, G. Krausch, V. Abetz and A. H. E. Müller, *J. Am. Chem. Soc.*, 2003, **125**, 3260–3267.
53. C. Boyer, X. Huang, M. R. Whittaker, V. Bulmus and T. P. Davis, *Soft Matter*, 2011, **7**, 1599–1614.
54. S. Shankar and J.-W. Rhim, *Carbohydr. Polym.*, 2016, **135**, 18–26.
55. T. V. Duncan, *J. Colloid Interface Sci.*, 2011, **363**, 1–24.
56. M. A. Khosa and A. Ullah, *J. Food Process. Beverages*, 2013, **1**, 8.
57. J. G. Rouse and M. E. Van Dyke, *Materials*, 2010, **3**, 999–1014.
58. J. Schweizer, P. E. Bowden, P. A. Coulombe, L. Langbein, E. B. Lane, T. M. Magin, L. Maltais, M. B. Omary, D. A. D. Parry, M. A. Rogers and M. W. Wright, *J. Cell Biol.*, 2006, **174**, 169.
59. C. A. Anker, *U. S. Pat.*, 3642498A, 1972.
60. Y. Kawano and S. Okamoto, *Kagaku to Seibutsu*, 1975, **13**, 291–292.
61. K. O. Havelka, R. Y. Lochhead and S. E. Morgan, *Cosmetic Nanotechnology: Polymers and Colloids in Cosmetics*, American Chemical Society, 2007.
62. M. H. Schmid-Wendtner and H. C. Kortting, *Skin Pharmacol. Physiol.*, 2006, **19**, 296–302.
63. E. Lee and B. Kim, *Korean J. Chem. Eng.*, 2011, **28**, 1347.
64. B. Tylkowski, M. Giamberini, T. Underiner, S. F. Prieto and J. Smets, *Macromol. Symp.*, 2016, **360**, 192–198.
65. L. M. Katz, K. Dewan and R. L. Bronaugh, *Food Chem. Toxicol.*, 2015, **85**, 127–137.
66. U. S. Food and Drug Administration, Guidance for Industry: Safety of Nanomaterials in Cosmetic Products, <https://www.fda.gov/Cosmetics/GuidanceRegulation/GuidanceDocuments/ucm300886.htm>, (accessed February 2019).
67. P. Khanna, C. Ong, B. H. Bay and G. H. Baeg, *Nanomaterials*, 2015, **5**, 1163–1180.
68. J. C. Salles and F. J. Deschamps, *Occup. Med.*, 2010, **60**, 662–664.
69. U. S. Food and Drug Administration, Don't be Misled by "Latex Free" Claims, <https://www.fda.gov/ForConsumers/ConsumerUpdates/ucm342641.htm>, (accessed February 2019).
70. U. S. Food and Drug Administration, Latex in Cosmetics, <https://www.fda.gov/Cosmetics/ProductsIngredients/Ingredients/ucm590045.htm>, (accessed February 2019).

71. R. Baran, *Am. J. Clin. Dermatol.*, 2002, **3**, 547–555.
72. O. Canizares, *AMA Arch. Dermatol.*, 1956, **74**, 141–143.
73. M. E. Gatica-Ortega, M. A. Pastor-Nieto and J. F. Silvestre-Salvador, *Actas Dermo-Sifiliogr.*, 2018, **109**, 508–514.
74. B.-I. Haukanes and C. Kvam, *Bio/Technology*, 1993, **11**, 60–63.
75. Environment and Climate Change Canada, Microbeads – A Science Summary, <http://www.ec.gc.ca/ese-ees/default.asp?lang=En&n=ADDA4C5F-1>, (accessed Feburary 2019).
76. R. E. J. Schnurr, V. Alboiu, M. Chaudhary, R. A. Corbett, M. E. Quanz, K. Sankar, H. S. Strain, V. Thavarajah, D. Xanthos and T. R. Walker, *Mar. Pollut. Bull.*, 2018, **137**, 157–171.
77. Johnson & Johnson Consumer Inc., Mircobeads, <https://www.safetyandcarecommitment.com/Ingredients/Microbeads>, (accessed Feburary 2019).
78. L'oreal, L'Oréal Completed the Reformulation of its Washoff Products Using Plastic Microbeads as Cleansing or Exfoliating Agents, <https://www.loreal.hk/en-hk/media/news/2017/feb/reformulation-of-products-using-microbeads>, (accessed Feburary 2019).

# Subject Index

- ACCENT™, 4  
advanced coatings  
    experimental  
        film formation, 353  
        film stretching, 353–354  
        purification, 354  
        sample resuspension, 354  
    latexes for  
        anisotropic latexes,  
            352–353  
        architectural coatings,  
            350–351  
        background, 349  
        industrial coatings,  
            351–352  
    results and discussion, 354–355  
anisotropic latexes, 352–353  
aqueous polyolefin, 15–18  
architectural coatings, 350–351  
  
binary *vs.* capillary breakup, 9  
BLUEWAVE™ technology, 3–5  
  
CANVERA™, 4  
charge adjustment, 167  
coatings. *See* advanced coatings  
colloidal polyelectrolyte brushes,  
    148–151  
colloidal polymer nanoparticles  
    glass transition  
        features of, 268–271  
        in geometrical confinement, 267–268  
        glassy dynamics in,  
            265–267  
    molecular mobility,  
        272–274  
physical aging in,  
    271–272  
semicrystalline colloidal  
particles, 274–276  
    chain conformation by,  
        278–279  
    crystallizable  
        nanoparticles, 281  
    crystallization in, 279–281  
    generation of nanoparticles, 276–278  
colloids  
    block copolymer microphase  
        separation in  
            block copolymers, 82–85  
            homopolymers, 82–85  
            molecular weight effect,  
                81–82  
        from homopolymer blends,  
            72–75  
        core–shell particles,  
            78–79  
        Janus particles, 75  
        patchy particles, 75–78  
confocal microscope, 216–217  
core–shell particles, 78–79  
core–shell polymer-based colloids  
    grafting from approach  
        ATRP reaction, 34–36  
        ionic, metal-catalyzed  
            and UV- or photo-induced polymerizations, 38–40

- NMP, 36–37  
 RAFT, 38  
 grafting to approach, 32–34  
 types of, 31
- core-shell structure, 150
- cosmetics and personal care
- applications of polymer colloids
    - facial makeup, 404–405
    - lipstick, liquid
      - lipstick, 407
    - mascara, 405–406
    - nail polish, 406–407
    - shampoo and conditioner, 407–408
    - sunscreen, 405
- environmental and safety concerns
- environmental safety, 412–413
  - health and safety, 410–412
- key polymer colloid properties
- adhesion, 402
  - chemistry modification, 402–403
  - film formation, 401–402
  - lubrication and tribology, 403
  - particle size, particle size distribution, 400
  - waterproofing, 402
- novel polymer particles
- amphiphilic particles, 409
  - Janus particle, 408–409
  - light-triggered microcapsules, 410
  - pH-sensitive polymer, 410
  - smart particles – stimuli responsive polymers, 409–410
  - sustainable particles, 409
- crystallizable nanoparticles, 281
- dispersion enabled heat activated pressure sensitive adhesive, 23–25
- droplet breakup theory
- beyond steady state – transient breakup, 8–9
  - classical droplet breakup theory, 6–7
  - concentrated emulsion systems, 7–8
  - confined boundaries, 10
  - emulsification in water, 11–13
  - surfactant effects on rheology and, 9–10
  - surfactant optimization, 10–11
  - wall effects, 10
- dynamic fragility, 270
- EAA. *See* ethylene acrylic (EAA) co-polymer
- ECOSMOOTH™, 4
- electro-jetting, 53–54
- electro-spraying, 53
- electron microscopes
- background, 220–223
  - focused ion beam system, 227–229
  - helium ion microscope (HIM), 229–230
  - ion microscope, 226–227
  - scanning electron microscope (SEM), 223–224
  - scanning transmission electron microscopy (STEM), 226
  - transmission electron microscope (TEM), 224–225
- environmental safety, 412–413
- ethylene acrylic (EAA) co-polymer, 20
- facial makeup, 404–405
- film formation, 353
- film stretching, 353–354
- flash nanoprecipitation (FNP) process
- aggregation, 62–66
  - characteristic times of, 65–66
  - equipment, 69–70

- flash nanoprecipitation (FNP) process (*continued*)  
 mechanism of stabilization, 67–69  
 nucleation, 62–66  
 polymer collapse, 62–66  
 solvent and polymer choice, 66–67
- flash precipitation method, 277
- flow lithography, in single- (and multi-) phase flows, 109–114
- fluctuation dissipation theorem (FDT), 266
- fluorescence microscope, 215–216
- FNP process. *See* flash nanoprecipitation (FNP) process
- focused ion beam system, 227–229
- gas–liquid region, 138
- geometrical confinement, 267–268
- glass transition, 264  
 features of, 268–271  
 in geometrical confinement, 267–268  
 glassy dynamics in, 265–267  
 molecular mobility, 272–274  
 physical aging in, 271–272
- glass-forming liquids, 265
- glassy dynamics, 265–267
- health and safety  
 acrylates, 412  
 allergies, 411  
 nanotechnology and nano-material, 410–411  
 natural rubber latex, 411–412
- helium ion microscope (HIM), 229–230
- High Internal Phase Emulsion (HIPE) process, 3, 5, 6
- homopolymer blends, colloids from, 72–75  
 core–shell particles, 78–79  
 Janus particles, 75  
 patchy particles, 75–78
- homopolymer colloids  
 concentration effects, 70–71  
 mixing time effects, 71–72
- homopolymers, 82–85
- hybrid polymer–inorganic colloids, 79–81
- HYPOD™, 4
- ideal glass transition, 271
- industrial coatings, 351–352
- internal phase viscosity, 7
- International Union of Pure and Applied Chemistry (IUPAC), 196, 198
- ion microscope, 226–227
- Janus particles, 75
- Janus-particle stabilized pickering emulsions, 331–332  
 Janus balance, 335  
 liquid–liquid interfaces, 332–334  
 stimuli-responsive pickering emulsion, 335  
 thermodynamically stable pickering emulsions, 334
- linear low density polyethylene (LLDPE) dispersion, 20
- linerless labels, 24
- lipstick, liquid lipstick, 407
- mascara, 405–406
- medical applications  
 clinical translation, 385–386  
 emerging applications  
 alternative routes of administration, 382–383  
 encapsulation of biologics, 381–382  
 immune engineering, 383–385  
 multifunctional particles, 381  
 material selection, 360–361  
 natural polymers, 361–362  
 synthetic polymers, 362–365

- nanomedicine, 359  
 physiochemical properties  
     mechanical properties,  
         377  
     PEGylation, 379–380  
     shape, 376–377  
     size, 375–376  
     surface charge,  
         378–379  
     surface chemistry,  
         377–378  
     targeting ligands,  
         380–381  
 processing methods  
     bottom-up methods,  
         367–371  
     complex coacervates,  
         370–371  
     continuous particle  
         generation *via* fluid  
         flows, 372–373  
     core–shell nanoparticles/  
         micelles, 370  
     emulsification methods,  
         371–372  
     layer-by-layer (LBL)  
         assembly, 370  
     polymersomes, 369–370  
     soft-lithography templat-  
         ing, 373–375  
     solvent displacement, 369  
     top-down methods,  
         371–375  
 responsive nanoparticle  
 platforms  
     chemoresponsive polymer  
         systems, 367  
     pH responsive, 365–366  
     temperature responsive,  
         366–367  
 microbeads, 412–413  
 microemulsions, 326  
 microfluidic approaches  
     capsule formation, 102  
     devices, 102  
     microparticle, 102  
 particle solidification, chemical  
 approaches to  
     (bio)polymer-containing  
         droplets, ionic  
         crosslinking of,  
             117–119  
     capsule formation, inter-  
         facial complexation  
         for, 119–122  
     monomer-containing  
         droplets, 104–109  
     polymer-containing drop-  
         lets, covalent cross-  
         linking of, 114–117  
     single- (and multi-) phase  
         flows, 109–114  
 particle solidification, physical  
 approaches to  
     double emulsions, block  
         co-polymer self-  
         assembly in, 128–131  
     particle assembly at  
         interfaces, 122–127  
     polymer-containing drop-  
         lets, solvent extraction  
         of, 131–138  
     single- and multi-phase  
         microfluidics, 102  
 microscopy  
     aberrations, 206–208  
     apertures, 208–209  
     atomic force microscope  
         (AFM), 218–220  
     of colloids, 232–233  
     diffraction limit of resolution,  
         210–211  
     electromagnetic radiation,  
         203–205  
     electron microscopes  
         background, 220–223  
         focused ion beam system,  
             227–229  
         helium ion microscope  
             (HIM), 229–230  
         ion microscope,  
             226–227

- microscopy (*continued*)
  - scanning electron microscope (SEM), 223–224
  - scanning transmission electron microscopy (STEM), 226
  - transmission electron microscope (TEM), 224–225
  - electron, ion, and X-ray microscope, 212–213
  - electrons, 203–205
  - history of, 194–196
  - instrument selection for colloid analysis, 230–232
  - lens basics, 205–206
  - magnification, 209
  - microscope probes, 202–203
  - natural opals and colloidal silica, 198–199
  - colloidal crystals, 199–200
  - colloids, characterization of, 200–202
  - optical microscopes
    - confocal microscope, 216–217
    - fluorescence microscope, 215–216
    - visible light microscope, 213–214
  - polymer colloids, 197–198
  - resolution, 209
  - resolution criteria, 211–212
  - specimen, 196–197
  - spectrum of, 213
  - wave-like nature of light, 203–205
  - X-ray microscope, 217–218
- miniemulsion method, 276
- molecular mobility, 272–274
- molecular weight effect, 81–82
- multi-layer film formation, 46
- multilayer deposition, 292
- nail polish, 406–407
- novel polymer particles
  - amphiphilic particles, 409
  - Janus particle, 408–409
  - light-triggered microcapsules, 410
  - pH-sensitive polymer, 410
  - smart particles – stimuli-responsive polymers, 409–410
  - sustainable particles, 409
- nucleation rate, 63
- optical hiding, hybrid particles for, 18–20
- optical microscopes
  - confocal microscope, 216–217
  - fluorescence microscope, 215–216
  - visible light microscope, 213–214
- particle formation strategies, 139
- particle solidification
  - chemical approaches to
    - (bio)polymer-containing droplets, ionic cross-linking of, 117–119
    - capsule formation, interfacial complexation for, 119–122
    - monomer-containing droplets, 104–109
    - polymer-containing droplets, covalent cross-linking of, 114–117
    - single- (and multi-) phase flows, 109–114
  - physical approaches to
    - double emulsions, block co-polymer self-assembly in, 128–131
    - particle assembly at interfaces, 122–127
    - polymer-containing droplets, solvent extraction of, 131–138

- pH-sensitive polymer, 410  
 phase-transitioned lysozyme (PTL), 43  
 poly(*N*-isopropylacrylamide (PS-PNIPA)), 7  
 polydopamine (PDA), 43  
 polyelectrolyte complexes (PECs)  
     flash nanocomplexation (FNC), 88  
     encapsulation *via*, 89–91  
     mechanism of, 85–86  
     mixing timescales on, 86–88  
 polymer colloid formation  
     kinetic Monte Carlo simulations, 252–259  
     particle-based modeling  
         general considerations, 241–246  
         model details, 246–252  
 polymer colloids  
     biopolymer colloid-stabilized pickering emulsions  
         cellulose nanocrystal-stabilized pickering emulsions, 342  
         fat crystal-stabilized pickering emulsions, 343–344  
         protein-stabilized pickering emulsions, 343  
     emulsions, 325–326  
     Janus-particle stabilized pickering emulsions, 331–332  
         Janus balance, 335  
         liquid–liquid interfaces, 332–334  
         stimuli-responsive pickering emulsion, 335  
     thermodynamically stable pickering emulsions, 334  
     microgel-stabilized pickering emulsions  
         high internal phase emulsions, 339–340  
     liquid–liquid interfaces, 338–339  
     microgels, 335–336  
     stimuli-responsive pickering emulsions, 337–338  
     pickering emulsions, 326–328  
         anisotropic homogeneous particles, 328–331  
         polymer-grafted particles, 340–341  
 polymer deposition  
     biopolymer coating, 43–45  
     layer-by-layer (LbL) deposition, 45–47  
     polydopamine coating, 41–43  
     resin, 41–43  
 polyolefin dispersions, 20–22  
     spray drying of, 14  
 polyolefin morphology, 15  
 porous media  
     colloidal particle transport  
         3D, 307–310  
         2D, 303–307  
         direct pore-scale assessments, 303–310  
         indirect pore-scale assessments, 299–303  
         macro-scale studies, 296–299  
     mathematical modeling  
         advection-dispersion equation (ADE), 291–292  
         filtration theory, 292–295  
         Lattice–Boltzmann method (LBM), 295–296  
         pore network modeling (PNM), 295–296  
 pressure sensitive adhesives (PSAs), 24  
 ProSperse<sup>TM</sup>, 4  
 protein corona, 377

- scalability, 139–140  
 scanning electron microscope (SEM), 24, 223–224  
 scanning transmission electron microscopy (STEM), 226  
 self-assembly  
     co-precipitation, 47–49  
     flash nanoprecipitation (FNP), 50–51  
     microfluidics, 51–53  
 semicrystalline colloidal particles, 274–276  
     chain conformation by, 278–279  
     crystallizable  
         nanoparticles, 281  
     crystallization in, 279–281  
     generation of nanoparticles, 276–278  
 shampoo and conditioner, 407–408  
 spherical polyelectrolyte brush (SPB)  
     bimetallic nanoparticles,  
         synthesis of, 154–155  
     catalytic performance, 155–156  
     controlled protein immobilization in  
         dynamic light scattering (DLS), 168–169  
         interactions between protein, 164–168  
         ionic strength, 178–179  
 isothermal titration calorimetry (ITC), 169–170  
 pH, 175–178  
 protein immobilization, 168, 173–175  
 small angle X-ray scattering (SAXS), 170–173  
 turbidimetric titration, 168  
 metallic compound nanoparticles, 156–161  
 metallic nanoparticles in, 151–153  
     synthesis of, 153–154  
 organic-inorganic hybrid nanoparticles, 161–164  
 styrene-isoprene (SI) oligomer, 12  
 styrene-isoprenestyrene (SIS), 24  
 sunscreen, 405  
 thermal plastic olefins (TPO), 21–22  
 transmission electron microscope (TEM), 224–225  
 visible light microscope, 213–214  
 wave-like nature of light, 203–205  
 X-ray microscope, 217–218